Developing a ground-based search system for transits of extrasolar planets

vorgelegt von

Diplom-Physiker Holger Voß
Berlin

Eingereicht an der Fakultät II - Mathematik und Naturwissenschaften der Technischen Universität Berlin

zur Erlangung des akademischen Grades

Doktor der Naturwissenschaften (Dr. rer. nat.)

genehmigte Dissertation

Promotionsausschuss:

Vorsitzender: Prof. Dr.-Ing. H. J. Eichler
Berichter/Gutachter: Prof. Dr. H. Rauer
Berichter/Gutachter: Prof. Dr. E. Sedlmayr

Tag der wissenschaftlichen Aussprache: 15.06.2006

Berlin 2006

D 83

Angefertigt am Institut für Planetenforschung des Deutschen Zentrums für Luft- und Raumfahrt (DLR) e.V., Berlin-Adlershof

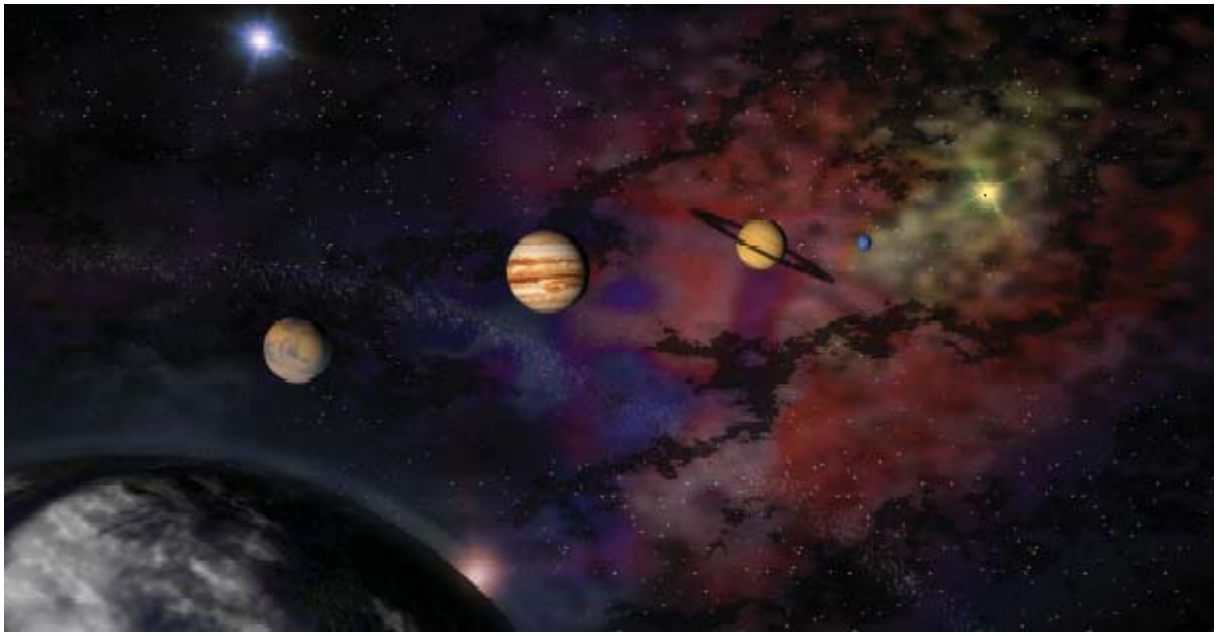

Exploration

By TMHIII

Off we go into the deep and black,
Riding high bright as a sun,
Leaving home riding on wings of thunder,
Throttle up, staging is done,

Putting out on a new sea full of wonders,
For distant shores under our sun,
Moon and Mars are just the start,

Planets around new stars,
We live to fly, we explore or die,
Nothing can stop the spirit of exploration.

Abstract

The search for extrasolar planets is a relatively new field in astronomical and astrophysical sciences that was boosted by the first discovery of the exoplanet 51 Peg b in 1995 by radial velocity measurements. The short orbital period of 4.2 days determined for this giant exoplanet encouraged the accelerated development of another search method due to the high probability that such a Hot Jupiter planet would cross its host star in the line of sight yielding a photometrically detectable signal during this crossing. This transit method (also known as the occultation or eclipse method) measures such a darkening signal as an evidence for an orbiting planet.

The first detection of a transiting exoplanet HD 209458 b in 1999 and the discoveries obtained for this planet during follow-up observations demonstrated the high scientific potential of planets discovered by the transit method. The size of the exoplanet and the inclination of the orbit were determined. Combined with the information obtained with radial velocity measurements the mass and the density of the planet were calculated identifying the planet as a gas giant. Atmospheric components like Sodium, Hydrogen, Oxygen and Carbon were identified with spectroscopic measurements made with the Hubble Space Telescope. Hydrogen evaporating from the surface of the giant planet due the high stellar pressure of the nearby host star was discovered. The direct flux centered around the secondary eclipse was determined in infrared bands by measurements with the Spitzer Telescope. This unique opportunity to study detailed physical and chemical properties of exoplanets is advantageous compared to planets proven only by other search methods.

In recent years only three additional transiting planets orbiting bright stars suitable for high-resolution follow-up spectroscopy have been discovered. A substantially higher number of detected transiting exoplanets are imperative to answer fundamental questions about Hot Jupiter planets. Deep surveys like OGLE (five transiting planets orbiting faint stars detected) will give higher number of detected transiting exoplanets, increasing the statistical database. Due to the faintness of the host stars the physical and chemical characterization of the detected planets will be limited. Furthermore the obtained large error estimations of the physical parameters for the planets will limit using the parameters for modeling purposes.

The transit method offers the unique possibility to detect small rocky planets orbiting solar-like stars if observations are carried out from space. Satellite missions like COROT and Kepler will open this new field in the exoplanet search in the near future monitoring ten thousands of stars simultaneously from space without the disturbing noise introduced by the earth atmosphere.

In this thesis the establishing of the ground-based transit survey Berlin Exoplanet Search Telescope (BEST) is described. This survey was initiated with the goal of widening knowledge about this relatively young search method for exoplanets to support the preparations for the French-led COROT satellite mission. The instrument of the search system, a 20cm Schmidt telescope, has a similar dimension as the telescope of the COROT satellite. The field of view (FOV) of BEST (3.1° x 3.1°) is comparable in size with the FOV of the COROT telescope.

The set-up and the successful implementation of the BEST system are described in this work. Furthermore the developed strategies for the photometric observations, the calibration and analysis of the data, follow-up observations and their optimization are commented.

Two transits of the exoplanet orbiting the star HD 209458 were already observed during the initial set-up phase of the BEST system demonstrating the feasibility that transit signals can be successfully measured with the system.

During the 2-year observational campaign (2001-2003) from the Thüringer Landessternwarte (TLS) Tautenburg, Germany, three target fields were observed for 90 nights. The collected data was calibrated and analyzed by the developed automatic data

pipeline. Photometric precision sufficient for detections of transits by Jupiter-sized planets orbiting Solar-like stars was obtained for several thousand stars.

Five transit candidates were discovered in the data set. Two candidates were identified as eclipsing binaries; one of the secondaries was determined to be one of the smallest main sequence stars with a known radius. A blending scenario was identified for one transit candidate: an eclipsing binary was blended by two more stars observed in the same point spread function (PSF) of BEST. A fourth candidate host star for a transiting planet was found to be a giant star too large that a transit signal of a planet-sized object could be detected. Candidate 5 is still under investigation; a planetary origin of the observed signal could not be confirmed so far.

Additionally variable stars were identified in the data set of the three observed target fields. Altogether 83 stars were identified as variable stars, all discoveries are new discoveries. For 53 of these variables periodic variability could be confirmed. Among the variables 38 objects were classified as eclipsing binaries.

The observational campaign from TLS turned out to be a useful investment for both collecting observational data and developing an automated data reduction process. Furthermore optimization of the photometric observations, data reduction and –analysis, follow-up analysis and observations could be conducted. Nevertheless the obtained orbital phase coverage during one observational season was not sufficient enough for detecting more than one transit event of short-periodic exoplanets eventually contained in the three target fields with high probability. Not optimal meteorological conditions were identified as the main limitation of the observations, thus that the planning for a movement of the search system to an observational site with better meteorological conditions was accelerated.

More than 20 transit search programs have already been established during recent years. Most of these are wide-angle searches monitoring bright and moderately faint stars (10 mag < V < 15 mag). Only one transiting exoplanet has been detected by a wide-angle survey: TrES-1. In this work it was analyzed how the detection rates of transit search systems can be maximized based on the knowledge obtained during BEST observations and from operational and proposed transit searches. Aspects of this optimization process were the analysis of the fraction of suitable targets stars in different magnitude ranges in typical target fields close and above the Galactic plane, the influence of stellar crowding, the maximization of the orbital phase coverage and the minimization of main noise sources worsening the photometric precision. The analysis showed that the BEST system allows higher detection rates for transits of exoplanets compared to other ongoing transit search systems. Nevertheless, as a result of this analysis, a new transit search system is proposed consisting of f/1 Schmidt telescopes with an aperture of 45cm able to monitor a FOV of 4.7° x 4.7° combined with a 4k CCD with a pixel size of nine μm. This system would combine the advantages of a wide FOV and a pixel scale well suited to monitor target fields close and above the Galactic plane. Nevertheless all analyzed search systems can reach sufficient detection probabilities if the target fields are well selected so that the pixel scale corresponds to the stellar density of the observed target fields.

Zusammenfassung

1995 begann mit der Entdeckung des ersten Exoplaneten, welcher einen sonnenähnlichen Stern umkreist, ein neues Kapitel in der Astronomie und Astrophysik. Die unerwartet kurze Umlaufzeit dieses Planeten 51 Peg b von 4.2 Tagen und die damit verbundene hohe Wahrscheinlichkeit der Bedeckung des Zentralsterns durch den Planeten eröffnete neue Perspektiven für die Transitsuche nach Exoplaneten. Mit der Entdeckung des ersten Transitexoplaneten HD 209458 b im Jahre 1999 und den umfangreichen Informationen über den Planeten, welche bei Nachfolgebeobachtungen gewonnen werden konnten, wurde diese Entwicklung weiter forciert. Mit dem COROT-Satelliten wurde eine Weltraummission unter französischer Führung in Planung genommen, welche als ein Hauptziel die Suche nach Transits von Exoplaneten hat. Das Deutsche Zentrum für Luft- und Raumfahrt beteiligt sich unter anderem mit dem bodengebundenen Transit-Suchsystem *Berlin Exoplanet Search Telescope* (BEST) an der wissenschaftlichen Vorbereitung dieser Mission.

In dieser Arbeit ist dieses System und seine erfolgreiche Inbetriebnahme an der Thüringer Landessternwarte (TLS) Tautenburg beschrieben. Als ein Schwerpunkt dieser Arbeit wurde zur Bearbeitung und Analyse der gewonnenen Daten eine automatische Software erstellt. Desweiteren wurde eine Strategie zur Unterscheidung von realen planetaren Transitsignalen und Signalen entwickelt, welche durch andere physikalische Phänomene verursacht werden.

Während der von der TLS durchgeführten Beobachtungskampagne wurden drei ausgewählte Zielfelder für insgesamt 90 Nächte beobachtet. Die gewonnenen Daten wurden kalibriert und photometrisch ausgewertet. Für bis zu 4000 Sterne pro Beobachtungsnacht wurde eine photometrische Genauigkeit erreicht, um Transits von jupitergroßen Planeten um sonnenähnliche Sterne entdecken zu können.

So konnten für fünf Sterne transitartige Signale gemessen werden, welche durch Planeten verursacht worden sein könnten. Mit Hilfe von Informationen aus Online-Datenbanken und Nachfolgebeobachtungen mit diversen Teleskopen (2-Meter TLS-, 9,2-Meter HET-, 09-Meter-Westerlund-Teleskop) konnten bisher für vier der beobachteten Signale nichtplanetare Ursachen bestimmt werden. Davon erwiesen sich drei Systeme als Bedeckungsveränderliche. Für ein System konnte die bedeckende Komponente als einer der weltweit kleinsten vermessenen M-Sterne identifiziert werden. Dieses Bedeckungssystem wird zur Erhöhung der Präzision der Messungen auch weiterhin beobachtet werden. Die gewonnenen Parameter des Sterns sind von Bedeutung für die Verbesserung von Modellen von M-Zwergen. Für Kandidat 5, mit einem M-Zwerg als Zentralstern, dauern die Nachfolgeuntersuchungen und Beobachtungen weiterhin an. Das beobachtete Signal könnte von einem Planeten kleiner als Saturn verursacht worden sein.

Die gewonnenen Daten wurden auch auf Veränderliche analysiert. 10 – 15 % der Sterne zeigten dabei Variabilität. Für 83 Veränderliche konnte die Art der Variabilität festgestellt werden, dies sind neue Entdeckungen. Für 53 Sterne wurde dabei die Periodizität der Veränderlichkeit bestimmt. 38 Sterne wurden als Bedeckungsveränderliche eingestuft.

Außerdem wurde eine Analyse zur Optimierung von Transitsuchsystemen einschließlich BEST durchgeführt. Für BEST konnte dabei im Vergleich mit gegenwärtig genutzten Weitwinkelsuchsystemen eine hohe Entdeckungswahrscheinlichkeit für Transits von Exoplaneten ermittelt werden. Gleichzeitig werden in der Analyse auch Empfehlungen zur optimierten Zielfeldauswahl, zur Erhöhung der Phasenabdeckung für mögliche Transitplaneten und zur technischen Optimierung der Systeme ausgesprochen. Weiterhin wurde basierend auf den heutigen technischen Möglichkeiten ein neues Suchsystem

vorgeschlagen, welches eine deutlich höhere Entdeckungswahrscheinlichkeit für Transitplaneten aufweisen sollte als gegenwärtig benutzte Systeme.

Contents

1. Introduction

The discovery of other worlds was a long enduring dream of the mankind beginning already with the knowledge that there are other stars than the sun in the sky. The Greek philosopher Epikur (341-270 B.C.) mentioned in a letter to Herodot that 'there are countless other worlds, worlds like our own and different, too'. It took more than 2000 years proving that his imagination based only on visual impressions is really true. In 1992 the first planets outside the Solar System were discovered orbiting the pulsar PSR1257 +12 (Wolszczan et al. 1992). Three planets were discovered orbiting this old neutron star derived by pulsar timing. The first planet orbiting a solar-like star other than the sun was detected three years later in 1995: 51 Peg b (Mayor & Queloz 1995). The discovery of this planet really opened a new field in astronomy and astrophysics: the detection of other worlds called extrasolar planets or exoplanets.

About 170 exoplanets were discovered in the following years most of them by the radial velocity (RV) method. Some surprising results were found: planets in highly eccentric orbits, planets in close-in orbits with orbital periods of a few days, planets with a few times more mass as Jupiter, free-floating planets, planets orbiting giant stars and pulsars.

A definition for 'planet' had to defined based on this new knowledge. In 2003 the International Astronomical Union (IAU) defined the following[1]:

(1) Objects with true masses below the limiting mass for thermonuclear fusion of deuterium (currently calculated to be 13 Jupiter masses for objects of solar metallicity) that orbit stars or stellar remnants are "planets" (no matter how they formed). The minimum mass/size required for an extrasolar object to be considered a planet should be the same as that used in our Solar System.

(2) Substellar objects with true masses above the limiting mass for thermonuclear fusion of deuterium are "brown dwarfs", no matter how they formed nor where they are located.

(3) Free-floating objects in young star clusters with masses below the limiting mass for thermonuclear fusion of deuterium are not "planets", but are "sub-brown dwarfs" (or whatever name is most appropriate).

The IAU stated that this is a "working definition", that has to "evolve as our knowledge improves". Based on the deuterium-burning mass limit and the formation process this definition is a compromise. The definition of the minimal mass of a planet is based on the definition of the minimal size for planets in the Solar System that is currently under discussion after the detection of Sedna, a Kuiper Belt object larger as Pluto.

An important point of the definition is the necessity to determine the true mass of the object. The most promising approach to determine real masses of planet candidates are combined measurements RV measurements and transit observations of transiting planets.

Therefore this introduction will give an overview concentrated on both detection methods transit search and RV measurements, which is by far the most successful method for detecting exoplanet candidates. An historical view id given to demonstrate how the influence of the planet detections by RV measurements has boosted the transit search. Furthermore the parameter space of the detected planet candidates and the status of the scientific research based on the observations is given.

[1] http://www.ciw.edu/IAU/div3/wgesp/definition.html

1.1. History of the radial velocity search for extrasolar planets

Ten years ago in October 1995 the first detection of an extrasolar planet orbiting a solar-like star was announced by Mayor and Queloz (1995) ending decades of endeavors of several groups of scientists to discover the first planet in a planetary system different from our own Solar System. The presence of a Jupiter-mass planet around the star 51 Pegasi was inferred from observations of the periodic variations in the star's radial velocity induced by the mass of the orbiting planet. The radial velocity (RV) measurements were made with the fiber-fed echelle spectrograph ELODIE of the Haute-Provence Observatory, France, starting in September 1994.

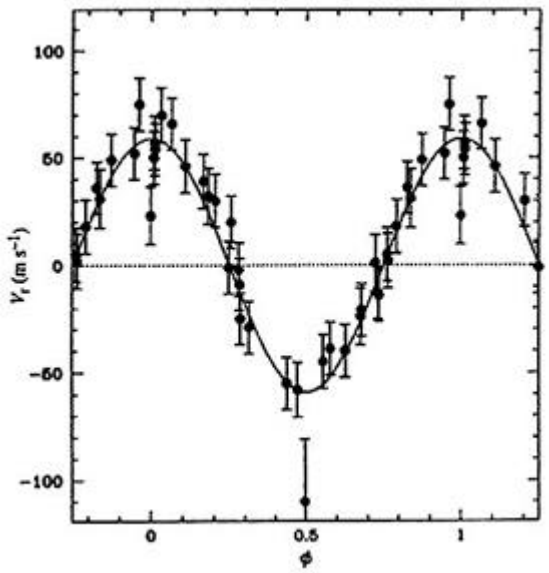

Figure 1.1.: The historical radial velocity data of the first discovered exoplanet 51 Peg b by Mayor and Queloz (1995.)

RV measurements determine the radial component (in the line of sight) of the movement of the primary object caused by the gravitational interaction with the secondary component. The RV semi-amplitude K can be expressed by (Bouchy et al. 2002)

$$K = 0.09 \frac{M_2(M_{earth})}{\sqrt{a(AU)M_1(M_{sun})}} ms^{-1} \qquad (1.1.)$$

where the mass of the secondary M_2 is directly proportional to the RV semi-amplitude K. The semi-major axis is given by a, the mass of the primary object by M_1. This formula assumes that the orbital plane is superposed with the line of sight. For transiting systems this is a good approximation. Thus a Jupiter-mass planet orbiting a solar-mass star in an orbit with a semi-major axis of 0.05 AU shows a semi-amplitude of 0.13 km/s. A low mass brown dwarf (20 M_{jup}) will cause a semi-amplitude of 2.5 km/s, a low mass M dwarf (0.1 M_{sun}) 13.3 km/s.

The possibility of discovering extrasolar planets orbiting their host stars within a period of a few days using RV measurements was first mentioned by Struve (1952). Based on the knowledge that binaries with orbital periods of a few days exist Struve proposed to probe solar-like stars if they are orbited by short-period giant planets, by measuring the stars' radial velocities. Oscillations of 0.2 km/sec were stated to be 'just detectable with the most powerful Coudé spectrographs in existence' (Struve 1952).

Nevertheless it took nearly three decades until serious efforts were undertaken to search for extrasolar planets with the RV method. The Canadian scientists Campbell and Walker started the first RV search program for exoplanets in 1980 as reported in Campbell et al.(1988). A

sample of 12 late-type dwarfs and 4 subgiants were observed 3 times/year over a 10-year period with the Coudé spectrograph of the 3.6m Canada-France-Hawaii (CFH) telescope. An absorption cell containing hydrogen fluoride was used as wavelength reference obtaining a remarkable RV precision of 13 m/sec. The program ran until 1992 but no planet was detected.

In 1983 Geoff Marcy and his team started to monitor a sample of 120 dwarf stars measuring the radial velocities (Marcy & Benitz 1989). First observations were carried out with the Coudé spectrograph of the Mount Wilson Observatory 2.5m telescope equipped with a Th-Ar lamp as a wavelength reference. A nightly uncertainty of 40 m/sec was obtained, the internal error was 150 m/sec. Due to the closing of the 2.5m telescope at Mt. Wilson the campaign was moved to use the 3m telescope at the Lick observatory. With the Coudé echelle spectrograph of this telescope an internal error of 200 m/sec was reached. During the early nineties the RV precision was improved to 15 m/sec using an iodine cell as wavelength reference.

In 1986 McMillan (University of Arizona) started a second RV search program for exoplanets using an echelle spectrograph of a 0.9m telescope (McMillan et al. 1986). The wavelength calibration was performed with a Fabry-Perot etalon that was calibrated with an Ar emission line lamp. A RV precision of 6 m/sec was obtained.

More researchers started RV monitoring campaigns in 1987. Bill Cochran and Artie Hatzes from the University of Texas in Austin started to monitor 33 F, G and K dwarfs and subdwarfs with the echelle spectrograph of the 2.7m telescope located at the McDonald Observatory (Cochran & Hatzes 1990). A RV precision of 5 m/sec was obtained with an iodine absorption cell as spectroscopic reference.

Although sufficient precision of the RV measurements was reached by all teams, no team reported the discovery of an exoplanet until 1995 when the first discovery of the planet 51 Peg b was reported by Mayor and Queloz as already mentioned above. This group started to monitor a sample of 142 G and K dwarf stars in April 1994 with the echelle spectrograph on the 1.93m telescope in Haute-Provence, France. Using a Th-Ar calibration lamp during the exposures led to a precision of 13 m/sec. A fast data reduction pipeline was developed able to quickly deliver the measured radial velocity of the observed star. This was the major advantage of the Swiss team in the race to discover the first exoplanet. Based on the assumption that only giant planets with orbital periods of several years exist (like in the Solar System and proposed by the existing planet formation theories) the RV data was not immediately analyzed for short-period behavior caused by masses of orbiting giant planets. Not following the recommendation of Struve (1952) to search for short-period giant planets was a fateful decision of the American teams, allowing the first detection of an exoplanet orbiting a Solar-like star to be made by the Mayor/Queloz team. The giant planet orbiting 51 Pegasi with a minimal mass of 0.47 M_{jup} (where M_{jup} is 1 Jupiter mass) is orbiting its host star in 4.23 days. The resulting RV amplitude of 57 m/sec was easily detectable with the RV precision attained.

Challenged by the discovery of 51 Peg b Marcy and Butler analyzed their RV data for short period planets and discovered one giant planet with a short orbital period of 116.6 days: 70 Virginis b with a minimal mass of 6.6 M_{jup} (Marcy & Butler 1996). The large RV amplitude of 318 m/sec would have been easily detectable within the collected data years before. RV observations of this system had already started in 1988. Another planet with a minimal mass of 2.4 M_{jup} was reported orbiting the star 47 Ursae Majoris with a period of 2.98 years (Butler & Marcy 1996).

In late 1996 the teams Cochran/Hatzes and Marcy/Butler reported jointly the independent discovery of another extrasolar planet 16 Cygni b (Cochran et al. 1997) orbiting its host star in an eccentric 800-day orbit.

The basis for future discoveries of several dozens of exoplanet in the next few years was established with these successful detections. More teams doing RV searches were formed, new and more precise instruments were established. They are listed in alphabetical order:

a) AFOE spectrometer at the Whipple Observatory, Arizona, USA;
b) The Anglo-Australian Planet Search (AAPS) with the 3.9m AAT telescope, Australia;
c) The California & Carnegie Planet Search at the Lick Observatory, and the Keck Observatory, USA (Marcy & Butler);
d) Coralie at the Leonard Euler Telescope at La Silla, Chile (Swiss team);
e) Elodie at the Haute-Provence Observatory (Swiss/French team)
f) ESO Coude Echelle Spectrometer (CES)
g) High Accuracy Radial Velocity Planet Search (HARPS) in La Silla, Chile;
h) Hobby-Eberly Telescope at the McDonald Observatory, Texas, USA (Cochran team);
i) SARG Exoplanet Search with TNG telescope at La Palma, Italian team;
j) TOPS (Tautenburg Observatory Planet Search) with the 2m telescope at Tautenburg, Germany (Hatzes team);
k) UVES spectrograph at the VLT UT2, Paranal, Chile.

How many and what kinds of planets detected so far by radial velocity searches is described in the next section.

1.2. Characterization of the exoplanets discovered by RV searches

165 extrasolar planets orbiting solar-like stars have been detected by RV searches until February 2006 following the statistics given by Jean Schneider's website about exoplanets[2]. These statistics include all confirmed detections of exoplanet candidates with a mass limit of 13 M_{jup} corresponding to the lower mass limit necessary to trigger a thermonuclear fusion. Additional companions with masses < 20 M_{jup} are listed if another planetary companion with M < 13 M_{jup} is detected already. Assuming a 2-sigma uncertainty for the planetary masses, a planet reported to have e.g. 19 M_{jup}-mass could actually have a mass below 13 M_{jup} with 12% probability. These 165 planets are located in 142 planetary systems. 17 multiple planets systems exist with up to 4 detected planets (55 Cnc b, c, d, e).

The orbital periods range from 1.94 days (Gliese 876 d) to 3177 days (HD 72659 b). More planets with orbital periods less than 10 days have been detected, defining the new class of so-called Hot Jupiters. 31 planets detected by RV searches belong to this class.

Gliese 876 d again shows the shortest semi-major axis with 0.021 astronomical units (AU), HD 72659 b is reported to have the largest distance to its host star: 4.16 AU.

The existence of these Hot Jupiter planets and more giant planets in the inner part of stellar systems was in contradiction to the common core accretion planet formation theories (for an overview about planet formation theories see Wuchterl, Guillot & Lissauer 2000), where first a rocky core is formed similar as for terrestrial planets, and this core accretes large amounts of gas from the surrounding protoplanetary disk. This assumed that the planet is formed beyond the so-called snow line, where water is condensed to ice particles, based on the knowledge of the structure of the Solar System with giant planets existing only beyond the snow line. Orbital migration theories were introduced to solve this discrepancy. Due to gravitational interactions with the circumstellar disk the giant planets are supposed to migrate

[2] http://vo.obspm.fr/exoplanetes /encyclo/catalog-main.php

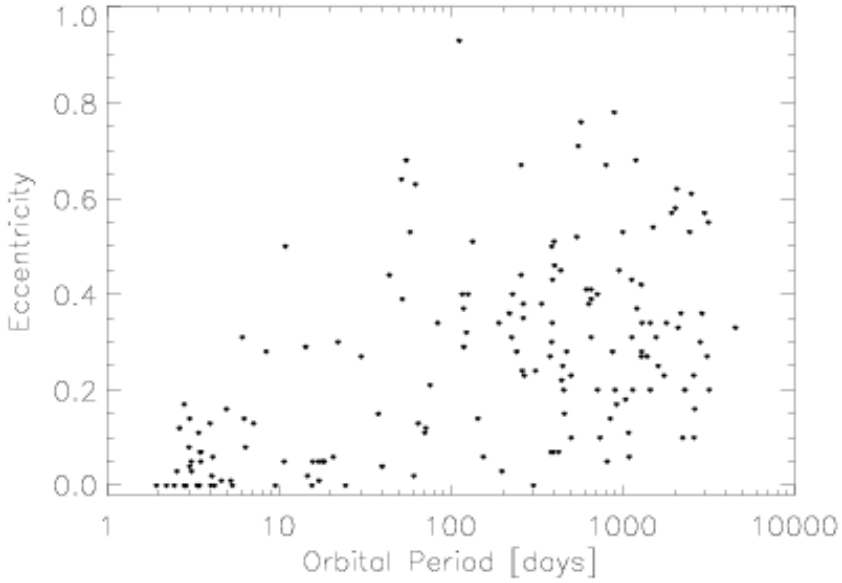

Figure 1.2.: Eccentricity of planetary orbits vs. orbital periods given for all exoplanets with known eccentricity[2]. Planets were found to have orbits with diverse eccentricities. For close-in exoplanets only low eccentricities were determined.

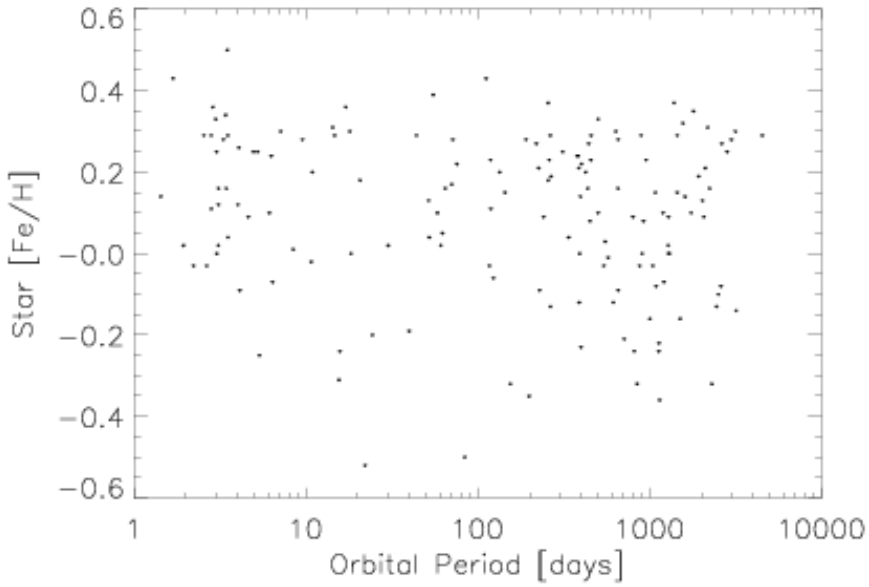

Figure 1.3. Metallicity of stars which harbor exoplanets against the orbital period of the planets[2]. Most planetary host stars are reported to show a higher metal content than the Sun (Fe/H > 0.0). Especially Hot Jupiter planets were found to orbit mainly metal-rich stars.

toward the host star to the orbits where they are observed now. On the path of this migration the planets clear the circumstellar disks. The stopping mechanism that prevents the planets from falling into the host stars is still under debate. For a review about planetary migration theories please see Thommes & Lissauer (2005).

Another difference to the Solar System is the detection of eccentric orbits for a large fraction of these exoplanets (see Figure 1.2.). The maximum eccentricity is detected for HD

[2] http://vo.obspm.fr/exoplanetes /encyclo/catalog-main.php

80606 with e = 0.927. The mean eccentricity is about e = 0.3 if the Hot Jupiter class planets are excluded. These Hot Jupiters show orbits with no or low eccentricities due to orbit circularization caused by tidal interactions with the close host stars.

The majority of the host stars were found to have a higher content of heavy elements compared to our Sun (see review Santos et al. 2003, Figure 1.3.). Metallicity seems to play an important role for giant planet formation. Santos et al. (2004) found that in the CORALIE RV sample 25% of stars with Fe/H > 0.3 were found to harbor a giant planet, This is reduced to 3% for metal-poor stars (Fe/H < 0.0).

Due to the unknown inclination, i, of the orbits for exoplanets characterized by RV searches only a lower mass limit, M sin i, can be concluded without further constraints. Thus in the extreme case of an orbit perpendicular to the line of sight (i = 0°) the real mass of the exoplanets characterized by RV measurements can easily exceed the upper mass limit for a planetary body.

Several planets are reported to have masses of a few Jupiter masses. But no heavy giant planets were detected in the inner regions of the planetary systems as reported by Pätzold & Rauer (2002). A possible explanation of this absence of massive planets at these distances are tidal interactions between planets and their central star that lead to a rapid decay of a planetary orbit toward the Roche zone of the star. The massive planets fall into their host star within a short timescale.

The lowest minimal mass of an exoplanet was found for the planet Gliese 876 d with 0.023 M_{jup} corresponding to 7.4 Earth masses. The detection of a planet with this low mass by RV measurements was possible due to the low mass of the host star (M4 type dwarf) yielding larger RV amplitudes compared to planets orbiting stars with higher masses. Additionally the improved RV precision (1 m/sec) and a high number of measurements with the Keck telescope over a period of eight years enabled the detection (Rivera et al. 2005).

Only for very few planets has the inclination of the orbit been determined by additional analyses.

For the planet Gliese 876 b the inclination was determined with the help of measurements of astrometric residuals (perpendicular to the line of sight) of the host star at different orbital phases of the planet by the fine guidance sensors (FGS) of the Hubble Space Telescope (Benedict et al. 2002). The inclination was determined to 84° ± 6° yielding a planetary mass of 1.89 ± 0.34 M_{jup}.

The astrometric mass determination for Gliese 876 b was not the first mass determination to be obtained for an extrasolar planet. In 1999 it was discovered that the Hot Jupiter planet HD 209458 b eclipses its host star. This transit has provided additional information about the inclination of the orbit. The history and the statistics of transiting exoplanets will be discussed in the following sections.

1.3. History of transit search for extrasolar planets

The astronomer Otto Struve (1952) mentioned the possibility of eclipses observable when a close-in giant planet crosses in front of its host star in his ‘proposal for a project of high-precision stellar radial velocity work’. The assumption was made that a loss of light up to 0.02 mag can be observed if a giant planet covers its host star. Struve estimated that this method ‘should be ascertainable by modern photoelectric methods’.

It took nearly 20 years before a more detailed proposal for a transit search was made by Rosenblatt (1971). Rosenblatt was the first to calculate the expected shapes of transit signals in different colors and estimated the detection rates for a proposed transit search system. This system consisted of 3 wide-field telescopes equipped with photometers and located at 3 different sites and hoped to be able to find one transiting planet per year of operation. The

detection rates were overestimated assuming that each star harbors a giant planet that would be photometrically detectable if the orbit is aligned correctly.

The next proposal was made by Borucki and Summers (1984). Again the use of photometers was proposed, which was improved by fiber-optic connections to the focal plane of 1m wide-field telescope to reach a detection rate of one transiting giant planet per year of observations. This estimation was based on the assumptions that giant planets have long-period orbits, that each star has one giant planet and that a photometric precision of 0.1% is reached for 10^4 stars. Space-based telescopes were proposed to reach these demanding goals.

The first established transit search program took a different approach. Starting in 1994 the TEP (Transits of Extrasolar planets) network consisting of 10 telescopes (0.7m to 2.5m apertures) observed the eclipsing binary CM Draconis for 5 years obtaining 1014 hours of observations (Deeg et al. 1998, Deeg et al. 2000). The binary system consists of two small M dwarfs orbiting each other in one day. Under the assumption that the angle between the plane of the eclipsing binaries and the plane of possible planets is small the system could detect transits of existing planets of a size of ≥ 1.5 R_E (Earth Radii) with high probability. Six suspicious small-amplitude events were recorded, but no planetary transit could be confirmed by follow-up observations. But the search demonstrated that transit detections are possible for the obtained photometric precision of better than 0.5%.

The discovery of the first short-period giant planet 51 Peg b in 1995 and the discovery of more planets similar to this Hot Jupiter planet accelerated the development of further transit searches. In 1999 the planet HD 209458 b was reported to have an orbital period of 3.5 days by RV measurements (Mazeh et al. 2000). Short-period exoplanets were monitored photometrically

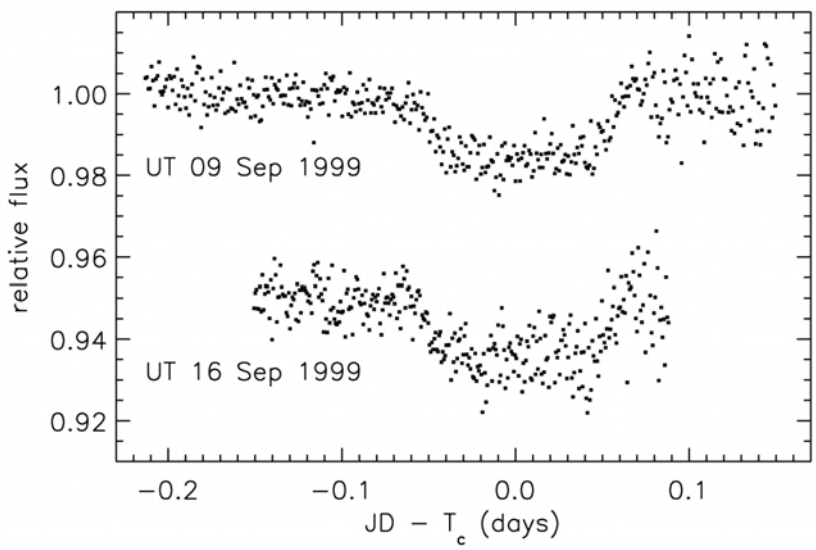

Figure 1.4.: Two transit signals of the planet HD 209458 b as reported by Charbonneau et al. (1999).

because they have a probability of a few percent of transiting their host stars. Charbonneau et al. (1999) and Henry et al. (1999) both reported the detection of transits of the exoplanet HD 209458 b (see Figure 1.4.). For the first time the transit of a planet in an extrasolar planet system was discovered. Based on the information contained in the transit signal the radius of the planet was determined to be 1.27 ± 0.02 R_{jup}; the inclination of the orbit was calculated to be $87.1° \pm 0.2°$. In combination with the lower mass limit M sin i from the RV measurements the mass and the density of the exoplanet were determined: 0.63 M_{jup} and 0.38 g/cm^3. Physical properties of the body of an exoplanet were determined for the first time. Notable is that photometric observations by Charbonneau et al. (1999) were made with the 10cm STARE telescope, one of the first operational wide-angle transit searches for planets.

The determination of the planetary parameters was improved by applying space-based photometry with the STIS instrument on board the Hubble Space Telescope (Brown et al. 2001, Figure 1.5.). The obtained photometric precision of about $1.1 \cdot 10^{-4}$ allowed to determine the planetary radius to 1.347 ± 0.060 R_{jup} and the orbital inclination to 86.6 ± 0.14 deg demonstrating the advantages of space-based photometry due to the missing influences of the atmosphere of the Earth.

After the detection of the transits of HD 209458 b more than 20 new ground-based transit search programs were established. Two major strategies were developed:

a) Wide-angle searches monitoring brighter stars,
b) 'Photometrically deeper' searches monitoring fainter stars.

Some of these transit searches and their observational strategies are described in appendix section A.

The next step to establish the transit method as a search tool for exoplanets was the first discovery of an exoplanet based on photometry and confirmed by RV measurements. It took until early 2003 to confirm the first exoplanet of this kind: OGLE-TR-56 b (Konacki et al. 2003a). This exoplanet was one of the 70 transit candidates found during photometric observations with the 1.2m OGLE-III telescope during the 2001 observational campaign and published by the OGLE group in 2002 (Udalski et al. 2002a, 2002b, 2003). The orbital period of the planet was found to be surprisingly short (1.21 days), establishing a new class of exoplanets: The very Hot Jupiters with orbital periods less than 2 days.

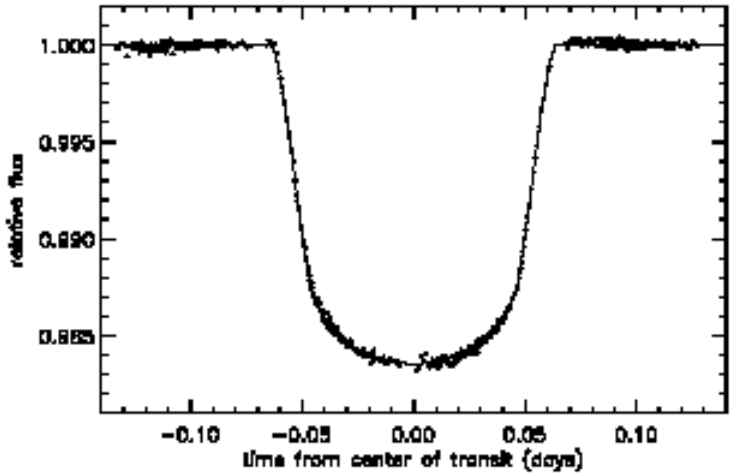

Figure 1.5. HST photometry of the transit of HD 209458 b (taken from Brown et al. 2001).

Most of the candidates were analyzed to be eclipsing binaries or blends. Later one more candidate discovered during the first photometric OGLE-III campaign could be confirmed to be a real transiting exoplanet: OGLE-TR-10 b (Bouchy et al. 2004b, Konacki et al. 2005).
More transit candidates of further OGLE observational campaigns were published. 68 transit candidates were discovered during the 2002 campaign observing target fields in the Carina region (Udalski et al. 2002c, 2003). RV follow-up observations confirmed 3 candidates to be transiting exoplanets: OGLE-TR-113 b and OGLE-TR-132 b (Bouchy et al. 2004a), OGLE-TR-111 (Pont et al. 2004). 40 additional transit candidates of the 2003 OGLE campaign were published in Udalski et al. (2004). RV follow-up observations are ongoing.

Several wide-angle surveys and deep search programs have published a smaller number of transit candidates, although most of them turned out to be false alarms. Only one candidate was confirmed to be a transiting exoplanet: TrES-1 (Alonso et al. 2004). This planet was detected first by the STARE telescope that is now a part of the Trans-Atlantic Exoplanet Survey (TrES) network.

The second generation of RV surveys have already yielded announcements of more transiting exoplanets orbiting bright stars. The N2K (next 2000 stars, Fischer et al. 2005) discovered a transiting Saturn-sized planet orbiting the star HD 149026 (Sato et al. 2005). Another consortium (the ELODIE metallicity-biased search for transiting Hot Jupiters survey, Da Silva et al. 2006) recently discovered a transiting exoplanet orbiting the bright star HD 189733 (Bouchy et al. 2005).

More transiting exoplanets will be detected in the future. Additional to the ground-based searches future satellite missions will detect more and smaller transiting extrasolar planets.

The first mission will be the French-led COROT (Baglin et al. 2002) satellite launching in 2006. This small satellite program with a wide European cooperation (A, B, D, E, ESA) is dedicated to two scientific goals: astroseismology and the search for transiting planets. During at least five observational campaigns 30,000 to 60,000 stars will be monitored for 150 days to search for transiting planets. The obtained photometric precision will be sufficient enough to detect transits of large terrestrial (rocky) planets with orbital periods up to 70 days.
The Kepler mission, to be launched in 2008, will be able to detect earth-sized planets in earth-like orbits: Kepler (Borucki et al. 2003).

1.4. Characterization of the transiting exoplanets

Planets that show a transit signal eclipsing their host stars offer the possibility for further characterization of orbital and planetary parameters. Based on the depth of the transit signal the radius of the transiting exoplanet can be determined knowing the size of the host star. Knowing the orbital period and fitting a modeled transit shape to the measured transit shape allows evaluating the inclination of the planetary orbit.

A wider range of parameters can be determined especially if RV follow-up observations can be successfully conducted to give values for M sin i and the semi-major axis. The mass of the extrasolar planet can be directly calculated using values for M sin i from the RV analysis and the orbital inclination i conducted from the transit signal. Furthermore knowing the mass and the radius allows determining the mean density of the exoplanet.

The basic parameters radius, inclination, semi-major axis, mass and density were determined for all nine detected transiting exoplanets and are listed in Table 1.1. The minimal orbital period of 1.21 days was detected for OGLE-TR-56 b, the maximal period of 4.02 days for OGLE-TR-111 b. The radii of the detected transiting exoplanets ranges from 0.72 R_{jup} to 1.35 R_{jup}. The mass interval of the transiting planets starts at 0.36 M_{jup} and ends at 1.45 M_{jup}.

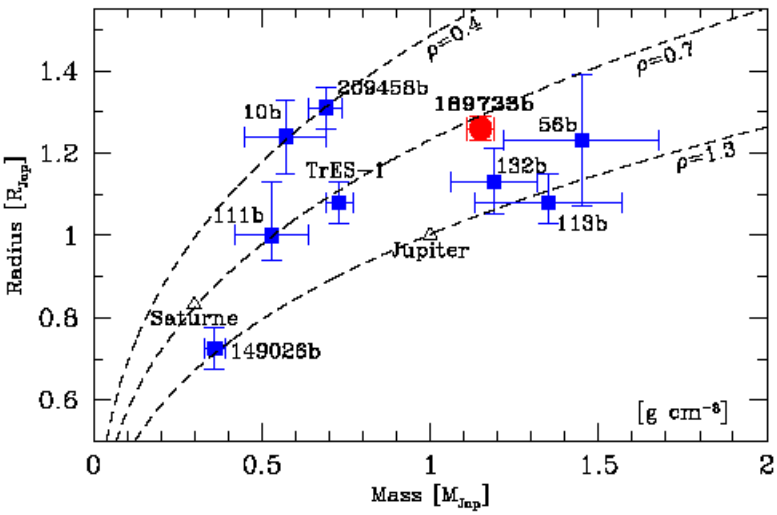

Figure 1.6.: Radius-mass diagram for the 9 transiting exoplanets. Note the low densities given for HD 209458 b and OGLE-10 b. The other transiting exoplanets show mean densities comparable to the densities of Jupiter and Saturn (taken from Bouchy et al. 2005).

Table 1.1.: Orbital period, planetary radius, inclination, eccentricity, semi-major axis, planetary mass and density for all known transiting extrasolar planets as known in early October 2005. Additionally the sources for the information are given. For HD 209458 b the eccentricity of the orbit was determined additionally. Note especially the diversity of the mean planetary densities ranging from 0.4-1.5 g/cm^3.

Planet	*Orbital period P [days]*	*Radius R [R_{jup}]*	*Inclination i [°]*	*Eccentricity e*	*Semi-major axis a [AU]*	*Mass M [M_{jup}]*	*Density ρ [g/cm^3]*	*Reference*
HD 209458 b	3.524744 ± 0.000003	1.347 ± 0.060	86.68 ± 0.14	0.07	0.045	0.69 ± 0.05	0.4 ± 0.1	Brown et al. 2001
HD 189733 b	2.2190 ± 0.0005	1.26 ± 0.03	85.3 ± 0.1	0 (fixed)	0.0313 ± 0.0004	1.15 ± 0.04	0.8 ± 0.1	Bouchy et al. 2005
HD 149026 b	2.8766 ± 0.0010	0.725 ± 0.05	85.3 ± 1.0	0 (fixed)	0.042	0.36 ± 0.03	$1.3^{+0.5}_{-0.3}$	Sato et al. 2005
TrES-1	3.030065 ± 0.000008	$1.08^{+0.18}_{-0.04}$	$88.5^{+1.5}_{-2.2}$	0 (fixed)	0.0393 ± 0.0011	0.75 ± 0.07	$0.8^{+0.2}_{-0.5}$	Alonso et al. 2004
OGLE-TR-56 b	1.211919± 0.000006	1.23 ± 0.16	81.0 ± 2.2	0 (fixed)	0.0225 ± 0.0004	1.45 ± 0.23	$1.1^{+0.8}_{-0.5}$	Torres et al. 2004
OGLE-TR-10 b	3.101386 ± 0.000030	1.24 ± 0.09	89.2 ± 2.0	0 (fixed)	0.0416 ± 0.0007	0.57 ± 0.12	$0.4^{+0.2}_{-0.1}$	Konacki et al. 2005
OGLE-TR-113 b	1.43250 ± 0.00001	0.765 ± 0.025	85 - 90	0 (fixed)	0.0228 ± 0.0006	1.35 ± 0.22	1.5 ± 0.5	Bouchy et al. 2004
OGLE-TR-132 b	1.689857 ± 0.000006	1.13 ± 0.08	78 - 90	0 (fixed)	0.0306 ± 0.0008	1.01 ± 0.31	$1.0^{+3.9}_{-0.5}$	Moutou et al. 2004
OGLE-TR-111 b	4.01610	$1.00^{+0.13}_{-0.06}$	86.5 - 90	0 (fixed)	0.047 ± 0.001	0.53 ± 0.11	$0.7^{+0.4}_{-0.3}$	Pont et al. 2004

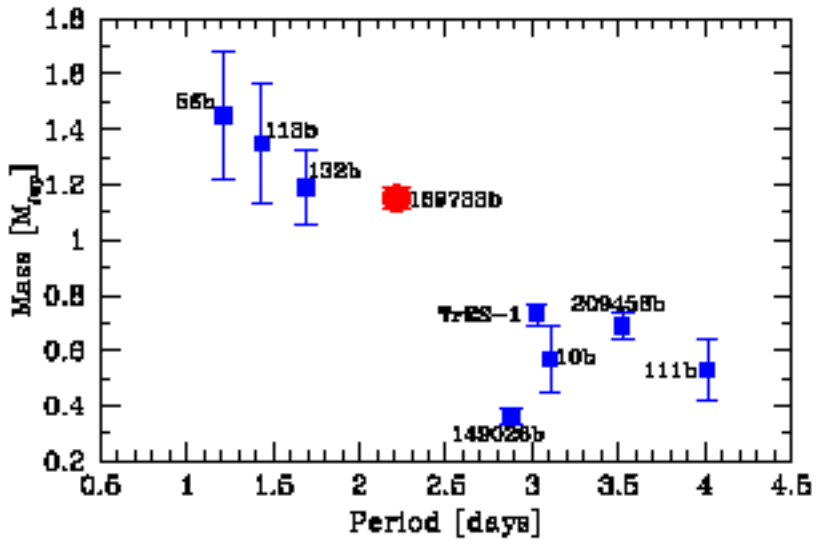

Figure 1.7.: Mass-orbital period diagram for the nine transiting exoplanets. An correlation between orbital period with masses of the transiting planet was reported by Mazeh et al. (2005) The Figure was taken from Bouchy et al. (2005).

The observed mean densities of the planets (see Figure 1.6.) are ranging from 0.4 g/cm^3 to 1.5 g/cm^3. Most of the transiting planets show densities similar to Jupiter (1.3 g/cm^3) or Saturn (0.7 g/cm^3), only for HD 209458 b and OGLE-TR-10 b lower densities of about 0.4 g/cm^3 have been reported. Several processes were proposed to explain the observed large radius and therefore the low density of HD 209458 b. Hot Jupiter planets are irradiated by the close host star resulting in high surface temperatures of about 1,000 K. Therefore the upper layers of the planetary atmosphere are extended. For HD 209458 b an additional energy source is necessary which explains the observed difference of 0.3 R_{jup} between the observed and modeled radius of the planet (Bodenheimer et al. 2001). Guillot & Showman (2002) proposed, that first a small fraction of the stellar flux has to be transformed into kinetic energy (winds) and then is converted to thermal energy at deeper atmosphere layers yielding a further extension of the atmosphere. But this process should take place for all Hot Jupiter planets extending their atmospheres. Bodenheimer et al. 2003 see an ongoing tidal circularization of the orbit of HD 209458 b as cause for the extended atmosphere. This scenario needs a second still undetected, smaller planet in a 80-day orbit using a model not containing a core for HD 209458 b. The resulting orbital eccentricity of 0.03 fits well to the RV data. If HD 209458 b has a solid core then an eccentricity of 0.1 is necessary, but this scenario is excluded by the RV data.

Note that Mazeh et al. (2005) reported a correlation between orbital period and masses of the transiting exoplanets (see Figure 1.7.). Note the larger error values for all parameters of the OGLE planets orbiting fainter stars. These larger errors are mainly based on the larger error values for the planetary mass due to low S/N of the RV follow-up measurements. The observed correlation could be explained with a critical mass limit in dependency upon the orbital distance of the planet as proposed in Baraffe et al. (2004). The atmospheres of planets below this critical mass are thermally evaporated by the flux of the host star in a short time scale. Therefore only the cores of the planets survive.

A more accurate mass determination is one of the advantages of transits observed for brighter host stars. Further follow-up analyses can be carried out. Infrared fluxes were measured for the HD 209458 planet (Deming et al. 2005) and the TrES-1 planet (Charbonneau et al. 2005) during the secondary eclipse. These measurements yielded estimates for the effective temperatures and albedos of the planets, which are basic parameters for atmospheric models. Ongoing improvements of atmospheric models for exoplanet are based on these data (f.e. see Figure 1.8.)

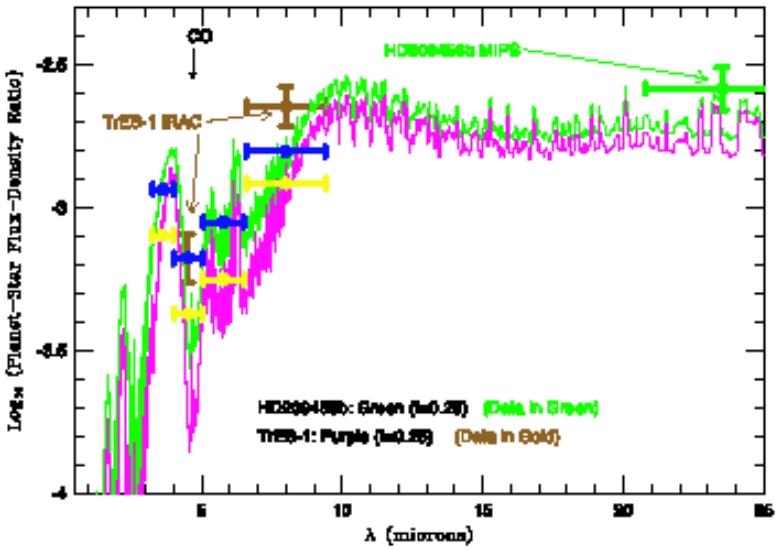

Figure 1.8.: The planet-to-star flux density ratio as a function of wavelength is given for models of the planets HD 209458 b and TrES-1. A comparison with measurements of the Spitzer satellite during secondary transits is done (from Burrows et al. 2005).

Some components of the atmosphere of the planets were also determined. Sodium was detected by Charbonneau et al. (2001). Oxygen and carbon were detected by Vidal-Madjar et al. (2004); an extended upper atmosphere of hydrogen was detected by Vidal-Madjar et al. (2003). All these detections were made with instruments of the Hubble Space Telescope. So far Ground-based observations have not been successful in detecting atmospheric components of the transiting exoplanets but progress is made towards the first ground-based detections. Arribas et al. (2006) reported recently about a new measurement technique. With the integral field-spectroscopy (IFS) a relative flux in the Na D band was measured for HD 209458 b only with an error 2 times higher as for the detection with Hubble STIS by Charbonneau et al. (2001).

1.5. Purpose of this study

The number of nine detected transiting exoplanets is not statistically significant. Therefore the number of detected transiting exoplanets has to be increased in the coming years. To detect a high number of transiting exoplanets a high number of dwarf stars has to be observed. These dwarf stars have to be small enough that a transit of a giant exoplanet is observable from the ground. Ground-based photometric observations are limited by the atmosphere (mainly scintillation and sky background) to obtain a precision of about 1 %. Therefore only smaller dwarfs (Solar like and smaller) are sufficient target stars for ground-based transit surveys. This favors the photometric monitoring of faint stars as observed by OGLE or even deeper searches.

The faintness of the host stars complicates the spectroscopic follow-up observations as seen for the OGLE candidates (V > 15). For some faint OGLE candidates no conclusive RV follow-up measurements could be carried out with the largest available telescopes (Konacki et al. 2003b, Bouchy et al. 2004a, 2004b). The RV characterization of brighter OGLE candidates lacks precise measurements due to the low S/N of the spectra contained with the largest telescopes resulting in large errors for the determined planetary parameters (see also Figures 1.6. and 1.7.). Thus much effort is needed to gain limited information about the discovered planets.

Transiting planets orbiting brighter stars more easily lead to further information about the chemical composition of close-in exoplanets than do darker stars. For the brightest host star of a transiting exoplanet HD 209458 atmospheric components were detectable by space-based

spectroscopy with the STIS spectrograph of the Hubble Space Telescope. Unfortunately the spectrograph failed in 2004.

Ground-based spectroscopic observations have so far failed to detect atmospheric signatures of transiting Jupiter exoplanets even when utilizing the most powerful telescopes of the world (Narita et al. 2005, Deming et al. 2005a, Moutou et al. 2001 and several others).

The number of transits for brighter stars will be limited for statistical reasons. The number of detectable bright small dwarf stars is rather limited, bright stars are more likely giants and early dwarf stars being too large that transits of giant planets can be detected by ground-based photometric monitoring. Deeg et al. (2004) estimate optimistically that 30 stars brighter than magnitude 10.5 will show detectable transits deeper than 1%. More realistic estimates suggest that only 10% of the observed bright stars are suitable targets stars (Brown 2003) and that only a fraction of 50% of the bright stars can be monitored with sufficient photometric precision due to sky background issues and crowding noise. These estimates reduce the number of photometrically detectable transits for bright stars to about six. But a significantly higher number of transiting giant planets has to be detected in order to obtain a statistically relevant sample of Hot Jupiter planets. RV searches can perform this task.

Future larger space-based (i.e. James Webb Space Telescope, Terrestrial Planet Finder-C) and ground-based telescopes will allow an improved characterization of transiting exoplanets orbiting moderately fainter stars in the near IR or optical wavelengths in the next decade.

Thus the photometric monitoring of moderately faint stars ($V < 14 \ldots 15$) should yield statistically relevant numbers of detected transiting giant planets. Furthermore basic characteristics like radius, mass and mean density with accurate error estimations can be obtained with current observational systems with a medium amount of effort.

Space-based photometric transit search systems are not exposed to the influences of the Earth atmosphere and therefore can detect smaller planets. The French space agency CNES (Centre National d'Etudes Spatiales) is developing the space-based transit search mission COROT (Convection, Rotation and planetary Transits, Baglin et al. 2002). One main goal of the mission is the monitoring of oscillations of stars (astroseismology), the other main goal is to search for transiting planets orbiting moderately faint stars. As part of the German participation the ground-based transit search system Berlin Exoplanet Search Telescope (BEST) was established. The development of BEST is a major part of this PhD thesis. This included initial tests and characterizing of the subsystems and the set-up of the system at the initial observing site Thüringer Landessternwarte (TLS) Tautenburg. Strategies for the photometric observations, had to be developed to obtain high quality data allowing the acquisition of high precision light curves. An automatic data reduction pipeline was prepared simultaneously with the observational campaign. The data obtained were used for further optimizing the data reduction and analysis software.

The observational campaign at the TLS endured nearly 2 years. The collected data of three regular target fields had to be calibrated. The obtained high-precision light curves were analyzed for transit-like events and variable stars. Spectroscopic (RV) and photometric follow-up observations of candidate objects for transits of exoplanets had to be organized and analyzed.

Furthermore an optimizing process was initiated to obtain a higher probability for the detection of transiting exoplanets for the given search system and alternative systems based on the knowledge about existing technology and the experience made with the BEST system.

To document how the aims of this work shall be approached the thesis is structured in the following way:

Chapter 2 describes the basics of the transit method and its main limitations.

Chapter 3 introduces the Berlin Exoplanet Search Telescope (BEST) system. Technical details about the system are described. The system is compared with other wide-angle systems described in the Appendix section.

Chapter 4 describes how the target fields for observations from the Thüringer Landessternwarte (TLS) Tautenburg were chosen. The strategies for both monitoring with BEST and the follow-up strategy of transit candidates are discussed.

Chapter 5 describes the developed data reduction and analysis software starting with the basic calibration of the CCD (charge coupled device) images. The data reduction pipeline further includes the extraction of the stellar signals, the assembling of the light curves, and their calibration and the systematic search for transit signals.

Chapter 6 contains the results of the observations carried out from the TLS. First a few general results, including observational statistics and photometric quality of the data are listed. Then discovered transit candidates are described, and follow-up analyses are presented.

Chapter 7 addresses an analysis of different aspects on how to optimize the BEST transit search system and transit search systems in general. Aspects such as minimizing noise contributions, maximizing the fraction of suitable target stars, minimizing crowding and maximizing orbital phase coverage are discussed. A new search system is proposed combining the advantages of a large field of view using a currently available 4k CCD well suited to the stellar densities as typically found for target fields close and above the Galactic plane.

Chapter 8 displays the results of the search for variable stars in the three target fields observed from TLS.

Chapter 9 contains a summary of the results of this work.

2. The transit method

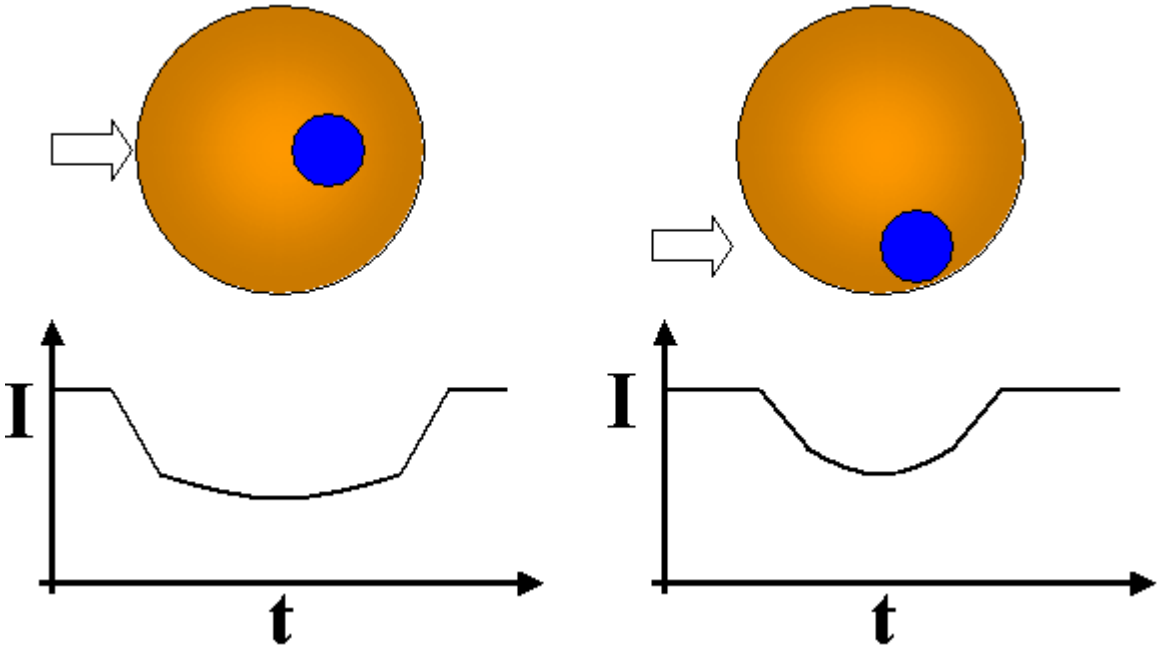

Figure 2.1: Schematic view of a transit (left plot: central transit, right: non-central transit): During the occultation of the star by a planet the observed stellar brightness, I, drops.

The transit method is one of several employed to discover planetary companions of stars. The search principle is very basic: the brightness of a star is monitored for decreasing stellar flux due to occultation of the star by an orbiting planet (see Figure 2.1.). In the following it will be described how to model a transit signal. Modeling the signal is the first step necessary to derive the planetary parameters that can be obtained with the transit method.

2.1. Simulating the transit shape

2.1.1. Simulations without limb darkening

The dimming signal for a full eclipse can be separated into three parts: ingress, full occultation and egress. For modeling transit signals the following parameters (see also Figure 2.2.) are defined:

- R_p is the radius of the planet
- R_* is the radius of the star orbited by the planet
- $R = R_p / R_*$ is the size ratio of planet and star
- D is the distance between the centers of the disks of the star and the planet as seen from the observer
- $k = D / R_*$ is the normalized center-to-center distance. Note that the minimum of k is often called the impact parameter.

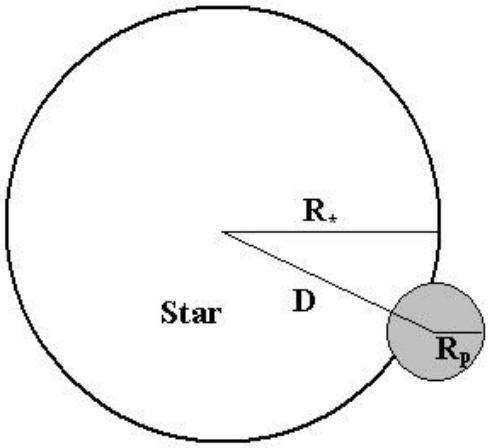

Figure 2.2.: Geometry of a planet with radius R_p orbiting a star with radius R_* as seen from the observer. D is the center- to-center distance between the star and the planet.

Assuming that the star is seen as a disk with a uniform flux of light and the planet as an opaque, dark disk (smaller than the orbited star), then the total flux relative to the unobscured flux can be expressed by:

$$S(R,k) = 1 - S_T(R,k)\,. \qquad (2.1.)$$

During the non-occultation phase ($k > 1 + R_p$) there is no reduction of the stellar flux and thus the relative signal depth S_T can be described as

$$S_T(R,k) = 0\,. \qquad (2.2.)$$

For the full occultation ($k \leq 1 - R_p$) results in

$$S_T(R,k) = R^2\,. \qquad (2.3.)$$

During the ingress and egress ($|1 - R_p| < k \leq 1 + R_p$) the reduction of the flux is expressed by

$$S_T = \frac{1}{\pi}\left[R^2 a + b - \sqrt{\frac{4k^2 - \left(1 + k^2 - R^2\right)^2}{4}}\right], \qquad (2.4.)$$

where

$$a = \cos^{-1}\left[\left(R^2 + k^2 - 1\right)/\left(2Rk\right)\right] \qquad (2.5.)$$

and

$$b = \cos^{-1}\left[\left(1 - R^2 + k^2\right)/\left(2k\right)\right] \qquad (2.6.)$$

according to Mandel and Agol (2002).

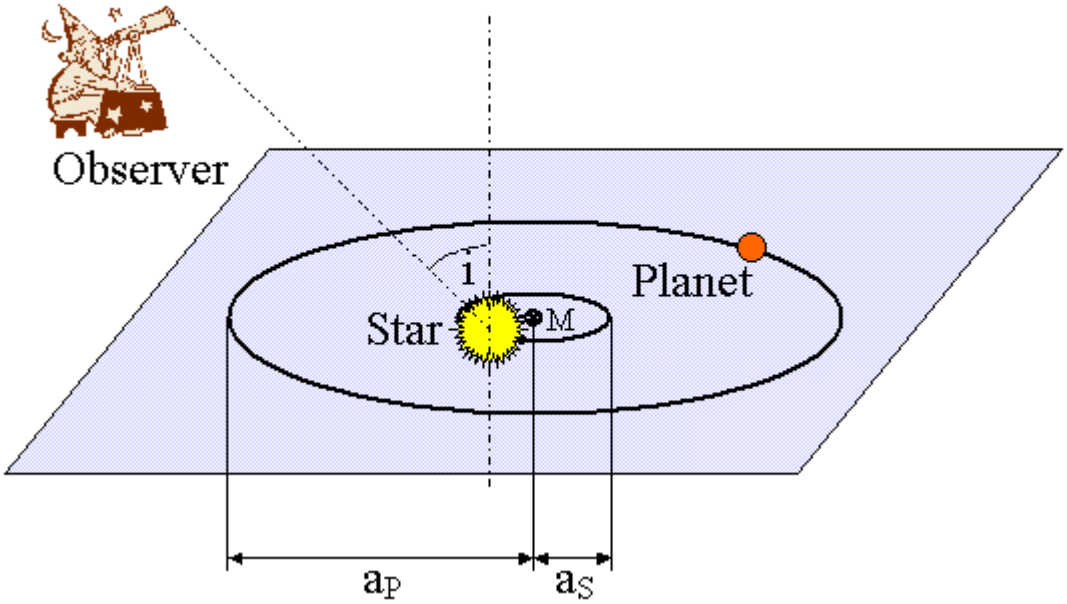

Figure 2.3.: A planet and a star orbiting both their common center of mass M. The orbit of the planet is described by its semi-major axis, a_p and the orbital period P. The inclination of the orbit, i is defined as the angle between the normal to the orbital plane (shown in grey) and the observer's line of sight.

These simulations of the transit shape without considering limb darkening can be used for the analysis of noisy data where no information about the curvature of the transit signal is attainable. A Jupiter-sized planet transiting a Solar-like star would cause a maximal signal depth of about 1%, whereas for Earth-sized planets this value reduces to 0.008%.

If the orbital period, P, of the planet is known, obtained from multiple transit detections or radial velocity (RV) measurements, then further calculations can be performed. Thus the normalized center-to-center distance k can be written as a function of time (assuming that the orbit is circular) according to Mandel & Agol (2002):

$$k = \frac{a_p \sqrt{(\sin \varpi t)^2 + (\cos i \cos \varpi t)^2}}{R_*} \qquad (2.7.)$$

where a_p is the semi-major axis of the planetary orbit, $\varpi = 2\pi/P$ is the orbital frequency and t the time measured from the center of the transit, and i is the inclination of the planetary orbit (see Figure 2.3.). The semi-major axis a_p can be derived from Kepler's third law knowing the mass of the host star M_*:

$$a_p^{\,3} = \frac{GM_* P^2}{4\pi^2} \qquad (2.8.)$$

where G is the gravitational constant. The mass of the planet is assumed to be small compared to the mass of the host star.

For a central transit (i = 90°) equation (2.7.) reduces to

$$k = \frac{a_p \sin \varpi t}{R_*}. \qquad (2.9.)$$

Then the time for the first/last contact of the planetary disk with the stellar disk can be calculated by replacing k with $(R_* + R_p) / R_*$

$$t = \frac{\sin^{-1}\left(\frac{R_* + R_p}{a_p}\right)}{\varpi} \quad . \qquad (2.10.)$$

Then the total duration of the transit event can be calculated

$$T = 2t = \frac{2\sin^{-1}\left(\frac{R_* + R_p}{a_p}\right)}{\varpi} = \frac{P\sin^{-1}\left(\frac{R_* + R_p}{a_p}\right)}{\pi} \quad . \qquad (2.11.)$$

Thus a Jupiter-like planet orbiting a Sun-like star with a period of 1.2 days and a semi-major axis of 0.0225 astronomical units (AU) (like the transiting planet around OGLE-TR 56) would cause a signal of 2.1 hours duration for a central transit. In an orbit similar to the HD 209458b orbit a central transit would take 3.1 hours, a 10-day orbit with a semi-major axis of 0.09 AU results in a transit duration of 4.2 hours. Thus the typical duration of a transit signal for giant planets orbiting Solar-like stars covers two to four hours. This timescale of a transit event for a Hot Jupiter class planet up to about four hours allows observation of full eclipse during a single observational night.

For planets with longer orbital periods the transit duration increases. A transit of the Earth across the Sun takes 13.1 hours, a transit of Jupiter takes 32.4 hours.

For non-central transits ($i \neq 90°$) the total transit duration can be calculated as (Seager & Mallén-Ornelas 2003)

$$T = \frac{P\sin^{-1}\left\{\frac{R_*}{a_p}\left(\frac{[1+R]^2 - k_{\min}{}^2}{1-\cos^2 i}\right)^{1/2}\right\}}{\pi} \qquad (2.12.)$$

yielding reduced transit durations for non-central transits compared to central transits.

2.1.2. Simulations considering limb darkening

The simulations of the transit signals considered so far were without limb darkening. If information about the curvature of full eclipse phase can be provided then limb darkening should be considered within the calculations. Limb darkening describes the following effect: the intensity peaks in the middle of the stellar disk with a minimum on the edge of the disk. Limb darkening is observed because the observer's line of sight passes through shallower, cooler and more absorbing layers of the photosphere as it moves away from the center of the stellar disk. The solar radius at which we can see the optical depth as being unity increases as we move the line of sight towards the edge (limb) of the star. The temperature of the stellar atmosphere is decreasing for an increasing distance from the center of the star. The intensity of the radiation emitted is a strongly increasing function of temperature (for a black body the intensity is proportional to the fourth power of the temperature). Therefore the intensity will be greater looking at the center of the star than looking at the limb.

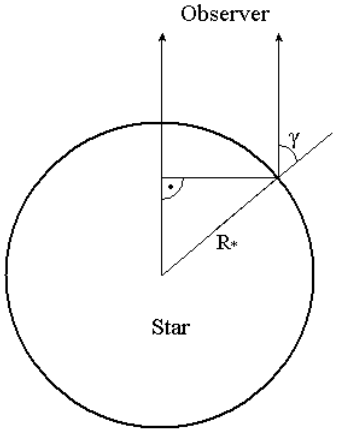

Figure 2.4. Geometry for the calculations of the limb darkening. The star is seen edge-on with the observer off the top of the page. The angle γ (necessary for limb darkening simulations) is the angle between the observer's line of sight

It is known that the distribution of the specific intensities depends on the effective temperature and local surface gravity of the star. For example, Díaz-Cordovés (1990) concludes that a quadratic limb darkening law represents a good approximation of the distribution for colder stars. For hot and larger main sequence stars a square root law is more adequate. For ground-based transit searches hot stars are generally not good targets because of their large size. For such stars, even eclipses of giant planets will cause very small transit signals not detectable from the ground for hot stars.
So the quadratic limb darkening law

$$I(r) = 1 - c(1-\mu) - d(1-\mu)^2 \qquad (2.13.)$$

is a good approximation useable for fitting transit signals detected by ground-based transit searches. Here r is the normalized radial coordinate of the star and I(r) is the specific intensity as a function of r with I(0) = 1, and μ = cos(γ), γ is the angle between the observer's line of sight and the normal to the stellar surface (see Figure 2.4.). c and d are the limb darkening coefficients depending on the effective temperature of the star, the local surface gravity of the star, the atmospheric transmission, and the transmission of the instrument (filter, mirror reflectivity, CCD sensitivity). These coefficients are available from Tables given by Claret (2000), who computed models of stellar atmospheres (Claret 1998) and used model atmospheres derived by Kurucz (1998). The coefficients are computed for 12 photometric bands, effective temperatures between 2000 K – 50000 K and with log g varying between 0.0 and 5.0. An additional parameter is the stellar metallicity ranging from 10^{-5} up to 10^{+1} solar abundances.

The flux of a star that is occulted by a planet considering limb darkening is given by

$$F(R,k) = \left[\int_0^1 dr\, 2rI(r)\right]^{-1} \int_0^1 drI(r)\frac{d\left(S(R,k)r^2\right)}{dr}, \qquad (2.14.)$$

where S(R, k) is the relative flux of a uniform source defined in equation (2.1.).

Numerical simulations were performed to model transit light curves considering quadratic limb darkening. Based on a subroutine by Mandel and Agol (2002) and the limb darkening coefficients of Claret (2000) these simulations allow the calculation of transit light curves for a given planetary size with high accuracy knowing the orbital parameters semi-major axis and orbital period, stellar parameters mass, radius, effective temperature and metallicity and the photometric band of the observations. These simulations were analyzed for obtainable transit depths and durations for Hot Jupiter planets for some typical star-planet systems.

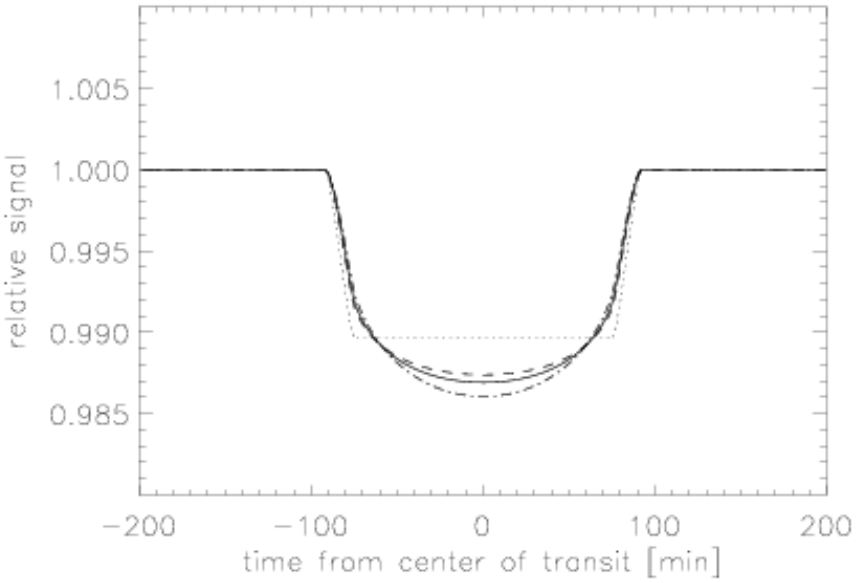

Figure 2.5.: Theoretical transit light curves with quadratic limb darkening effect for a Solar-like star occulted by a Jupiter-sized planet with an orbital period of 3.5 days in comparison with the light curve without consideration of limb darkening (dotted line) based on equation (2.14.). Remaining line styles mark calculations considering limb darkening for different photometric bands: V band (dashed-dotted line), R band (solid line) and I band (dashed line). Note that the signal depth in different bands does not vary significantly.

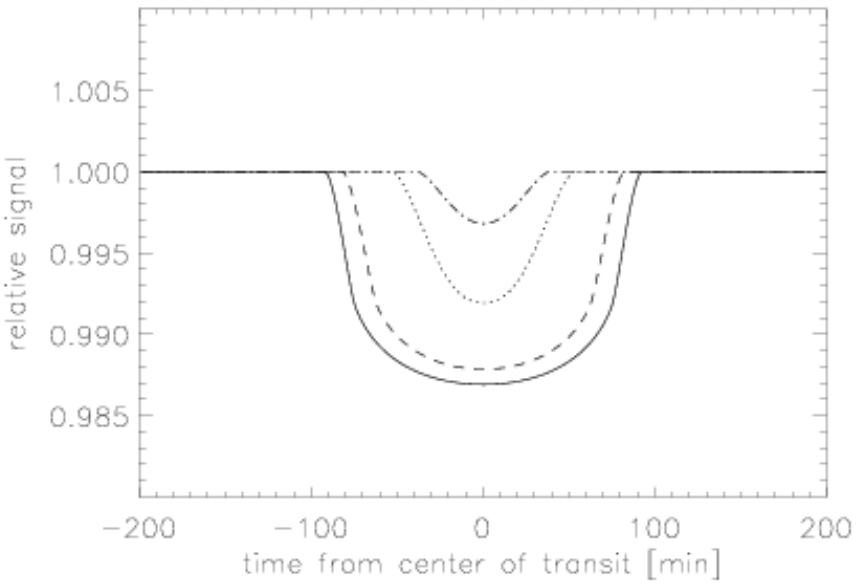

Figure 2.6.: Theoretical transit signal shapes of a Jupiter sized planet transiting a Solar like star computed for different minimal normalized center-to-center distances k_{min} (impact parameter): 0 (solid line), 0.5 (dashed line), 0.9 (dotted line) and 1.0 (dashed-dotted line). Note that the signal depth and the integrated signal for central transits ($k_{min} = 0$, $k_{min} = 0.5$) is larger compared to the theoretical signal not considering limb darkening (refer e.g. to the 1% signal in Figure 2.5.) due to the brighter central region of the stellar disk that is passed. However, for a full occultation far away from the center ($k_{min} = 0.9$) a signal depth smaller than 1% is calculated due to the fainter surface brightness of the occulted regions of the disk. The total integrated signal for all k_{min} equals for simulations with and without limb darkening.

Table 2.1.: The maximal signal depth in percent caused by transits of planets with a radius R = 1.0 R_{jup} is given for some main sequence stars. The stellar parameters were derived from Krautter et al (1994). The quadratic limb darkening was calculated with the limb darkening coefficients of Claret (2000), assuming central transits and solar metallicity of the host stars.

Spectral type of host star	*Signal depth no limb darkening*	*Signal depth limb darkening B band*	*Signal depth limb darkening V band*	*Signal depth limb darkening R band*	*Signal depth limb darkening I band*
F0 V	0.44	0.55	0.58	0.54	0.52
F5 V	0.59	0.74	0.76	0.71	0.68
G0 V	0.83	1.09	1.08	1.01	0.97
G2 V (Sun)	1.00	1.36	1.33	1.23	1.19
G5 V	1.19	1.61	1.58	1.46	1.41
K0 V	1.39	2.02	1.91	1.73	1.70
K5 V	1.93	2.96	2.88	2.66	2.52
M0 V	2.78	3.90	4.15	3.94	3.77

In Figure 2.5. theoretical transit signals considering the quadratic limb darkening effect for a Solar-like star occulted by a Jupiter-sized planet with an orbital period of 3.5 days are displayed for the VRI photometric bands. No significant differences of the signal shapes can be detected. A strong dependency of the signal shape can be reported for different impact parameters k_{min} as seen in Figure 2.6. Only transiting planets passing close to the bright center of the stellar disk can cause signals with maximal depth. Transits occurring close to the edge of the stellar disk show V-shaped signals with significantly smaller signal depths than for central transits. Note that the total transit signal integrated for all possible transit paths is of the same size as for the modeled transit signal not considering limb darkening.

Table 2.2.: The same calculations as made for Table 2.1, except the transiting planet has a larger radius R = 1.3 R_{jup} (comparable to the size of HD 209458b) Transiting planets of this size will be detectable orbiting F type main sequence stars.

Spectral type of host star	*Signal depth no limb darkening*	*Signal depth limb darkening B band*	*Signal depth limb darkening V band*	*Signal depth limb darkening R band*	*Signal depth limb darkening I band*
F0 V	0.75	0.93	0.98	0.92	0.88
F5 V	1.00	1.12	1.13	1.20	1.15
G0 V	1.39	1.83	1.82	1.69	1.63
G2 V	1.69	2.29	2.24	2.08	2.00
G5 V	1.99	2.69	2.63	2.46	2.36
K0 V	2.34	3.38	3.21	2.98	2.86
K5 V	3.28	5.00	4.86	4.50	4.26
M0 V	4.70	6.56	6.97	6.63	6.35

In Table 2.1. and 2.2. simulated transit depths are listed investigating the dependence of the transit signal depth and the photometric band used for the observations upon the quadratic limb darkening. Jupiter-sized planets transiting G type main sequence stars or smaller stars will be detectable, assuming that signal depths of 1 % are detectably in the light curves of these stars. The modeled signals considering limb darkening for central transits are by 30 % deeper compared with signals not assuming limb darkening for the simulations, especially for

K and M dwarfs 50 % deeper signals were calculated. On the other hand non-central transits show a decreased signal (see Figure 2.5.). With a detection limit of 1 % signal depth Jupiter-sized planets are detectable orbiting G0 V dwarfs or smaller stars.

2.2. Derivable parameters from transit signals

In the following it is described which planetary parameters can be derived from measured planetary transit signals. It is assumed that the transit depth can be measured and that the orbital period was derived from the light curve (or complementary RV measurements). Furthermore circular orbits are assumed. Information about the shape of the transit signal during the full occultation phase cannot be derived from the light curve due to photometric noise typical for ground-based observations. Therefore limb darkening is not considered. Then the planetary radius can be determined from the relative signal depth S_T:

$$R_p = R_* \sqrt{S_T} \qquad (2.15.)$$

The impact parameter k_{min} can be written as (Seager & Mallén-Ornelas 2003):

$$k_{\min} = \frac{a_p}{R_*} \cos i = \left\{ \frac{\left(1-\sqrt{S_T}\right)^2 - \left[\sin^2\left(T_F \pi / P\right) / \sin^2\left(T\pi / P\right)\right]\left(1+\sqrt{S_T}\right)^2}{1-\left[\sin^2\left(T_F \pi / P\right) / \sin^2\left(T\pi / P\right)\right]} \right\}^{1/2} \qquad (2.16.)$$

where T_F is the duration of the full occultation (excluding ingress/egress). With the known orbital period, mass M_* and radius R_* of the host star the orbital inclination can be determined with the help of Kepler's third law (equation 2.8.):

$$i = \arccos\left(\frac{R_* k_{\min} \left[4\pi^2\right]^{1/3}}{\left[GM_* P^2\right]^{1/3}} \right) \qquad (2.17.)$$

The semi-major axis a_p of the orbit is then derived from the first part of equation (2.16.). Thus the planetary parameters radius R_p, the impact parameter k_{min}, the semi-major axis of the orbit a_p and the orbital inclination i can be determined from the photometric light curve if the signal depth S_T and the orbital period P are determinable. Additionally the stellar mass M_* and the stellar radius R_* of the host star has to be known with the best precision available.

If information about the shape of the transit signal during the full occultation phase is available from high precision light curves then limb darkening has to be taken into account for the calculations. This however assumes better knowledge about the host star (effective temperature, the local surface gravity, metallicity) and the instrument (bandpass) for the determination of the limb darkening coefficients (for details see section 2.1.2.). Then theoretical light curves simulated by the method of Mandel & Agol (2002, equation 2.14.) can be fitted to the light curve data yielding determinations for the planetary parameters.

The combination of information obtained by RV measurements and transit observations yields some additional advantageous results. RV measurements provide information about the low mass limit $M_p \sin(i)$ for the planetary companion. With the known orbital inclination derived from the transit observation the real mass of the planet M_p can be derived confirming the planetary nature of the eclipsing object. Furthermore the mean density of the planet can be derived via

$$\rho_P = \frac{M_P}{{R_P}^3} \qquad (2.18.)$$

These determined planetary parameters are basic physical input parameters for models of planetary formation and evolution. Therefore the determination of these parameters with high precision for more planets is a main goal of transit search programs.

2.3. Probabilities for detecting a transit

How many stars have to be monitored to achieve a significant chance for detecting a transiting planet? To answer this question an equation is proposed:

$$N_{transit} = N_{phot} \cdot f_{tar} \cdot f_d \cdot f_{geom} \cdot f_{HJ} \cdot f_c \qquad (2.19.)$$

Main aspects like geometrical probability for a transit, f_{geom}, the fraction of suitable target stars, f_{tar}, the fraction of transit signals detectable from the ground, f_d, the fraction of stars that harbor a Hot Jupiter planet, f_{HJ}, the obtained duty cycle to reach a significant probability for the detection of three transit events, f_c and the number of high-precision light curves, N_{phot} , obtainable by ground-based transit searches are discussed. The latter is mainly limited by different photometric noise terms which will also be discussed in this section.

2.3.1. The fraction of stars harboring a Hot Jupiter planet

The most successful detection method for exoplanet candidates is the radial velocity (RV) method. This method is able to detect all Jupiter-mass planets in close-in orbits with $P < 10$ days (= Hot Jupiters) without biases. This enables an analysis of the frequency of such planets. Marcy et al. (2005) have summarized the results of the American RV search programs stating that about 1.2 ± 0.3% of the observed stars (mainly F, G, K dwarfs) harbor a Hot Jupiter planet.

A more extensive calculation of the fraction can be done using the data given by Schneider's Extrasolar Planets Encyclopaedia[4]. The six Hot Jupiter planets found by the new RV search programs N2K (Fischer et al. 2005) and the ELODIE metallicity-biased search for transiting Hot Jupiters survey (Da Silva et al. 2006) are excluded due to the incompleteness of the search programs. Another reason for excluding their discoveries is that these programs favor metal-rich stars as target stars. Additionally the six planets discovered first by transit searches are also excluded due to the strong bias for extremely short orbital periods of this search method. Then, 25 Hot Jupiter planets remain in the sample of 135 planetary systems, that harbor exoplanets, yielding that 18% of the known planetary systems harbor a Hot Jupiter planet. Further we assume that about 7 percent of all solar-like stars were detected to harbor giant exoplanets by RV searches (Udry, private communication, Marcy et al. 2005). Adding all statistical uncertainties leads to a fraction of 1.3 ± 0.3% of all solar-like stars that harbor a Hot Jupiter class planet very similar to the result reported by Marcy et al. (2005).

[4] http://vo.obspm.fr/exoplanetes /encyclo/catalog-main.php

2.3.2. The geometrical probability for a transit

A significant limitation of the transit method is the low geometrical probability that a planet crosses its host star in the observer's line of sight. For a full eclipse the probability is $(R* - R_p)/a_p$, if grazing occultations are included it is $(R* + R_p)/a_p$ (Koch & Borucki 1996). The geometrical probability for a transit of a typical Hot Jupiter planet (R_p = 1 R_{jup}, P = 3.5 days) orbiting a Solar-like star is about 10% (this number will be used for further analyses), for an orbital period of 10 days it drops to about five percent. A Very Hot Jupiter (P = 2 days) shows a geometrical probability for a transit of about 15 - 20% (see Figure 2.7.).

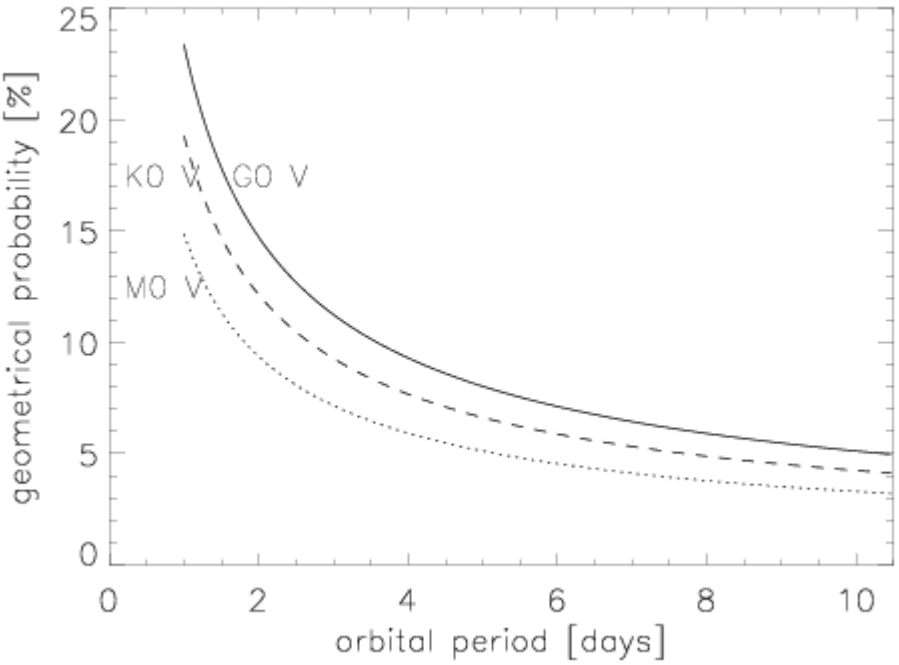

Figure 2.7.: Geometrical probabilities for transits of Jupiter-sized planets in close-in orbits for host stars of spectral types G0 V, K0 V and M0 V comprising typical target stars for ground-based transit surveys. The stellar parameters are derived from Krautter et al. (1994), the geometrical probabilities are computed as $(R* - R_p)/a_p$.

In Table 2.3. geometrical probabilities are listed for very Hot Jupiters (OGLE-TR-56b), hot Jupiters (HD 209458b and a Jupiter-sized planet orbiting a Solar-sized star in a 3.52-day orbit), the inner planets of the Solar System and Jupiter are listed for comparison. The transit probabilities include only full occultations. Grazing eclipses have a smaller signal depth and duration and will be harder to detect and are therefore excluded. Additionally maximal transit depths (V band), and maximal transit durations are listed (based on simulations made in section 2.1.2.). For observing a transit (with a full eclipse) of the Earth from a random direction outside the Solar System a probability of only 0.42 % is given, detecting a Jupiter transit is even more unlikely with a probability of about 0.1 %. This means that from a statistical point of view one would have to observe more than 1,000 stellar systems comparable to our own system to find one transiting Jupiter-like planet in an orbit like Jupiter. The fraction of stellar systems that contain a Jupiter-sized planet in a similar orbit is yet to be determined, the RV survey are still ongoing. Therefore the total number of Solar-like stars that have to be monitored to have a good chance to detect a Jupiter analogue planet is undetermined. The observations need to be uninterrupted for a full orbital period of about 12 years to detect one transit. The transit depth of up to 1.3% for a Jupiter-sized transit should be detectable for most ground-based search systems.

Table 2.3.: Characterization of transit signals of planets of the Solar System in comparison with the planets HD 209458 b and OGLE-TR-56 b orbiting a Solar-like star. For the calculations of the transit depth and duration it is assumed that the inclination of the orbits of the planets is 90°. For the geometrical probability of a transit only full eclipses are considered.

Planet	*Orbital Period [days]*	*Max .transit depth in V band [%]*	*Transit duration [hours]*	*Geometrical probability [%]*
OGLE-TR-56 b	1.212	1.7	2.4	20.5
HD 209458 b	3.525	2.0	3.1	10.4
Hot Jupiter	3.525	1.3	3.1	9.3
Mercury	87.969	0.0016	8.1	1.2
Venus	224.256	0.0101	11.2	0.64
Earth	365.256	0.0111	13.1	0.42
Mars	686.980	0.0032	16.1	0.30
Jupiter	4335.223	1.3	32.4	0.08

Transits of smaller, rocky planets with orbits like those of the inner planets in the Solar System are unlikely be detectable from the ground due to the small signal depth of around 0.01%. Additionally the probability to see the planetary orbit edge-on is small and makes a detection unlikely even for Jupiter-sized planets.

2.3.3. The fraction of suitable target stars

Transits with depths of around 1% and deeper will be detectable for ground-based transit searches. A typical size of a giant exoplanet is assumed to be 1 R_{jup}. The upper size limit of irradiated close-in gas giant planets resulting from models of gas giants in an evolved Solar System is approximately 1.5 Jupiters (Bodenheimer et al. 2003). Additional effects like kinetic heating as proposed by Guillot & Showman (2002) or dissipation of energy arising from ongoing tidal circularization of the planetary orbit by an additional planetary companion (Bodenheimer et al. 2001) can enlarge the atmosphere of the planets up to radii of about 2 R_{jup}. Gas giants located in younger stellar systems can still have larger radii up to 2.5 R_{jup}. This has to be kept in mind when 'transit cases' based on observations are investigated. But for the statistical approach made here these planets are neglected.

We assume an upper limit of 1.5 R_{jup} for the radii of close-in gas giants for this statistical approach to estimate the number of suitable target stars. Therefore transit signals with depths of about 1% and deeper will be detectable for stars with an upper limit of about 1.5 solar radii. This is approximately the size of an evolved F5 dwarf (Krautter et al. 1994).

A galaxy model was used to estimate the number of these kinds of small target stars in the observed target fields: the model of the stellar population synthesis of the Galaxy developed at the Besançon observatory (hereafter named Besançon model, Robin et al. 2003). Based on results of the Hipparcos satellite mission and parameters adjusted with the near-infrared survey DENIS[5] this dynamically self-consistent model can reproduce reliable predictions of star counts in any given direction but not the Galactic center. Additionally the Besançon model gives the following parameters:

a) Absolute luminosity, M_v

[5]The DENIS database, 2nd Release, http://vizier.u-strasbg.fr/viz-bin/ViZier?-source=II/252

b) Luminosity class
c) Spectral type
d) Effective temperature
e) Surface gravity
f) Age
g) Mass
h) V magnitude and magnitude differences to Johnson U, B, R, I, J, H, K, L magnitudes
i) Metallicity, [Fe/H].

To classify stars into two groups, namely less than or greater than 1.5 R_{sun} the absolute luminosity was used. According to Cox (2000) stars with an absolute luminosity larger than 3.5 have a radius < 1.5 R_{jup}. The absolute luminosity is a parameter that is dependent upon the age of the stars, thus the dependency upon the stellar size from the age of the object is included in this model.

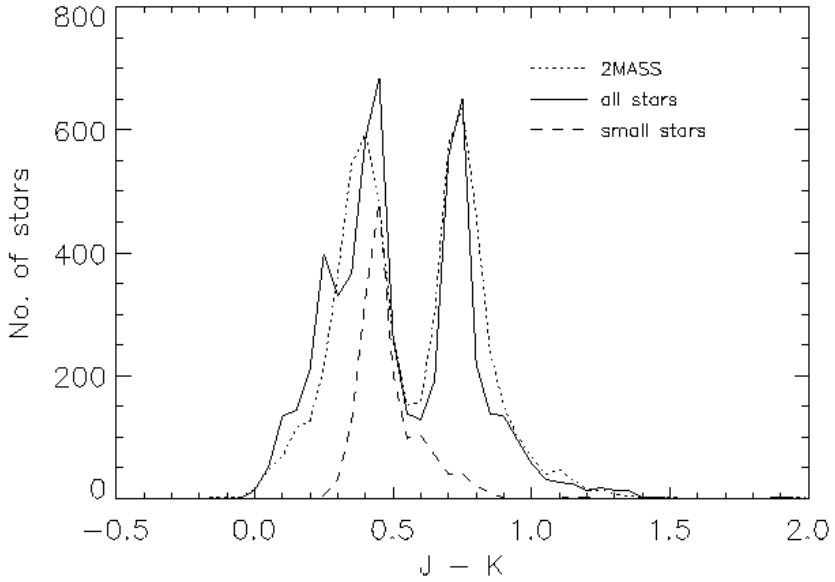

Figure 2.8..: The number of stars binned into 0.05 mag intervals is plotted versus the (J-K) color index for a typical Galactic target field (FOV 3.1° x 3.1°) from the Besançon model (V < 14). The solid line gives the total number of stars; the dashed line the stars with radii less than 1.5 solar radii. The J-K color index allows discriminating between giants and dwarf stars. The peaks with J-K < 0.5 contain mainly dwarf stars, whereas the peaks with J-K > 0.5 are mainly giants. Only about 27 % of all stars are small stars (dashed line) and therefore suitable targets for ground-based transit searches. For comparison with observational data 2MASS data are overplotted (dotted line). Note that the 2MASS stars were selected according to the (J-K) color given by the Besançon model.

Wide-angle searches monitor stars with sufficient precision down to magnitudes of 12-15. For this magnitude range typical target fields in the Galactic Plane are dominated by large main sequence stars and giants (see example in Figure 2.8.). Only about 20 percent of all stars are small enough to be sufficient target stars. The fraction strongly depends on the magnitude of the observed stars and the location of the target field in the Galactic plane.

Bright stars are usually giants or large main sequence stars due to the high absolute luminosity of this object. Small dwarf stars are objects with lower absolute luminosity and are therefore favored objects for deep searches. Thus, M dwarfs as the majority of the stars in the galaxy are present only with a very low number at magnitude ranges observed by wide angle searches.

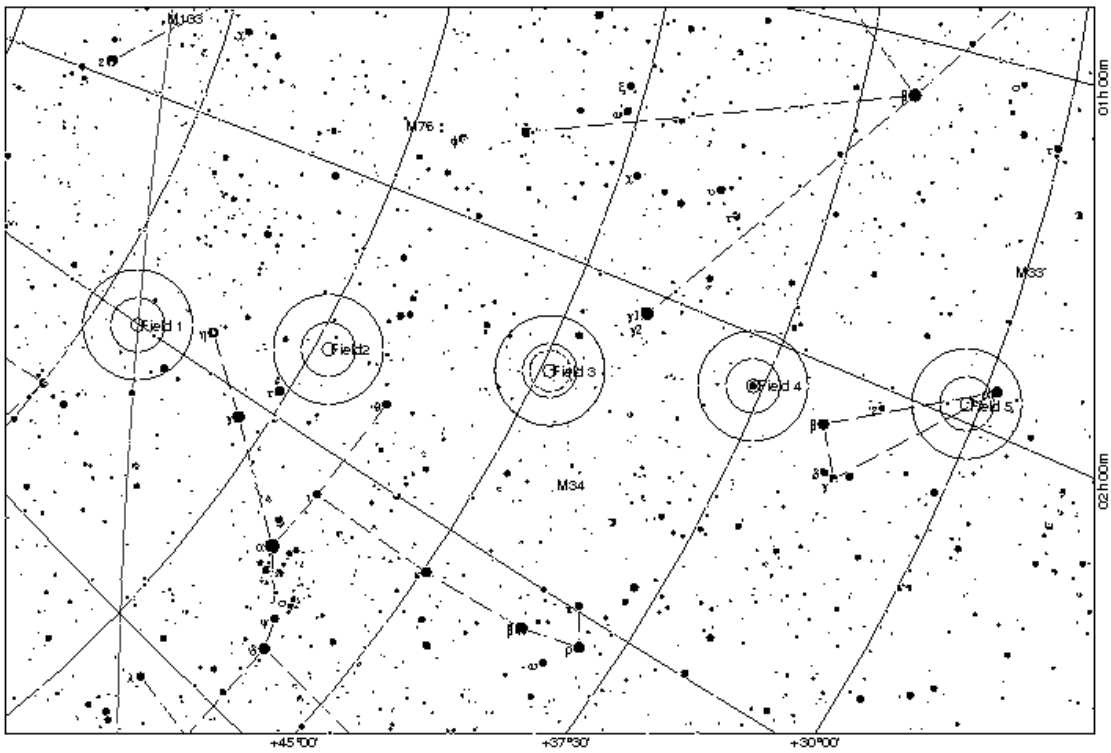

Figure 2.9.: Map (made with TheSky) of target fields that were modeled with the Besançon model to evaluate the fraction of small target stars. The single solid straight line on the left side (going through field No. 1) is the center of the Galactic plane. The distance of the target fields from the Galactic plane is increased stepwise by 7.5 deg with increasing field number.

The fraction of suitable target stars depends also on the location in the Galactic plane. If the line of sight form Earth goes through the Galactic plane or the Galactic bulge, then many background objects with large absolute luminosities can be seen. More favorable are observing directions above the Galactic plane to reduce the number of background objects. The fraction of suitable target stars was estimated for five target fields with different distances to the center of the Galactic plane (see Figure 2.9.) with the help of the Besançon model. This fraction is shown for different limiting R magnitudes in Figure 2.10. Target field No. 1 is centered in the Galactic plane, the distance to the Galactic plane is increased stepwise by 7.5° with increasing field number. For a limiting magnitude of R = 10 less than 10% of all stars are considered to be sufficient target stars. For magnitude R = 12 a stronger dependency upon the location of the target field is reported. In and close to the Galactic plane about 10% of the stars are good targets for transit search. This is increased to 30% for target field No. 5 with the largest distance from the Galactic plane. Going to deeper magnitudes further increases this effect, especially for magnitudes 15 – 16 the fraction of suitable target stars depends strongly on the location relative to the Galactic plane. For a limiting magnitude R = 14 target fields in the Galactic plane show a fraction of good target stars of about 20%, for fields above the Galactic plane of 40 – 60% is obtained.
Due to the decreasing total number of stars/deg^2 with increasing distance to the center of the Galactic plane it is important to count the number of suitable target stars/deg^2. These numbers for the five modeled target fields are given in Table 2.4. The maximal number of suitable target stars for the different target fields shifts from the fields above the Galactic plane for limiting magnitude R < 12 to the target fields centered in the Galactic plane for R < 18.

Therefore an optimized target field selection is an important factor to obtain a high probability for detecting a transiting planet. Note that the number of suitable target stars is more important than simply selecting the highest total number of stars.

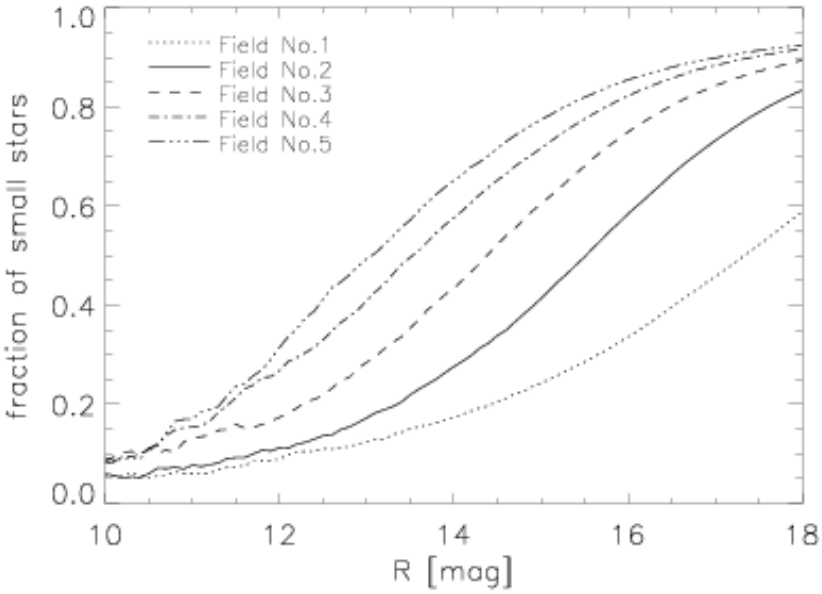

Figure 2.10.: The fraction of small stars for the 5 modeled target fields each separated by 7.5 deg to the center of the Galactic plane is plotted versus the R magnitude. The target field centered on the Galactic plane (No. 1) has the lowest fraction of suitable (= small) stars for all magnitudes > 10.5. The fraction of small stars increases with the distance to the Galactic plane for all magnitudes > 10.8. Note that for the brighter stars the number of small stars is low resulting in small number statistics.

Table 2.4.: Galactic coordinates and stellar densities are given for the five modeled target fields (Besançon model). The maximal number of suitable target stars for the different limiting magnitudes is shaded. Note that a typical reddening of 0.70 mag/kpc for all fields was assumed as recommended by the authors of the model. This is a good approximation for large FOVs in the Galactic plane. Local variations of the reddening can lead to different stellar densities especially for small FOVs.

Field No.	*l [deg]*	*b [deg]*	*Suitable target stars [# / deg^2] R < 12 mag*	*Suitable target stars [# / deg^2] R < 13 mag*	*Suitable target stars [# / deg^2] R < 14 mag*	*Suitable target stars [# / deg^2] R < 15 mag*	*Suitable target stars [# / deg^2] R < 18 mag*
1	130	+0.0	12	49	148	394	6640
2	130	+7.5	15	58	169	528	6150
3	130	+15.0	16	65	183	520	3650
4	130	+22.5	22	70	181	453	2465
5	130	+30.0	22	69	176	371	1688

2.3.4. The fraction of detectable transit signals

In this section it is estimated which fraction of transit signals can be detected by ground-based photometry. The detection limit is assumed to be 1%, so only signals of 1% depth and deeper will be detectable. Based on the definition of a suitable target star ($R < 1.5\ R_{sun}$) and the assumption that the distribution of planet sizes is uniform up to the maximal planet size of 1.5 R_{jup}, estimations for the fraction of detectable transiting planets can be made. The stellar distribution can be taken from the Besançon model, the radii of the stars, R_* are calculated from the surface gravity and the mass given by:

$$R_* = \sqrt{\frac{GM_*}{g}} \qquad (2.20.)$$

based on Newton's definition of the gravitational force.

Then the planets with different sizes are randomly distributed amongst the suitable target stars of the stellar distributions given by the Besançon model. The same target fields and limiting magnitudes as for the calculation of the fraction of the suitable target stars were chosen. In a next step the depth of the resulting transit signals was calculated according to equation 2.3. The resulting distribution of the signal depths were analyzed for signals with depths of 1% and deeper. An example for target field No. 2 can be seen in Figure 2.11. For a limiting magnitude $R < 14$ about 58% of all transit signals would have a depth of 1% and deeper. This fraction is not strongly dependent on the target field selection. Larger differences were found for different limiting magnitudes. For a limiting magnitude of $R < 12$, 50 – 55 % of the transit signals are detectable, for the limiting magnitude 14 this ranges from 55 – 60 %, for magnitude $R < 16$ the fraction is increased to 60 – 65 %.

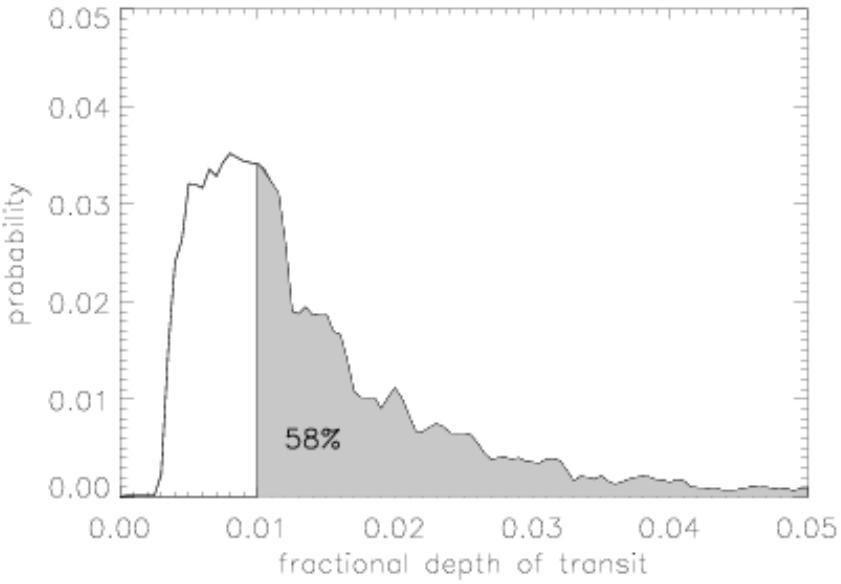

Figure 2.11.: The probability of finding a transit of different fractional depths is plotted for main sequence stars with $R < 1.5\ R_{sun}$ for the distribution of target field No. 2 given by the Besançon model ($R < 14$). The distribution of planetary radii was assumed to be uniform up to 1.5 R_{jup}. The percentage of transits with signals larger than 1% is 58%.

2.3.5. Photometric error budget

The number of high precision light curves that is obtainable with a photometric survey system depends on several factors: transparency of the atmosphere, throughput of the instrument, the number of undisturbed stellar PSFs that can be imaged on the CCD (charge coupled device, a semi-conductor image-sensing device usually in the form of a plane rectangular matrix of pixels, that converts the optical image into electrical signals) and the photometric errors of the measurements. The errors of the photometric measurements will add noise to the light curves, such that the scatter of the light curves of fainter stars will exceed the maximal noise level for which a transit signal can be detected.

To calculate the maximal number of high precision light curves (RMS < 1%) the photometric error budget for CCD images has to be analyzed. A CCD image consists of different kind of signals. Additionally to the signals originating to the imaged object(s) several other signals are contained. In the image a constant zero point is set for all pixels. This bias signal is disturbed by read-out noise. The read-out noise consists of Gaussian noise caused by the electronics of the CCD and the computer and is therefore specific for the used imaging system. For high-precision measurements like a search for transits of extrasolar planets read-out noise should not be the dominant noise term. The read-out noise relative to the stellar signal is called σ_r in the further.

The stellar signal itself consists of photons. The photons, that reach the pixels of the CCD detector, introduce free electrons due to the photoelectrical effect. The number of electrons is the real measured signal and is affected by statistical noise. This noise is often called photon or shot noise. For N stochastically emitted electrons the photon noise is given by Poisson statistics as $\sqrt{N}$, the relative photon noise σ_P is then calculated as (Newberry 1991):

$$\sigma_p = \sum_{i=1}^{n} \frac{\sqrt{N_i}}{N} \qquad (2.21.)$$

N is the integrated 'stellar' signal of n pixels, N_i is the signal of pixel i. The number of emitted electrons N_i is calculated as the product of the measured pixel values in ADU (analog-digital units) and the gain of the CCD.

Another noise source is introduced by the subtraction of the sky background signal from the total signal for an object measured in the image. The relative sky background noise σ_{Sky} is given as the summation of the photon noises for the n pixels used for the measurements of the stellar signal:

$$\sigma_{Sky} = \sum_{i=1}^{n} \frac{\sqrt{N_{Sky,i}}}{N} \qquad (2.22.)$$

where $N_{sky,i}$ is the pixel value of the sky background estimation for pixel i given in counts of e^- (Newberry 2001).

Further noise is introduced by thermally generated electrons. The number of these electrons is dependent upon the cooling temperature of the CCD and the exposure time. It is very specific for the used CCD detector. This noise is called thermal noise or dark noise. The relative thermal noise is called σ_t in the further.

Another major contribution for the total noise of light curves is scintillation noise. The relative scintillation noise was characterized by (Young 1993) as:

$$\sigma_s = 0.09 D^{-2/3} A^x e^{-h/h_0} (2T)^{-1/2} \qquad (2.23.)$$

Table 2.5.: Estimated scintillation noise (equation 2.23.) for some typical observational situations and wide-angle instruments.

Telescope Aperture D [cm]	*Integration time [sec]*	*Observational altitude h [m]*	*Airmass*	*Scintillation noise σ_s [%]*
5	15	0	1.5	0.011
10	15	0	1.5	0.0072
20	15	0	1.5	0.0045
30	15	0	1.5	0.0035
10	240	0	1.5	0.0018
20	240	0	1.5	0.0011
20	240	0	2.0	0.0019
20	240	0	3.0	0.0038
20	240	0	1.0	0.0006
20	240	4000	1.5	0.0007

where D is the diameter of the main mirror given in cm, A is the airmass (= 1/cos Z, Z = zenith distance of the observed star), h is the altitude of the telescope in meter, h_0 = 8000m is the scale height of the atmosphere and T the exposure time in seconds. The exponent x varies from 1.5 to 2.0 dependent upon the angle between the observing direction and the wind direction in the upper troposphere. An average exponent of 1.75 is recommended for observations at moderate airmasses.

In Table 2.5. scintillation noise for some typical wide-angle search systems as a function of integration time, altitude of the observational site and airmass is listed. For systems with small apertures (5-10cm), short integration times yield scintillation errors of about 1%. Taking longer exposures could decrease the scintillation noise to an acceptable level (0.2%). For medium-sized telescopes (20-30cm) scintillation noise is negligibly low except for high airmasses and short exposure times.

Further noise is added by all stages of data reduction, including corrections for bias, dark current and interpixel variations in detector sensitivity (flat field correction) and is called calibration noise σ_c.

All noise sources mentioned before are uncorrelated to each other. Therefore they can be combined in quadrature, the relative total noise σ is calculated as:

$$\sigma = \sqrt{\sigma_r^2 + \sigma_p^2 + \sigma_{Sky}^2 + \sigma_t^2 + \sigma_s^2 + \sigma_c^2 + \sigma_o^2} \qquad (2.24.)$$

where σ_o contains all other additional undefined noise sources. Thus, the largest single noise contribution always dominates the total noise.

For an optimal detector the relative read-out noise σ_r and the relative thermal noise σ_t should be negligible low for the measured signal range. An observational site with a low sky background level minimizes σ_{Sky}. CCDs with a small pixelsize are advantageous giving a smaller collecting area per pixel and therefore yield lower sky background signals. As shown in table 2.5. scintillation noise σ_s can be minimized by large apertures of the chosen telescope and longer exposure times. The calibration noise σ_c has to be minimized by an optimized image calibration process. Thus, in an optimized observational situation all such contributions to the total noise should be negligibly low. Then photon noise becomes the dominating noise source.

Photon noise can be estimated applying some simple assumptions typical for wide-angle transit surveys. If the point spread function (PSF) of a star shows a Full Width Half Maximum (FWHM) of about two pixels (= Nyquist sampled PSF as recommended for high precision photometry for transit searches, see Bakos et al. 2004, Howell & Everett 2001), then a typical signal of a bright but unsaturated star on a 14-bit CCD (typical for wide angle transit surveys) has a strength of about 10^6 electrons yielding a minimal photon noise of 0.1%. according to equation 2.21. A signal 100 times weaker (N=10^4 electrons) results in a photon noise of 1%. The counts in electrons N can be converted in magnitudes M:

$$M = C_M + 2.5 \log N \qquad (2.25.)$$

where a C_M is a constant magnitude number to convert the instrument magnitude 2.5logN to a photometric system. Then the range of 10^4 to 10^6 corresponds to a range of five magnitudes where a photometric precision < 1% could be obtained assuming photon noise is the dominating noise term for the whole magnitude range.

2.3.6. The number of obtainable high precision light curves

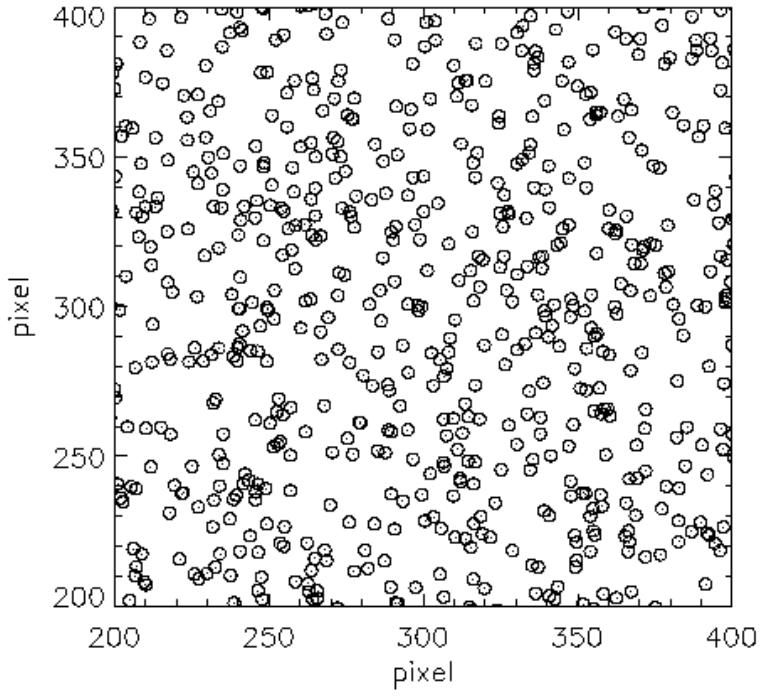

Figure 2.12.: Crowding simulation. A 200 pixel by 200 pixel cut is plotted. The aperture radius was set to four pixels.

In the previous section it was suggested, that in the ideal case of photon noise limited transit search, high precision light curves (RMS < 1%) could be obtained for a magnitude range of five mag. In the following it will be estimated how many undisturbed stellar PSFs can be imaged onto one CCD based on information about the magnitude range.

The stellar images are assumed to exhibit a PSF with a FWHM of 2 pixels (see section 2.3.5.). Further, we assume a photometry with an aperture radius of 4 pixels to obtain maximal signal to noise (S/N, see Howell & Everett 2001). A disturbed PSF is defined as having at least one more PSF within a center-to-center distance of two aperture radii (= 8 pixels). A conservative magnitude limit of four magnitudes is defined, thus PSFs with a signal 4 mag lower than the inspected PSF have no influence and cannot disturb this PSF.

The distribution of the stellar magnitudes is again taken from the Besançon model. With target field No. 2 a typical target field in the Galactic plane was chosen for the statistical simulations. The number of stars in the CCD image was varied from 4000 to 30000 in the observed magnitude interval with a range of 5 mag.

Most wide-angle transit searches use a CCD with 2048 by 2048 pixels (called a 2k CCD). The PSF of the stars were distributed randomly on the CCD (see Figure 2.12.). The number of stars with no disturbing neighbors according to the definition given above was analyzed. A maximal number of 4680 PSFs from a total number of about 15000 PSFs in the image were found to be undisturbed. This fraction of undisturbed PSFs of about 30% will be used as the number of obtainable high precision light curves N_{phot} for further analyses.

Note that photometric procedures like PSF fitting or image subtraction can improve this 'crowding' problem giving higher numbers of undisturbed signals.

2.3.7. Orbital phase coverage

The coverage in orbital phase has to be good enough to observe at least one transit event to be able to start with the follow-up analysis. The ideal case is to detect three transit events to be able to determine the orbital period of the planet and to be able to detect weak transit signals in folded light curve data. Observing only one transit event will make follow-up observations more intensive, but a high number of false alarms can be identified in this early stage already reducing the total amount of follow-up observations. Nevertheless a higher number of RV measurements will have to be made to determine the orbital period if only one single transit detection was made. Additional photometric observations will be necessary to make sure that the phases of the radial velocity changes and the transit are the same. Photometric observations at a phase shift of about 0.5 are important to exclude secondary eclipses for binaries where a smaller occultation signal is detected (small star is covered by large star).

Approaching 100% orbital phase coverage would be optimal. An advantage of reaching full orbital phase coverage for the suggested orbital period is the possibility to identify grazing eclipses of binaries with a high mass ratio between secondary and primary components due to the gravitational darkening effect (gravitational forces lead to deformed stars which show deformed light curves). In this case ellipsoidal variations in the light curves of binaries with a minimal mass ratio of 0.4 caused could be detected to identify such systems with the photometric data.

Which orbital phase coverage can be obtained for ground-based transit surveys? Several limitations of different origins exist. The most common limitations are:

a) Altitude constraint: As already concluded in section 2.3.2. observations at airmasses > 2 (altitudes < 30 degree) are not recommended because of quickly increasing scintillation noise and stronger extinction effects.
b) Seasonal limitations: Target fields are typically observable night by night for up to 4 months per season from a central European site for more than three hours at a time.
c) High background due to moon: It was assumed that a period between 5 -10 days around full moon has to excluded because stray light worsens the photometric quality. The duration of the excluded period depends on the distance between the target field and the moon and the phase angle of the moon. If the moon is closer to the field than 30 degrees observations are not useful. Also, five days centered on full moon are always excluded due to the brightness of the sky.
d) Bad weather

Another limitation is added by the use of a German mount (as used for BEST) that limits the maximal duration of the observations to 8-10 hours per night depending on the hardware limitations (collision of mount and telescope tube or CCD) of the mounts used. This is a minor disadvantage because only during the winter period longer observations would be possible.

With these limitations it is possible to observe about 630 hours for 84 nights in four months in spring or autumn from a central European site like the TLS. Target fields with this maximal observability are circumpolar fields that move through the zenith position. A model was developed to estimate the phase coverage of potential transiting exoplanets for the attainable total duration of observations for a chosen target field. The orbital period was chosen to be a free parameter along with the epoch of the transit event. Both parameters were determined in a Monte Carlo approach within given limits of 0.5 to 10 days for the orbital period and all possible epochs within the first and the last observation with a minimal number of epochs of one million to reach a high statistical basis. Detection was defined to be an event of a minimal duration of 1.5 hours that occurred during the observational times.

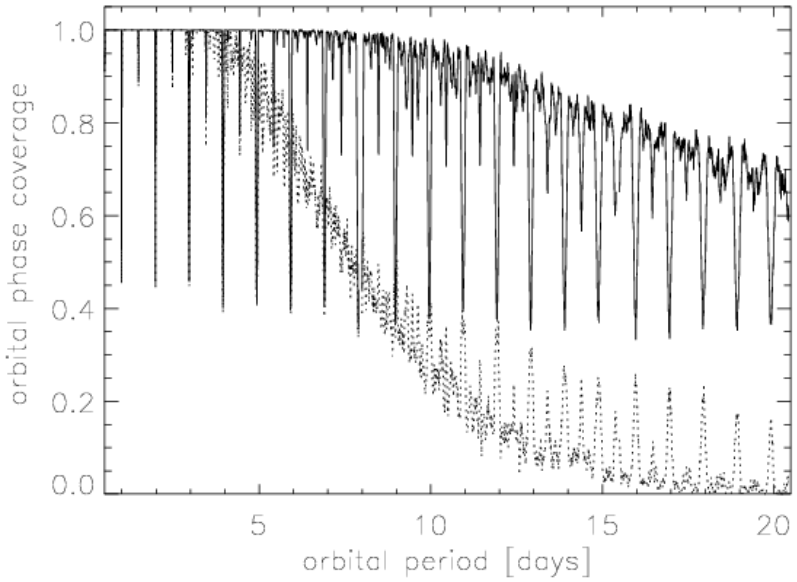

Figure 2.13.: Orbital phase coverage vs. orbital period for a duty cycle of 80 percent as can be obtained on an observational site with very good meteorological conditions. 100 percent orbital phase coverage for one detection is reached for hypothetical planets with orbits up to 7.5 days. For three detections full phase coverage is obtained for periods of up to 3.5 days. Similar orbital phase coverage can be reached by the OGLE-III campaigns from Las Campanas, Chile.

These simulations were provided for different duty cycles (efficiency of the observations during time not excluded from observations so far). A duty cycle of 100 percent is rather unrealistic. Only very few observational sites (e.g. Chile) feature nearly optimal weather. A duty cycle of 80 percent can be reached there (see OGLE campaigns, Udalski et al. 2002a, 2002c). Thus a duty cycle of 80 percent for a 4-month observational campaign from Chile during spring or autumn is assumed for a realistic simulation of the orbital phase coverage (see Figure 2.13). 100 percent orbital phase coverage for one detection is reached for hypothetical planets with orbits of up to 7.5 days. For periods of about 10 days there is still phase coverage of 95 percent reached which would imply the detection of Hot Jupiter planets with detectable transit signals at least once. For three detections full phase coverage is obtained for periods of up to 3.5 days. Nearly all transits of planets with orbital periods up to

five days could be monitored. Thus an observational site with a duty cycle of 80 percent would be an ideal observational place for a one-site/one instrument transit search concerning sufficient orbital phase coverage.

Most observational sites in Europe with an existing infrastructure allow lower duty cycles of 40 to 60 percent. Thus the orbital phase coverage was simulated for a duty cycle of 50 percent (see result in Figure 2.14). 100 percent orbital phase coverage for one detection is

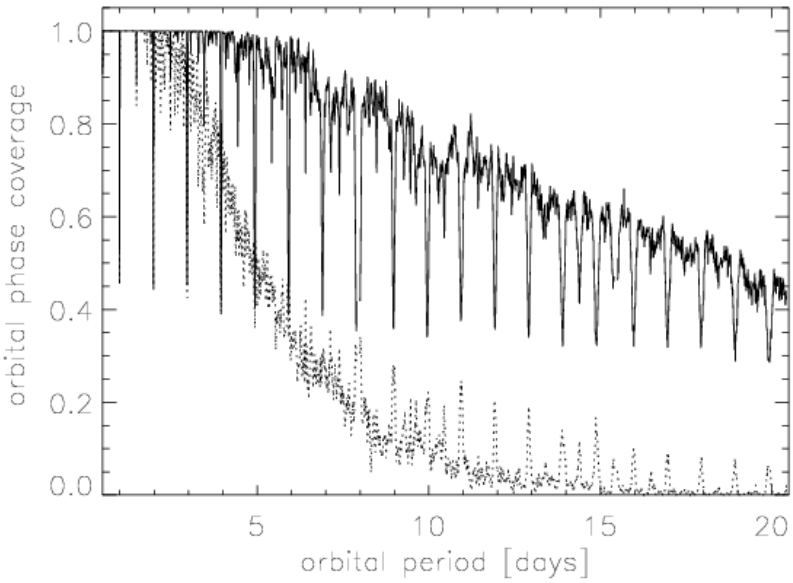

Figure 2.14.: Orbital phase coverage vs. orbital period for a duty cycle of 50 percent as can be obtained on a typical site with good meteorological conditions like OHP. 100 percent orbital phase coverage for one detection is reached for hypothetical planets with orbits up to 4.5 days. For three detections full phase coverage is obtained for periods of up to 2 days.

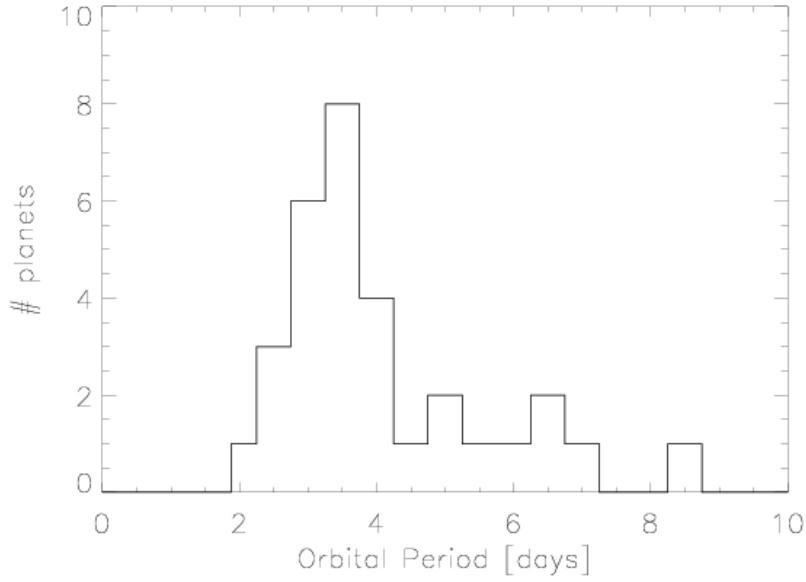

Figure 2.15. Number of Jupiter-sized exoplanets detected by RV searches vs. orbital period as given by the Extrasolar Planets Encyclopaedia[6]. The number peaks at about 3 - 4 days. 24 of 31 planets have an orbital period less than 5 days. The RV measurements are not biased for

[6] http://vo.obspm.fr/exoplanetes /encyclo/catalog-main.php

orbital periods less than 5 days; the RV precision reached allows detecting Neptune-mass planets in close-in orbits and the RV campaigns are going on for several years now**.**

for hypothetical planets with orbits up to 4.5 days. For three detections full phase coverage is obtained for periods of up to two days. Thus most of the Hot Jupiter planets will be detected once assuming that most of them have orbital periods up five days as suggested by RV searches (see Figure 2.15.). Three detections could be made for planets with typical orbital periods of three to five days with 50 – 80 % certainty (with an average of 65 % for further calculations).

2.3.8. Resulting detection probabilities

In sections 2.3.2.-2.3.7. the following parameters of equation 2.19. were estimated: The fraction of stars that harbor Hot Jupiter planets, f_{HJ}, the geometrical probability for a transit of Hot Jupiter planets, f_{geom}, the fraction of suitable target stars, f_{tar}, in typical Galactic target fields, the fraction of transit signals that exceed the detection limit of ground-based photometry and are therefore detectable, f_d, the number of obtainable high precision light curves, N_{phot} and the attainable orbital phase coverage for three detections, f_c, from a good European observing site. These numbers are now applied to formula 2.19., the used values for the parameters and the resulting detection probabilities for transiting exoplanets can be seen in Table 2.6 for target fields in the Galactic plane (field No. 1 and 2). For a limiting magnitude of R < 12 (typical for 10cm telescopes) a probability of 21 ± 6% per observed target field can be attained. In Brown (2003) a detection probability for the 10cm STARE telescope is given: 0.39 detectable transits for 10,000 stars observed. This corresponds to a detection probability of 18% for one observed target field in this analysis in good agreement with the calculated 21% here. Observing with a 20cm telescope (BEST, R < 14) could double the detection probability mainly due to the higher fraction of observed suitable stars.

Table 2.6.: Estimates for the parameters of equation 2.19. and resulting detection probabilities for the detection of one transiting planet per observed target field for the limiting R magnitudes 12 and 14 for typical target fields in the Galactic plane (field No. 1 and 2).

Limiting R magnitude	N_{phot}	f_{tar}	f_d	f_{geom}	f_{HJ}	f_c	*Detectable transiting planets*
12	4680	0.10	0.50-0.55	0.10	0.013	0.50-0.80	0.21 ± 0.06
14	4680	0.20	0.55-0.60	0.10	0.013	0.50-0.80	0.45 ± 0.13

If three target fields per year can be observed then the annual detection probabilities are increased. For the limiting magnitude R < 12 a transiting Hot Jupiter could be detected with about 63 ± 18% certainty, for deeper observations (R < 14) more than one planet (1.35 ± 0.39) can be detected.

The detection probabilities could be improved by:

- Maximizing the duty cycle to attain a phase coverage close to 100%.
- Optimized target field selection to maximize the number of suitable target stars.
- Observing at deeper magnitudes to maximize the fraction of suitable target stars.

2.4. Summary of chapter 2

In this chapter an overview is given on how to simulate transit signals and derive the planetary parameters from the transit signal. The initial simulation does not include the limb darkening effect for the stellar host. This can be used for noisy signals where no information about the curvature of the signals during the phase of full occultation can be obtained. In a next step limb darkening is included in the simulations. Based on the article of Mandel & Agol (2002) the quadratic limb darkening law is implemented using limb darkening coefficients of Claret (2000). For typical cases like Hot Jupiter transits and transits of the planets in the Solar System the resulting transit signals are calculated and analyzed mainly for signal depth and duration. Jupiter-sized planets transiting a Solar-like star causes a signal of 1% depth and 3 hours duration for a typical 3.5 day orbital period. The maximal depth for a transit signal is calculated to be about 5-10% if a M dwarf is occulted.

Generally the signal depth depends mainly upon the ratio of the radii of planet and star. For non-central transits where the planet covers only the outer regions of the stellar disk a significantly reduced transit signal depth and duration of the signal results. Additionally the duration of the transit signal mainly depends upon the stellar size and the orbital period of the planet. Therefore it is recommended to simulate transit signals of non-central transits with models considering limb darkening.

In section 2.2. it is described which parameters can be derived from measured transit signals. Single signals allow the determination of the radius of the transiting objects and give a first approximation for the orbital inclination of the planet. If further signals have been measured and the orbital period is known then the inclination of the planetary orbit can be calculated more accurately. In combination with radial velocity measurements (which give the lower mass limit for the planet M sin i) the mass of the planet can be derived. The mass determination allows discrimination between eclipses by small M dwarfs, brown dwarfs or Jupiter-sized planets, which can all have the same size. Additionally the combination of the planetary parameters radius and mass allows the determination of the mean density of the transiting object.

Some estimations have been derived for the probability of detecting a transiting Hot Jupiter planet orbiting a Solar-like star ($R < 14$) with a typical wide-angle search system in section 2.3. Aspects like the probability that a star harbors a Hot Jupiter, the geometrical probability that this planet transits its host star and the obtainable coverage of the orbital phase with a duty cycle of 50% are considered for this analysis. Additionally the fraction of suitable host stars (stars with a radius less than 1.5 R_{sun} for which a transit signal can be detected by ground-based photometry) is analyzed with the help of the Besançon model of the stellar population synthesis of the Galaxy (Robin et al. 2003) yielding only 10 - 20% percent of suitable host stars for the monitored magnitude range of typical target fields in the Galactic plane. The number of obtainable high precision light curves (RMS < 1%) has been determined by an analysis of the photometric error budget (including photon noise, background noise, scintillation noise) to calculate the observable magnitude range. Further the crowding situations (overlapping of stellar signals) are simulated to calculate the maximal number of undisturbed stellar signals for a 2k CCD as used by most wide-angle transit searches. According to equation 2.1. all these limitations contribute to the detection probability for a transiting Hot Jupiter. This probability is estimated to 20-50% for a 4-month observational campaign of a typical target field in the Galactic plane. It mainly depends on the monitored magnitude range and the number of obtained high precision light curves for a given instrument.

3. The Berlin Exoplanet Search Telescope (BEST)

The Berlin Exoplanet Search Telescope (BEST) is a search program initiated in 2001 by Heike Rauer at the Institute for Planetary Research of the German aerospace agency 'Deutsches Zentrum für Luft-und Raumfahrt' (DLR). The main goal of this initiative was to support the French-led satellite mission COROT scientifically. Ground-based observations to search for transits of Jupiter-sized exoplanets with a small telescope system similar to the size of the COROT satellite were carried out to widen the knowledge about the relatively new transit search method.

In the following sections the instrumental set-up of BEST during the initial observation phase at the Thüringer Landessternwarte (TLS) Tautenburg will be described and some comparison with other transit search systems will be provided.

3.1. The instrument

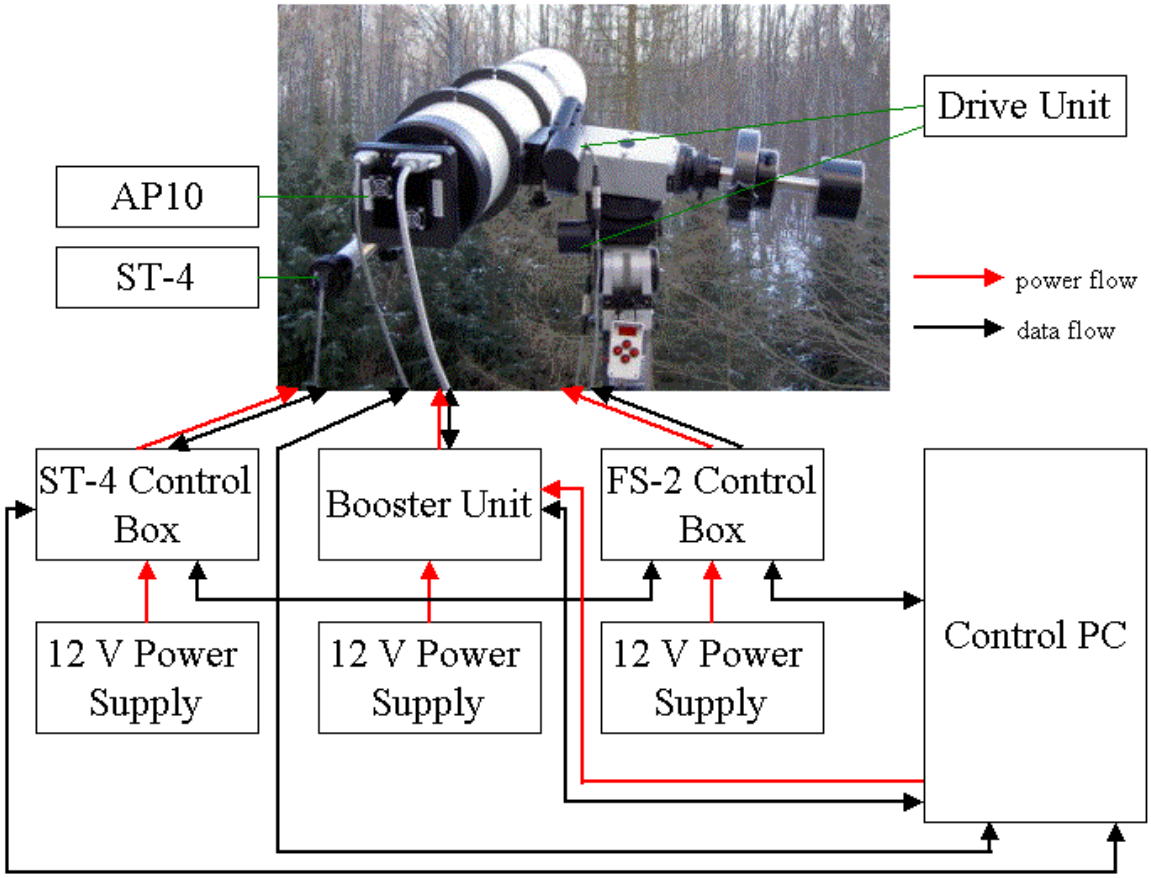

Figure 3.1.: Scheme of the Berlin Exoplanet Search Telescope system. Red lines show the flow of power, black lines the flow of data. Note that crossing lines are not connections between the lines. The control PC and all 12 V power supply boxes are supplied by a single power source.

The Berlin Exoplanet Search Telescope (BEST) system consists of a telescope, a German equatorial mount, a CCD camera, an autoguider system, a control PC and an enclosure as weather protection. All parts of the telescope system are commercially available, so it is straightforward to set up additional similar systems or replace defect subsystems. An

overview of the system is given in Figure 3.1. A more detailed description of the single components is given below.

3.1.1. The telescope

To be able to detect a transit of an exoplanet it is important to observe a high number of stars simultaneously over a long period with high photometric precision. Therefore it is very important to have a large field of view (FOV). All stars in this FOV should have the same good photometric precision. To achieve this we selected a Flat Field Camera (FFC) as our optical instrument. A FFC is a Schmidt-Cassegrain telescope. In contrast to the Schmidt telescope the focal point occurs outside the telescope, and it is therefore easier to connect an instrument at the external focal plane instead at a the location of an internal focal as typical for a conventional Schmidt telescope (see scheme of the telescope in Figure 3.2.).

A main component of the selected FCC 2.7 of Lichtenknecker Optics is the correcting lens. The correcting lens used is a special design of Lichtenknecker Optics to give a flat image in the focal plane in contrast to the normal Schmidt design with a curved image in the focal plane. Additionally the Lichtenknecker lens corrects for aberration as normal Schmidt lenses do, so a wide area of the sky can be observed.

The 230-millimeter diameter mirror is made from Duran borosilicate glass, a material with a low thermal expansion coefficient, developed by SCHOTT.

The aperture of the telescope is 200 millimeters, the focal length of the FFC is 540 millimeters. This results in flat images with a diameter of 28 mm in the focal plane, showing a 3.1-degree square field of the sky. The total tube length is about 700 mm long and 230 mm in diameter.

For focusing the secondary mirror has to be moved manually. The focus position is in most cases stable over single nights. Refocusing is only necessary when the temperature has changed by several degrees.

A dew cap with the same diameter as the tube and a length of 270 mm is mounted atop of the telescope above the corrector plate. Both dew cap and corrector plate can be heated with a Kendrick Dew Remover system to prevent condensation in high humidity weather conditions.

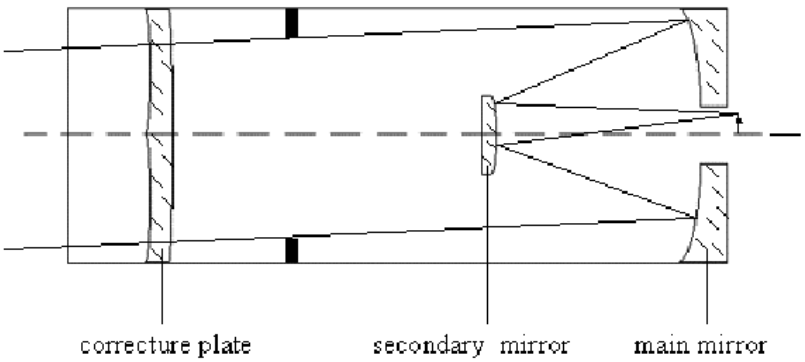

Figure 3.2.: Optical scheme of the Flat Field Camera (FFC) of Lichtenknecker Optics. The light enters through the correcting lens. The main mirror collects the light and reflects it to the secondary mirror. The secondary mirror redirects the light through the central hole in the main mirror to the focal plane behind the main mirror.

3.1.2. The CCD

In combination with the telescope an AP10 camera system of Apogee Instruments Inc., USA is used. This CCD (Charged Coupled Device, see section 2.3.5) camera has a Thomson TH7899M grade E chip with 2048 x 2048 pixels, the pixel size is 14 x 14 micrometer square with 100 % free aperture. The pixel scale is about 5.5 arcsec. The resulting image zone is 28.67 mm x 28.67mm, comparable to the size of a small format photographic film. The well depth is approximately 200,000 electrons; the gain was set to 11.4 ADU for the grade E CCD by Apogee Instruments Inc. The digital resolution is 14 bit, resulting in a saturation level of 16384 ADU and a short readout time of about 9 seconds at 1.3 MHz speed. Therefore, the dead time of the system due to readout is negligibly small. The quantum efficiency of the Thomson chip peaks at almost 40 % between 650-800 nm (see Figure 3.5.).

Defocusing is necessary to get well-sampled point spread function of the stars (Full Width Half Maximum FWHM > 2 pixel, see section 2.3.5. for details).

The bias level (for definition see section 2.3.5.) shows a nightly variation depending on the ambient temperature. Temperature dependence of the bias level yields leads to some long-term instability with a bias level range of about 25 ADU during the different seasons. The readout noise can be influenced by other noise sources; the orientation of the TLS 2m telescope and the ambient temperature and humidity was found to be important in this respect. The bias frames show a relatively constant pattern, a few bad (but stationary) columns and some bad pixels.

The dark current is highly dependent on the cooling temperature of the CCD. The grade E CCD chip had several thousand hot pixels, which do not completely disappear after dark correction.

Figure 3.3.: Apogee AP10 camera system (front). In the centre the entrance window is seen.

Figure 3.4.: AP10 camera system as seen from the back mounted on the telescope. The cooling system, the data transfer cable and the control cable can be seen.

During the first 2 years of operation we used the grade E chip for the CCD described above. This chip was damaged by a power surge inside the CCD system in April 2003 and had to be replaced. To reduce the influence of the dark current and hot pixels, a grade H CCD chip with a dark current reduced by a factor of three was chosen to be the new CCD chip for the BEST system. This upgraded system was only used during one night at TLS to collect data of

regular target fields in September 2003. Main characteristics for both CCDs are given in Table 3.1.

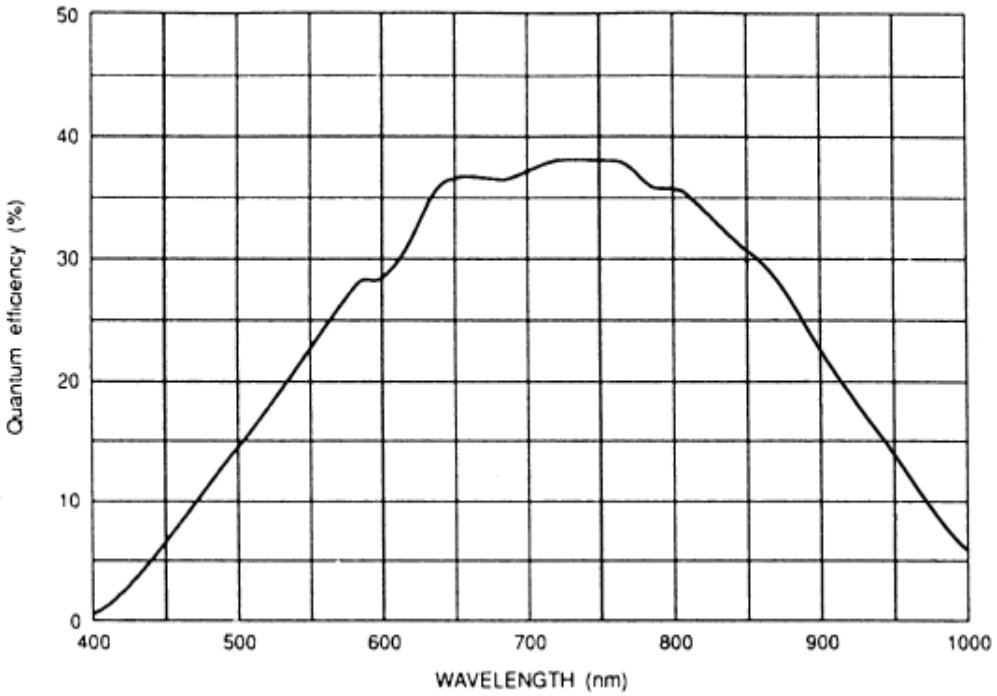

Figure 3.5.: Typical spectral response curve of a Thomson TH7899M CCD (©Thomson-CSF). The visible wavelength range and some near-IR wavelength range is covered.

Table 3.1.: Characteristics of the CCD performance given for both CCD chips.

	Grade E CCD	*Grade H CCD*
Format [pixels]	2048 x 2048	2048 x 2048
Pixel size [μm]	14	14
Gain [e^-/ADU]	11.4	12.5
Well depth [ADU]	16384	16384
Well depth [e^-]	186777	204800
Bias level setting [ADU]	311	361
Nightly variation of bias level [ADU]	±2	±2
Readout noise [ADU]	1.9-2.2	1.6-1.8
Dark current/sec at T = -20°C [ADU]	0.09	0.03
Dark current/sec at T = -29°C [ADU]	0.05	-
Dark current/sec at T = -48°C [ADU]	0.02	-

The CCD is cooled with a 2-stage thermoelectrical Peltier cooler with forced air. Cooling temperatures of 38 K below ambient temperature were reached with the cooling system of the grade E system, the upgraded system of the grade H CCD reached 42 K temperature difference. The cooling process takes about 20 minutes, and temperature stabilizing takes 15

additional minutes. Cooling of the CCD is necessary to reduce the number of thermal emitted electrons in the pixels of the CCD (= dark current).

The camera is controlled by an ISA-card (PCI bus card) mounted in a Windows-NT4.0-PC. During our observations in Tautenburg the PC was situated in the control room of the 2m-telescope at a distance of 35m from the Berlin Exoplanet Search telescope system, so we had to use a data transfer cable (37 pin D connectors on each end) and control cable (15 pin connectors) with a length of 35m. Data transfer was only possible with a remote booster unit made by Apogee. The ISA card is connected to the remote boost unit with the data transfer cable, and the remote boost unit is connected to the CCD with a 3m data transfer cable. The boost unit also supplies power to the AP10. The boost unit is powered by a 12V power supply unit (see also the electrical scheme Figure 3.1.).

The CCD is controlled by the software MaxIm DL (version 3) of Diffraction Limited, Canada. This software allows to control the cooling temperature of the CCD. Taking images of different kinds (bias, dark, light) is initiated by the software, the images are downloaded on the hard disc of the control PC.

3.1.3 . The mount

The requirements for a mount used for monitoring the brightness of stars with accurate precision for up to 12 hours per night are high and include:

- highest stability in all orientations
- never losing orientation
- good pointing accuracy.

Equatorial mounts can meet these requirements. It was decided upon a German equatorial mount instead of an equatorial fork mount because of the higher stability and flexibility of the former. Balancing is often easier to achieve with the help of the counterweights and more accessories may be added to the optical tube without taxing the mount.

As a base for our system we use a German equatorial mount M100B of Lichtenknecker Optics, Belgium. Standing on a tripod pier with adjustable feeds, the mount is easily aligned with the help of two spirit levels. A polar axis finder scope with reference star constellations helps to achieve an exact polar alignment. A polar height adjustment range from 0 deg to 90 deg allows to use the mount for observations all over the world.

Two stepper motors of the FS2 telescope drive unit of the German company Astro-Electronic allow adjustment of both the right ascension and the declination axis with high precision. Automatic slewing to selected objects (>3700 including all stars brighter than 3rd mag) and to all desired coordinates (RA, DEC) is possible with a handheld control pad. A serial connection to a PC enables interaction with sky map programmes like GUIDE, TheSky, SkymapPro and Starry Night, so that the telescope can be moved from the control room of the observatory, whereas a further serial connection makes interactions with an autoguider system possible. For our observations we use TheSky 5.0 Level II of Software Bisque, USA to move the telescope system from the control room.

3.1.4. The autoguider system

No telescope can ever be aligned perfectly. Imperfect stability for different orientations will introduce pointing errors. The drive units are adding further errors. Additionally refraction at

Figure 3.6.: ST-4 CCD and control box (photo: SBIG).

Figure 3.7.: ST-4 mounted at the end of the guide refractor.

lower airmasses will yield to pointing errors. Thus it is necessary to use an autoguider system to reduce drifting of the monitored star field during observations lasting several hours.

That is why a refractor combined with a ST-4 autoguider (Santa Barbara Instrument Group) is a subsystem of the Berlin Exoplanet Search Telescope. The guide refractor (see Figure 3.7.) was supplied by Lichtenknecker Optics and has an aperture of 90 mm and a focal length of 900 mm.

Autoguiding is accomplished by placing the ST-4 camera (see Figure 3.6.) at the prime focus of the guide refractor mounted on the primary telescope. The ST-4 uses a CCD detector with 192 ×165 pixels. The pixels are not square. Their dimensions are 13.75 × 16.0 micrometer and result in an active area of 2.64 by 2.64 millimeter. A micro controller built in the ST-4 control box takes exposures, reads out the pixels values, determines the drift of the tracked star and calculates the necessary telescope corrections. These corrections are sent over a serial link to the FS2 telescope drive unit.

The operations of the autoguider are controlled by the PC in the control room with the help of the MaxIm DL software. Transmitting the data is provided by a serial link. Because of the cable length of 35 meters it is necessary to convert the data with RS232/RS485 converters. This allows downloading of full frames in a few seconds. For tracking operations only part-frames with negligible download time are employed. So it is possible to control all kinds of tracking operations with the PC the whole observational night long.

The guide tube is equipped with a dew cap and is heatable with a Kendrick Dew Remover system to prevent condensation on the objective lens during phases of high humidity.

3.1.5. The control PC

A single control PC with a 1Ghz Intel Pentium 3 processor and a memory of 512MB Shared DDR SDRAM at 333 MHz was employed for our purposes. Two hard disks with a data storage capacity of 80 GB are used for temporary storage. A CD-R burner is used for permanent data storage.

Outgoing connections are the two control cables of the AP10 CCD camera and two serial cables, one controls the ST-4 autoguider, and the second transmits signals between the TheSky software and the FS2 drive unit of the telescope. These serial cables are protected

against power surges. Power is supplied by the stabilized power net of the TLS observatory. Additionally a power surge protector is used for the power supply of the control PC.

Windows NT4.0 is used as an operating system because of its high stability and the necessity to use a Windows based PC for some of the control programmes, namely MaxIm DL and TheSky.

3.1.6. The enclosure

The enclosure is a simple and robust housing for the telescope (see Figure 3.8.). It was built and provided by the Thüringer Landessternwarte. The skeleton of the housing is a stable construction made of wood. Coated metal sheets are fixed on it as an outer layer. The dimensions of the enclosure are 1.33 x 1.45 meters wide and 2 meters high, allowing the storage of the completely mounted telescope with all subsystems in its park position. For observations the whole housing has to be moved manually on two rails.

Figure 3.8.: The Berlin Exoplanet Search Telescope observing site at the Thüringer Landessternwarte Tautenburg, Germany. The enclosure has been moved to the observation position.

The housing provides protection against wind and rain. It has no lightning protection, so all electrical systems have to be unmounted during unstable weather situations where lightning may occur. During stormy weather conditions the housing is fixed with tightenable bands.

3.1.7. Summarized description of the BEST system

Telescope	20cm Schmidt-Cassegrain telescope Lichtenknecker FFC2.7
CCD	Apogee AP-10 CCD with 2048 × 2048 pixels Pixelsize 14 μm
FOV	3.1° × 3.1°
Pixelscale	5.5 arcsec
Mount	Lichtenknecker M100B with FS-2 drive unit by Astro Electronic
Autoguider	SBIG ST-4 Autoguider on 9cm refractor
Control-PC	Windows NT4 PC with 1Ghz Intel Pentium 3 processor
Software	Diffraction Limited MaxIm DL 3 (CCD + autoguider control) Software Bisque TheSky5.0 (Telescope control)

3.2. Comparison with other transit search systems

Most of the wide-angle transit search systems (see description of the systems in Appendix A) use a lensing system with apertures up to 110 mm. The effective throughput of light is lower due to the smaller aperture and the reduced throughput of the lenses compared to the throughput of our system. Only brighter stars (V < 12 mag) are observable with an accurate sampling rate and photometric precision < 1% (Brown & Charbonneau 2000).

Using filter systems further limits the light throughput and declines the efficiency of the system. But a limitation of the throughput in the red and blue parts of the spectrum is essential for ground-based observations. In the red portion of the spectrum emissions from the sky background are an additional noise source. At higher airmasses there are rapid changes of extinction at short wavelengths, additionally the scintillation noise is increased for observations at higher airmasses (see section 2.3.5. & Borucki et al. 2001). For this reason we have limited our observations to a maximal airmass of 2 corresponding to an altitude of 30 degrees above the horizon. Additionally the low quantum efficiency of the used AP10-CCD in the blue wavelength range reduces the influence of high extinction noise in the blue spectral range.

For a wider field of view observed with a lensing system differential extinction will be more important, most likely the FOVs have to be split into subframes for the relative photometric analysis.

The advantage of wide-angle lensing systems is the ability to monitor a high number of bright stars at once. For brighter stars it will be much easier to do follow-up observations, i.e. spectroscopy for spectral typing or measurement of the variation of the radial velocity.

Most of the ground-based wide-field transit search programmes are using lensing systems monitoring brighter stars. Only BEST, STARE and APT are using Schmidt telescopes as an optical instrument. The Automated Patrol Telescope (APT) has an aperture of 50 cm, but the focal ratio of f/1 results in a pixel scale of 9.4 arcseconds/pixel and undersampled point spread functions (PSF). Only a few pixels are covered with the light of one star, resulting in higher noise due to the influence of intra-pixel variations. To reduce negative effects of the undersampled PSF the APT has to be moved slightly during exposures to distribute the light of one star onto more pixels (see Hidas et al. 2003).

The STARE telescope with an aperture of 100 mm is resulting in a reduced light throughput compared with our telescope system. The STARE pixel scale is 11 arcseconds/pixel, so the PSFs are undersampled (Alonso, private communication) and additional noise caused by intra-pixel variations should be resulting.

The pixelsize of the Vulcan photometer CCD is 9 μm resulting in a pixel scale of 6 arcsec/pixel. This is comparable with our pixel scale of 5.5 arcsec/pixels. But the PSFs of the Vulcan photometer are oversampled (Borucki et al. 2001) characterizing the lower quality of the optical lensing system compared to a Schmidt-Cassegrain system.

The PSF of the BEST system is undersampled so we have to defocus during observations. The quality of the CCD is an important factor to achieve optimal results. The full field of view of the telescope/lenses system should be covered, and the pixelsize should be chosen in a way that the PSF is slightly oversampled (FWHM > 2 pixel) and it is not necessary to spread the PSF in any way (Howell & Everett 2001). Spreading the PSF means that more stars will have overlapping PSFs. This is an important noise source especially in star-rich crowded observational fields. But financial aspects have to be considered, too. For this reason we have chosen a 2k x 2k CCD with a pixelsize of 15 μm. The AP10 of Apogee Instruments Inc. is a robust low price CCD camera. The 2-stage Peltier cooling system is capable of reducing the dark current in an adequate way and it is simpler to operate in comparison with a liquid nitrogen cooling system.

The BEST FOV of about 3.1 x 3.1 degrees is smaller than the FOV of most other wide-angle search systems, but we have the highest light throughput and the smallest pixel scale with 5.5 arcseconds/pixel.

All well-known operational transit search systems use an equatorial mount with computer controllable drives. Only one axis has to be moved to follow a single star field over one night. Commercial tracking systems originally built for amateur astronomers are used to correct minor alignment errors. As already mentioned, we preferred a German equatorial mount instead of an equatorial fork mount, because it is a stable system and can be very flexibly adapted to different instrument set-ups, being balanced with the help of counterweights. Additionally, fork mounts for this size class of instruments are not commercially available and have to be custom-made for high costs.

4. Target field selection, observational and follow-up strategy

The field selection is an important factor that clearly influences the probability of detecting a transiting exoplanet. A high number of solar-like stars have to be monitored simultaneously with high photometric precision and a sampling rate sufficient to determine the shape of the transit event. The target fields have to be monitored for several months to obtain high orbital phase coverage for potentially detectable transiting Hot Jupiters. The planetary nature of the detected transit events has to be confirmed by follow-up analyses. Rough spectral typing based on available catalogue data is used to reduce the number of false alarms. Both photometric and spectroscopic follow-up observations are necessary to exclude further false alarms.

4.1. Target field selection

The observatory at the observational site Tautenburg was founded in 1960 as an affiliated institute of the former German Academy of Sciences (East Berlin). In 1992, the institute was refounded as 'Thüringer Landessternwarte (TLS) Tautenburg' indicating that it is operated as a State Observatory of the Freistaat Thüringen.

The observatory is running a 2m telescope which can be used in configurations as Schmidt telescope, Cassegrain telescope or Coudé telescope.
The TLS Tautenburg is located in central Germany at the following coordinates:

- Latitude: 50° 58' 48.4'' North.
- Longitude:11° 42' 40.2'' East.

The height above sea level is 341m. The location of the site influences which fields in the sky are observable and is therefore an important influence for the selection of target fields.

Target fields with high numbers of stars in or close to the Galactic plane are observable from this site with a maximal duration of 13.5 hours per single night if they are moving through the zenith positions. This is based on the assumption that the target fields should be observed at airmasses < 2 (corresponding to an altitude of 30° above the horizon) to reduce the influence of atmospheric effects like scintillation, extinction and transparency changes. Thus a maximal zenith distance of 5 deg (when the target field moves through the meridian) was chosen to be a main criteria for target fields that could eventually be observed by BEST from TLS. An additional criteria was that the target fields did not contain bright background objects like nebulae, cluster and galaxies because these would reduce the S/N ratio of the stars in front of these bright background objects. Furthermore no star brighter than magnitude 5 should be contained in the field of view to avoid heavy saturation of the CCD chip. 16 different target fields were proposed (see Table 4.1. and map in Figure 4.1). Most of the proposed target fields are located close to the Galactic plane guarantying a high number of stars. The maximal number of stars is contained in target field No. F16 with 41,000 stars, followed by target field No.F15 with 31,000 stars. Both target fields are located close to the Galactic plane and were observable during the initial observations in the summer of 2001. Both target fields were observed; target field F15 was chosen to be the first regular target field observed by BEST because field F16 showed a heavier crowding with many overlapping PSFs compared to field F15.

Table 4.1. Proposed target fields for BEST observations from TLS. The given coordinates are for the center of the fields (epoch 2000.0). The given data are based on the SIMBAD Astronomical Database.

Target field No.	*RA [deg]*	*DEC [deg]*	*# Stars 5-12 mag*	*Total # of stars*	*# Stars F8 –K7 (6-10 mag)*	*Brightest star [mag]*	*Θ (Airmass < 2)*
F1	1h 20	52	370	23,000	32	6.97	18h 12 – 8h 27
F2	2h 40	52	395	25,000	29	6.66	19h 32 – 9h 47
F3	4h 30	49	182	11,000	24	6.2	21h 41 – 11h 18
F4	5h 20	50	244	15,000	31	6.92	22h 25 - 11h 14
F5	6h	48	288	18,000	29	5.73	23h 17 – 12h 42
F6	7h 45	50	133	8,000	30	5.32	0h 50 – 14h 39
F7	10h 30	49	126	8,000	37	6.44	3h 41 – 17h 18
F8	10h 30	50	127	8,000	28	6.44	3h 35 – 17h 18
F9	12h 30	50	114	7,000	26	7.09	5h 36 – 19h 25
F10	14h 31	50	145	9,000	31	5.59	7h 36 – 21h 25
F11	15h 20	50	115	7,000	32	6.47	8h 25 – 22h 14
F12	16h	50	152	10,000	36	6.04	9h 05 – 22h 54
F13	18h	49	246	15,000	56	6.23	11h 12 – 0h 49
F14	19h 20	48	394	25,000	60	6	12h 37 – 2h 42
F15	20h	48	497	31,000	71	5.63	13h 17 – 2h 42
F16	22h	50	651	41,000	43	6.41	15h 05 –4h 54

In October 2001 the second target field had to be selected for observations. Target field F15 reached the altitude limit of 30 deg (airmass = 2) during the night due to the seasonal movements of the sky with more than 3 hours left for observations during the astronomical night. Two target fields of the proposed fields were within the limits of the movement of the German mount of BEST (without flipping the mount): F2 and F3.

Target field F3 contains about 11,000 stars. This is significantly less compared to target field No.2 with about 25,000 stars. Thus the decision was made to choose F2 as the next target field for BEST observations.

In January 2002 target field F2 observations ended 3 hours earlier than the astronomical night. Thus another target field was chosen: field F8. Only target field F7 was also close to the zenith within the limits of the German mounts. Both target fields are overlapping (see map in Figure 4.1.) with a center-to-center distance of 1deg. The only major difference between the fields is that F8 passes the meridian 1deg closer than field F8, thus F8 was preferred for BEST observations.

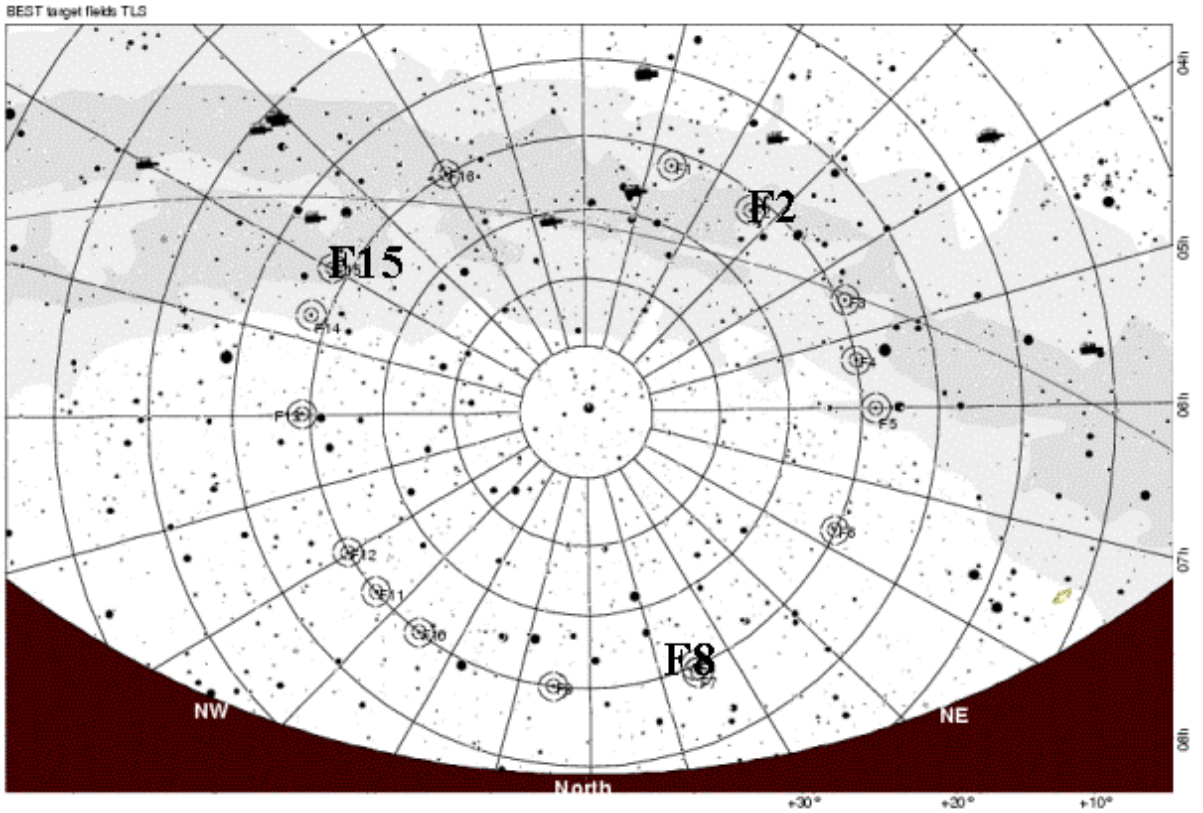

Figure 4.1. Target fields proposed for BEST observations from TLS. 16 different target fields were selected to allow observations during the entire year. Further criteria for target field selection were minimal contamination with bright stars (< 5 mag) and bright background objects like nebulae, clusters and galaxies. The observed target fields F15, F2 and F8 are marked. The picture was constructed by the TheSky astronomy software.

4.2. Observational strategy

Different calibration CCD images have to be taken during an observational run. These kind of images has to be defined:

- Bias frame: An image with a duration of zero seconds and in absence of any light is taken to measure the basic signal of all CCD pixels.
- Dark frame: A frame with a given exposure time is taken in absence of any light (shutter closed) to measure the dark current due to thermally emitted electrons in the CCD.
- Flat field images: The telescope system is exposed to an uniform source of light to record the variation of the light sensitivity of single CCD pixels and to be able to correct for dust on optical surfaces, reflections from baffles or poorly aligned optics, vignetting, and other instrumental effects in the final data. The uniform light source could be an illuminated flat field screen or the sky in the twilight.

Our observational sequence started with taken flat fields in the evening twilight if the weather permitted. The telescope was directed to the flat field screen mounted on the protective enclosure of the system in observation position. Up to 20 single flat exposures were taken per night to obtain a high total signal for maximizing S/N. Then flat field procedure was carried out in the twilight about 0.5 hours after sunset.

In a next step the telescope was pointed to a bright known star. The star was centered on the CCD and then the actual telescope position was synchronized to coordinates of the centered star.

Further the telescope was pointed to the target field; if necessary the telescope pointing was corrected again to cover the target field. Before the observations of the target field could start the autoguider was pointed to a suitable guide star. Then the system was ready to start the observations of the target field.

To observe a wide dynamic range of stars and to be able to detect transiting planets around brighter stars we have chosen to use three different exposure times:

- 15 seconds for stars with V > 8 mag
- 40 seconds for stars with V > 9 mag
- 240 seconds for stars with V > 10.5 mag.

The readout time of the CCD is about ten seconds, so it is possible to take a frame with the same exposure time every 325 seconds. The sampling rate would be 11 frames per hour and exposure time. However, the performance of the Apogee AP10 CCD had some shortcomings. Heavily saturated objects yield remnant signals in the following exposure (remanence). Therefore it is necessary to take 5 bias frames after an exposure of 240 seconds. This adds 50 seconds to the duration of the observational sequence.

Additionally it is necessary to take dark frames between the observations. One reason for this is that the dark current is high and depends on the cooling temperature of the CCD. Therefore it is important to reach the minimal cooling temperature each night, and this strongly depends upon the outdoor temperature. Nevertheless the dark current shows night-to-night variations using the same cooling temperature. Furthermore the dark current for dark exposures taken between observations can be higher compared with the dark current measured before or after the observations. Tests were performed using dark frames not taken during the time series. The resulting dark current calibrated images showed higher background noise compared to images calibrated with that taken during the time series. Thus it was decided to take dark frames for each of the three exposure times after a sequence of two normal frames. So the typical observational sequence is:

1. Star field 15 seconds
2. Star field 40 seconds
3. Star field 240 seconds
4. 5 x bias frame
5. Star field 15 seconds
6. Star field 40 seconds
7. Star field 240 seconds
8. 5 x bias frame
9. Dark frame 240 seconds
10. Dark frame 40 seconds
11. Dark frame 15 seconds

.

This sequence takes about 16.4 minutes, resulting in a sampling rate of about 7.3 normal frames per hour and 3.7 dark frames per hour for each exposure time. For observations that will take probably more than three hours during one night it is possible to reduce the sampling rate for the dark frames and get a higher sampling rate for the normal frames. Generally a number of about 10 dark frames per exposure time are needed for the dark current calibration.

The observation of a target field continued until the airmass limit (<2) was reached or as long as the weather permitted. Eventually a new target field was observed before the observational night ended about one hour before sunrise.

4.3. Follow-up strategy

Unfortunately detected transit-like signals can originate from different non-planetary eclipsing events. Eclipsing binaries can mimic transit-like signals in the following configurations (see Brown et al. 2003):

a) A main sequence star is eclipsed by another main sequence star. If the smaller star fully eclipses the larger star and if the ratio of the radii of the stars is of about 1/10 or smaller, then the signal can be misinterpreted as a planetary transit signal. Especially eclipses of M dwarfs with similar sizes as Jupiter-sized planets can be misinterpreted as transits of a giant exoplanet.

   Another possibility is that grazing eclipses reduce the signal depth of binaries with larger ratios of the stellar radii. Even binaries consisting of the same spectral spectral type can show these grazing eclipses, looking similar to planetary transit signals in noisy data.

b) A main sequence star is eclipsed by a brown dwarf. Brown dwarfs have sizes similar to Jupiter-sized planets; thus the eclipse of a brown dwarf yields the same photometric signal as the transit of a Jupiter-sized planet.

c) The signal of an eclipsing binary is blended by one or more stars. This dilution of the eclipse signal reduces the total signal depth thus it can have similar amplitude as a transit signal of an exoplanet. The blending third component can be a dwarf or a giant, bounded to the binary or a foreground star.

d) Stellar spots can mimic a transit-like signal.

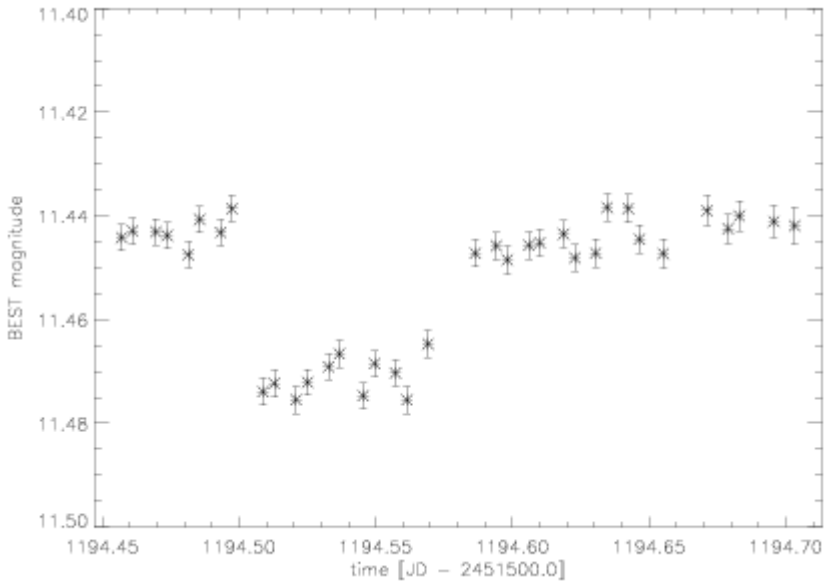

Figure 4.2. Signal found for a star drifting on the CCD chip. The chip was partly covered by a dirt particle. Drifting of the star image over the covered part of the CCD caused the lower signal. The flat field calibrations did not fully compensate the lost flux yielding a signal comparable to a transit signal with very short ingress/egress phase.

Additionally system effects related to the CCD or the optics can cause transit-like signals and therefore introduce false alarms. CCD defects like dead pixels or dirt in the optical path (see example in Figure 4.2.) can mimic single transit-like events.

Follow-up analyses and observations must first rule out all such false alarm cases. An effective strategy was developed to discriminate between these false alarms and real planetary transits. In the following it is described how catalogue data is used for spectral typing and how photometric and spectroscopic data helps distinguish the real planetary transits.

4.3.1. Catalogue data

The follow-up analysis starts just after the first transit-like signal is detected in data of the single nights. After first tests to rule out that sensor defects (defect pixels, bad CCD lines, particles in the optical path) have caused the signals have been passed successfully, a rough spectral typing is done based on online available photometric and astrometric data. Several resources were already available or were made available during the TLS observational campaign. It is important to discriminate if the host star is a giant or dwarf. Thus the spectral class and the luminosity class of the host stars have to be evaluated. Therefore we need at least three colors to be able to calculate 2 color indices to estimate both the spectral and luminosity class of the main component of the eclipsing system.

Tokunaga (2000) gives the following color indices for all spectral types and the most common luminosity classes V (dwarf), III (giant) and I (super giant): V-K, J-H and H-J. Additionally the effective temperature is given. These values can be compared with values given in catalogues. The 2MASS catalogue (Cutri et al. 2003) gives the colors in the bandpasses J, H, K. Because the index (H-K) is nearly the same for stars of the same effective temperature but of different luminosity classes it is not sufficient to evaluate the luminosity class. However, (J-H) or (J-K) can be used for this purpose. Unfortunately the 2MASS catalogue does not contain V colors for the stars. But it can be found in other catalogues:

The Tycho Input Catalogue (Egret et al. 1992) gives the V colors for stars brighter than V = 12.1 mag, Karchenko (2001) provides V colors for stars brighter than V=12-14 mag. This covers most of the magnitude range observed with BEST.

Using more than one catalogue needs some caution. The photometric measurements used are most likely different for different catalogues yielding to magnitude shifts that cannot be determined precisely yielding uncertain error values for the color indices. Often different photometric systems are used. Thus the resulting spectral/luminosity classes are uncertain beyond a certain level.

Some further evidence for the luminosity class of a star can be gained by analyzing the proper motion of the star. If the star moves with a significantly lower proper motion than the majority of the neighboring stars then it is most likely a giant. But note this is no final proof. Proper motions can be found in catalogues like UCAC-2 (Zacharias et al. 2003), The ACT Reference Catalogue (Urban et al. 1997), the USNO-B1.0 catalogue (Monet et al. 2003) or the All-sky Compiled Catalogue of 2.5 million stars by Kharchenko (2001).

Additional checks are made to identify possible blends. Because of the large pixel scale of BEST (5.5 arcsec/pixel) a relatively high number of objects cannot be resolved. In POSS (Palomar Observatory Sky Survey) images with higher resolution available in the Aladin database (Bonnarel et al. 2000) some unresolved objects can be identified. With the help of the rough spectral typing as described earlier in this section it is possible to decide if the observed transit-like signal arose from planetary transit or not.

4.3.2. Photometric follow-up observations

Additional photometric detections have to be made if only one or two transit-like signals were detected during the regular photometric campaign done with BEST. At least three detections are necessary to determine the periodicity of the eclipsing event photometrically.

The main instrument used for photometric follow-up of BEST candidates is the 90cm Westerlund telescope provided by the collaborators at Uppsala University in Sweden. The telescope is installed in a dome on top of the Ångström laboratory. The classical Cassegrain reflector has two focii for semi-permanent mounting of different types of instrumentation. The main purpose of the telescope is to introduce students to astronomical observations but it is also used for professional research projects. The main mirror has a mechanical diameter of 92 cm, 90 cm are optically free.

The focal ratio of the main mirror is f/3. The total focal ratio of the system (both primary and secondary mirror) is f/10. The imaging camera is a Santa Barbara Instrument Group (SBIG) STL-1001E detector with a Kodak KAF-1001E CCD. The chip of the 1k x 1k CCD with a pixel size of 24 μm covers an area of 24.6 mm x 24.6 mm.

The monitored field of view (FOV) is about 18.8' x 18.8' in the Nasmyth 1 f/5 focus (with focal reducer). A smaller FOV of 8.9' x 8.9' is monitored in the Nasmyth 2 focus with f/10.5 with a pixel scale of 0.52'' compared to the pixel scale of 1.1'' in the Nasmyth 1 focus. The available small pixel scales resolves objects which cannot be resolved by BEST. The resolved objects can be monitored separately to identify the eclipsed object.

Five UBVRI filters are available for photometric observations mounted in an internal SBIG wheel. These imaging filters with a diameter of 48 mm are UBVRI Johnson-Cousins filters. For the detection of additional transit signals white light images (no filter) or R filter images are used because of the higher throughput in these bandpasses to increase the signal to noise (S/N) ratio.

For the identification of transit-like signals caused by eclipsing binaries, observations in two bandpasses can be carried out. If the spectral types of the binary components are significantly different then the signals have different depths in different wavelength bands. The smaller and therefore cooler component emits additional flux in the red part of the spectrum; thus the signal depth is increased in the blue bandpasses compared to the red bandpasses. In-transit observations switching from blue bandpasses (U or B if the U flux is low) to red bandpasses (R or I) are useful to identify eclipsing binaries where both components are of different spectral type. But note that grazing eclipses of systems consisting of objects of nearly the same spectral type cannot be identified.

4.3.3. Spectroscopic follow-up observations

In recent subsections it was shown that several but not all false alarms can be identified with the help of information contained in online databases or photometric follow-up observations. For remaining candidates a more precise spectral typing is necessary to better evaluate the dimension of the secondary object. Thus taken high or medium resolution spectra can be compared with reference spectra (i.e. Montes et al. 1999). This allows a more precise determination of the size of the secondary object to be able to decide if the object is planet sized or not. Giant planets orbiting are expected to have an upper limit radius of about 1.5 R_{jup}, but younger planets can be larger, up to 2 R_{jup} (see Bodenheimer et al. 2003).

If the size of the secondary is estimated to be 2 R_{jup} or less then measurements of the radial velocity (RV) have to be carried out to identify whether the object responsible for the detected transit signal is a planet (less than ~ 13 M_{jup}), a brown dwarf companion (~ 13 M_{jup} – 80 M_{jup}) or a small main sequence star. The radius of objects with masses between 0.001 and 0.2 M_{sun}

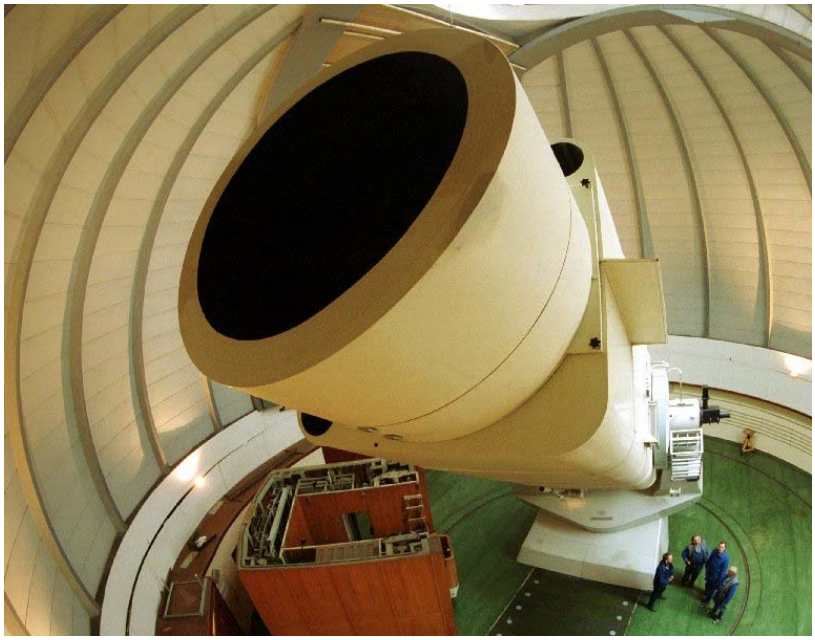

Figure 4.4.: The 2m Alfred Jensch telescope at the Thüringer Landessternwarte (TLS). This telescope is used for RV confirmation of transit candidates detected by BEST.

is nearly constant in the range of 0.5 R_{jup} to 2.0 R_{jup} (see Bodenheimer et al. 2000, Pont el al. 2004).

Spectroscopic measurements both for spectral typing and RV analysis for transit candidates detected with BEST are carried out with the 2m Alfred Jensch telescope at the Thüringer Landessternwarte (TLS) Tautenburg (see Figure 4.4.). The spherical primary mirror of the telescope has a focal length of 4m. This multi-purpose telescope can be used in 3 different optical modes: Coudé mode, Nasmyth mode for spectroscopic measurements and Schmidt mode for photometric monitoring. The focal length in Coudé mode is 92m.

The white-beam Echelle spectrograph allows taking spectra with a resolution of up to 67,000. The spectrograph is temperature-stabilized and uses an Echelle grating with 31.6 lines per millimeter. Three different grisms can be used: the UV grism (340nm – 547nm), the VIS grism (463nm – 737 nm) or the IR grism (538nm – 927nm). The highest sensitivity is reached with the VIS grism. With an hour exposure a S/N of 30 per pixel (low resolution spectra) can be reached for stars as faint as magnitude 13. Sufficient RV measurements can be obtained using the temperature stabilized iodine cell to generate a very dense reference system of absorption lines superimposed on the stellar spectrum for wavelength calibration.

For most of the BEST candidates only low-resolution spectra will be available. This allows the RV identification of candidates where the transit-like signal is caused by a brown dwarf or stellar companions. For bright stars (11 mag – 12 mag or brighter depending on seeing and transparency conditions) medium resolution spectra can be obtained allowing determination of the orbital parameters and the mass of Jupiter-mass exoplanets.

More details about the instrument and the report about the first planetary discovery with this instrument can be found in Hatzes et al.(2005).

For faint candidates additional spectroscopic analysis has to be carried out. Collaboration partners at the McDonald Observatory in Texas, USA provide access to the 2.7m Harlan J. Smith telescope and the 9.2m Hobby-Eberly Telescope (HET).

The Harlan J. Smith telescope uses a cross-dispersed 2dcoudé spectrograph (Tull et al. 1995) in combination with an iodine cell for wavelength calibration and monitoring of the instrumental profile very similar to the instrumental set-up of the TLS 2m telescope for RV measurements. Due to the larger main mirror of the 2.7m telescope spectra with higher S/N can be obtained compared to spectra taken with the 2m TLS telescope for the same stars. More details about the 2.7m telescope and its instrumental set-up can be found in Hatzes et al.(2000). Nevertheless the performance does not allow obtaining high-resolution spectra for

most of the BEST transit candidates. A much larger collecting area is necessary to reach a S/N ratio of 100 or better.

A well-suited and well-located telescope for this purpose is the Hobby-Eberly Telescope (HET) at the McDonald Observatory. The HET consists of an array of 91 hexagonal-shaped mirrors (1m diameter) with a resulting effective aperture of 9.2m. The main mirror is fixed in a truss that can be rotated in the azimuth direction only. Tracking is done with fiber optics directly moved in the spherical focal plane. The truss is tilted at 35 deg zenith angle. This construction limits the accessible regions of the sky to objects at declinations between –11 deg and +72 deg, but significantly reduces the technical and financial efforts to built and maintain a telescope of this dimension.

Targets within the BEST target fields with declinations between 46.5 deg and 53.5 deg are observable with the HET telescope. The High Resolution Spectrograph (HRS; Tull et al. 1998) was designed to be able to make RV measurements with a precision of 3 m/s or better for stars as faint as V = 10 mag. A resolving power of 60,000 is used for RV measurements. Two CCDs cover a large wavelength range centered on 594nm. An iodine cell is used for wavelength calibration and analysis of the instrumental profile. For more details about the telescope and the set-up of the HRS refer to Cochran et al. (2004).

If RV measurements confirm the orbital period of the eclipsing object derived from photometric signals and the mass of the secondary object is evaluated to be in the range typical for planets then the transit of an exoplanet is confirmed. If only a few RV measurements can be taken or the RV data is too noisy for an orbit to be fitted to the RV data then some tests must be carried out to rule out a blending scenario.

The spectra can be analyzed for secondary components to rule out that eclipsing binaries are the source of the observed transit-like signals. The first step is to search for directly visible lines from the secondary component of the binary in the spectra. In high-resolution spectra double lines of grazing eclipsing binaries of nearly the same spectral type are visually easily identified. Note that this test can be carried during the analysis of the first spectrum of the primary.

If no secondary components can be detected this way then precise analyses of the shapes of the spectral lines can be provided using several spectra of the primary object. During this bisector analysis one searches for spectral line asymmetries that are caused by a secondary stellar component that cannot be detected directly in high-resolution images or in spectra (e.g. Gray 1992). This secondary component can be an eclipsing binary that is blended by the primary component. The measured spectra are fitted with a modeled spectrum to determine any variations of the line shapes with time. If variations are detected then they have to be analyzed, if they correspond to the periodicity of the photometric signal in order to identify the non-planetary character of the transit-like signal. Some of the OGLE candidates have been identified to be blends by this method. Thus Torres et al. (2004) reported that the candidate OGLE-TR-33 is an eclipsing binary blended by a brighter star located in the same line of sight.

4.3.4. Summary of the developed follow-up strategy

After the detection of a single transit-like event in the light curve data the following tests, analyses and procedures are carried out:

a) Test if CCD defects or dirt in the optical path has mimicked a transit-like signal.
b) Check if the signal is diluted by unresolved stars in the same PSF with help of high resolution images.

c) Rough spectral classification based on catalogue data to estimate the size of the eclipsing object and to search for spectral lines of secondary objects.
d) Spectral classification based on a single spectrum of the primary taken with 2m TLS telescope.
e) RV measurements with the TLS 2m telescope.
f) Precise RV measurements with the 2.7m HJS telescope or the 9.2m HET telescope to determine the mass of the secondary object.
g) Bisector analysis to rule out blending scenarios.

All these tests have to successfully passed to identify, that a transit-like signal was caused by a planet.

Additional photometric observations can be ordered to detect further transit signals allowing to determine the orbital period independently from by determination by RV measurements.

5. Data reduction and analysis

Monitoring several thousand stars every night with suitable meteorological and photometric conditions results in several Gigabytes of data each night. The data has to be calibrated, all stars must be detected in every frame and a photometric measurement has to be carried out. All light curves with an accurate enough photometry have to examined for transit-like events. This large amount of work has to be done directly after each observational night to be able to start follow-up analysis and observations as soon as possible after a star is observed to show a transit-like event.

Therefore the development of an automated data reduction and analysis process was defined as a main task in this thesis work. The goal was to develop a reduction pipeline that is able to analyze the data in near real time without loss of data quality. This allows to optimize the following observations for candidate stars (i.e. prevention of candidate stars being located on a bad column of the CCD).

The International Data Language (IDL) is a language compatible with most of the computing platforms, including UNIX, Windows and Macintosh platforms. Therefore the platform independent IDL was chosen to be the language of the reduction pipeline.

The developed pipeline called 'BESTRED' only needs input lists for the calibration frames (bias frames, dark frames, flat field frames) and normal (star) frames.

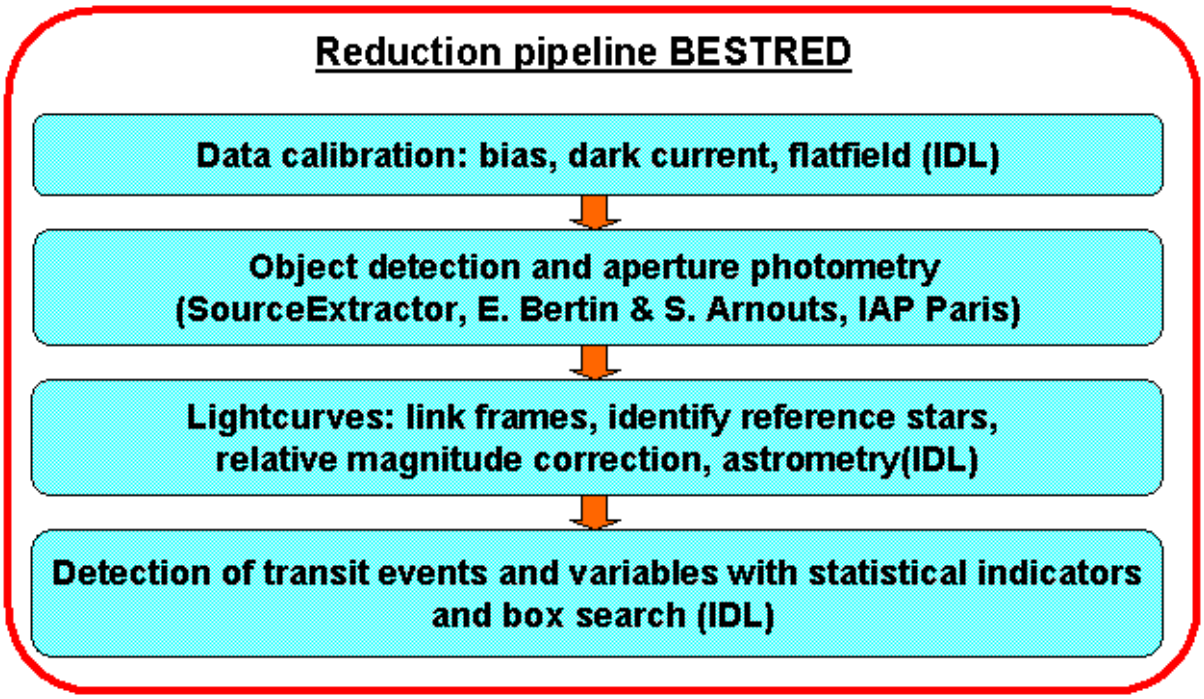

Figure 5.1.: Scheme showing the single steps of the developed reduction pipeline.

The single steps of the data pipeline are data calibration, source detection and photometry, the assembly and calibration of the light curves, and the detection of transit like events (see scheme in Figure 5.1.) and will be described in the following sections.

5.1. Data calibration

The collected data have to be calibrated as a preparatory step for the photometry. The single steps of the calibration are described in the same sequence as they are carried out in the data reduction pipeline.

In a first step all calibration frames are checked for anomalies like unusually high noise patterns and cosmic hits. Then the first kind of calibration images are processed: **bias frames**. For the definition of the kinds of calibration frames please see section 4.2. All selected undisturbed bias frames are used to create the median-filtered masterbias using standard procedures for CCD image calibration. The masterbias is normalized based on the analysis of the mean bias level of the oversampled margin region of the CCD images.

Further all **dark** frames are checked in a similar procedure as for the biasframes, dark frames with suspicious signals are excluded for further processing. Masterdarks for all exposure times used are obtained by subtracting the scaled masterbias from the single dark frames and averaging these bias-subtracted dark frames.

In the following step all **flat field** images are bias- and dark-subtracted, the individual flat field frames are co-added. Then the co-added flat field frame is normalized yielding the masterflat.

The standard calibration process for the **star field** images contains the following processes. The scaled masterbias and the dark frame corresponding to the exposure time of the star field frame are subtracted from the raw star field exposures. Finally these exposures corrected for bias and dark current are divided by the masterflat frame yielding the calibrated star field exposures. The calibration procedure can be expressed by the following equation:

$$\text{Calibrated image} = \frac{\text{Raw image - scaled normalized masterbias - masterdark}}{\text{Normalized masterflat}} \qquad (5.1.)$$

The data calibration is relatively CPU intensive, that means the calibration for data of one night takes several hours due to the large amount of data. For a normal night 200 – 300 images (including calibration images) each with a size of 8 Mbytes are taken resulting in a total amount about 2 Byte of data that has to be processed in the described single steps.

5.2. Source detection and photometry

The source detection and the photometric extraction of the signal is a very important step in the reduction process of the data. Several routines with these capabilities (DAOPHOT, SourceExtractor …) have already been developed, intensively tested and used for similar astronomical purposes. The Source Extractor software by E. Bertin of the Institute d' Astrophysique de Paris and S. Arnouts of the European Southern Observatory (Bertin & Arnouts 1996) is an automatic routine that optimally detects, deblends, measures and classifies sources of astronomical images. It is suited to automatically analyze large amounts of data with high photometric precision but without being too computationally intensive.

The complete analysis of an image is done in six steps: **estimation of the sky background**, **thresholding**, **deblending**, **filtering**, **photometry** and star/galaxy separation. The last step is the most computationally intensive step using a neural network as a classifier between stars and galaxies. For the purpose of a fast data reduction of time series of star rich target fields it is not necessary to do this separation. Faint galaxies can be treated as nonvariable objects. Bright and extended galaxies are excluded during the field selection process because of their introduction of additional background noise for many surrounding sources. Therefore the star/galaxy separation functionality of SourceExtratcor is not used for BESTRED.

How the SourceExtractor (Version2.0) is optimized for the use in the BESTRED pipeline is described in the following sections:

a) **Background estimation**: A precise estimation of the background is needed to measure the fluxes of the stars accurately. SourceExtractor constructs a background map of the image. A grid is applied with a user-defined mesh size. Objects are excluded from the background map so that the local background histogram is clipped iteratively until convergence at $\pm 3\sigma$ around its median. The resulting background map is the basis for a bicubic-spline interpolation between the meshes of the grid. In order to be able to reproduce small scale variations of the background this mesh size must not be too large. If the mesh size is too small, objects and random noise can heavily affect the background estimation. Tests were carried out to find the optimal size of the background grid. Artificial star signals were introduced into starless regions of real images and measured with different photometry procedures to find the optimal grid size. Grid sizes of 16 – 32 pixels resulted in the best photometric measurements, a grid size of 32 was chosen because it requires less computational time for calculating the background map. Finally the background map is subtracted from the image.

b) **Thresholding**: SourceExtractor is using thresholding for the detection of objects in the frame. A threshold limit has to be defined. Signals of faint objects are noisy. This yields very noisy light curves for which no transit signals can be detected. Therefore a relatively high detection threshold of 5σ relative to the background RMS was chosen. A second parameter is the minimal number of neighboring pixels above this threshold which have to be contained in a detected object. By choosing 5 pixels individual 'hot' pixels are not considered as an object, but fainter stars with only 5 pixels above the threshold can still be detected.

c) **Deblending**: In frames of crowded star fields a large number of PSFs of neighboring stars are overlapping. With the detection method used many of these overlapping objects can be detected as single objects. To be able to separate the fluxes of these objects a deblending procedure has to be carried out. A multiple isophotal analysis is used in the SourceExtractor routine. Each extracted set of pixels is re-thresholded at several levels exponentially between the highest peak value and the detection threshold. Objects that are so close that no saddle point can be located in their profile cannot be separated and will be treated as a single source. Possible transit signals will be diluted and are most likely no longer detectable anymore. Considering that the precision of photometric measurements will always be influenced if the PSFs of the stars are overlapping it was decided to use the recommended (by the authors of SourceExtractor) parameters for the deblending procedure. The minimum contrast parameter was set to be 0.0005 and the number of deblending thresholds to 32, thus that 32 individual but overlapping objects can be detected. Note that changes in seeing during the night can result in different numbers of detections for the same number of real objects and therefore lead to confusion when creating the light curves. Therefore these stars are not good targets for a transit search.

d) **Filtering**: A simple filtering approach is used. A 3 x 3 convolution mask with FWHM = 2 pixels is applied to filter single bad pixel signals and signals on the boundary of the image in the background. The pixels of the filtered signals are set to zero. This makes sense because images are already background subtracted.

e) **Photometry**: SourceExtractor offers the possibility to use four different kinds of photometric measurements: isophotal, corrected-isophotal, fixed-aperture and adaptive-aperture magnitude. **Isophotal** magnitudes are a simple summations of pixel

values, using the detection threshold as the lowest isophote. Large fractions of flux are lost depending on the setting of the detection threshold.
For the **corrected-isophotal** magnitudes a Gaussian shape for the PSFs is adopted. Then, the additive correction is given by the approximation 2.5 log η, where η is given by:

$$\eta = 1 - 0.1961\left(A \cdot t / I_{iso}\right) - 0.7512\left(A \cdot t / I_{iso}\right)^2 . \qquad (5.2.)$$

t is the detection threshold and A the area related to this threshold (see Maddox et al. 1990). This approximation works best for Gaussian-shaped PSFs.

The **fixed-aperture** magnitude is measured within an aperture with an user-defined radius. Each pixel is divided into 5 x 5 sub-pixels. Therefore a non-integer radius of the aperture is possible and pixels on the edge of the aperture with noisier signals are not overestimated.

For the calculation of the **adaptive-aperture** magnitude an elliptical aperture is fitted to the star signal. This method is based on the 'first moment' algorithm developed by Kron (1980). A minimal radius for the aperture is given. Then the shape of the objects is analyzed within a second, larger radius and the elliptical optimized aperture is fitted to the stellar signals optimizing the signal-to-noise ratio (S/N) for the measured signals within the larger radius. With a scaling factor k = 2 for the larger radius (compared to the first radius) it is guaranteed that an almost constant fraction of the flux (~ 90%) is lying within the aperture (Infante 1987). A good balance between systematic and random errors is achieved, pixels with low values are not considered and therefore the S/N is increased. For signals with low S/N a minimum radius has to be defined to avoid the use of erroneously small apertures. Tests showed that the highest S/N was reached for a minimal radius of 3.0 pixels corresponding to a radius of about 1.5 – 2.0 FWHM. This results in a measurement of the flux within an ellipse with semi-minor axis of between 3 and 4 pixels and a very small elongation e < 1.2 for the majority of the stars.

The apertures for fainter stars are generally larger. Faint stars have a wider FWHM. A larger aperture is needed to measure the same fraction of the total flux as measured for bright stars. Only an increased aperture size allows further comparisons of the measured fluxes from fainter stars with the fluxes of brighter stars. Thus the average size of the semi-major axis is about 4 pixels due to the dominating number of faint stars.

For detected overlapping PSFs a correction is applied. Suspected contaminated parts are replaced by the mirrored opposite side of the aperture eclipse.

All four kinds of photometric measurements described in e) above were tested. Artificial but well-defined signals were introduced into real data containing sky background signals and only very faint background stars more than three magnitudes fainter than the artificial star signals. The stellar signals introduced had Gaussian profiles with FWHMs in the range of 1.5 to 2.5 pixels (see example in Figure 5.3). This pixel range corresponds to the range that is typical in the data of the BEST system. In real BEST data it was found, that in a single frame a FWHM variance interval of 0.5 pixels is typical. Additionally, during observations the FWHM of the PSFs are not constant. A possible reason for this change is the appearance of a temperature gradient that leads to distortions of the mirrors and the telescope tube. Another problem that makes it more complicated to reach optimal photometric precision are strong changes in the transparency of the atmosphere at the observational site, Tautenburg. In many of the nights, changes of up to 0.5 magnitudes due to increasing haze were observed. These

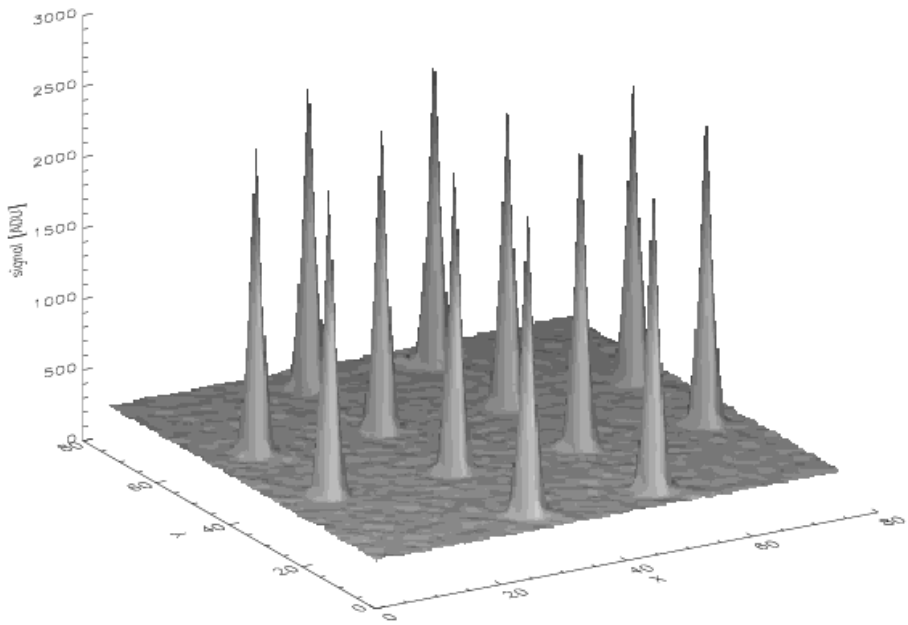

Figure 5.3.: 3D plot of an image used for the optimization of the parameters for SourceExtractor photometry. 12 PSFs with a FWHM of pixels are placed on real background data. This image was used to examine the precision of the different photometric measurement procedures of SourceExtractor. The background of the image was extracted from real data taken by the BEST system. The signal strength and the FWHM of the star signals were varied to simulate more realistic conditions in further tests.

Table 5.1.: Results of tests to optimize the photometric measurements of the SourceExtractor software. Artificial star signals of stars with a Gaussian profile and a constant FWHM of 2.0 pixels were measured with different kinds of the photometry. Only the results of the best measurements for the fainter objects are listed. The adaptive aperture photometry has the lowest errors of the photometric measurements in combination with a high S/N) ratio.

Kind of photometry used	***Integrated signal 10,000 ADU***	***Integrated signal 5,000 ADU***	*Integrated* ***signal 2,000 ADU***
Isophotal photometry Threshold 5σ	9,977.2 ± 33.1 (S/N = 225)	4,976.5 ± 29.7 (S/N = 137)	1,986.7 ± 26.4 (S/N = 67)
Isophotal photometry Threshold 3σ	10,014.0 ± 71.3 (S/N = 134)	5,000.9 ± 68.1 (S/N = 49)	2,005.0 ± 33.1 (S/N = 56)
Corrected isophotal photometry threshold 5σ	1,0167.3 ± 39.4 (S/N = 206)	5,159.3 ± 32.4 (S/N = 133)	2,271.0 ± 23.5 (S/N = 83)
Fixed Aperture Diameter 7 pixels	9,993.2 ± 35.1 (S/N = 220)	4,994.8 ± 34.8 (S/N = 123)	1,996.7 ± 35.0 (S/N = 53)
Adaptive aperture	9,995.1 ± 34.1 (S/N = 222)	4,989.4 ± 26.5 (S/N = 148)	1,995.5 ± 26.6 (S/N = 67)

conditions make it more difficult to define an optimal procedure to reach the best photometric precision. Extensive tests were necessary to find the most optimal procedure.

In a first test, signals with different strengths and constant PSF with a FWHM of 2.0 pixels were measured with the four possible photometric procedures (see Figure 5.3.). Typical values

of the signal strength were chosen within a range from the brightest non-saturated objects to the faintest objects with a photon noise smaller than 1%: 50,000, 20,000, 10,000, 5,000 and 2,000 ADU. The artificial stars were placed on 12 different locations within the real background image to evaluate the measurements independently from the location of the object. All four kinds of photometric measurements performed well for the brighter objects, but for the fainter ones there are significant differences (see Table 5.1). Apart from the corrected isophotal photometry method all other kinds of photometry are able to measure the signals close compared to the real signal. The signals determined by corrected isophotal photometry are overestimated. The relative overestimation increases with decreasing signal strength. Comparison of signals with different strength will yield additional errors for the relative photometry. Therefore the corrected isophotal photometry is not suitable for our purposes.

The uncorrected isophotal photometry method with a low threshold of 3σ results in measurements with exceptionally lower S/N compared to the measurements with a threshold of 5σ. A higher threshold yields to underestimation of the signal. An optimized threshold has to be chosen, but this choice depends on the FWHM of the signals. For the BEST observations with time-dependent, non-uniform PSFs in the FOV this threshold has to be varied with a high computational effort. A constant threshold produces a larger RMS of the measurements.

Table 5.2.: Artificial signals of 10,000 ADU and 2,000 ADU with different FWHM in an interval from 1.5 pixels to 2.5 pixels on real background data measured with different kind of photometric procedures. For faint stars the adaptive aperture photometry performs best, for bright stars the performance of all listed photometric procedures show no significant discrepancies of statistical relevance, but the adaptive aperture photometry gives the closest average measurement of the signals.

Kind of photometry used	***Integrated*** *signal 10,000 ADU*	***Integrated si****gnal 2,000 ADU*
Isophotal photometry Threshold 5σ	9,977.2 ± 25.8 (S/N = 252)	1,974.8 ± 32.5 (S/N = 56)
Fixed Aperture Diameter 7 pixels	9,978.4 ± 27.7 (S/N = 245)	1,991.9 ± 28.5 (S/N = 63)
Adaptive aperture	9,988.8 ± 26.8 (S/N = 248)	1,995.7 ± 22.9 (S/N = 76)

Additional tests were carried out for Gaussian signals with different FWHM to simulate varying seeing and focus conditions. The FWHM for different signal strength was varied in an interval from 1.5 pixels to 2.5 pixels. Results of these tests are listed in Table 5.2. For bright signals the tested kinds of SourceExtractor photometry show no significant differences of statistical relevance. For faint signals the adaptive aperture photometry performs best. Therefore the photometric measurement with an adaptive aperture was chosen to be implemented in the pipeline reaching high S/N even for fainter objects with varying FWHM and signal strength.

Furthermore the detection and deblending capabilities of SourceExtractor were tested. Test data was constructed in the same way as for the tests previously described. Overlapping signals were added onto real background data (see Figure 5.4.). Objects separated only by 3-4 pixels were not detectable as single objects, objects at larger distances were detected.

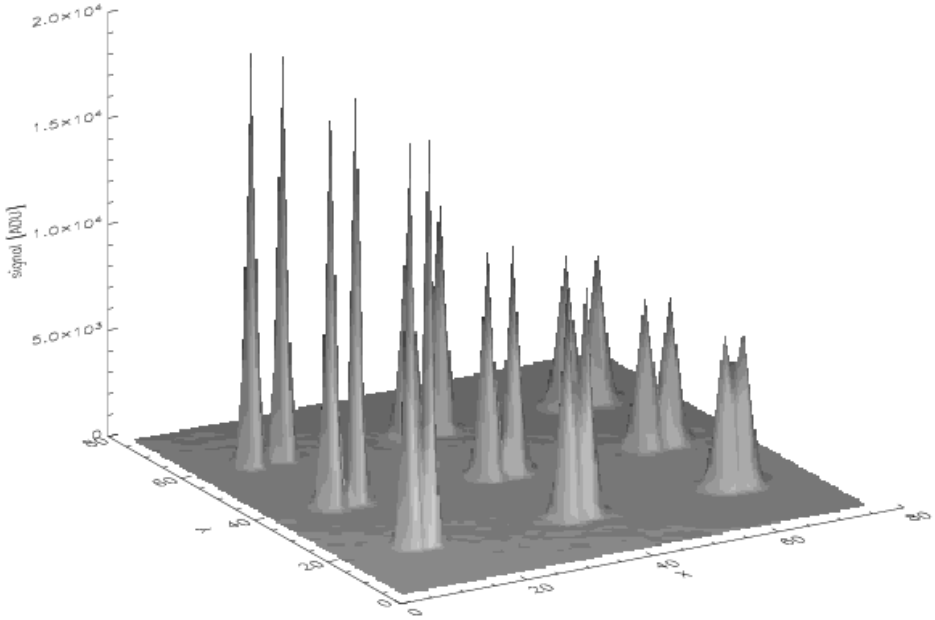

Figure 5.4.: Artificial 'stellar' signals with overlapping PSFs. This image was used to test the potential masking tools for the photometric measurement of the SourceExtractor software. Mirroring the parts of the not affected PSF to replace the affected parts yields to results with better precision. Compared to the 'blanking' method yielding a small additional error in the dimension of 0.01% for all kinds of tested photometry.

Two kinds of masking tools are available in SourceExtractor: 'correct' or 'blank'. The blanking procedure replaces the values of pixels that are affected by overlapping PSFs with a value of zero, leading to a loss of signal. The 'correct'-procedure replaces the affected parts of the PSFs by mirroring the not affected part. Best results were obtained with the 'correct' procedure leading to small additional errors for the photometric measurements in the order of 0.01%. Therefore the 'correct' procedure was chosen for implementation in BESTRED.

For stars close to this SourceExtractor confusion limit of 3-4 pixels a degrading of the photometric precision was detected in real. Depending on seeing and focus variations neighboring objects (especially faint ones) are sometimes not detected in a few single frames. Then the pixels of the faint, undetected objects above the detection threshold are interpreted to belong to the brighter, detected object yielding the measurement of a combined signal. Especially for very crowded target fields this can yield to additional noise for a high number of light curves. Therefore in Karoff et al. (2006) it was analyzed, how the photometric precision for light curves in very crowded target fields (f.e. the target fields of the COROT satellite) can be improved. The tested image subtraction software ISIS (Alard 2000) was found to deliver better results for crowded target fields. Nevertheless, for the light-curves of non-crowded stellar images SourceExtractor applying the adaptive aperture photometry obtained lower RMS as ISIS.

SourceExtractor additionally determines the positions of the objects measured in pixel coordinates X and Y of the CCD. The parameters are derived from the spatial distribution of those pixels detected to be above the detection threshold. The barycenter of these pixels is then calculated. This is a good approximation for circular objects, especially for our main targets: stars.

5.3. Assembling the light curves

Ideally the positions of the stellar PSFs should not vary from CCD image to image. This ensures that no additional errors introduced by pixel-to-pixel variations of the sensitivity of the CCD chip worsen the photometric precision of the light curves. In reality a constant object position on the CCD cannot be reached. Alignment errors of the telescope are not negligible for observations over several hours. Additionally the stepping motors (drives) do not compensate the rotation of the Earth perfectly and the mounting will always be a little bit unstable and therefore causes pointing errors.

To reduce the influence of these errors an additional guiding system (see section 3.1.4.) is used to track a single star. But with the tracking of a single star the orientation of the observed target field is not locked. Rotations of the field stars around the tracked star are still possible. Fortunately exposures of the target fields are taken every few minutes resulting in drifts of less then one pixel in both directions from exposure to exposure for the BEST system. Therefore objects can be easily detected again in the following frame. But if observations are interrupted for any reason (clouds, technical problems, etc.) for longer times, the objects will drift more than the SourceExtractor confusion limit of four pixels (distance where neighboring objects can be separately detected, see section 5.2.). If a drift is dominant in one direction (drift in the second direction is less then the confusion limit), then the drift can be assumed to be linear. Linear interpolation constants can be calculated and used to find all the objects once more in the following frame.

This principle is used and the necessary linear drift parameters are calculated. Therefore the position of the 11 brightest stars are automatically identified in each frame and cross-correlated with the coordinates in the next frame. Then the linear drift parameters are used to assemble to light curves.

The created 'raw' light curves contain the following information: number of the exposure, instrumental magnitude, error of the instrumental magnitude, the pixel coordinates. The instrumental magnitude m is calculated as $m=-2.5 \log N_{ADU}$, where N_{ADU} is the number of counts for the signal given in ADU by SourceExtractor.

In a next step a 'flag' parameter is inserted containing information about known pixel anomalies: defect columns, pixels with strongly non-constant dark current.

5.4. Calibration of the light curves

The calibration of the light curves is an important step of the data reduction. Ideally a non-variable star should always have the same measured signal strength apart from statistical uncertainties like photon noise, scintillation noise and from uncertainties of the measurement introduced by the background noise. But the changing transparency of the atmosphere leads to measurements with additional variations. The transparency of the atmosphere can be changed by different factors, i.e. changing airmass. The extinction of light by the atmosphere is color dependent. Nevertheless, a correction of this extinction is possible in a certain scope for most of the stars. Differential photometric corrections (as proposed by Howell et al. 1988, Honeycutt 1992) can be carried out. A mean differential magnitude correction can be determined for all stars in the limited FOV of BEST. Additionally the fact that the majority of the stars have nearly the same color (because they are preferred in that magnitude range), helps to calculate a sufficient mean magnitude correction for the majority of the stars. How the mean magnitude correction is applied in BESTRED is given step-by-step in the following:

1) All light curves of stars in a defined magnitude range are identified. The magnitude range is defined thus, that only non-saturated stars are selected, for

which the photometric measurement is dominated by photon. The number of the selected reference objects ranges from a few hundred to a few thousand depending mainly on the stellar density of the target field and the exposure time.

2) The mean magnitude differences Δm_i of the selected stars in all frames compared to the first frame of the daily time series are computed:

$$\Delta m_i = \frac{1}{n}\sum_{k=1}^{n}\left(m_{i,k} - m_{1,k}\right) \qquad (5.3)$$

where n is the number of selected reference stars, and $m_{i,k}$ is the magnitude of the reference star k in the i-th image of the time series.

3) The calculated mean magnitude differences Δm_i are used to correct the magnitudes of all the light curves of the potential reference stars:

$$m_{i,k}^{kor} = m_{i,k} - \Delta m_i \qquad (5.4)$$

.

4) In an iterative selection process the corrected (via equation 5.4.) light curves are searched for non-variable stars based on the RMS of the corrected light curves. A defined number of light curves with the lowest RMS is selected. The number of the selected light curves depends upon the stellar density of the observed target field and the exposure time. It is chosen in such a way, that variable stars (with large RMS) are excluded.

5) Now the selected light curves of the non-variable reference stars are used to recalculate the mean magnitude differences via equation 5.3. Note that the number of light curves considered n is reduced compared to step 2) as described in 4).

6) Finally the magnitudes of all light curves are corrected with the mean magnitude differences recalculated in step 5).

All light curves are now calibrated for extinction.

The described calibration process of the light curves is the result of an optimization process to reach the best results, especially to achieve the highest number of stars with a RMS < 1%. As already shown in section 5.2. the use of the adaptive aperture photometry procedure gives the results with highest photometric precision especially for unstable signals (mainly due to strong chances in transparency) as observed from the observational site in Tautenburg. Tests with real data confirmed this result.

Tests were made to find an effective selection process for the reference objects. The general idea is to select a high number of reference objects with signals that are photon-noise limited. Random errors do not affect the resulting photometry strongly anymore using high numbers of non-variable reference objects. A range of the instrumental magnitude was selected to limit the total number of potential reference objects. Under the assumption that the high majority of all stars are non-variable a mean magnitude difference from frame-to-frame can be calculated for all potential reference objects. This average change of magnitude is used to correct the light curves of all potential reference objects. Then light curves of non-variables showing the lowest RMS can easily be selected as final reference objects. The number of final reference objects is another parameter which can be varied to find as much as possible light curves with a sufficiently low RMS to search for transit-like signals caused by exoplanets. Results of these

Table 5.3.: Results of tests to determine an effective procedure for the selection of the reference objects. Only data for one typical night (5.5 hours, BEST target field 8) are displayed here for comparison. Similar tests were carried out for data of different nights and target fields. The range of the instrumental magnitude for potential reference stars (first column) and the number of selected reference stars (first number of the second column, the second number gives the number of all potential reference stars) were varied to get a high number of light curves with high precision. A magnitude range from –12.50 to –10.50 and a number of 100 selected reference objects (red marked) is a good compromise to reach a high number of light curves with precision better 0.5 percent and 1.0 percent without to high computational effort. The tests for different data sets yielded the same result.

Magnitude range of reference objects [mag]	*Number of reference objects*	*Number of light curves with a RMS < 0.5%*	*Number of light curves with a RMS < 1.0%*	*Number of light curves with a RMS < 1.5%*
-12.50 - -11.50	10/69	187	608	915
-12.50 - -11.50	50/69	198	608	916
-12.50 - -11.00	10/128	195	610	917
-12.50 - -11.00	50/128	199	605	916
-12.50 - -11.00	100/128	200	609	914
-12.50 - -10.50	10/219	196	609	920
-12.50 - -10.50	30/219	194	610	918
-12.50 - -10.50	50/219	199	606	916
-12.50 - -10.50	70/219	202	607	915
-12.50 - -10.50	90/219	199	610	916
-12.50 - -10.50		200	609	917
-12.50 - -10.50	125/219	200	605	915
-12.50 - -10.50	150/219	199	606	917
-12.50 - -10.50	175/219	198	608	918
-12.50 - -10.50	200/219	200	608	917
-12.50 - -10.00	10/313	194	610	919
-12.50 - -10.00	50/313	200	606	917
-12.50 - -10.00	100/313	199	610	918
-12.50 - -10.00	200/313	199	608	919
-12.50 - - 9.50	10/481	194	610	920
-12.50 - -9.50	50/481	200	610	916
-12.50 - -9.50	100/481	200	609	918
-12.50 - -9.50	150/481	201	607	918
-12.50 - -9.50	200/481	202	608	919
-12.50 - -9.50	300/481	202	608	920

tests are displayed for data of one typical night in Table 5.3. More tests were done for data of different nights and different target fields to select the final parameters for differential photometric correction of the reduction pipeline.

Howell at al. (1988) proposed confining the entire photometric calibration process to small subsections of the CCD. The systematic errors that neighboring stars in the same CCD subsection have in common are correctable in this way. To test this calibration method we divided the CCD images in 4 by 4 subsections. Differential photometric corrections were determined and the light curves were thus calibrated in the single subframes. Only minor improvements of the photometric precision were reached for the total number of light curves. Because of the minor improvement of the precision and the associated high computational effort this method was not considered viable for photometric corrections.

5.5. Astrometry

Astrometric coordinates are needed to be able to connect the light curves of the objects from night to night and to identify the objects in data bases of interest. The calculation of the astrometric coordinates of the observed objects in the first frame of the data set is following the light curve calibration process.

The coordinate system that is used so far is the pixel coordinate system of the CCD with the coordinates x and y. The observed FOV is not exactly the same for data sets of different nights due to pointing errors. Therefore the star signals are not centered on the same pixel position.

Standard astronomical software (e.g. MIDAS) includes astrometry packages, but our goal to develop an automated software based on IDL useable on all kinds of computer platforms has made it necessary to develop an IDL program that determines the astrometric coordinates for our purposes. The limitation that no coordinates of the frame center are to be contained in the fits header of the frames (due to software inabilities) made it impossible to use any of these already existing routines.

For a first approach of the determination of the relative standard coordinates right ascension (RA) α and the declination (DEC) δ linear approximations were used:

$$\begin{aligned} \alpha_i \cos\delta_i &= a + bx_i + cy_i \\ \delta_i &= d + ex_i + fy_i \qquad i = 1,2,3. \end{aligned} \qquad (5.5.)$$

This simple system of equations as given by (Rackham 1972) is able to handle errors like small orientation errors, non-perpendicularities of the axes in the pixel coordinate system, centering errors and tilt errors due to non-perpendicularity of the optical axis to the plane of the CCD chip, as long as these errors are small (< 1°). Displacement of the stellar images by refraction for airmasses less than 2 and aberration can be treated by these linear approximations.

Three bright but not saturated reference stars (suffixes 1, 2, 3 refer to the three stars) at larger distances (well-distributed over the whole FOV) were used to calculate the linear 'plate' constants a, b, c, d, e and f. a and d are the standard coordinates of the image center. The pixel coordinates x_i and y_i were calculated as barycenters of the PSFs of the stars by the SourceExtractor software. The standard coordinates of the three identified stars were taken from the HST Guide Star Catalog Version 1.2 (Lasker et al. 1996). Absolute position errors of that catalog are about 0.3-0.4 arcsec corresponding to 0.055 – 0.073 pixels on our CCD. The errors of the determination of the pixel coordinates of SourceExtractor are comparable in range to the errors of standard coordinates. The combined error will be smaller than one arcsec and therefore precise enough for the purpose of linking the star signals.

Note that the coordinates of epoch 2000.0 were used without corrections for the proper motions. Based on information given by the Tycho-2 Catalogue (Hog et al. 2000) typical

annual proper motions of dwarf stars in the observed target fields are about 20-30 mas/yr corresponding to $5 \cdot 10^{-3}$ pixel of our CCD. For giant stars the proper motions are smaller than 10 mas/yr. Therefore corrections by the proper motions are negligible for our purpose of linking star signals of a maximal time difference of 2 seasons.

The standard coordinates of any other star are calculated by using the determined 'plate' constants and the pixel coordinates measured by SourceExtractor.

The resulting astrometric standard coordinates especially for stars with larger distances to the three reference stars showed large discrepancies of up to 30 arcsec compared with the catalog data. Using more reference stars to calculate averaged plate constants has reduced the errors of the calculated standard coordinates, but unacceptably large and systematic errors remained.

These errors were caused by the special optical system that we use: a Schmidt-Cassegrain system. The Schmidt corrector plate transforms the spherical image into a flat image. Because of this transformation second and third order terms have to taken into account as given by Montenbruck & Pfleger (1994):

$$\alpha_i \cos\delta_i = a + bx_i + cy_i + c_a x_i y_i + c_b x_i^2 + c_c y_i^2 + c_d x_i^3 + c_e y_i^3 + c_f x_i y_i^2$$
$$\delta_i = d + ex_i + fy_i + f_a x_i y_i + f_b x_i^2 + f_c y_i^2 + f_d x_i^3 + f_e y_i^3 + f_f x_i y_i^2, \qquad i = 1,2,3...,9. \quad (5.6.)$$

At least nine reference stars have to be identified in an image to be able to calculate the plate constants. These nine resulting homogenous equations can be written as a matrix system. The matrix system for the calculation of the declination δ is structured in the following way:

$$\begin{pmatrix} 1 & x_1 & y_1 & x_1y_1 & x_1^2 & y_1^2 & x_1^3 & y_1^3 & x_1y_1^2 \\ 1 & x_2 & y_2 & x_2y_2 & x_2^2 & y_2^2 & x_2^3 & y_2^3 & x_2y_2^2 \\ 1 & x_3 & y_3 & x_3y_3 & x_3^2 & y_3^2 & x_3^3 & y_3^3 & x_3y_3^2 \\ 1 & x_4 & y_4 & x_4y_4 & x_4^2 & y_4^2 & x_4^3 & y_4^3 & x_4y_4^2 \\ 1 & x_5 & y_5 & x_5y_5 & x_5^2 & y_5^2 & x_5^3 & y_5^3 & x_5y_5^2 \\ 1 & x_6 & y_6 & x_6y_6 & x_6^2 & y_6^2 & x_6^3 & y_6^3 & x_6y_6^2 \\ 1 & x_7 & y_7 & x_7y_7 & x_7^2 & y_7^2 & x_7^3 & y_7^3 & x_7y_7^2 \\ 1 & x_8 & y_8 & x_8y_8 & x_8^2 & y_8^2 & x_8^3 & y_8^3 & x_8y_8^2 \\ 1 & x_9 & y_9 & x_9y_9 & x_9^2 & y_9^2 & x_9^3 & y_9^3 & x_9y_9^2 \end{pmatrix} * \begin{pmatrix} d \\ e \\ f \\ f_a \\ f_b \\ f_c \\ f_d \\ f_e \\ f_f \end{pmatrix} = \begin{pmatrix} \delta_1 \\ \delta_2 \\ \delta_3 \\ \delta_4 \\ \delta_5 \\ \delta_6 \\ \delta_7 \\ \delta_8 \\ \delta_9 \end{pmatrix} \quad (5.7.)$$

The 9 by 9 matrix is called A in the following. Solutions for the plate constants d, e, f, …, f_f can be calculated. The determinant of the matrix A is determined. In a next step a new matrix called B is formed; whereby the first column of A is replaced by the known declinations of the 9 reference stars δ_1, δ_2, …, δ_9 according to the Cramer Rule. Now the solution for the first plate constant is calculated:

$$d = \frac{\det B}{\det A}. \quad (5.8.)$$

The remaining plate constants are calculated in a similar way. To determine the second plate constant e the second column of A is replaced by δ_1, δ_2, …, δ_9 to form B, for the third constant the third column is replaced and so on.

After the determination of all nine plate constants related to the declination δ, the plate constants a, b, c, c_a, …, c_f related to the right ascension have to be calculated. The matrix

system is formed in a similar way as for calculations of the right ascension parameters in equation 5.7. The solution is determined with the same method as used for the calculation of the plate constants related to the declination.

The third order terms are necessarily taken into account. The typical dimension of the constants is about 10^{-12}, this yields to a maximal correction of about 30 arcsecs.

To reach the highest possible precision for all stars it is important to choose reference stars which are well distributed over the whole FOV. The resulting astrometric precision corresponds to one pixel, only the coordinates of few single stars have errors of up to two pixels. This precision is sufficient enough for the purpose of linking light curves from night to night under the consideration that only stars with distances larger three pixels can be separately detected by SourceExtractor.

An additional task is to determine a relation between the instrumental magnitude and a magnitude of a known photometric system. Observations of the Berlin Exoplanet Search Telescope system are carried out without a filter system and are therefore white light observations dominated by the sensitivity of the CCD chip (see Figure 3.5.). The effective wavelength of the CCD is about 720 nm in the red part of the visual spectrum. Only combinations of wide band filters in this part of the spectrum can be used to derive a relation for the instrumental magnitude. The USNO-B1.0 catalog (Monet et al. 2003) offers two R magnitudes R1 and R2 for stars up to magnitude 20. The differences of the mean of the R1 and R2 catalogue magnitudes to the BEST instrumental magnitude is determined for the nine reference stars. The averaged difference is then added to the instrumental magnitude of all stars yielding a to a roughly calibrated R magnitude. Further tests were carried out with photometric data given by other catalogues, but the averaged R1 and R2 magnitudes used for magnitude calibrations showed the smallest deviations in magnitude shift for stars of different spectral type.

After the calculations of the astrometric coordinates and the R magnitude for all stars in the first frame of individual nights the light curves can be linked from night to night.

5.6. Search for transit-like signals

All the light curves have to be analyzed if there are any detectable transit-like signals contained. Transit signals have a relatively short duration compared to the orbital period. For Hot Jupiter planets the duration of the transit signal is typically less than 5% of the orbital period. Due to the short duration of the transit signal compared to the non-occultation phase the light curve is non-sinusoidal. The transit signal shows a special spatial form which can be used for detection. Due to the short ingress/egress times relative to the total signal length for most of the transit signals (grazing transits are excluded) the signal can be assumed to be box-shaped. This neglects the limb darkening effect. But this effect is one order of magnitude lower than the signal depth and can therefore be neglected without losing too much S/N (see section 2.1.). Thus a box-fitting algorithm was developed to search for transit-shaped signals. As a first step the algorithm was developed to search for signals in light curves obtained during single night observations.

5.6.1. Search for transit signals in data of single nights

The following steps are performed in preparation for the box search. First a sigma clipping routine is applied to exclude data points that are significant outliers. All data points lying more than 3σ above the mean value were excluded. A lower clipping limit was not applied to

avoid loosing signals that could be part of deeper transit signals. Instead of a lower clipping limit the data point with the lowest signal is excluded from further analysis.

In a second step a linear least square fit is applied to the light curves to reduce the influence of long-term variability and trends.

Furthermore the light curve data is binned to increase the signal to noise (S/N) ratio. All data points within 0.5 hours are averaged to a single data point. Longer bin intervals would further increase the S/N ratio, but short and shallow transit-like signals (i.e. grazing transits) could be lost for longer bin intervals.

The possible transit duration was limited to an interval between one and four hours corresponding to 2 - 8 data points (binned) in series as typical for Hot Jupiter transits including grazing transits. A lower limit of about 0.4% is set for the signal depth; no upper limit is set to avoid missing deep transit signals of giant planets orbiting small K or M dwarfs. This flexible transit depth reduces the computational efforts compared to other search algorithms with fixed box depths like the BLS algorithm of Kovács et al. (2002). For these algorithms different runs with different box depths have to be applied to detect transit signals of all possible depths. The disadvantage of a flexible box depth is an increased number of false alarms mainly due to assemblies of noisy data points and signals of eclipsing binaries. The number of these false alarms is reduced by comparing the intra-signal noise with the noise of the light curve outside the transit signal. As a final test the S/N of the signal is calculated. This S/N ratio depends on the signal depth, δI, the number of data points within the transit signal, n, and the photometric precision of the light curve outside the signal σ assuming that the noise during the transit phase is the same as outside the transit phase (Pont 2005):

$$S/N = \frac{\delta I \sqrt{n}}{\sigma} \qquad (5.9.)$$

The signal within the transit signal is excluded from the S/N calculation. Fitting a box to a signal that is not boxed-shaped would decrease the S/N. Note that there is no risk of missing a transit signal in a light-curve of a short-period variable. These stars of spectral types A, B, F are too large that a transit of a Jupiter-sized planet could be detected in the noise of data of ground-based photometry.

The photometric precision is calculated as

$$\sigma = \frac{1}{m}\sum_{i=1}^{m}\left|I_i - \bar{I}\right|, \qquad (5.10.)$$

where I_i represents the signal strength of the m'th data point and $\bar{I}$ is the mean signal strength.

Next, the detection limit of the S/N has to be chosen to discriminate between random noise events and possible reliable signals. Kovács et al. (2002) has shown for box searches, that pure noise signals almost exclusively have a S/N ratio below 6. Real signals have higher S/N ratios. Tests were carried out confirming this result. Thus we considered a S/N of 7 to be the detection limit for our transit search.

What kind of single signals will be detectable with this detection limit? A typical transit signal of 3 hours duration has about 16 single data points that can be identified to belong to the signal (ingress/egress are excluded). A Jupiter-sized planet transiting a Solar-like star every 3.5 days causes a signal with about 1% depth. For a light curve with 1% photometric precision a S/N of 4 results. Such a signal is plotted in Figure 5.5. It can barely be seen as a significant detection.

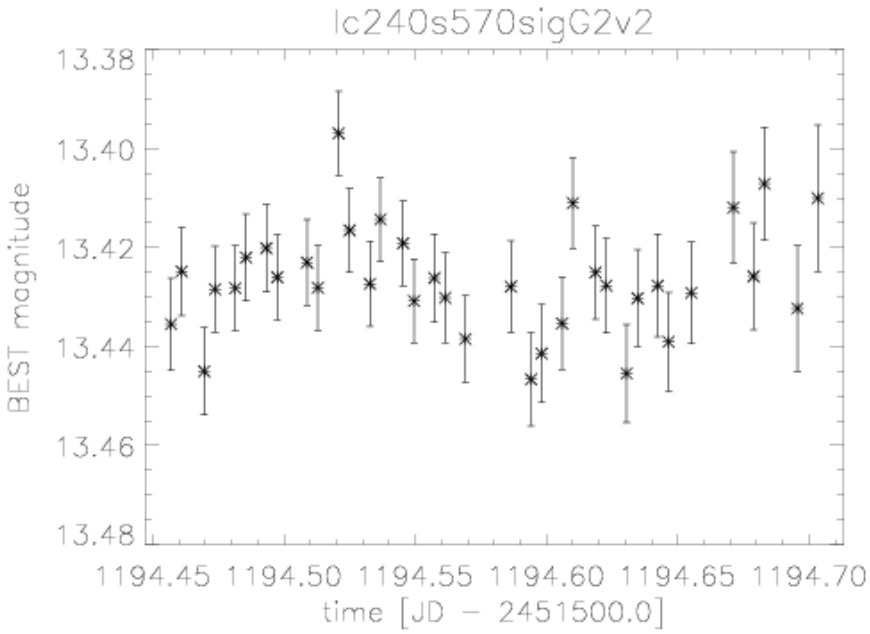

Figure 5.5.: An artificial transit signal (based on the model by Mandel and Agol (2002), see section 2.1.) was inserted into real data with a photometric precision of 1%. The inserted 3-hours transit signals caused by a Jupiter-sized planet orbiting a Solar-like stars in 3.5 days has a mean depth of about 1%. This signal has a low S/N of 4 (see equation 5.8.) and cannot be clearly classified as a significant detection. Signals with S/N < 7 can origin from pure noise with high probability.

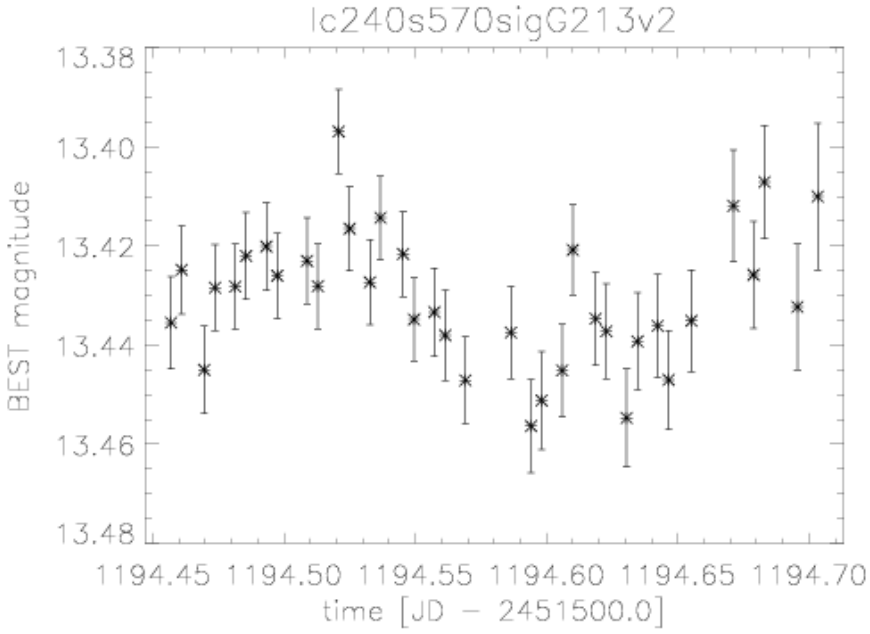

Figure 5.6.: An artificial transit signal was inserted to a real data light curve with a photometric precision of 1%. The 3-hours transit signals caused by a planet with 1.3 R_{jup} orbiting a Solar-like stars in 3.5 days has a mean depth of about 2.0%. This signal has a S/N of 8 and can be seen as a significant detection.

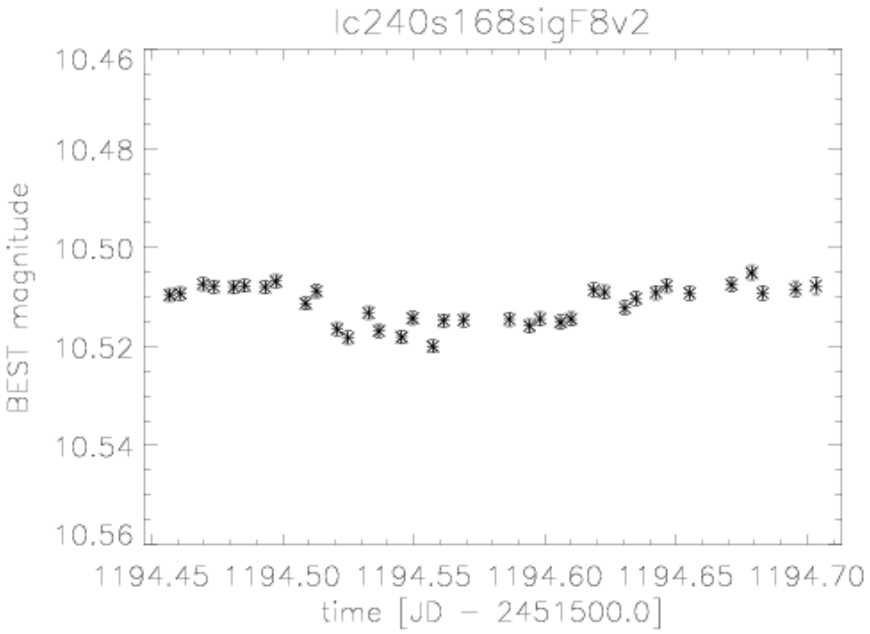

Figure 5.7.: Transit signal of a Jupiter-sized planet orbiting a F8 dwarf in a 3.5 day orbit (depth 0.7%) inserted into a light curve with a precision of 0.2%. Note that the magnitude is scaled similar to Figure 5.5. and 5.6. The S/N of the signal is 14; even smaller signals down to 0.4% can be detected (S/N = 7).

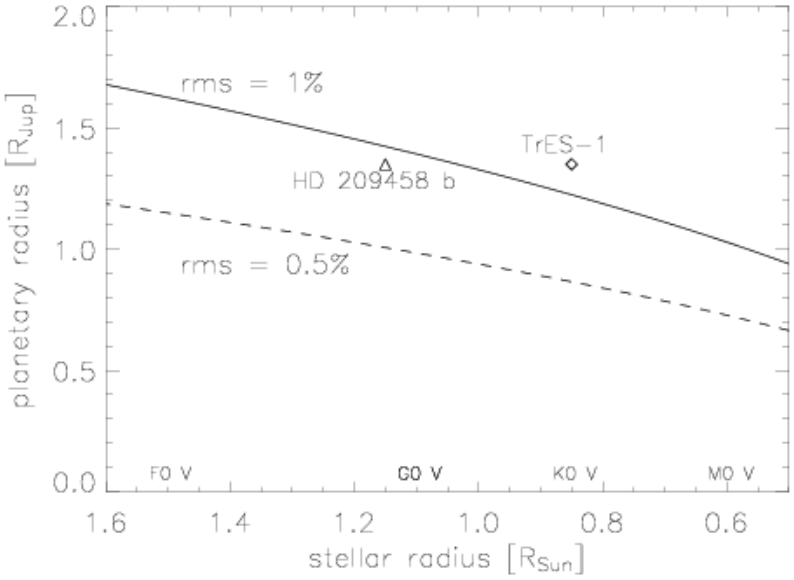

Figure 5.8.: Detectable planet sizes vs. stellar radii of the host stars for planets orbiting in a 3.5 day orbit for one detected signal. Planets above the lines giving the photometric precision of 1% (solid line) and 0.5% (dashed line) could be detected.

A S/N of 8 is obtained for a signal with a mean depth of 2.0% assuming the same duration and orbital period as before. Such a signal is plotted in Figure 5.6. for comparison. Note that this signal is comparable to the transit signal caused by the HD 209458 b planet in depth and duration.

In additional tests the detection limits for different sized host stars were determined. The following spectral types were included: from A0 V ($R = 2.4\ R_{sun}$) to M2 V ($R = 0.5\ R_{sun}$). The stellar parameters of the stars were assumed to be similar as in Krautter et al. (1994).

Observations are assumed to be made in R band filter. Again a 3.5-day orbit was considered for the calculations. An example light curve can be seen in Figure 5.7.

For light curves with 1% photometric precision, transits of Jupiter-sized planets can be detected for host stars with a radius less than 0.9 R_{sun} (corresponding to spectral class G8 V). For light curves with a better photometric precision of 0.5% this limit increases to spectral class G2 V (solar-like). Even planets with a radius of 0.8 R_{jup} would then be detectable.
In figure 5.8. the detection limits for photometric precisions of 0.5% and 1.0% are given for the examined range of radii of the host stars.

For light curves with the highest precision of 0.2% reached with BEST observations single transit with a depth of about 0.4% could be detected. This corresponds to a transit signal of a Jupiter-sized planet orbiting a late A-type star. If a maximal planet size of R=1.5 R_{jup} is assumed then planets could be detected for host stars with a radius up to R=2.5 R_{sun} (early A-type star). For a M dwarf with half solar radius even planets with a radius of 0.3 R_{jup} are detectable with a photometric precision of 0.2%. But note that these are extreme cases. Only very few stars are monitored with this precision. The monitoring of M dwarfs is very unlikely due to their limited absolute magnitude.

5.6.2. Search for transit signals in folded light curves

For light curves assembled from data of several nights some additional preparations have to be made before signals can be detected. One feature of the BEST light curves are magnitude offsets up to a few percent between data from night to night. The detection of a transit event requires only that the relative precision is maintained over a single night due to the relatively short duration of a transit in the order of three hours. In this way the need for long-term stability is reduced. This allows to concentrate on obtaining very high precision for hour-to-hour measurements. For variations of the stellar flux with longer duration than a single night this yields to lower detection probabilities, but the main purpose is of the BEST survey is transit search.

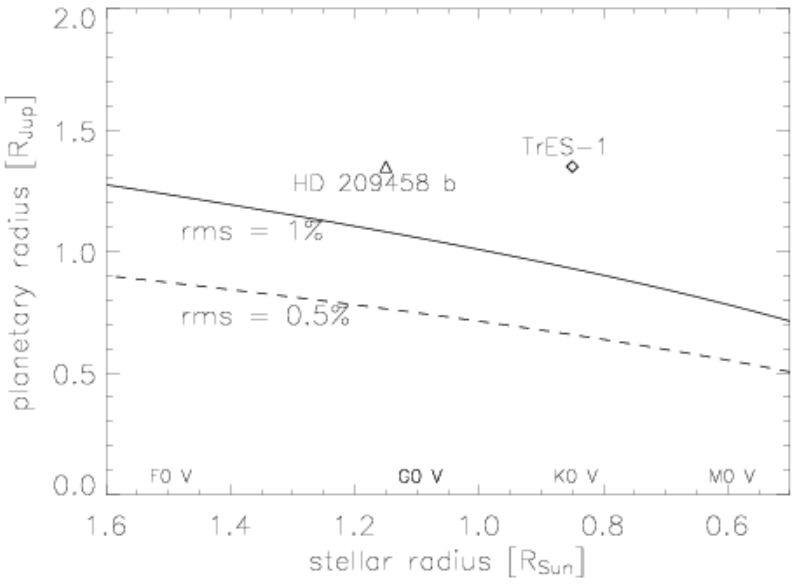

Figure 5.9.: The same as in Figure 5.8. but now for three detected signal in folded data. The detectable planet sizes are significantly decreased in comparison for signals that were detected once.

Remember that long-term stability needs high efforts to maintain especially for a transit search where the nightly set-up varies for most of the nights. For BEST we had to unmount/mount the CCD after nightly observations. Sometimes the entire telescope tube was unmounted due to bad weather. Flat field images were collected every night, but the flat field calibration was not perfect. Imperfect pointing during flat fielding yielded small gradients in the illumination of the flat field images. This gradient differed from night to night. Additionally the use of a photometric aperture with a flexible size to improve the nightly photometric precision in combination with variable PSF sizes resulted in small magnitude offsets for the reference stars for the magnitude calibration. Therefore the magnitude offset depends on the position of the stars on the CCD, even this position was variable in a dimension of a few dozens of pixels. Altogether these effects yielded the magnitude offsets especially in the vignetted area of the FOV. Note that in a next reduction pipeline these offsets will be reduced either by using of local PSF fitting that reduces the influences of the flat field errors or by a more sophisticated method of flat field calibration. Nevertheless, the chosen procedure was able to reach high nightly photometric precision that is needed for transit search.

How are these magnitude offsets treated for the signal detection? First all zero signals were removed, and then all data gaps longer than 0.5 hours were identified. The small time span of 0.5 hours was chosen to include data gaps when the guide star was exchanged. In most cases the guide star was changed to a brighter star when the transparency of the atmosphere degraded yielding unstable guide operations. This exchange of the guide star resulted in shifts of the FOV and thus resulted in magnitude offsets for the stars especially in the vignetted

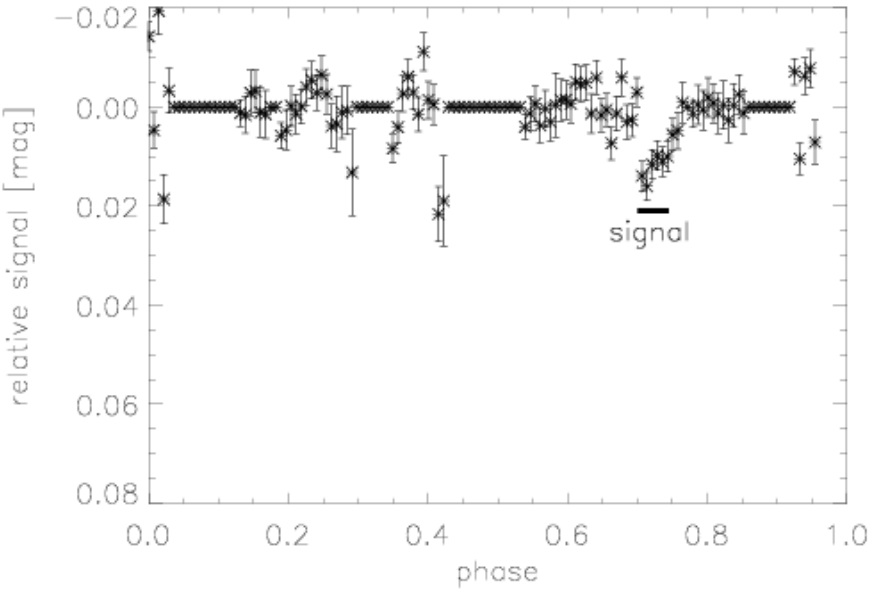

Figure 5.10.: Artificial transit signal of 1% depth (duration three hours) detected in a folded light curve based on real data. The light curve shows an overall photometric precision of 1% (unbinned). Three transit signals have to be recorded to reach a significance of 7σ. A single transit event can be seen in Figure 5.5. Note that the data points with no error bars are data gaps.

area of the CCD image. Therefore these data gaps were treated in the same way as data gaps from one observation to the next one.

The data are separated into data subsets based on the identification of the data gaps. The signals in these subsets are normalized to remove the magnitude offsets. Outlying data points are removed as described in the subsection before. A linear least-square fit is applied to the

subset of the data to remove long-term trends. In a next step the data are folded with trial periods. These trial periods range from 0.5 days to 10.0 days with a step size of 0.01 days to be able to detect transit signals of Hot Jupiters. Then all data points within 0.5 hours are binned.

Finally the detection algorithm searches for transit-like signals in a similar way as described for the signal search in nightly data.

The detection algorithm was tested as for data of single nights. Artificial transit signals were inserted into light curves of real data. Again 7σ signals were found to be significant detections. This means that a typical transit signal of a Jupiter-sized planet orbiting a Solar-like star in 3.5 days with a signal depth of 1% can be detected in folded light curves if it was observed three times with a photometric precision of 1% (see Figures 5.9. and 5.10.). If an M dwarf ($R=0.5R_{sun}$) were to be monitored with a photometric precision of 1%, then transits of planets with a radius down to 0.5 R_{jup} are detectable if 3 detections were recorded. For better photometric precisions of 0.5% or 0.2% and 3 recorded transit events even planets with smaller radii can be detected: 0.35 R_{jup} or 0.22 R_{jup}. The latter corresponds to 2.4 R_{earth}. Nevertheless, as stated before, the numbers of monitored M dwarfs are rare. F and G type main sequence stars are more commonly monitored and therefore a Solar-like star is a more realistic reference object for the determination of the detectable planet size.

5.6.3. Comparison with other detection methods

Several detection algorithms for transit signals have been proposed in the recent literature: the BLS (Boxfit Least Squares) method of Kovács et al. (2002), matched filters (Jenkins et al. 1996) and Bayesian algorithms (Doyle et al. 2000; Defaÿ et al. 2001 and Aigrain & Favata 2002). Tingley (2003) carried out a theoretical comparison test of these algorithms concluding that 'no detector is clearly superior for all transit signal energies' and the best method for identifying transit events is to apply all filters.

In preparation for the COROT satellite mission (Baglin et al. 2003) a comparative blind test for detection of transit-like signals in simulated data of the COROT satellite was conducted in 2004. Five teams including a DLR team have participated testing different approaches for identifying transit events. The results of this test were published in Moutou et al. (2005).

For this test 1,000 synthetic light curves were built based on the instrumental model and models for stellar variability. The instrumental model constructed by Auvergne et al. (2003) contains effects like environmental perturbations, radiation flux, jitter from pointing errors of the satellite, temperature variations, scattered light from the earth combined with a CCD noise model. Stellar variability was added using two different models. Lanza et al. (2003) constructed a stellar model based on a rotational modulation of three active stellar regions and a uniformly distributed background. The rotational period and the areas of the active regions were varied to simulate a wide range of stellar types with different states of activity and ages. The SIMLC tool of Aigrain et al. (2004) was the second tool to simulate stellar variability. Based on a fit to solar data an artificial power spectrum is computed and rescaled. A set of 45 light curves for stars of spectral types F5 V to K5 V and different ages was modeled.

Twenty transit signals of planets with sizes from 1.6 Earth radii to 1.3 Jupiter radii and orbital periods from four to 90 days were inserted. The host stars were chosen such that the transit signals were close to the detection limit.

Additionally the signals of 6 grazing binaries, 4 background binaries, 1 triple system and 5 different short-period background variables were inserted. To simulate crowding an additional stellar signal 0-6 mag fainter than the main signal was added to each light curve.

In the COROT blind test five methods were used to detect the transit events:

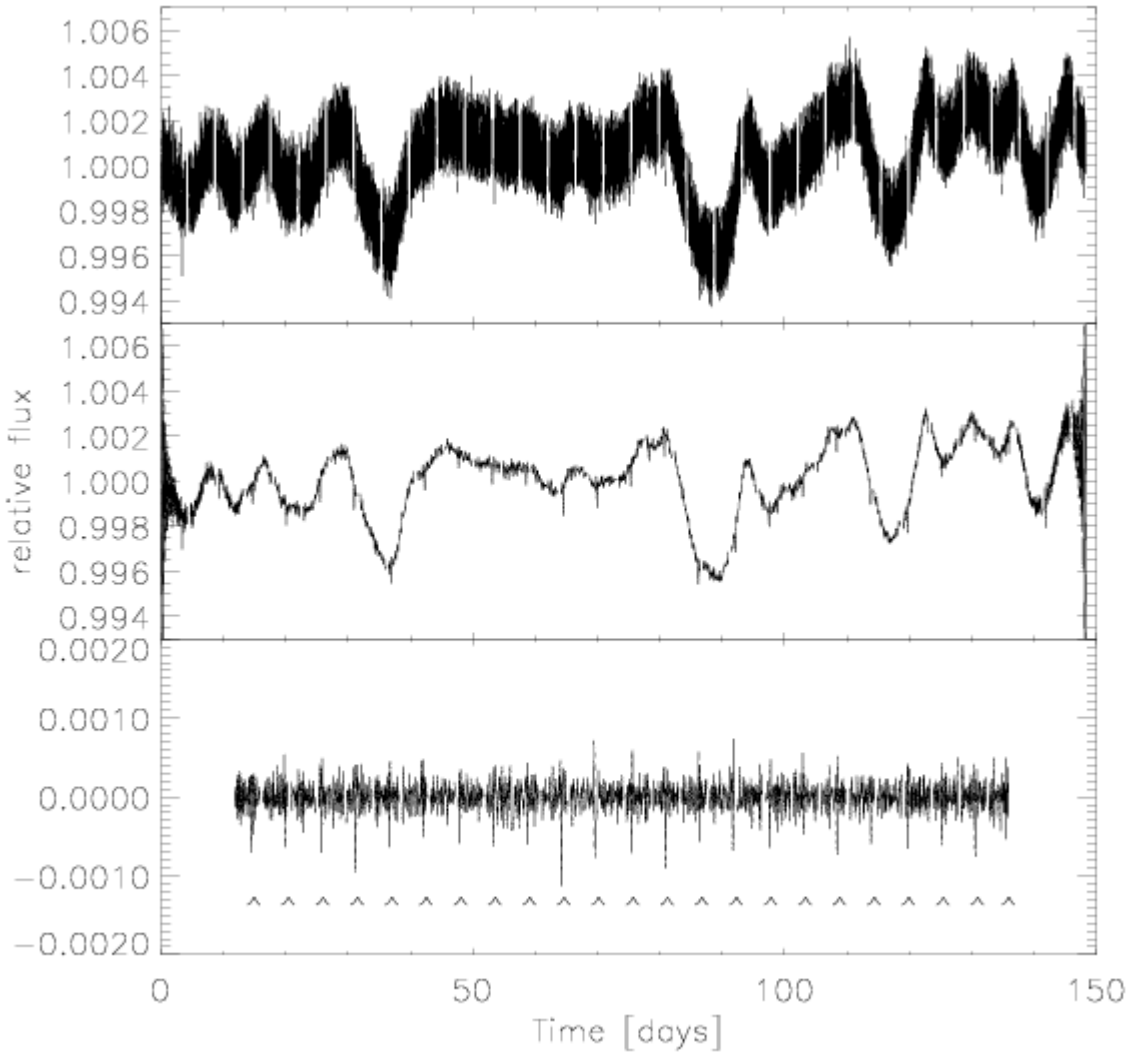

Figure 5.11.: The different steps of the transit search process are displayed. The raw data are normalized (top), then the data gaps are interpolated and a lowpass-filter is applied to the data (middle). Finally the stellar variability is modeled, a search for transit-like signals is performed and their periodicity analyzed (bottom). The detected signals are marked.

a) The first algorithm applies a single sliding transit template to the data and computes the correlation function between template and data. Before detection short-term systematic noise is removed by applying a linear noise model to the data. The detected single transit-like events were finally chosen by eye (for details see Moutou et al. 2005).
b) The light curves were detrended via fitting by 200 harmonics. The transit signals were detected by a box fit on phase folded data (for details see Moutou et al. 2005) .
c) A detection method described in Guis & Barge (2005) is performed: the data is denoised with the 'Gauging Filter' and a matched filter is used for signal detection.
d) Systematic noise residuals from scattered light is removed by 1-D filtering light curves folded at the best fit period. Long periodic stellar variability is

treated by applying an iterative non-linear filter (Aigrain & Irwin 2004). A box search is used to find transit-like events.

e) The DLR team used an approach based on the box search for single events as described in section 6.7.1. First the data are normalized, then data gaps with a maximal time span of 43 min are interpolated. A standard lowpass-filter with a variable cut-off frequency (maximal 0.177 day^{-1}) is applied to the data to remove systematic residuals of the scattered light contribution and other short-term variabilities. Long-term variability is fitted locally for subsets of data with variable timespan. The fit is subtracted from the data (see example in Figure 5.11.). A box-search is performed in unfolded data detecting single transit-like events. The depth of the box-signal is kept variable, the length of the signal can vary between one hour to 30 hours (duration of Jupiter transit 29 hours). The mean epochs for the detected signals are analyzed for periodicity. Both single and periodic events were recorded.

Nine of twenty transit events were detected by all teams. The smallest planet detected by all teams had a radius of 2.5 Earth radii demonstrating the detection limit for the COROT satellite mission. Seven transiting planets with radii of 1.8 to 2.5 Earth radii were not detected by any team.

Our team detected 11 transiting planets. For most of the non-detections some individual single events were detected on a very low confidence level, but most of the signals were below the chosen detection level of 3σ. To maximize the S/N of the signals a search in folded data is necessary to be able to detect the fainter signals. Note that the detection threshold can be raised for the box search in folded data to avoid false detections as made for the single false detection with the mimimal confidence level of 3σ.

Only one detection was missed due to confusing stellar variability with a timescale comparable to the timescale of the transit event. Note that for ground-based transit search this variability is typical for stars that are too large to be sufficient target stars for transit search.

The five applied detection methods were able to find the majority of inserted transit-like signals. Best results were achieved by more evolved and specialized search algorithms especially for the detection of shallower signals.

5.7. Summary of chapter 5

In this chapter it has been described how the data are calibrated and analyzed by a automated reduction and analysis pipeline.

In a first step the raw images are calibrated. This includes the creation of an median-filtered masterbias, which is normalized based on the analysis of the mean bias level of the oversampled margin region of the CCD images. Masterdarks for all exposure times used are obtained by subtracting the scaled masterbias from the single dark frames and averaging these bias-subtracted dark frames. In the following step all flat field images are bias- and dark-subtracted, the individual flat field frames are co-added. Then the co-added flat field frame is normalized yielding the masterflat. Then the scaled masterbias and the dark frame corresponding to the exposure time of the stellar frame are subtracted from the raw light exposures. Finally these light exposures corrected for bias and dark current are divided by the masterflat frame yielding the calibrated light exposures.

In the individual calibrated light exposures the stellar signals are detected by thresholding of the SourceExtractor software (Bertin & Arnouts 1996) after the subtraction of the background map. In a next step a flexible aperture is applied to the signals guarantying that a constant fraction of the total flux is measured within the aperture for the whole magnitude

range of the signals analyzed. This procedure was chosen after intensive tests with artificial data simulating changes in transparency and seeing as typical for BEST observations from TLS. Tests with real data of typical observational nights additionally supported using the flexible aperture approach for the photometric measurements in the BESTRED pipeline.

Further the light curves of individual nights are assembled by determing the mean linear shifts for the pixel coordinates of the brightest 11 stellar signals in the images and applying these mean shifts to all other objects detected in the images.

The resulting light curves are calibrated by applying a mean extinction term to all light curves. This extinction term is calculated as a mean of the magnitude changes from frame to frame for a high-number of selected non-variables. These reference stars are chosen from all stars (within a large, defined magnitude range covering the brighter, non-saturated stars) by an iterative process, that searches for the minimal RMS scatter for all light curves.

In a next step an astrometric solution for the images is calculated based on the identification of nine bright, but non-saturated stars in a single image of the observational night. Observations with a Schmidt telescope make it necessary to calculate nine plate constants up to third order for each of the astrometric coordinates right ascension and declination. The calculated astrometric coordinates are used to link the light curves from different nights.

All light curves are analyzed if they contain transit-like signals. In a first step the data of individual nights are analyzed just after the creation of the single-night light curves to allow an immediate start of the follow-up analyses and observation. Single outlying data points with higher signals than the mean signal are clipped. A linear fit is applied to minimize nightly trends in light curves. The data are binned in 0.5-hour intervals to increase the S/N for the detection of signals. After this preparatory work a box search algorithm is applied to the light curves identifying the transit-like signals.

The search for transit-like signals in light curves combined from all observations is applying the same preparatory steps as for light curves of single nights: clipping, linear detrending in nightly intervals and binning. Additionally the light curve data are normalized on a nightly basis and folded for periods from 0.5 days to 10 days. Then the box search algorithm is applied to the data searching for transit-like signals with durations up to five hours.

Detected transit-like signals are inspected and analyzed if they exceed the detection threshold of 7σ. Signals below this detection threshold are mainly random noise, signals above the limit have a high probability to be real signals. In light curves with a RMS of 1% single signals > 1.8% depth exceed this detection threshold for a typical transit duration of three hours. In folded light curves the minimal detectable signal depth is reduced to 1.0% for a signal combined of three single signals. For light curves with a photometric precision better than 1% smaller signals could be detected. Thus in 0.5% precision data single signals of about 0.9% depth are still detectable with an acceptable confidence level.

The detection procedure for single signals was compared with other detection algorithm in a blind test on simulated data of the COROT satellite mission. The detrending techniques were adopted to the characteristics of the simulated light curves. Short duration data gaps were interpolated. Periodic short-term variability mainly due to imperfectly removed scattered light contributions were reduced by a standard low-pass filter. These procedures were additionally carried out to the clipping, normalizing, linear detrending and binning of the light curve data. The signals were detected by a box fitting. Further the detected signals were analyzed for a periodic appearance. The detection algorithm was able to detect signals down to the detection limit and has shown a comparable performance in comparison with the other tested detection algorithms.

6. Results of the observations from the TLS

6.1. General information about the TLS observations

Regular field observations with BEST from the Thüringer Landessternwarte Tautenburg (TLS) started at the end of July 2001; the last observations were carried out in September 2003. Due to initial technical problems during the implication of the SBIG ST-4 guiding system only short exposures of 15 and 40 sec were taken. The technical problems could be solved finally in October 2001 and longer exposures of 240 sec were taken additionally.

Three targets fields (for more details about the field selection see chapter 4) were observed on a regular basis. These regular observations were interrupted on April 1, 2003 due to a failure of the Apogee AP-10 CCD caused by a power surge of unknown origin that destroyed the CCD chip and most of the readout electronics. The CCD mishap was then used to upgrade the system with a CCD chip of higher grade to reduce the readout and dark current noise. During first tests of the upgraded CCD system in September 2003 target field No.15 was observed for one additional night ending the regular observations from TLS.

6.1.1. Observational statistics

Totally during 90 nights observations of three target fields were carried out:

- Target field No.15 (Cygnus):49 nights observed (= 163.3 hours)
- Target field No.2 (Perseus):22 nights observed (= 105.2 hours)
- Target field No.8 (Ursa Major):37 nights observed (= 169.6 hours).

A total observation time of 438.1 hours (= 18.25 days) was obtained. The average duration for the observation of the target fields was about 146 hours. A nightly observation took only 4.1 hours on average. The main reason for shortened observations during the autumn and winter was bad weather at the observational site, mainly high humidity. More information about the single observations is listed in the appendix section C.

Only monitoring phases longer than two hours can give at least some information about stellar variability for the given sampling rate (6-8 images/hour). Only observations with a high number of monitored stars can give a sufficient probability for the detection of a planetary transit. The number of additional light curves of brighter stars gained through the short exposures, that are not contained with higher precision in the time series consisting of 240 sec exposures, are limited to about 10% of the number of high-precision light curves of the 240 sec data. Therefore only observations with the longest exposure time of 240 sec are stated to be efficient for the transit search and are statistically counted for this purpose. This yields to a corrected observational statistic relevant for the transit search:

- Target field No.15 (Cygnus):17 nights observed (= 65.1 hours)
- Target field No.2 (Perseus):14 nights observed (= 69.2 hours)
- Target field No.8 (Ursa Major):32 nights observed (= 148.4 hours) .

The high number of observations for target field No.15 that were not considered to be relevant for the transit search is mainly to be seen as a result of the early observations in 2001 carried out with short exposure times.

Most of the observations for target field No. 2 were carried out during long but dry winter nights with the technically limited maximal duration of about 12 hours resulting in the

relatively high average observational duration of about 5 hours compared to 3.8 hours for target field No. 15.

Observations of target field No. 8 took place mainly in the springtime with more favorable weather conditions resulting in a higher number of observations. Spring and summer have the most favorable conditions. But only in early spring and late summer do the nights have a relatively long duration sufficient for the detection of transit signals with duration of about 3 hours. During the spring there is no access given to observe the star-rich regions of the Milky Way at low airmasses.

Which orbital phase coverage results for the three observed target fields from the selected observational times? A model was developed to estimate the phase coverage of potential transiting exoplanets for the observations of each target field. These simulations were introduced in section 2.3.7. Now the real observation times were used for the calculations. The orbital phase coverage determined is plotted over the possible orbital period of transiting planets for one and three detections (see Figures 6.1., 6.2., 6.3.).

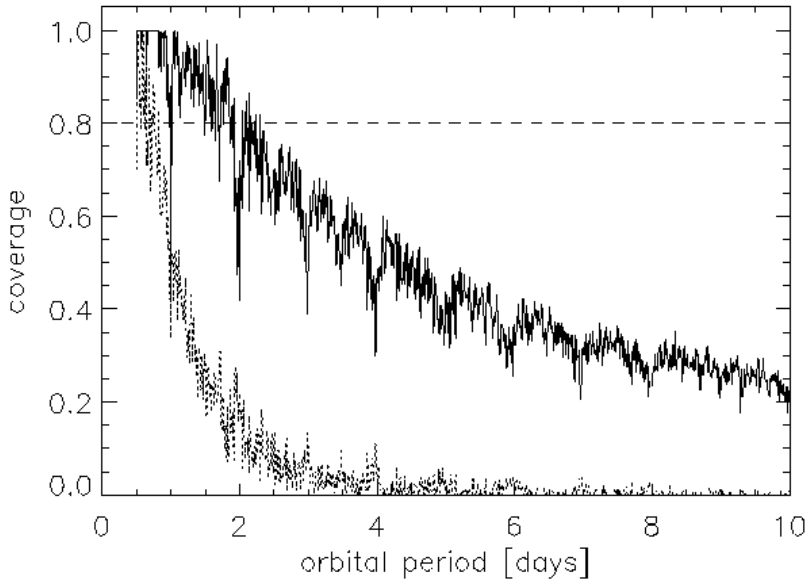

Figure 6.1.: Coverage plotted vs. orbital period of hypothetical transiting exoplanets for observed target field No.15. A phase coverage of 80% for one detection was reached for orbital periods less than two days (solid line). The dashed line gives the coverage for three detections and it is rather low for all orbital periods.

A probability of 80% for the detection of one transit event was obtained for orbits of up to two days for target field No. 15, up to 3 days for field No.2 and up to five days for field No. 8. Therefore all detectable transits of very Hot Jupiters ($P < 2$ days) should have been observed in all three target fields with a probability of 80% or higher depending on the target field. The BEST survey has reached a sufficient coverage for three events only for target field No. 8 for orbits of about one day. The phase coverage for three detections sufficient for the determination of the orbital period of a detected planet for target fields No. 2 and 15 was rather low. Any detections of this kind are unlikely.

Nevertheless, a high number of observations were made. The detected transit-like events are described in the following sections.

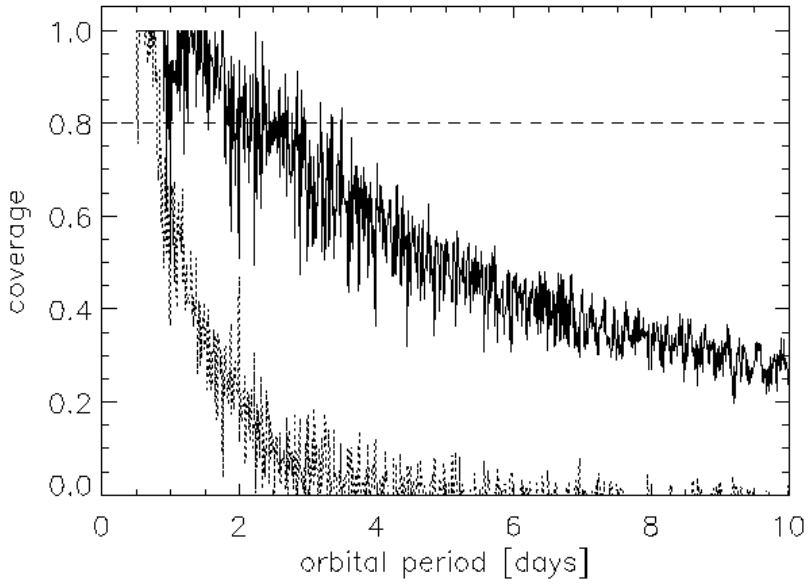

Figure 6.2.: The same plot as in Figure 6.8. this time for the observations of target field No. 2. Sufficient phase coverage was reached for 2-day orbits. Note the higher coverage obtained in spite of a similar total duration of the observations compared to the observations of target field No. 15. This is explained by the relevantly longer durations of the single observational runs.

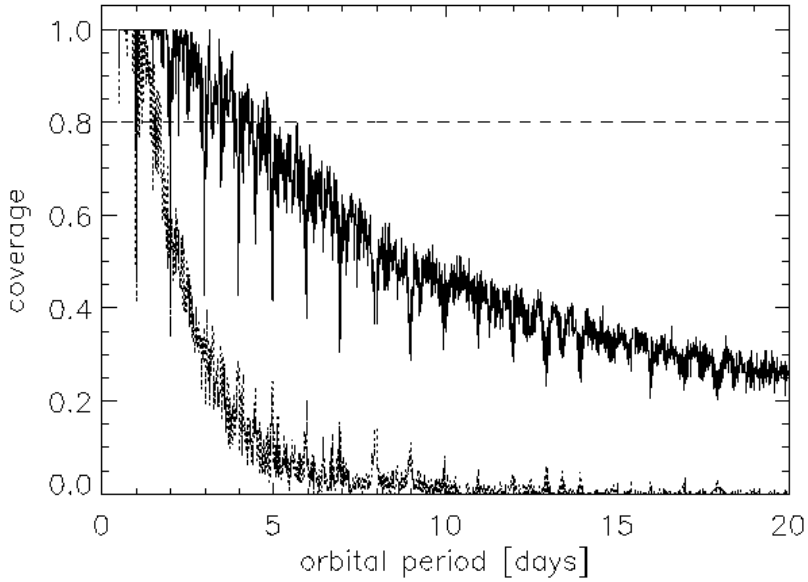

Figure 6.3.: Coverage vs. orbital period up to 20 days plotted for target field No. 8. Phase coverage of 80% was obtained for orbital periods up to five days for one detection. Three detections would have been made for transits with orbits of less than two days.

6.1.2. Photometric quality

The photometric quality of the collected data is clearly of importance. For the detection of single transit events with a depth of one percent a high photometric precision of about 0.5% RMS is necessary. For three detections of the same depth in folded data this is reduced to about 1% RMS (see section 5.7.). The number of stars that provide these quality levels for the

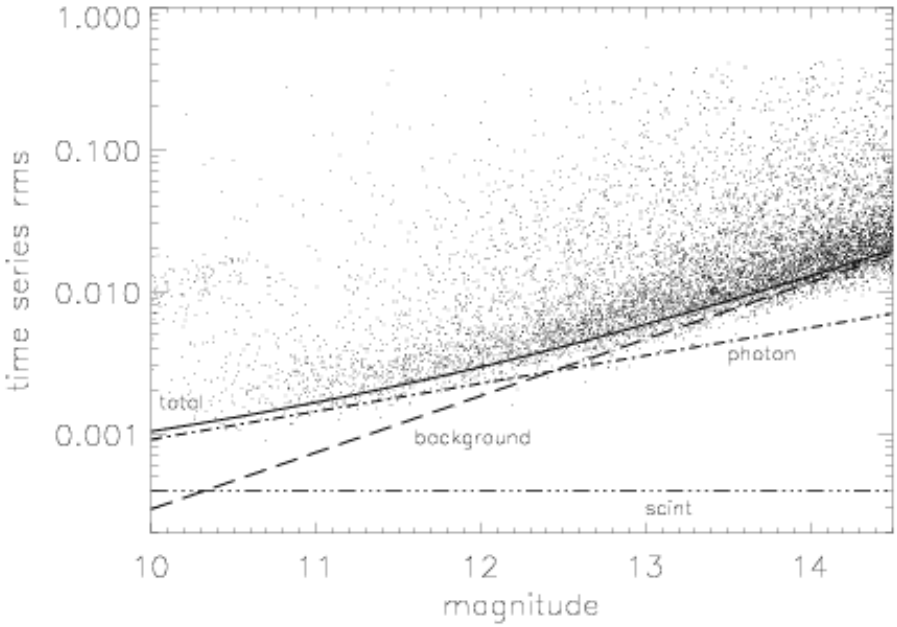

Figure 6.4.: Light curve RMS plotted vs. R magnitude for the 6 hours time series observations of Target field No. 2 from October 14/15, 2001. About 4,000 light curves have a photometric precision better than 1% for 240 sec exposures up to magnitude 14. The noise levels were calculated by equation 2.21, 2.22, 2.23 and 2.24. The light curves of the brighter stars are dominated by photon noise, but the majority of light curves (fainter stars) are dominated by background noise. Light curves of stars with an RMS well above the total noise can be affected by different additional noise sources: stellar variability, increased background noise due to crowding and pixel defects, passing satellites and aircrafts.

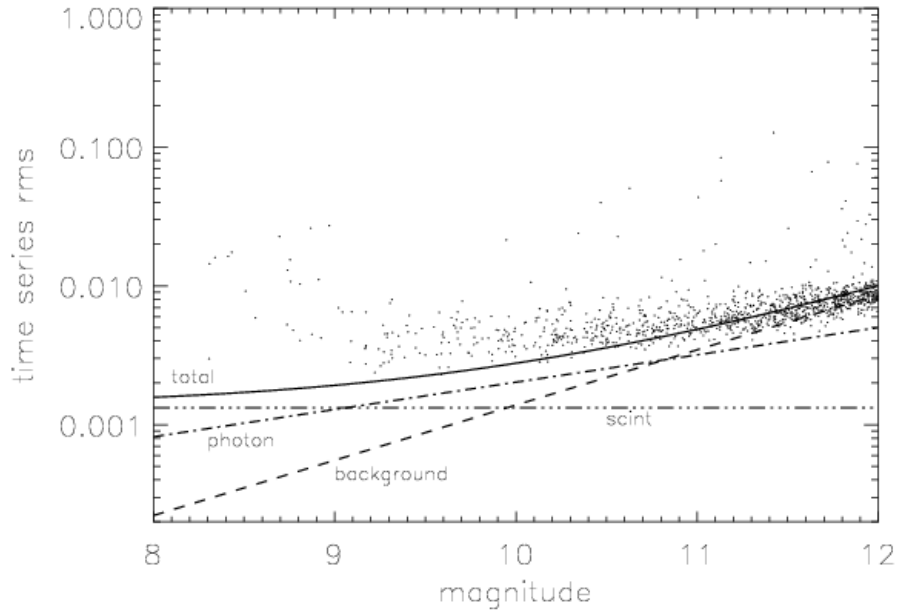

Figure 6.5.: The same as in Figure 6.4. but with an exposure time of 40 sec instead of 240 sec. 383 additional light curves with a photometric precision better than 1% were obtained (magnitude < 11). The precision of these light curves is photon noise limited. More light curves with RMS < 1% are obtained for fainter magnitudes, but light curves for these stars were obtained with higher precision in the time series assembled of 240 sec exposures.

photometry can be used as indicator for the photometric quality of the data.

How many high precision light curves are obtained is mainly dependent on the level of different noise sources. There are three major contributors to noise: Photon noise, background noise and scintillation noise. These contributions can be estimated according to equation 2.21, 2.22 and 2.23 of chapter 2. The total noise could be calculated as in equation 2.24. In Figure 6.4., 6.5. and 6.6. the RMS of light curves of an exemplary night for exposures of 240 sec, 40 sec and 15 sec is displayed. The different noise terms are overplotted.

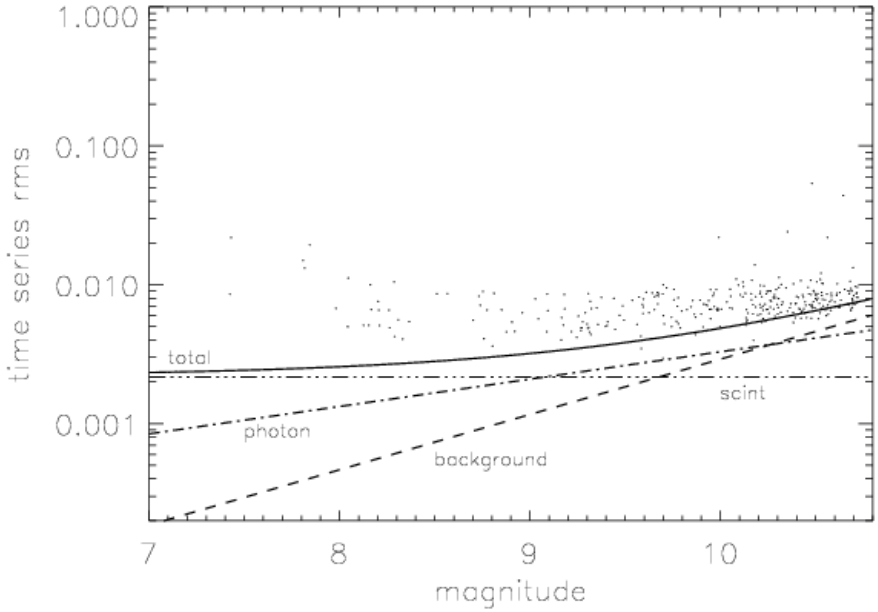

Figure 6.6.: The same as in Figure 6.4.and 6.5. but with an exposure time of 15 sec. 38 additional light curves with a photometric precision better than 1% were obtained (magnitude < 9.2). For most observations this number is further reduced yielding to a low efficiency of the 15 sec observations. Therefore it was decided to cancel further 15 sec exposures to improve the sampling rate of the 40 sec and 240 sec time series.

A comparison of the theoretically obtainable total noise with the actually obtained noise for the light curves can be used to evaluate the photometric quality of the data. The light curves composed of longer exposures (240 sec and 40sec) are dominated by background noise (see Figure 6.4. & 6.5.); only the light curves of the brightest objects are dominated by photon (shot) noise. Scintillation noise is negligible low. Scintillation noise has only a mayor influence on the noise for light curves of bright stars in the 15 sec exposures (Figure 6.6.). Additionally the photon noise contributes in the same order as the scintillation noise. Background noise influences the light curves of the fainter stars (>10 mag) in the time series of the 15 sec exposures. Light curves of stars down to magnitude 14 with a photometric precision better than 1% were obtained during the darkest nights with 240 sec exposures (see Figure 6.4.). 1% precision was reached for time series of 40 sec exposures down to magnitude 12 (Figure 6.5.), for 15 sec exposures down to magnitude 11 (Figure 6.6.).

Only the reduction of the background noise will give a significantly higher number of high precision light curves of fainter stars. Analyses showed that the sky background noise for observations from TLS is linearly dependent from the sky signal, because readout noise and thermal noise are negligible low. Only the detected single hot pixels introduce additional noise, the noise of the general dark current is low enough to be not dominant for the total noise of the light curves.

The plots 6.4.- 6.6. represent observations of the star-rich target field No. 2 during the night of October 14/15, 2001. This night stands out from most of the nights when observations of

star-rich target fields were carried out. The transparency of the atmosphere was high and stable, and the sky background was low yielding a high number of high precision light curves (about 4,000 light curves with precision < 1% for all three exposure times). The number of high precision light curves obtained in the time series of the shorter exposure times 15 sec and 40 sec which are not covered in the time series of 240 sec exposures with higher precision are limited. This number is of about one tenth of the number of light curves resulting from the time series of 240 sec exposures for good photometric conditions. For the common photometric conditions the number of additional light curves especially from exposures of 15 sec is further limited. In good nights only a few dozens additional light curves with a photometric precision just below 1% were obtained. Therefore it was decided to cancel the 15 sec exposures in early 2003 to improve the time sampling for the time series of 40 sec and 240 sec.

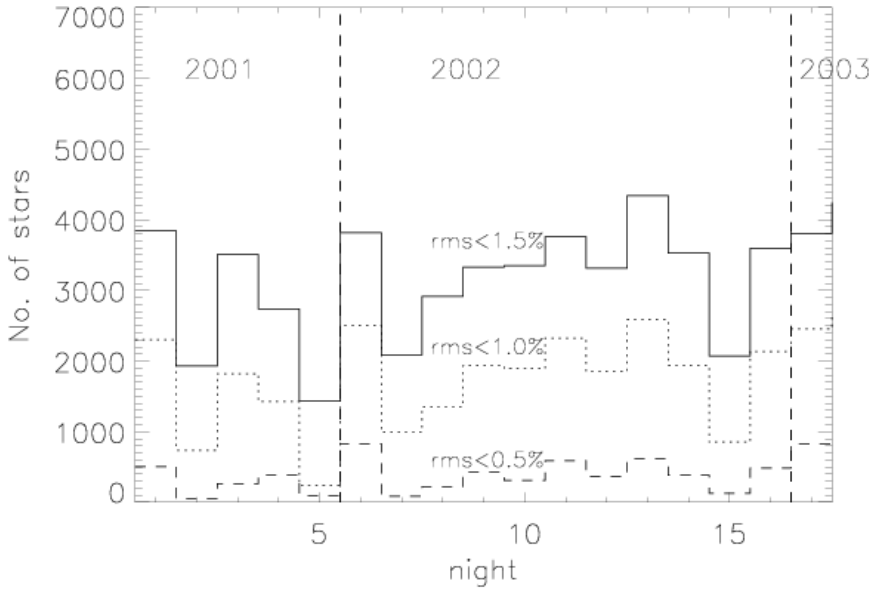

Figure 6.7. The number of stars that reach the photometric precision levels of 0.5%, 1.0% and 1.5% for the 240 sec observations of target field No.15. In the first half of the diagram observations during the late autumn and winter show a variable number of stars with distinct precision levels demonstrating the changeable conditions during this time (bad transparency, high background signal due to snow, …). The observations in the second half were made mainly during a 2-week period in September 2002 with more stable but not perfect weather conditions.

Less suitable photometric conditions for most of the observations reduced the number of high precision light curves. The numbers of light curves resulting from the 240 sec exposures with precisions better than 0.5%, 1.0% and 1.5% are plotted for comparison in the Figures 6.7. (target field No. 15), 6.8. (field No. 2) and 6.10.(field No. 8).

Some general trends can be detected. During the summer time the photometric precision decreases because of the higher sky background, during the winter the same problem can be observed when reflection from snow increases the background level significantly. Only in stable phases of the weather is a constant number of high-precision light curves obtained as seen for observations of field No. 15 and field No. 2.

Obtaining constant transparency is another major issue to reach high photometric precision as it can be seen for the third night of observations of target field F2 (October 14/15, 2001) in.

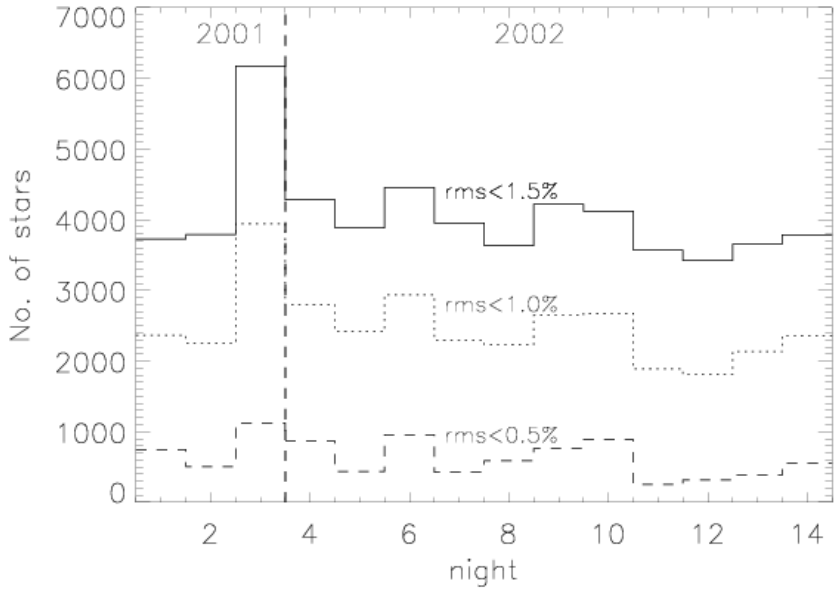

Figure 6.8. The same as Figure 6.7. but for field No. 2. The number of stars with the same precision is relatively constant during the winter season when this target field was observed. Only night No.3 (October 14/15, 2001) shows an exceptionally high photometric quality. Both transparency and seeing were very stable during that night, the background signal was low.

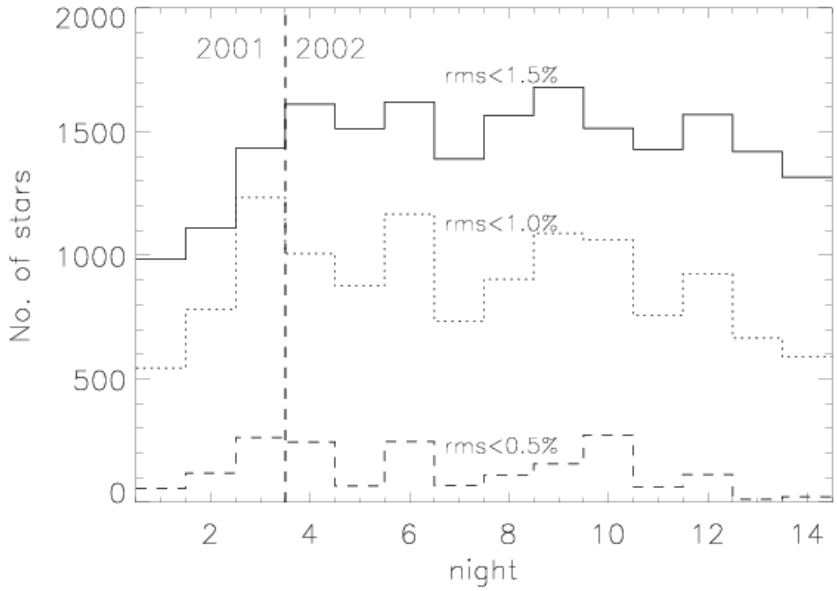

Figure 6.9. The same as Figure 6.8. but for 40 sec exposures. 877 light curves had a photometric precision better than 1% on average. About 530 of these light curves were covered by light curves of 240 sec exposures with higher precision. Thus 350 additional light curves (precision < 1%) were recovered from 40 sec exposures for the transit search.

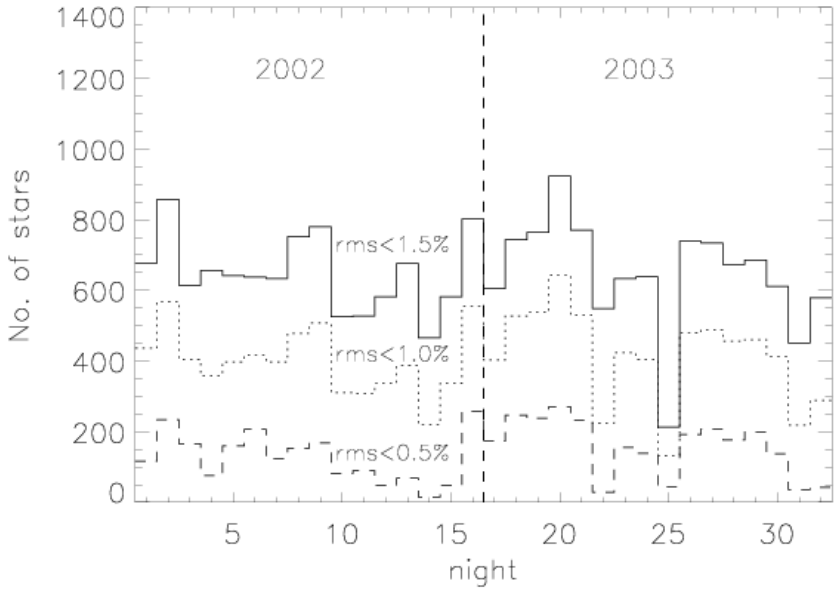

Figure 6.10. The same as for Figure 6.7. but for field No. 8. Note the trend of a decreasing photometric precision in both halves of the diagram corresponding to the two observed seasons 2002 and 2003. The number of stars that reach a photometric precision level is mainly influenced by the increasing sky background signal. Night No. 25 featured an exceptionally high background signal due to a close and bright moon three days before full moon.

The influence of the photon and scintillation noise increases with reduced exposure times. The number of high precision light curves obtained with 40 sec exposures is influenced mainly by background noise (see Figure 6.9.) and varies in a similar way as for light curves of 240 sec exposures (compare Figures 6.8. and 6.9.). Photon noise is of the same order for stars with light curves that are not covered with higher precision by 240 sec exposures. Thus the number of additional high precision light curves obtained with 40 sec exposures is nearly constant.

Going to shorter exposure times (15 sec, Figure 6.6.) increases the noise especially for the brighter unsaturated stars that are not covered by longer exposures (40 sec, 240 sec.). This additional noise further reduces the number of light curves with high precision in the observed target fields with a limited number of stars in the magnitude range from 8-9 that is not covered by longer exposures. Additionally it is known that the objects in this magnitude range are mostly giants or large main sequence stars. The low efficiency of the 15 sec observations for transit search was the main reason for the decision to cancel further 15 sec exposures to improve the sampling rate of the 40 sec and 240 sec time series.

In Table 6.1. the average number of light curves with distinct precision levels per target field is given. The highest number of high precision light curves is reached for target field No. 2 despite the fact that the total number of stars that is higher in target field No.15. A higher sky background in the summer and unstable weather conditions in the autumn (changing transparency) are the reason for this. Field No. 2 was mainly observed under such stable conditions in the winter season when cold but dry air was dominating. But high humidity during the winter season made it impossible to carry out observations more frequently.

Another important aspect for the number of high precision light curves is the crowding situation of the target fields. Even though target field No.8 has about 10 times (V<14) less target stars than field No.15 and seven times less stars than field No.2 a relatively higher number of high precision light curves was nevertheless reached: only 4.5 times less high-precision light curves than field No. 15 and 6 times less for field No. 2 (1% precision). Higher

Table 6.1.: Average number of stars with distinct light curve precision levels listed for the individual target fields. The number of additional light curves obtained by 40 sec exposures and not covered by 240 sec exposures is given in parenthesis.

	Target field No.15	Target field No.2	Target field No. 8
RMS < 0.5%	**427 ± 243 (78 ± 40)**	**632 ± 247 (105 ± 67)**	**138 ± 76 (37 ± 12)**
RMS < 1.0%	**1849 ± 703 (261 ± 69)**	**2468 ± 492 (337 ± 36)**	**405 ± 113 (68 ± 9)**
RMS < 1.5%	**3285 ± 831 (366 ± 49)**	**4012 ± 640 (372 ± 19)**	**647 ± 130 (75 ± 5)**
RMS < 2.0%	**4660 ± 884**	**5328 ± 798**	**853 ± 156**
RMS < 2.5%	**5935 ± 1002**	**6540 ± 906**	**1023 ± 180**

background levels can partly explain the large discrepancy for field 15. For field 2 with nearly the same background levels as field 8 additional noise caused by crowding is responsible for the observed discrepancy. Crowding plays an important role decreasing the photometric quality and has been analyzed more accurately in chapter 7.

Nevertheless, the obtained number of high-precision light curves with RMS < 1.0% and better will allow the detection of Jupiter-sized planets in short-period orbits according to the determined detection limits for one detection (section 5.7.1.) or three detections (see section 5.7.2.) in folded data.

6.2. Observations of transits of the exoplanet orbiting the star HD 209458

The observation of already known events has the advantage to know when and where to observe to find a transit. Therefore the first discovered transiting planet HD 209458b (Charbonneau et al. 1999, Henry et al. 1999), discovered by radial velocity measurements (Mazeh et al. 2000), was a good target to test the BEST system in the summer of 2001. This transit with a depth of about 1.7 percent and good observability from TLS during the initial observational phase has made this object to an almost ideal target to demonstrate the capabilities of the BEST system.

During the initial phase of the observations from TLS two opportunities, arising from good weather conditions, enabled the monitoring of this transit. The first observation of the transit could be provided in the morning hours of 2001, July 24, a second observation took place on August 24, 2001 starting in the evening twilight. The light curves obtained for the transit events are plotted in Figure 6.11 and were first reported in (Rauer & Voß 2002).

The relative brightness of the star (V = 7.65 mag) forced us to defocus the images to avoid saturation of the CCD. The exposure time was limited to 15 sec; a shorter exposure time would have lead to unacceptably high scintillation noise.

Both observations covered only a part of the transiting event: the first observations showed the ingress, the second observations covered more than half of the event (see the light curve in Figure 6.11.). To reduce the influence of the scintillation noise the data points shown in the Figure were binned by a factor of 3. The transit event was clearly detected during both observations demonstrating the capability of the BEST system even for short exposures.

All further observations of the transit were prohibited by unfavorable weather conditions at TLS in 2001.

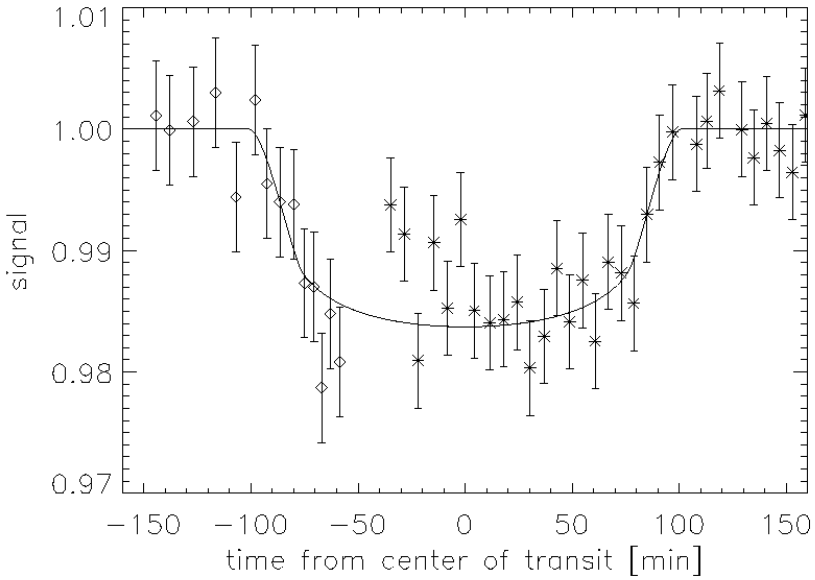

Figure 6.11.: Transit of the planet orbiting the host star HD 209458 observed with BEST. The first transit was observed during the night July 23/24, 2001 in the morning twilight (diamonds). The second transit event was monitored in the beginning of the night August 24/25, 2001. The solid line gives a transit fit based on the model of Mandel and Agol (2002) (for details about the model see section 2.1.) using the planetary and stellar parameter derived from HST times series photometry given by Brown et al. (2001).

6.3. Transit candidates discovered by the BEST system from the TLS

Transit candidates are stars that have shown at least one transit-like signal that could have been caused by an object of planetary size. The significance of the detected transit-like signal has to exceed 7σ to gain a high probability that it is no random event (for details see section 5.7.).

Three detections are not absolutely necessary to start the follow-up analysis. The planetary character of transiting events can be ruled out for many possible cases like eclipsing binaries with an early large main sequence star as primary just after the first detection is made. Gravitationally induced modulation of the light curves outside the transit-like signal can be detected for many high-mass secondaries.

The early discrimination of potential candidates as false alarms reduces the false alarm rate and enables an earlier start of the confirmation by radial velocity (RV) measurements.

The detection of at least two additional transit events remains a necessary part of the final confirmation process. Eventually this can be done by photometric follow-up observations with different small-FOV instruments to reduce the observational effort for the search instrument BEST. This way allows a more effective transit search program. A more detailed description of follow-up strategy is given is section 4.3. In the following sections the follow-up analysis and observations of transit candidates are described in chronological order.

6.3.1. Candidate 1 (BEST C 1)

The first candidate for a transiting extrasolar planet was observed around the star GSC 3566-1556 (RA=19h 55min 2.1sec, DEC=+49° 12' 36''), hereafter referred to as BEST C 1. Coordinates of the candidate are given in table 6.The first detection of a complete transit-like signal (16σ) was made in the night of September 8/9, 2002 (Figure 6.12.). The light curve obtained with BEST showed a drop in intensity of about 2.9 % and with a duration of 2.6 hours. Partial eclipses could also be observed 5 nights from the main event giving a first estimate for the orbital period: 4.89 days.

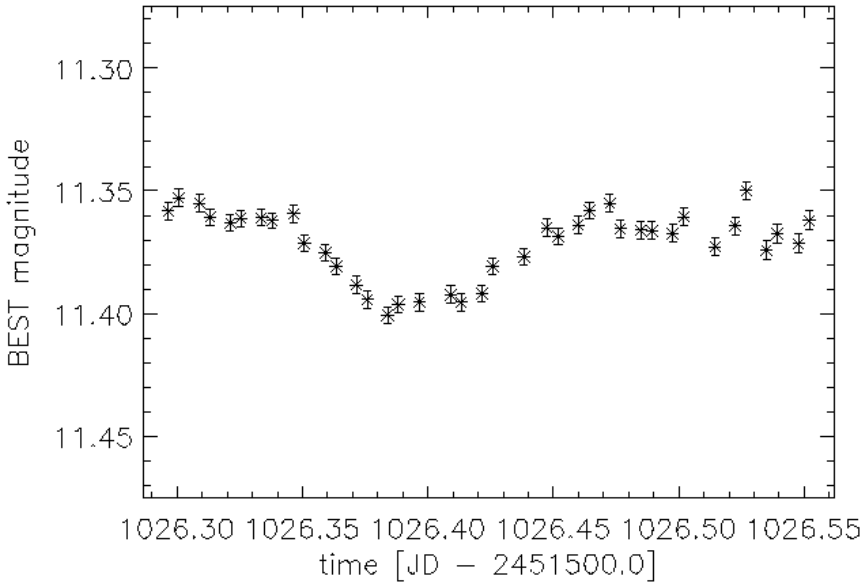

Figure 6.12.: Light curve of BEST C 1 showing a relatively deep (2.9%) eclipsing event with a duration of about 2.6 hours. Ingress and egress phase are relatively long, only a short flat bottom was observed. The data consists of 240 sec single exposures.

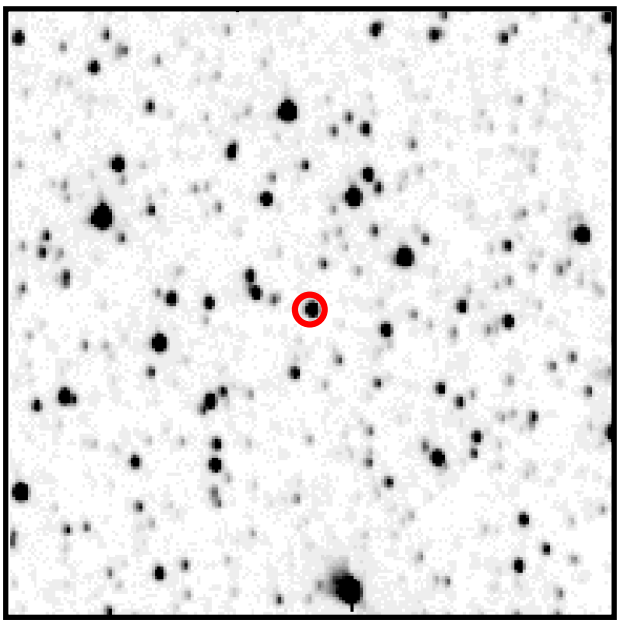

Figure 6.13.: BEST C 1 as seen by BEST. The object is marked by the circle that gives the aperture size. The image displays an area of 18 by 18 arcmin in the sky.

The shape of the light curve showed relatively long ingress/egress phases of about one hour typical for eclipsing binary systems, but because of the short flat bottom the system was still considered to be a possible transit of an extrasolar planet.

Table 6.2.: Catalogue data available for BEST C 1.

Parameter	*Value*	*Source*
J	10.440 ± 0.023	(Cutri el al. 2003)
K	10.100 ± 0.021	
J – K	+0.340 ± 0.044	
V	12.10 ± 0.01	(Egret et al. 1992)
V	11.689	(Kharchenko 2001)
B	12.019	
B-V	+0.33	
pmRA [mas/yr]	1.59	
pmDE [mas/yr]	11.00	
PmRA [mas/yr]	1.2	(Urban et al. 2004)
pmDE [mas/yr]	-8.0	

The host star was observed to have a luminosity of about 11.38 magnitudes by the BEST system and is located in the target field No.15 (for coordinates of the target fields see section 4.1.).

A preliminary characterization of the host star parameters was carried out based on available catalogue data (see Table 6.2.). Only the All-sky Compiled Catalogue of 2.5 million stars (Kharchenko 2001) was available in September 2002 as a useful source for information. B and V magnitudes were given, the resulting (B-V) of +0.330 yields a spectral type between F0 and F2 for both dwarf and giant case (Krautter et al. 1994). Kharchenko (2001) also gives relatively low proper motions for the star indicating that it could be a giant. But a first high-resolution spectrum taken with the 2m telescope at TLS (for more details about the RV observations see section 4.3.3. and Hatzes et al. 2005) implied a G type dwarf star. The spectral type was estimated to be G0 V within three spectral classifications. The resulting determined size interval for the host star could not completely rule out that an object with a radius of about 1.5 R_{jup} had caused the transit-shaped signal.

In 2003 more catalogue data were published. The 2MASS catalogue gives a (J-K) index of +0.340 ± 0.044 corresponding to spectral type F6 V to G3 V, the giant case is excluded, all giants have a larger (J-K) value.

The wrong identification of the spectral type with (B-V) colors is a good example that catalogue data can be misleading and can only give a first rough estimation. If a spectral type later than A is determined a spectra has to be taken to be able to discriminate the spectral type.

Radial velocity measurements with the 2m telescope at TLS were started on September 29, 2002. A 30-minute exposure yielded a spectrum with a S/N of 30 per resolution unit. Five more RV measurements were made in the following 5 months. These six RV measurements were used along with the epochs of the transit centers (where RV was set to zero assuming a circular orbit) to calculate the orbit as shown in Figure 6.14. The RMS scatter of the RVs is about 0.15 km/s. The mass of the primary was assumed to be 1.05 M_{sun} yielding a mass of 0.22 M_{sun} for the secondary. This high mass for the secondary characterizes the object as an M dwarf. The spectral type of the secondary is determined to be M3 V following the mass-spectral class relationship for M dwarfs of Baraffe & Chabrier (1996). The M dwarf orbits a solar-type primary at 0.0611 AU orbital distance. Note however, that the parameters derived for the secondary depend on the parameters of the primary object. The spectral type of the primary is only determined within 3 spectral classifications. Therefore the parameters of the companion are somewhat uncertain.

Additional observations of the eclipse were made in July 2003 using the TLS 2m telescope in Schmidt mode. A target field centered on BEST C 1 was monitored in V band during the night July 23/24. Advancing clouds stopped the observations shortly after the predicted start

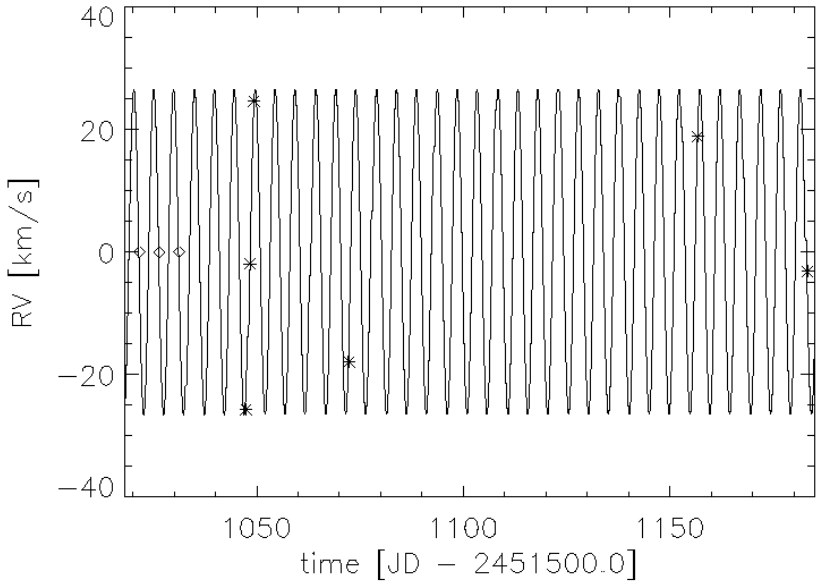

Figure 6.14.: Radial velocity measurements of the BEST C 1 system. Crosses mark the 6 direct RV measurements made by the 2m telescope at TLS. The diamonds show the center times of the observed transits, the corresponding RVs were set to zero assuming a circular orbit. The continuous line shows the calculated orbit.

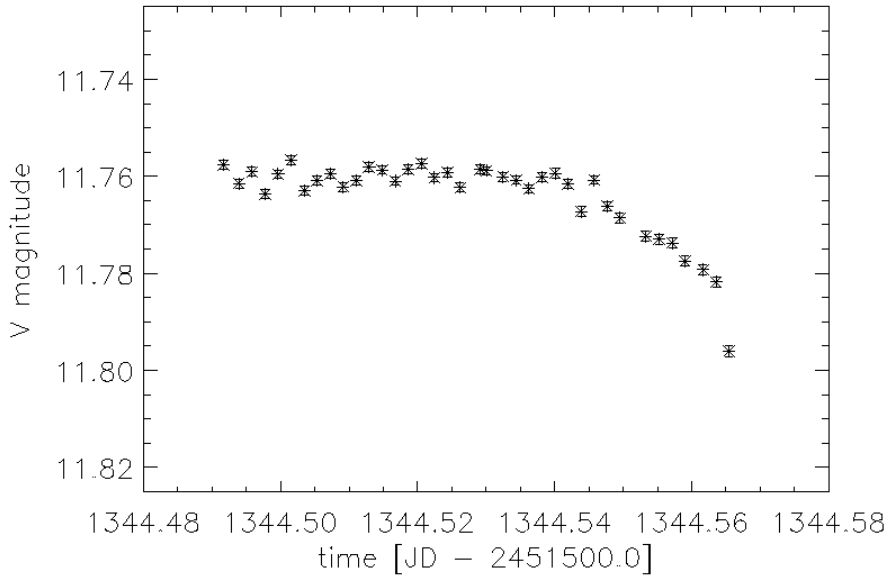

Figure 6.15.: Detection of the beginning ingress phase of the eclipsing BEST C 1 system made during the night July 23/24, 2003 with the TLS 2m telescope in Schmidt mode. The photometric precision reached before the ingress was about 0.17%. Unfortunately advancing clouds prevented further observations.

of the ingress phase of the eclipse. Unfortunately further observations of the system had to be cancelled five nights later due to bad weather. The photometric data were reduced by the data pipeline BESTRED developed for the BEST system. The resulting light curve (see Figure 6.15.) shows clearly the beginning of the ingress phase of the eclipse. The ingress phase started about 20 minutes later than expected allowing to precise the orbital period more accurately. The reduced error will allow further direct observations of the eclipse within the next 10 years.

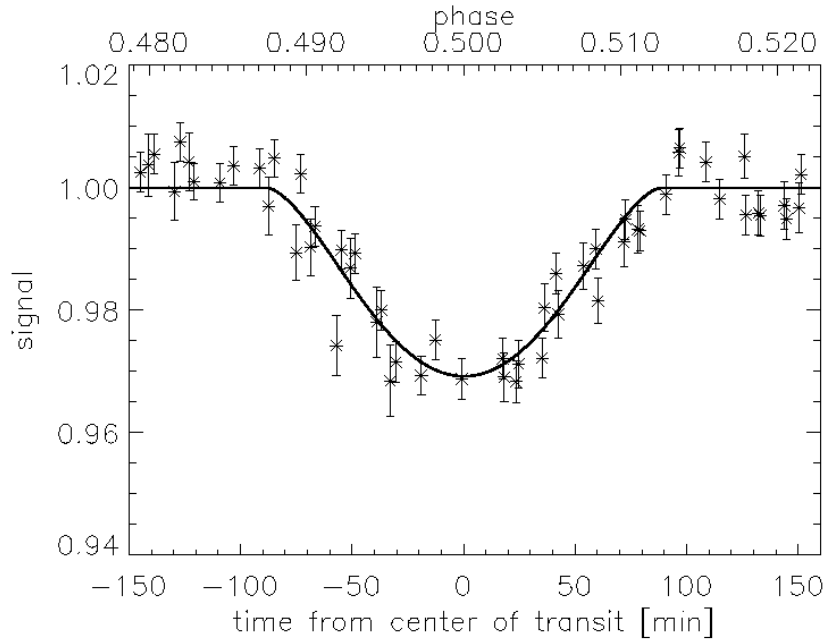

Figure 6.16.: Phased light curve for BEST C 1 containing the signals of three detections. The solid lines gives a fit for light curve using the method suggested by Mandel & Agol (2002). The radii of the primary and the secondary are fit parameters. A radius of 1.27 R_{sun} for the primary was determined, the radius of the secondary is 0.27 R_{sun}. Further parameters are given in Table 6.3.

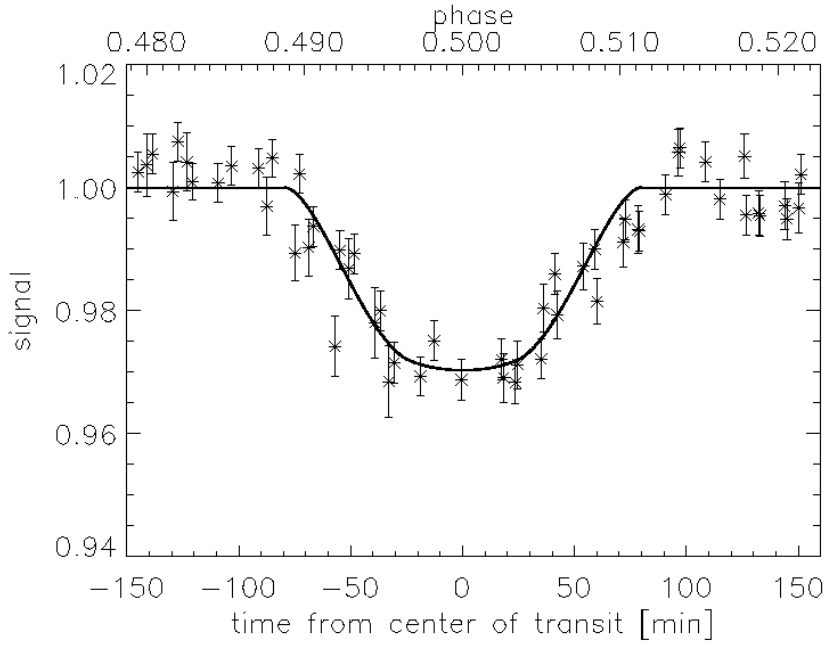

Figure 6.17.: Plot of the phased light curve similar as in the Figure above. This time the radius of the primary was fixed to be 1.05 R_{sun}. The best fit resulted in a radius of 0.18 R_{sun} for the secondary. Further parameters of the fit are given in Table 6.3.

Based on the method suggested by Mandel & Agol (2002) (for details see section 2.1.) further parameters of the binary system were determined by fitting the transit light curves assuming quadratic limb darkening. In a first fitting approach the parameters radius of the primary, radius of the secondary and inclination of the orbit were optimized. In a Monte Carlo test these parameters were independently varied, and the sum of least squares of the difference

Table 6.3.: Parameters of the binary system BEST C 1 based on the photometric and spectroscopic observations. For fit 1 the radii of both components have been determined by fitting the transit light curves using the model based on Mandel & Agol (2002). Only the radius of the secondary and the inclination were optimized for fit 2, the radius of the primary was fixed to 1.05 R_{sun} according to the size of an evolved G0 V star. For both fits the eccentricity of the orbits was fixed to be zero based on the cut period of 6-10 days for tidal circularization for orbits of G binaries (Mayor et al. 1992).

Parameter	Fit No. 1	Fit No. 2
Primary:		
R.A.	$19^h55^m02^s.22$	
Dec.	+49°12'36''.3	
Epoch	2000	
BEST Magnitude	11.38	
Type	G0 V (F7 V-G3 V)	G0 V
Radius (R_{sun})	1.27 ± 0.06	1.05 (fixed)
Mass (M_{sun})	1.05 (0.95-1.3)	1.05 (fixed)
Secondary:		
Type	M3 V	M3 V
Radius (R_{sun})	0.27 ± 0.05 (0.22-0.32)	0.18 ± 0.02 (0.16-0.20)
Mass (M_{sun})	0.22 (0.21-0.26)	0.22 (0.21-0.24)
T_0 (MJD)	52,526.397 ± 0.004	52,526.397 ± 0.004
Orbital period (days)	4.89543 ± 0.00006	4.89543 ± 0.00006
Semi-major axis (AU)	0.0611 ± 0.0002 (0.0591-0.0657)	0.0611 ± 0.0002
Inclination (deg)	85.0 ± 0.4	86.5 ± 0.2
Eccentricity	0 (fixed)	0 (fixed)
RMS [%]	0.27	0.32

between the fit and the light curve data were minimized. The differences were weighted by the errors of the photometric measurements to minimize the influence of low quality data. A radius of about 1.27 R_{sun} was derived for the primary object giving a larger size than expected for an evolved G0 V star. A possible explanation is that the star is an earlier type star (F7 V) within the range of the spectral classification. Or the star has a larger radius because it is less evolved. A more precise spectral classification is therefore essential to give a precise solution. A radius of about 0.27 R_{sun} for the secondary object at an inclination of about 85° was found to fit best (see Figure 6.16.). All parameters of the fit are listed in Table 6.3. (fit No.1). The RMS scatter for the in-eclipse data points is about 0.27 %. The eclipse based on the determined parameters is a grazing eclipse. This is in contrast to the observed short but flat bottom of the light curve that is expected only for a full eclipse. Because the bottom of the light curve is short compared to the combined ingress/egress phase and the two partial detections only cover the ingress/egress phase a higher number of data points for the ingress/egress phase results in a more precise fit for this phase.

In a second light curve fitting approach (Fit No. 2, see Figure 6.17.) the radius of the primary was fixed to be 1.05 R_{sun} typical for a G0 V star of five Giga years age. This yields an eclipsing object with about 0.18 solar radii at an inclination of about 86.5%. The RMS of the fit is now 0.32% and therefore less precise especially for the ingress/egress phase. The flat bottom is fitted better compared to fit No. 1, now the event has more the appearance of a full eclipse.

Note that in the paper of Rauer et al. (2004a) a first description of the binary system was given based on light curves resulting from a first version of the data reduction pipeline giving

higher radii for both objects compared to fit No. 1 presented in this work. The radius of the primary was determined to be 1.37 ± 0.06 R_{sun}, the radius of the secondary to 0.30 ± 0.05 R_{sun}. The flatter bottom of the light curves presented here leads to a decrease in the estimated size of both stars.

If we obtain a more precise characterization of the secondary object, then the photometric precision and the time sampling of the light curves has to be improved together with a more precise spectral typing of the primary object. As shown in Pont et al. (2005) the sizes of only a very few small M dwarfs have been determined so far. Only six M dwarfs with masses below 0.3 M_{sun} radii have been determined so far giving very scant observational constraints on the mass radius-relation (Figure 6.18.). The eclipsing system which we have discovered may potentially yield a very precise size determination for an M dwarf useful for comparison with existing evolutionary models. However, further observations both photometric and spectroscopic are needed to accomplish this goal. More precise photometry in different bands can be obtained with the 2m TLS telescope in Schmidt mode to reduce the uncertainties of the size determination. Also, more RV measurements are needed to confirm the circular orbit.

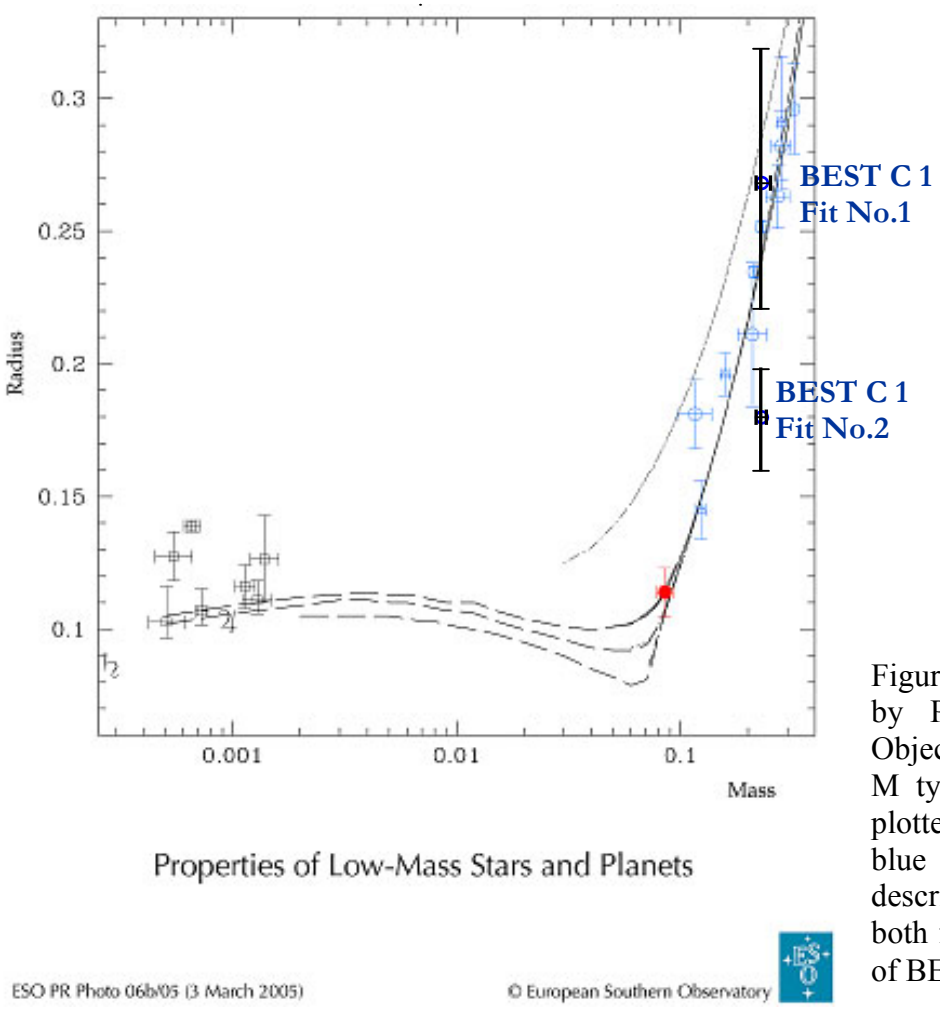

Figure 6.18.: Figure given by Pont et al. (2005). Objects plotted in blue are M type stars, planets are plotted in black. The dark blue plotted objects describe the results for both fits for the secondary of BEST C 1.

For the case that the binary system can be identified as young system a direct measurement of the infrared flux of the M dwarf during the secondary eclipse, similar as done for the planets TrES-1 by Charbonneau et al.(2005) and HD 209458 b by Deming et al. (2005b), could be performed with the Spitzer space telescope to get additional information about the surface temperature of the star. Direct information about young M-dwarfs is rather rare, a system with determined mass, density and temperature would be very useful to compare with model data for young M dwarfs.

6.3.2. Candidate 2 (BEST C 2)

BEST Candidate 2 showed a first full transit-like event during the night December 11/12, 2002 (displayed in Figure 6.19. marked by crosses). The relatively flat-bottomed eclipsing event with duration of about 2.6 hours and a depth of 3.2% was observed for a 11.56 magnitude star (GSC 0370-1739, (BEST C 2, RA= 2h 40min 51.5sec, DEC=+52° 45' 6'')) in the BEST target field No.2.

A second partial drop in the light curve of the star was found later in the data of October 14/15, 2001 (see Figure 6.19., diamonds). The ingress phase was missed, but the bottom and the egress phase were monitored. Both are in good agreement with the observed phases of the full event. The time difference between the two events was determined to be 422.935 days.

The available catalogue data (see Table 6.4.) were evaluated to determine the spectral class of the main object. The (J-K) index (Cutri el al. 2003) indicates that the object is of spectral type F0 V to F5 V. The given (B-V) colors of +0.43 (Urban et al. 2001) and +0.42 (Kharchenko et al. 2001) limit the spectral class from F4 V to F5 V according to Krautter et al. (1994). The given proper motions (see Table 6.4.) are close to the mean proper motions of the neighboring objects.

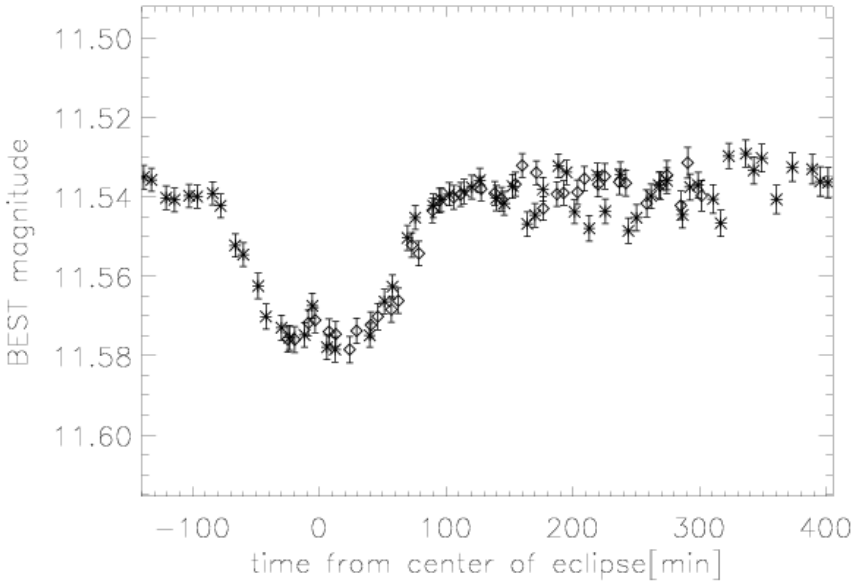

Figure 6.19.: Eclipsing event detected for a star (BEST C 2) in target field 2 with a duration of about 2.6 hours and a depth of 3.2% as seen in unbinned data consisting of 240 sec exposures. Because of the relatively flat bottom this event was eventually considered to be caused by a transiting planet. The crosses mark the full detection with a time from center of the eclipse T2 = 2452620.400. The center of the earlier partial detection was detected at T1 = 2452197.465 (diamonds).

Therefore the eclipsing secondary has a minimal size of about 2.7 times Jupiter size assuming that the star has a radius of about 1.5 R_{sun} (Krautter et al. 1994) and is too large to be planet.

Nevertheless one spectrum was taken by the coudé echelle spectrograph of the TLS 2m telescope yielding that the primary is a fast rotating A type star. The radius of the star should be about 2 R_{sun} or larger, the minimal radius of the secondary 0.35 R_{sun}. Consequently the secondary object is a M type dwarf with high probability.

Further analysis of the eclipsing binary system could be useful to analyze the physical parameters of the secondary M dwarf (especially for the case of a young system).

Table 6.4.: Catalogue data available for BEST C 2.

Parameter	*Value*	*Source*
J	10.771 ± 0.028	(Cutri el al. 2003)
K	10.564± 0.026	
J - K	+0.207 ± 0.054	
V	11.60 ± 0.40	(Egret et al. 1992)
V	12.222	(Urban et al. 2001)
B	12.65	
B-V	+0.43	
V	12.173	(Kharchenko et al. 2001)
B	12.595	
B-V	+0.42	
pmRA [mas/yr]	-6.12	
pmDE [mas/yr]	-10.79	
pmRA [mas/yr]	-8	(Monet et al. 2003)
pmDE [mas/yr]	-12	
pmRA [mas/yr]	-1.9	(Zacharias et al. 2004)
pmDE [mas/yr]	-5.4	

6.3.3. Candidate 3 (BEST C 3)

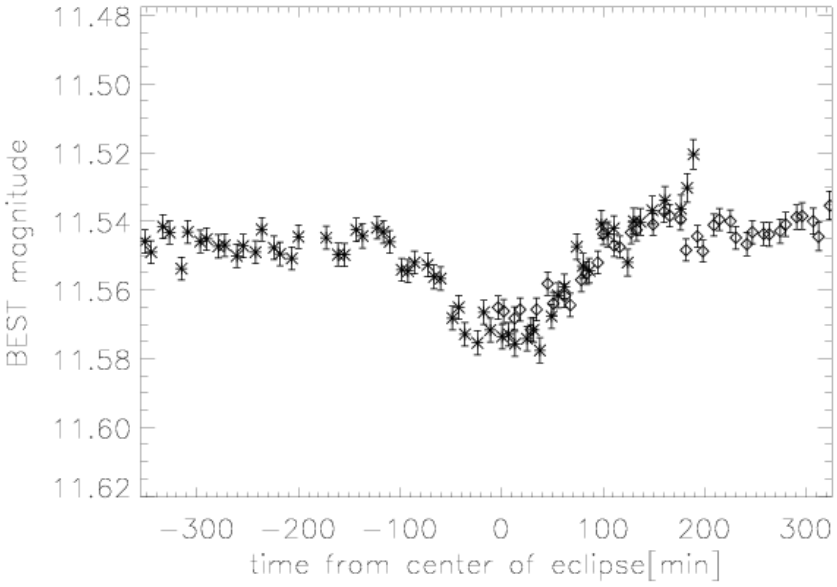

Figure 6.20.: The phased light curve of BEST C 3 is displayed (unbinned 240 sec exposures). The 2.7% deep decrease in the light curve continues for about 3.3 hours. The full detection (crosses) was made during the night December 11/12, 2002 (center time T_2 = 2452620.548). The first partial detection (diamonds) was made more than a year earlier (T_1 = 2452197.450).

A first full transit-like event was detected with a confidence level of about 17σ for an 11.56 mag star (RA=2h 36min 39.4sec DEC=+53° 10’ 58’’) in the BEST target field No. 2 during monitoring on the night December 11/12, 2002 (see Figure 6.20., crosses). A first partial detection had already been made in 2001 on October 14/15, 2001 (Figure 6.20., diamonds). Only a half event was found at the beginning of the observations. The shape of the partial

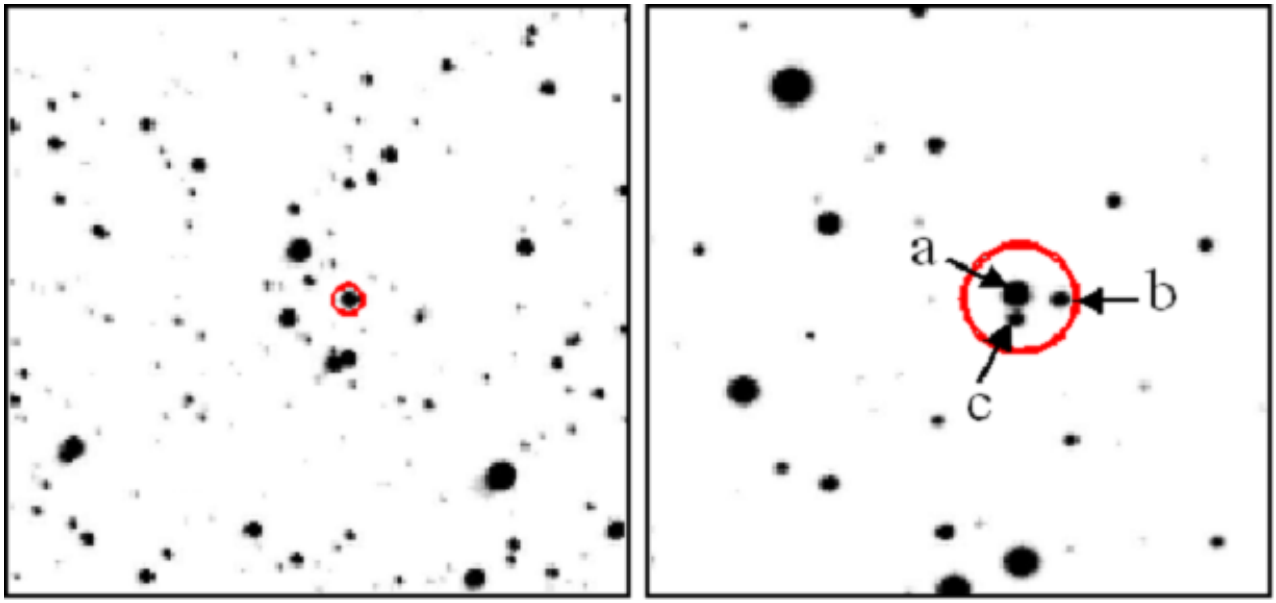

Figure 6.21.: BEST C 3 as seen by BEST (left) and the TLS 2m telescope. The TLS image resolves three objects within the BEST PSF. The circle gives the size of the aperture used in the BEST aperture photometry.

signal does not fully match the shape of the full signal, although note the somewhat variable signal of the star outside of the eclipsing event. The potential variability of the star can distort the transit signal. But it cannot be completely ruled out that the two observed events have different origins based on the light curve data.

In one of the regular checks to search for images with higher resolution with the help of the Aladin interactive sky atlas (Bonnarel el al. 2000) three objects were detected to be present within the PSF of BEST in POSS-I data (see Figure 6.21.). Any of these it could have been the eclipsed object, it is now to address which of the objects is the eclipsed one.

In early 2003 only very sparse photometric data about objects in that region was available. Therefore photometric follow-up observation of the objects with the TLS 2m telescope in Schmidt mode were ordered and carried out by the colleagues Jochen Eislöffel and Alexander Scholz on February 4, 2003. Exposures in U, B and V filters were taken. No photometric standard stars were observable on the same declination. Only one star of known spectral type included in the same FOV was used for a rough calibration. The star had a very low U flux, excluding calibration for the U band observations. The results for the B and V fluxes of the objects are listed in Table 6.5 additionally to the catalogue data.

The brightest star (object a, GSC 3687-414, for identification labels see Figure 7.21.) has a (B-V) of about +1.0 and a (J-K) of about +0.70. According to Krautter et al. (1994) and Tokunaga (2000) the star can be identified either as a K3/K4 main sequence star or a K0/K2 giant. The proper motion as given by Monet et al. (2003) is close to the mean proper motion of the surrounding objects and cannot be used to decide which luminosity class the object belongs to. If it is a K dwarf with a radius of about 0.75 R_{sun} then the signal could be caused by an object with a radius of about 1.3 R_{jup}. A planetary origin of the signal cannot be ruled out.

For object b the (B-V) value of about +0.7 and (J-K) of $+0.118 \pm 0.056$ give no conclusive result whether for the spectral type nor the luminosity class. But it can be ruled out that the star is a K or M dwarf. If the transit-like signal is caused by the eclipse of this object then the signal should show a depth of about 20-30% and cannot be caused by a planetary companion.

Object c shows a (B-V) of +1.6 and (J-K) of +1.1 and can be identified as a M type star. The high proper motion indicates that it is a dwarf star. For that case it cannot be ruled out that a planetary companion of this star causes the detected signal.

Table 6.5.: Catalogue data available for BEST C 3. Additionally the photometric data collected with the TLS 2m telescope is listed.

Parameter	*Value object a*	*Value object b*	*Value object c*	*Source*
J	10.283 ± 0.022	12.571 ± 0.031	11.486 ± 0.026	(Cutri el al. 2003)
K	9.584 ± 0.020	12.453 ± 0.025	10.367 ± 0.022	
J - K	+0.699 ± 0.042	+0.118 ± 0.056	+1.119 ± 0.048	
V	12.00 ± 0.01			(Egret et al. 1992)
B	13.5	-	14.9	(Monet et al. 1998)
pmRA	-20	0	196	(Monet et al. 2003)
[mas/yr]	-14	0	60	
V	12.7	14.6	14.9	TLS 2m (Eislöffel, Scholz)
B	13.7	15.3	16.5	
B-V	+1.0	+0.7	+1.6	

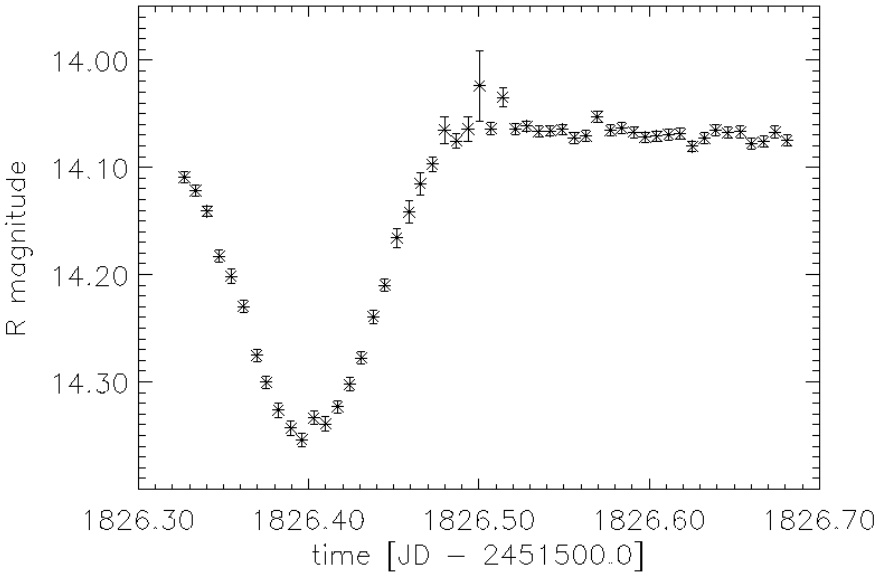

Figure 6.22.: Eclipsing event observed for star b on November 16/17, 2004 with the Westerlund telescope from Uppsala, Sweden. This measurement identified the BEST C 3 case as an eclipsing binary system blended by two additional stars.

Photometric follow up observations were necessary to identify which of the three objects is really eclipsed. The 90cm Westerlund telescope at Uppsala, Sweden with a pixel scale of 1.1 arcsec was a suitable instrument that allowed resolving the three stars photometrically. A target field centered at the three stars (see Figure 6.22.) was observed with the Westerlund telescope during three nights in October/November 2004 by Pär Nilsson (for details of the observations see in the appendix section C). During the night November 16/17 an eclipsing signal was detected for object b (see Figure 6.22.). The signal with a depth of 26% and duration of about 3.4 hours corresponds to the depth and duration to the observed combined signal of the three stars observed by the BEST system.

The BEST C 3 case could be identified to consist of an eclipsing binary blended by two additional stars within the PSF of the BEST system.

6.3.4. Candidate 4 (BEST C 4)

With a confidence level of about 8σ a potential transit event was detected for the star GSC 3445-546 (RA=10h 36min 10.1sec DEC=+48° 55' 41'') in BEST target field 8 during the night of April 8/9, 2002 (see Figure 6.23.). Unfortunately the ingress of the event was not observed during the twilight of the night. But the first 4 data points can however be interpreted as part of the ingress phase but only on a low confidence level. The potential full transit event would have duration of about 2.9 hours, but the measured partial signal was about 2.4 hours. During the following night (1.122 days later) a signal that could be interpreted as an egress phase was observed (Figure 6.23., diamonds) .

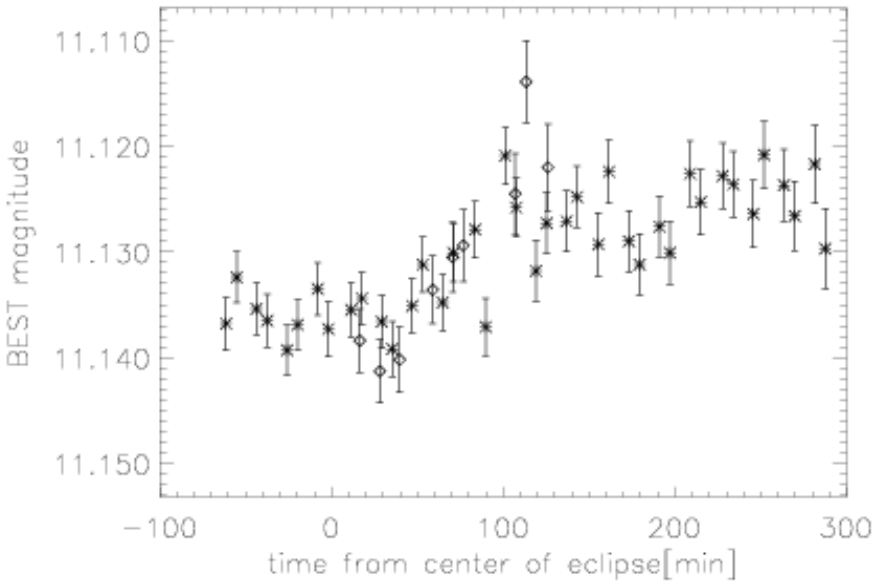

Figure 6.23.: Phased light curve showing a possible transit event that was detected for BEST C 4 (unbinned 240 sec exposures). Note the flat bottom of the signal shape. The event has a duration longer than 2.4 hours, the 'dip' has a depth of about 1.0%. Unfortunately the ingress phase was missed at the beginning of the night for the first detection (crosses, center time = 2452373.418 assuming that the first 4 data points are part of the ingress phase). The second detection covers only the egress phase (diamonds) and is therefore somewhat uncertain.

Table 6.6.: Catalogue data available for BEST C 4.

Parameter	*Value*	*Source*
J	9.592 ± 0.022	(Cutri el al. 2003)
K	8.682 ± 0.022	
J - K	+0.910 ± 0.044	
V	11.55 ± 0.40	(Egret et al. 1992)
B	13.4	(Monet et al. 1998)
pmRA [mas/yr]	1.2	(Zacharias et al. 2004)
pmDE [mas/yr]	-8.0	

The potential host star has a brightness of about 11.13 mag observed by the BEST system.

Additional catalogue information is summarized in Table 6.6. The color index (J-K) of +0.910 ± 0.044 from the 2MASS catalogue (Cutri et al. 2003) allows a rough spectral typing. If the candidate is a dwarf star the spectral type should be in the range from K9 V to M5 V

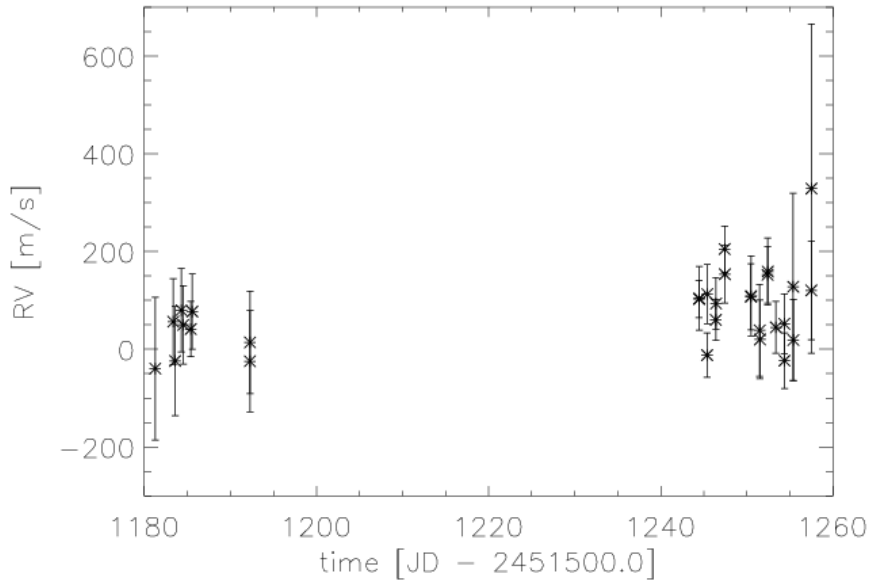

Figure 6.24.: Radial velocity measurements made for BEST C 4 with the 2m telescope of the TLS from February to April 2003. A periodic variation larger than 80 m/s was not detectable. The RV data are listed separately in appendix section D.

(Tokunaga 2000). For the giant case K3 III to M0 III could be the spectral type. A third color or another color index is needed to determine the luminosity class. A V magnitude of 11.55 ± 0.40 is given by the Tycho Input Catalogue (Egret et al. 1992). Therefore (V-K) could be range from 2.45 to 3.29. The large parameter range does not allow discriminating between a dwarf and giant character of the object. But if the candidate is a K dwarf the transiting object could have a size comparable to the size of Saturn or less.

A first spectrum was taken by the TLS 2m telescope was indicating that it is a K type star. It was not possible to decide the luminosity class of the object because of the low S/N.

The BEST team decided to continue the photometric and spectroscopic follow-up observations in 2003. The potential detection of an eclipsing exoplanet with sub-Saturnian size would have been an important scientific discovery. A campaign of radial velocity (RV) measurements was started additionally to the photometric monitoring by BEST.

30 RV measurements were carried out by Eike Guenther, Artie Hatzes and the author between February 10, 2003 and April 28, 2003 (see Figure 6.24.). A periodic signal larger than 80 m/s was not detectable. Because of the uncertainty of the measured RV data no planet with a mass less than about 0.5 M_{jup} is detectable without knowing the period of the signal given by photometry.

In mid 2003 the UCAC catalogue presented precise proper motions for objects in the observed magnitude range (Zacharias et al. 2004). For BEST C 4 a proper motion of about 1.2 mas/yr in RA (right ascension) and –8.0 mas/yr in DEC (declination) was measured. The average proper motion in the of about 1.2 mas/yr in RA and –8.0 mas/yr in DEC had been measured. The average proper motion in the surrounding area of the star is of about 10.1 mas/yr in RA and 13.6 mas/yr in DEC. BEST C 4 shows a lower proper motion indicating that the star is located at a larger distance and therefore has to be a K giant with much larger size of a K dwarf. Nevertheless, the low proper motion is no final proof for the giant character of the star.

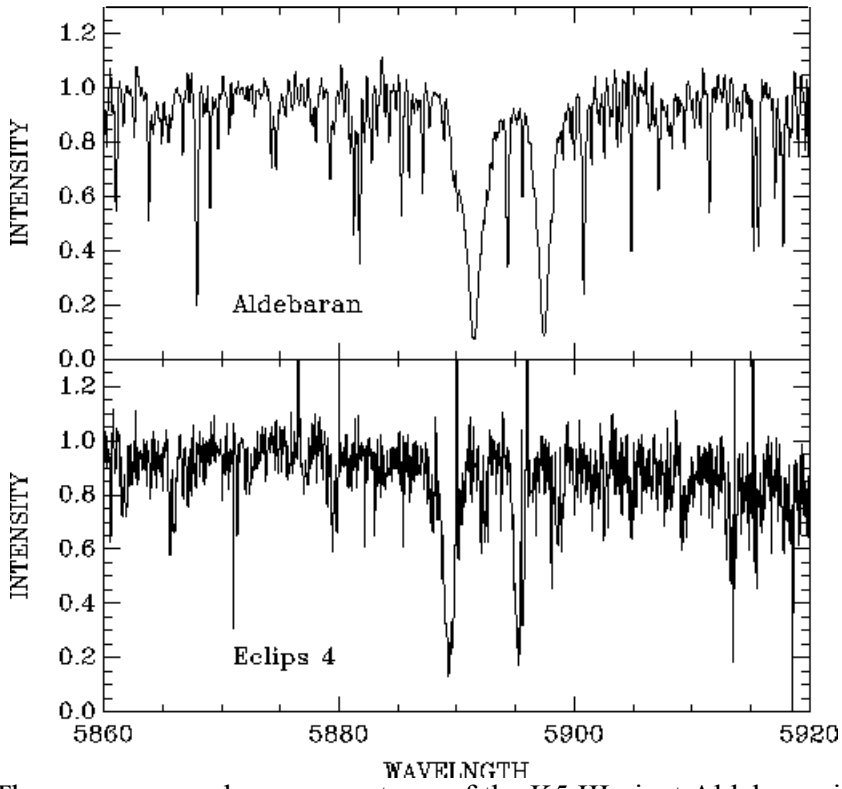

Figure 6.25.: The upper curve shows a spectrum of the K5 III giant Aldebaran in the region of the gravity-sensitive Sodium-D line taken with the echelle spectrograph of the TLS 2m telescope. The lower curve gives the co-added spectrum of BEST C 4 (labeled as 'Eclips 4' in the plot provided by the colleagues from TLS) in the same region showing narrower Sodium lines. This indicates the giant luminosity class of BEST C 4.

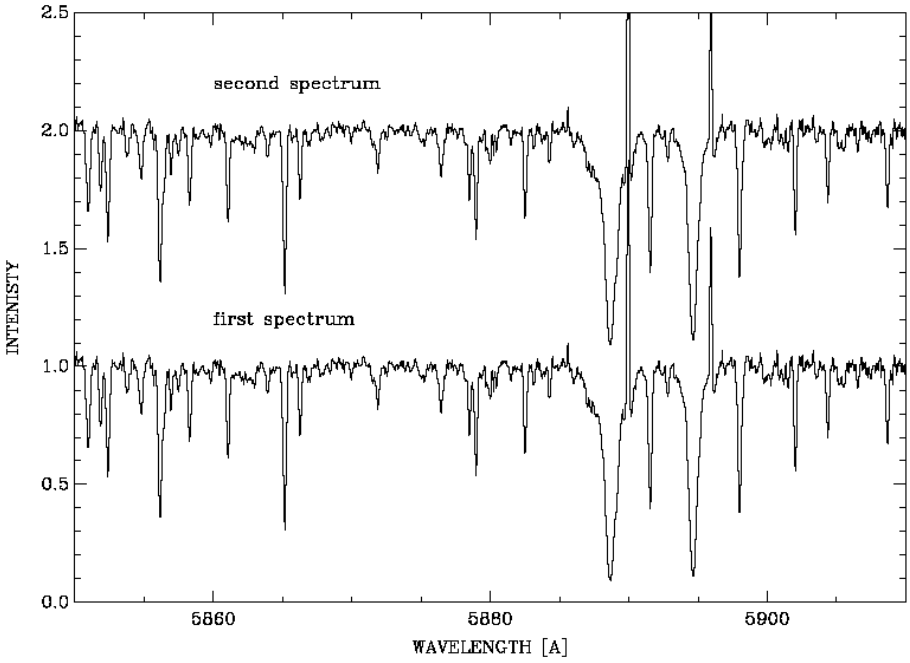

Figure 6.26.: Two high resolution spectra of BEST C 4 taken with the HET telescope during the night of November 8/9, 2004. The region around the Sodium-D lines is displayed. The surrounding area of the star is of about 10.1 mas/yr in RA and 13.6 mas/yr in DEC. BEST C4 shows a lower proper motion indicating that the star is located in a larger distance and spectra were compared to reference spectra given by Montes et al. (1999) indicating that the star is a K5 giant.

One possible way of deciding which luminosity class an object belongs to is to analyze the influence of the surface gravity to gravity-sensitive spectral lines like the Sodium D lines (see Charbonneau et al. 2004). Therefore Eike Guenther of the TLS co-added the echelle spectra taken with the TLS 2m telescope the reach higher S/N and compared the spectrum to a spectrum of the star Aldebaran. The spectrum of this K5 III star was taken with the same instrumental set-up. The broader sodium lines of Aldebaran (see Figure 6.25. for a comparison) indicate that BEST C 4 is a giant star. A dwarf star has broader sodium D lines resulting from the influence of the higher surface gravity.

Unfortunately the spectra of BEST C 4 and Aldebaran did not match completely. Thus it was decided to take additional spectra of the object with the echelle spectrograph of the 9.2 Hobby Eberly telescope (HET) at the McDonald Observatory, Texas, USA to compare it with reference spectra given in Montes et al.(1999). Collaborator Michael Endl has observed the

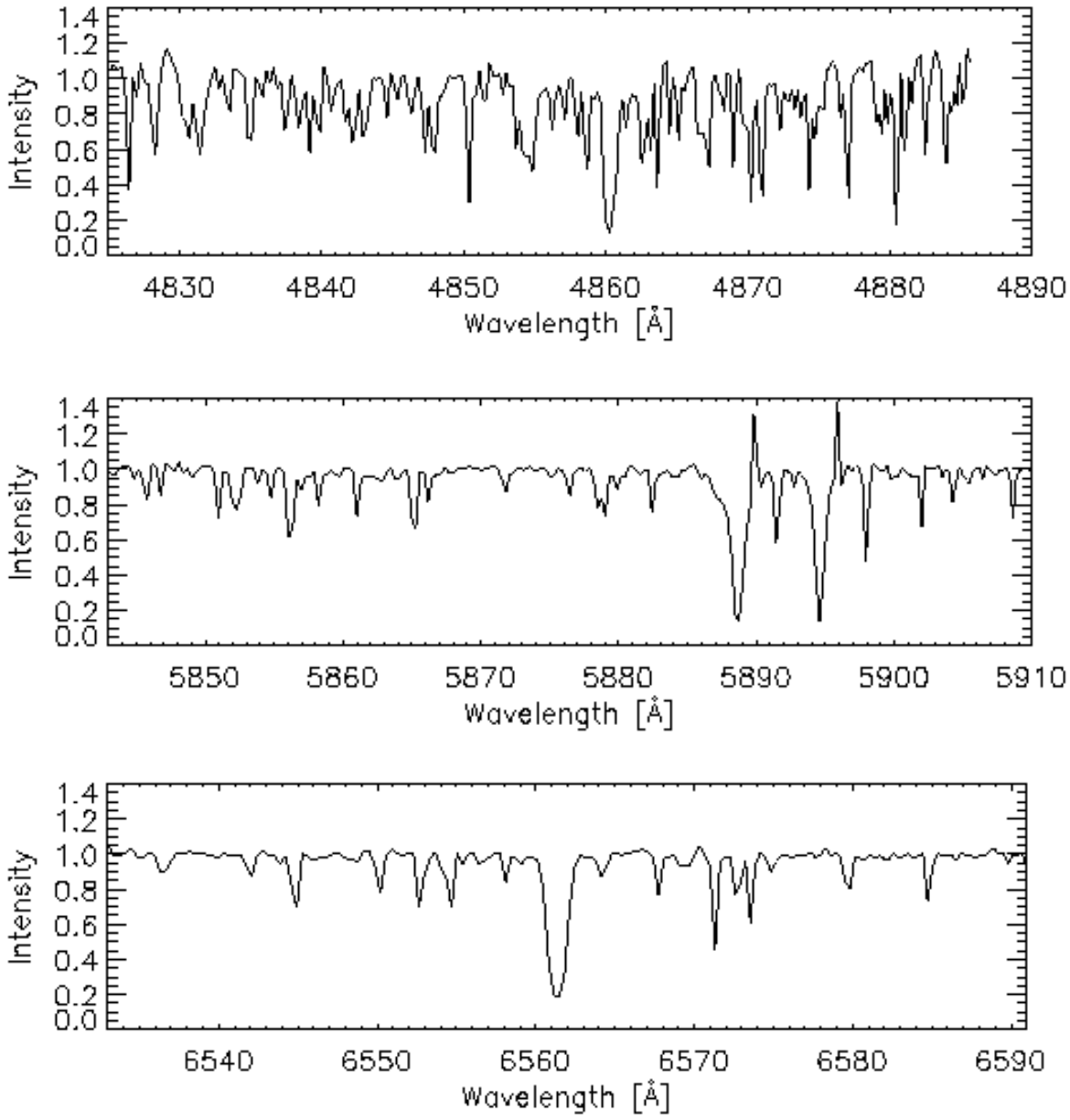

Figure 6.27.: Plots of the spectral regions (rebinned HET data) that were compared with the reference data by Montes et al. (1999, see example in Figure 6.28.). The upper plot gives the spectral region around the Hβ line at 4860 Å. In the middle the region around the Sodium-D doublet is plotted. In the lower plot the region around the Hα at 6561Å is displayed.

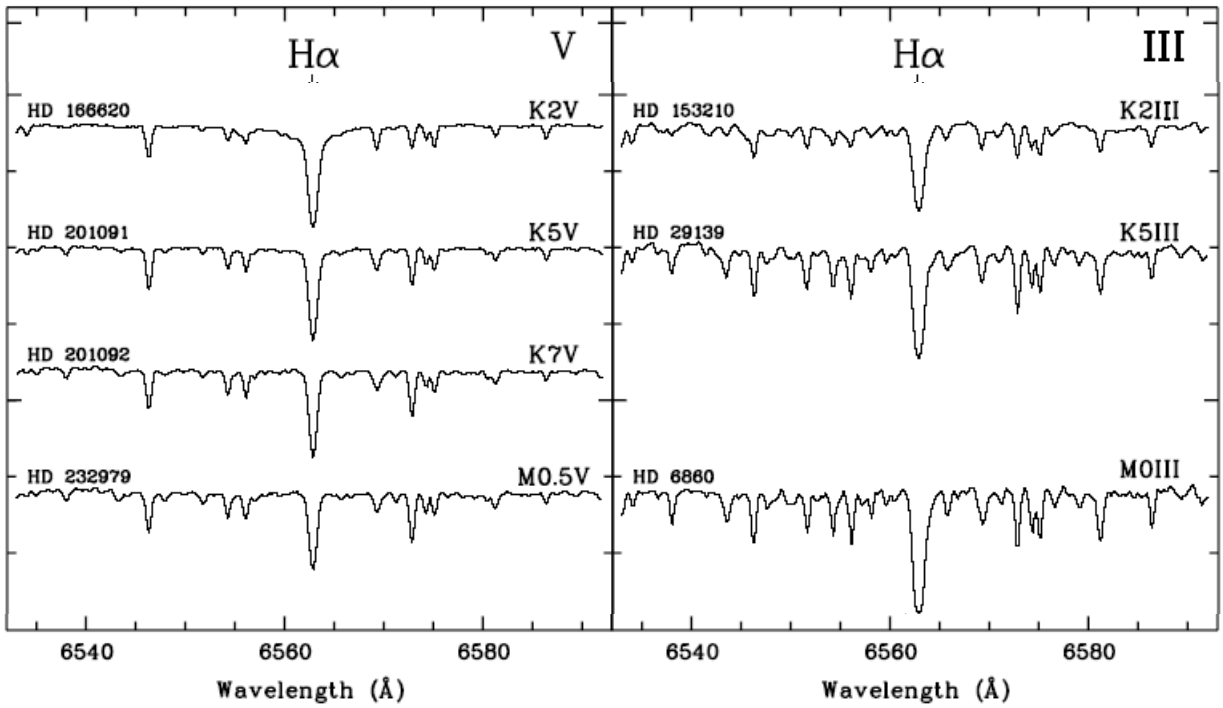

Figure 6.28.: Reference spectra centered around the Hα line for K type stars of the luminosity classes dwarf and giant as given by Montes et al. (1999).

object BEST C 4 during the night of November 8/9, 2004 with the HET. Two spectra (see Figure 6.27.) were taken with the echelle spectrograph of the telescope. The data were reduced and calibrated by Michael Endl and Eike Guenther. The following regions of the spectra were used for comparison with the reference spectra of Montes et al. (1999):

a) 483 – 489 nm including the Hβ line (Figure 6.27. upper plot)
b) 584 – 591 nm including the Sodium-D duplet (Figure 6.27. center plot)
c) 653 – 659 nm including the Hα line (Figure 6.27. lower plot).

The data were rebinned by a factor of 4 (see Figure 6.27.) to reach a comparable wavelength resolution as in the reference spectra (see Figure 6.28.). The best match with the reference spectra was identified to be for spectral type K5 III. The line width of the Sodium-D lines is so narrow typical for a giant. Only dwarfs earlier than type G8 have such narrow gravity-sensitive spectral lines as observed. The observed number and intensity of spectral lines in the Hα region is typical for a K5 giant star, a dwarf star has less intensive lines. The observed Hβ line is too intense for a late type K dwarf. The observed spectrum in the surrounding region again fits best for a K5 III star.

In agreement with results from the photometric data and the observed proper motions the spectroscopic data implies BEST C 5 to be a K giant. The spectral type was identified as K5 III within 3 spectral classifications. A typical radius of 25 R_{sun} for a K5 giant does not permit the detection of a photometric signal caused by a planet-sized object. A stellar companion was ruled out by the non-detection of a strong RV signal. Possible explanations for the observed signal are stellar variability that mimics a transit-like signal or a blend of an eclipsing binary in the foreground directly in the line of sight. In POSS-I images the closest object has a distance of about 37 arcsec. In an aperture with a radius of 4 pixels (corresponding to 22

arcsec) as used for the photometry only a very low part of the flux of the faint object is measured additionally to the flux of BEST C 4. The faint object is more than 5 magnitudes fainter in the R band, thus even for the case that its flux is completely blocked it cannot be responsible for the observed signal.

6.3.5. Candidate 5 (BEST C 5)

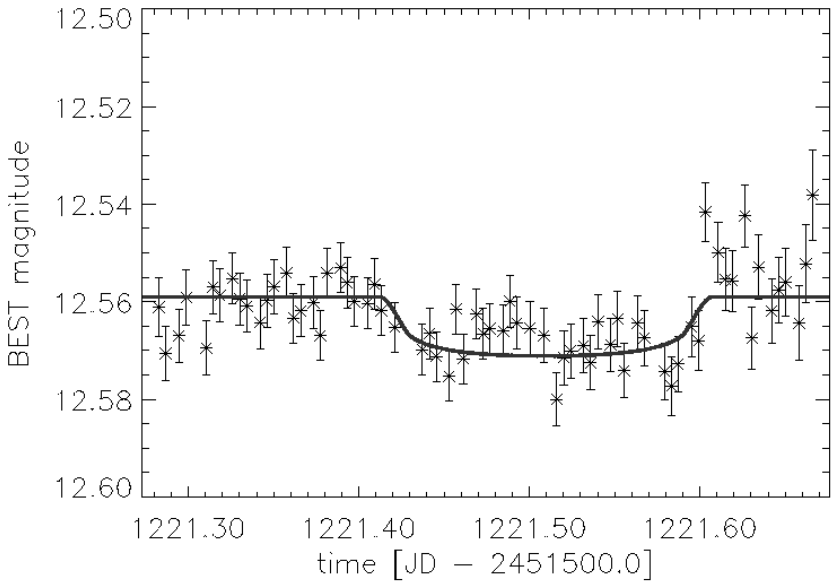

Figure 6.29.: Light curve for BEST C 5: detection (8σ) of a transit like event with a duration of about 4.5 hours and a depth of about 1% as seen in unbinned data consisting of 240 sec exposures. A modeled transit shape is overplotted assuming a M0 V primary star with a radius of about 0.8 R_{sun} eclipsed by a planet with a radius of about 0.75 R_{jup} in an orbit of 13 days.

The transit-like event of BEST Candidate 5 (displayed in Figure 6.29) has a relatively long duration of about 4.5 hours and a depth of about 1%. This detection was made in the data collected during the night of March 22/23, 2003. No further signals have been found for this star in the additional photometric data. The event was detected for a field star of target field No. 8 with a determined magnitude of about 12.56 with a detection confidence of about 8σ. The relatively high confidence level for a signal depth of 1% results from the relatively long duration of the event and the improved sampling rate of images per hour.

According to the 2MASS catalogue (Cutri el al. 2003) (J-K) is +0.848 ± 0.039, leading to a rough spectral type range from K7V to M4V for the case that it is a dwarf star (Tokunaga 2000). Several other indications for the dwarf characterization were found in catalogues as listed in Table 6.7. The (B-V) color index of Kharchenko (2001) indicates that the host star is an M5 dwarf or an M super giant according to Krautter et al. (1994). The super giant character of the object is however very unlikely because of the high proper motion detected by several surveys but cannot completely ruled out. Combining the given V magnitudes to an average V magnitude gives 14.66 ± 0.06; the resulting (V - K) of 5.64 ± 0.08 is a clear indication for the M dwarf nature of the host star (Tokunaga 2000). The spectral type can be determined to be M4V to M5V. Additionally a ROSAT X-ray detection is listed in the ROSAT All-Sky Survey Faint Source Catalog (Voges et al. 2000) indicating that the object is eventually a young star. No second star (3 magnitudes fainter) closer than 30 arcsec was found in data archives (see figure 6.30.).

Table 6.7.: Catalogue data given for BEST C 5.

Parameter	*Value*	*Source*
J	9.866 ± 0.021	(Cutri el al. 2003)
K	9.018 ± 0.018	
J – K	+0.848 ± 0.039	
V	14.73	(Salim & Gould 2003)
V	14.617	(Kharchenko 2001)
B	16.263	
B-V	1.646	
pmRA [mas/yr]	223.92	
pmDE [mas/yr]	-212.95	
spectral type	M	
pmRA [mas/yr]	254	(Monet et al. 2003)
pmDE [mas/yr]	-190	
V	14.64	(CMC 1999)
spectral type	M	(Luyten 1979)

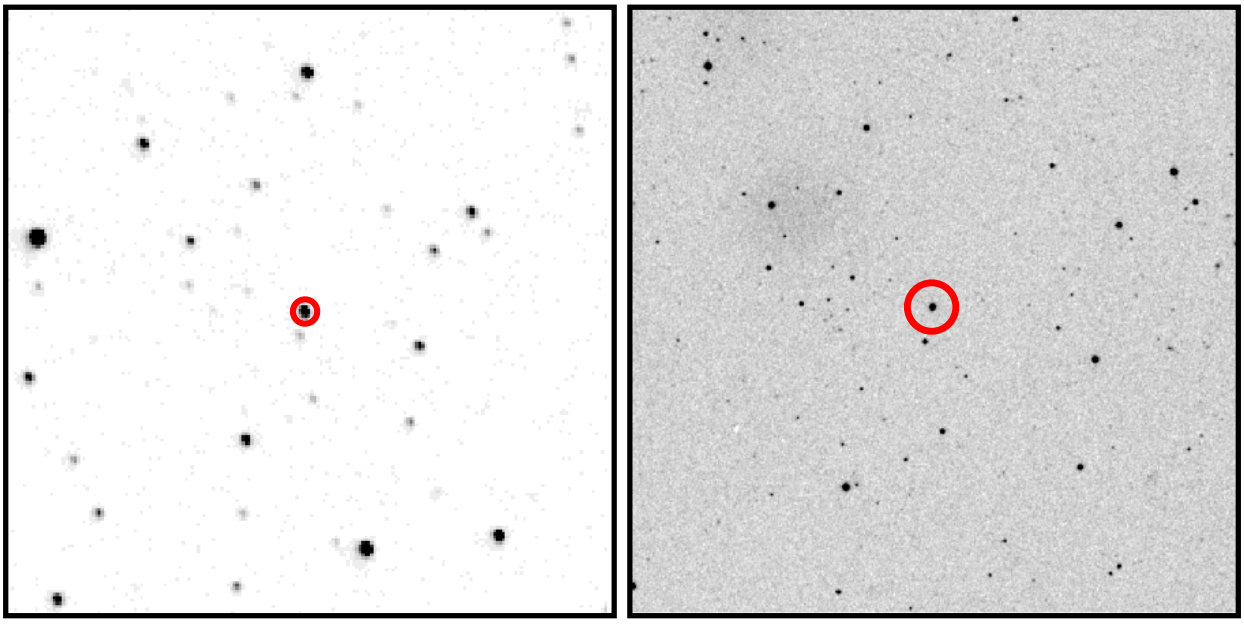

Figure 6.30.: BEST C 5 as seen by BEST (left image). The image displays an FOV of 18’ x 18’. The red circle gives the size of the aperture for photometry used in the BEST images. A POSSII image (right) in the R band with a size of 8.6 x 8.6 arcmin and a pixel scale of 0.5 arcsec shows no evidence for a star within the PSF as seen by BEST.

Photometric and spectroscopic follow-up observations are still ongoing. Additional photometric data is being collected with the 90cm Westerlund telescope. Spectroscopic measurements are being made with the 2.7m Harlan J. Smith telescope in Texas to better characterize the possible host star and to rule out that it is a close-in binary.

6.4. Summary and discussion of the results searching for transits

6.4.1. Overview of the detected transit candidates

During the observations at TLS from July 2001 to September 2003 five candidates objects were found with transit-shaped signals (see Table 6.8.).

Table 6.8 : Transit candidates discovered by BEST from TLS and the cause of transit-like signal

Transit candidate	*Cause of transit-like signal*
BEST C 1	Grazing eclipse of M dwarf
BEST C 2	Eclipsing binary, primary is A type star
BEST C 3	Eclipsing binary blended by 2 other stars
BEST C 4	Eclipsing binary blended by a giant or stellar variability
BEST C 5	unknown

The light curve of the first candidate BEST C 1 showed one full transit-shaped event, two additional partial events were detected 5 days earlier and later during an atypically long phase of stable good weather conditions at the TLS. Thus the orbital period of the event of about 4.9 days could be determined with the photometric data. This demonstrates a typical case of a preferred multiple detection for eclipsing objects with orbital periods close to whole numbers of days. Note that the orbital periods of the photometrically detected planets with orbital periods larger than 2 days TrES1 (3.03 days), OGLE-TR-10 b (3.10 days) and OGLE-111 (4.02 days) are also close to whole-day numbers. Ground-based observations are biased to find these objects with a higher probability if the orbital periods are determined photometrically.

The spectral type of the host star was determined by spectroscopy with the 2m TLS telescope. The resulting determined size interval for the host star could not completely rule out that an object with a radius of about 1.5 R_{jup} has caused the transit-shaped signal. Thus six radial velocity measurements were obtained with the TLS 2m telescope. The mass of the object was determined to be about 0.22 M_{sun} clearly identifying the object as an M3 dwarf. The size of the secondary object was determined by fitting the light curves data. The transit candidate was identified as a false alarm: a grazing eclipse of a low-mass star orbiting a solar-like G type star has caused the observed signals. Radii for objects with a mass less than 0.3 M_{sun} have only been determined a few times up to now. With our discovery it was possible to determine the size for one of the stellar objects with the lowest mass. The accuracy of the derived size determination was limited by the given uncertainties for the size of the primary. Further follow-up observations will be needed to determine the improved size of the primary. An additional photometric detection of the eclipse decreased the uncertainties of the orbital period allowing a more precise timing for future observations of the eclipse during the next years.

Transit-shaped signals were detected twice for transit candidate BEST C 2, one event was partially observed in 2001, the second one more than one year later. But the short duration of the signal indicated that the event has a period of only a few days. Single spectra taken by the TLS 2m telescope identified the eclipsed object as a fast rotating A type star too large that a

planet-sized body could have caused the signal. BEST C 2 was identified as another eclipsing binary system.

Two transit-like signals were detected in the light curve of BEST C 3 which implied a full eclipse. During standard tests which involved analyzing archived high-resolution images, it was found that BEST observed two additional objects within the same PSF. Both observed objects were about two magnitudes fainter than the main star. Color data taken with the 2m TLS telescope as well as archived photometric data were used to determine the spectral types of the three objects. Only one object was identified to be too small enough that the signal could be caused by a planet-sized object. Photometric time series data with higher spatial resolution were needed to find out which of the objects was being eclipsed. A collaborator from Uppsala, Sweden, observed the object for three nights in the autumn of 2004. During one night an eclipse was detected for one of the fainter stars corresponding in depth and duration with the combined signal observed by BEST. BEST C 3 was identified to be an eclipsing binary system blended by two other stars observed simultaneously within a PSF of BEST.

The cause for the false alarm of candidate BEST C 4 could not be identified clearly. Finally the object was identified as a K giant much too large that a planet-sized object could cause a transit signal detectable from the ground. Only one confident signal was observed (a second possible signal was too noisy to be seen as a detection); it was determined that only the beginning of the ingress phase of the transit has been missed with some confidence. The spectral type was determined to be K type with photometric colors and spectroscopic data. The giant character of the K type object could not be ruled out based on this data. The photometric colors had too large uncertainties, the spectra taken by the TLS 2m showed too low S/N. Thus a RV campaign was started with the TLS 2m telescope for this object. No RV variations larger than 80 m/s were detected. Finally it was decided to take a spectrum having high S/N with the 9.2m HET telescope by collaborators in Texas, USA. Finally the object could be identified as a K giant by comparison of the HET spectrum with reference spectra. The transit case was ruled out. A possible explanation could be that a blended eclipsing binary system directly in the line of sight not detectable in high-resolution images or some kind of variability of the giant mimicked a transit signal.

Candidate BEST C 5 is still under investigation. In 2003 one transit signal was detected with a relatively long duration of about 4.5 hours indicating an orbital period longer than 10 days. It will be extremely difficult to detect the transit signal again by a single-site ground-based search system due to the expected long orbital period. Further observations have to be made for this object: the photometric campaigns of BEST and the Westerlund telescope are ongoing. Additionally spectroscopic measurements are being made with the 2.7m Harlan J. Smith telescope in Texas to better characterize the possible host star and to rule out that it is a close-in binary.

To summarize, five candidates showing transit-like events were identified in the data of the observations made from TLS Tautenburg. Four candidates were identified as false alarms: two eclipsing binaries consisting of main sequence stars, one blended eclipsing binary system and one giant star showing a transit-like signal. Publications about other ground-based transit searches (Charbonneau et al. 2004, Brown 2003) report about similar false alarm rates. A relation of 10 false alarms to one real planet detection or worse is expected. For the target field that contained the transiting TrES-1 planet a total number of 16 transit candidates were reported by Brown (Winter school ‘Extra solar planets’ Tenerife 2004). 14 candidates were identified to be false alarms, 10 of them were grazing eclipsing binaries, four were blends and one candidate is still under investigation. The number of the expected detectable transiting exoplanets has decreased with time during the last few years. Early estimations were too optimistic.

6.4.2. Approximations of the expected detection rates for transiting exoplanets

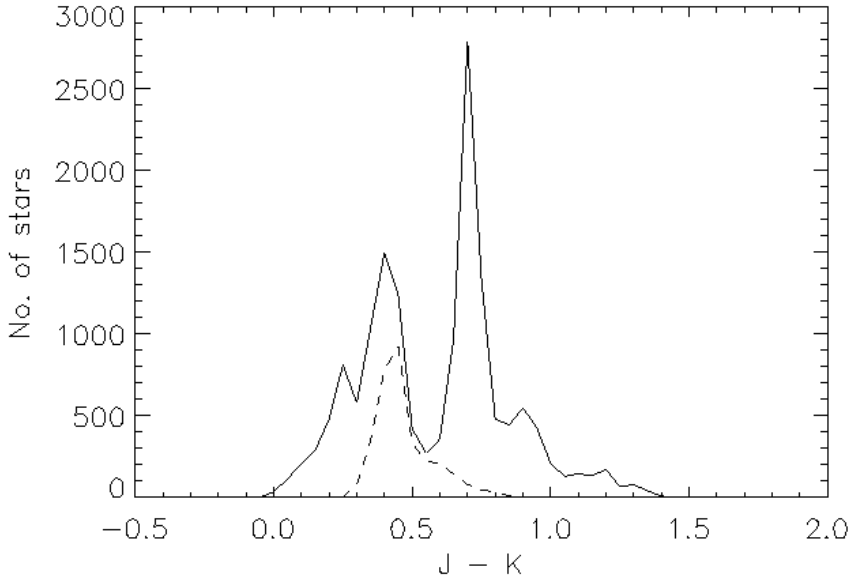

Figure 6.31.: Besançon model for target field No.15 as observed by BEST. A fraction of 21% (dashed line) of the stars is targets small enough that a transit signal could be detectable from the ground. The field is dominated by K giants (J-K ~ 0.7).

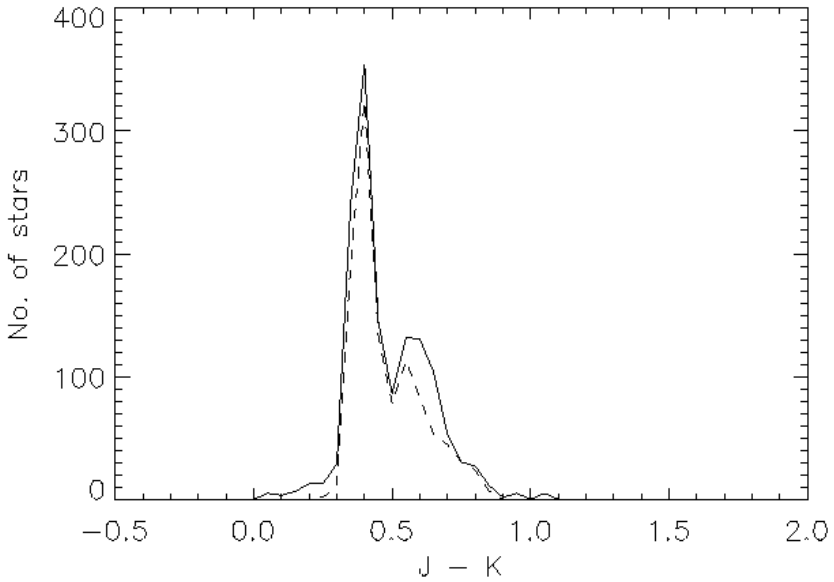

Figure 6.32.: Besançon model for target field No.8 as observed by BEST. A fraction of 78% of the stars (dashed line) is small enough that a transit signal could be detectable from the ground. The total number of good targets is limited due to the low star density in the region far from the Galactic plane.

Does the non-detection of a transiting exoplanet during the observational campaign of BEST from TLS meet the expectations? In section 2.3. estimations for expected detection rates of transiting exoplanets have already been addressed. The expected number of detected transiting exoplanets for an observed target field was expressed by relation 2.19 addressing the

parameters geometrical probability for a transit f_{geom}, the fraction of suitable target stars f_{tar}, the fraction of transit signals detectable from the ground f_d, the fraction of stars that harbor a Hot Jupiter planet, the obtained duty cycle to reach a significant probability for the detection of three transit events f_c and the number of high-precision light curves N_{phot} obtainable by ground-based transit searches. Some of the parameters are dependent from the observed target field. Therefore the calculations are adopted in the following starting with the fraction of suitable target stars.

Models were calculated for the observed target fields. Target field No. 2 and No. 15 are both close to the Galactic plane. Therefore the fraction of good target stars is limited. For target field No.2 a fraction of 27 % of all stars was determined to be good targets, for field No.15 closer to the Galactic plane the percentage reduces to 21% (see Figure 6.31.). Target field No.8 is located more than 30 deg above the Galactic plane and contains only 1/10 of the stars compared to target field 15. But the fraction of good target was determined to be higher: about 78 % percent of the stars are small enough that a transit signal could be detectable from the ground (see Figure 6.32.). Note that the fractions of suitable stars in the real target fields can be different compared to fractions given by the model.

The obtained phase coverage f_c for the observed target fields was already calculated in section 6.1. The number of light curves with sufficient photometric precision of 1% and better N_{phot} was already determined in section 6.1.2. The fraction of detectable transit signals (>1%) was calculated as in section 2.3.4. These parameters and the resulting probabilities for the detection of one transit event are listed in table 6.9. for the observed target fields. For the observations of target field 2 the highest probability for one detection was given with 33% mainly due to the higher N_{phot} compared to observations of field 15 and 8. Target field 15 additionally shows a lower fraction of suitable target stars leading to a further reduction of the detection probability. For field 8 the low number of high precision light curves N_{phot} is partly compensated by the high fraction of suitable target stars f_{tar} and the better orbital phase coverage f_c compared to field 2 and 15.

Table 6.9.: The numbers of detectable single transit signals are given for the target fields observed from TLS (in combination with the parameters of equation 2.19 used for the estimation). Note that the probability of a single detection for target field No. 2 is high due to the high number of light curves with sufficient precision and the higher fraction of suitable target stars compared to target field No. 15.

Target field	N_{phot}	f_{tar}	f_d	f_{geom}	f_{HJ}	f_c	*Detectable transiting planets*
15	2110 ± 772	0.21	0.51	0.10	0.013	0.54	0.16 ± 0.06
2	2805 ± 528	0.27	0.58	0.10	0.013	0.58	0.33 ± 0.06
8	473 ± 122	0.78	0.64	0.10	0.013	0.81	0.25 ± 0.06

The total probability to detect one real transit event during the TLS observations was of about 74% ± 18%. This is in agreement with the result of the detection of zero real transit events (BEST C 5 is still under investigation and is not included in this analysis).

The orbital phase coverage of Hot Jupiter planets for three detections was low especially for the target fields 2 und 15: 4-8% making any detection unlikely. For target field 8 a phase coverage of 20% was obtained for three detections of a transit yielding a detection probability of 8%. This demonstrates that the low orbital phase coverage was the main limiting factor of the BEST transit survey from TLS.

The class of very Hot Jupiters (P < 2 days) was not included in this discussion so far because only statistics based on RV detections were used as reference. Three planets detected by the OGLE search have orbital periods less than 2 days: OGLE-TR-56 b, OGLE-TR-113 b, OGLE-TR-132 b defining the new class of very Hot Jupiters. For all three target fields observed by BEST the phase coverage was sufficient enough to detect at least one transit of a very Hot Jupiter if it exists.

The number of high precision light curves from BEST was limited compared to the OGLE search. During the two campaigns monitoring stars in the Galactic bulge and in the Carina region more than 150,000 light curves with a precision better than 1.5% were observed by OGLE (Udalski et al. 2002a, Udalski et al. 2002c). The number of light curves with the same precision observed by BEST was limited to about 8750 (see section 6.2.1). Therefore the BEST system should have found one very Hot Jupiter with a probability of 18% during the 2-year observational campaign at TLS assuming an orbital phase coverage for very Hot Jupiters of 100% obtained by BEST. The non-detection of very Hot Jupiters for the BEST observations from TLS are in good agreement with the statistical basis given by the OGLE search.

The detection probability for observations done from TLS reached for the BEST system has to be increased. The search has to be optimized. The number of good target stars has to be maximized; the number of light curves reaching sufficient photometric precision has to be increased by improving the photometry procedures and observations of less crowed target fields. The main limitation of the transit search was the low duty cycle obtained at TLS. Only for target field No. 8 sufficient orbital phase coverage for three transit detections for a hypothetical Hot Jupiter planet was reached. Unfortunately this target field contained the lowest number of dwarf stars being located far away from the Galactic plane.

7. Optimizing of ground-based transit searches

7.1. General considerations for optimizing ground-based transit searches

To obtain a high probability of detecting a transiting planet the monitoring of as many suitable stars as possible with high photometric precision as often as possible to obtain high phase coverage according to equation 2.19 is required.

One approach to optimize ground-based transit searches is to analyze which kind of target fields have maximal detection probabilities for different instrumental set-ups. Target fields with a wide range of stellar densities exist. The range goes from very crowded fields in stellar clusters and fields close to the Galactic bulge, to crowded target fields centered close to the Galactic plane, to moderately crowded target fields above the Galactic plane and finally, to non-Galactic fields with very low content of stars. None of these kind of target fields should be excluded from transit searches. An optimized target field has to be selected for an existing search system to obtain a sufficient detection probability, or an optimized telescope system has to be chosen to monitor the selected kind of target fields.

An optimized ground-based transit search system has to meet the following requirements:

a) The telescope should have a low focal ratio (defined as the focal length divided by the aperture size) to cover a large field of view (FOV) to observe as many stars as possible simultaneously.
b) The telescope should have a large aperture to limit the exposure times for target fields that contain a high number of faint stars to reach a sampling rate of 6 exposures per hours or better (to get information about the shape of the transit signal),
c) The CCD should have a large format that can cover the full unvignetted image in the focal plane.
d) A pixel size of the CCD sensor is required, that corresponds to the observed point spread function (PSF) of the stars in a way that a compromise is found between large full width half maxima (FWHM) to minimize the influence of intra- and inter-pixel variations (typical for front-illuminated CCDs) and a low number of overlapping PSFs in the total FOV. A Nyquist-sampled PSF with a FWHM of two pixels is thought to be such compromise (Howell & Everett 2001, Bakos et al. 2004). Oversampled images (FWHM > 2.0 pixels) will yield higher background noise and increase the crowding problem. Undersampled PSFs (FWHM < 2.0) will introduce additional noise by pixel-to-pixel and intra-pixel effects. Thus optimal PSFs should have a FWHM of two pixels.
e) The search system has to be placed at one (or more) observing site(s) with good photometric and meteorological conditions to obtain maximal phase coverage and a high number of light curves with high precision.

Concerning a) the telescope with the lowest focal ratio that is technically feasible is a telescope with a focal ratio of 1, as built for the Kepler satellite (Borucki et al. 2003) and the Automated Patrol Telescope (see appendix section A.1.8.). An optimized transit search system should have a similar low focal ratio 1. A Schmidt correction plate should be used to minimize the distortion of the image in the focal plane.

Another aspect is the pixelsize of the available large format CCDs (c,d). The largest commercially available and moderately priced CCD chip is the 4k Kodak KAF16801 chip with a size of 36.9 mm x 36.9 mm and a pixel size of 9 μm. Assuming an instrumental

Table 7.1.: Parameters of the existing and proposed transit search systems that were used for the analysis sorted in the order of increasing aperture size. For more details about the search systems see appendix section A. Note that for BEST4k the FOV is limited to 3.1 deg x 3.1 deg due to vignetting.

System	*Aperture [cm]*	*Focal ratio 1/F*	*FOV [deg x deg]*	*CCD*	*Pixel size[µm]*	*Pixelscale [arcsec/pixel]*
PASS prototype	2.5	2.0	32 x 32	2k x 2k	14	56.2
KELT	4.2	1.9	26 x 26	4k x 4k	9	22.9
TrES (STARE)	10	2.8	6.1 x 6.1	2k x 2k	14	10.7
BEST	20	2.7	3.1 x 3.1	2k x 2k	14	5.5
BEST4k	20	2.7	3.1 x 3.1	4k x 4k	9	3.5
TEST	30	3.2	2.25 x 2.25	4k x 4k	9	2.0
BEST-2	25	5.0	1.66 x 1.66	4k x 4k	9	1.5
OTSS	45	1.0	4.7 x 4.7	4k x 4k	9	4.1

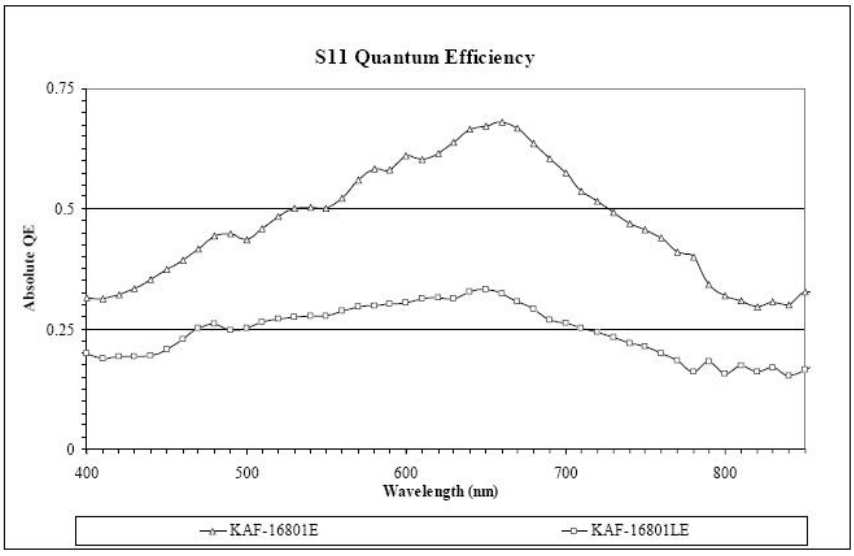

Figure 7.1.: Quantum efficiency of the Kodak KAF-16801E CCD chip as given by Kodak. The quantum efficiency is much higher than for the Thomson TH7899M CCD used for BEST (see Figure 3.5. for comparison). For the wavelength range up to 750 nm the KAF-16801E chip shows nearly double quantum efficiency compared to the Thomson chip.

dominated PSF (as is typical for wide-angle systems with a low focal ratio) similar to that reached with the BEST telescope (FWHM = 8.25 arcsec for focused images) for a f/1 telescope a pixel scale of about 4.1 arcsec would be necessary to reach a Nyquist-sampled PSF for this CCD chip. This can be reached by a f/1 Schmidt telescope with a main mirror of 45 cm. The FOV covered by the proposed CCD chip would be 4.7° x 4.7°. This proposed system is referred to as the Optimized Transit Search System (OTSS) in the following discussion.

In the following the detection probabilities for the proposed system will be analyzed. Its performance will be compared with the performance of typical transit search systems which already exist or have been proposed (see Table 7.1.). The systems PASS prototype, KELT, STARE and TEST are operational or in the commissioning phase; more details about the systems can be found in appendix A.

BEST4k is an upgraded BEST system: a CCD with a KAF-16801E chip replaces the current 2k CCD, the FOV is assumed to be the same as for BEST. Comparing the

performances for crowding and photometric noise limits of the BEST system with the performance of the BEST4k system will demonstrate the influence of an optimal choice of the CCD sensor. Additionally the CCD chip has a better quantum efficiency (see Figure 8.1.) compared to the Thomson TH7899M chip used.

BEST-2 is a system to study the variability of stars in the most crowded target fields of the COROT satellite mission consisting of a 25cm F/5 Baker Ritchey-Chretien telescope and a CCD with the KAF-16801E chip. It will be located to the Atacama desert, Chile during 2006.

This analysis includes wide-angle searches only. Deeper searches will monitor higher fractions of suitable small stars and thus will have higher detection probabilities (see section 2.3.3.). But the observation of faint stars also implicates some disadvantages. The OGLE search (for details see the appendix A.) observes stars in the magnitude range I = 14 mag to I = 17 mag and is a moderately deep transit search. But the confirmation of candidates of this search program by RV measurements has already shown that it is relatively intensive using 8-10m class telescopes. For some candidates it was reported that they were too faint to reach enough S/N for conclusive RV measurements (Konacki et al. 2003a, b, 2004; Bouchy et al. 2004a). The planetary parameters derived for the planets show large uncertainties. Furthermore follow-up measurements to determine the composition of the planetary atmosphere with the existing instruments are not possible because of the faintness of the stars.

Confirmation by RV measurements can not be determined for searches deeper than OGLE. Only upper limits of the masses will be determinable to rule out that the transit-like signals are caused by grazing eclipsing binaries or brown dwarfs. Furthermore the exclusion of blends will be impossible. Additionally most of the deep searches can only monitor target fields for a few days or weeks. The observational time has to be shared with other scientific projects. Technological and financial efforts are significantly higher for the deep searches than for wide-angle searches. Wide-angle searches can be fully dedicated to transit search.

Aspects of the analysis to optimize wide-angle transit searches will include: how to reach sufficient orbital phase coverage and how to optimize the target field selection to monitor a high number of small target stars with undisturbed signals. Additionally it is important to analyze how the different noise sources will affect the photometric performance of the different systems.

7.2. Analysis of the noise source terms for selected wide-angle transit searches

As already seen in section 2.3.5. photon noise is the dominating noise source for wide-angle searches especially for brighter non-saturated stars. It is given by Poisson statistics as described in equation (2.21.) A lower relative photon noise can be reached by increasing the number of photons collected per star. This can be achieved by increasing the ratio of the collecting area/main mirror, by improving the optical throughput of the search system (using CCDs with higher quantum efficiencies and broad-band or no filters, mirrors with higher reflectivity, etc.), or by longer exposure times.

An optimized transit search system should be dominated by photon noise over the entire useable magnitude range for which the total noise results in 1% RMS noise or less for the light curves. But for faint stars often sky background noise is the dominating (as seen for the BEST system, see section 6.1.2.).

The background signal in CCD images includes mainly the signal from the sky background. This signal consists of light from background stars, galaxies, night glow, light scattered from the interstellar medium and stray light as a product of the human civilization. The latter is the major contributor to the total background signal (for most observational sites) and characterizes whether an observational site is well-suited for a high-precision photometric

monitoring campaign. Dark observational sites show sky brightnesses of about 21 mag/arcsec^2. 21.9 mag/arcsec^2 for the V band and 21.1 mag/arcsec^2 for the R band are reported for La Silla in Chile (Vanzi & Hainaut 2003). Benn & Ellison (1998) give similar results for La Palma: 21.9 mag/arcsec^2 in the V band and 21.0 mag/arcsec^2 in the R band. These measurements are done in dark, moonless nights. Regions close to the zenith position that do not contain any detectable object were analyzed for these results. For TLS we measured a minimal background signal of about 20.1 mag/arcsec^2 in BEST images, one magnitude brighter than measured in the R band for dark observational sites. Remember that the magnitudes of the stars were calibrated by comparison with R magnitudes of reference stars. More commonly, values were determined to be 19.7 mag/arcsec^2 for uncrowded target fields and 19.5 mag/arcsec^2 for crowded target fields containing more background objects. 19.5 mag/arcsec^2 corresponds to about 500 ADU/pixel (gain of the CCD 11.4 e^-/ADU) in 240 sec exposures of the BEST system with an AP-10 camera.

The sky background noise for aperture photometry can be calculated as described in equation 2.22.

The third major contributor for the total noise of light curves is scintillation noise as calculated in equation 2.23.

Furthermore it is assumed that additional noise sources, such as readout noise and thermal noise of the CCD, are negligibly low. Then the total noise for light curves of the systems included in this analysis can be calculated as

$$\sigma = \sqrt{\sigma_p^2 + \sigma_{Sky}^2 + \sigma_s^2} \qquad (7.1.)$$

Well-sampled data with Nyquist sampled PSFs with a FWHM of 2 pixels are assumed for all systems as recommended by Howell & Everett (2001) to reach highest photometric precision. The radius of the aperture for photometry was set to 4 pixels based on the findings in an analysis to determine the best photometric procedure using SourceExtractor (see section 4.2.). Note that different photometric measurement techniques can lead to different results.

Another assumption made is, that the measured signals for the brightest non-saturated stars have a value of 10^6 electrons, typical for 14-bit CCDs (FWHM = 2 pixels). This is a good estimation for all the systems considered in this analysis, because all systems use AP-10 CCDs, AP-16 CCDs or very similar CCDs (see also section 2.3.5).

The exposure times used for the calculations of the scintillation noise were set to the exposure times used by the operating systems. For systems larger than BEST the exposure time was limited so that the brightest, non-saturated stars have a magnitude R=11.0 to avoid that stars too faint for RV follow-up observations are observed. The optical throughput is assumed to be the same as for the BEST system.

The limiting magnitude was determined for all systems when the total noise level reached 1%.

The noise terms were analyzed for two different observational sites. The first part of the analysis was carried out for a site at a height of 2500m above sea level with a sky background of 21.0 mag/arcsec^2 in the R band as typical for a dark observational site. The calculations are based on the assumption that the average airmass is 1.4 as typical for observations of target fields going through the zenith down to an altitude of 30 degrees. The results of this study for this site are given in Table 7.2.

Scintillation noise is dominating only for the bright non-saturated stars for the observing strategy of the KELT (for more information about this system see Table 7.1. and section A.9.1.) system with an exposure time of 30 sec. A strategy to limit the influence of the scintillation noise for the KELT system is to increase the exposure time. A minimal total noise of 0.23% could be reached with an exposure time of 240 sec instead of the 0.60% noise for

Table 7.2.: Noise sources and resulting limiting magnitudes for existing or proposed transit search systems located at a site with a height of 2500m above sea level and with a sky background of 21.0 mag/arcsec^2 in the R band .

System (exposure time)	*Minimal R magnitude*	*Minimal RMS [%]*	*Limiting magnitude (RMS < 1%)*	*Photon noise [%]*	*Background noise [%]*	*Scintillation noise [%]*
PASS (900 sec)	7.4	0.22	9.7	0.26	0.96	0.15
KELT (30 sec)	4.9	0.60	8.2	0.42	0.69	0.59
KELT (240 sec)	7.1	0.23	10.6	0.47	0.87	0.21
STARE (120 sec)	8.2	0.19	11.8	0.49	0.85	0.16
BEST (240 sec)	10.5	0.12	14.4	0.56	0.82	0.07
BEST4k (240 sec)	10.5	0.12	14.8	0.67	0.76	0.07
TEST (170 sec)	11.0	0.12	15.8	0.84	0.57	0.07
BEST-2 (240 sec)	11.0	0.11	16.0	0.85	0.52	0.06
OTSS (80 sec)	11.0	0.12	15.6	0.76	0.66	0.07

Table 7.3.: Noise sources and resulting limiting magnitudes for existing or proposed transit search systems. A background signal of 20.0 mag/arcsec^2 for an observational site at a height of 341m (like TLS) was here assumed.

System (exposure time)	*Minimal magnitude*	*Minimal RMS [%]*	*Limiting magnitude (RMS < 1%)*	*Photon noise [%]*	*Background noise [%]*	*Scintillation noise [%]*
PASS (900 sec)	7.4	0.29	9.2	0.21	0.96	0.20
KELT (30 sec)	4.9	0.78	7.5	0.30	0.56	0.77
KELT (240 sec)	7.1	0.29	10.2	0.38	0.89	0.27
STARE (120 sec)	8.2	0.24	11.3	0.40	0.89	0.22
BEST (240 sec)	10.5	0.14	14.0	0.46	0.89	0.10
BEST4k (240 sec)	10.5	0.14	14.4	0.56	0.84	0.10
TEST (170 sec)	11.0	0.12	15.5	0.73	0.69	0.07
BEST-2 (240 sec)	11.0	0.13	15.6	0.76	0.66	0.08
OTSS (80sec)	11.0	0.14	15.2	0.65	0.76	0.10

the 30sec exposures. But the longer exposure time would reduce the capability to ‘jump’ between 10 different pointings in the horizontal coordinate system as proposed by the KELT team.

All other systems are dominated by photon noise for the brightest non-saturated stars. A minimal total noise term will be reached for the proposed BEST-2 system with a value of

0.11%. The systems BEST, BEST4k, TEST and OTSS reached a minimal value of 0.12% for the total noise of light curves of the brightest non-saturated stars.

The dynamic range (minimal R magnitude – limiting magnitude) with a photometric precision better than 1% ranges from 1.7 mag for the PASS system (mainly due to noise caused by the background signal) to 5.0 mag for the BEST-2 system. The noise terms for the photometry of the BEST-2 system are dominated by photon noise for all light curves with RMS < 1%. The observations of the systems BEST-2, TEST and OTTS can be described as photon noise limited. This mean that photon noise is dominating for light curves with RMS=1% and therefore for the majority of stars. Due to the smaller pixelscale compared to the other systems background noise is not the dominating noise term.

Note the wider dynamic range of the BEST4k system (+0.4 mag) compared to the BEST system. The collecting area of a single 9μm pixel of BEST4k is 2.4 times smaller than for the 14-μm pixel of BEST yielding to a reduction of the background signal by a factor of 2.4 in relation to the measured stellar signals (assuming the same quantum efficiency for stellar and background signals).

For the second part of the analysis of the noise terms it was assumed that all systems are hypothetically located at the TLS with a higher background signal of 20.0 mag/arcsec^2 and a height of 340m above sea level (see results in Table 7.3.). Thus the increased background noise and scintillation noise further reduces the magnitude range suitable for transit search. The dominating noise source for light curves obtained with KELT (30 sec) is scintillation noise with a value of 0.77%. This and the higher background noise limit the magnitude range to 2.6 mag. PASS would have a suitable magnitude range of 1.8 mag mainly due to the higher background signal. TLS would be an unsuitable observational site for both searches.

Searches with smaller pixelscale show a reduced influence of the high background signal. The magnitude range suitable for transit search is reduced by 0.4 to 0.6 mag compared to the 21.0 mag/arcsec^2 sky signal. For the systems with the smallest pixel scales TEST (2.0 arcsec/pixel) and BEST-2 (1.5 arcsec/pixel) photon noise will dominate the suitable magnitude range, but the influence of the background noise is in the same order as the photon noise for the stars with a photometric precision of 1%. For the OTSS system background noise is the dominating noise source for the faint stars at the limiting magnitude. The suitable magnitude range of 4.2 mag is however still better than for STARE, BEST or BEST4k.

Pepper et al. (2003) used different parameters for their noise analysis of the proposed KELT system. Scintillation noise was underestimated using an exponent x = 1.5 in equation (8.3.) as proposed in an earlier paper of Young (1967) that was corrected to 1.75 later by Young (1993). Another major difference is the usage of DoPhot photometry with very small apertures containing only 13 pixels to reduce the influence of the background noise. Nevertheless the limiting magnitude of 10 for 30 sec exposures expected by Pepper et al. (2004) seems to be too optimistic. First tests of the KELT system published by Pepper et al. (2004) showed an attained photometric precision of 1-4% for stars with V = 6 – 10 mag closer to the prediction made in this analysis. A longer exposure time could significantly improve the limiting magnitude. For exposures of 240 sec a limiting magnitude of 10.6 could be reached mainly due to the reduced scintillation noise. But then the sampling rate or the number of observed target fields has to be reduced. The latter would eliminate the character of the system as an all sky survey.

Generally wide-angle searches are background noise limited. Only photometry of all-sky surveys taking short exposures can be mainly degraded by scintillation noise. The introduction of CCDs with smaller pixelsize reduces the influence of the background noise, but only search systems with large apertures (D > 20 cm) can be photon noise up to the limiting magnitude (light curve RMS<1%) limited using currently available CCDs with 9-μm pixelsizes, even on dark observational sites.

7.3. The fraction of suitable target stars

For ground-based searches only transits with depths of around 1% and deeper will be detectable. Host stars can have a maximal dimension of 1.5 solar sizes to show transit signals of 1% and larger (see section 2.3.3.). The fraction of these suitable target stars in a target field can vary for the BEST target fields based on the calculations of the Besançon model of the stellar population synthesis of the Galaxy (Robin et al. 2003, see section 2.3.3. for details). Simulations were already carried out for five typical target fields in and above the Galactic plane (called field 1, 2, 3, 4, 5) in section 2.3.3. Target field No. 2 (= F2) was observed by the BEST survey. Two more fields were observed: F15 and F8 (see target field selection 4.1.). For the three observed target fields Besançon model were applied in section 6.4.2. already. Remember that target field No. 15 with the highest stellar density showed the lowest fraction of suitable target stars of about 21 %. Target field No. 2 was enriched in small target stars with a fraction of 27 %, and target field No. 8 had a fraction of about 78 % for a limiting magnitude of 14. For this study the simulations were expanded to different limiting magnitudes so that the results can be applied to all search systems included in this analysis. Thus, this analysis includes Besançon models for seven target fields (see Table 7.4. for coordinates and stellar densities) with limiting R magnitudes from 10 to 18.

The models of the target fields showed that the distribution of stellar types is inhomogeneous leading to varying fractions of stars being small enough to be suitable target stars for ground-based transit searches. In Figure 7.2. and Figure 2.8. the fraction of suitable target stars is plotted for the modeled target fields against the limiting magnitude R. The fraction of good target stars is generally lower for brighter stars compared to fainter stars. For a limiting magnitude R = 10 the fraction is below 10 % for most target fields among the simulated target fields. Only target field No.8, with the lowest stellar density, has a higher fraction of good target stars. Thus the number of suitable target stars is limited for all-sky searches like PASS or KELT. According to Deeg et al. (2004) there are 250,000 stars of all spectral and luminosity classes in the northern hemisphere to be monitored from a single site

Table 7.4.: Galactic coordinates and stellar densities are given for the 7 potential or observed target fields (observed target fields are marked with an additional 'F', the fields are listed with decreasing stellar densities) used for the analysis of the content of stars small enough for ground-based transit searches. Note that a typical reddening of 0.70 mag/kpc for all fields was assumed. This is a good approximation for large FOVs in the Galactic plane. Local variations of the reddening can lead to different stellar densities especially for small FOVs.

Field No.	*l [deg]*	*b [deg]*	*Stellar density [# / deg^2] R < 12 mag*	*Stellar density [# / deg^2] R < 13 mag*	*Stellar density [# / deg^2] R < 14 mag*	*Stellar density [# / deg^2] R < 15 mag*	*Stellar density [# / deg^2] R < 18 mag*
F15	83	+9.0	200	485	1070	2288	17813
1	130	+0.0	148	374	847	1789	11447
F2	130	+7.5	139	306	627	1229	7407
3	130	+15.0	105	217	426	841	4098
4	130	+22.5	78	160	329	630	2651
5	130	+30.5	64	132	263	476	1796
F8	163	+54.5	22	48	97	171	588

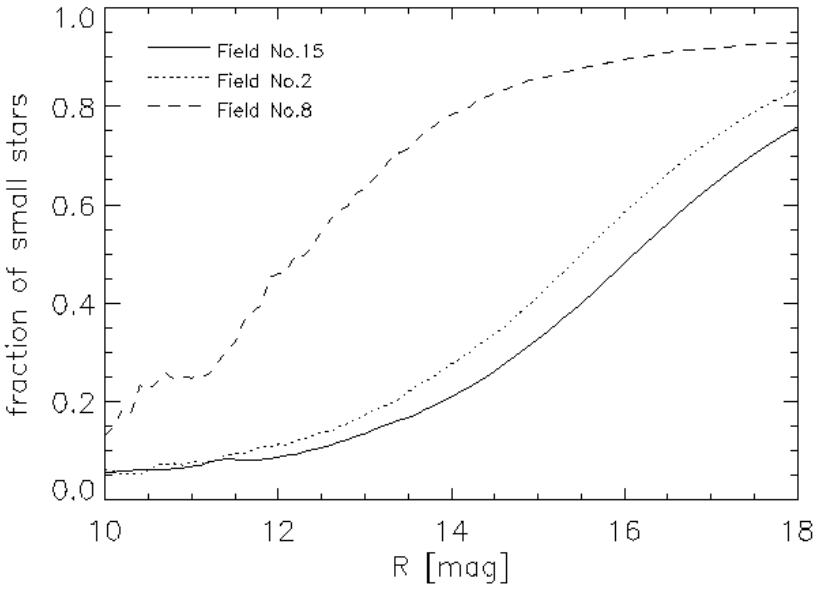

Figure 7.2.: The fraction of target stars small enough to be targets of a ground-based transit search for the three observed target fields is plotted versus the R magnitude limit where a photometric precision of one percent is obtained. The fraction increases with the limiting magnitude. The fraction is significantly enriched for target field No. 8 compared to the target fields No. 2 and 15 in the Galactic plane for all magnitudes.

Table 7.5.: The average number of suitable target stars/deg^2 is computed for potential or observed target fields by the Besançon model. The fraction of small stars in percent is given in parenthesis.

Field No.	R < 12 mag	R < 13 mag	R < 14 mag	R < 15 mag	R < 18 mag
F15	17 (8.7 %)	65 (13.4 %)	224 (20.9 %)	750 (32.8 %)	13502 (75.8 %)
1	13 (8.9 %)	46 (12.4 %)	147 (17.4 %)	435 (24.3 %)	6742 (58.9 %)
F2	16 (11.3 %)	53 (17.3 %)	173 (27.6 %)	508 (41.3 %)	6177 (83.4 %)
3	18 (17.6 %)	62 (28.7 %)	186 (43.6 %)	510 (60.6 %)	3668 (89.5 %)
4	21 (26.9 %)	66 (41.0 %)	190 (57.8 %)	452 (71.8 %)	2434 (91.8 %)
5	20 (31.5 %)	65 (49.4 %)	172 (65.3 %)	369 (77.5 %)	1663 (92.6 %)
F8	10 (46.0 %)	30 (63.2 %)	76 (78.4 %)	146 (85.6 %)	547 (93.1 %)

all-sky survey with magnitude 10 or brighter at airmasses below 2. With the estimated fraction of 1ß% of small stars at most 25,000 stars (mainly late F and early G stars) are small dwarfs and therefore suitable targets for transit search.

The fraction of suitable target stars increases steadily with increasing R magnitude. For target fields above the Galactic plane (b > +10°) a higher fraction of good targets is observed than for target fields in the Galactic plane. The fraction of good target stars increases with the distance to the center of the Galactic plane. A percentage of about 90% good target stars is reached for all target fields above the Galactic plane for R magnitude 18.

The percentage and the number of suitable target stars per deg^2 for selected limiting R magnitudes for the seven target fields analyzed is given in Table 7.5. The density of suitable stars is nearly the same for all target fields for R magnitudes < 14, only target field F8 shows a lower density because of the extremely low stellar density. For deeper searches the fraction of small stars is maximal for the target fields close to the center of the Galactic plane with the highest stellar densities. Note that for the brighter stars this is a small number statistics and results should be treated carefully.

7.4. Stellar crowding

In section 2.3.6. a model for analyses of crowding (overlapping of stellar PSFs) was already introduced. Undisturbed signals were defined as objects which have no neighbors within a distance of two times of the aperture radius used for photometry and within a magnitude range of 4 mag. In section 6.1.2. it was addressed that crowding noise could be an important contributor to the total noise budget for the photometry of star-rich target fields.
The SourceExtractor software shows some capabilities to improve the photometry for some crowding cases (see section 5.2.) Therefore a more detailed analysis was carried out.

Three different kinds of disturbances exist that can worsen the photometric precision of the resulting light curves:

a) A neighboring object is resolved but contributes to the measured signal within the aperture (or the measured PSF) of the neighboring object and therefore weakens transit signals. Noise is added if the additional signal is from a variable object. This case is called '**dilution**' in the following discussion. Note, that the SourceExtractor software used corrects this case by mirroring the 'undiluted' part of the PSF, if both objects are detected separately.

b) A neighboring object cannot be spatially resolved. A combined signal of both objects is measured; transit signals are weakened. Additional noise is added if one of the contributing signals is variable. This case is called '**unresolved**'.

c) A mixture between case a) and b). Due to variations of the seeing or transparency a neighboring object is not detected in all frames. The resulting light curve consists of combined measurements and corrected measurements. Mainly due to changes in the transparency this case is relatively common for observations performed at the TLS. The limiting distance where neighboring objects can be resolved was found to be 3-4 pixels using the SourceExtractor software on BEST data (see section 5.2.). In the following text this case is called '**confusion**'.

For the case of 'dilution' a significant weakening of transit signals can reduce their detectability. The majority of the transit signals is expected to have a depth of about 1 % close

to the detection limit for ground-based searches. Thus a weakening of the signal by more than 20 % was considered to be relevant for the following analysis of crowding situations.

Simulations of crowded fields for the search system included in this study were carried out. Based on the star numbers and the brightness function given by the Besançon models for the seven target fields the spatial distribution of the stars was simulated. Random coordinates on the CCD chip were created for each single star. Then each single star was analyzed if any of the crowding cases a), b) or c) were appearing. It was assumed that the PSFs are Nyquist sampled with a FWHM of 2 pixels. The radius for the aperture was set to be 4 pixels. An average radius of 4 pixels was found to yield to light curves with the highest precision for observations of BEST from TLS (for details see section 5.2.).

Note that the decision to use the Besançon model data for the crowding analysis in combination with random coordinates is based on several facts. First, all available observational data for target fields are limited in spatial resolution. Additional tests with POSS-I and GSC-II data showed that several objects are listed twice or more with different magnitudes or different coordinates with 2-dimensional distances close to the supposed resolution limit. The latter cases often affect large areas and could be the result of an underestimation of the position errors scanning overlapping plates to produce these catalogues. Objects listed with different magnitudes were often identified as variables in the BEST data set.

Another way was found to check the modeled data with real data. For the observed target fields F2, F8 and F15 overlapping objects can be flagged by the SourceExtractor software. The number of overlapping objects detected in 240 sec exposures (R < 14 mag) was counted and compared with the total number of overlapping objects resulting from the crowding models for these target fields. For target field No.15 48.6% of the stars (R < 14) were detected to be overlapping with other stars; the model computed a fraction of 44.9%. For field F2 SourceExtractor identified 43.8% of overlapping objects; the simulation gives 43.3%. Target field No.8 with the lowest stellar density showed a fraction of 7.4% of overlapping objects detected by SourceExtractor, the model computes 5.5%. So the model gives reasonable, but slightly underestimated estimates of the stellar crowding.

For simplification all stars were assumed to be single stars, any stars that cannot be resolved are assumed to be not bounded.
The following are counted:

- Unresolved objects: objects which are closer than 3 pixels to another star.
- Diluted objects: the signal within the aperture originates with a fraction of 20 percent or more from one or more neighboring objects (resolved und unresolved).
- Signals that are eventually disturbed by detection ‘confusions’ caused by neighboring objects close to resolving limit. The number of ‘confused’ objects strongly depends upon variations of the seeing and the transparency. The given fraction of confused objects is an average value for the use of the SourceExtractor as a tool for detection and photometry and can differ for other detection tools.

First simulation for BEST were carried out. Ten single simulations for every target field are averaged to increase the statistical basis. Results of this analysis of target field F2 for the R magnitude range 12 – 15 for the BEST system are plotted in Figure 7.3. and can be compared to results of field F15 in Figure 7.4.. The fraction of disturbed signals (dilution, confusion) doubles for target field F15. The frequency of confused cases is higher than for diluted cases for both target fields if the dilution limit is 20%. Note that the number of dilution cases is nearly the same as for confusion if a lower dilution limit of 10 % is set.

Results of the simulations for all target fields included in this analysis at the limiting magnitude R = 14 mag (reached for observations under good photometrical conditions with

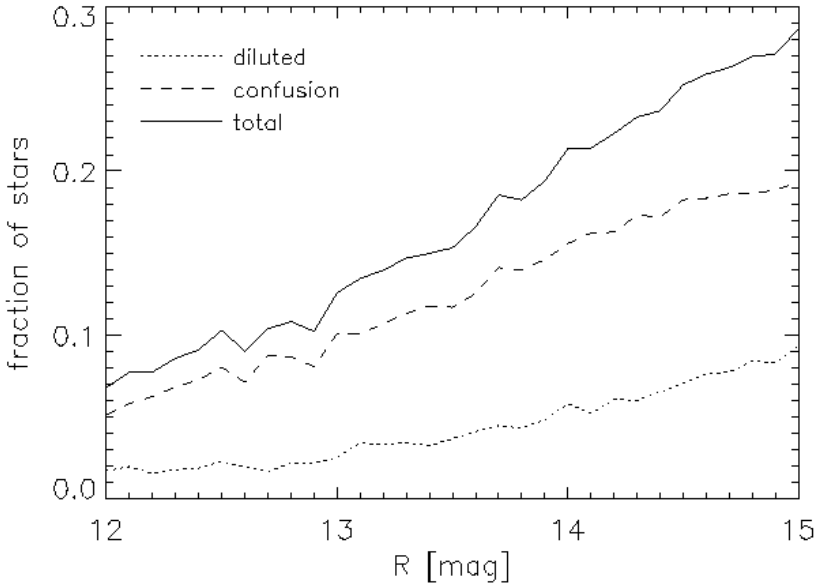

Figure 7.3.: The fractions of potentially disturbed star signals is given for target field F2 observations by BEST for different magnitudes as a result of the analysis of the stellar crowding based on the Besançon model. The 'confusion' cases have a higher influence for all magnitudes than the 'dilution' cases. Note that cases with signal dilution less than 20 % are not counted as diluted objects. The number of 'dilution' cases is nearly the same as for confusion cases if a lower 'dilution' limit of 10 % is set. A percentage of 23 % of the stellar signals at the magnitude R = 14 is diluted or disturbed by detection problems. Note, that the number of unresolved objects is subtracted from the total number of objects in the frame to make the result of the analysis comparable to the analysis of real data. Therefore the number of unresolved objects is not displayed here, but the dilution cases due to unresolved objects are still counted.

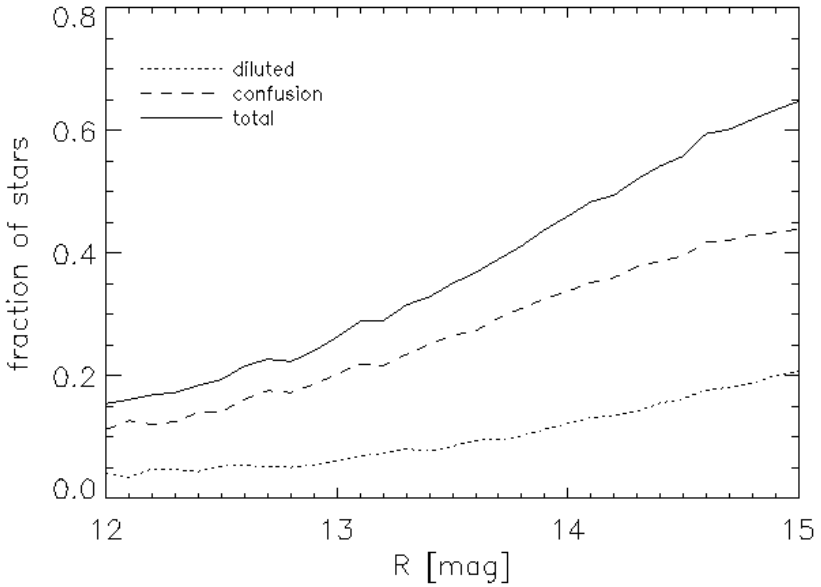

Figure 7.4.: The same as for Figure 7.3. but for field F15. Note the significantly higher rates of 'confusion' and 'dilution'. A fraction of 43 % of the stellar signals at the magnitude R = 14 is diluted or disturbed by detection problems.

Table 7.6.: Results of the crowding simulations for target fields of different stellar density for the BEST system as given by the Besançon model. The given number of stars for R < 14 is not corrected for the number of unresolved objects. Note that the number of undisturbed stellar signals is higher for target field 1 and 2 than for target field F15 with higher stellar densities. Thus fields with stellar densities like field No.1 and No.2 should be preferred target fields for BEST if an optimal crowding situation were to be the only consideration.

Target field No.	*# stars R < 14 mag in FOV*	*Unresolved [%]*	*Diluted > 20%[%]*	*Confusion [%]*	*Fraction of undisturbed signals*	*# stars undisturbed*
F15	9821	4.2	7.8	31.3	56.7	5569
1	9378	4.1	6.9	23.4	65.6	6152
F2	7323	3.0	4.3	15.8	76.9	5631
3	5016	2.2	3.4	8.3	86.1	4319
4	3364	1.5	1.9	6.2	90.4	3041
5	2566	0.9	1.6	3.6	93.9	2409
F8	824	0.1	0.2	1.6	98.1	808

BEST at TLS) are listed in Table 7.6. The percentage of unresolved objects is relatively low with 0.1 – 4.2 %. In reality this percentage will be higher because unresolved binaries are not included in this study.

Target field F15 with the highest stellar density shows the lowest fraction of undisturbed signals with 56.7%. The majority of the disturbances are caused by confusion cases, dilution is a minor case. Generally the confusion potential grows fast with the stellar density in comparison to the dilution potential (field F8 is excluded because of the low statistical basis).

For the target fields 1 and F2 the number of undisturbed star signals is higher than for the more star-rich target field F15. Target field 1 has the highest number of undisturbed signals with 6152.

The absolute number of undisturbed stellar signals will be lower for target fields above the Galactic plane (fields No. 3, 4, 5 & F8) as for the fields in the Galactic plane. But still some thousand stars can show an undisturbed signal.

The number of overlapping PSFs may actually be higher as in this simulation; many of the dilution cases yield a lower additional signal than the limit of 20 %. Thus, SourceExtractor lists 48.6 % of all detected stellar signals as influenced by neighboring objects, as mentioned before. Note that this does not include the number of unresolved objects (unbound objects, binaries and triples). The probability of observing blended eclipsing binaries that can mimic transit-like signals decreases with the stellar densities of the observed fields. Additionally the photometric performance is degraded by the high number of faint background objects, which increase the background signal locally and reduce the S/N of the observed brighter stars.

Similar crowding simulations were computed for the systems STARE, BEST4k, TEST, BEST-2 and OSST (see selected results in Table 7.7.). The limiting magnitudes for the different systems were given by TrES team members or are based on the experience with BEST.

Comparing the crowding for the current BEST system with the BEST4k system shows an improved crowding situation. The percentage of undisturbed stellar signals of target field F15 is 85.1% for BEST4k giving 10,800 undisturbed signals up to magnitude 14.5. The current BEST system will monitor 5,600 stars without disturbances up to magnitude 14.0 corresponding to a percentage of 57%. Although the exposures of BEST4k are deeper (due to

Table 7.7.: Results of crowding simulations for target fields F15 and F2 for different existing or proposed transit search systems similar to the simulations performed for BEST. Again it was assumed that the FWHM = 2.0 pixels and radius of aperture = 4.0 pixels. The replacement of the 2k CCD of BEST by a 4k CCD will double the number of undisturbed stellar signals for field F15. More crowded target fields can be observed with the larger instruments to be able to monitor higher numbers of undisturbed (by crowding) stellar signals.

system	*Target Field No.*	*Limiting R mag-nitude*	*# stars in FOV*	*Unresol-ved [%]*	*Diluted > 20% [%]*	*Confusion [%]*	*Fraction of undisturbed signals[%]*	*# stars undisturbed*
STARE	F15	12	7092	3.2	6.2	33.1	57.5	4078
STARE	F2	12	6732	3.2	5.5	20.7	70.6	4753
BEST4k	F15	14.5	14415	2.6	4.4	17.9	75.1	10825
BEST4k	F2	14.5	10033	1.9	3.0	7.8	87.3	8729
TEST	F15	15.0	11426	1.2	2.1	6.9	89.8	10261
TEST	F2	15.0	7163	0.7	1.1	2.9	95.3	7271
BEST-2	F15	15	6295	0.6	1.1	2.9	95.4	6005
BEST-2	F2	15	3946	0.4	0.6	1.4	97.6	3851
OTSS	F15	15	49772	5.4	9.1	27.0	58.5	29116
OTSS	F2	15	31204	3.2	5.1	11.6	80.1	24994

the higher quantum efficiency of the CCD chip) crowding is a much less disturbing issue for high precision photometry. But this assumes that the PSF of the stars can be adjusted to keep a FWHM of 2 pixels using the proposed 4k CCD and a focusing unit. Thus the replacement of the 2k CCD with the proposed 4k CCD will nearly double the number of undisturbed star signals for the star-rich target field F15. Target fields with a higher stellar density than for field F15 will be observable with the systems BEST4k, the 30cm TEST equipped with a 4k CCD and the 25cm BEST-2 with a 4k CCD.

The 10cm telescopes of the TrES-network with 2k CCDs reach similar performances for unresolved, diluted or 'confused' signals as the BEST system. The lower number of stars up to the limiting magnitude R = 12 mag yields however to a reduced absolute number of undisturbed stellar signals compared to BEST.

The larger proposed transit search systems BEST-2 and TEST show relatively low rates for dilution and confusion. Observations of more dense target fields than the target field analyzed in this study will yield higher detection probabilities. The OTSS system has higher but nevertheless acceptable rates of dilution and confusion for target fields in the Galactic plane. Here, a high number of undisturbed stellar signals can be monitored leading to a high detection probability.

The crowding situation for the all-sky surveys PASS (prototype) and KELT was also simulated (see Table 7.8., a description of the systems can be found in appendix B). Due to the large FOVs of these surveys no even distribution of the stars in the total FOV can be assumed anymore especially for regions close to the Galactic plane. Most of the target fields of the all-sky surveys are located outside the Galactic plane. It is known that about 400,000 stars exist brighter than magnitude 10.5 (Deeg et al. 2004). Thus 10 stars brighter than 10.5

Table 7.8: Results of the crowding simulation for PASS and KELT observing target field 5 as a typical target field above the Galactic plane and a typical target field not located in Galactic plane (labeled 'NG'). KELT is able to monitor all kinds of target fields due to the smaller pixelscale of the 4k CCD used. The crowding for PASS observations is very strong even for the field above the Galactic plane. Only target fields not correlated with the Galactic plane show a high number of undisturbed stellar signals.

system	*Target Field No.*	*Limiting R mag-nitude*	*# stars in FOV*	*Unre-solved [%]*	*Diluted > 20% [%]*	*Confusion [%]*	*Fraction of undisturbed signals [%]*	*# stars undisturbed*
PASS	NG	10	5120	1.9	6.2	30.5	61.4	3144
PASS	5	10	29692	8.1	20.2	62.5	9.2	2732
KELT	NG	10	3380	0.3	1.1	5.8	92.8	3137
KELT	5	10	19604	2.0	3.5	16.9	77.6	15213

mag per 1 deg x 1 deg field should be the stellar density for a typical target field not in the Galactic plane. Target field F8 shows a density of 8 stars per 1 deg x 1 deg field. Thus the number of stars contained in target field 5 was rescaled to reach the higher mean density of 10 stars per 1 deg x 1 deg for the crowding analysis. Target field F5 was chosen as a typical less crowded target field above the Galactic plane whether such regions can be monitored by all-sky surveys. The limiting magnitude was set to be 10.0 for both searches in agreement with the expected limiting magnitudes given in the publications of both groups operating these systems. The crowding situation for KELT is much more moderate than for PASS. If PASS observes regions in the Galactic plane all objects will be affected by crowding using photometric apertures with a radius of four pixels. Smaller apertures or smaller pixels can improve the crowding situation. For fields above the Galactic plane the crowding situation improves, nevertheless the percentage of undisturbed stellar signals is rather low (10%). But fields not in the region of the Galactic plane show a moderate crowding. KELT observations of moderate crowded target fields close to the Galactic plane (like field F5) will be possible if the crowding situation is the only consideration. The number of stellar signals undisturbed by crowding can be rather high and reach numbers similar to the larger transit search systems using 4k CCDs included in this study.

7.5. Orbital phase coverage

Estimates of the necessary orbital phase coverage to be able to detect one or three transit event of a Hot Jupiter planet were already addressed in section 2.3.7. For duty cycles of 40 to 60 percent typical for good observational sites in Europe about 100 percent orbital phase coverage for one detection is attained for hypothetical planets with orbits up to 4.5 days within one season. For three detections full phase coverage is obtained for periods of up to two days. Thus, most of the Hot Jupiter planets will be detected once. This assumes that the transit signal is deep enough (about 2%) to be detectable as an individual signal. Shallower signals with a depth of about 1% will not be detected. For this kind of signals more observations has to be done to obtain a phase coverage for three detections.

One solution is to monitor the same target field for a second season or longer as it was done for the observations by BEST from TLS. The orbital phase coverage obtained for the three observed target fields can be seen in section 6.1.

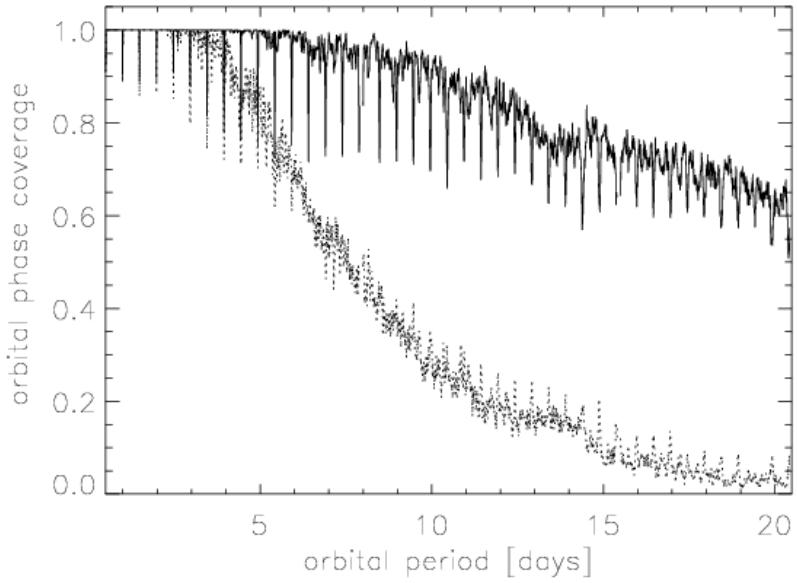

Figure 7.5: Orbital phase coverage vs. orbital period for an observational network consisting of two instruments located on sites with the same geographical latitude and opposite longitude each with a duty cycle of 40 percent. 100 percent orbital phase coverage for one detection is obtained for orbital periods of up to 6.5 days, for three detections up to 3.5 days within one season. Note that the detection probability for events occurring on daily intervals (or multiples thereof) has improved compared to observations from a single site.

Another way is to build up a network of similar telescopes at different locations with the same geographical latitude. Overlapping observations can be reduced if the second site is located on a different longitude. The ideal case is a longitude difference of 180 degree to avoid any overlapping observations even during longer winter nights. Such cases were modeled again for different combinations of the duty cycles. One example is given for a 40% duty cycle for both sites (see Figure 7.5.). 100 percent orbital phase coverage for one detection is obtained for orbital periods up to 6.5 days, for three detections up to 3.5 days. Most of the transit cases for 4-day orbits or shorter will be observed three times allowing discovery of most of the detectable Hot Jupiter transits. The phase coverage for events occurring on daily intervals (or multiples of it) has improved compared to observations from a single site, the phase coverage for other periods is lower than for single site observations with a duty cycle of 80 percent.

Another option is to choose a second observational site on a location that often experiences the opposite weather situation. Clearly, simultaneous observations from both sites can now occur; nevertheless these simultaneous observations can be advantageous. The S/N of the combined light curves from both observations is increased allowing the detections of fainter transits. The simultaneous observation of a transit improves the reliability of the detected event significantly.

7.6. Resulting detection probabilities

The number of the expected detectable planets for the different existing or proposed transit search systems is estimated based on the calculations made in chapter 2 using equation 2.19. The percentage of stars harboring a Hot Jupiter planet h_e is 1.3 ± 0.3%, analogue to section 2.3.1. The geometrical probability for a transit of a Hot Jupiter f_{geom} is assumed to 10% (see

section 2.3.2.). The number of high-precision light curves (RMS < 1%) N_{phot} is calculated as the product of the number of stars in the total FOV up to the limiting magnitude given by the Besançon model of the stellar population synthesis of the Galaxy (see section 7.3.) and the fraction of 'undisturbed' signals given by the crowding analysis in section 7.4. The fraction of detectable transit signals (depth >1%) f_d is calculated as in section 2.3.4. The orbital phase coverage f_c was set to 50% to give a system-specific result independently from duty cycle. The results for the detection rates are given in Table 7.9.

The single 10cm telescopes of the TrES network show the lowest detection probabilities of the non-all-sky surveys mainly due to the low fraction of small stars in the modeled target fields. In reality this will be compensated by the networking giving a better orbital phase coverage. Higher detection probabilities are resulting for the BEST system due to higher fractions of small stars in the observed magnitude range. Target fields above the Galactic plane should be preferred target fields for TrES and BEST.

The replacement of the 2k CCDs by 4k CCDs improves the detection probability as demonstrated for the system BEST4k. Higher detection probabilities resulting especially for target fields in the Galactic plane which should be preferred target fields for a BEST4k system. But for target fields above the Galactic plane only moderately less detection probabilities are obtained. A reduced background signal due to the smaller pixel scale of the 4k CCD will be an additional advantage.

The TEST survey will have higher detection probabilities for target fields like field F15 in the Galactic plane. The influence of the crowding is still moderate. This allows the observation of target fields with higher stellar densities than field F15.

The BEST-2 system features lower detection probabilities due to the small FOV. The observation of more crowded target fields as accessible in the skies of the Southern hemisphere is recommended.

The highest detections probabilities are reached for the proposed OTSS system. It is well suited to observe target fields in and above the Galactic plane with nearly the same detection rates. Such detection rates are at least two times higher than for the other systems analyzed in this work. Further analysis should be done to evaluate whether such a system with a low focal ratio is feasible for moderate costs.

The all-sky surveys analyzed will be able to detect a few transiting planets around bright stars. The detection rate for the full single-site PASS system can reach 1.2 planets if 100% phase coverage is obtained. A second PASS system on the opposite half of the earth could monitor the bright stars not monitored by the first system and reach a similar detection rate. The KELT system will be able to reach an annual detection rate of 0.72 transiting planets per year assuming that only 3 paintings can be carried out to take long exposures of 240 sec.

To compare these annual detection rates of PASS and KELT with the detection rates of the other analyzed systems the latter detection rates should be multiplied by 2.5. Each system could monitor 3 different target fields per year. One of the three target fields observable in one year will not be located in or close to the Galactic plane and will contain significantly less stars yielding lower detection rates. Thus a 10cm telescope of the TrES network obtains an annual detection rate of 0.45 transiting planets (target field No.5), BEST 1.1 planets (field No. 4), BEST4k 1.8 planets (field F15), TEST 2.2 planets (field F15), BEST-2 1.3 planets (field F15) and OTSS 7.1 planets (field No.3).

The OTSS shows a superior performance with a very high detection probability for transits of exoplanets in comparison to all systems included in this study. Further studies for the OTSS seem to be appropriate.

Table 7.9.: Estimates for the planet detection probability for different existing or proposed search systems for mid-northern or mid-southern observational sites. Only the target fields with the highest detection probabilities are listed for the single field surveys. For PASS and KELT yearly detection rates are given. For the other surveys, the planet detection rate is given per observed target field within one season. Three target fields can be observed per year, but one target field per year will not be located close to the Galactic plane and will show lower detection rates. Thus a good assumption to evaluate the yearly detection rate is to multiply the single field detection rates by a factor of 2.5.

	Target field No.	Limiting R mag-nitude	# stars in FOV	Small stars f_{tar} [%]	Number of undisturbed signals [%]	Detectable signals f_d [%]	Number of good targets	# detected planets
PASS (15 systems)	**NG**	**10.0**	**26 x 5120**	**10.0**	**61.4**	**40.0**	**15 x 171**	**15 x 0.08**
KELT	**NG**	**10.0**	**9 x 3338**	**10.0**	**92.8**	**40.0**	**3 x 674**	**9 x 0.08**
TrES	**F15**	**12.0**	**7442**	**8.7**	**57.5**	**51.8**	**193**	**0.13**
TrES	**3**	**12.0**	**3907**	**17.6**	**79.9**	**53.1**	**292**	**0.19**
TrES	**5**	**12.0**	**2381**	**31.5**	**91.5**	**59.3**	**407**	**0.26**
BEST	**F15**	**14.0**	**10283**	**20.9**	**56.7**	**57.1**	**696**	**0.45**
BEST	**F2**	**14.0**	**6025**	**27.6**	**76.9**	**57.0**	**728**	**0.47**
BEST	**3**	**14.0**	**4094**	**43.6**	**86.1**	**59.7**	**918**	**0.60**
BEST	**4**	**14.0**	**3161**	**57.8**	**90.4**	**61.5**	**1014**	**0.66**
BEST	**5**	**14.0**	**2527**	**65.3**	**93.9**	**64.0**	**992**	**0.64**
BEST4k	**F15**	**14.5**	**14184**	**26.1**	**75.1**	**57.5**	**1588**	**1.03**
BEST4k	**F2**	**14.5**	**7957**	**34.2**	**87.3**	**59.6**	**1416**	**0.92**
BEST4k	**3**	**14.5**	**5423**	**50.8**	**92.3**	**61.8**	**1571**	**0.71**
TEST	**F15**	**15.0**	**11583**	**32.8**	**89.8**	**57.7**	**1969**	**1.28**
TEST	**F2**	**15.0**	**6222**	**41.3**	**95.3**	**60.5**	**1482**	**0.96**
TEST	**3**	**15.0**	**4258**	**60.6**	**97.6**	**63.9**	**1609**	**1.05**
BEST-2	**F15**	**15.0**	**6381**	**32.8**	**95.4**	**57.7**	**1152**	**0.75**
OTSS	**F15**	**15.0**	**50456**	**32.8**	**58.5**	**57.7**	**5585**	**3.63**
OTSS	**F2**	**15.0**	**27102**	**41.3**	**80.1**	**60.5**	**5424**	**3.53**
OTSS	**3**	**15.0**	**18546**	**60.6**	**87.4**	**63.9**	**6277**	**4.08**
OTSS	**4**	**15.0**	**13893**	**71.8**	**93.4**	**66.7**	**6214**	**4.04**

7.7. Summary of the optimization analysis

The ongoing process of finding an optimized transit search system has to consider several different kinds of aspects. An important aspect is to select the magnitude range of the stars that will be monitored. Transits of bright stars (V < 10 mag) will be preferred targets because spectroscopic analysis of the atmosphere of the planet will be possible as already demonstrated for the planet HD 209458b (Charbonneau 2002, Vidal-Madjar 2003 & 2004). But the number of transiting planets orbiting bright stars will be limited mainly because most of the bright stars are large main sequence stars or giants. Transit signals of these kinds of stars are not detectable from the ground. Furthermore the stellar density of the bright stars is rather low. Thus all-sky surveys seem to be the only way to monitor a high number of bright stars. But the small apertures of these systems will yield high scintillation noise for short exposure times. Longer exposure times will increase the background noise for the all-sky surveys with large pixel scales. Additionally the large pixel scales of these systems will lead to a high number of false alarms due to the high number of blends especially for regions with higher stellar density. But all-sky surveys like PASS or KELT should be able to find some few transits of exoplanets orbiting bright stars.

Another way to find Hot Jupiter transits for bright stars is to monitor bright stars by radial velocity surveys. The spectral types of many bright stars are known and these stars can be selected by these RV surveys. The N2K survey (Fischer et al. 2005) has started to monitor 2000 metal-rich F and K type dwarfs brighter than 10.5 mag. All Hot Jupiters found will be photometrically probed for transit signals. A first transiting planet has already been discovered by this survey: HD 149026 b (Sato et al. 2005). This planet is of Saturnian size ($0.725 \pm 0.05\ R_{jup}$) with a transit signal of 0.3% depth that would be hard to detect in an all-sky survey like PASS or KELT because of their high minimal noise levels.

If the goal of a transit search is to find as many transiting planets as possible then fainter stars (V > 15) have to observed. Going to deeper magnitudes increases the fraction of stars small enough that transits can be detected from the ground. Large meter-class telescopes (e.g. 1.3m OGLE-III telescope) with mosaic CCDs have to be used to monitor faint stars for at least 4 months to reach a sufficient orbital phase coverage. High logistical and financial efforts to build and operate such systems are hard to justify by the scientific output of statistics for Hot Jupiters. The RV confirmation exceeds high efforts using the largest telescopes of the world. No spectroscopic analyses of the planetary atmospheres are possible with current telescopes and near-future facilities.

Therefore it seems to be a good compromise to monitor stars at medium magnitudes (10 < V < 15). For the brighter objects the RV confirmation can be done with smaller telescopes like the 2m TLS, for the fainter ones only a few RV measurements are necessary with larger telescopes to confirm the planetary character of the transit events. In-transit spectroscopy will be possible with larger telescopes in the near future. And, most important, photometric monitoring is still possible with low-cost telescopes combined with single-chip CCDs, that can be dedicated completely to transit search.

Based on the commercially available 4k CCD technology an optimized system to search for transits is proposed: a 45cm aperture telescope with a focal ratio 1/F = 1 combined with a CCD using the 4k chip KAF 16801 with a FOV of 4.7 degree by 4.7 degrees. It was analyzed how to choose optimal target fields for this proposed OTSS system and other existing or proposed transit search systems. The proper field selection is important to have a high probability of detecting a transit. Therefore field selection has to be optimized for the different instrumental set-ups. Several aspects have to be considered:

- Possible phase coverage from the observational site (observability, technical limitations, photometrical limitations, weather, etc.)

- Content of stars small enough to be able to detect transits from the ground
- Crowding of the potential target field (number of undisturbed stellar signals).

An optimized field selection should consider all these aspects to reach high search efficiency. The analysis showed that smaller systems using 2k CCDs like STARE and BEST should preferentially observe target field above the Galactic plane. Target fields in the Galactic plane have a too high stellar density for these systems. Furthermore the number of small stars in fields of the Galactic plane is larger or the same than target fields in the Galactic plane which are dominated by large main sequence stars and giants in the observed magnitude range.

Larger search systems with 4k CCD can observe both target fields in and above the Galactic plane with higher detection probabilities. The highest detection probability is reached for the proposed OTSS system with an optimized pixel scale to obtain Nyquist-sampled PSFs without defocusing.

To obtain higher detection probabilities for transiting exoplanets good orbital phase coverage has to be reached. The meteorological constraints on most of the observational sites do not allow the achievement of necessary duty cycles of 80 percent or better. Thus new strategies have to be developed to increase the observational time base. The observations of single target fields for more than one season are proposed for single-instrument surveys. Another way is to build up networks of two or more telescopes to improve the orbital phase coverage.

8. Results of the search for variable stars in the TLS data set

Photometric monitoring campaigns dedicated to search for transits of extrasolar planets observe typically a few thousand stars simultaneously with high precision. The observations cover a high number of nights; the target fields are observed for several months. Observations of two or more seasons enlarge the time bases; multi-site campaigns improve the phase coverage. Typical sampling rates of more than 4 exposures per hour lead to a high probability for the discovery of nearly all types of variable stars with periods above 0.01 days. The expected frequency of variable stars is of about 10% for dwarf stars (RMS > 1.4%) for timescales of one to a few months based on HIPPARCOS data (Grenon 1993, Eyer & Grenon 1997) and ground-based observations (Bordé et al. 2003). A typical scaling factor of 0.16 is found from longer (months) to shorter (hours) timescales which implies 1.6% of all stars could show variations on short timescales. Additionally most of the giant stars show variability on larger timescales. Typical target fields are dominated by main sequence stars, the percentage of dwarf stars is about 60% or higher depending mainly on the magnitude range of the observed stars. Therefore several thousand variable stars will be monitored by the existing ground-based transit search surveys during the next few years.

The main goal of the BEST survey is the discovery of transits of exoplanets, nevertheless the detection and analysis of light curves of variable stars in the data set of BEST is an important secondary goal of the program. Especially the characterization of the variability of stars within the target fields of the COROT satellite mission will be an important aspect of the preparatory work for that mission. The variability will be one of the criteria for the selection of the limited number of target stars.

The strategy to search for variables in the BEST data set of the TLS observations and the analysis of the light curves of the variables will be explained in the following subsections.

8.1. Strategy for the detection of variables

There are several ways to identify variables in large datasets. Most methods are optimized to search for variables in datasets with an absolute photometric calibration. The light curves of the BEST data are relatively calibrated to maximize the observational time base avoiding observations of standard stars. Flat fields were taken on a nightly basis to reach a higher precision of the light curves for the respective set-up of the instrument that differs from night to night (alignment of telescope and CCD after daily mounting/unmounting, focus, temperature effects, dust particles in the optical path). This yields different gradients of the illumination of the flat field exposures for different nights mainly due to pointing errors of the telescope and changes of the direction of the light source (stray light in the twilight, see also section 5.7.2.). As described in section 5.5., nine stars well-distributed over the FOV are used to calibrate the instrumental magnitude to the R magnitude. The different gradients of the flat field exposures from night to night yield to different nightly amplifications of the stellar signal depending on the position of the stellar signal on the CCD chip. Thus nightly offsets between the stellar signals from night to night of up to a few percent in extreme cases are resulting. A limited detection capability for long-term variability is resulting, only large magnitude variations can be distinguished from night-to-night magnitude offsets. The detection method for variable objects has to be adapted accordingly to this characteristic of the BEST observations from TLS.

Further constraints for the selection of the detection method for variable objects are:

a) Limited computational effort for the high number of light curves (~10,000 - 20,000 for typical target fields),

b) Robustness against isolated spurious signals (due to satellites, airplanes, Hits of cosmic rays, etc.).

Accordingly to these constraints a variability index VI was defined (Zhang et al. 2003) as the ratio of the averaged point-to-point magnitude difference and the theoretically expected RMS for a light curve of a non-variable star:

$$VI = \frac{\frac{1}{N-1}\sum_{i=1}^{N-1}\left|m_i - m_{i+1}\right| \cdot w_i}{\sigma_t} \qquad (8.1.),$$

where N is the total number of measurements for the same object and m_i is the magnitude of the object in the image i. The weight w_i defined as

$$w_i = 1/e^{\frac{t_{i+1}-t_i}{\overline{\Delta t}}} \qquad (8.2.)$$

was introduced to limit the influence of different time intervals between the two measurements i and i+1 (especially for night-to-night magnitude offsets described before) on the VI index. The mean time interval between two neighboring measurements is expressed by $\overline{\Delta t}$. The theoretically expected RMS σ_t is calculated as described in equation 2.24. Following this definition a light curve of a non-variable star should have a variability index VI of about 1 under the assumption that no other noise sources as for σ_t exist. Variable stars should show a variability index larger than 1. Due to statistical uncertainties and errors for the determination of the noise sources non-variable stars show a variability index scattered around the unity value (see examples in Figures 8.1. –8.4.).
A limit has to be defined to discriminate between variable and non-variable objects in a way that minor changes of the limit do not change the fraction of variable stars dramatically. A value of VI = 1.5 was found to fulfill these criteria from statistical point of view (see Figure 8.1.). Nevertheless, some short-periodic stars were identified in data of individual nights showing a lower variability index down to VI = 1.2. Thus two approaches were defined for the identification of variable stars: In light curves combined of data from all observations a variability index V > 1.5 was set as a limit for variability. In the second approach light curves of selected individual nights were analyzed for stars showing a VI > 1.2.

8.2. The fraction of variable stars for the target fields observed from the TLS

8.2.1. Target field F8

12% of all stars (158/1316) up to magnitude 14 show a higher variability index VI than 1.5 and can therefore be classified as variable stars. The V index was calculated to be larger than 1.5 for about 28% of the stars in the magnitude range from 11 to 12 (see Table 8.1).

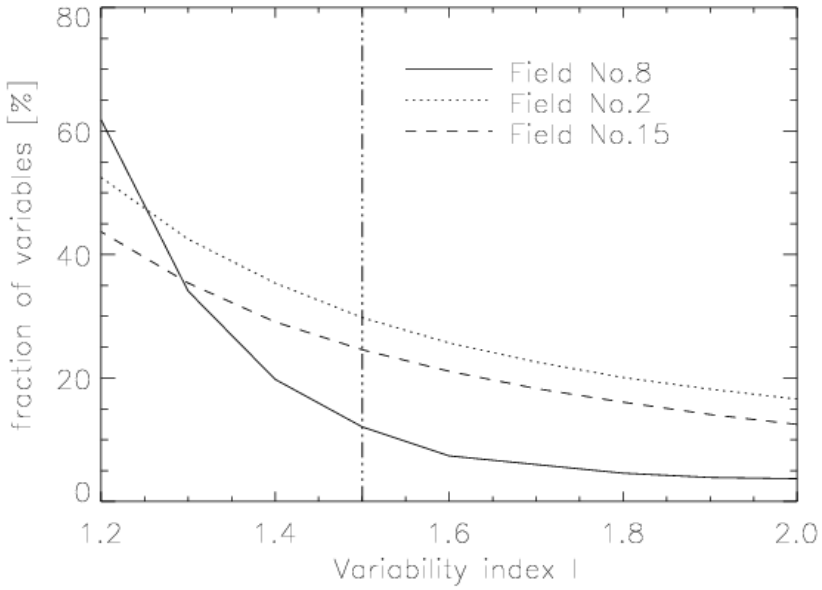

Figure 8.1.: Fraction of detected variables over the variability index for the data of the three target fields observed from TLS. A variability index of 1.5 (dashed-triple-dotted line) was chosen to discriminate between variable and non-variable stars.

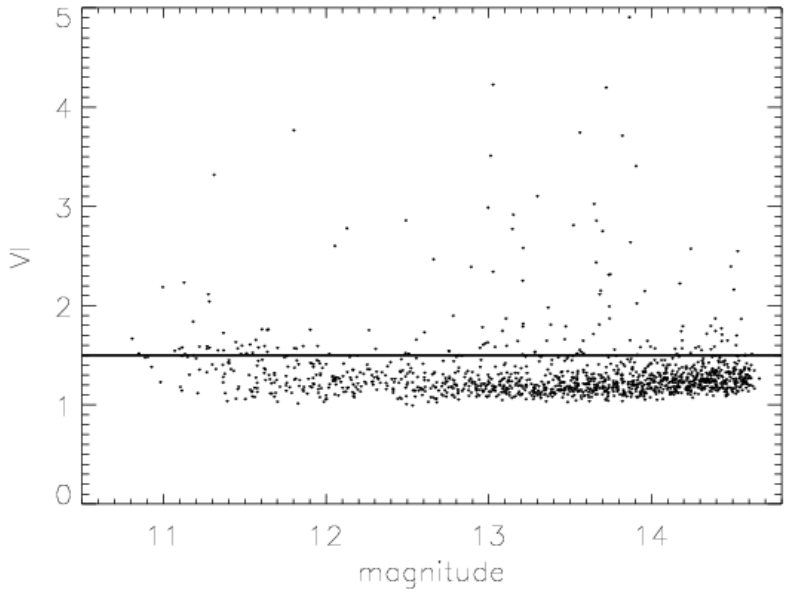

Figure 8.2.: The variability index VI plotted vs. the mean magnitude of the analyzed objects in target field No. 8. The variability limit of $V = 1.5$ is shown as a thick line.

About 10% were found to be variable for fainter stars. Target field 8 is dominated by dwarf stars, thus 12% variables stars is in agreement with the expected number of about 10%. Only for the brighter stars a higher number of variable stars is detected. The number of stars in this magnitude range is relatively small and statistically not relevant. Additionally a higher number of giant stars that are often variable is expected to be observed in this magnitude range.

8.2.2. Target field F2

The fraction of stars with $V > 1.5$ is found to be about 30% (3771/12627) for all stars up to magnitude 14. It increases with the brightness of the objects (see Table 8.1.). Such a high number of candidate variables is mainly caused by detection problems for crowded objects. Fainter neighboring stars are often not detected anymore when seeing/transparency conditions are unstable resulting in noisy light curves of different modes where overlapping signals are temporarily not corrected.

Background noise is more dominant for fainter objects reducing the fraction of candidate variables. A general trend is seen for brighter stars in Figure 8.3.: The average variability index increases with the magnitude of the stars. Additional noise sources like spatial extinction during non-photometric conditions and pixel-to-pixel variations increase the total noise. Additionally more variable giant stars are dominating in the brighter magnitude range and increase the fraction of potentially variable objects.

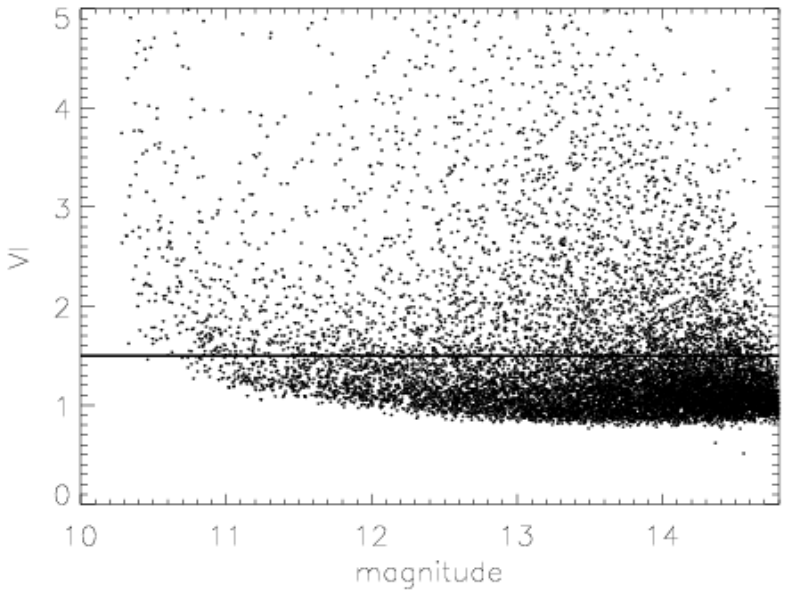

Figure 8.3..: The variability index VI plotted vs. the mean magnitude of the analyzed objects in target field F2. The variability limit of $V = 1.5$ is plotted as a thick line. 30 % of all stars have a variability index larger than 1.5. The high number results mainly from problems for the detection and the photometry for crowded objects. The high fraction of giants, that typically show long periodic variability, further increases the fraction of stars with $V > 1.5$

8.2.3. Target field F15

The fraction of all stars with a variability index larger 1.5 is of about 25% (2274/9261) up to magnitude 14. It is very high for bright stars and decreases rapidly with increasing magnitude. Although this target field is the most crowded one of the observed target fields, less stars than for target field F2 are examined. The selection criteria that the stars have to be detected in 90% of all frames yields a reduced number of stars. Due to the detection problems especially for crowded fainter stars the objects ('confusion', see section 7.4. & 6.1.2.) were not detected often enough to be chosen as variables. Under consideration of this aspect the fraction of stars with $V > 1.5$ is larger than for target field F2 as demonstrated for the bright, well-detectable stars.

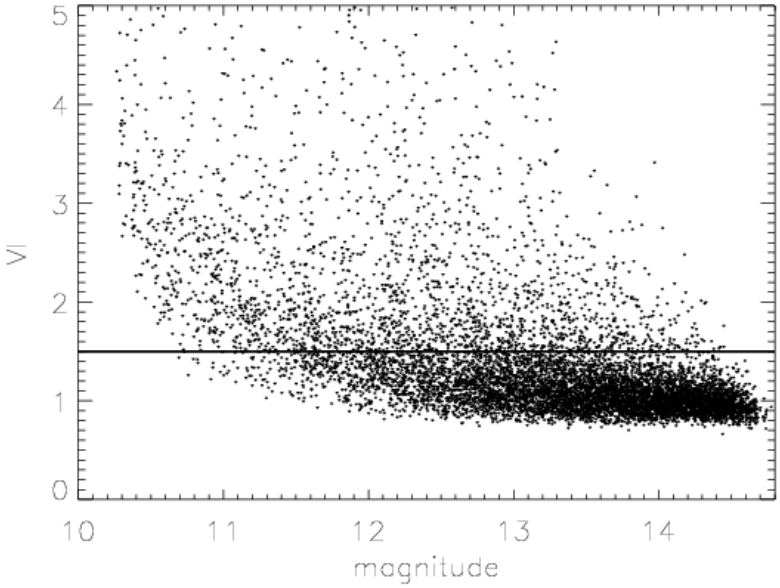

Figure 8.4.: The variability index VI plotted vs. the mean magnitude of the observed objects in target field F15. The variability limit of $V = 1.5$ is plotted with the thick line. 25 % of all stars have a variability index larger than 1.5.

Table 8.1.: Fraction of stars with a variability index V > 1.5 for different magnitude ranges of the observed target fields. The higher fraction of potential variable stars for target field F2 and F15 is caused be detection problems (confusion) due to crowding. The fraction of real variables is estimated to be around 10-15% in agreement with the 12% variable stars detected for the less crowded target field F8.

Magnitude	*11 - 12*	*12 -13*	*13 -14*	*>14*
Fraction of variable stars of field 8 ($V > 1.5$)	28%	10%	11%	7%
Fraction of variable stars of field 2 ($V > 1.5$)	46%	36%	31%	19%
Fraction of variable stars of field 15 ($V > 1.5$)	68%	33%	13%	3%

8.3. The search for periodic variables

The search for periodicity in time series data is one of the main aspects in astrophysics because regular periodicity can often be easily correlated to physical mechanisms, such as pulsation and rotation of the object.

Astronomical time series collected by ground-based monitoring surveys are always unevenly sampled and incomplete due to meteorological and photometrical constraints. Standard Fourier analysis is impossible due to the data gaps. Only modified Fourier methods have been developed to deal with this kind of data (see review in Cuypers 1987). But these algorithms are computationally intensive for a high number of light curves that have to be analyzed for a wide range of possible periods.

A less time-consuming method was proposed by Cincotta et al. (1995) using the information entropy of the light curve. The information entropy gives the degree of order or

disorder for the observed data as a function of phase for every trial period and shows minimal values for periodicities. It is calculated by:

$$S = -\sum_{i=1}^{m} \mu_i \ln \mu_i \; ; \qquad \forall \mu_i \neq 0 \qquad (8.3.).$$

μ_i estimates the probability of finding a data point within each of the m elements of the partition in the unit square where the light curve is defined. μ_i is determined by the ratio of the numbers of points falling inside the element i and the total number of points. This method is well-suited to handle large amounts of light curve data within an acceptable time frame. It is mathematically well-defined within the frame of information theory formalism and can deal with noisy, incomplete and unevenly-sampled data.

Note too that it has to be considered that nightly sampling could introduce alias periods of about one day.

An example for a calculation of the information entropy of a variable is given in Figure 8.5.

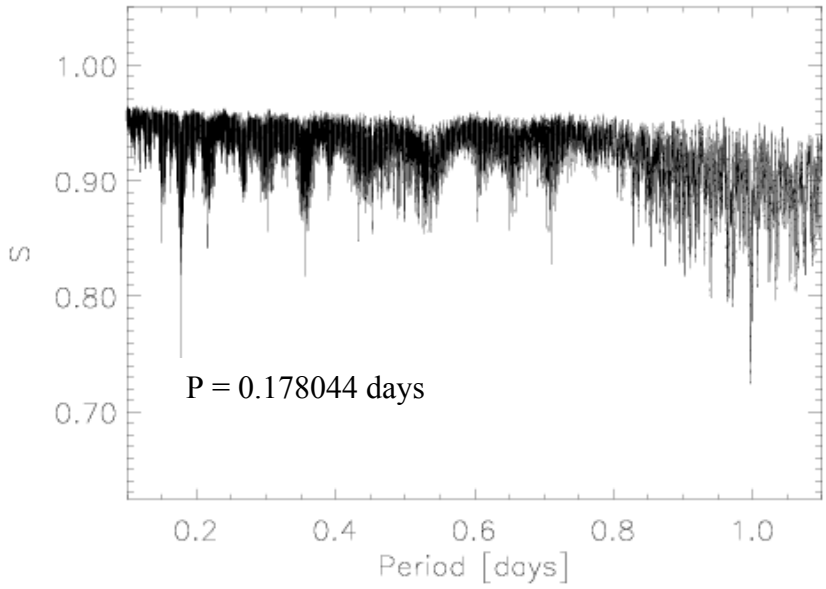

Figure 8.5.: The information entropy S vs. the trial periods for the detached eclipsing binary BEST F2 Var 11 calculated as proposed by Cincotta et al. (1995). A local minimal entropy value was found for P = 0.178044 days corresponding to the orbital period of the binary. The nightly mode of observations has introduced the signal for about one day.

8.4. Detected periodic variables

All light curves of objects showing a variability index larger than 1.2 were examined for short-type periodicity (< 1 day) using the method described above. Minima of the information entropy S found in this way were checked if they are based on real periodic behavior of the light curves. Light curves with V > 1.5 were searched for long-term periodicity (>1.5 days).

All light curves showing periodic behavior are listed in the following tables 8.2, 8.3 and 8.4. In these tables the coordinates of the variable objects showing a defined type of variability, their variability Index VI and the preliminary classification. The preliminary classification is based on the shape of the light curves using the following definitions (Krautter et al. 1994):

EA	eclipsing binary Algol type (undetectable deformation of the light curve during the non-eclipse phase);
EB	eclipsing binary β Lyrae type (eclipsing binary system consisting of 2 stars of different size orbiting each other in about 1 day, both stars are deformed by the gravity forces of the other component, thus the light curves are deformed during the non-eclipse phase);
EW	eclipsing binary W Ursae Majoris type (eclipsing binary system consisting of 2 stars of nearly the same size and luminosity orbiting each other in less than 1 day, both stars are strongly deformed by the gravity forces of the other, a permanent exchange of matter results, thus the light curves is deformed during the non-eclipse phase and both primary and secondary eclipses have the same depth and shape);
RR	short-periodic Cepheids with periods between 0.2 to 1.2 days, the magnitude varies up to a maximum of 1 to 2 mag;
RRc	RR Lyrae stars with symmetric sinusoidal light curves, the light curve can often not be differentiated from light curves of eclipsing binaries of the EW type;
RRab	RR Lyrae stars with asymmetric light curves
SX Phe	SX Phoenix variables have periods less than 2 days, the amplitude of the light curves varies between 0.3 to 0.8 mag;
δ Sct	δ Scuti type stars, the periods of the pulsation is less than 0.2 days, the amplitude of the light variation does not exceed 0.1 mag;
L	irregular variables.

8.4.1. Periodic variables for target field F8

Table 8.2: Stars contained in target field F8 showing periodic signals.
Additionally the coordinates of the stars, the variability index VI and the preliminary variability type is given together with some remarks.

BEST ID	*RA [hours]*	*DEC [deg]*	*VI*	*type*	*remarks*
F8 Var 1	10 29 37.6	+49 55 22	1.5932978	EB	
F8 Var 2	10 29 40.8	+50 55 50	1.8703993	SX Phe/ δ Sct	More modes
F8 Var 3	10 31 31.6	+50 15 01	1.6479941	RRab	
F8 Var 4	10 38 09.1	+50 36 31	1.5882194	L	
F8 Var 5	10 39 00.4	+50 41 06	2.2339598	RRc	
C 4	10 36 10.1	+48 55 41	1.5042250	K giant	Multiple modes

Note that light curves of the stars F8 Var 2 and F8 Var 3 were already published in Rauer et al. (2004c).

8.4.2. Periodic variables for target field F2

Table 8.3.: Stars contained in target field F2 showing periodic signals.

BEST ID	*RA [hours]*	*DEC [deg]*	*VI*	*type*	*remarks*
F2 Var 1	02 32 22.0	+52 16 30	7.5693501	EW	Blended ?
F2 Var 2	02 47 17.2	+50 45 07	1.9401805	δ Sct	More modes ?
F2 Var 3	02 45 45.1	+52 59 21	8.7454370	EW	
F2 Var 6	02 33 03.5	+52 13 30	1.7662871	RRc	Multiple modes
F2 Var 9	02 33 48.1	+53 32 08	2.1500652	EA	No secondary eclipse
F2 Var 11	02 41 00.9	+51 10 41	2.9760682	EW	
F2 Var 14	02 34 22.4	+52 22 08	2.7734593	RRab	Short period
F2 Var 24	02 35 37.1	+52 24 37	1.6933219	RRc	
F2 Var 25	02 41 52.7	+50 33 08	1.5011748	δ Sct	
F2 Var 27	02 47 34.5	+51 08 41	1.4187887	RRc	
F2 Var 28	02 47 17.1	+51 21 44	1.2297308	RRc	
F2 Var 29	02 46 00.1	+51 04 39	1.5562972	EB	
F2 Var 30	02 30 00.2	+51 53 38	1.4428716	EA	Eventually double period
F2 Var 31	02 47 44.5	+50 44 05	1.4059216	SX Phe	More modes ?
F2 Var 32	02 44 49.5	+51 25 44	1.4270477	RRc	
F2 Var 35	02 40 20.4	+51 54 39	1.3561590	RRc	
F2 Var 36	02 31 56.0	+50 50 14	1.2372062	SX Phe/ δ Sct	
F2 Var 38	02 40 02.6	+51 20 45	1.3389014	RRc	More modes ?
F2 Var 39	02 45 07.5	+52 58 56	1.2561440	SX Phe	More modes
F2 Var 40	02 44 07.6	+52 16 55	1.6578122	EW	
F2 Var 41	02 43 32.4	+53 29 24	2.7807480	SX Phe	
F2 Var 42	02 40 19.1	+53 00 25	1.5525370	SX Phe ?	More modes
F2 Var 43	02 42 42.8	+51 58 20	1.5131166	SX Phe	More modes
F2 Var 47	02 34 04.4	+53 28 48	1.5077743	EA	
F2 Var 48	02 40 11.2	+52 12 01	1.2327383	EA	
F2 Var 49	02 34 35.3	+50 32 23	1.3444194	EW	
F2 Var 50	02 32 16.1	+51 53 04	1.2198812	EA	Period uncertain
F2 Var 51	02 41 37.7	+52 29 38	1.5478201	EA	Period decreasing with time?
F2 Var 53	02 45 20.0	+52 08 48	2.3517777	EA	

8.4.3. Periodic variables for target field F15

Table 8.4. All detected stars of target field F15 showing periodic variability are listed.

BEST ID	*RA [hours]*	*DEC [deg]*	*VI*	*type*	*remarks*
F15 Var 3	19 52 35.6	+47 16 41	4.8077405	EW	
F15 Var 5	19 56 09.4	+46 39 42	2.0434163	EA	No secondary eclipse
F15 Var 6	19 56 04.2	+47 13 18	2.5026991	EW	
F15 Var 9	19 53 28.9	+47 48 51	1.8564404	EA	
F15 Var 13	19 59 35.1	+47 25 22	3.3535861	RRc	
F15 Var 14	20 01 18.3	+48 51 28	2.0122699	EW	
F15 Var 15	20 05 26.3	+47 33 23	7.8229063	SX Phe/ δ Sct	Blended?
F15 Var 20	20 03 35.0	+47 02 20	1.2076668	RRc	More modes?
F15 Var 24	20 05 47.4	+46 56 54	1.2051812	EB	
F15 Var 25	20 03 31.8	+46 47 48	1.21712244	EW	
F15 Var 29	20 07 19.5	+49 02 44	1.2840712	RRc	
F15 Var 30	20 06 10.2	+48 52 17	1.4238514	EW	
F15 Var 32	20 05 01.5	+47 35 17	1.2432635	RRc	
F15 Var 41	19 54 40.7	+48 44 38	1.5528648	EB	
F15 Var 44	19 56 04.1	+49 25 14	1.3155568	EB	
F15 Var 45	19 59 21.7	+48 58 10	1.2042211	EB	
F15 Var 46	19 58 15.6	+48 32 14	3.3488986	EW	
F15 Var 49	19 55 56.7	+49 19 06	1.8443079	EW	
F15 Var 56	19 53 58.6	+48 46 55	1.2068456	RRc	

For a few of the detected variables no constant periodicity was determable. The light curves of these stars are plotted for some selected nights in the second parts of appendix B additionally to the light curves of the periodic variables.

The following catalogues were checked it the detected stars are already known variables:

a) General Catalogue of Variable Stars, 4th ed., vol.V (Artyukhina et al. 1995)
b) New Catalogue of Suspected Variable Stars (Kukarkin et al. 1982)
c) New Catalogue of Suspected Variable Stars. Supplement (Kazarovets & Durlevich 1998)
d) The Washington Double Star Catalog (Mason et al. 2001).

Altogether 83 stars were identified as variable stars, all discoveries are new discoveries. For 53 of these variables periodic variability could be confirmed. Among the variables 38 objects were classified as eclipsing binaries.

9. Summary and main results

I. The Berlin Exoplanet Search Telescope (BEST) system consisting of a telescope, a CCD camera, a mount with a computer-controllable drive system, a autoguiding system and a control PC was set up at the Thüringer Landessternwarte (TLS) Tautenburg. The components were tested and successfully implemented building up a system capable of detecting transits of Hot Jupiter planets.

II. An automated data reduction and analysis pipeline was developed with the capabilities of calibrating the image data, extracting the light curves, applying an extinction correction and analyzing the resulting light curves for transit-like events in near real time. The data pipeline was optimized to deliver light curves with high photometric precision on a nightly basis.

III. A follow-up strategy was developed allowing the identification of real planetary transit events and excluding possible false alarm cases. The strategy includes the analyses of data in online data bases (Aladin, ViZier) and catalogues (2MASS, USNO B1.0, UCAC) as well as spectroscopic and photometric follow-up observations (2m TLS, 2.7m HJST, 9.2m HET, 0.9m Westerlund telescope). Based on a precise knowledge of the host star parameters a transit model can be fitted to the observed signal to identify if the transit-like signal could be caused by a planet-sized object. Radial velocity measurement are used to determine the mass of the secondary object to discriminate between giant planets, brown dwarfs and M dwarfs (all Jupiter-sized companions).

IV. An observational campaign lasting from 2001 to 2003 was conducted at the TLS monitoring three target fields during 90 nights with a total observing time of 438 hours. Target field F15 was observed for 163 hours, target field F2 for 105 hours and field F8 for 170 hours. The target fields F15 and F2 are located in the Galactic plane showing a high stellar density (F15: 37,000 detectable stars, F2: 32,000; both at a 1.5σ level). Target field F8 with 6,000 detectable stars is located above the Galactic plane thus it contains less stars. The target fields were observed with three exposure times (15 sec, 40 sec, 240 sec) to cover a large magnitude range ($8 < R < 14$) with a photometric precision better than 1% thereby sufficient for the detection of transits of Jupiter-sized planets orbiting Solar-like stars.
Additional observations were performed to observe two transits of the planet orbiting the star HD 209458. Both transits were successfully detected demonstrating the capabilities and the feasibility of the BEST system for monitoring of planetary transit events.

V. The collected data were calibrated and the resulting light curves were analyzed for transit-like events on a nightly basis. A box search routine was applied to the data searching for single transit events allowing to detect these events in near real time after the observations. A photometric precision better than 1% was obtained for up to 4,000 light curves per night monitoring target fields in the Galactic plane sufficient to detect transiting planets of the size of HD 209458 b orbiting Solar-like stars. For light curves with the best precision of 0.2% planets with radii larger than 0.5 R_{jup} could have been detected. In a second step of the data analysis the light curves of the

individual nights were combined to composite light curves covering all observations. These combined light curves were phase-folded with trial periods to be searched for low-amplitude transit signals with the box search routine. Transits of planets with Jupiter size orbiting Solar-sized stars could have been detected for 1% precision light curves if the detection consists of three single transit signals in the folded data.

VI. Five transit candidates were identified in the BEST data acquired at TLS. Four of the candidates were identified as false alarms. The majority of the false alarms (three) are due to eclipsing binaries with a small secondary component including one blending case. One of these secondaries (BEST C 1) was characterized as being among the smallest M dwarfs with a determined radius. The observations and analysis of this system will continue to allow a more precise determination of the physical parameters of the M dwarf. These parameters are of great importance for the improvement of models of low mass stars. Candidate BEST C5 is still under investigation since a potential planet around this M star causing the signal could have a radius of 0.3 Rjup. Further photometric monitoring is ongoing to divulge the true nature behind the detected transit-like signal.

VII. In an analysis it was investigated how to optimize BEST-like transit survey considering aspects like optimal target field selection, pixelscale and crowding, noise terms of the photometry and orbital phase coverage. The analysis showed that the BEST system allows higher detection rates for transits of exoplanets compared to other ongoing transit search systems. Nevertheless, a new optimized transit search system is proposed. Based on present technological limits an optimal transit search system was defined with a maximal detection probability for transits of planets orbiting stars with $R < 15$. This magnitude limit was proposed to allow precise spectroscopic follow-up measurements. The proposed system consists of a F/1 Schmidt telescope with an aperture of 45cm combined with a CCD with 4096 x 4096 pixels and a pixelsize of 9 μm. As a new telescope design the manufacture of such a kind of telescopes would be, however, cost-intensive. This system could monitor a FOV of 4.7°x 4.7° with a pixelscale of 4.1 arcsec and Nyquist-sampled stellar PSFs with a FWHM of 2 pixels. The expected yield is a detection rate of up to four transiting exoplanets per observed target field in the galactic plane. The detection probability of this system was compared with other typical wide-angle transit surveys, which all show lower detection probabilities for transits of exoplanets. For these systems an optimized target field selection is proposed to get higher detection probabilities. Systems with an aperture less than 20cm should preferably observe target fields moderately above the Galactic plane to reduce degradation of the photometry by crowding. Larger systems can observe both target fields centered in the Galactic plane and above. Generally the pixelscale of the instruments has to be adopted to the stellar density in the observed fields. For BEST an upgrade of the system with a 4k CCD and an automatic focusing unit is recommended to reach an optimal pixelscale without defocusing. This allows to double the detections rates for transiting planets and to improve the quality of the data due to more controlled focusing. Finally, the orbital phase coverage has to be improved by observing from a site with better photometrical conditions. At the new observing site of BEST, Observatoire de Haute-Provence (OHP), the duty cycle was doubled during the first season. Other strategies to improve the orbital phase coverage are to observe the same target field for a second season or the introduction of telescope networks enabling even better duty cycles to reach coverage sufficient for three detections of a transit.

VIII. The data set of BEST observations from TLS was analyzed for variable stars. In total 83 stars were identified as variable stars showing typical light curves, all of them are new discoveries. For 53 of these variables the periodicity was determined. Among the variables 38 objects were classified as eclipsing binaries. The total number of light curves that show some kind of variability with the BEST duty cycle is estimated to be 10-20%.

Appendix A:
Overview of ground-based transit search systems and strategies

Following the successful detection of the first transiting extrasolar planet HD 209458b in 1999 several other ground-based transit searches were developed worldwide. Two main directions of transit searches have been developed. Several meter-class telescopes were used for temporary deep transit searches in small field of views and several smaller wide-angle search systems were established dedicated to long-term transit search only. In this chapter an overview of both kinds of ongoing and future ground-based transit search projects and their observing strategies starting with wide-field systems will be given.

A.1. Wide-angle search systems

Transit search systems with a field of view (FOV) larger than 1deg x 1deg are classified as wide-angle search systems in the following. The systems are fully dedicated for transit search and variable star detection (with one exception: APT).

A.1.1. STARE (STellar Astrophysics & Research on Exoplanets)

This system is well known for the first detection of the transit of HD209458b (see Figure A.1.) in 1999 (Charbonneau et al. 1999). It is one of the first instruments that are dedicated to search for transit of extrasolar planet. It was initiated by the High Altitude Observatory (HAO) at Boulder, Colorado, USA and supported by the NASA Origins program. Principal Investigator is T. M. Brown.

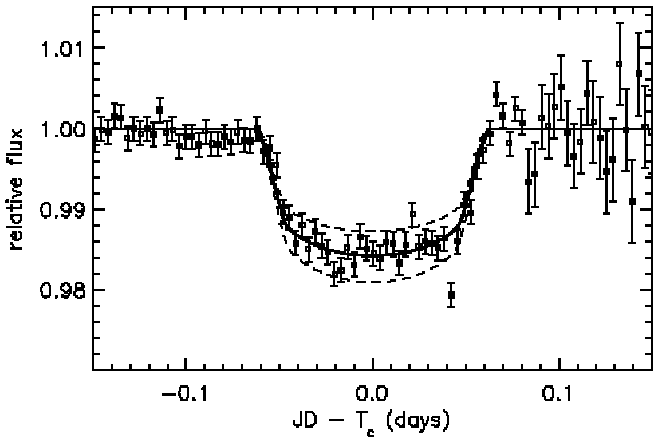

Figure A.1.: Transit of the exoplanet HD209458b observed with the STARE telescope (taken from Charbonneau et al. 1999).

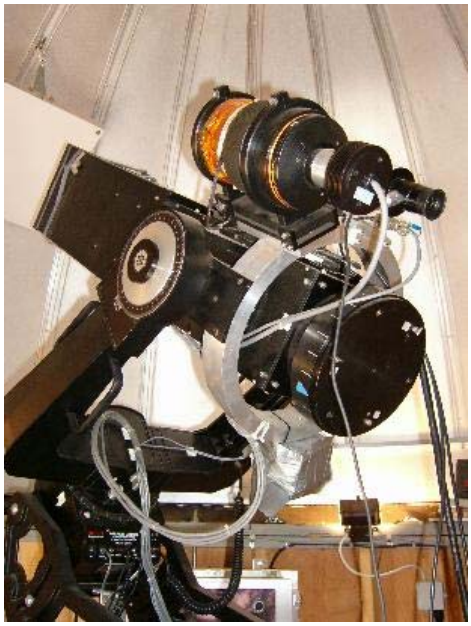

Figure A.2.: The STARE telescope.

A Schmidt camera of a focal length of 286 mm, 10cm diameter and focal ratio f/2.9 is used as optical instrument, giving of flat field of view (FOV) of 5.7 x 5.7 degree. This FOV is imaged onto a 2034 x 2034 pixel CCD (Pixelvision) with a pixel size of 15 μm corresponding to an spatial resolution of 10 arcseconds per pixel. The frames for the time series are taken through a Johnson R filter.

Prior to 1999 July, the main instrument was a lensing system (Aero-Ektar lens) giving the same field of view, but a throughput lower by a factor 2 and point spread function with lower quality.

The telescope rests on a Meade LX200 equatorial fork mount. A small tracking telescope coupled with a SBIG (**S**anta **B**arbara **I**nstrument **G**roup) tracking CCD and a finderscope are mounted additionally.

The telescope is operational since 1999. During the first few years it was operated from Bolder, Colorado. Since July 2001 the STARE telescope is located at the Teide observatory on the island of Tenerife in the Canaries. Several fields in the star constellations of Auriga, Perseus, Boötes and Cygnus have been observed for 1 or 2 seasons. Time series of 10000 stars in a typical field centered in the Galactic Plane with a sampling rate of 2 minutes are delivered. The range of the V magnitude of these stars is 9-14 mag, 1% photometric precision is obtained for stars V < 12 mag..

In 2004 the STARE telescope discovered a transiting planet called TrES-1 orbiting a 11.8 mag star in 3.03 days. For a first time an exoplanet was detected with an wide-angle search system and confirmed by the RV technique (Alonso et al. 2004).

For more details see (Brown & Charbonneau 2000) or the project website at:
http://www.hao.ucar.edu/public/research/stare/stare.html .

A.1.2. The Vulcan Photometer

Under the leadership of PI William Borucki a ground-based search for transiting extrasolar giant planets called Vulcan was developed. This project is sponsored by the NASA Ames Research Center.

Three versions of the system were built and used until now, the newest is the 'Camera-III' and is operational since November 1999 at Mt. Hamilton in California, USA. It consists of a Canon EF300 f/2.8 lens with a focal length of 300 mm and a 560-series camera of Spectral Instruments with a Kodak KAF16800 CCD. This 4k x 4k CCD has a pixelsize of 9 μm corresponding to 6 arcsec pixelscale. The field of view of Vulcan photometer is 7 x 7 degrees.

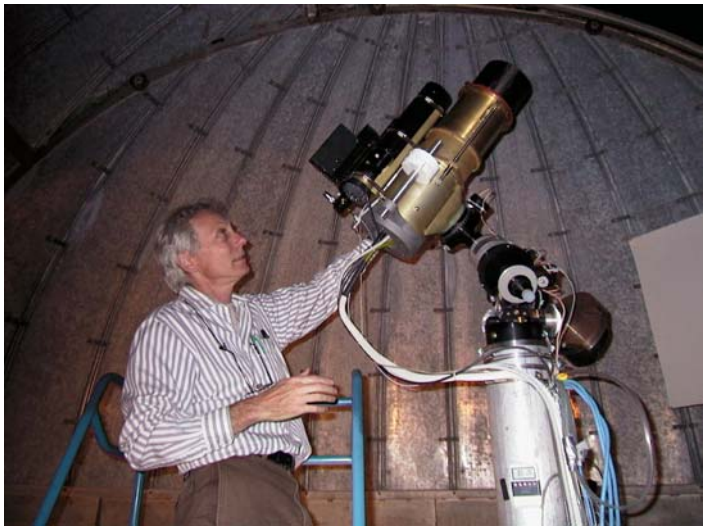

Figure A.3: The Vulcan Camera-III inside the dome at the Mt. Hamilton, California (taken from http://web99.arc.nasa.gov/~vulcan/).

An autoguider consisting of a Celestron Pixel 255 CCD and a refractor with an effective focal length of 600 mm and an aperture of 80 mm is used for tracking. This system is mounted on custom-made German equatorial mount. For observations a custom-designed filter is used. It covers the spectral range associated with both the V and the R bands of the UBVRI photometrical system.

Time series of up to 6000 stars (V magnitude 8.5-13) in a target field centered in the Galactic Plane with a sampling rate of 1 image/7.5 minutes are taken.
For more details see (Borucki et al. 2001) or the website of the Vulcan project:
http://web99.arc.nasa.gov/~vulcan/.

A.1.3. Vulcan South – Antarctic Planet Finder

Installing a transit search system in Antarctica has several advantages. During the 3 month polar night uninterrupted observations will be possible if weather conditions permit. And most of the stars are circumpolar, they do not rise or set. A disadvantage is the cold temperatures at the south polar region. Special equipment allowing observations at temperatures around –50 °C has to be developed. Nevertheless, the Vulcan South team under the leadership of PI Doug Caldwell initiated the challenging Vulcan South project: establishing a transit search system in Antarctica. Since 2000 after funding was acquired by the NASA Ames Research Center the necessary equipment was developed and tested. The instrument is a lensing system of 203 mm diameter and a focal ratio of f/1.5 combined with a 4k x 4k CCD camera. Per pixel an area of 6.1 x 6.1 arcseconds will be imaged, resulting in an FOV of 6.9 x 6.9 degree. The system was deployed in 2004, but suffered from serious technical problems with the CCD. Thus in the summer of 2005 first data was acquired despite continuing camera problems.
For more details see the Vulcan South website at:
http://www.polartransits.org/

A.1.4. WASP0 (Wide Angle Search for Planets) and SuperWASP

Figure A.4.: WASP0 is the small systems system mounted 'piggy-pack' on top of the larger one.

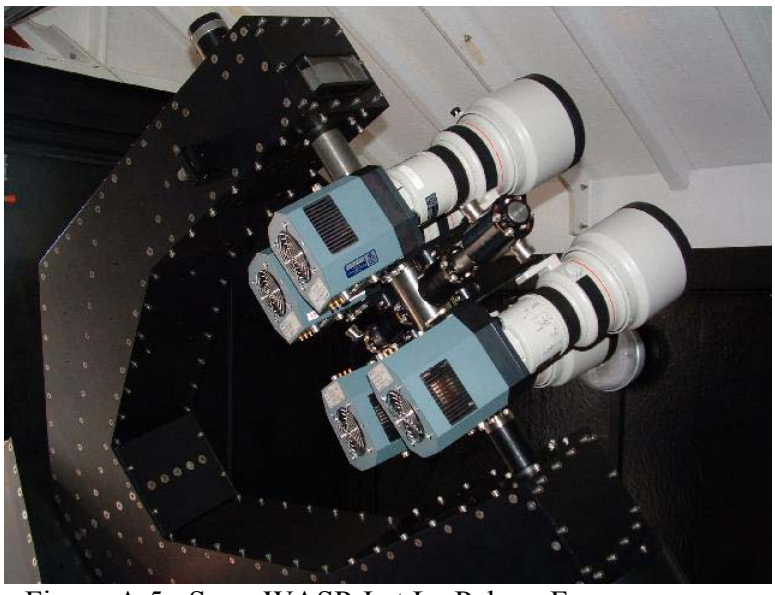

Figure A.5.: SuperWASP-I at La Palma. Four camera are supported by a fork mount.

The WASP project started 1999 as a collaboration of the Queen's University of Belfast and the University of St. Andrews.

A first prototype system was built and tested on the Canary Island of La Palma in 2000. It consisted of a 14-bit AP10 camera by Apogee Instrument Inc with a 2k x 2k CCD and an f/2.8 Nikon lens with 63 mm diameter. The resulting FOV had the dimension of 9 x 9 degrees yielding to a pixelscale of 16 arcseconds. This simple system was mounted on a commercial Celestron telescope on an equatorial mount.

A target field in the Draco constellation and HD209458 were observed. In 2002 WASP0 was relocalized to Kyroneri in Greece to carry out further observations. For more details about WASP0 see (Kane et al., 2003).

In mid 2000 Cambridge University, Leicester University and the Isaac Newton Group joint the collaboration of the universities of Belfast and St. Andrews to establish a robotic transit search system called SuperWASP. A robotic Optical Mechanics Inc. fork mount is the base for this system, consisting of 4 single cameras each with a field of view of 7.8 x 7.8 degrees. These cameras are equipped with 2k x 2k CCD produced by Andor, Belfast. The pixelsize is 13.5 µm, the pixelscale is 13.9 arcseconds. A Canon 200 mm f/1.8 lens with a diameter of 111 mm is used as optical instrument.

The SuperWASP system has reached the operational status in 2004 located on the Canary Island of La Palma. The system aims to monitor a large number of stars (~20,000) in the magnitude range of 7-13 with a precision < 1%.

The construction of a second unit started in the second half of 2003. This system was deployed in 2005 at the South African Astronomical Observatory in South Africa and will be operational soon.

More information about SuperWASP is available in (Street et al., 2003) and on the SuperWASP website:
http://www.superwasp.org/index.html .

A.1.5. SLEUTH (formerly known as PPS - Palomar Planet Search)

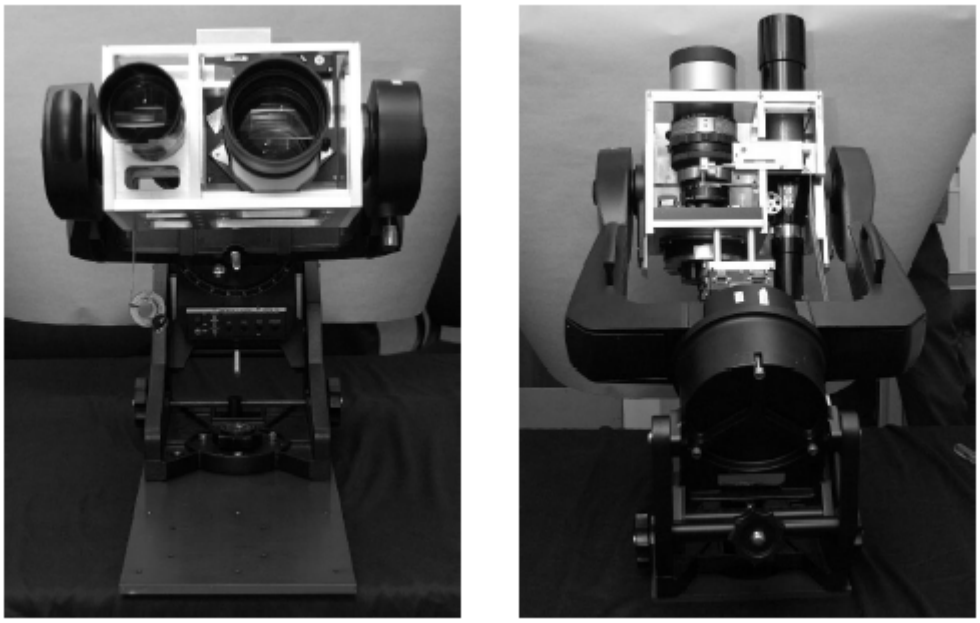

Figure A.6.: SLEUTH - the Palomar Planet Search system (from Charbonneau 2003)

David Charbonneau assembled together with J.T. Trauger's team of NASA/JPL the Palomar Planet Search system. A 2k x 2k CCD combined with a 280 mm f/2.8 commercial lens system monitoring a field of view of 5.7 x 5.7 degrees. Each pixel is 13.5 x 13.5 μm and images an area of 9.9 x 9.9 arcseconds. For tracking is a commercial tracking CCD in combination with a lens with a focal length of 440 mm and a diameter of 70 mm used.

SLEUTH is mounted in an equatorial fork mount and located at the Palomar Observatory, California.
For more details see Charbonneau (2003).

A.1.6. PSST (Planet Search Survey Telescope)

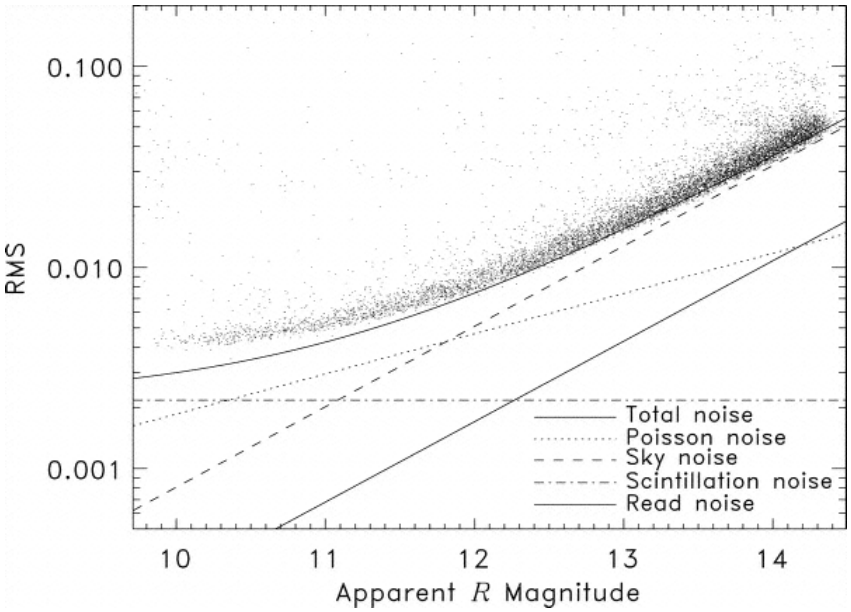

Figure A.7.: RMS versus R magnitude of the PSST system. The minimal photometric precision reached for the brightest stars is 0.4% (taken from (Dunham et al. 2004).

PSST is a system located in northern Arizona, PI is E.W. Dunham. It consists of a lensing system with an aperture of 107 mm diameter and a focal ratio of f/2.8. The field of view is ~5.7 x 5.7 degrees, the pixelscale of the used 2k x 2k CCD is 10.0 arcseconds The lens forms images with a FWHM of 1.6 pixels, the FOV is vignetted. An ST-4 autoguider is implemented for pointing corrections. The single exposure time is 90 sec for the taken R band time series. All information was taken from Dunham et al. (2004).

STARE, PPS and PSST form a network of transit search systems (Transatlantic Exoplanet Survey) to obtain a improved orbital phase coverage. The same fields are observed during observing campaign of 2 months duration.

A.1.7. HATnet (Hungarian Automated Telescope net)

Figure A.8.: HAT-1 at the Steward Observatory, Kitt Peak, Arizona

The HAT system was initiated by Bohdan Paczynski of the Princeton University in collaboration with the Konkoly Observatory, Hungaria. A custom-built horseshoe mount supports the CCD camera with a lensing system. The lensing system has an aperture of 110 mm diameter and focal ratio f/1.8, giving a field of view of 8deg x 8deg. The first HAT system (HAT-5) is operational at the Whipple Observatory at Mount Hopkins, Arizona, since February 2003, four additional systems using CCDs and lenses of the discontinued ROTSE-I (Robotic Optical Transient Search Experiment-I) project were operational later in 2003. HAT-6 and HAT-7 had first light in September 2003 located at the same observatory as HAT-5 monitoring different target fields. 2 additional systems are operational since November 2003 at Mauna Kea, Hawaii, establishing an observational network with the HAT systems in Arizona.

A similar system was deployed on the Wise Observatory in Israel in 2004 in collaboration of the Konkoly Observatory (Hungary) with the Wise Observatory of the Tel Aviv University: WHAT (**W**ise observatory **HAT**).

The prototype of the HAT systems HAT-1 was operational for more than one year at the Steward Observatory at Kitt Peak, Arizona. It consisted of an AP-10 CCD camera and a Nikon lens with a foal length of 180 mm and a focal ratio of f/2.8. The FOV had a size of 9 x 9 degrees, the pixelscale was 16 arcseconds/pixel. For more information see the website of the HAT project:
http://www.cfa.harvard.edu/~gbakos/HAT/ .

A.1.8. APT (Automated Patrol Telescope)

Figure A.9.: The Automated Patrol Telescope (APT) at the Siding Spring Observatory, Australia.

The Automated Patrol Telescope is operated by the University of New South Wales at the Siding Spring Observatory, Australia. It is a Schmidt like telescope, but the corrector plate is a system of 3 lenses to achieve a wide corrected field of view. The aperture is 500 mm and the focal ratio f/1, giving a flat field of 5deg x 5deg. Only a 2 x 3 degrees sized field is imaged with a CCD of Wright instruments, containing 770 x 1152 pixel. The pixel size is 22.5 µm, resulting in a pixelscale of 9.4 arcsec/pixel. This system is only temporary used for transit search. For more details see Hidas et al. (2003) and the website of the transit search program with the APT:
http://www.phys.unsw.edu.au/astro/research/planetsearch.html .

A.1.9. KELT (Kilodegree Extremely Little Telescope)

The goal of this system is to monitor bright stars with V = 6 -10 mag to search for planetary transits. A lensing system with an aperture of only 4.2 cm and f/1.9 focal ratio is combined with an 4k x 4k CCD Apogee AP-16 with 9 μm pixelsize, giving a FOV of 26 degree x 26 degree. The pixelscale is about 23 arcsec/pixel. The system was tested in Ohio, but it is planned to install the KELT system in New Mexico. All areas of the sky about 45° of the zenith will be covered with 30 sec exposures with 10 different pointings and a sample rate of 11 minutes. Find more information about this system in (Pepper et al. 2004).

A.1.10. PASS (Permanent All-Sky Survey)

The PASS project was initiated by Hans Deeg of the Institute for Astrophysics of the Canary Islands (IAC) with the goal to monitor all bright (V < 10.5) stars visible from one observing site. Up to 15 large CCDs combined with lensing systems will monitor the entire sky above 30deg altitude. The f=50mm 1/f = 1.4 lenses will be combined with 2k CCDs each obtained a FOV of 30deg x 30deg. The systems will be permanently mounted on a fixed platform, the star images will drift across the CCDs. 20sec exposures will be co-added to 900sec exposure to minimize the scintillation noise and increase the signal to noise (S/N) ratio.
A prototype was deployed in early 2004 at the Teide Observatory for testing For more details see Deeg et all (2004).

A.1.11. TEST (Tautenburg Exoplanet Search Telescope)

The TEST system combines a 30cm aperture 1/f = 3.2 Schmidt-Cassegrain telescope with an AP-16 4k CCD. This system will cover a FOV of 2.2deg x 2.2 deg with an pixelscale of 1.9 arcsec. The system is located at the Thüringer Landessternwarte, Tautenburg and is currently undergoing the commissioning phase.

A.1.12. Other wide-angle transit search systems

Some other wide-field transit search systems similar to the described ones exist useable for transit search. More information about these system can be found in the Table (A.1.) following this section and on the website of Keith Horne listing most of the known transit searches (http://star-www.st-and.ac.uk/~kdh1/transits/Table.html).

A.2. Meter-class telescope transit searches

Several larger telescopes are used for transit searches, all of them have to split their observational time budget with other scientific programs. According to the larger size of their optics and mosaic CCDs it is possible to monitor several thousand to ten thousands of fainter stars in smaller FOVs compared to the wide-angle systems. Star clusters and other fields with very high density of stars are observable. The high number of monitored stars will increase the possibility of the detection of a planetary eclipsing event. Additionally the fraction of small main sequence stars suitable for ground-based transit detection will be increased compared to the wide-angle systems due to deeper exposures.

But the faintness of the transit candidate stars will make it much more complicated to confirm the planetary character of the eclipsing events by mass determination with radial velocity follow-up observations. 8 -10 meter class telescopes will have to be used intensively. Blended scenarios (i.e. a giant is blending an eclipsing binary) will be ruled out extremely difficult. Spectroscopic follow-up observations to determine the chemical composition of the planetary atmospheres will not be possible. To concentrate on search systems close to the BEST system I will only describe one search program using larger telescopes in the following.

A.2.1. The Optical Gravitational Lensing Experiment III (OGLE-III)

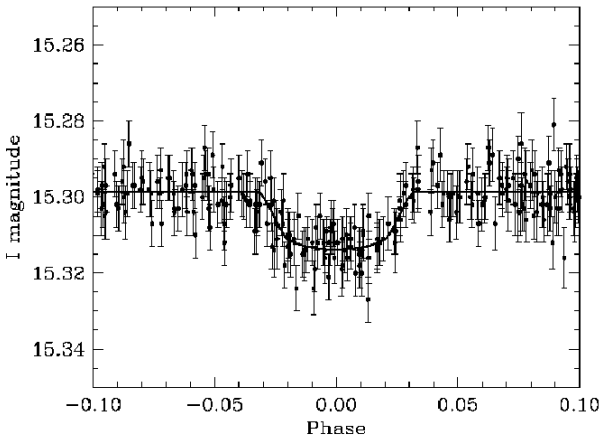

Figure A.10.: Photometric data of OGLE-TR 56 (taken from Torres et al. 2004).

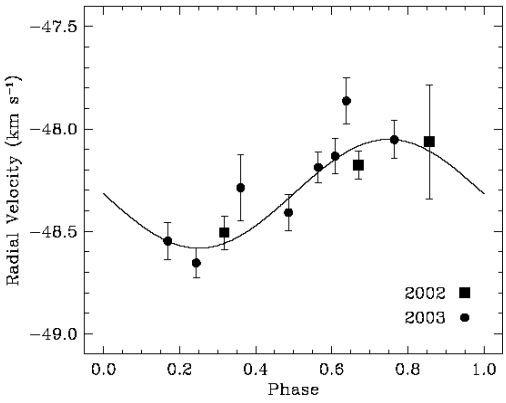

Figure A.11.: Radial velocity measurements made with the 10m Keck telescope confirming the planetary origin of the eclipsing event (from Torres et al. 2004).

Well known for the publishing of 177 partly controversial transit candidates is the OGLE-III project. Intensive observational campaigns were carried out since 2001 with the 1.3m Warsaw Telescope (f/9.2) at the Las Campanas Observatory, Chile. It is equipped with a mosaic CCD camera consisting of 8 SITe 2k x 4x chips giving a FOV of 35 arcsec square with 0.26 arcsec/pixel. The first campaign (Udalski et al. 2002a, Udalski et al. 2002b) started in June 2001, 3 target fields in the direction of the Galactic center were observed flipping from one field to another one. I band exposures with a sampling rate of approximately 11 minutes were taken during 32 nights. In 2002 a second campaign (Udalski et al. 2002c) was started observing 3 fields in the Carina constellation for 76 nights. A third observational campaign monitoring 6 target fields was carried out from February-July 2003 and in early 2004. 40 more stars were reported to show transit-like events (Udalski et al. 2004). Altogether 177 candidates for transits of exoplanets with transit depths up to 8 % were published.
Radial follow-up observations for the most promising candidates confirmed 5 transiting planets so far. The first exoplanet discovered by a transit searches was the planet orbiting the host star OGLE-TR 56. RV measurements confirmed that it is indeed a planetary transit (Konacki et al. 2003a, Torres et al. 2004) orbiting its host stars in 1.21 days. In the later 4 more candidates were characterized as planetary transit events by RV confirmation:

- OGLE-TR-113 (Bouchy et al. 2004a, Konacki et al. 2004)
- OGLE-TR-132 (Bouchy et al. 2004a)
- OGLE-TR-111 (Pont et al. 2004)
- OGLE-TR-10 (Konacki et al. 2005, Bouchy et al. 2004b).

Most of the candidates were identified as grazing eclipsing binaries or eclipsing binaries blended by another star (for example see Konacki et al. 2003b). Blended stars are very likely in these observed very star rich regions of the sky. Nearly 50 % of the candidates of the 2001 campaign could be identified as eclipsing binary systems with a lower mass ratio due to effects of gravitational darkening observable in the light curves (Drake 2003, Sirko & Paczynski 2003). The radial velocity follow-up observations with 10m class telescopes are still ongoing and further results will be reported in the future. More details about the OGLE project are to be found at the web page: http://bulge.princeton.edu/~ogle/

A.2.2. Other deep searches

Several other projects searching for transiting exoplanets using larger instruments are listed in the following Table (A.2.). The Table includes also the wide-field search projects mentioned above and gives some additional information about telescope parameters, status and observational site. Updated information can be found at the web page of Keith Horne: http://star-www.st-and.ac.uk/~kdh1/transits/Table.html .

Table A.1.: All known operating wide-angle transit search systems.

system	*Aper-ture [cm]*	*focal ratio 1/F*	*FOV [deg]*	*Observatio-nal site*	*status*	*remarks*
PASS prototype	3.6	1.8	30 x 30	Tenerife	Single lens prototype testing since 2004	15 systems planned for future, drift scans
KELT	4.2	1.9	26 x 26	New Mexico	testing	Lensing system 4k x 4k CCD
WASP-0	6.4	2.8	8.8 x 8.8	La Palma, Greece	Tests only	Lensing system AP-10 camera
ASAS-3	7.1	2.8	2 x (8.8 x 8.8)	Las Campanas, Chile	Operational since August 2000	Lensing system AP-10 cameras
SLEUTH (PPS)	10.0	2.8	5.66 x 5.66	Palomar Observatory	Operational since May 2003	Lensing system
STARE	10.0	2.9	6.03 x 6.03	Tenerife	Operational since 1999	TrES-1 detected
PSST	10.7	2.8	5.29 x 5.29	Arizona	operational	
XO	11.0	1.8	2 x (7.2x 7.2)	Maui, Hawaii	Operational since 2003	Drift scanning
HATnet	11.0	1.8	8.2 x 8.2	FLWO (3) Mauna Kea (1) Israel (1)	HAT-5 operational since February 2003, HAT-6 & HAT-7 operational since September 2003, 1 systems at Mauna Kea operational since November 2003, WHAT operational since 2004	Lensing system 5 systems
Super-WASP	11.1	1.8	4x (15.86 x 15.8)	La Palma, South Africa	Operational since April 2004, second system was deployed in South Africa	4 lensing systems

Vulcan	12.0	2.5	7.04 x 7.04	Mt. Hamilton, California	Operational since November 1999	4k x 4k CCD
RAPTOR-P	14.0	2.8	5 x (4.19 x 4.19)	Fenton Hill, New Mexico	Operational	AP-10 CCD
BEST	20.0	2.7	3.1 x 3.1	Observatoire de Haute Provence	Operational 2001-2003 TLS Since 2004 OHP	Schmidt-Cassegrain telescope
Vulcan-South	20.3	1.5	6.94 x 6.94	Antarctic plateau	First light 2004, 1 field in Carina region observed	4k x 4k CCD
TEST	30.0	3.2	2.2 x 2.2	TLS, Germany	Commisioning	Schmidt-Cassegrain telescope
APT	50.0	1.0	5 x 5 (2 x 3 used)	Siding Spring, Australia	Operational, only temporarily used for transit search	Schmidt telescope

Table A.2. All known operating meter-class transit search systems.

system	*Aper-ture [cm]*	*focal ratio*	*FOV [deg]*	*observational site*	*status*	*remarks*
TeMPEST	76.0	3.0	0.77 x 0.77	Mc Donald Observ., Texas	operational	
STELLA-II	80.0	8	0.50 x 0.50	Tenerife	Start of commissioning is planned for 2006	AIP led project
EXPLORE-OC	101.6	7.0	0.25 x 0.40	Las Campanas, Chile	operational	Open cluster survey
PISCES	120.0	7.7	0.38 x 0.38	Mt. Hopkins, Arizona	operational	
STELLA-I	120.0	8	0.37 x 0.37	Tenerife	Commissioning started in 2005	AIP led project
MONET	120.0	8	0.19 x 0.19	Sutherland, South Africa MDO, Texas	Commissioning	Led by University of Göttingen
ASP	130.0	13.5	0.17 x 0.17	Kitt Peak, Arizona	operational	
OGLE-III	130.0	9.2	0.58 x 0.58	Las Campanas, Chile	operational	177 transit candidates, 5 planetary transit confirmed
STEPPS	240.0		0.41 x 0.41	Kitt Peak, Arizona	operational	
INT	250.0	3.0	0.57 x 0.57	La Palma	operational	Used by UStAPS
EXPLORE-N	360.0	4.2	0.57 x 0.57	Mauna Kea, Hawaii	operational	
EXPLORE-S	400.0	2.9	0.61 x 0.61	Kitt Peak, Arizona; CTIO Chile	operational	

Appendix B:
Light curves of variable stars detected in the TLS data set

B.1. Folded light curves of periodic variables

In this section the light curves are plotted phase-folded with the detected periodicity. The re the following additional information is also given:

1.) The name given for the object in the BEST system: BEST FX Var Y, Where Y is a number given to the variable stars of the target field No. X;
2.) The Guide Star Catalogue (GSC) for the object if an identification was unambiguously possible;
3.) The preliminary variable type based on the shape of the light curve using the definitions given in section 8.4.
4.) The period of the light variation is given;
5.) The minimal and maximal measured magnitude is given, spurious measurements are marked with a question mark.

B.1.1. Target field 8

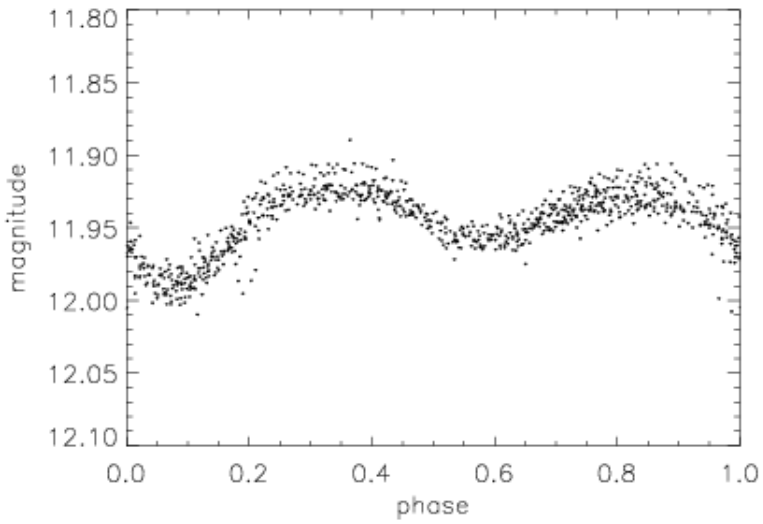

BEST F8 Var 1:
GSC 3438-424
Var. Type: EB
P: 0.565209 days
Max. 11.89 (?)
Min: 12.02

Appendix B: Light curves of variable stars detected in the TLS data set

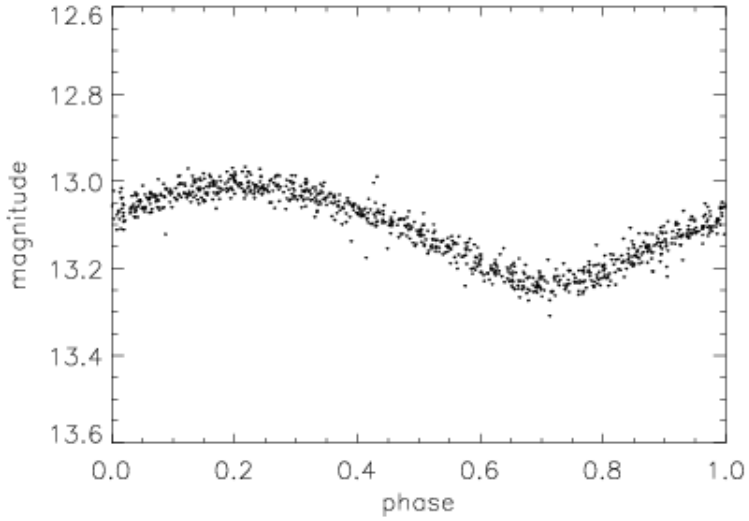

BEST F8 Var 2:
GSC 3441-858
Var. Type: SX Phe/ δ Sct
P: 0.171240 days
Max. 12.97
Min: 13.31 (?)

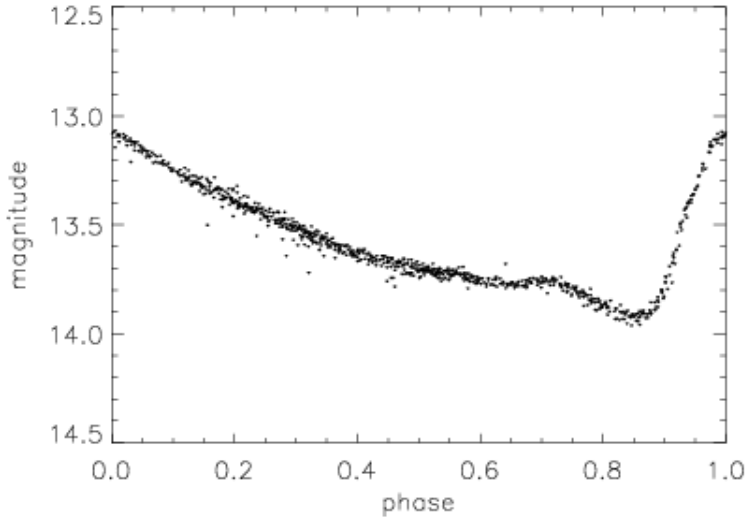

BEST F8 Var 3:
GSC 3448-901
Var. Type: RRab
P: 0.64634 days
Max. 13.07
Min: 13.96

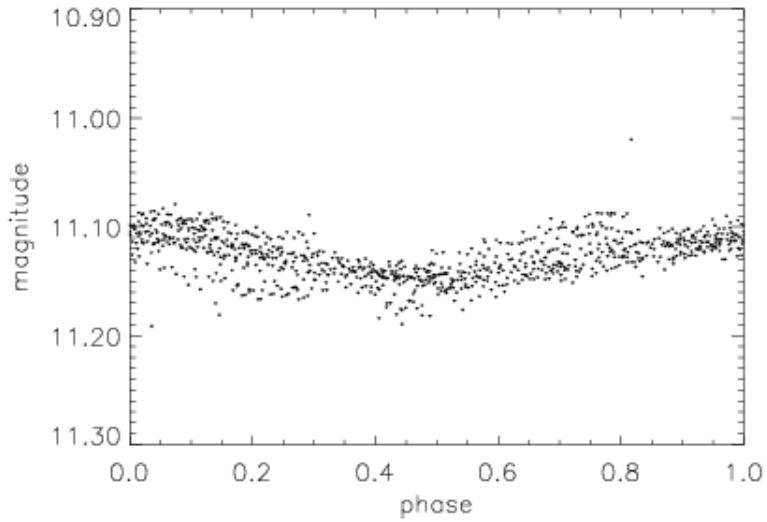

BEST F8 Var 5:
GSC 3448-582
Var. Type: RRc
P: 0.627292 days
Max. 11.02
Min: 11.19

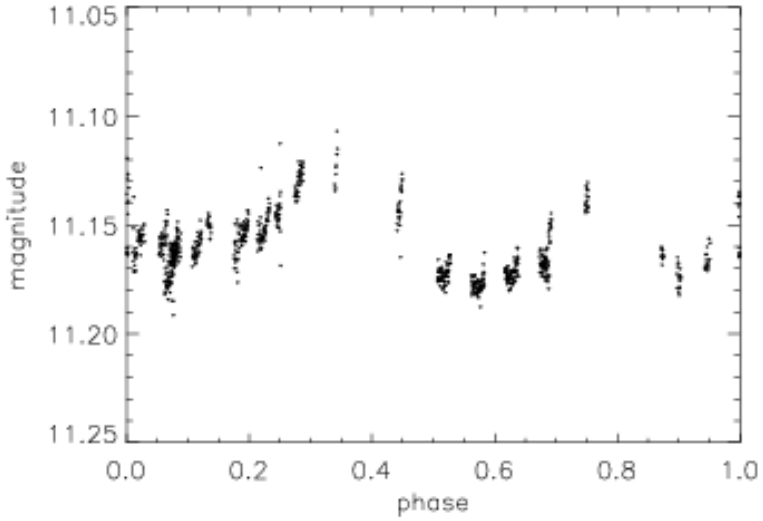

BEST F8 C 4:
GSC 3445-546
Var. Type: Giant
P: 18.0377 days
Max. 11.11
Min: 11.19

B.1.2. Target field 2

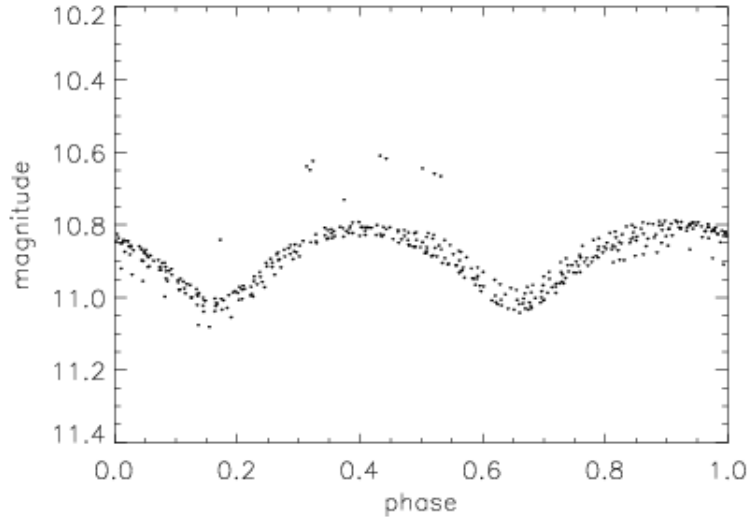

BEST F2 Var 1:
GSC 3307-1574
Var. Type: EW
P: 0.421662 days
Max. 10.61 (?)
Min: 11.08 (?)

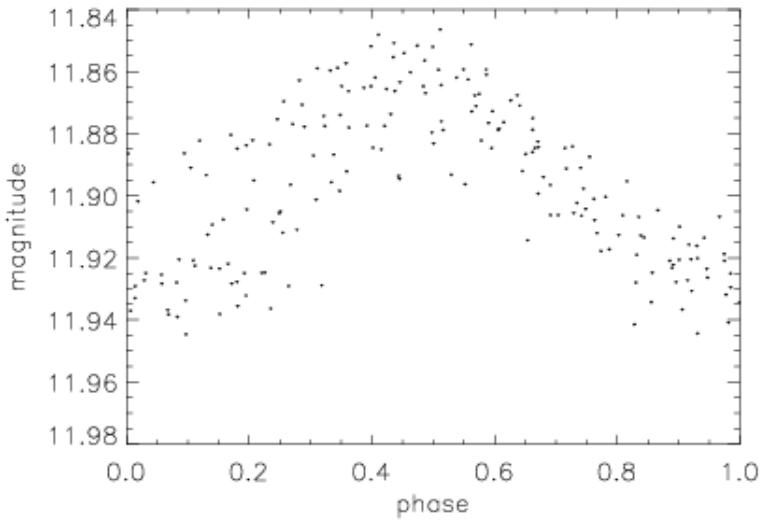

BEST F2 Var 2:
GSC 3308-462
Var. Type: δ Sct
P: 0.14908 days
Max. 11.85
Min: 11.94

Appendix B: Light curves of variable stars detected in the TLS data set

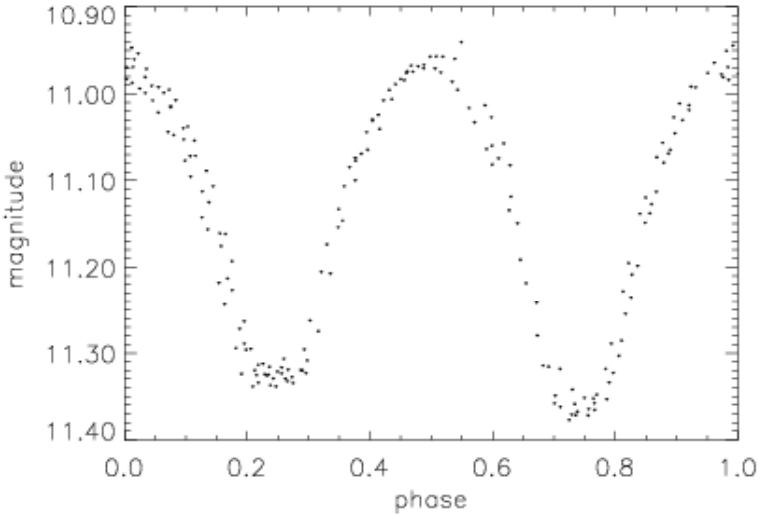

BEST F2 Var 3:
GSC 3700-1384
Var. Type: EW
P: 0.407449 days
Max. 10.94
Min: 11.38

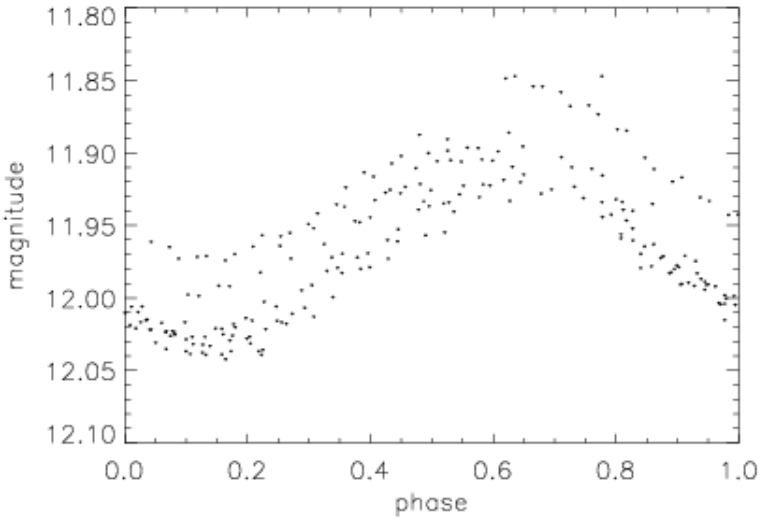

BEST F2 Var 6:
GSC 3307-1757
Var. Type: RRc
P: 0.250563 days
Max.: 11.85
Min.: 12.04

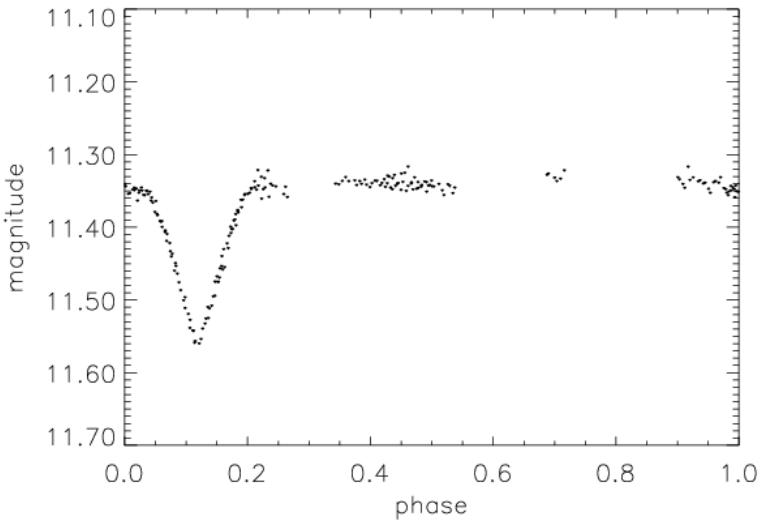

BEST F2 Var 9:
GSC 3687-1661
Var. Type: EA
P: 1.5081 days (?)
Max.: 11.32
Min.: 11.56

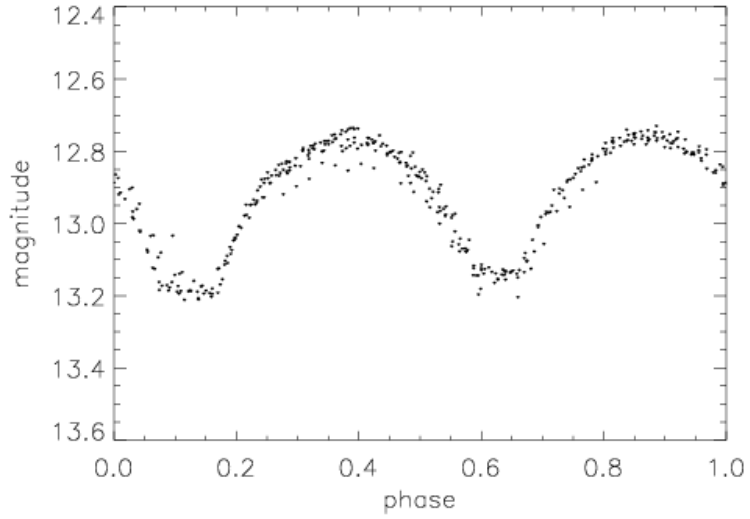

BEST F2 Var 11:
GSC 3687-1112
Var. Type: EW
P: 0.356084 days
Max.: 12.73
Min.: 13.21

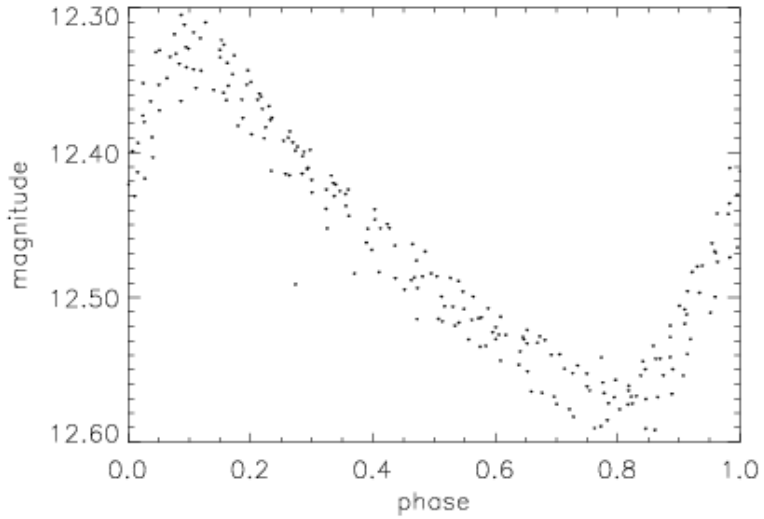

BEST F2 Var 14:
GSC 3307-2025
Var. Type: RRab
P: 0.182116 days
Max.: 12.30
Min.: 12.59

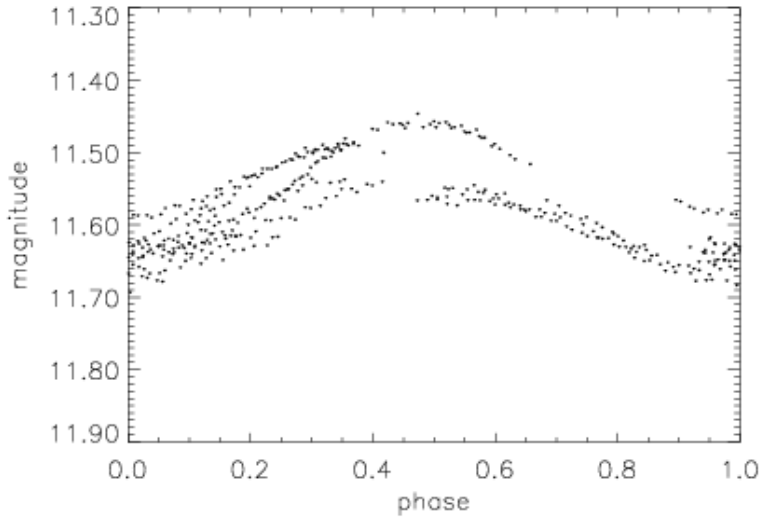

BEST F2 Var 24:
GSC 3307-1571
Var. Type: RRc
P: 0.50121 days
Max.: 11.45
Min.: 11.69

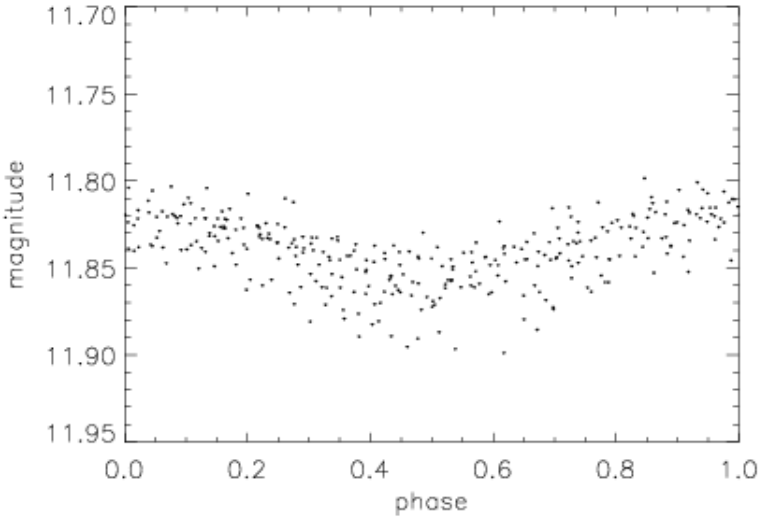

BEST F2 Var 25:
GSC -
Var. Type: δ Sct
P: 0.144414 days
Max.: 11.80
Min.: 11.90

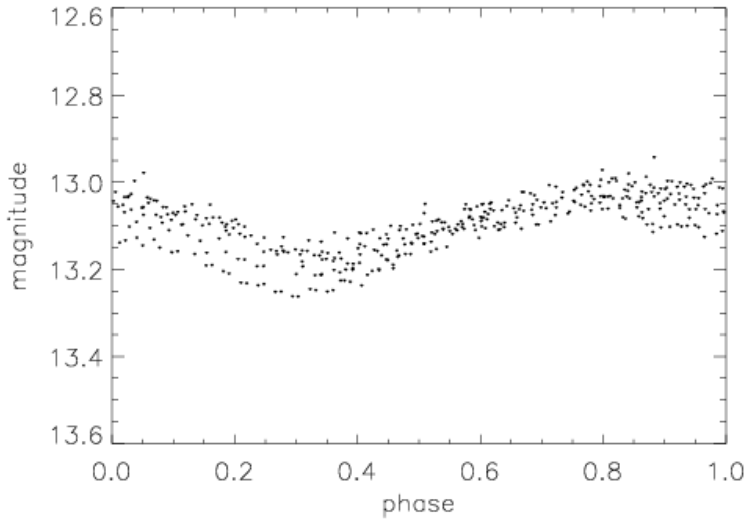

BEST F2 Var 27:
GSC 3308-952
Var. Type: RRc
P: 0.402182 days
Max.: 12.94
Min.: 13.25

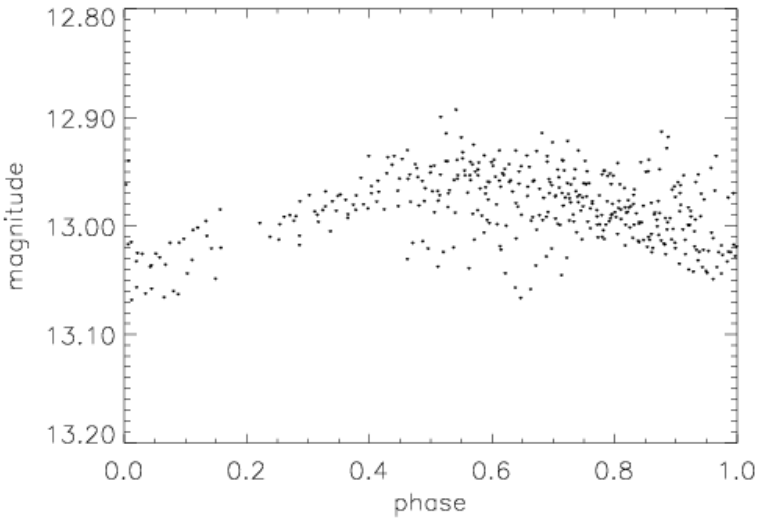

BEST F2 Var 28:
GSC 3308-617
Var. Type: RRc
P: 0.499506 days
Max.: 12.88
Min.: 13.07

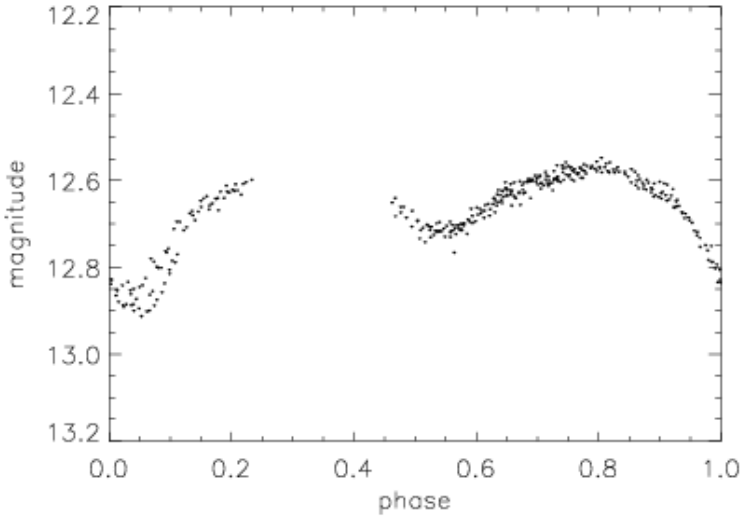

BEST F2 Var 29:
GSC 3308-582
Var. Type: EB
P: 0.903985 days
Max.: 12.55
Min.: 12.92

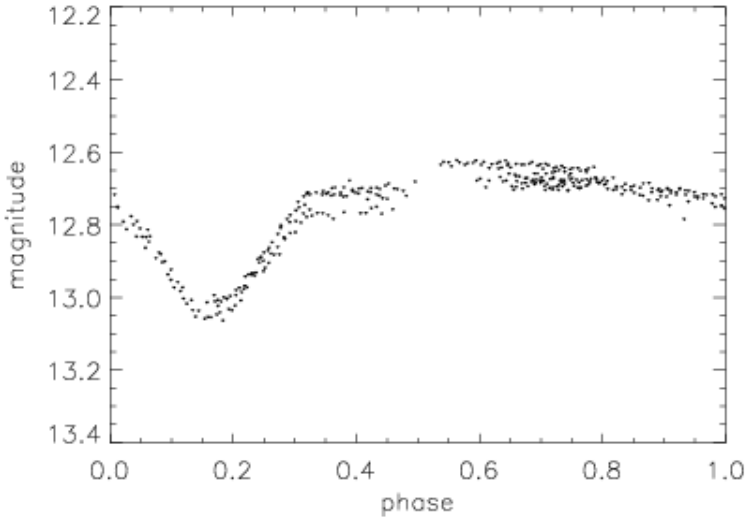

BEST F2 Var 30:
GSC 3307-1711
Var. Type: EA
P: 0.86588 days (x2 ?)
Max.: 12.62
Min.: 13.06

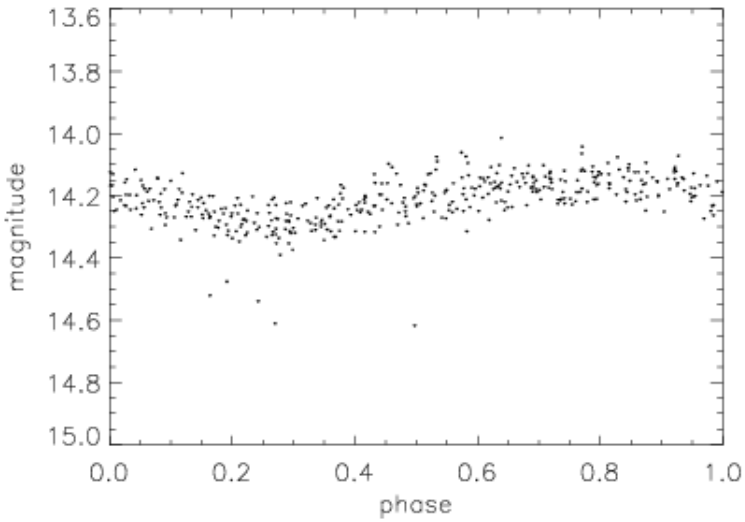

BEST F2 Var 31:
GSC -
Var. Type: SX Phe
P: 0.157758 days
Max.: 14.03
Min.: 14.62 (?)

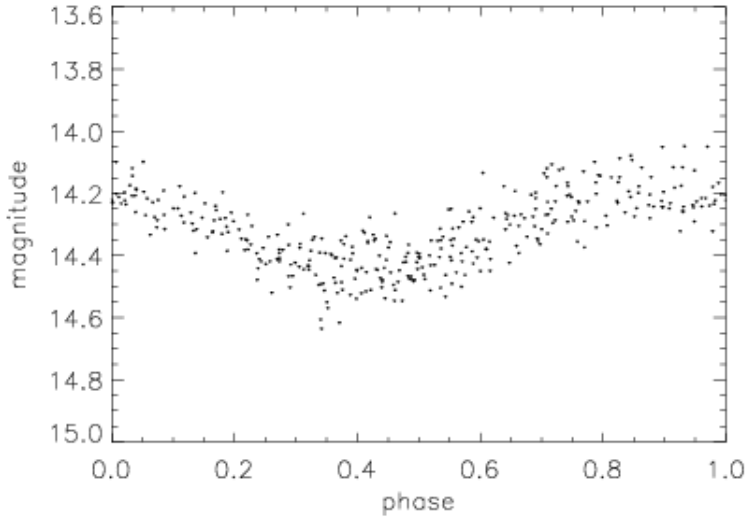

BEST F2 Var 32:
GSC -
Var. Type: RRc
P: 0.241685 days
Max.: 14.05
Min.: 14.63 (?)

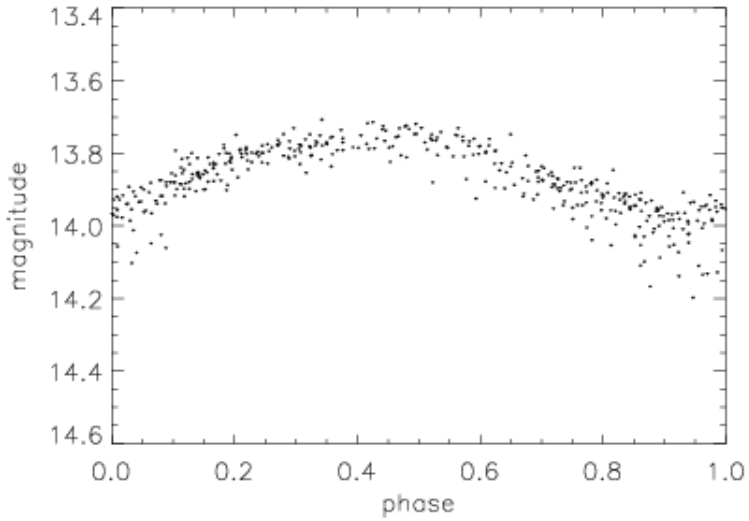

BEST F2 Var 35:
GSC 3308-2285
Var. Type: RRc
P: 0.481217 days
Max.: 13.71
Min.: 14.20 (?)

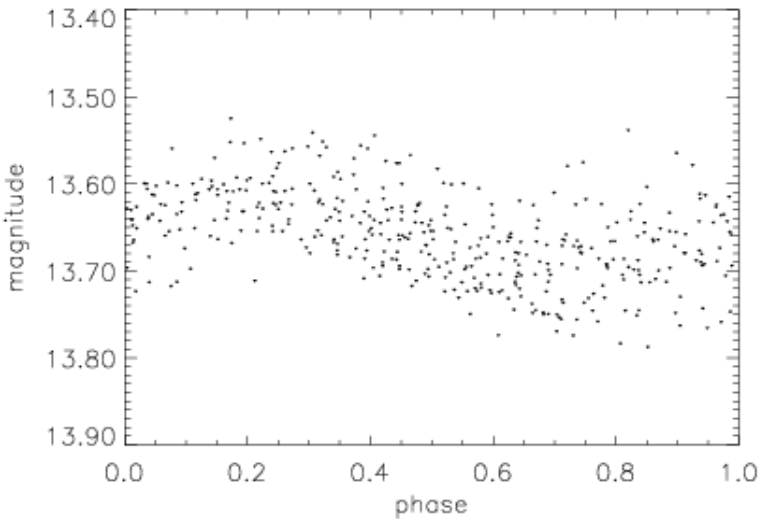

BEST F2 Var 36:
GSC 3307-1404
Var. Type: SX Phe/ δ Sct
P: 0.168315 days
Max.: 13.53
Min.: 13.79

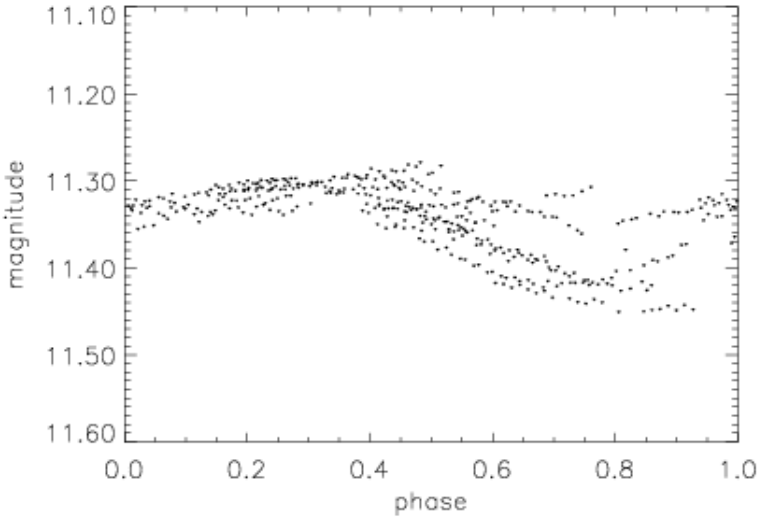

BEST F2 Var 38:
GSC 3308-969
Var. Type: RRc
P: 0.5645 days
Max.: 11.28
Min.: 14.46

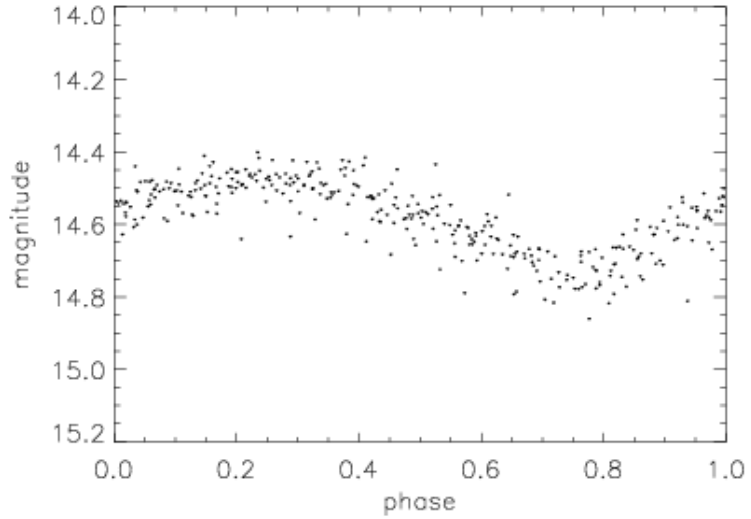

BEST F2 Var 39:
GSC -
Var. Type: SX Phe
P: 0.187196 days
Max.: 14.40
Min.: 14.86

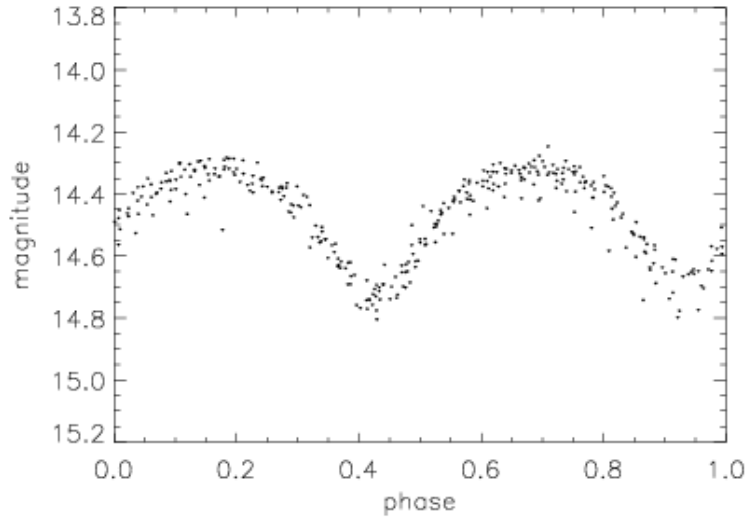

BEST F2 Var 40:
GSC -
Var. Type: EW
P: 0.267532 days
Max.: 14.25
Min.: 14.80

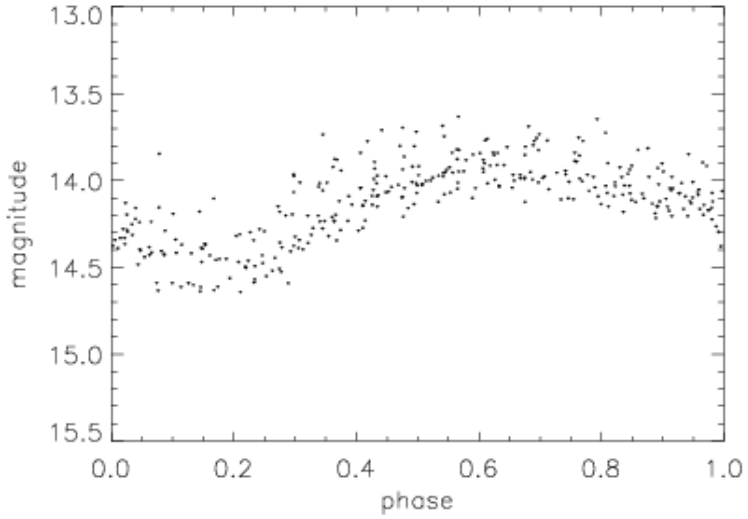

BEST F2 Var 41:
GSC -
Var. Type: SX Phe
P: 0.188916 days
Max.: 13.63
Min.: 14.64

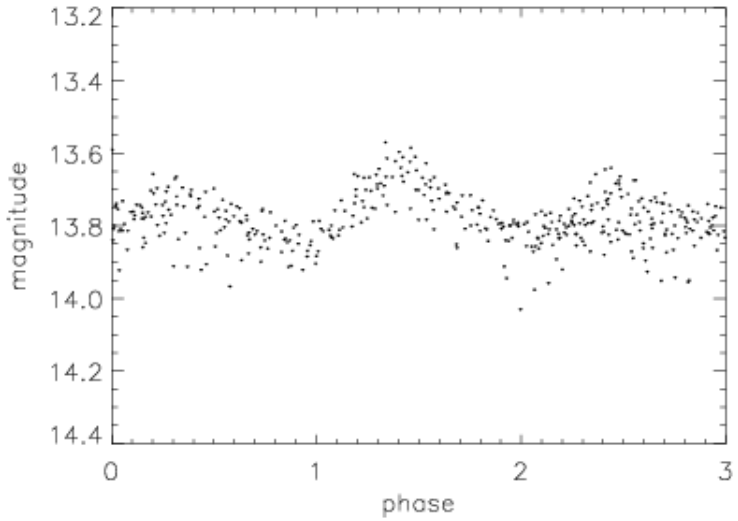

BEST F2 Var 42:
GSC -
Var. Type: SX Phe ?
P: 0.110372 days
Max.: 13.57
Min.: 14.03

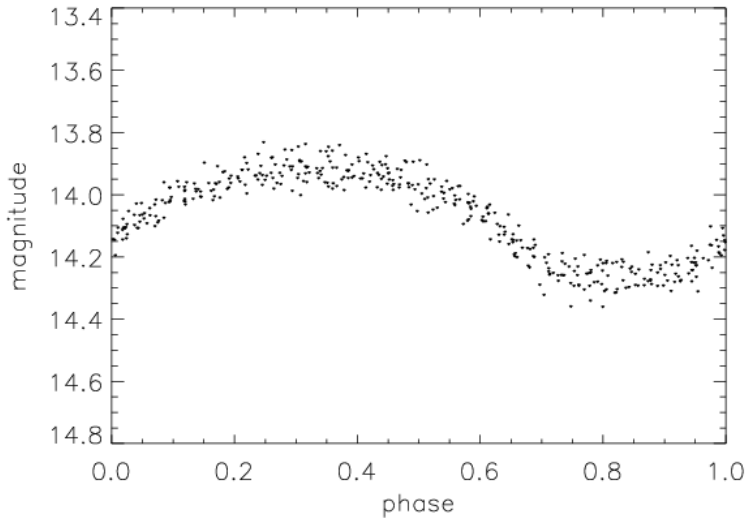

BEST F2 Var 43:
GSC -
Var. Type: SX Phe
P: 0.172062 days
Max.: 13.83
Min.: 14.36

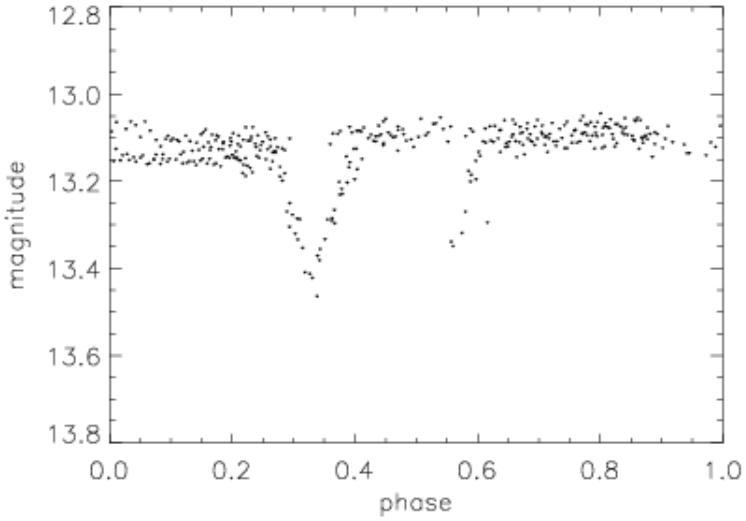

BEST F2 Var 47:
GSC -
Var. Type: EA
P: 1.0426 days (?)
Max.: 13.04
Min.: 13.46

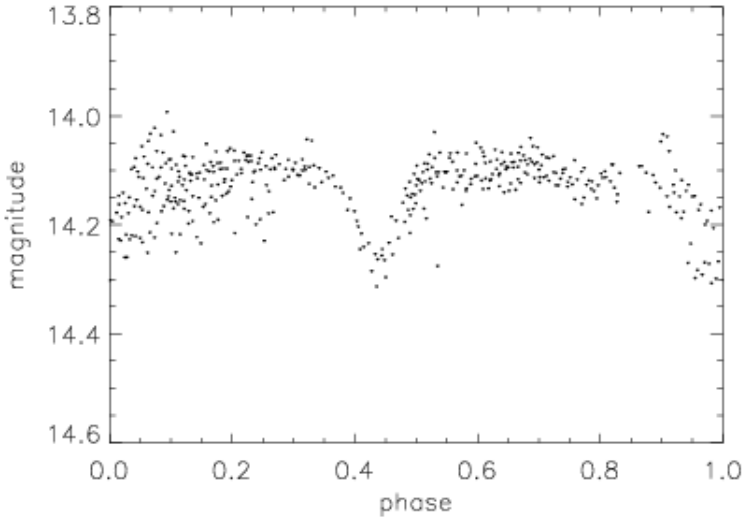

BEST F2 Var 48:
GSC -
Var. Type: EA
P: 1.10237 days (?)
Max.: 13.99
Min.: 14.31

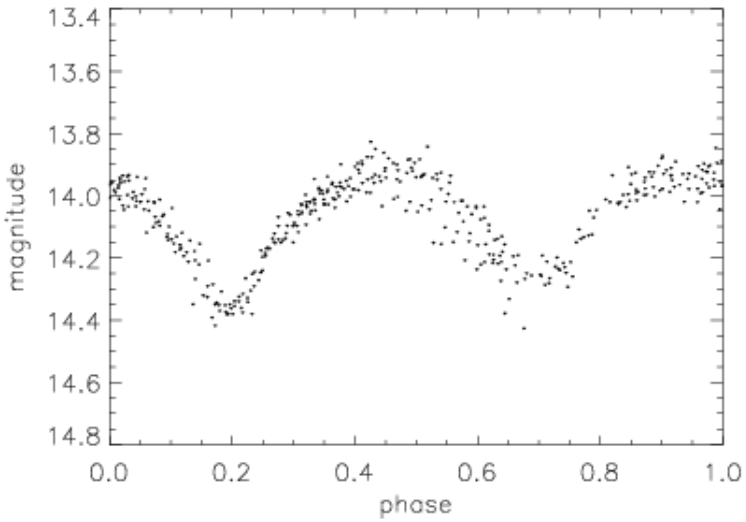

BEST F2 Var 49:
GSC -
Var. Type: EW
P: 0.587476 days
Max.: 13.83
Min.: 14.43

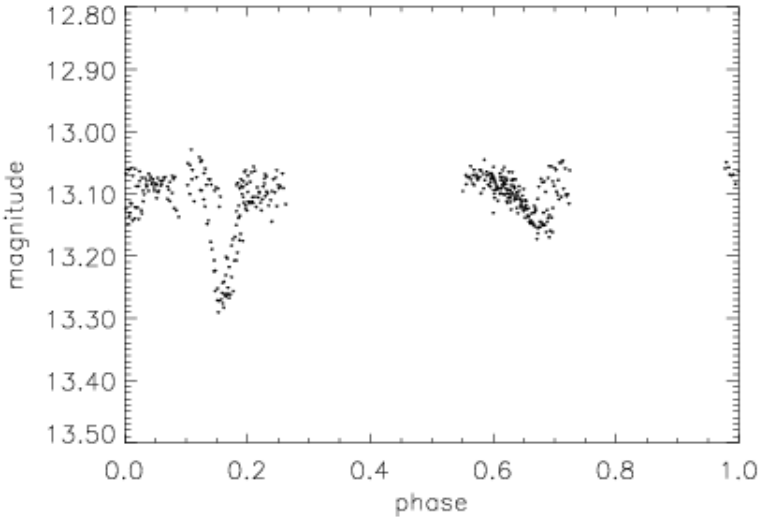

BEST F2 Var 50:
GSC 3307-1846
Var. Type: EA
P: 2.2378 days (?)
Max.: 13.12
Min.: 13.30

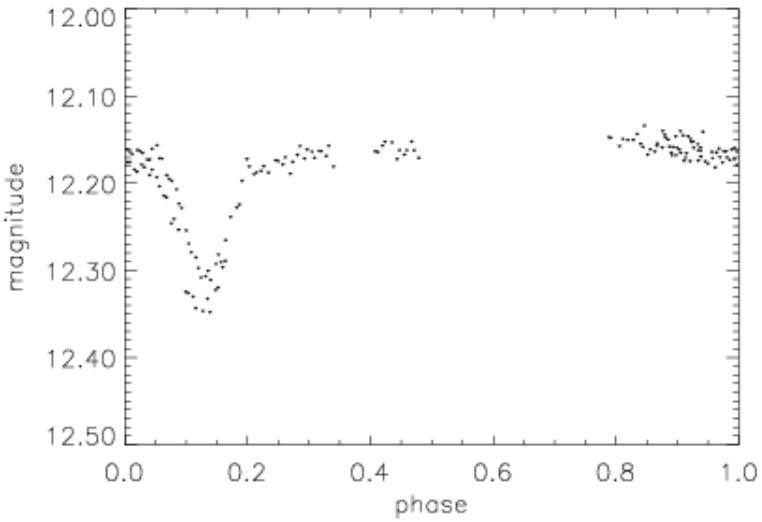

BEST F2 Var 51: season 1
GSC 3308-1667/1657
Var. Type: EA
P: 1.068 days (?)
Max.: 12.13
Min.: 12.35

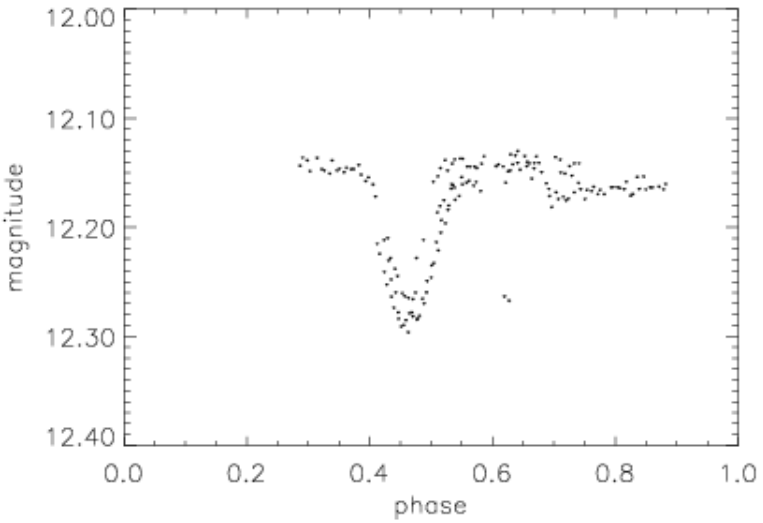

BEST F2 Var 51: season 2
GSC 3308-1667/1657
Var. Type: EA
P: 1.066 days (?)
Max.: 12.13
Min.: 12.35

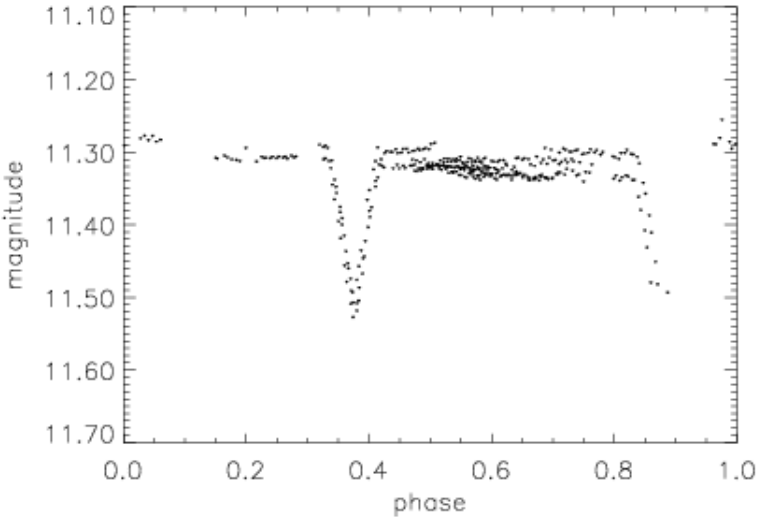

BEST F2 Var 53:
GSC 3308-2243
Var. Type: EA
P: 1.251 days (?)
Max.: 11.25
Min.: 11.53

B.1.3. Target field 15

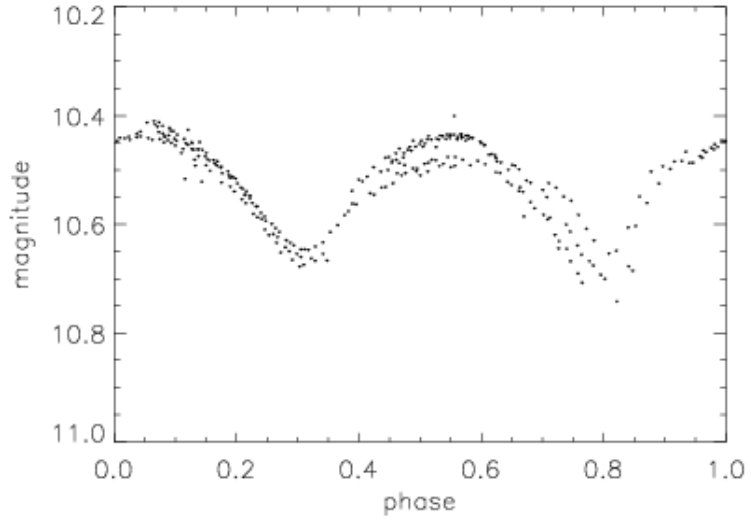

BEST F15 Var 3:
GSC 3562-1866
Var. Type: EW
P: 0.66065 days
Max.: 10.40
Min.: 10.74

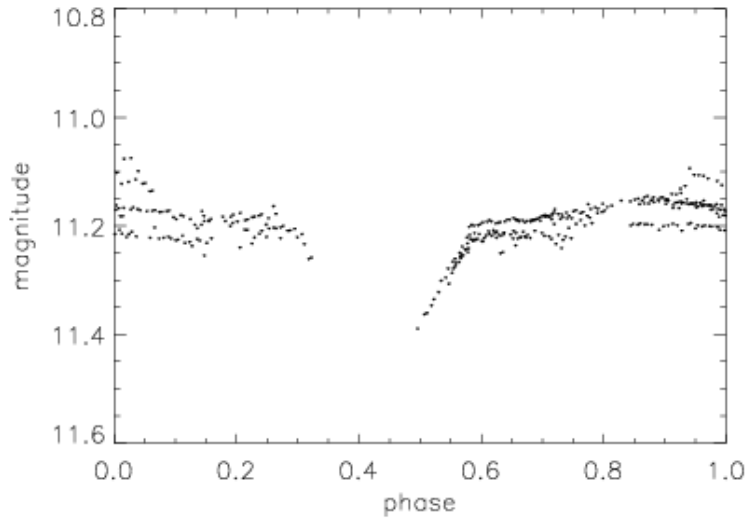

BEST F15 Var 5:
GSC 3558-939
Var. Type: EA
P: 1.08187 days (x2 ?)
Max.: 11.07
Min.: 11.39

Appendix B: Light curves of variable stars detected in the TLS data set

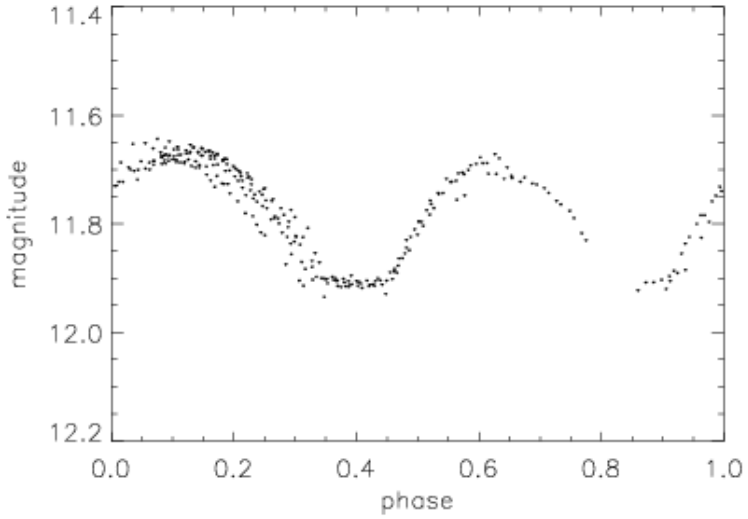

BEST F15 Var 6:
GSC 3562-1353
Var. Type: EW
P: 0.628748 days
Max.: 11.64
Min.: 11.93

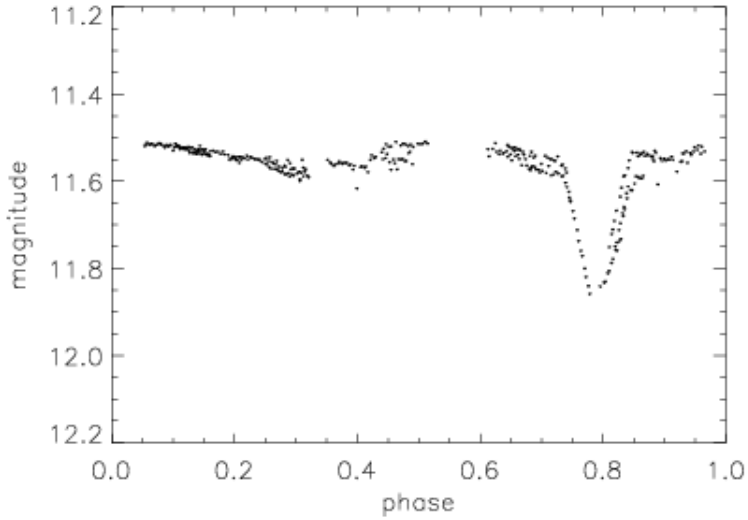

BEST F15 Var 9:
GSC 3562-985
Var. Type: EA
P: 2.04506 days
Max.: 11.51
Min.: 11.86

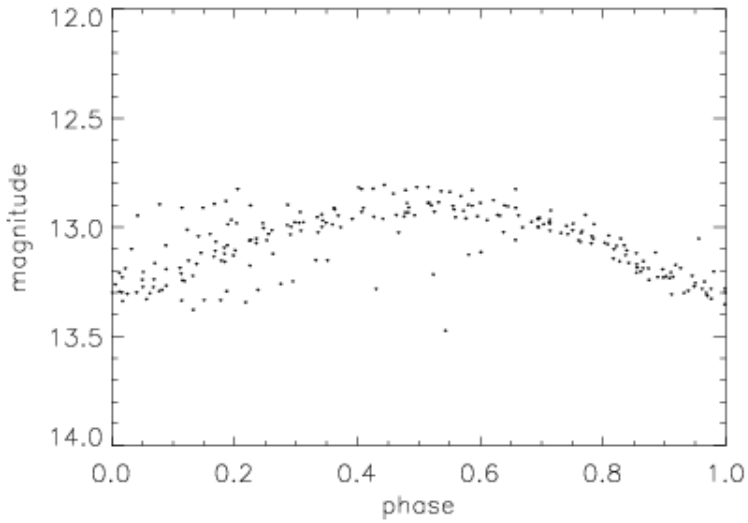

BEST F15 Var 13:
GSC 3562-1392
Var. Type: RRc
P: 0.219743 days
Max.: 12.89
Min.: 13.47

Appendix B: Light curves of variable stars detected in the TLS data set

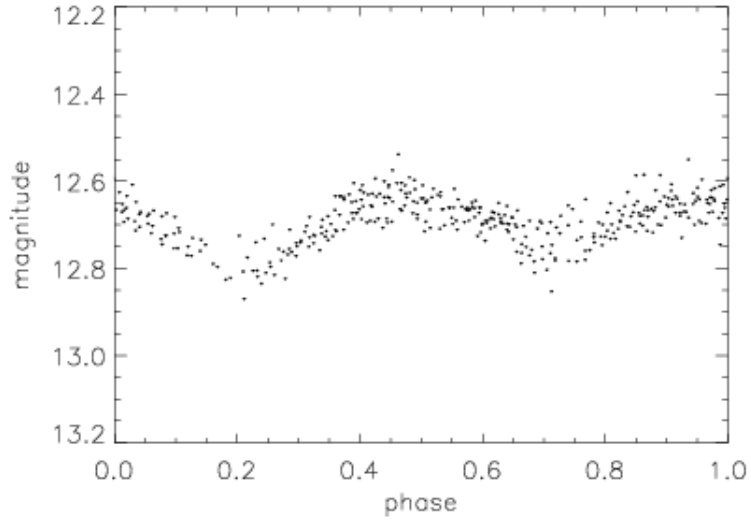

BEST F15 Var 14:
GSC 3566-373
Var. Type: EW
P: 0.591338 days
Max.: 12.54
Min.: 12.87

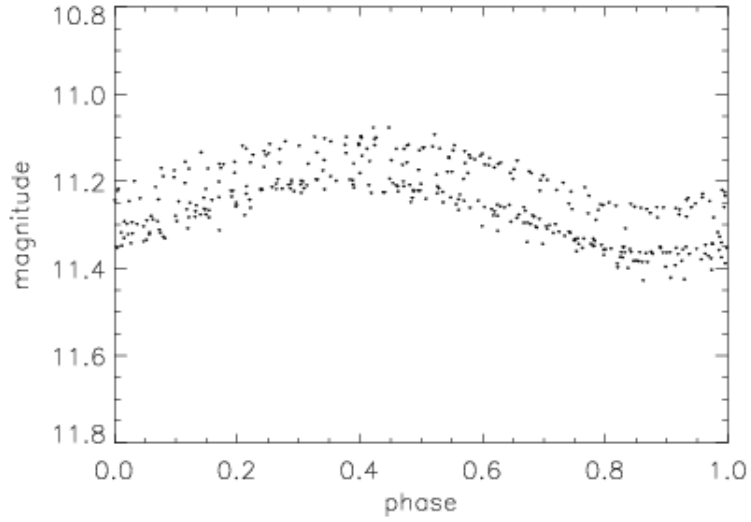

BEST F15 Var 15:
GSC 3563-334
Var. Type: δ Sct/ SX Phe ?
P: 0.169115 days
Max.: 11.08
Min.: 11.43

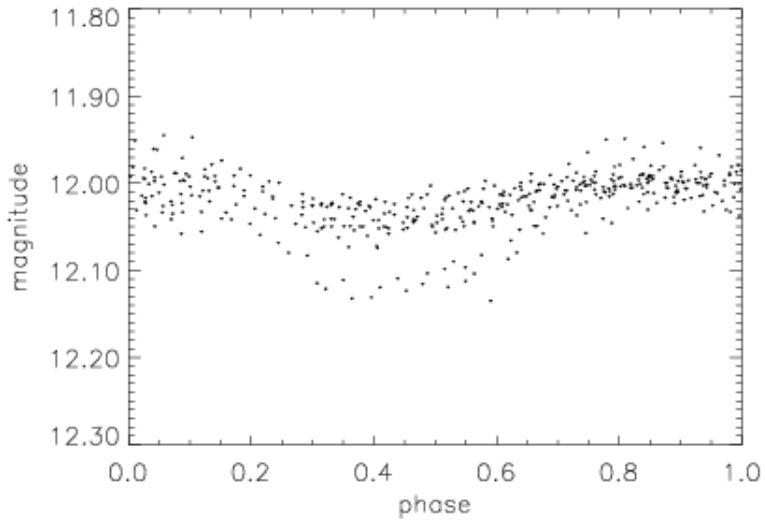

BEST F15 Var 20:
GSC 3562-2345
Var. Type: RRc
P: 0.265071 days
Max.: 11.94
Min.: 12.10

Appendix B: Light curves of variable stars detected in the TLS data set

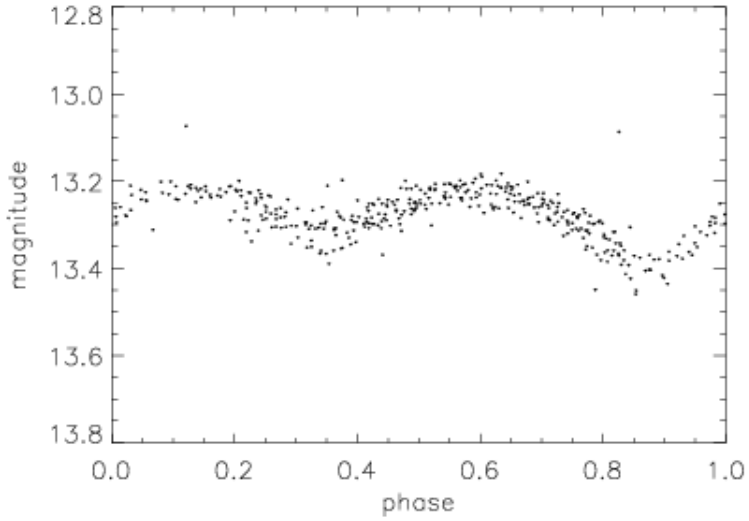

BEST F15 Var 24:
GSC 3563-1861
Var. Type: EB
P: 0.513142 days
Max.: 13.07
Min.: 13.46

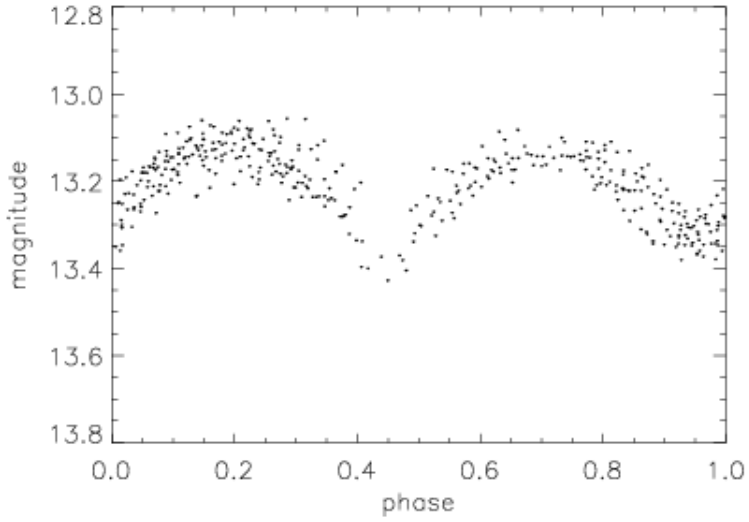

BEST F15 Var 25:
GSC -
Var. Type: EW
P: 0.414922 days
Max.: 13.06
Min.: 13.43

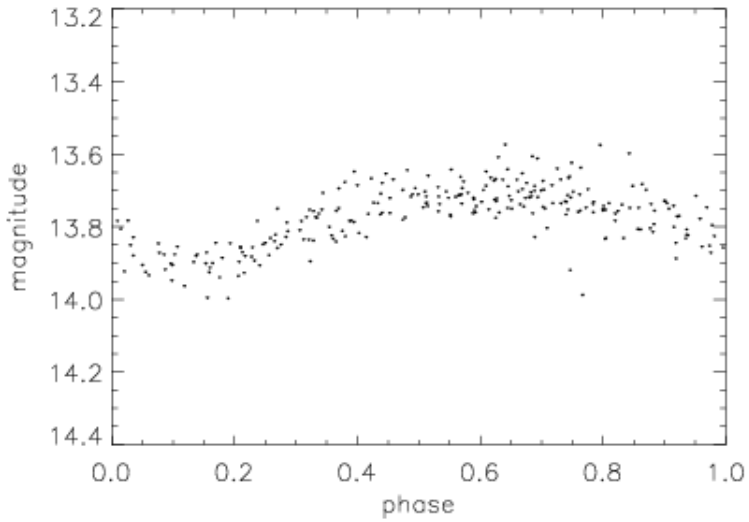

BEST F15 Var 29:
GSC -
Var. Type: RRc
P: 0.217298 days
Max.: 13.57
Min.: 14.00

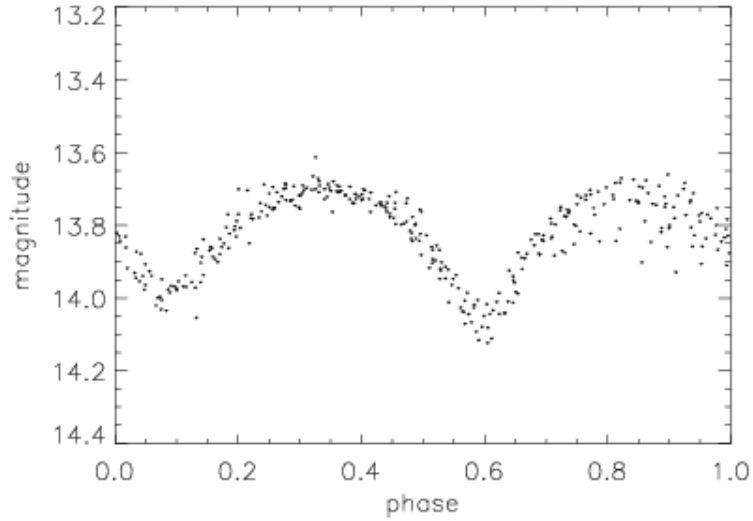

BEST F15 Var 30:
GSC -
Var. Type: EW
P: 0.301652 days
Max.: 13.61
Min.: 14.12

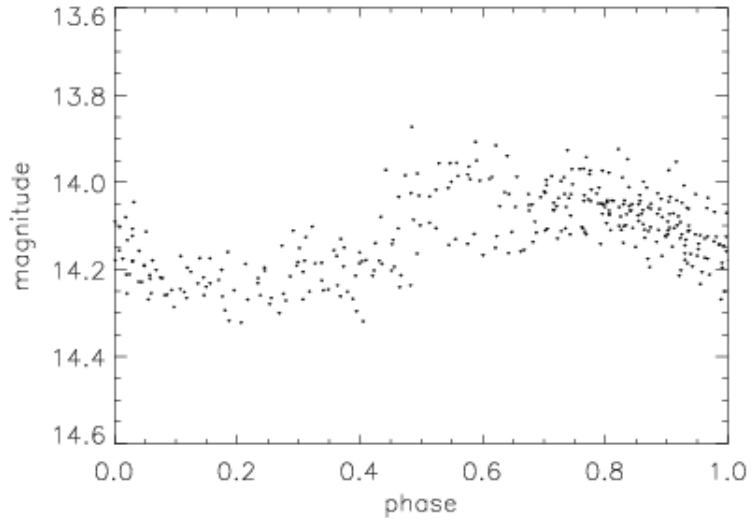

BEST F15 Var 32:
GSC -
Var. Type: RRc
P: 0.404801 days
Max.: 13.87
Min.: 14.32

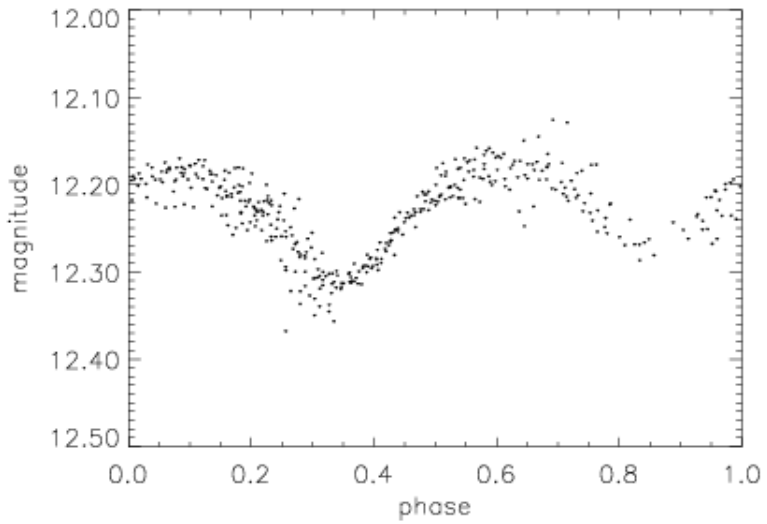

BEST F15 Var 41:
GSC 3562-946
Var. Type: EB
P: 0.529668 days
Max.: 12.13
Min.: 12.37

Appendix B: Light curves of variable stars detected in the TLS data set

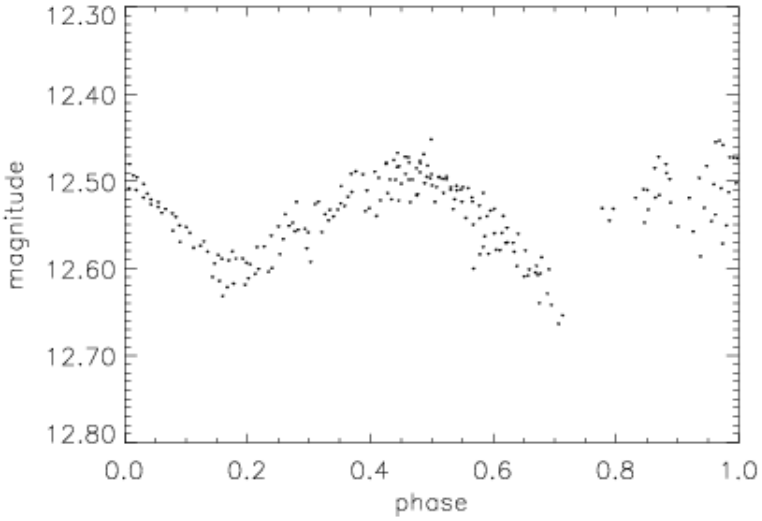

BEST F15 Var 44:
GSC 3566-935
Var. Type: EB
P: 0.683614 days
Max.: 12.45
Min.: 12.66

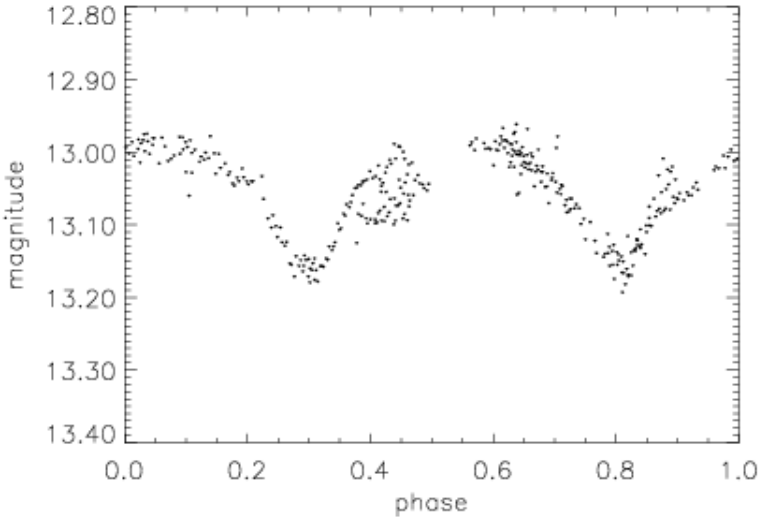

BEST F15 Var 45:
GSC 3566-33
Var. Type: EB
P: 1.66582 days
Max.: 12.96
Min.: 13.19

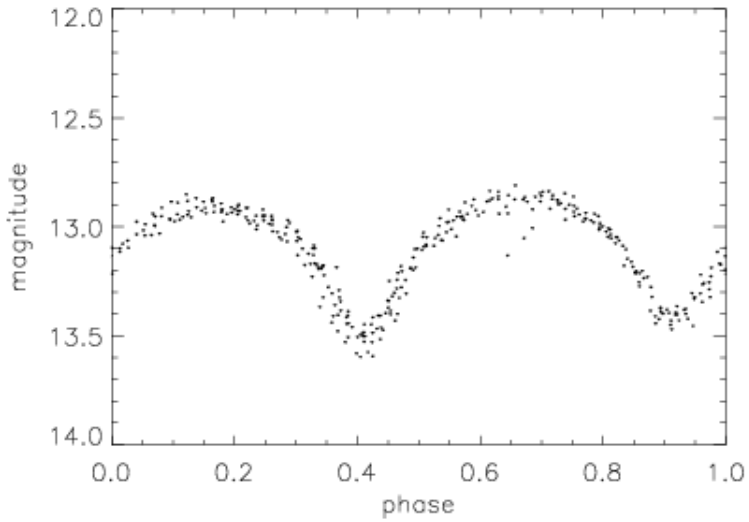

BEST F15 Var 46:
GSC 3562-464
Var. Type: EW
P: 0.306942 days
Max.: 12.80
Min.: 13.59

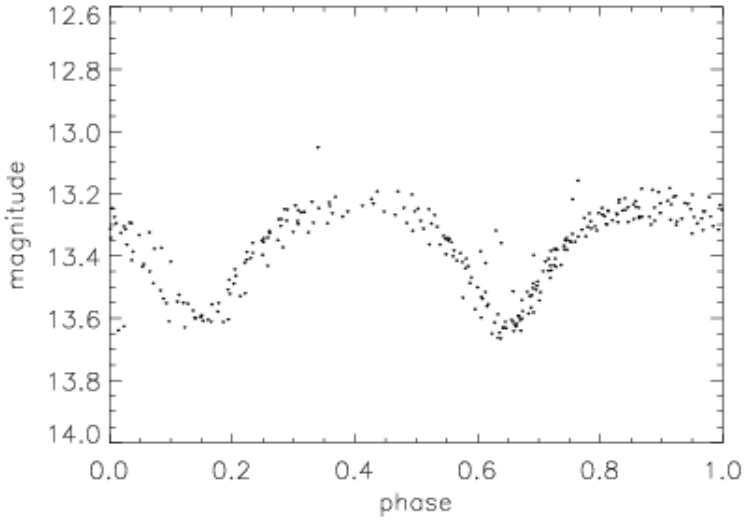

BEST F15 Var 49:
GSC -
Var. Type: EW
P: 0.45434 days
Max.: 13.05
Min.: 13.66

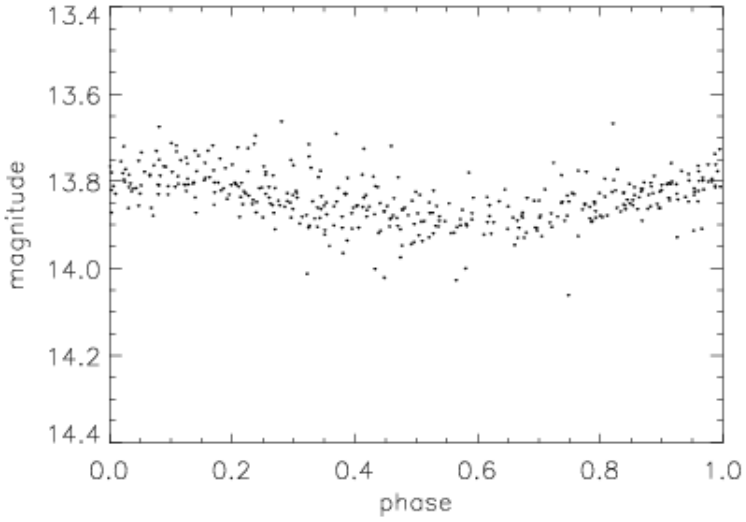

BEST F15 Var 56:
GSC -
Var. Type: RRc
P: 0.280851 days
Max.: 13.66
Min.: 14.06

B.2. Light curves of variables for selected nights

In the following light curves of identified variables in the three observed target fields will be displayed for selected nights. To identify these variables all light curves with VI > 1.5 were visually checked if nightly magnitude offsets are responsible for the high variability index. Note that this includes the variables found to be periodic. Additionally the light curves of the transit candidates are displayed for comparison.

The coordinates of the stars and the VI index (see section 8.1.) are displayed in the top line of the plots. Above the top line the ID code for the variable star is given (see Tables 8.2, 8.3, 8.4))

B.2.1. Target field 8

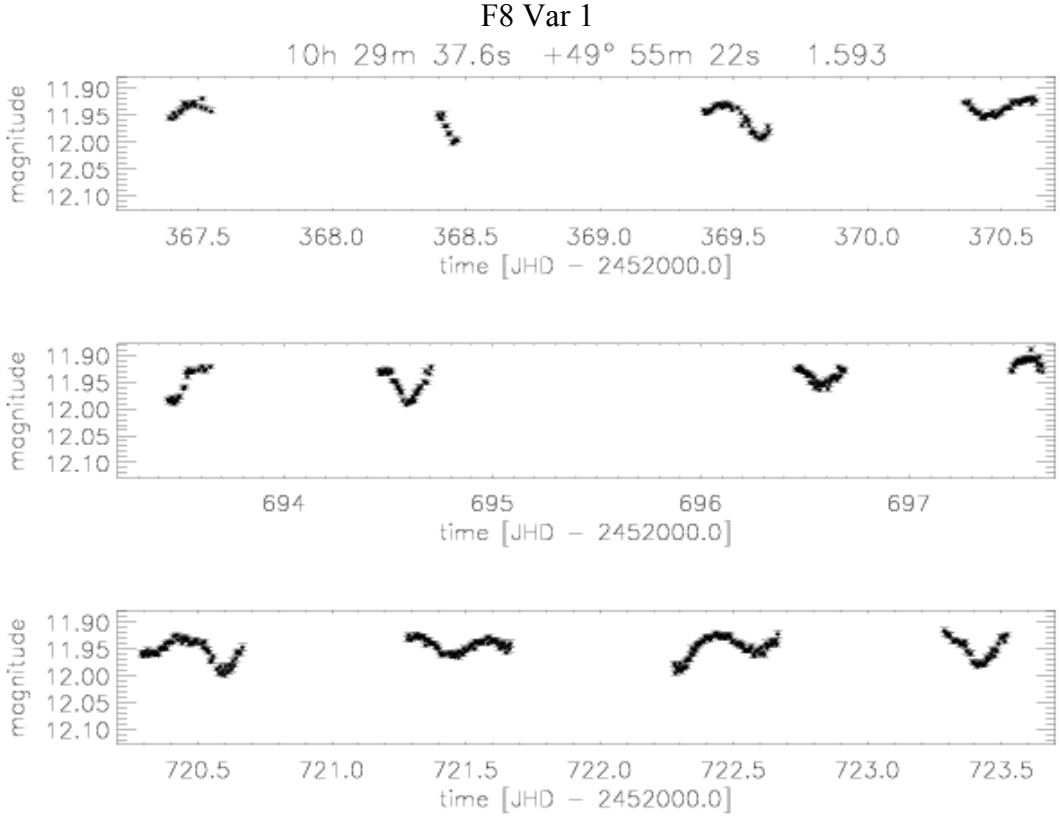

Appendix B: Light curves of variable stars detected in the TLS data set

F8 Var 2

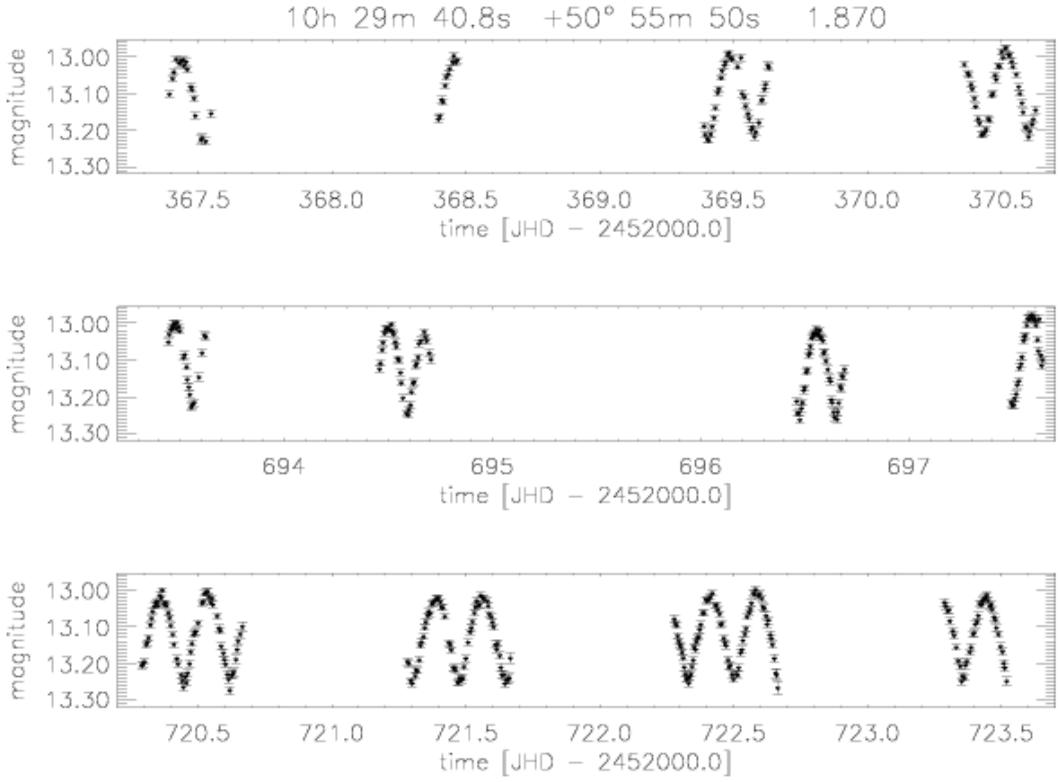

F8 Var 3

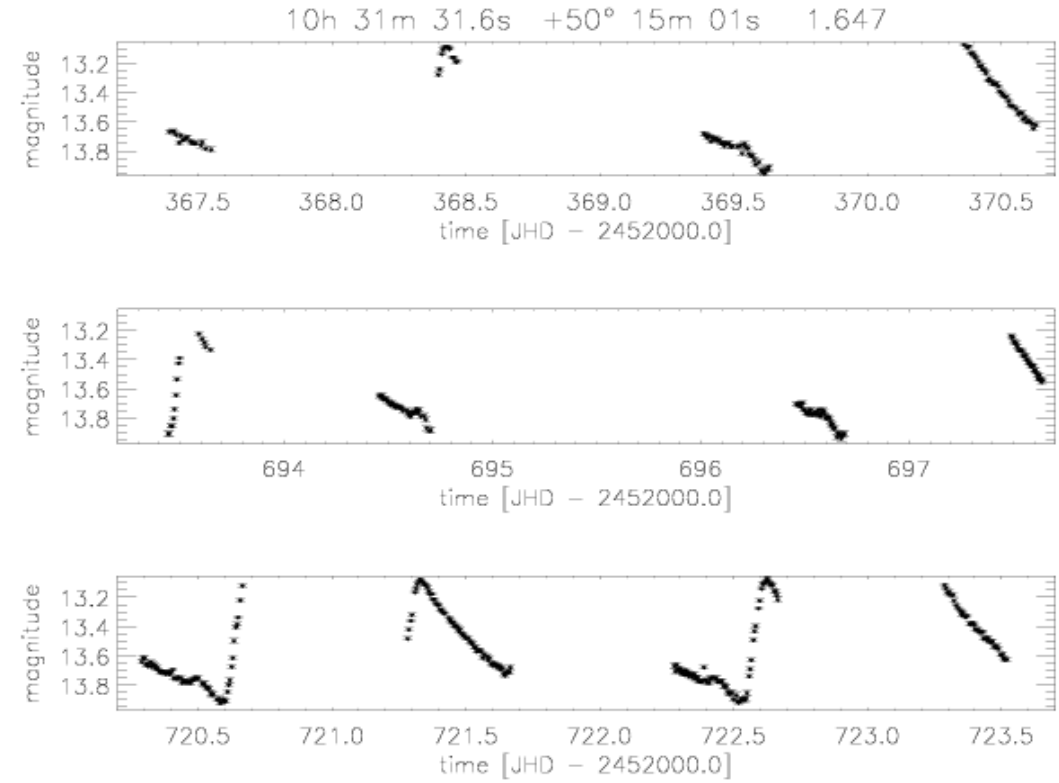

Appendix B: Light curves of variable stars detected in the TLS data set

F8 Var 4

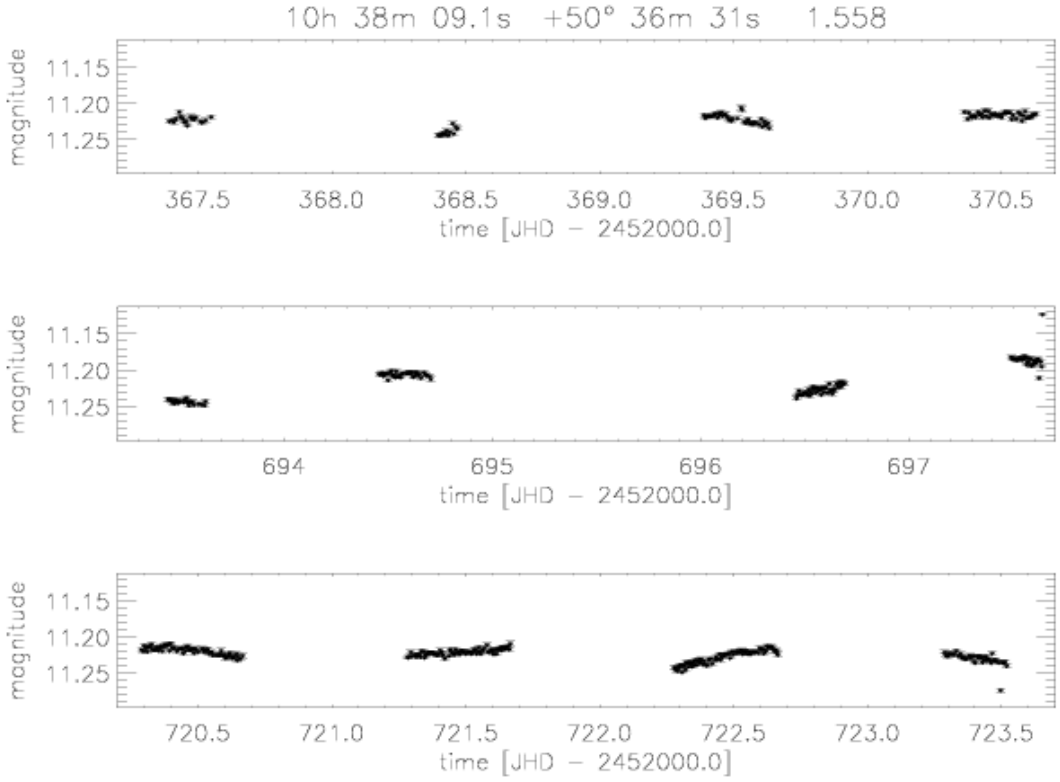

F8 Var 5

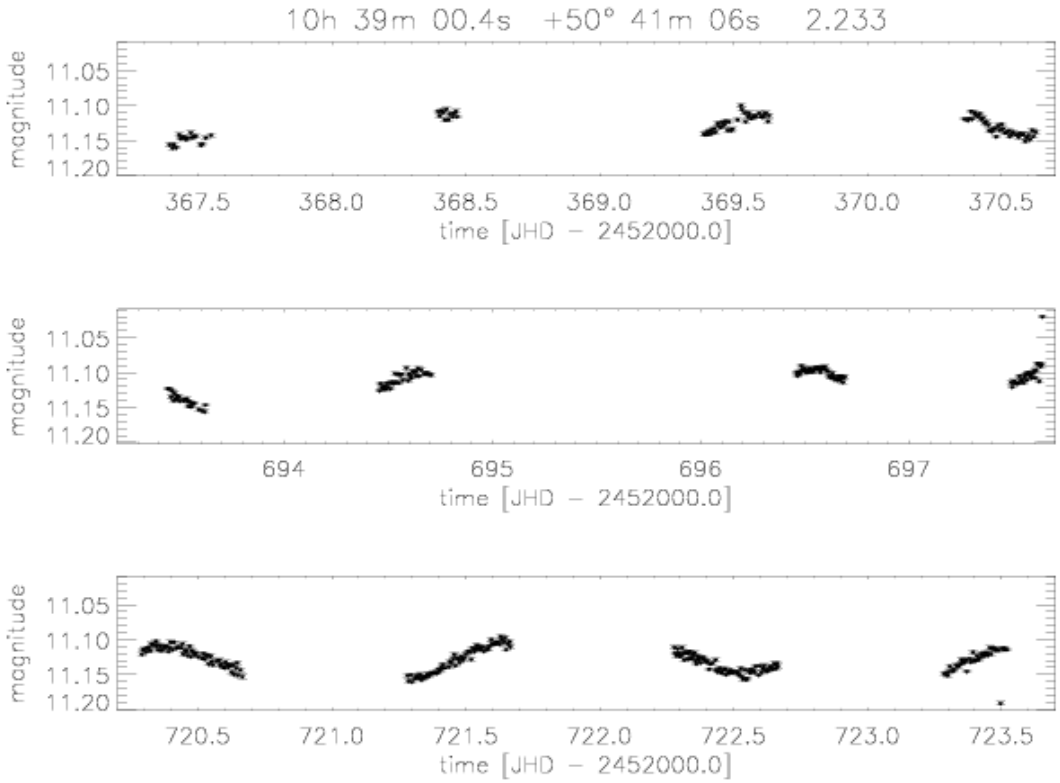

F8 Var 6

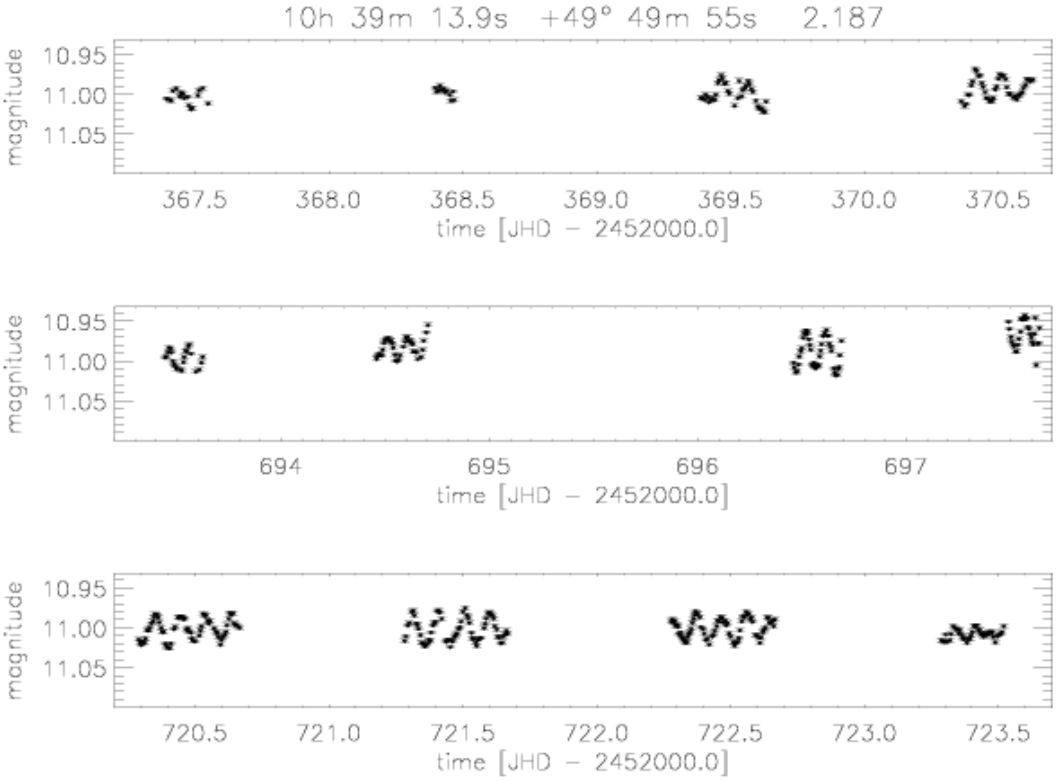

B.2.2. Target field 2

F2 Var 1

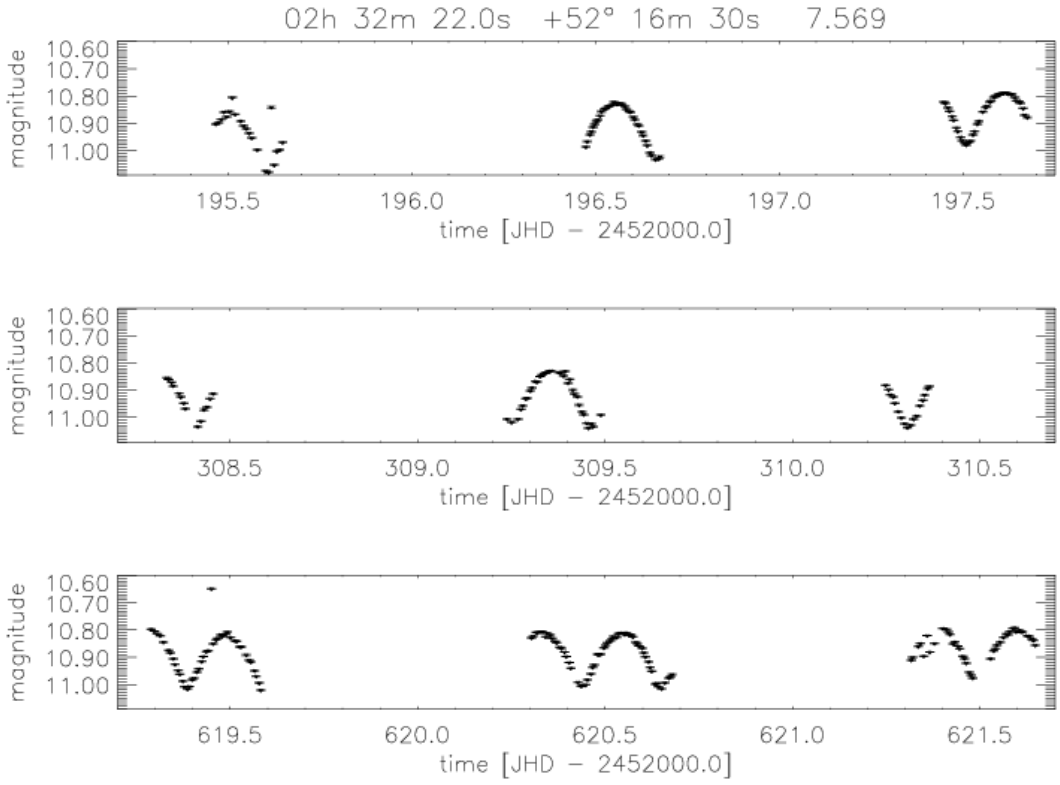

Appendix B: Light curves of variable stars detected in the TLS data set

F2 Var 2

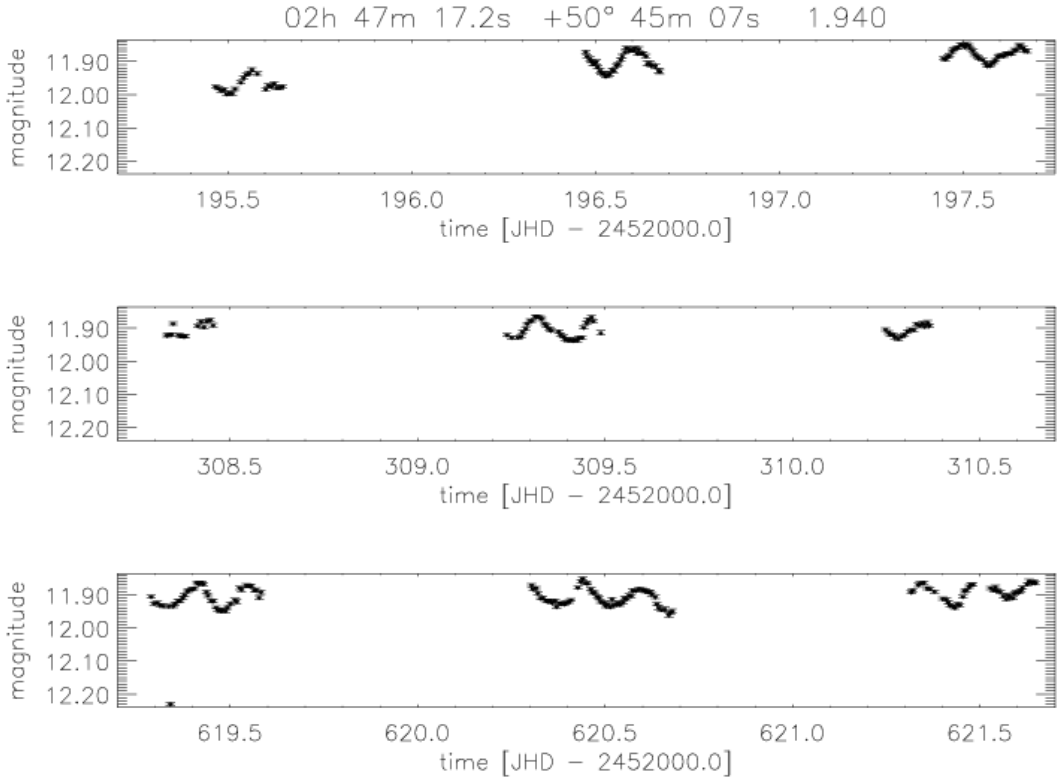

F2 Var 3

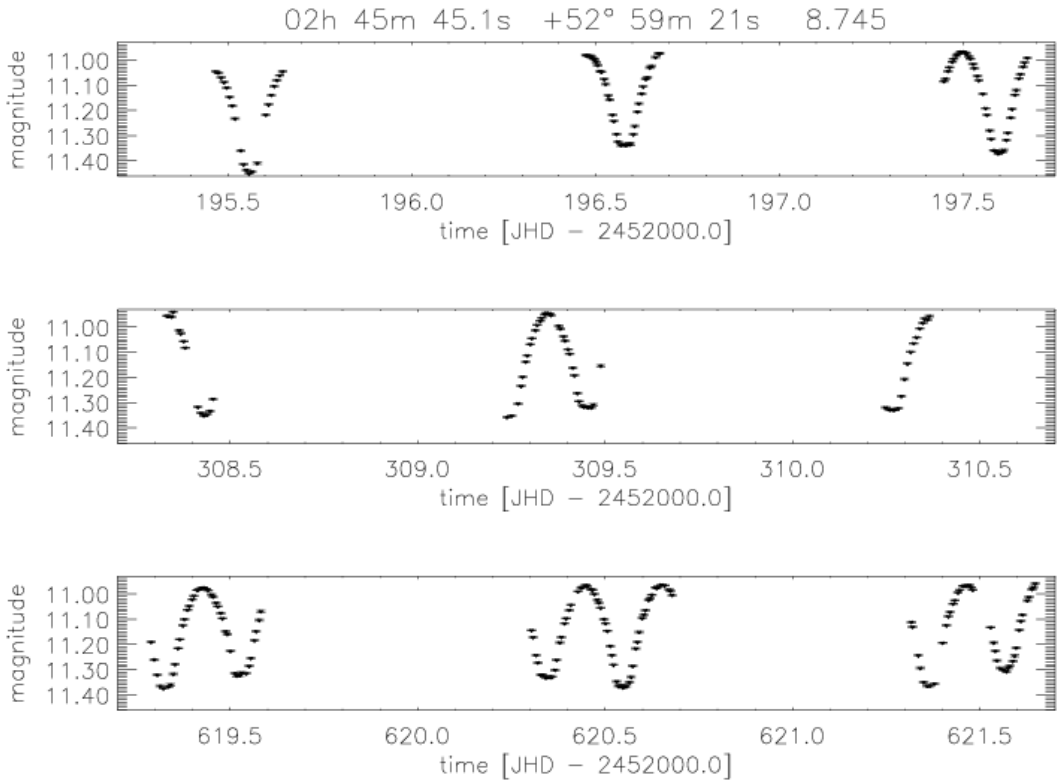

Appendix B: Light curves of variable stars detected in the TLS data set

F2 Var 4

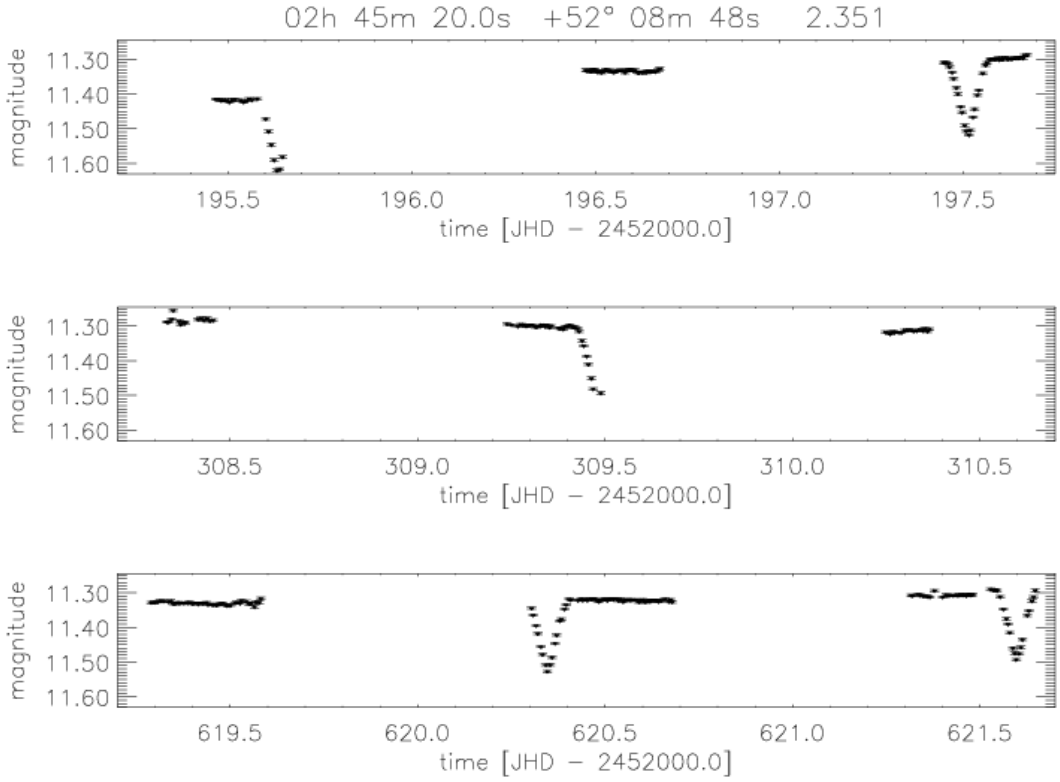

F2 Var 6

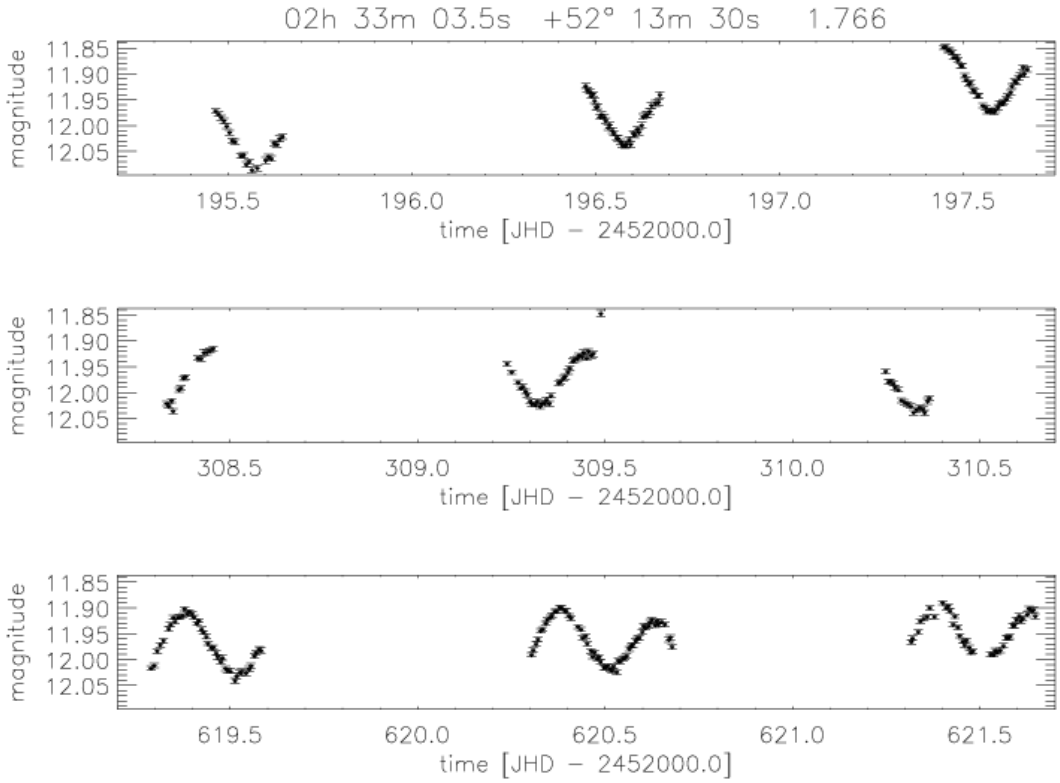

Appendix B: Light curves of variable stars detected in the TLS data set

F2 Var 7

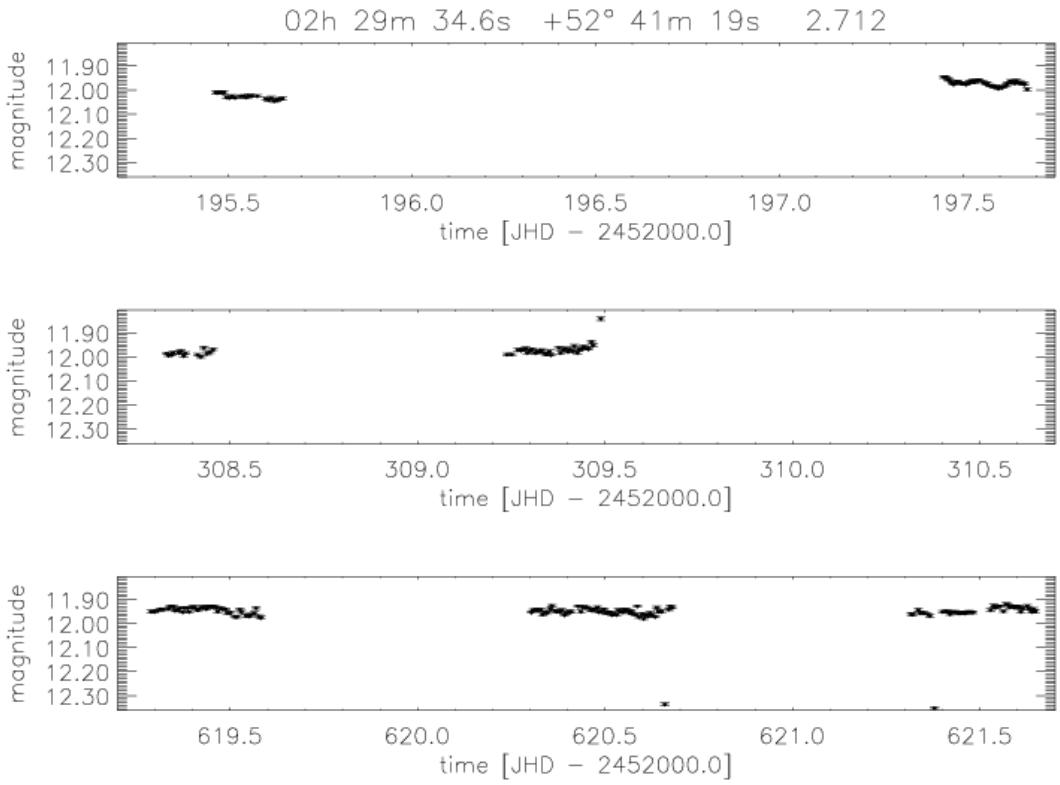

F2 Var9

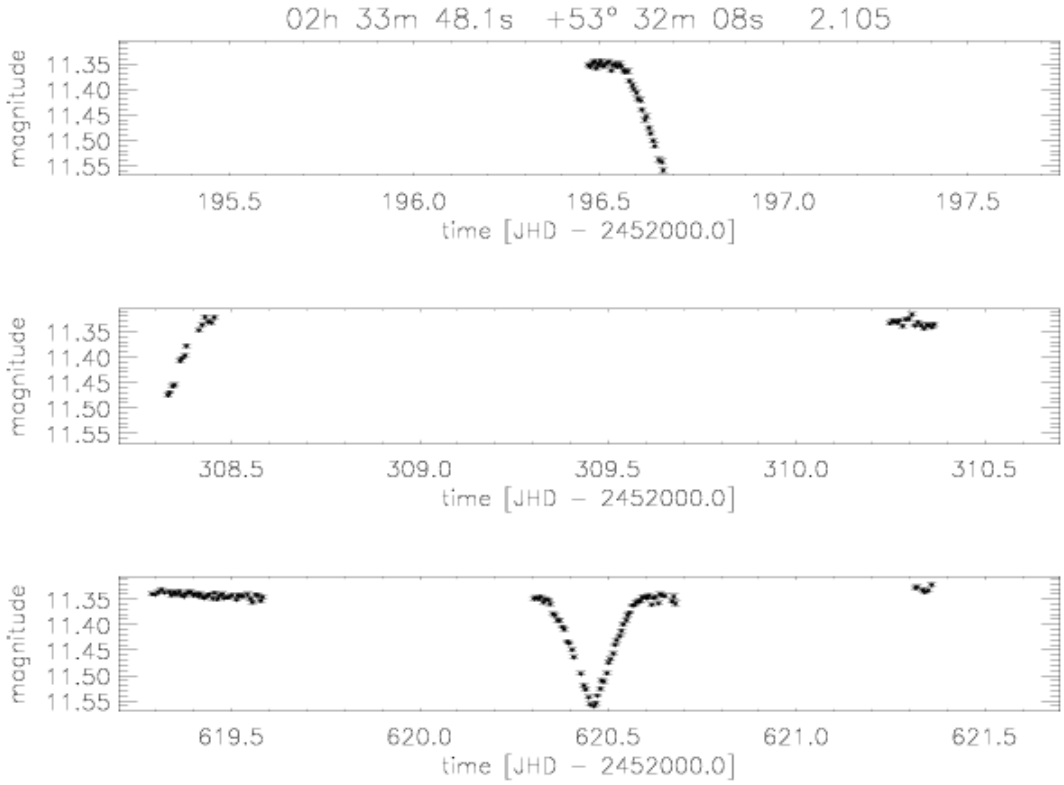

F2 Var 10

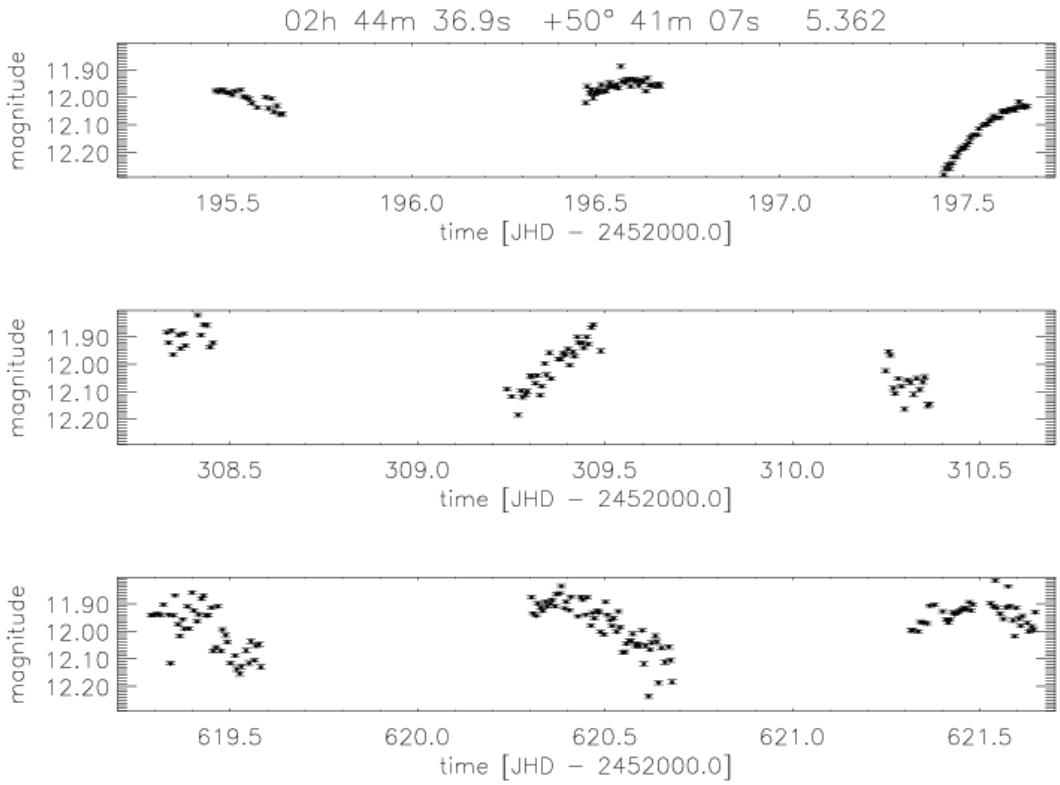

F2 Var 11

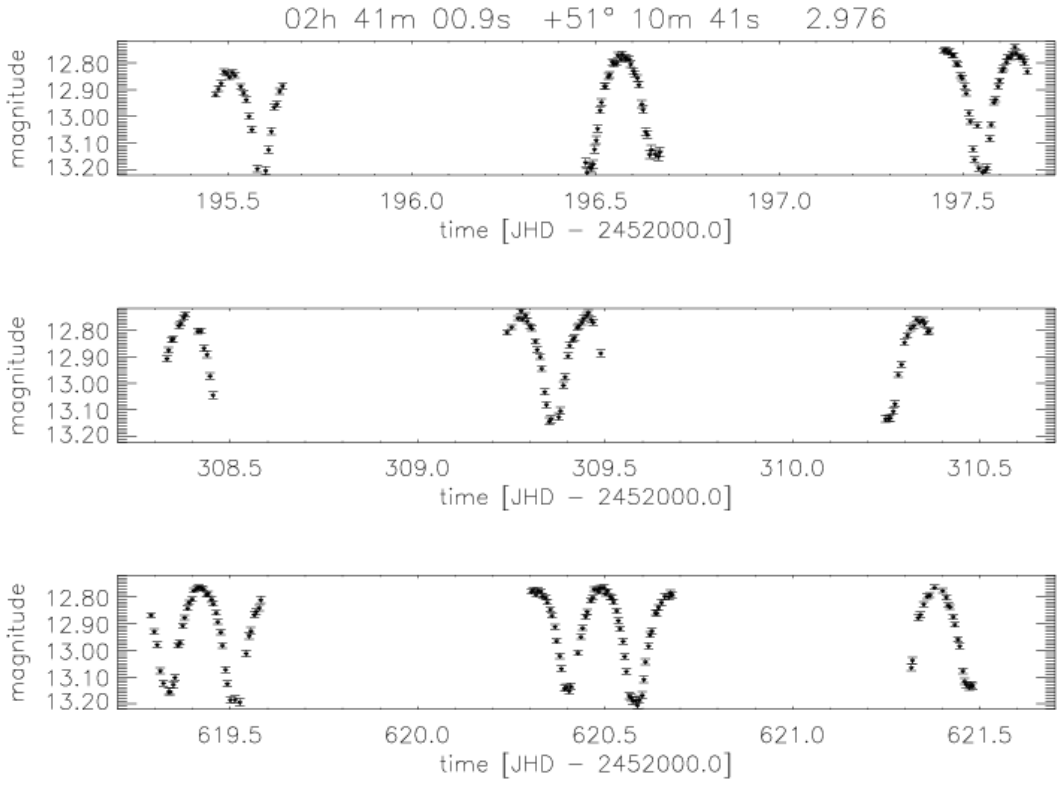

Appendix B: Light curves of variable stars detected in the TLS data set

F2 Var 12

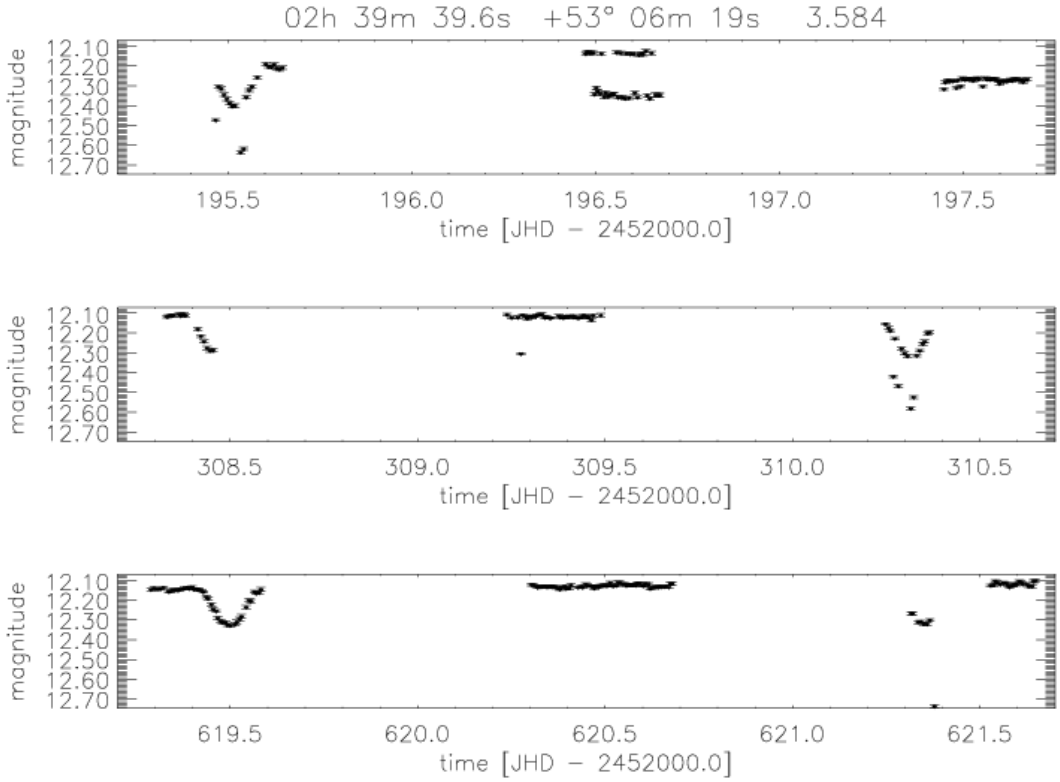

F2 Var 14

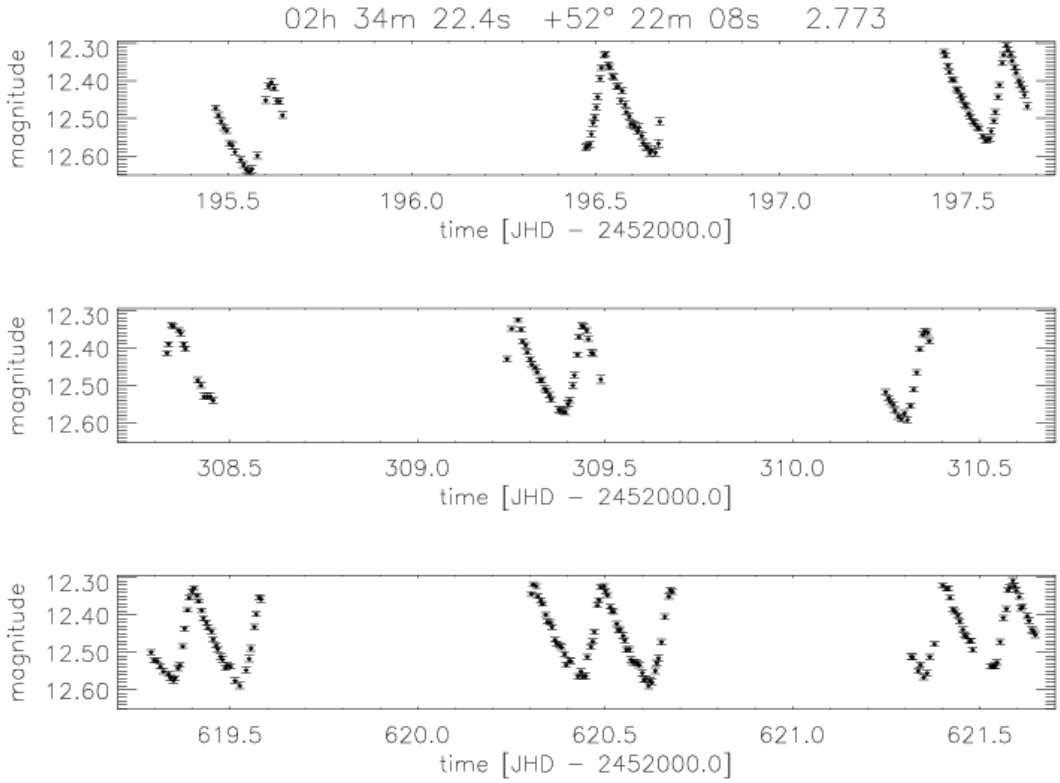

F2 Var 15

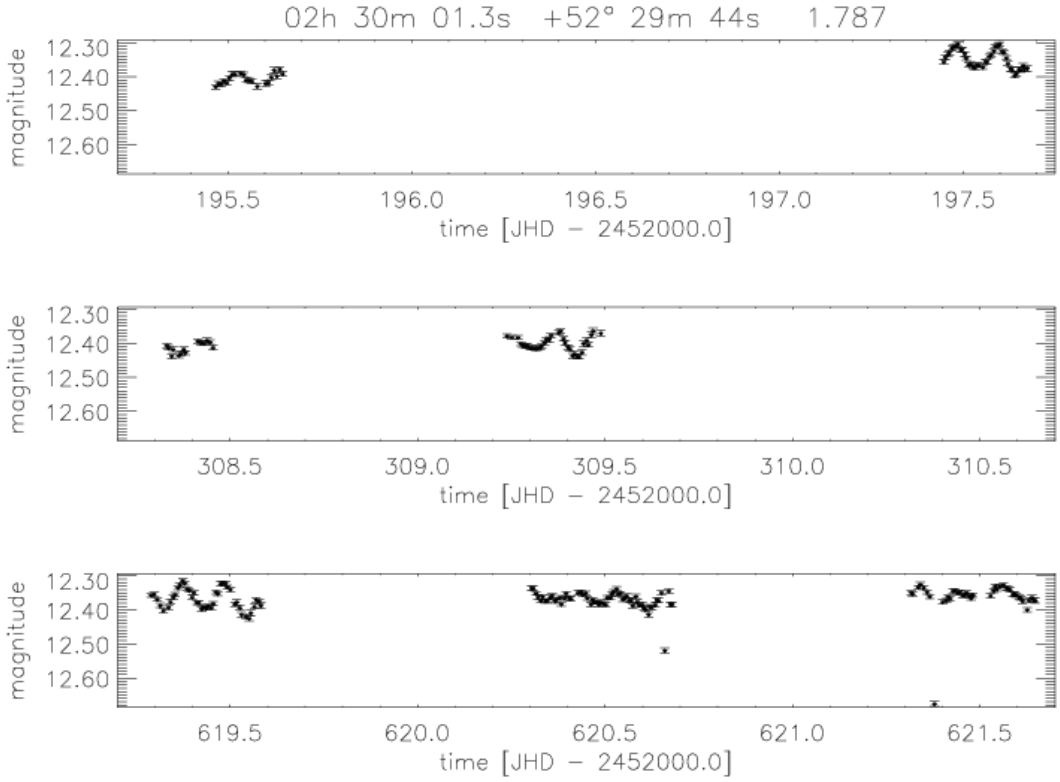

F2 Var 16 (blended !)

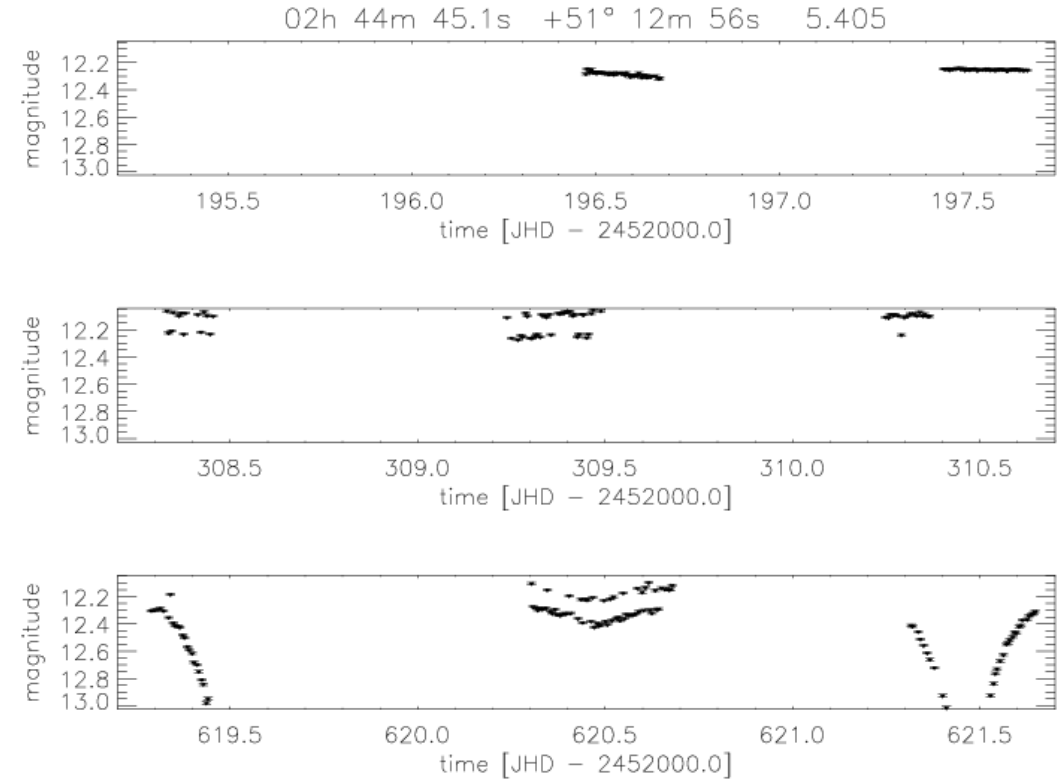

Appendix B: Light curves of variable stars detected in the TLS data set

F2 Var 18

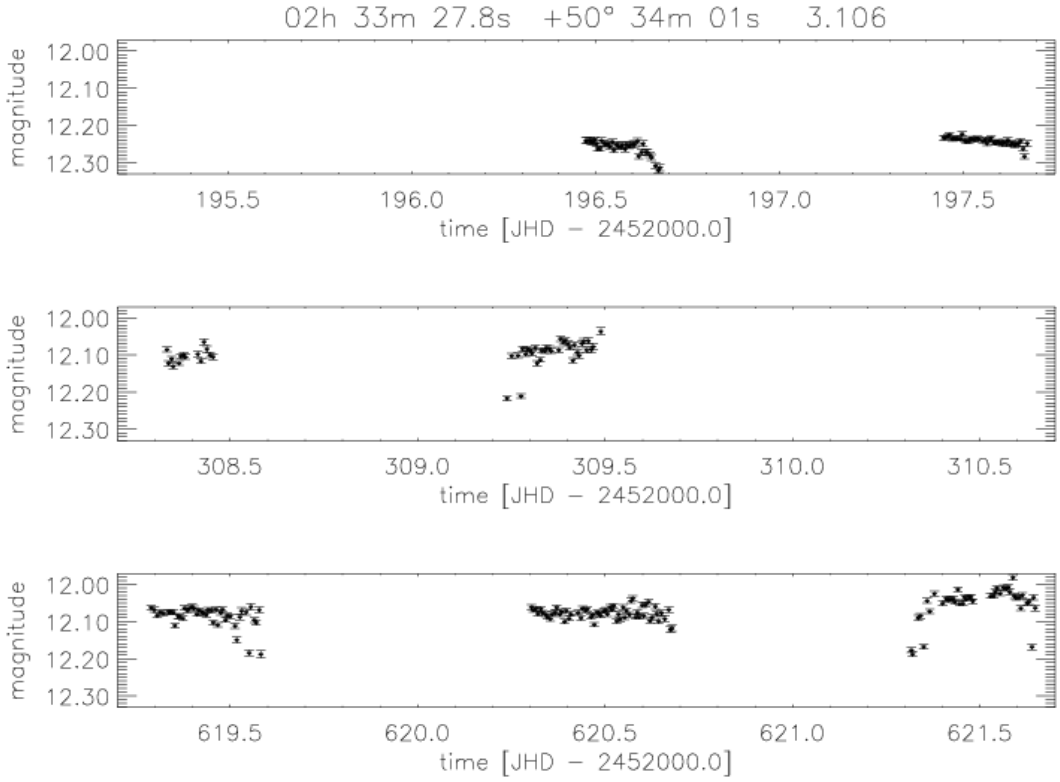

F2 Var 21

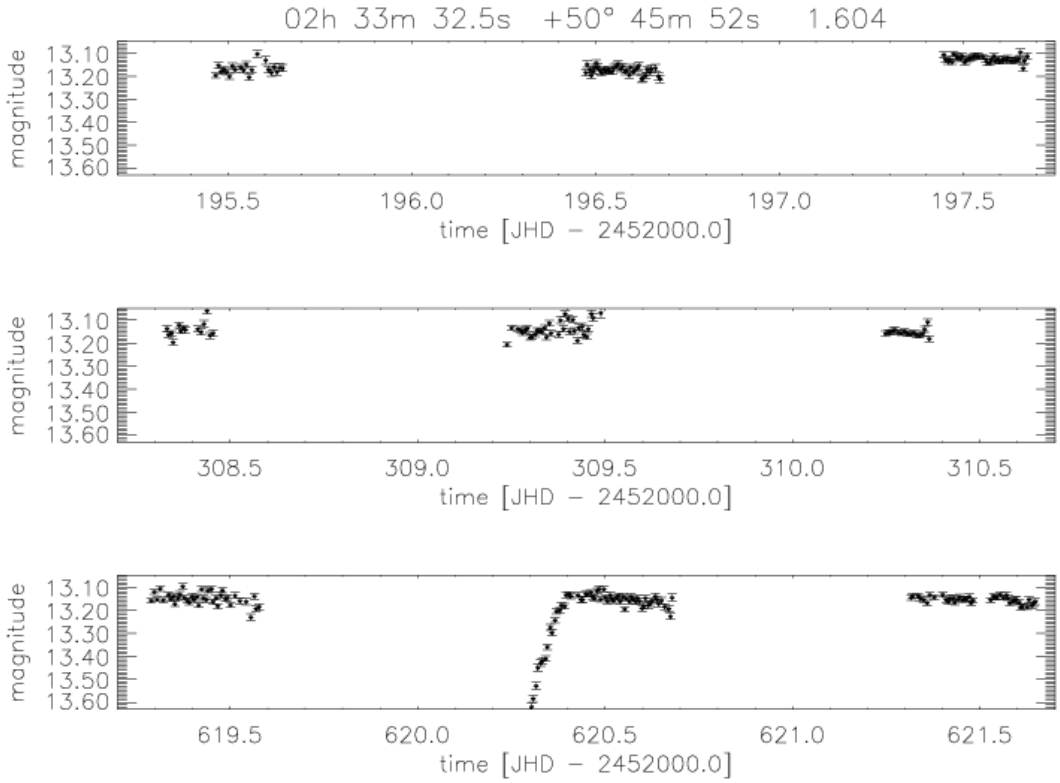

F2 Var 22

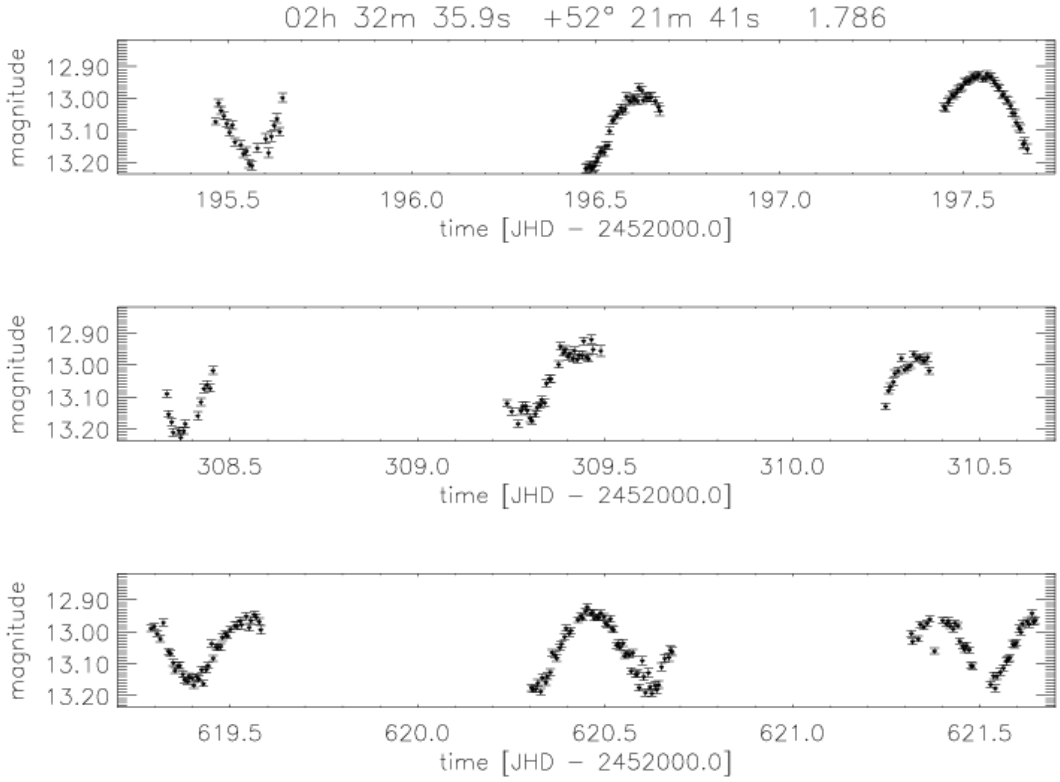

F2 Var 23

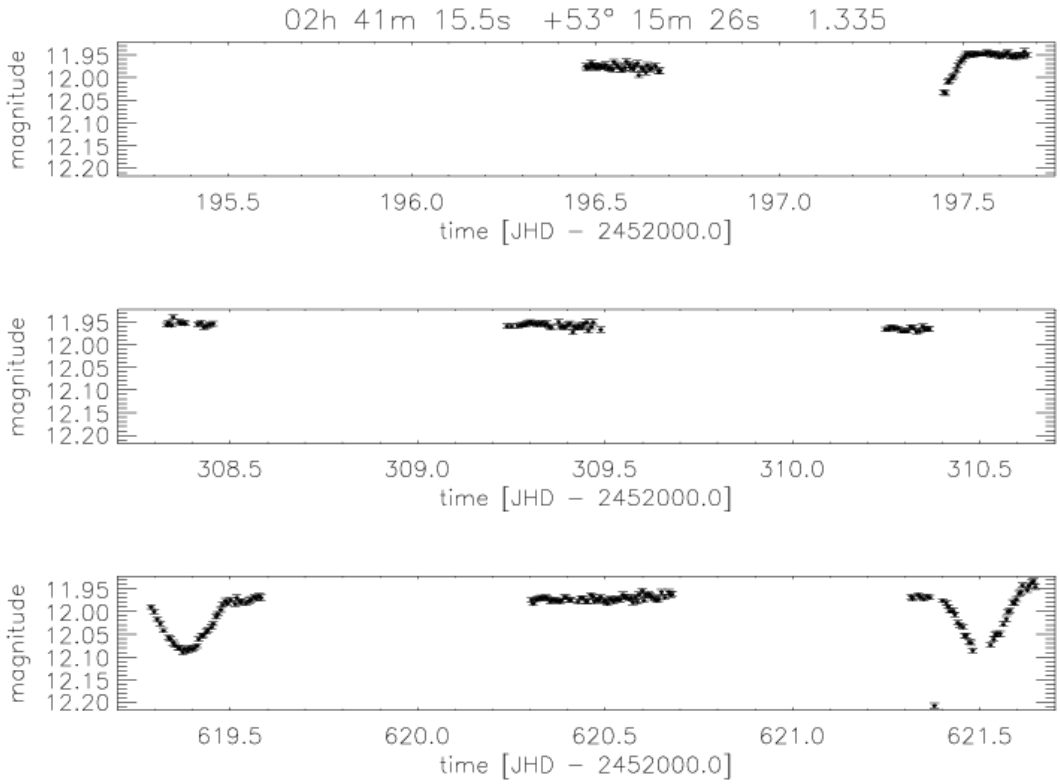

Appendix B: Light curves of variable stars detected in the TLS data set

F2 Var 24

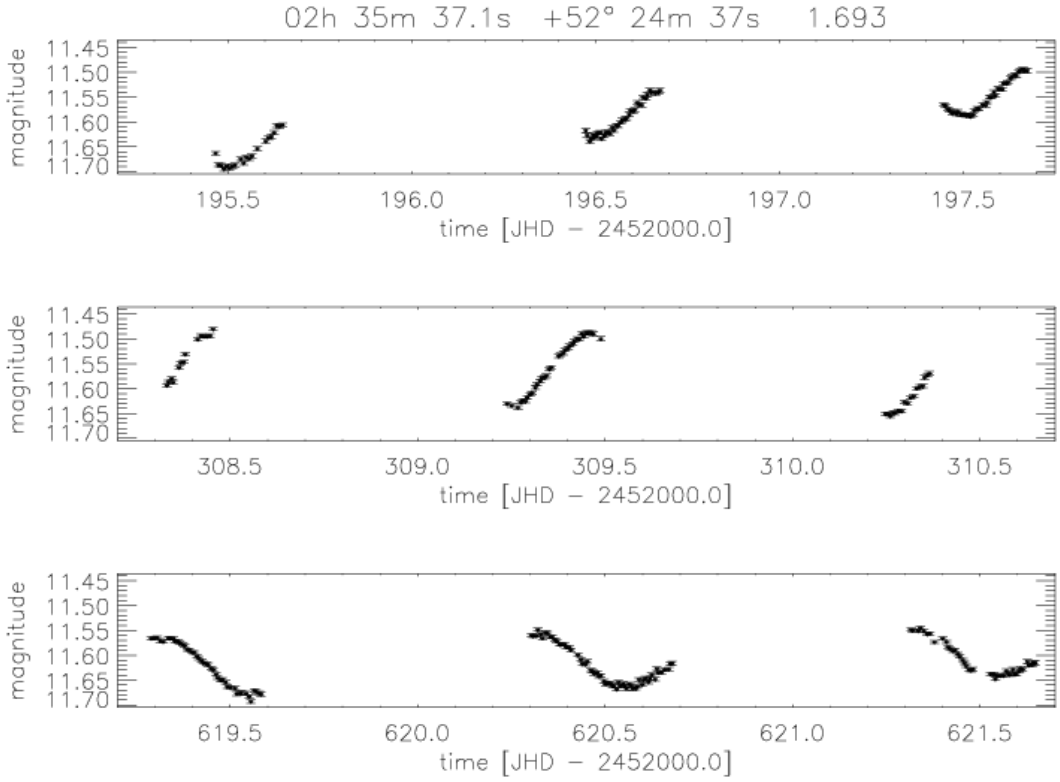

F2 Var 25

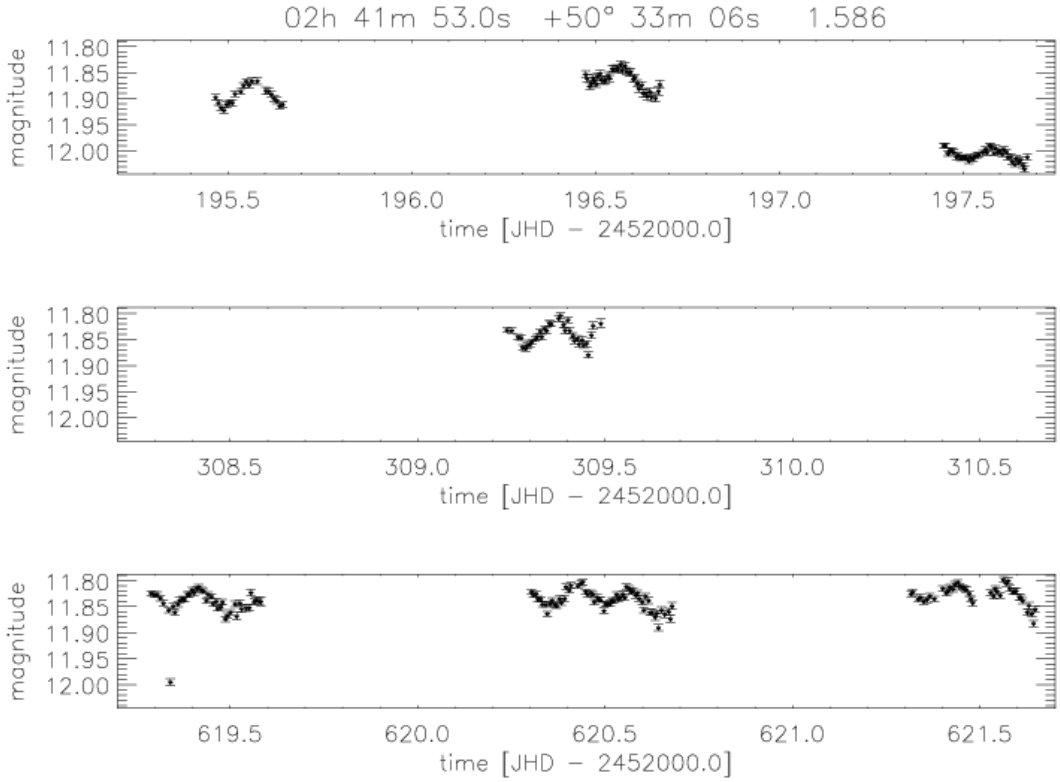

F2 Var 26

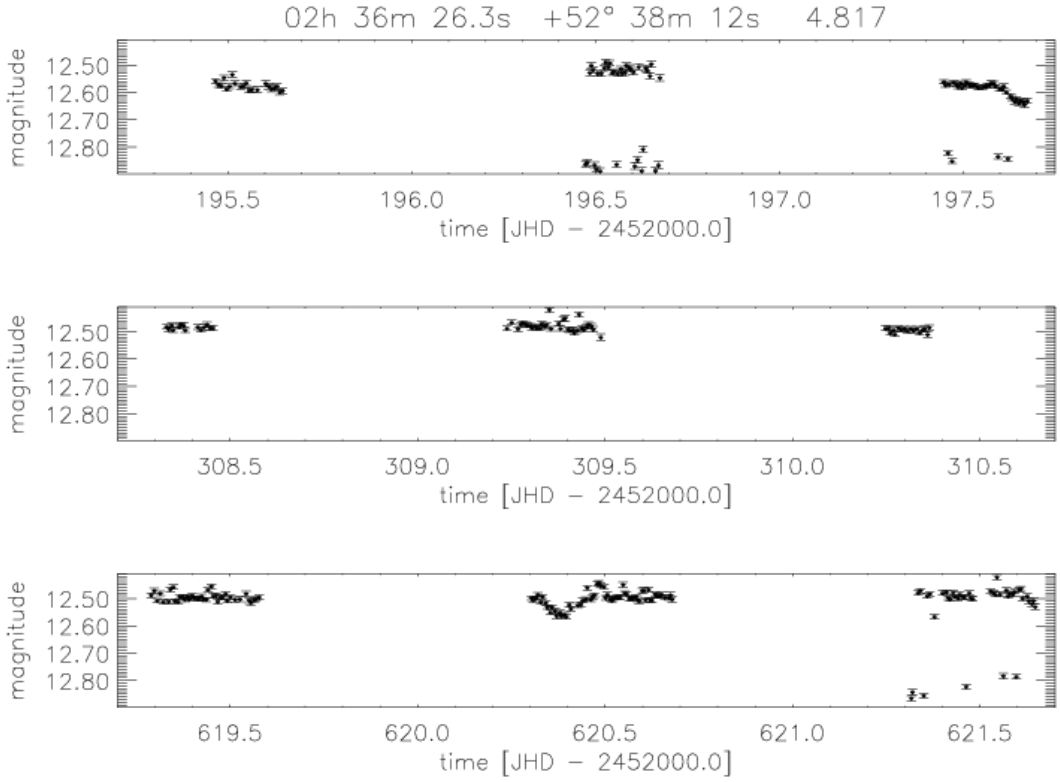

F2 Var 27

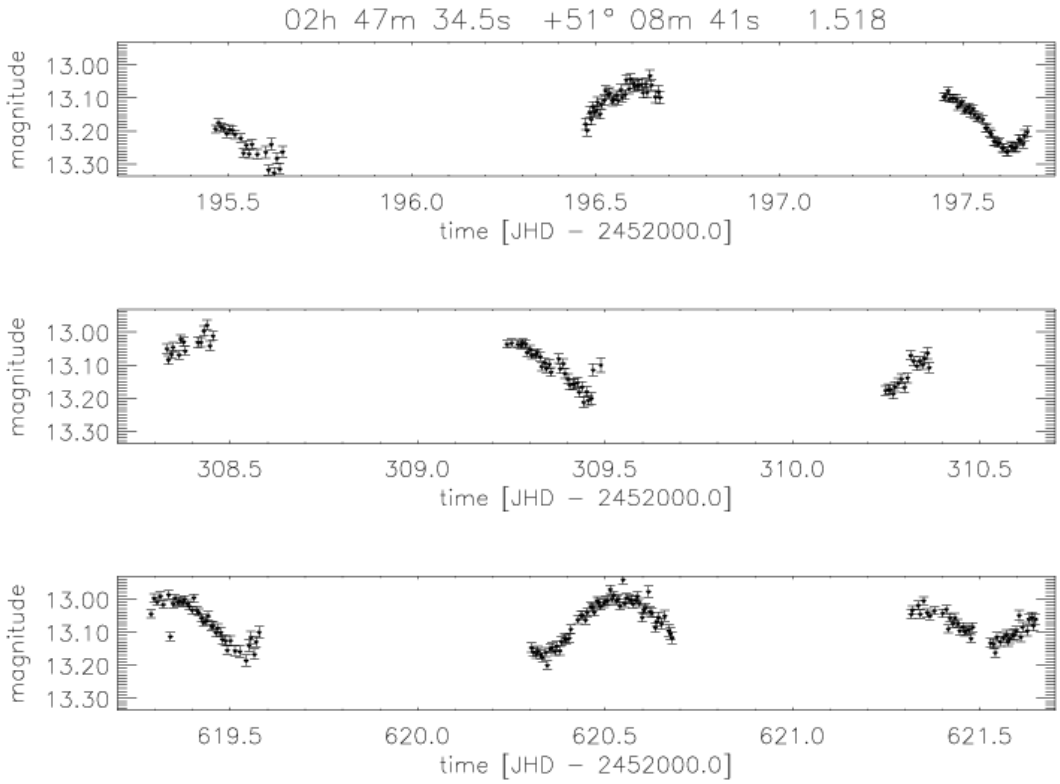

Appendix B: Light curves of variable stars detected in the TLS data set

F2 Var 28

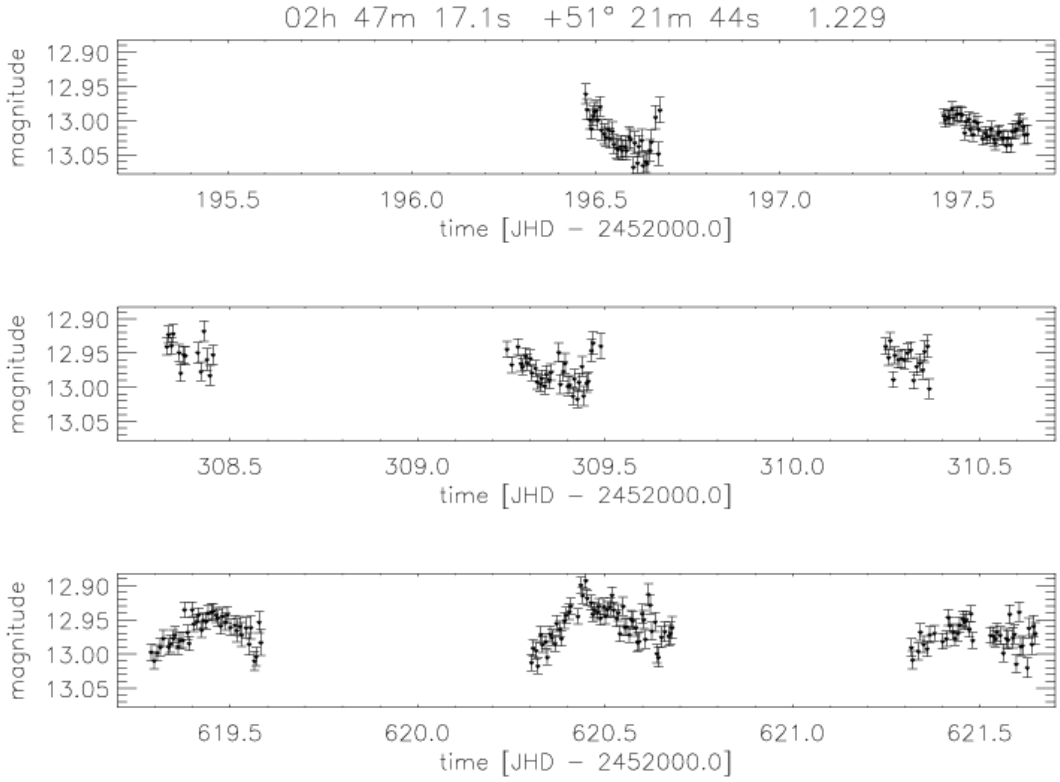

F2 Var 29

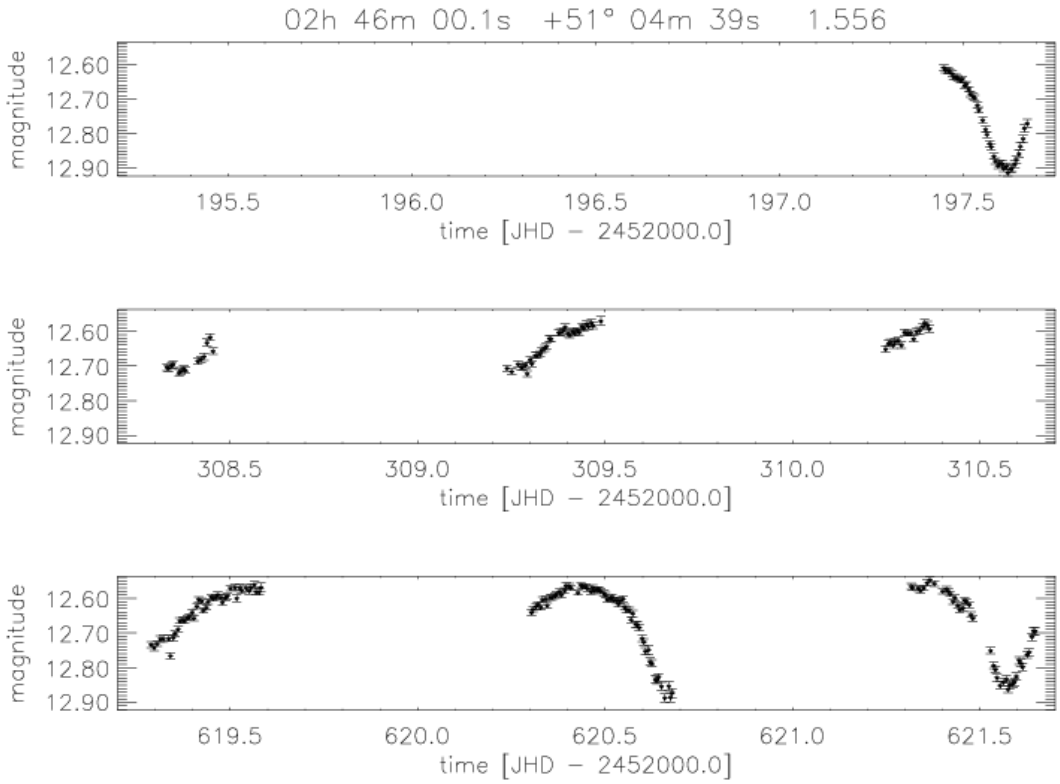

F2 Var 30

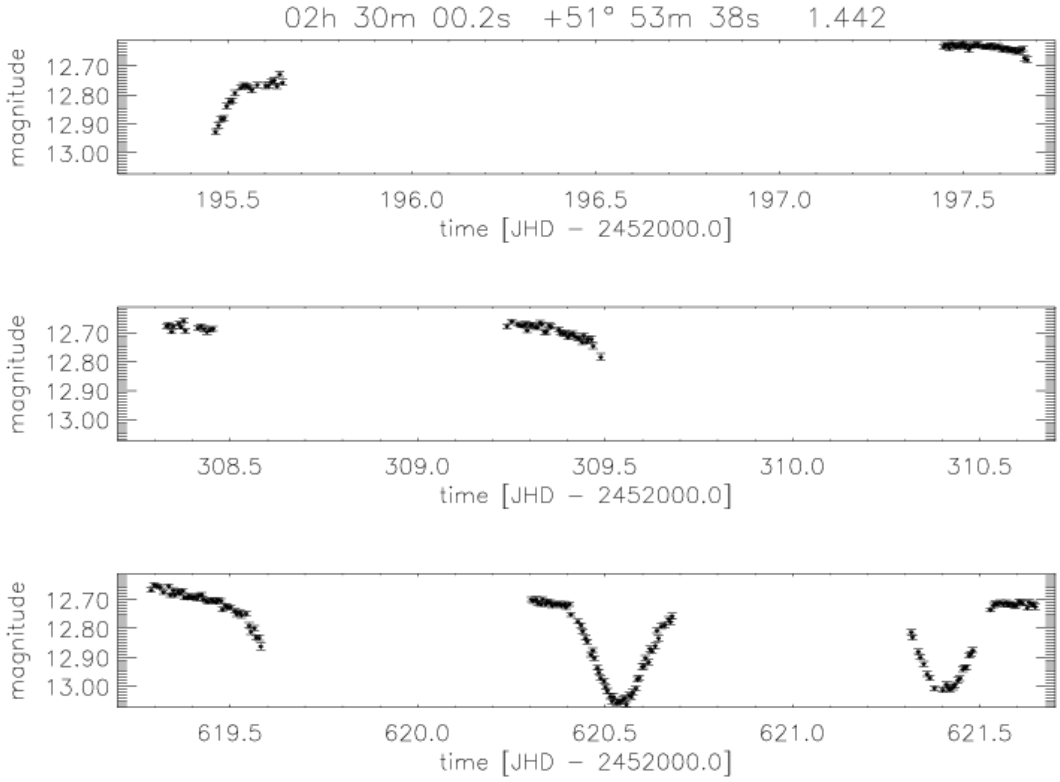

F2 Var 31

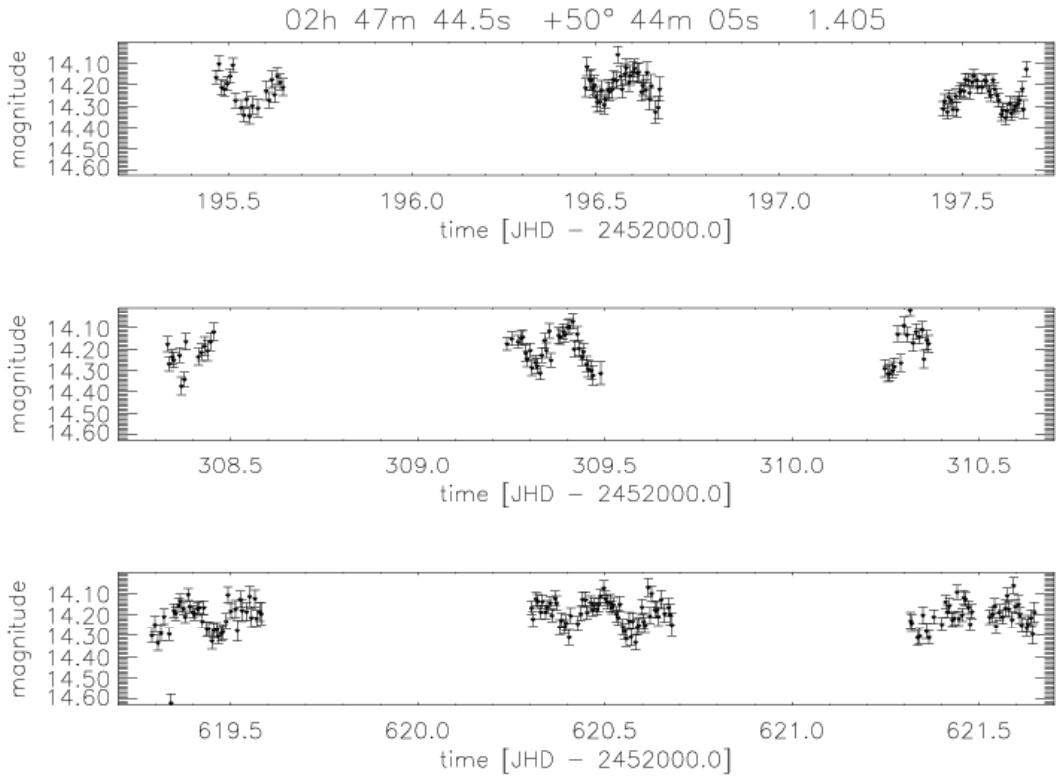

Appendix B: Light curves of variable stars detected in the TLS data set

F2 Var 34

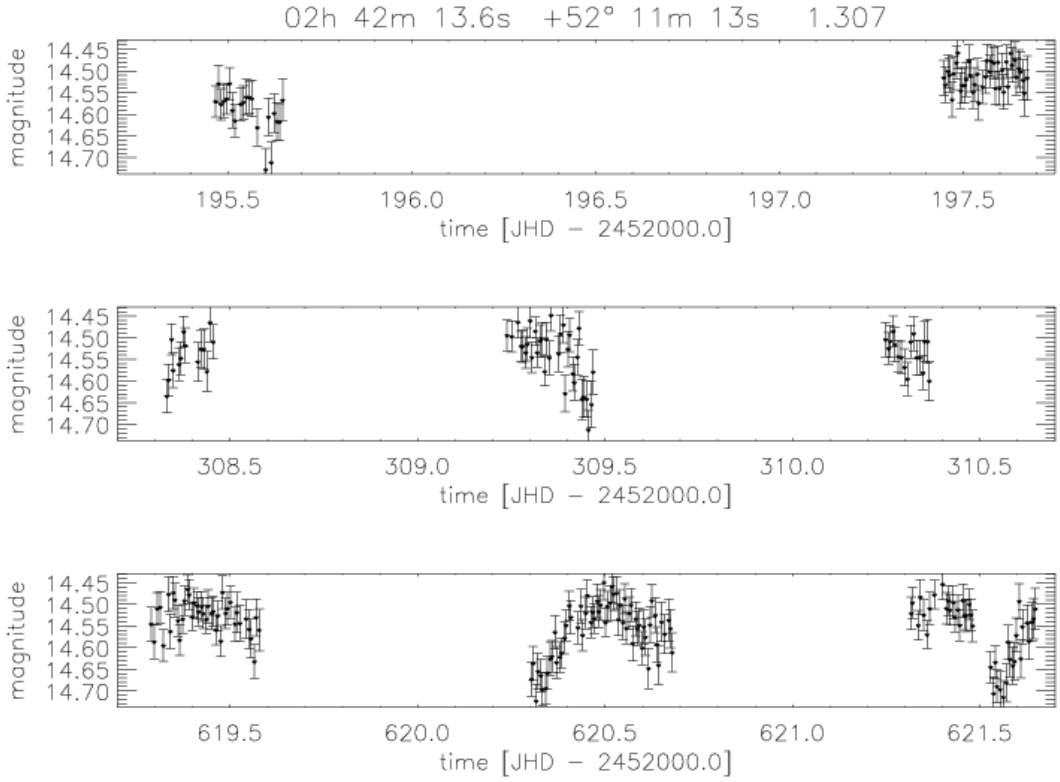

F2 Var 35

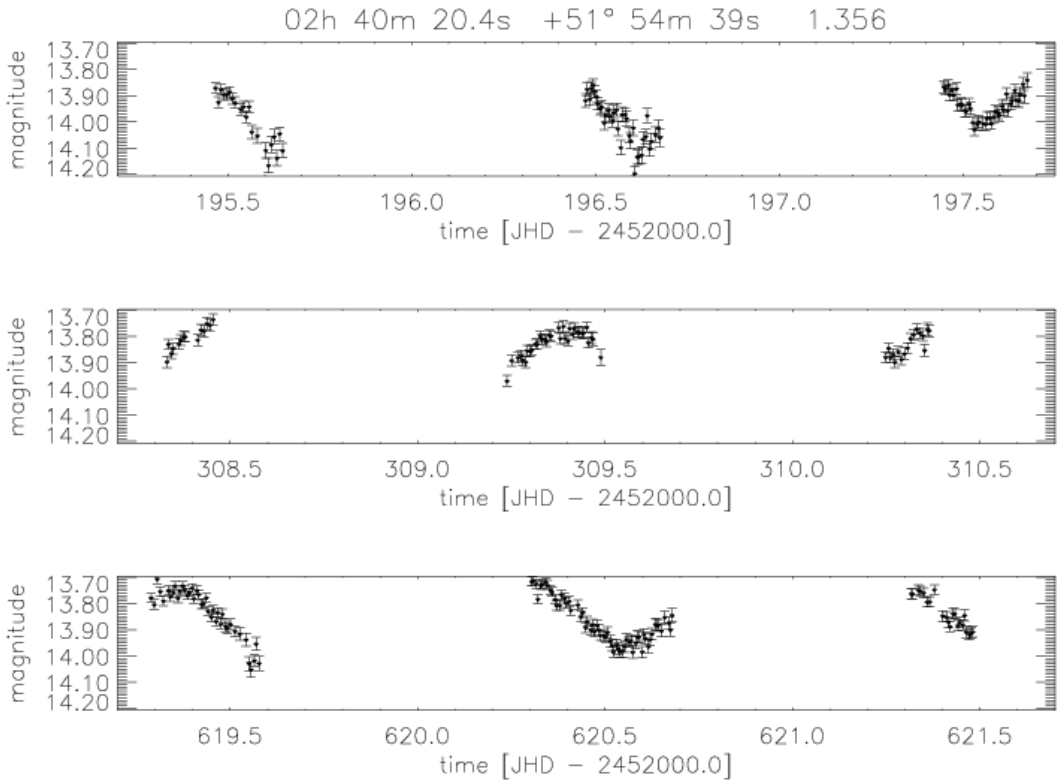

F2 Var 36:

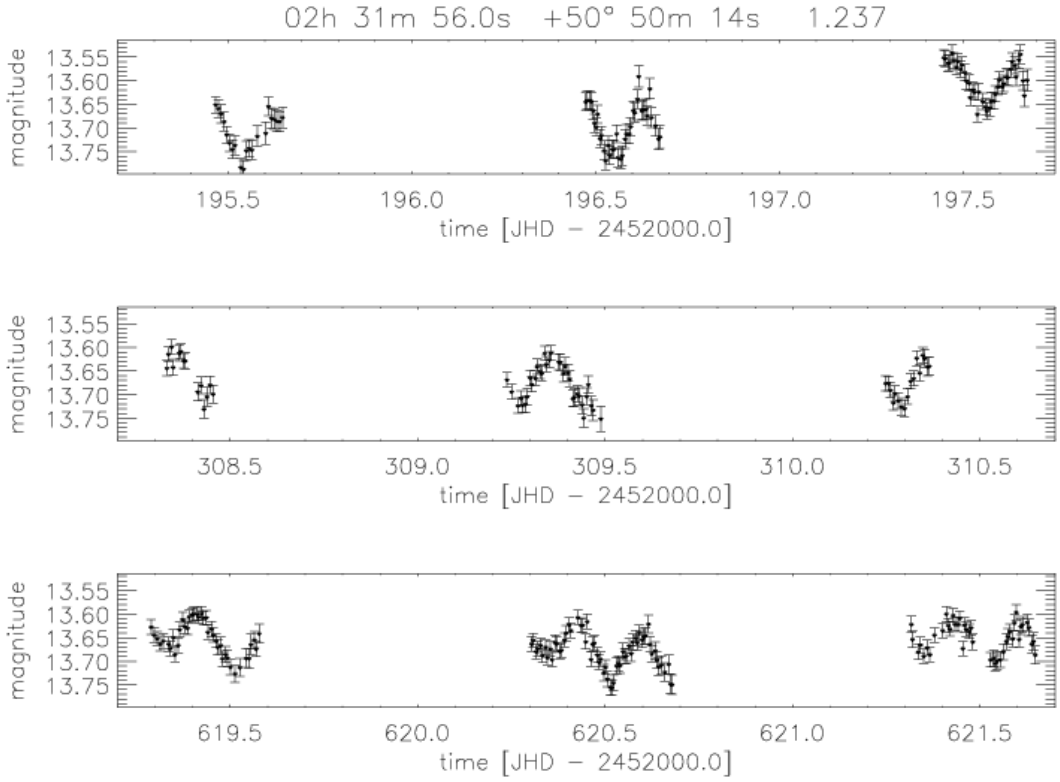

F2 Var 38:

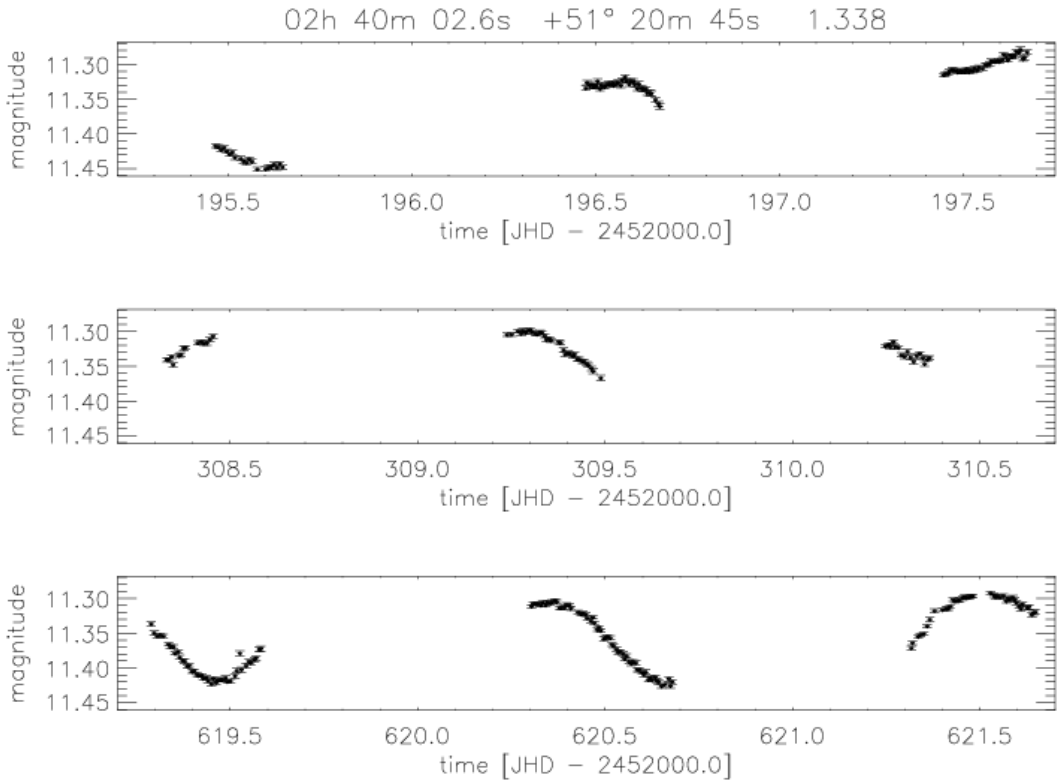

Appendix B: Light curves of variable stars detected in the TLS data set

F2 Var 39

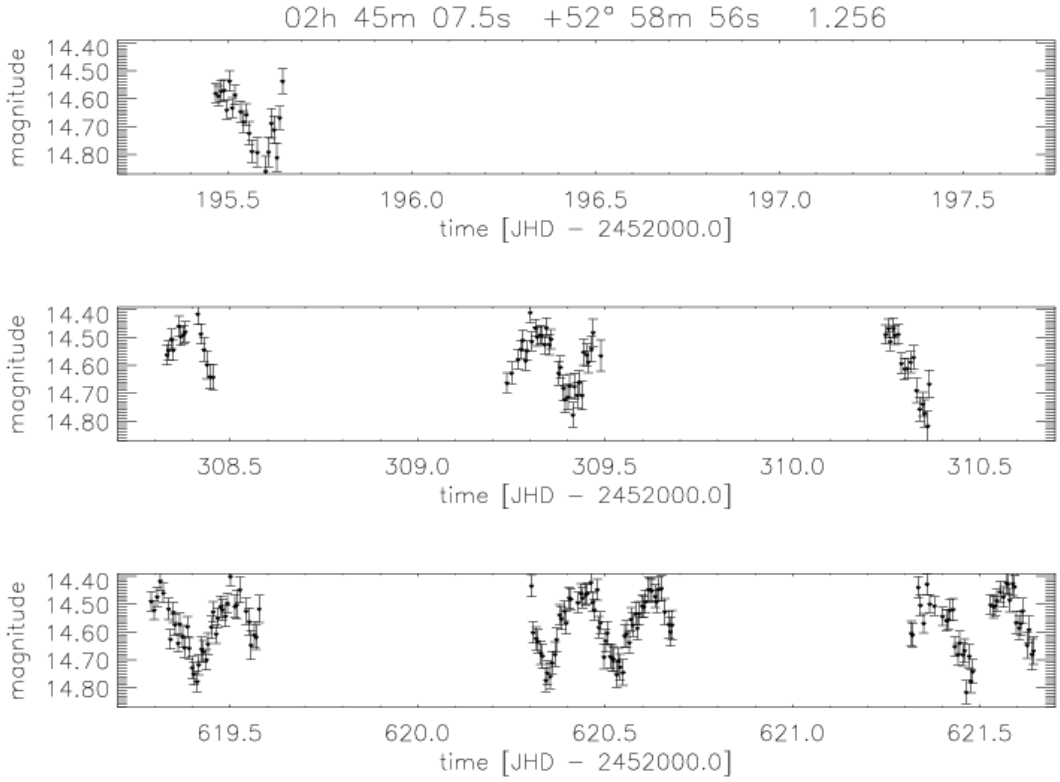

F2 Var 40

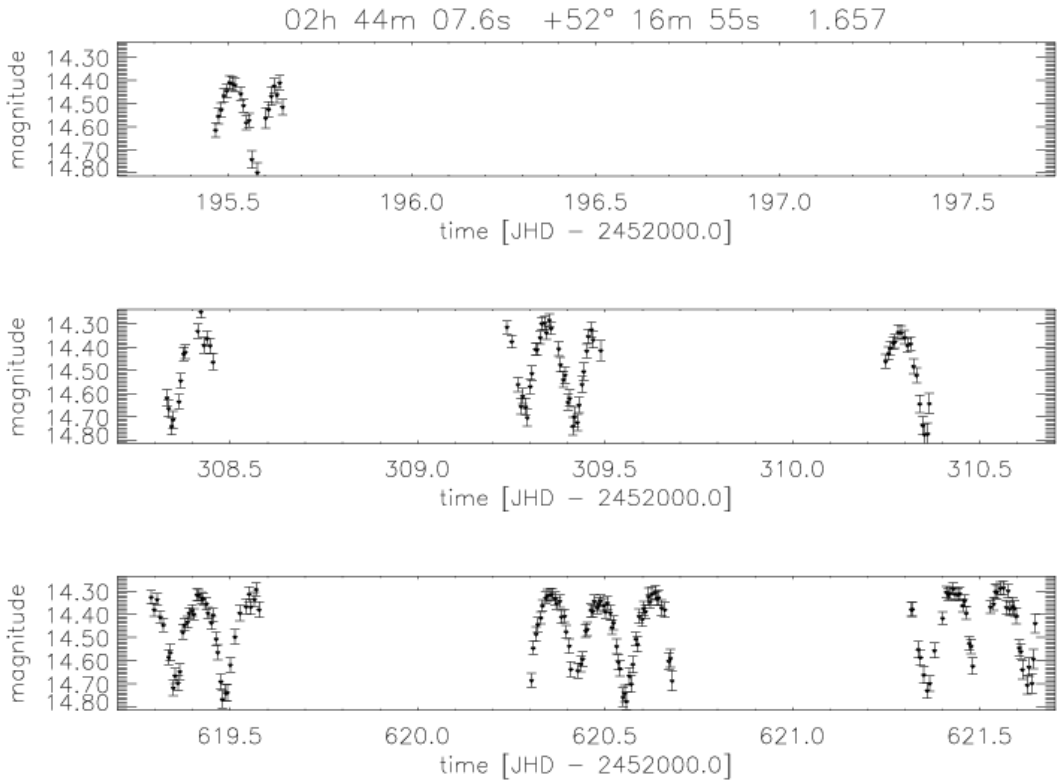

F2 Var 41

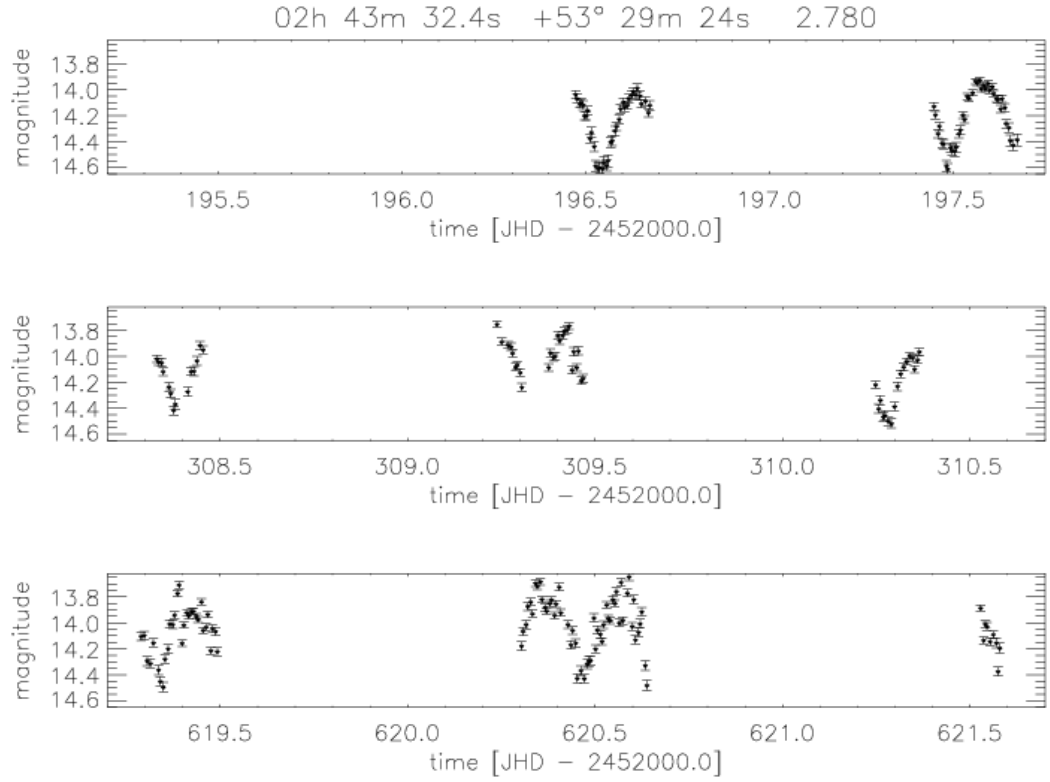

F2 Var 42

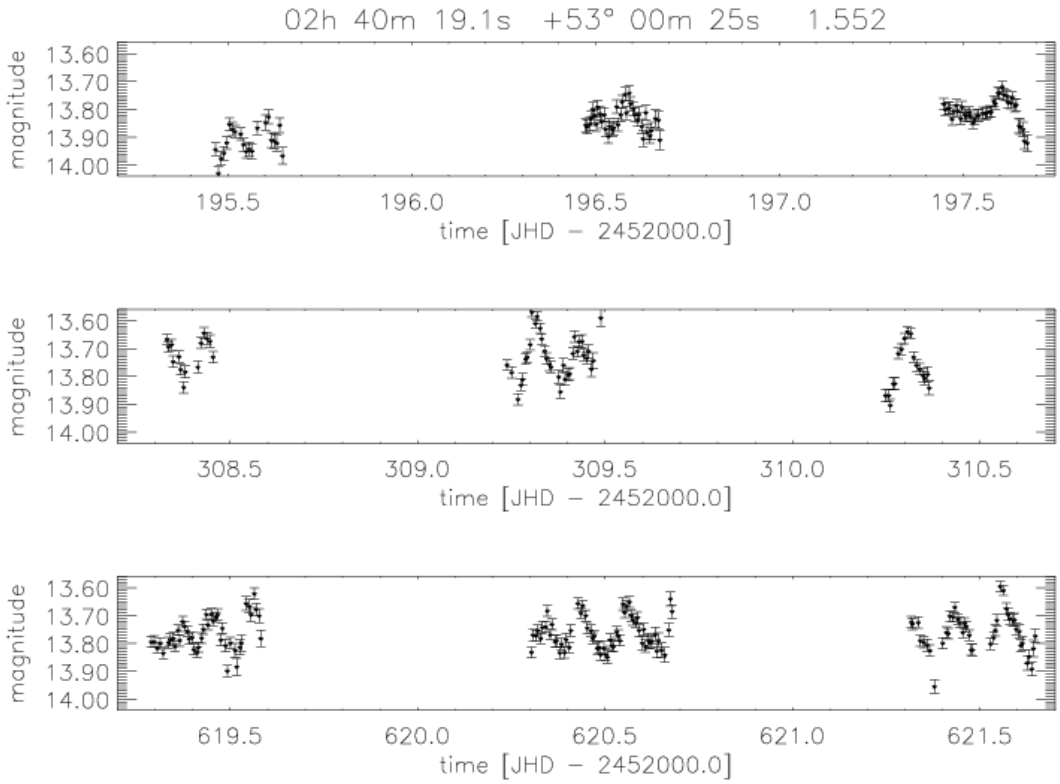

Appendix B: Light curves of variable stars detected in the TLS data set

F2 Var 43

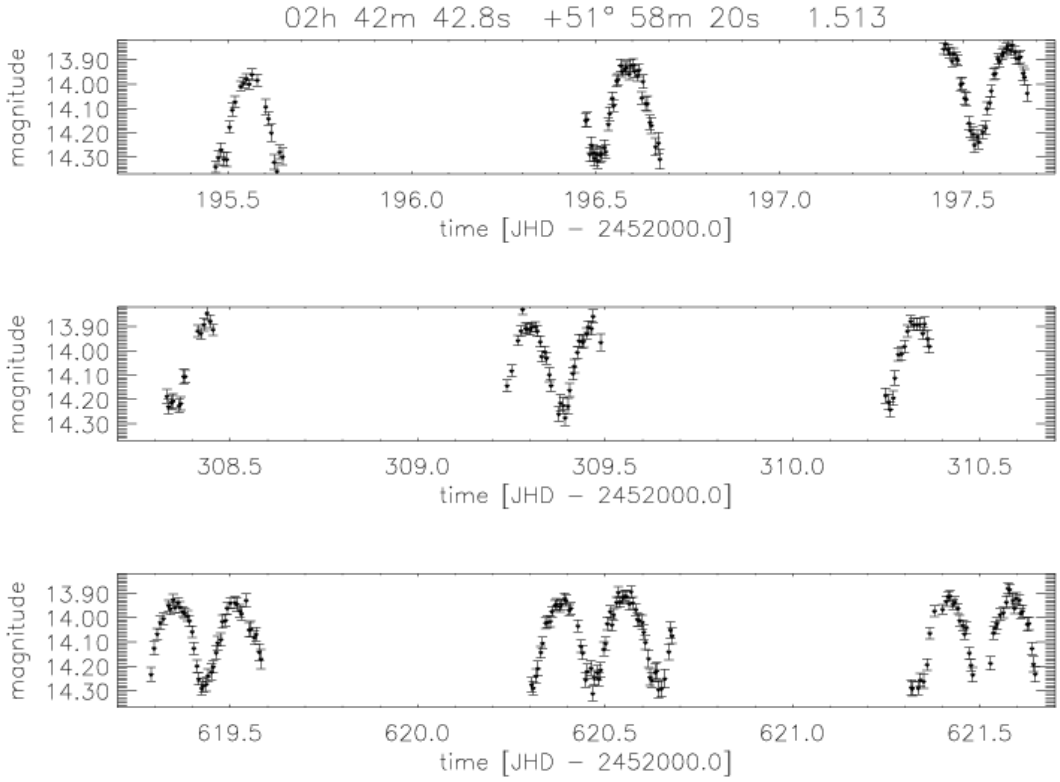

F2 Var 44

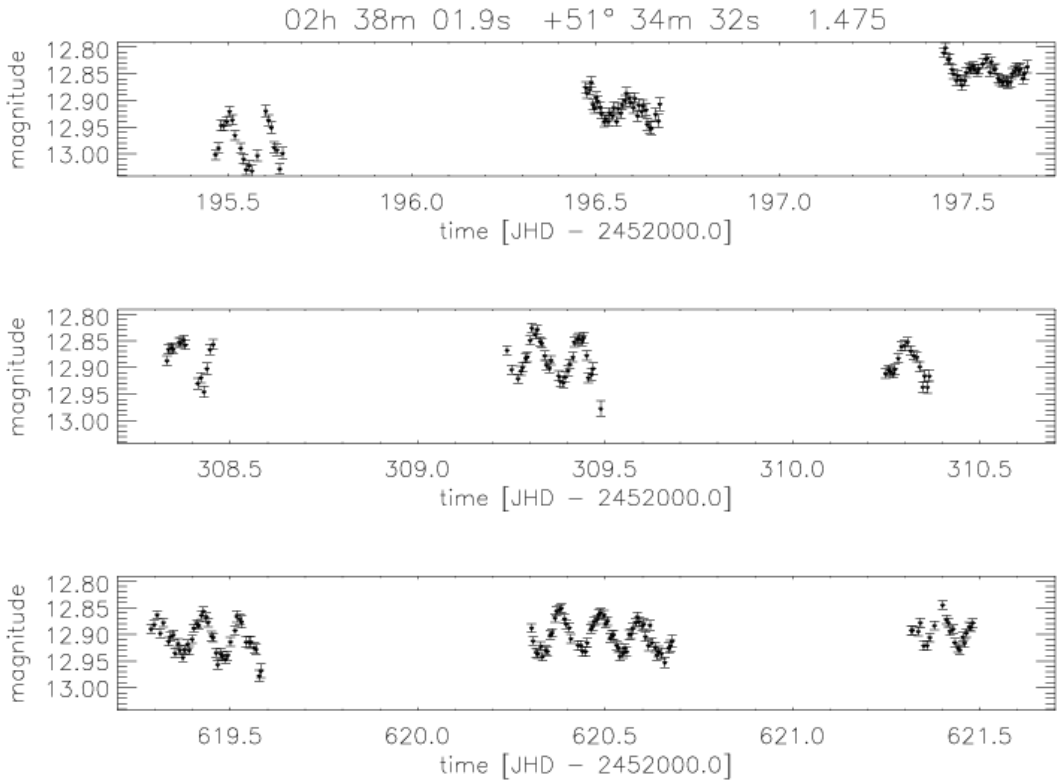

F2 Var 46

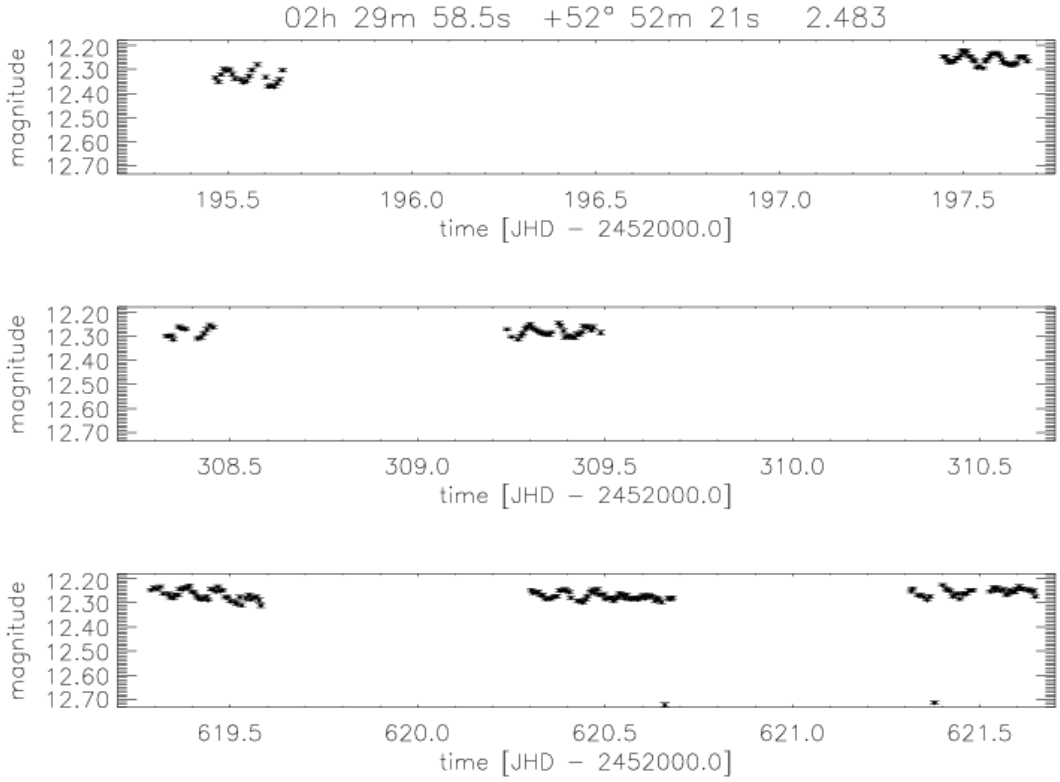

F2 Var 47

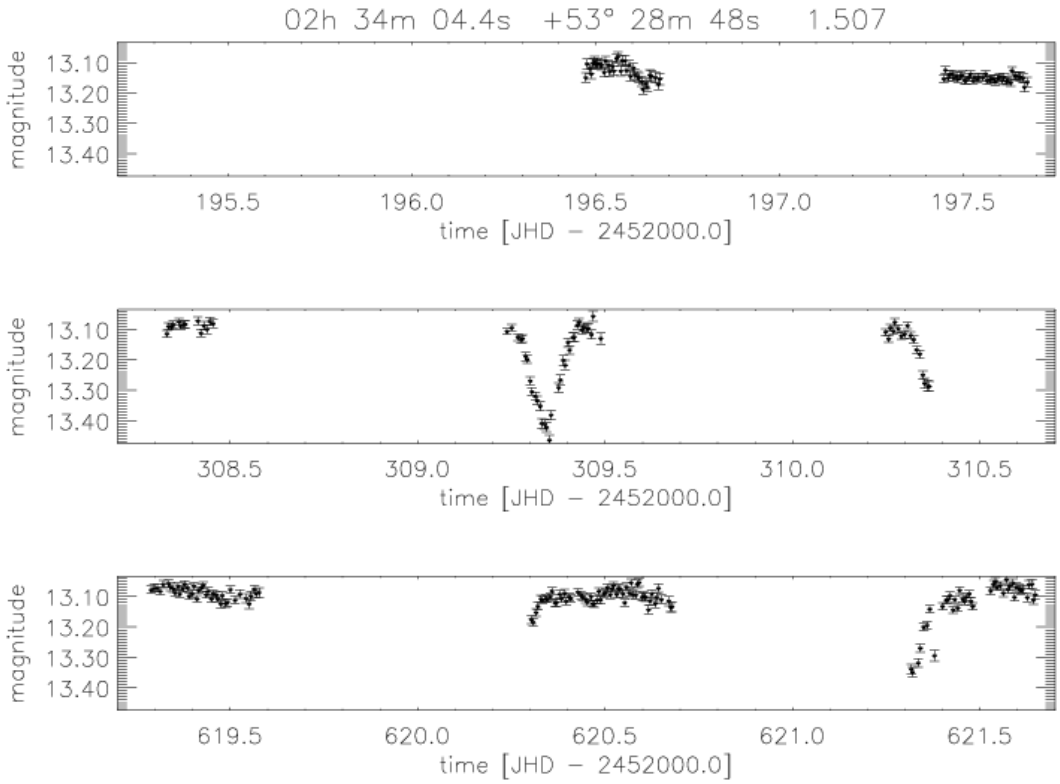

Appendix B: Light curves of variable stars detected in the TLS data set

F2 Var 48

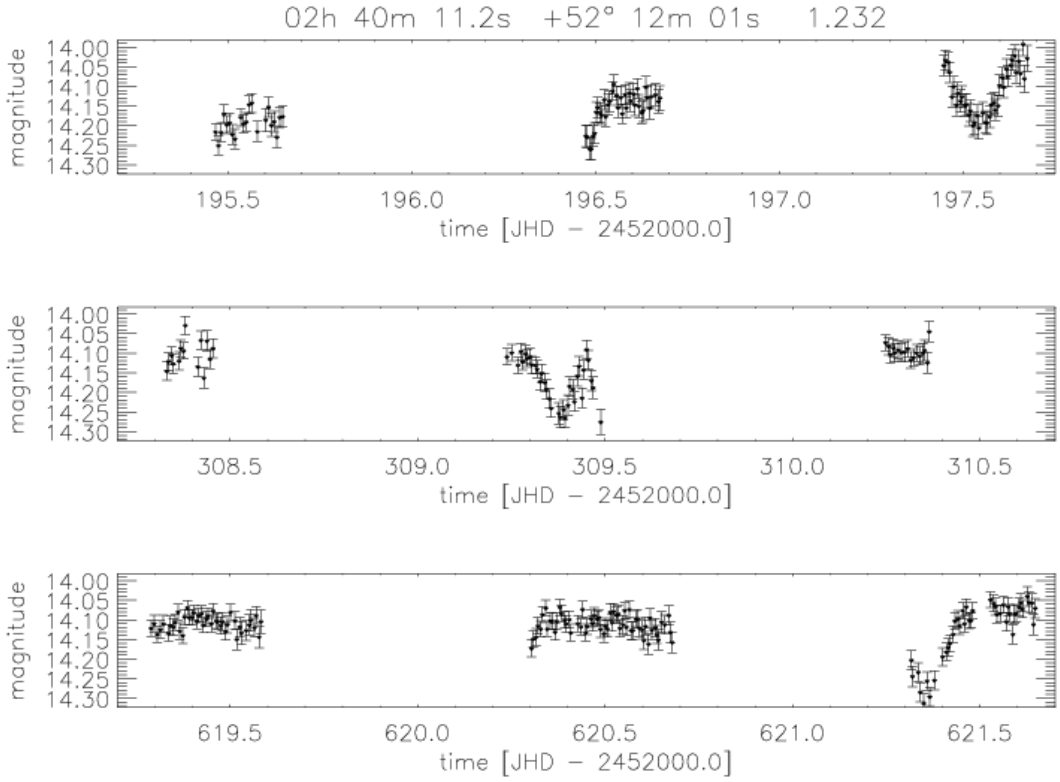

F2 Var 49

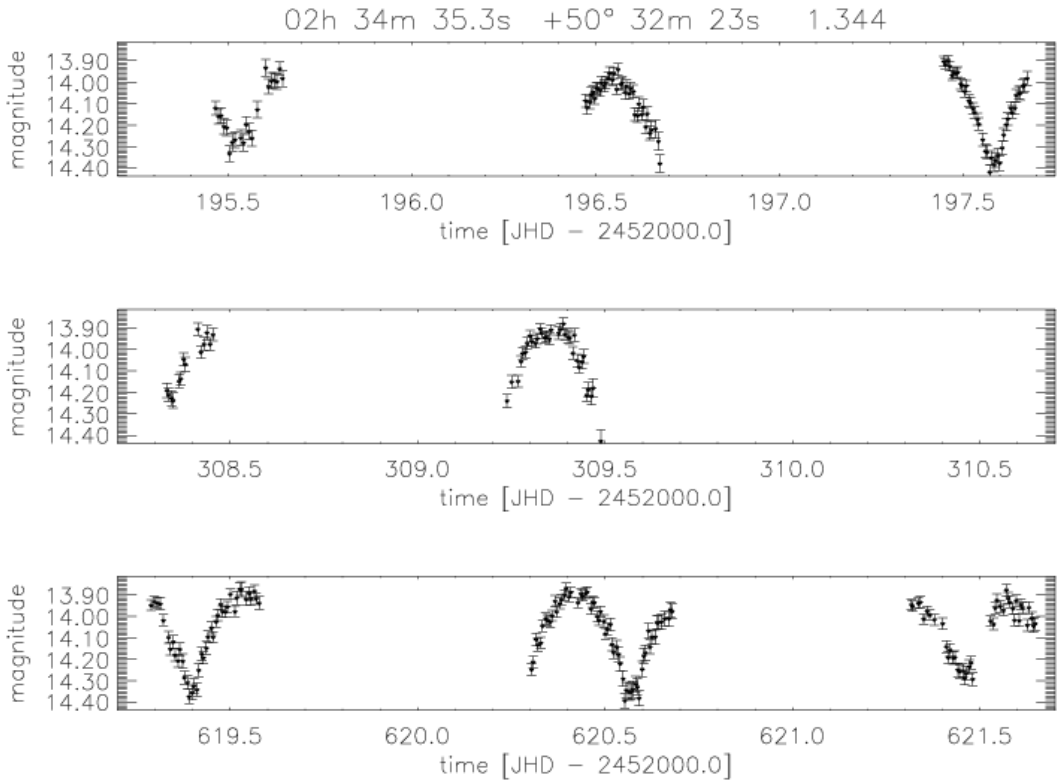

F2 Var 50

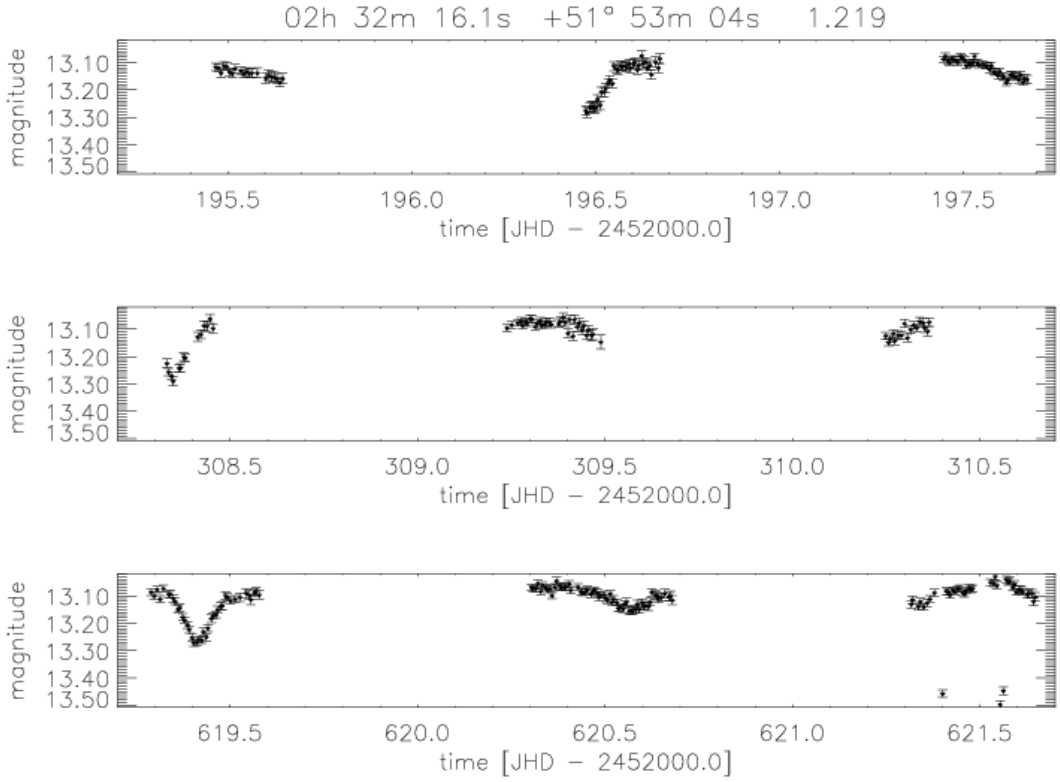

F2 Var51

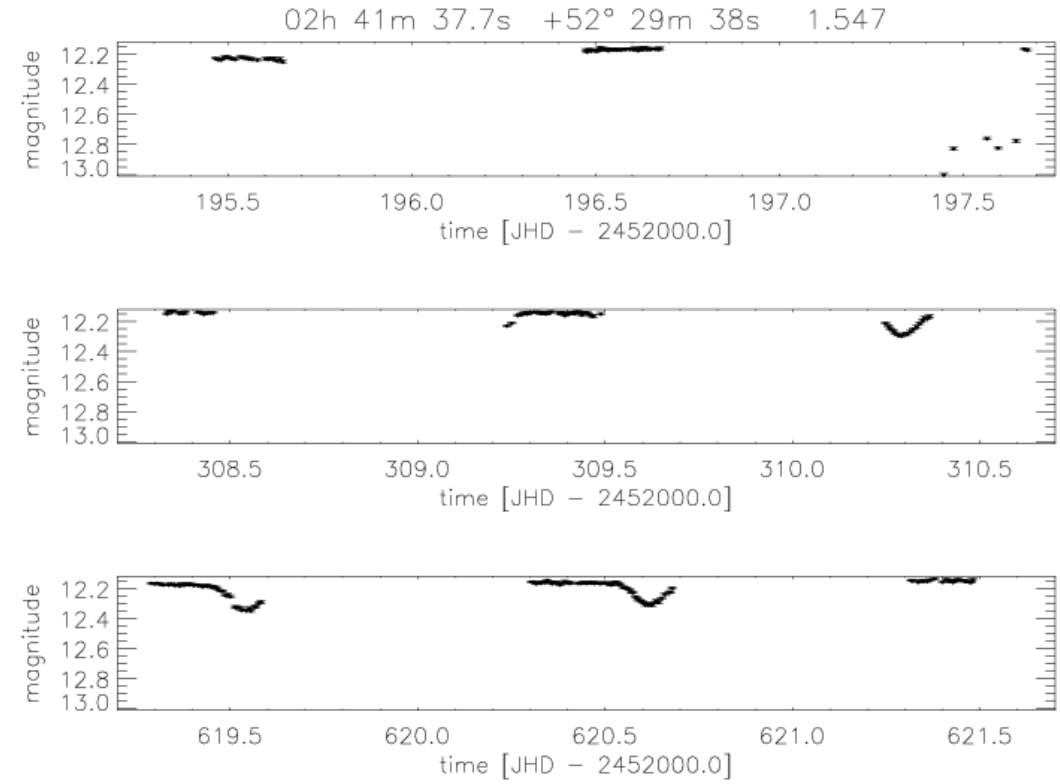

Appendix B: Light curves of variable stars detected in the TLS data set

F2 Var52

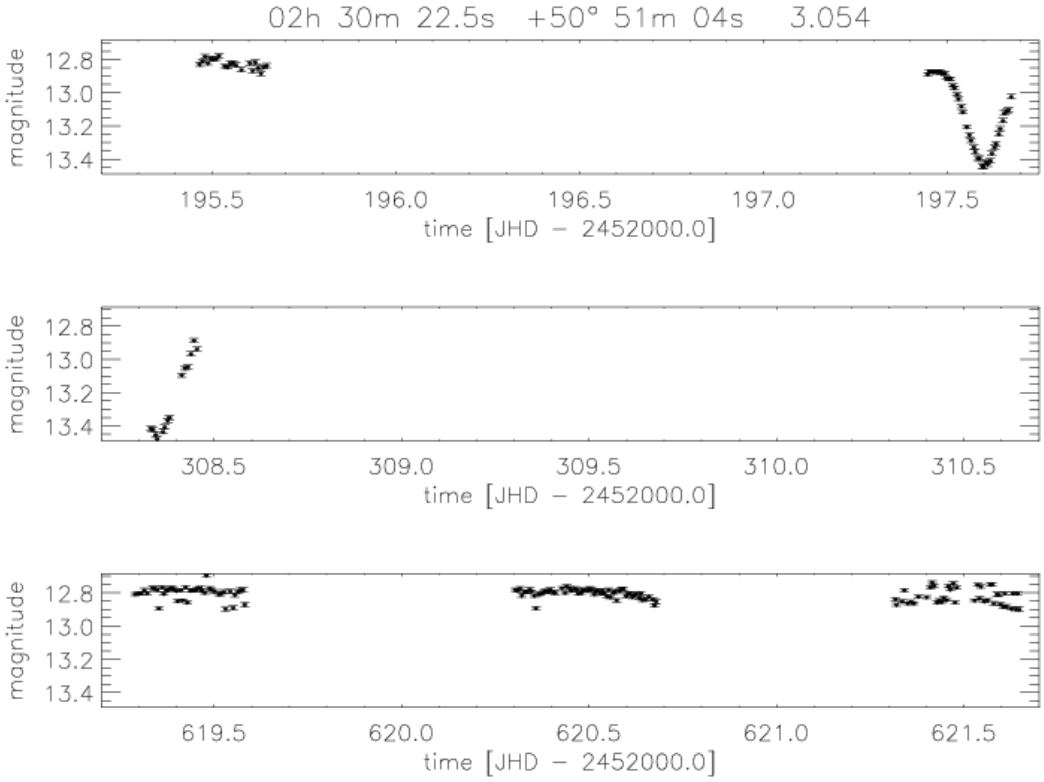

F2 Var 53

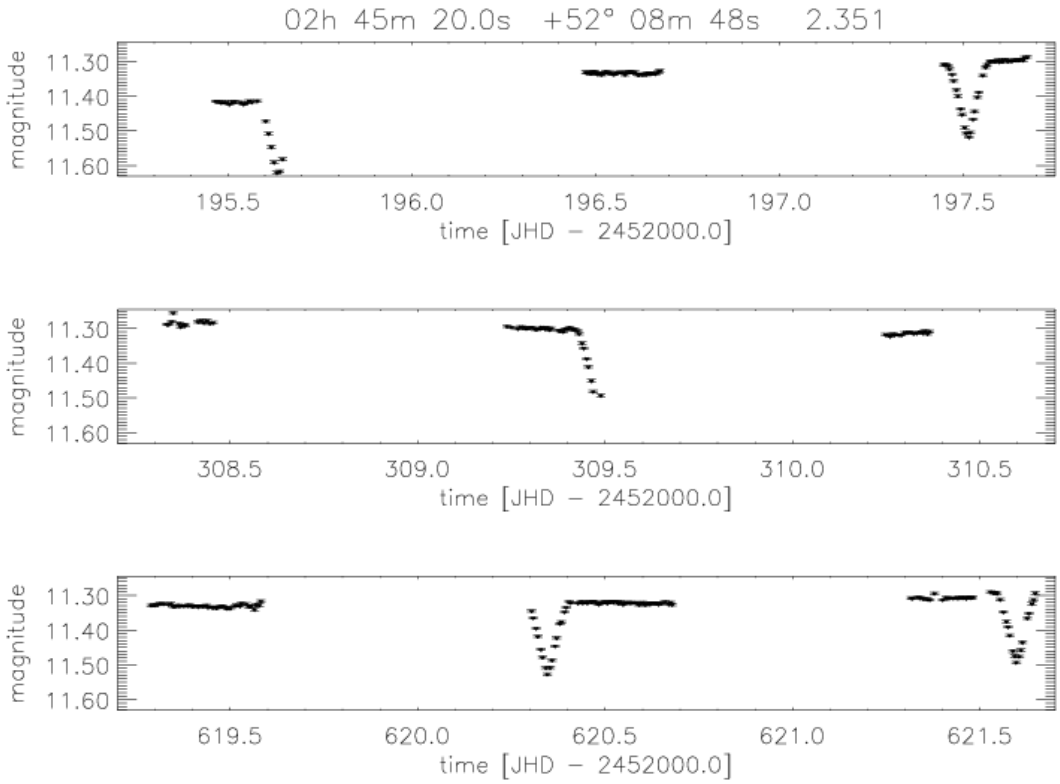

Appendix B: Light curves of variable stars detected in the TLS data set

F2 Var 54

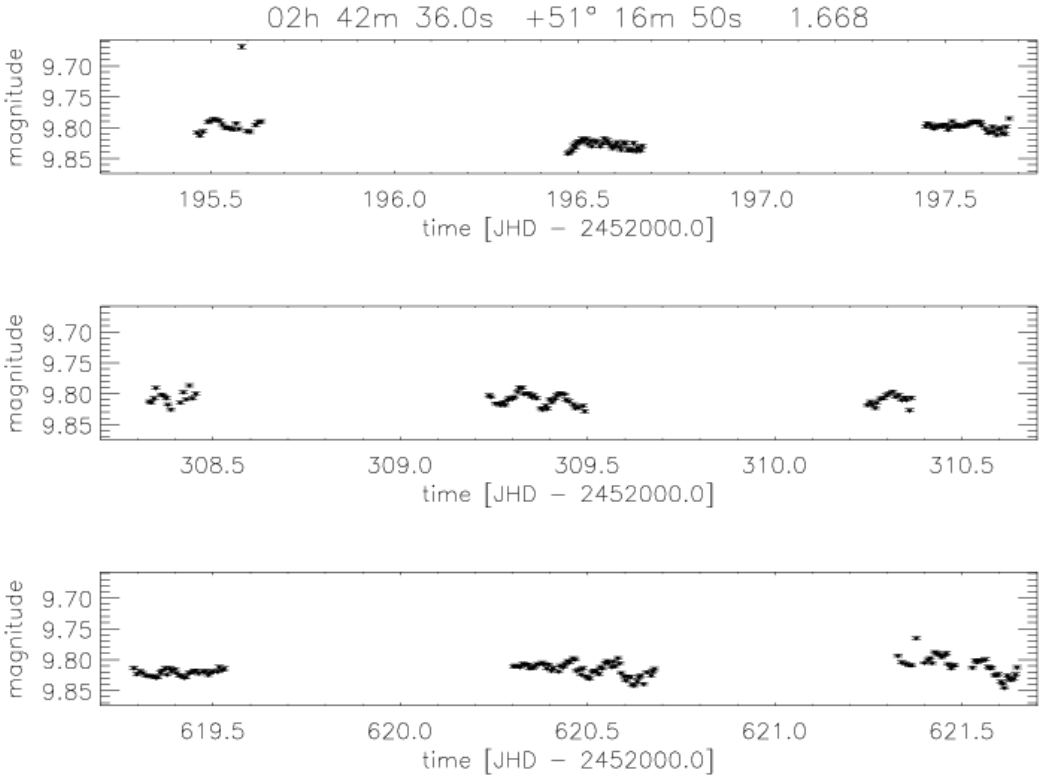

F2 Var 55

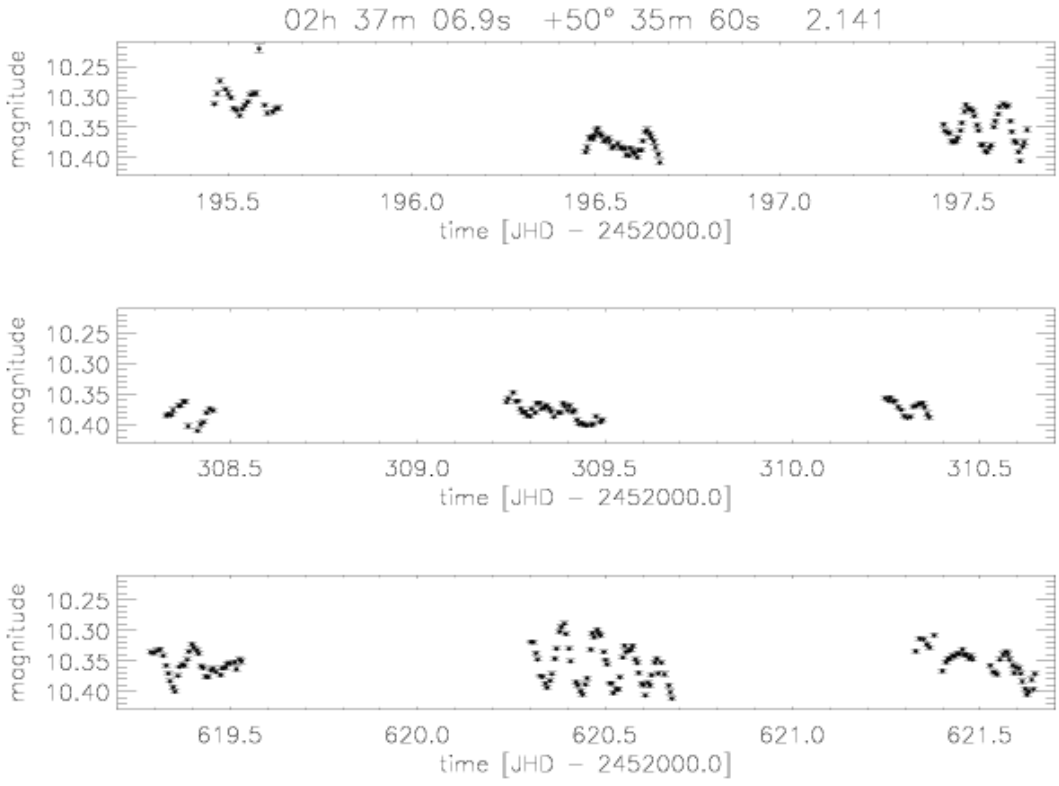

Appendix B: Light curves of variable stars detected in the TLS data set

F2 Var 56

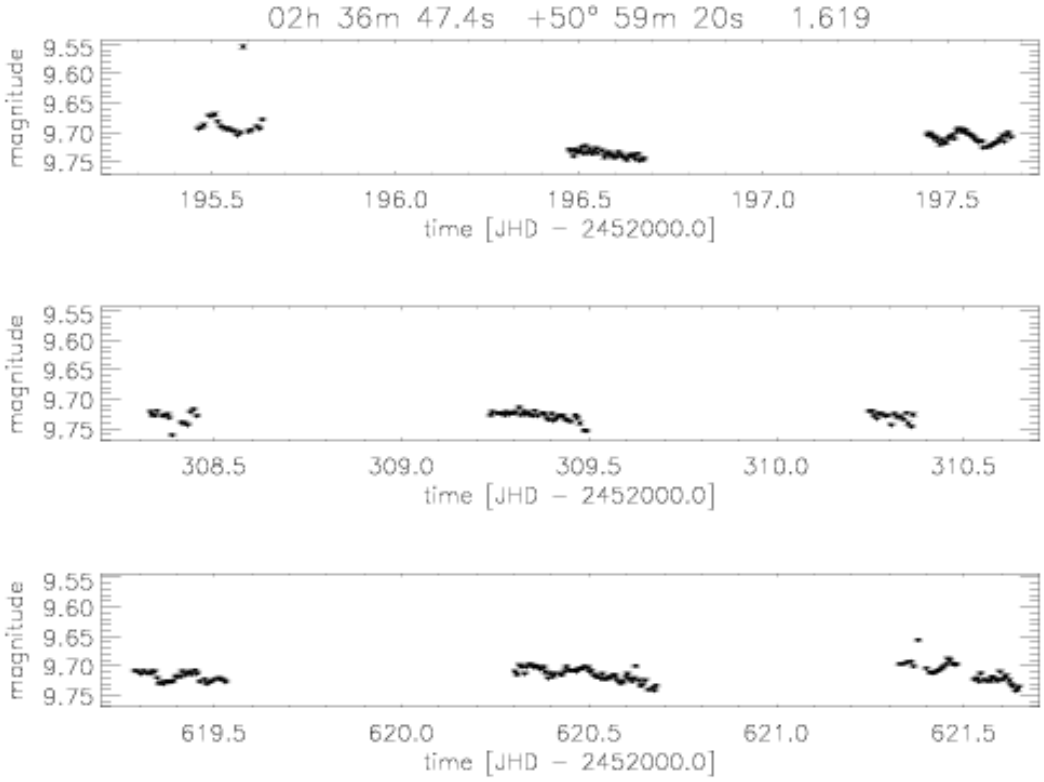

BEST C2

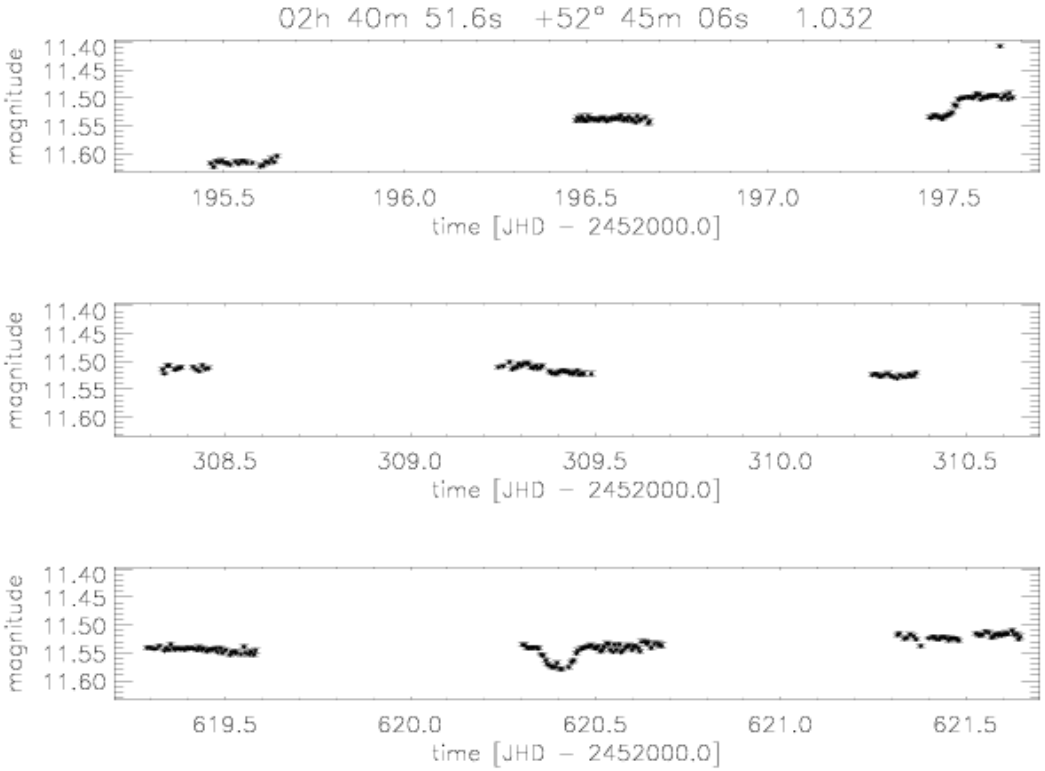

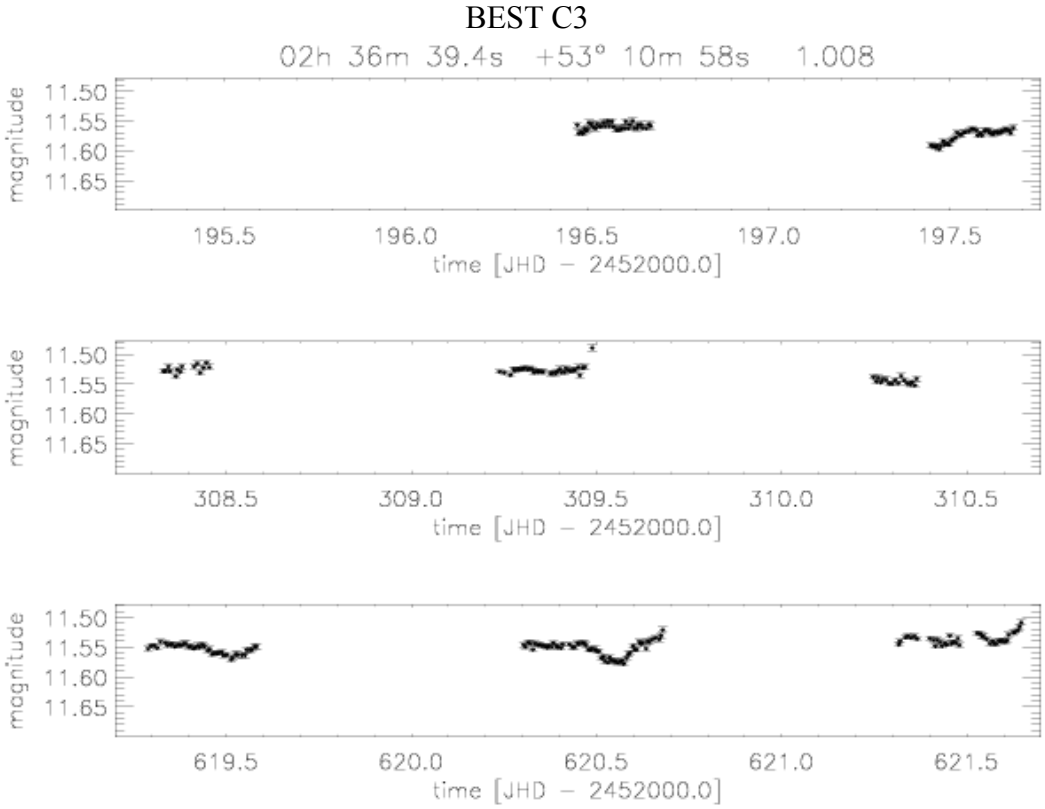

B.2.3. Target field 15

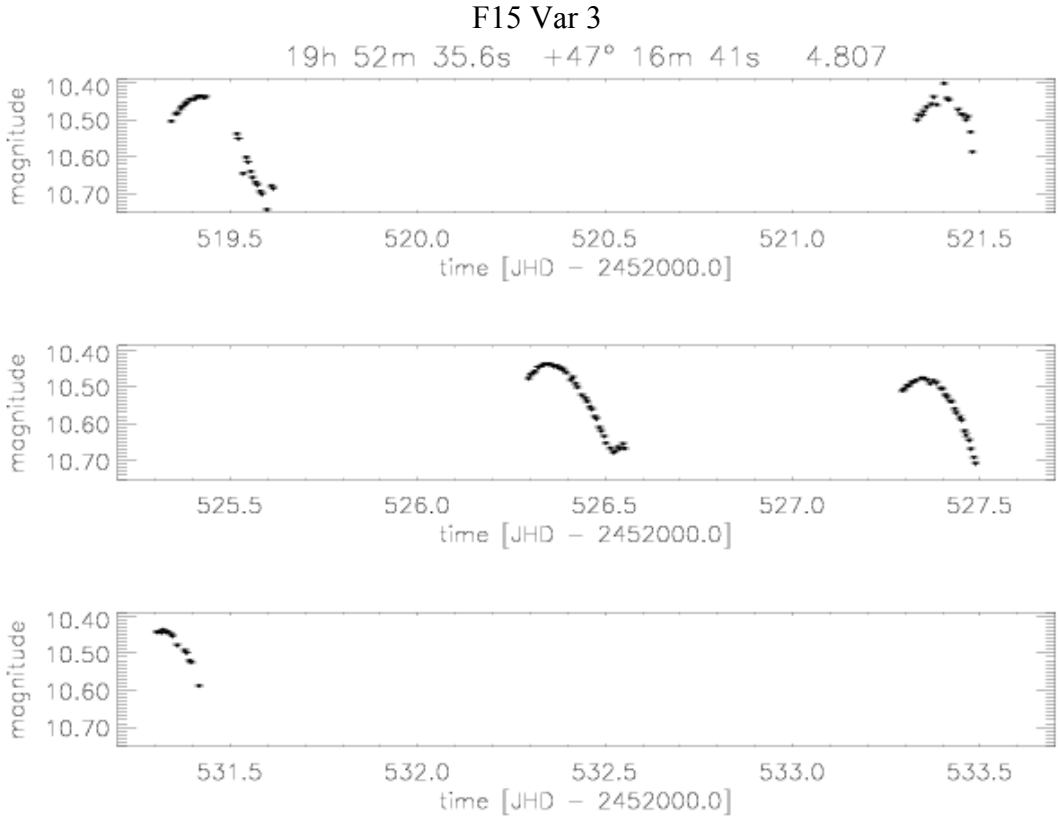

Appendix B: Light curves of variable stars detected in the TLS data set

F15 Var 5

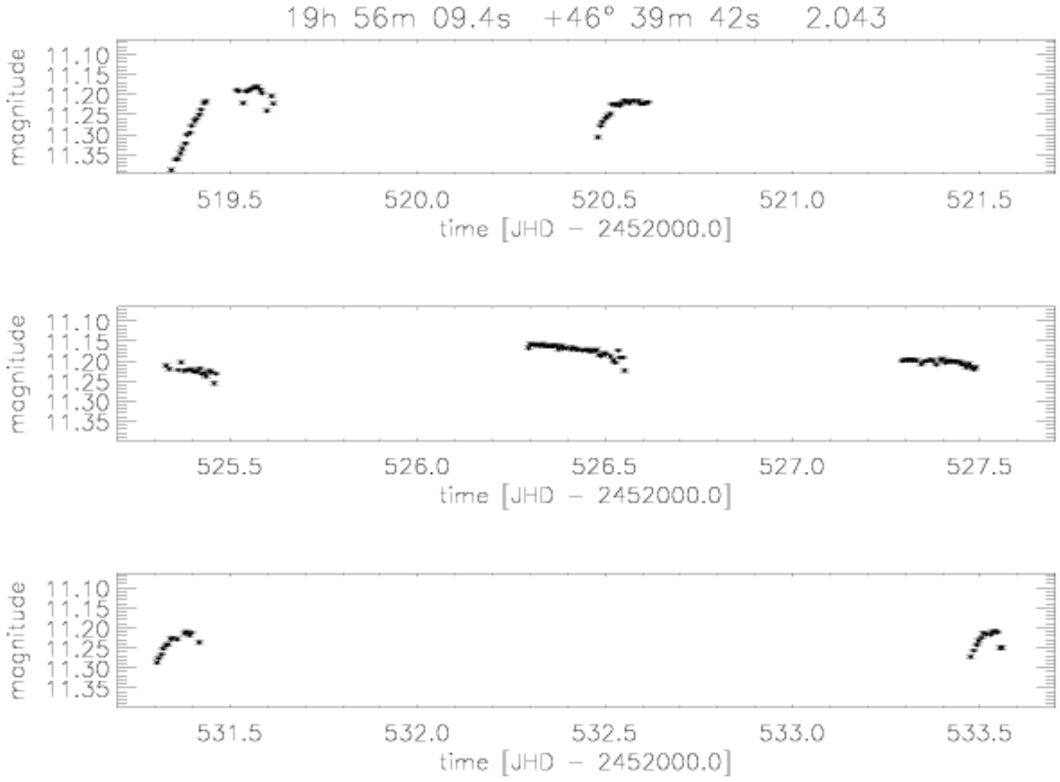

F15 Var 6

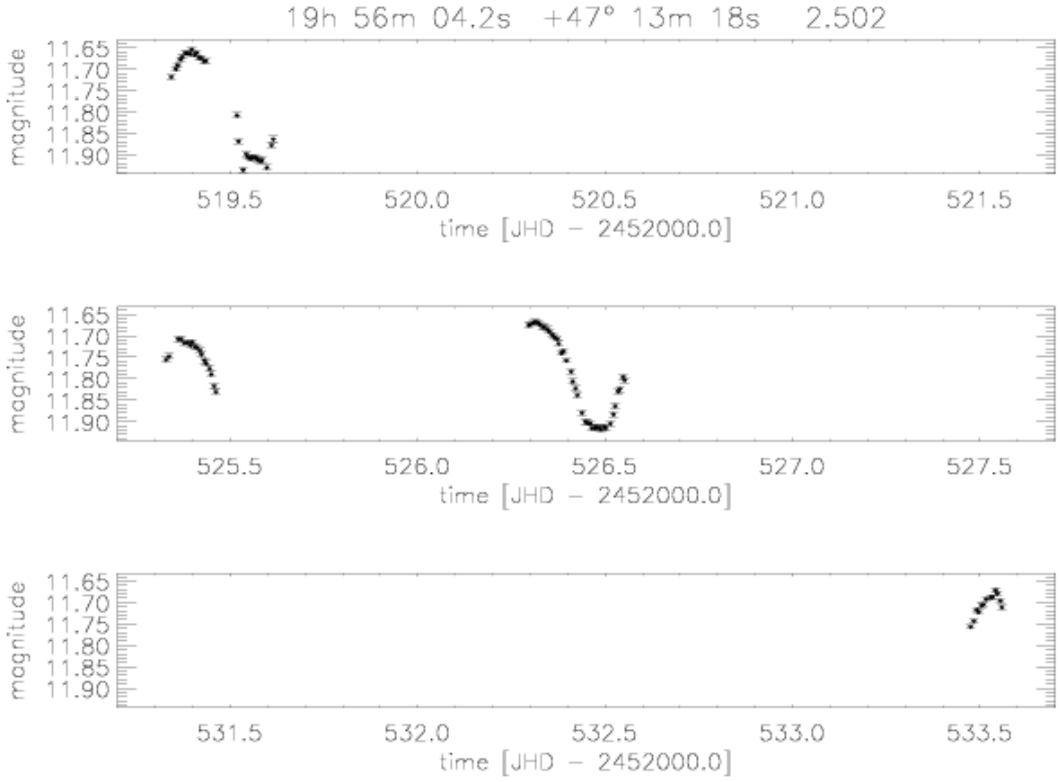

F15 Var 8

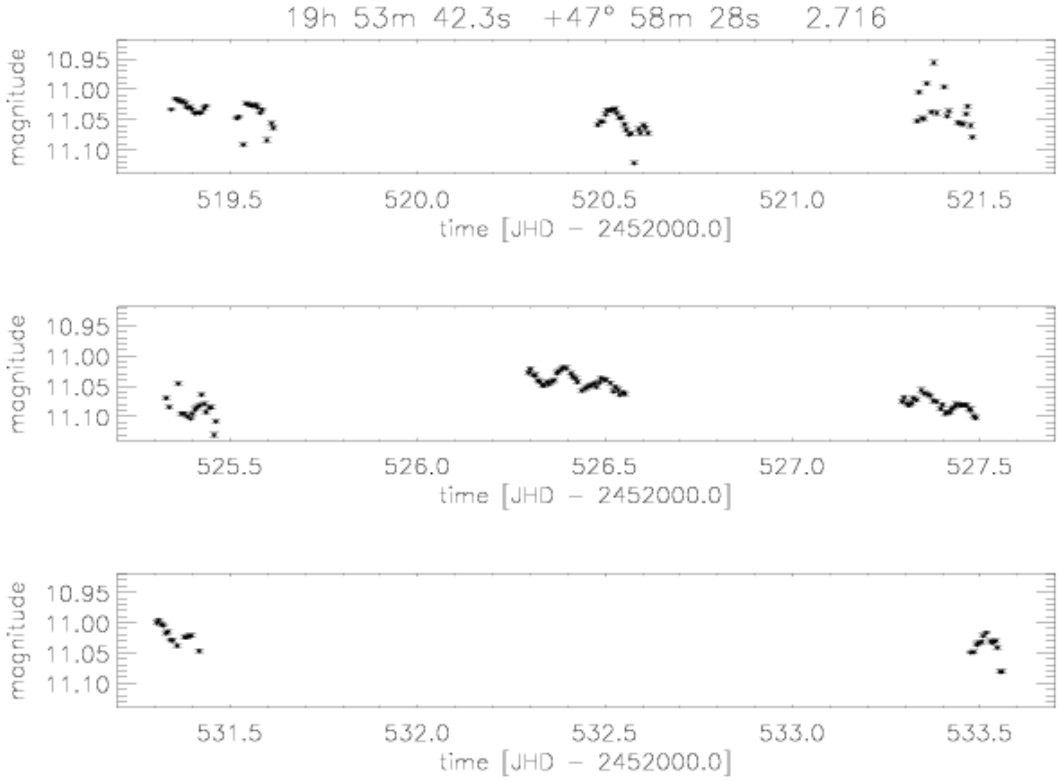

F15 Var 9

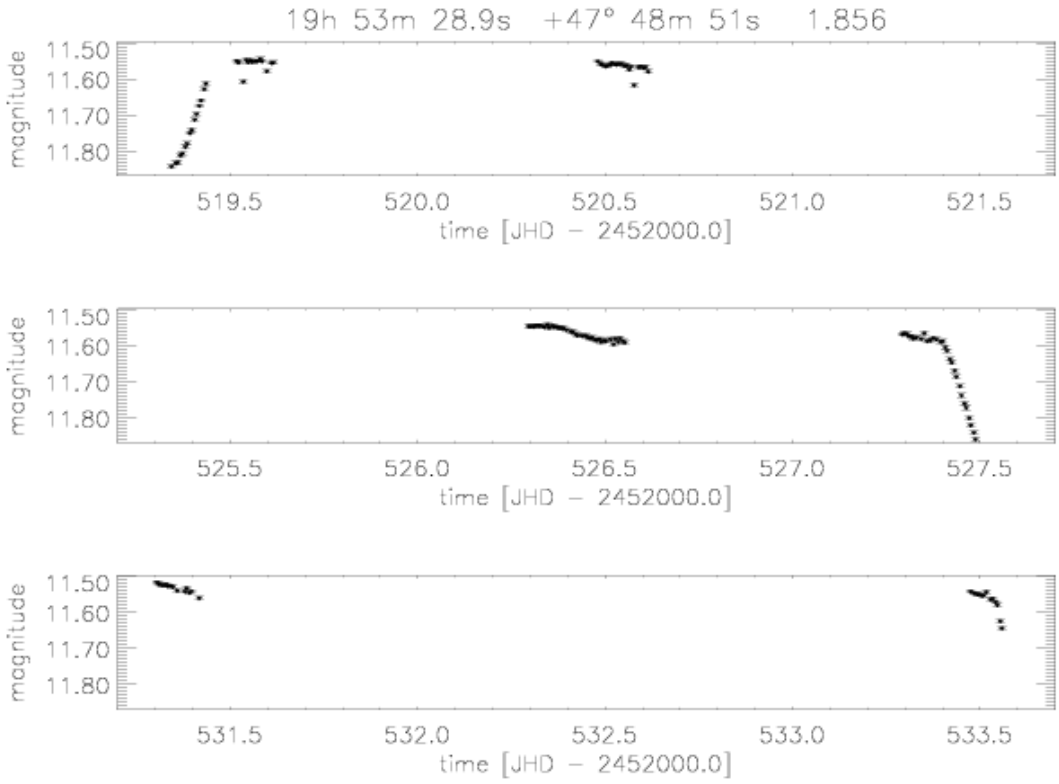

Appendix B: Light curves of variable stars detected in the TLS data set

F15 Var 11

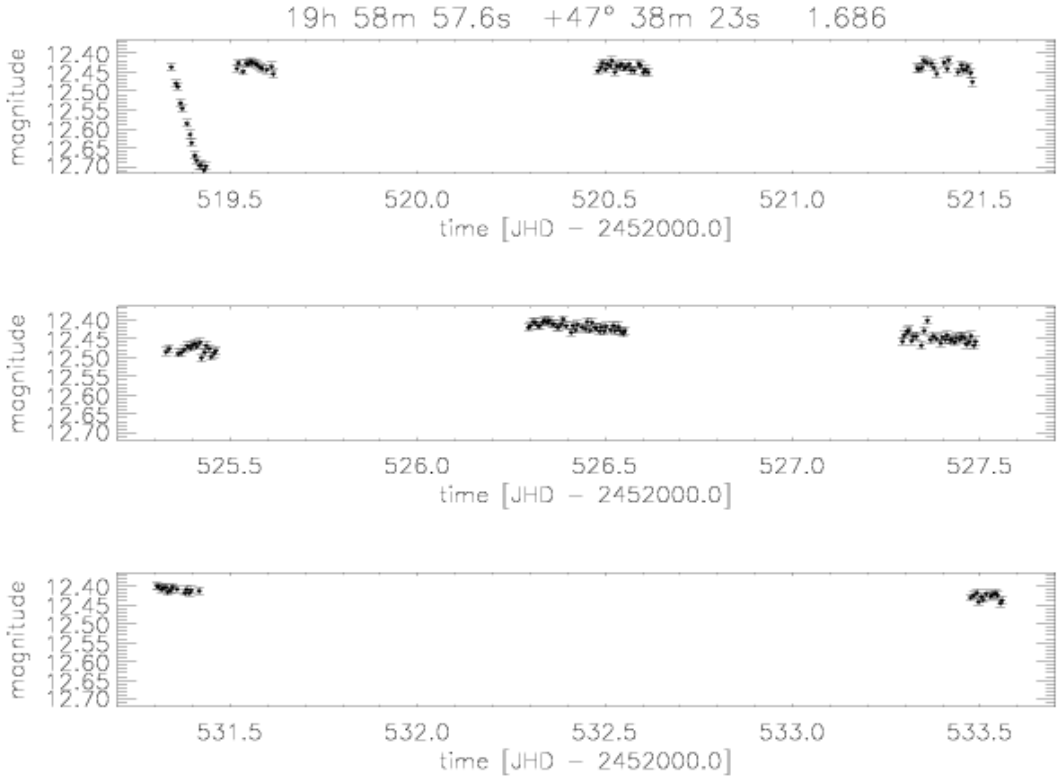

F15 Var 14

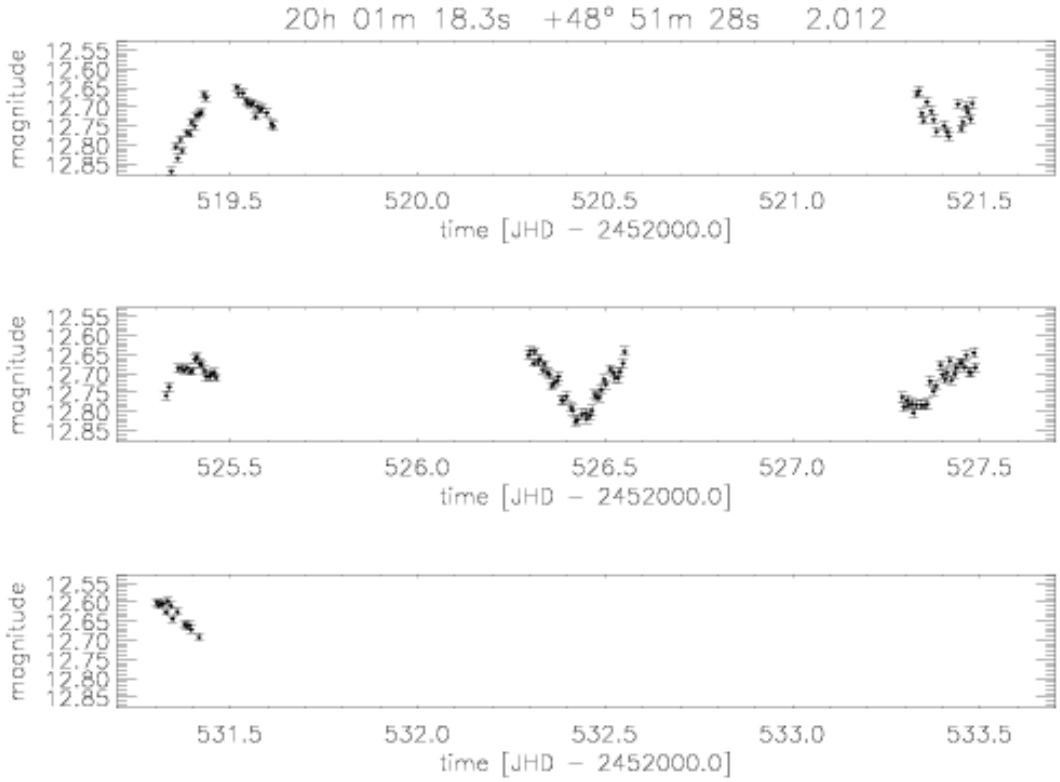

Appendix B: Light curves of variable stars detected in the TLS data set

F15 Var 15

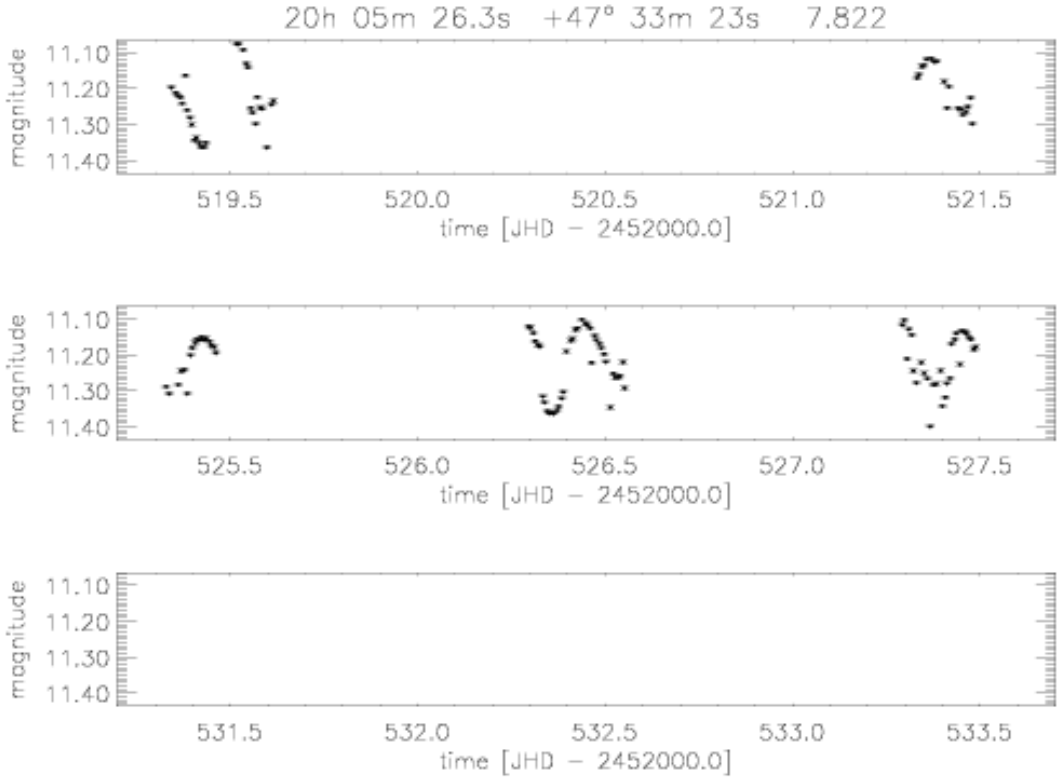

F15 Var 16

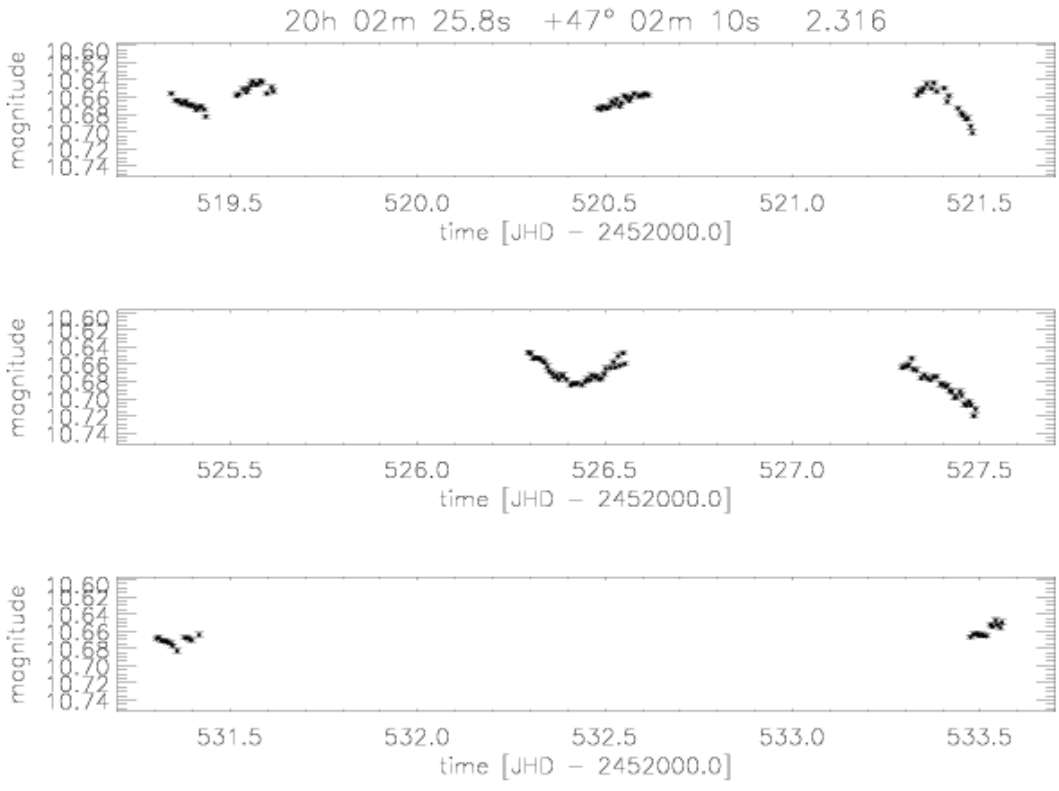

Appendix B: Light curves of variable stars detected in the TLS data set

F15 Var 20

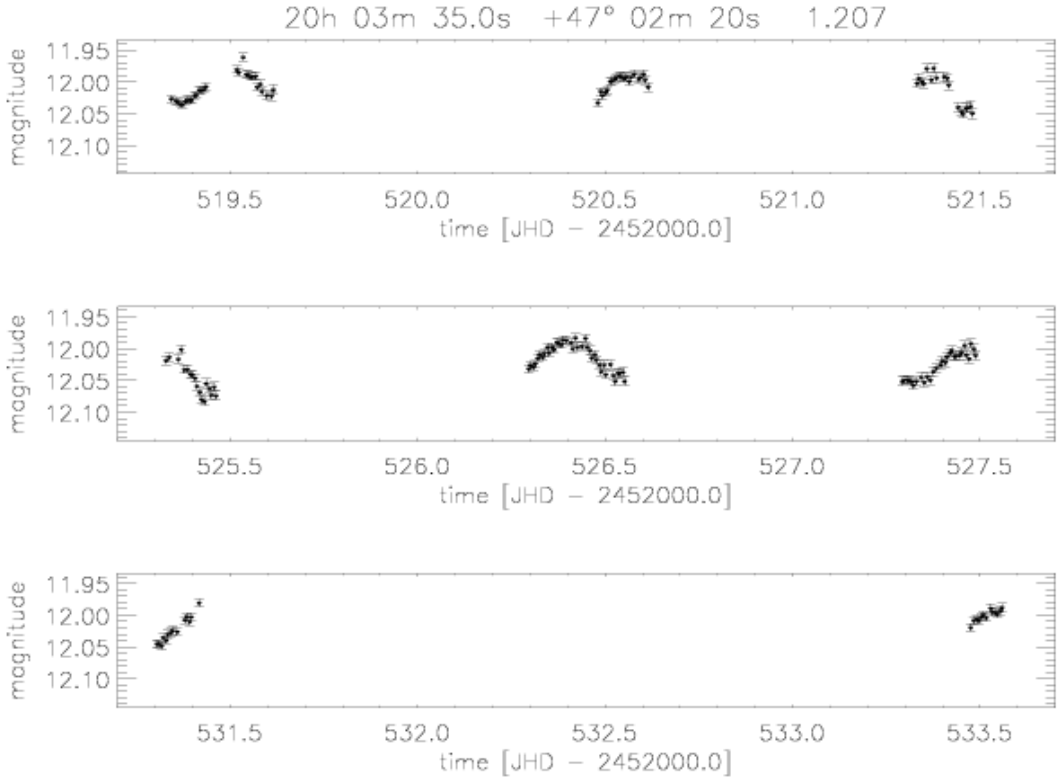

F15 Var 21

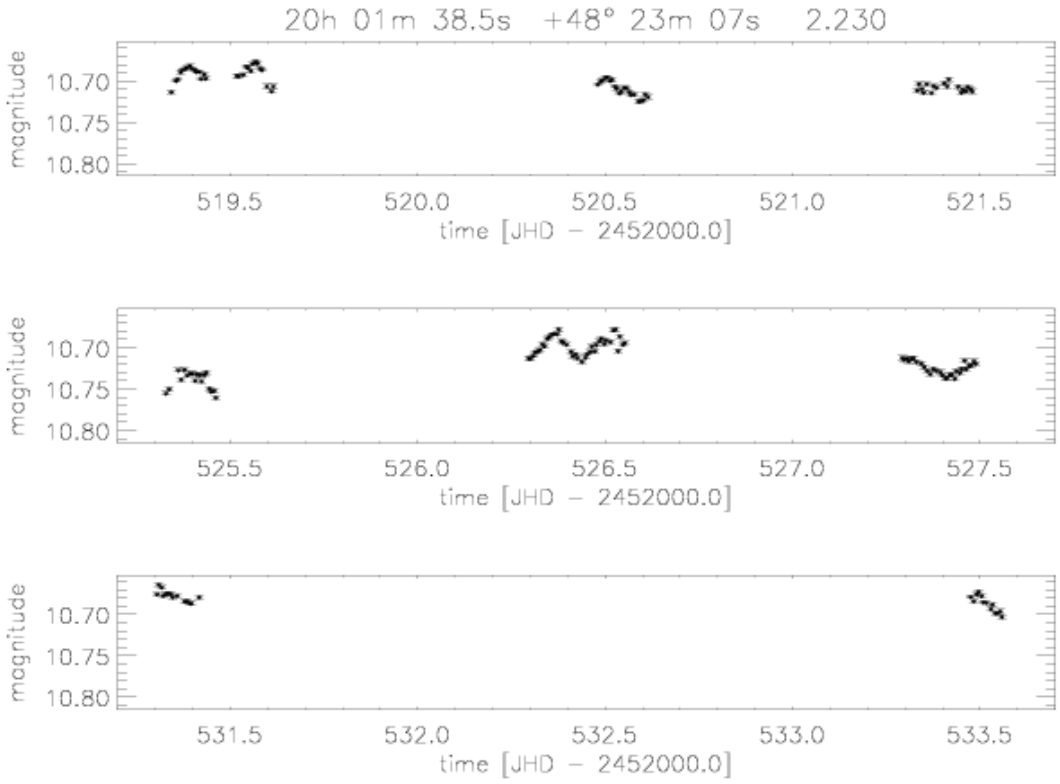

Appendix B: Light curves of variable stars detected in the TLS data set

F15 Var 24

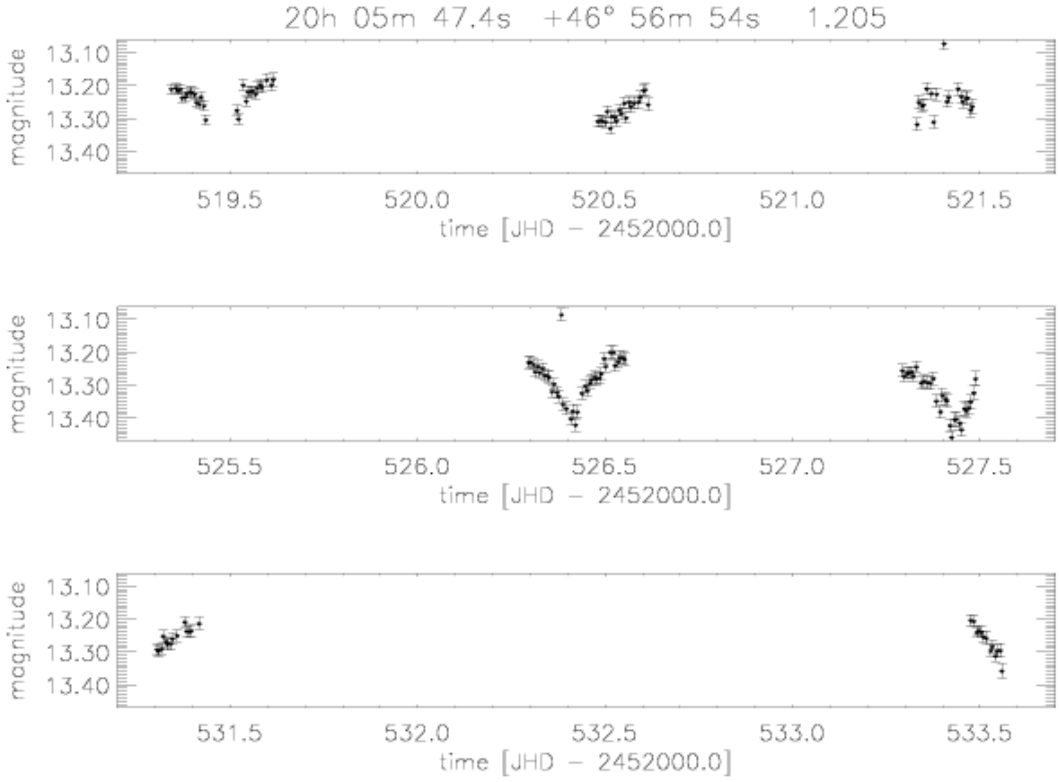

F15 Var 25

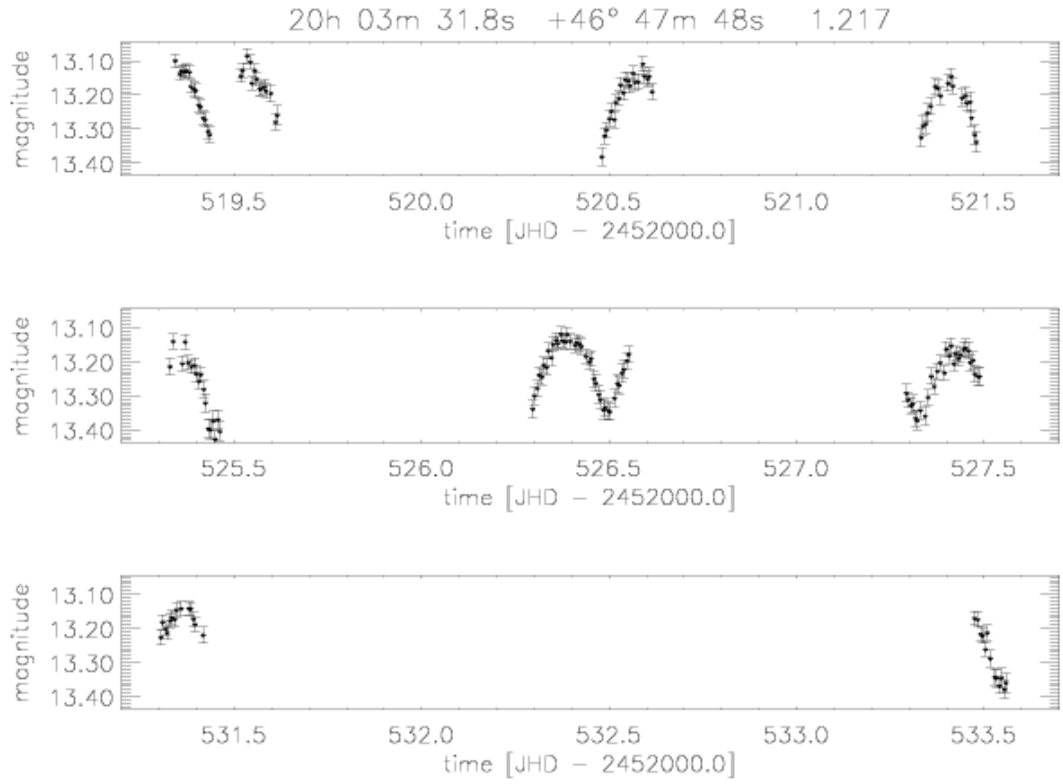

Appendix B: Light curves of variable stars detected in the TLS data set

F15 Var 28

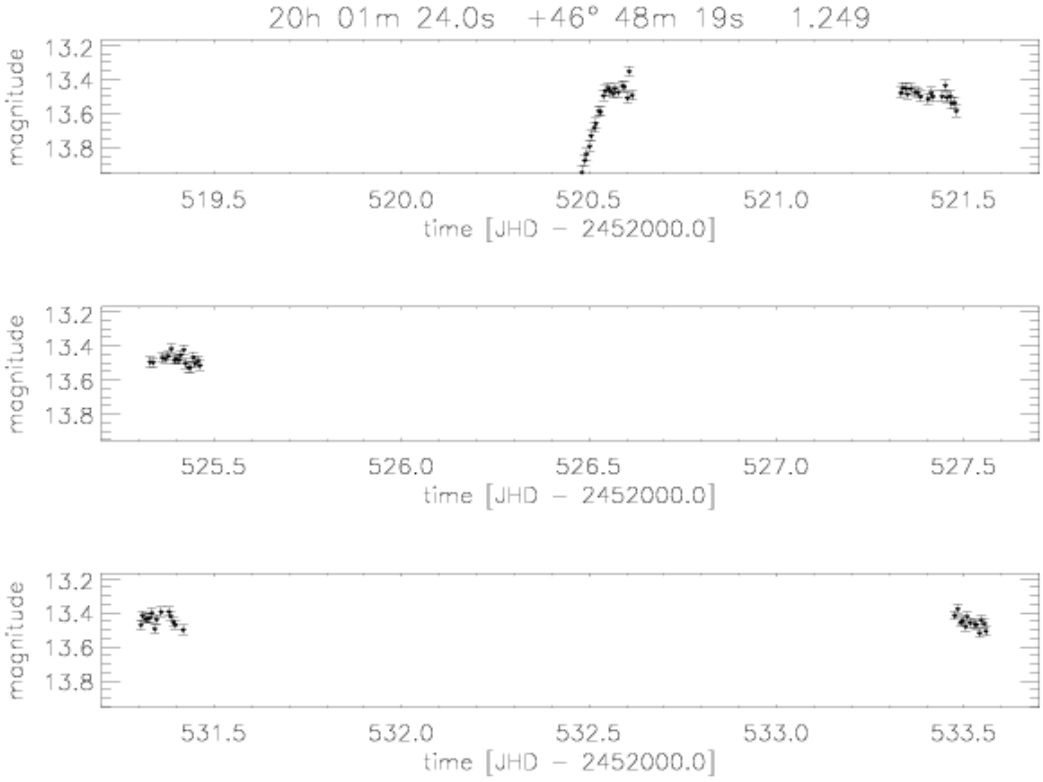

F15 Var 29

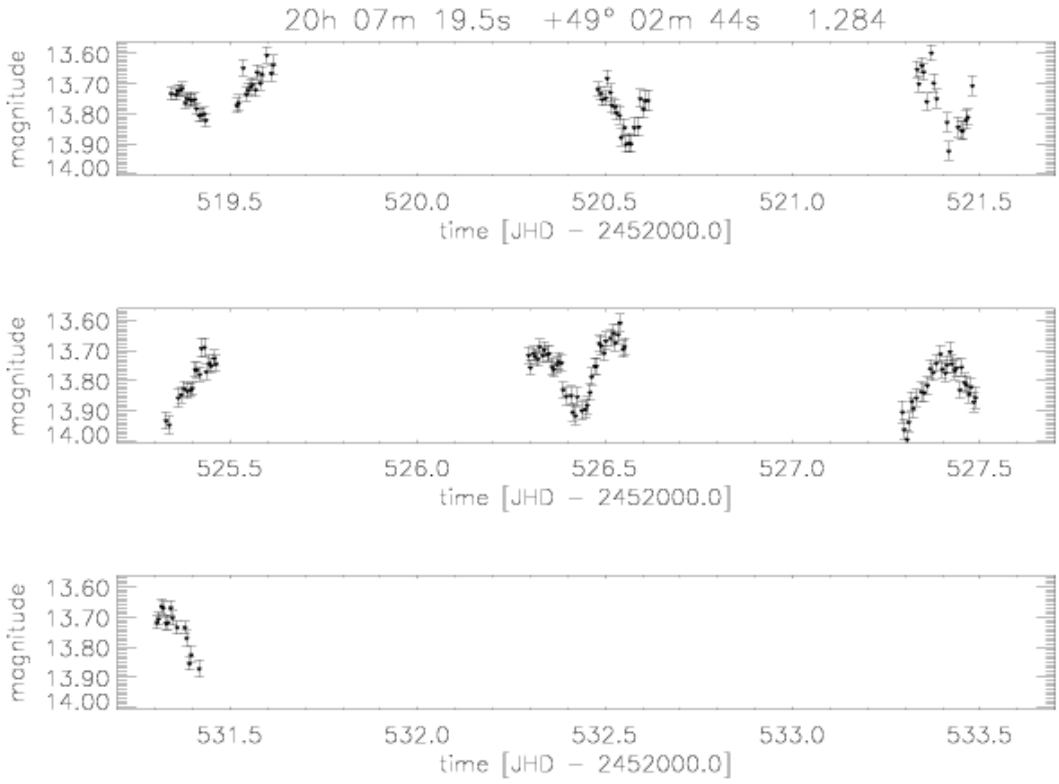

F15 Var 30

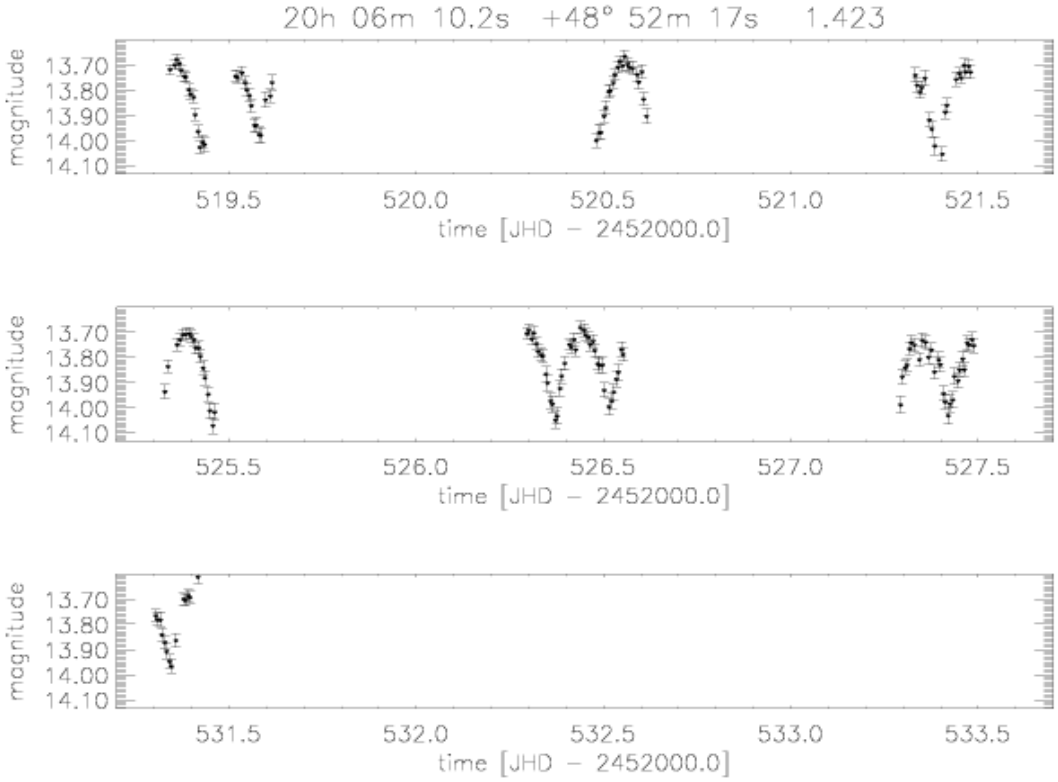

F15 Var 32

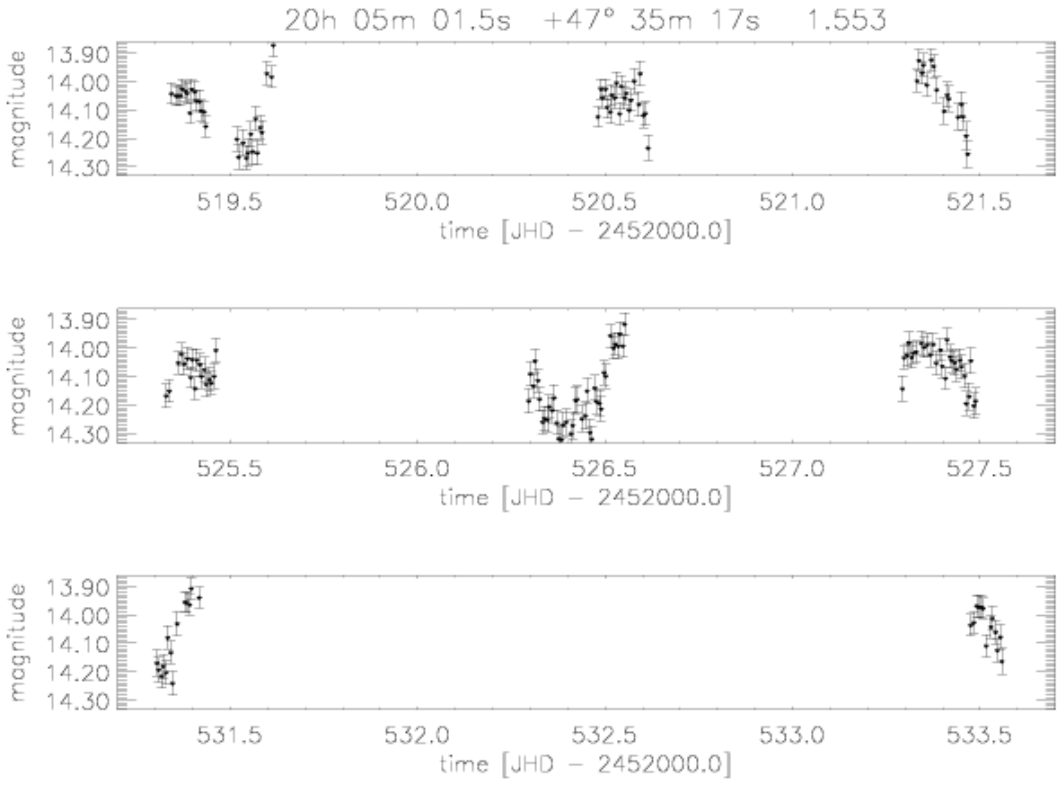

Appendix B: Light curves of variable stars detected in the TLS data set

F15 Var 33

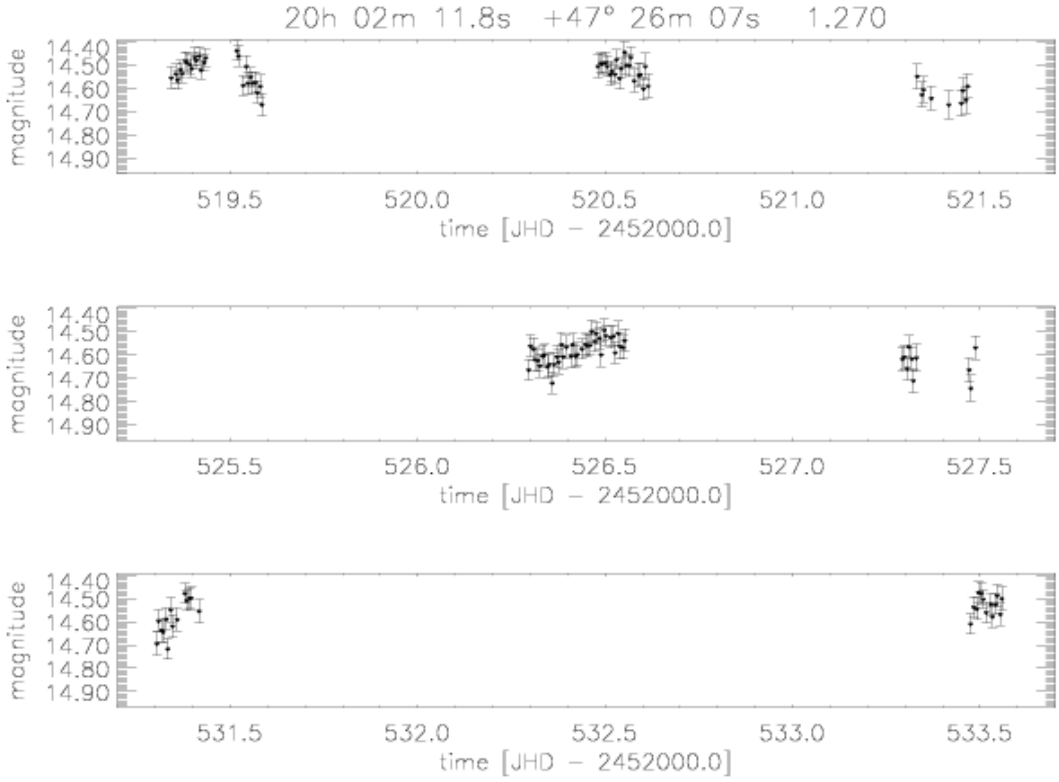

F15 Var 35

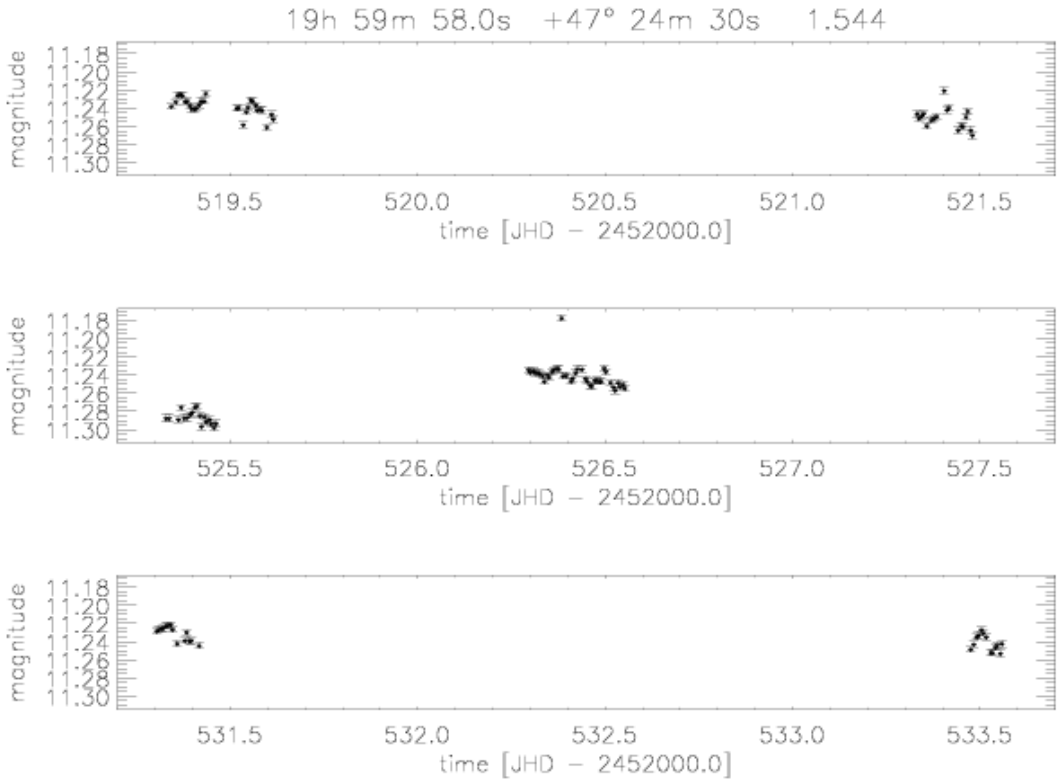

Appendix B: Light curves of variable stars detected in the TLS data set

F15 Var 36

F15 Var 37

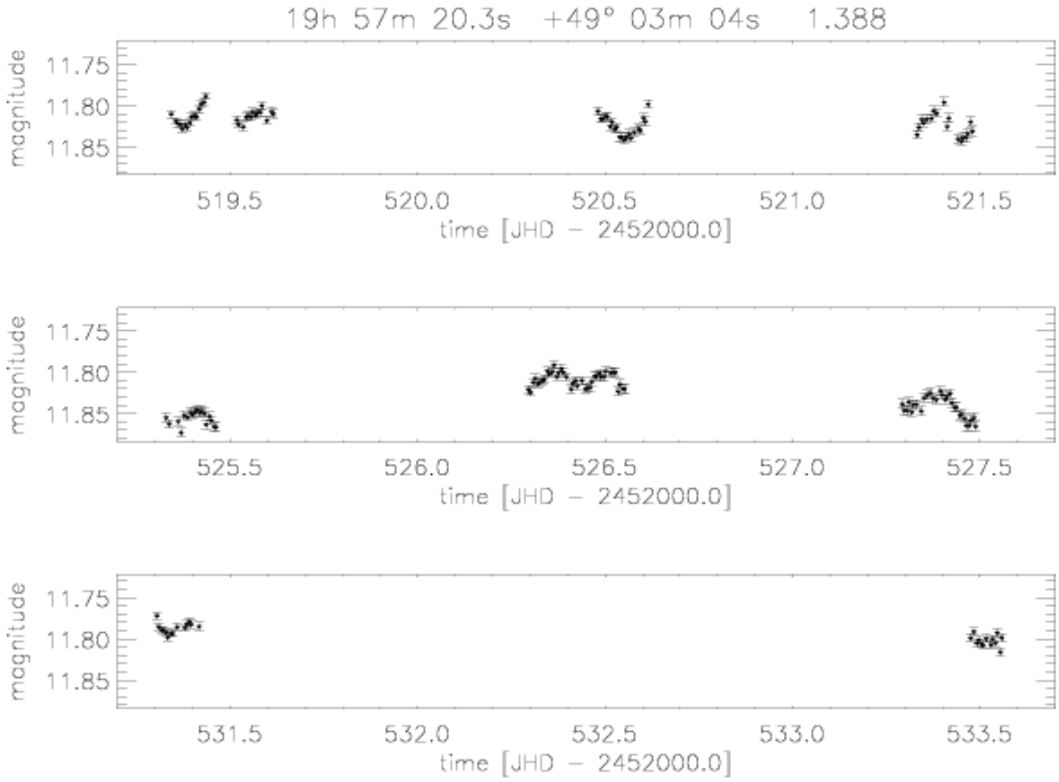

Appendix B: Light curves of variable stars detected in the TLS data set

F15 Var 38

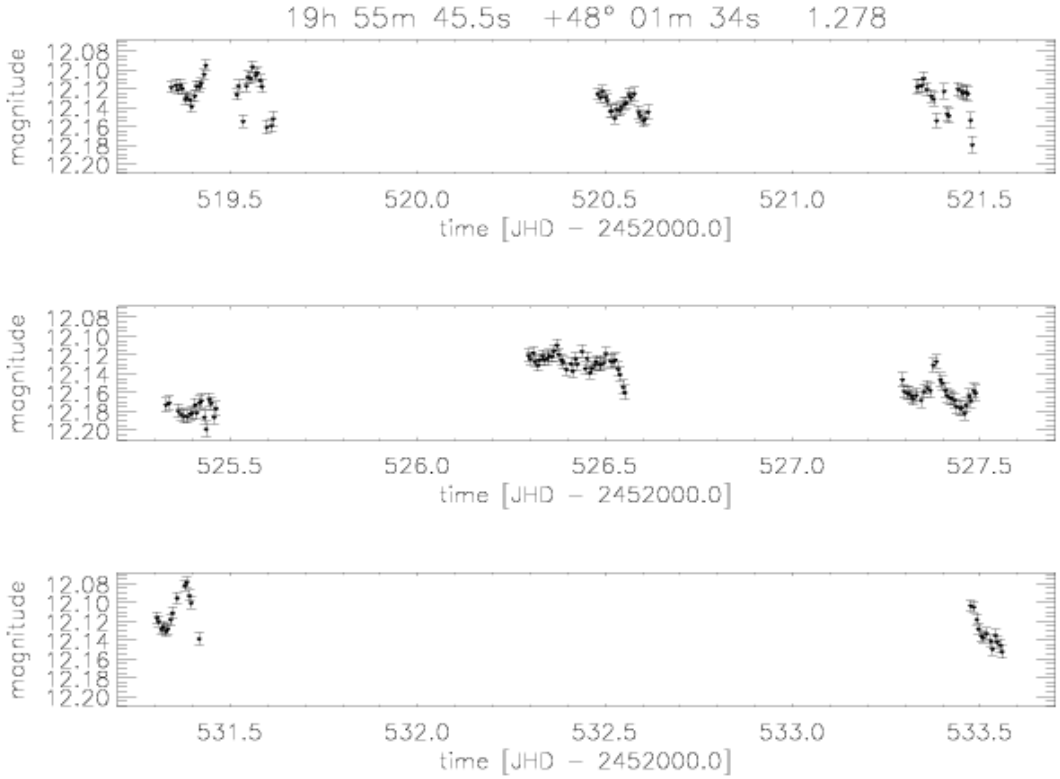

F15 Var 45

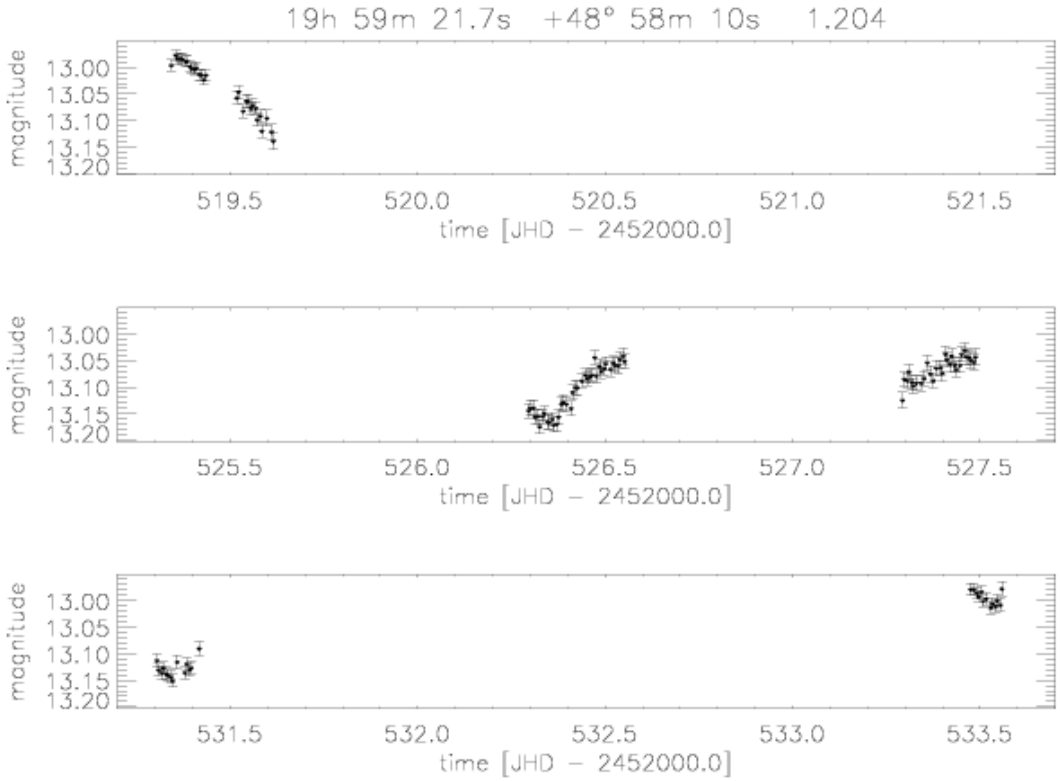

F15 Var 46

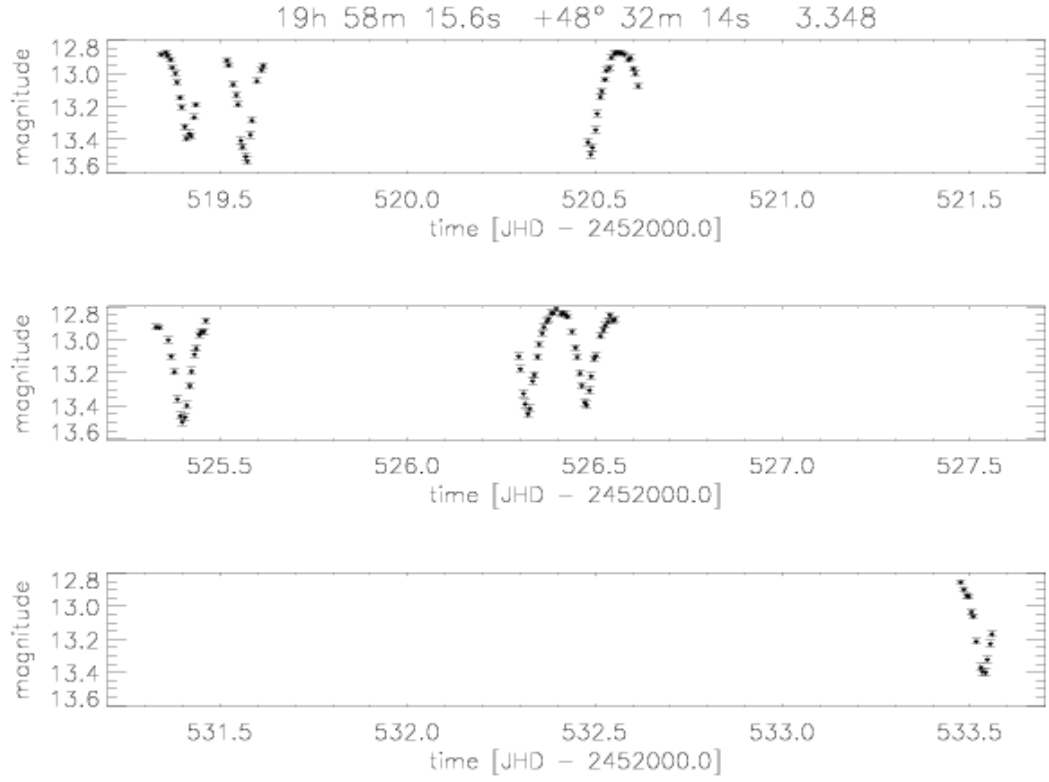

F15 Var 47

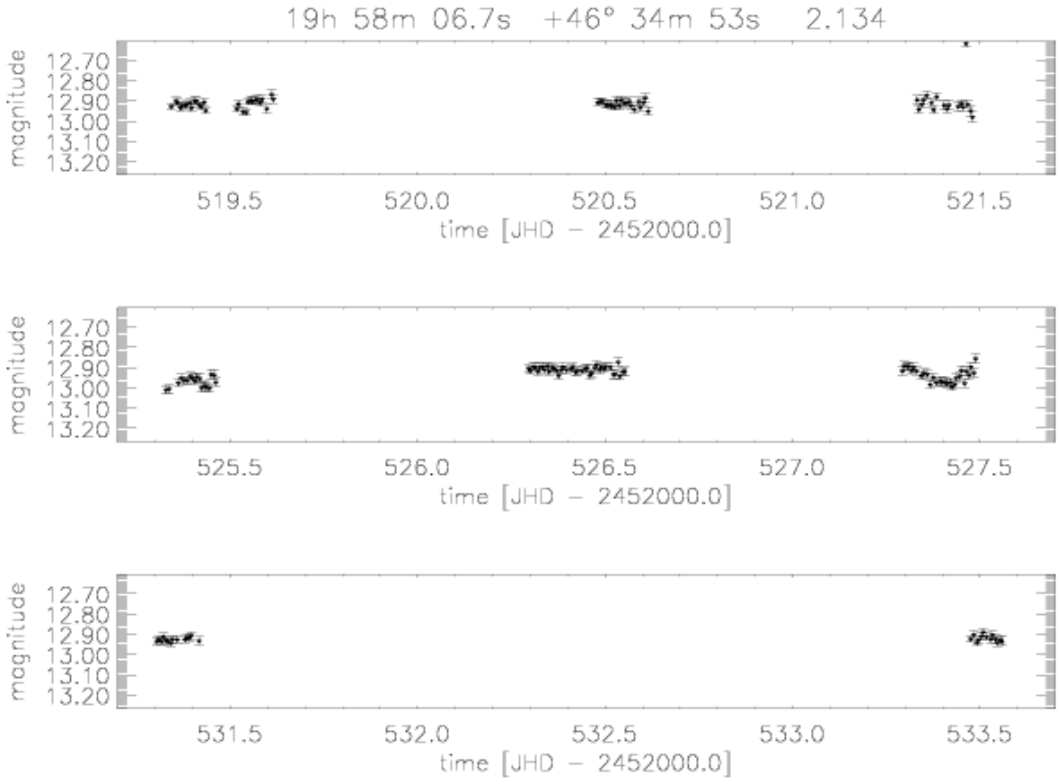

Appendix B: Light curves of variable stars detected in the TLS data set

F15 Var 48

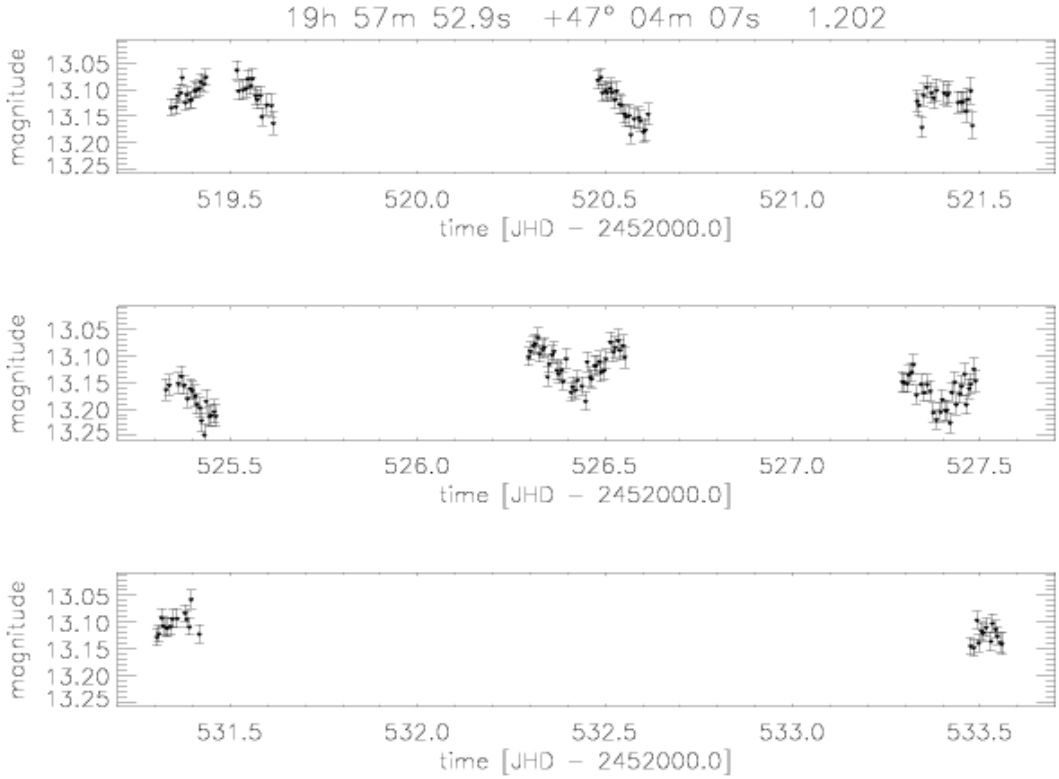

F15 Var 49

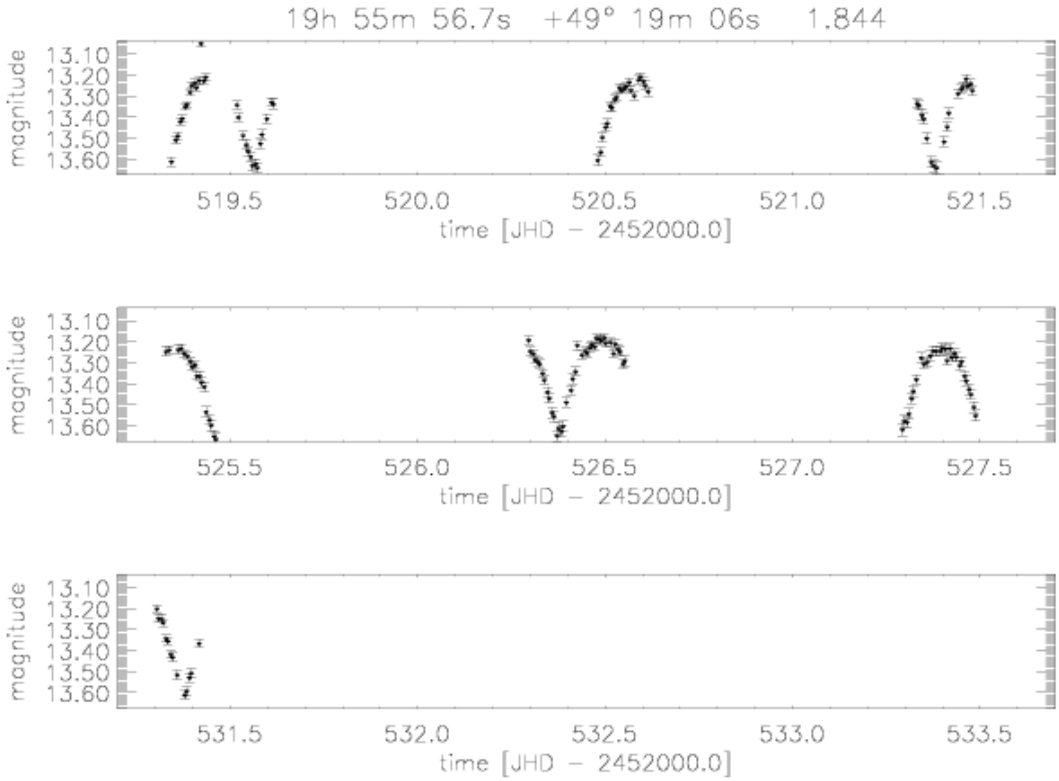

Appendix B: Light curves of variable stars detected in the TLS data set

F15 Var 50

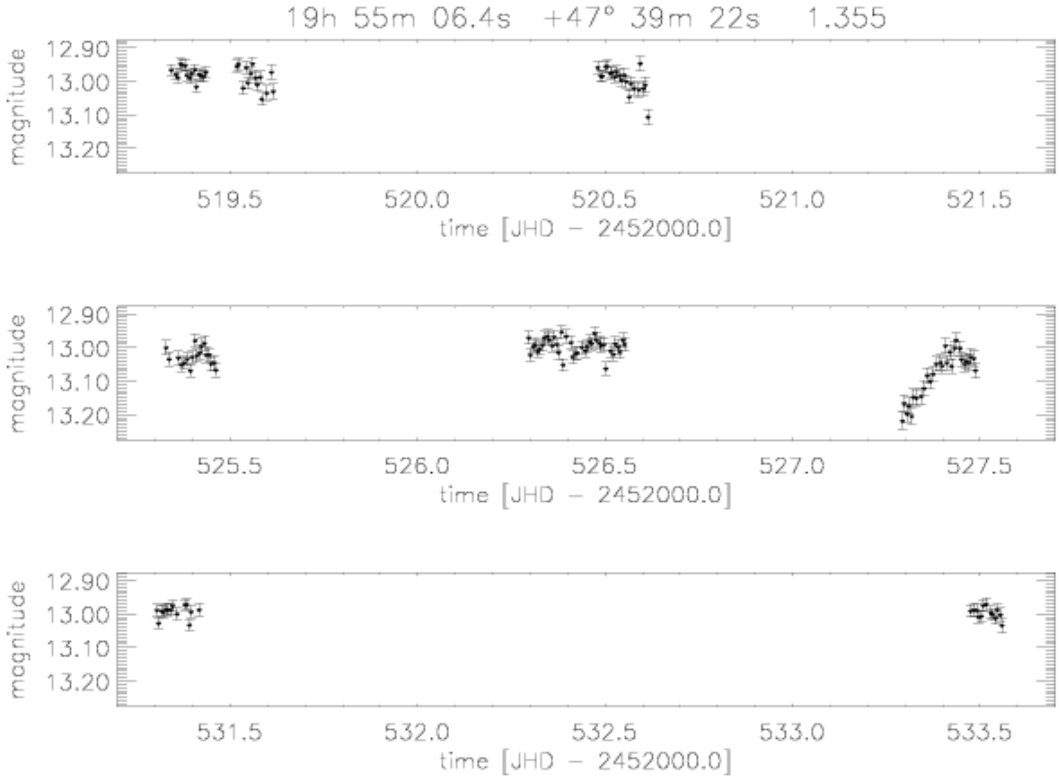

F15 Var 56

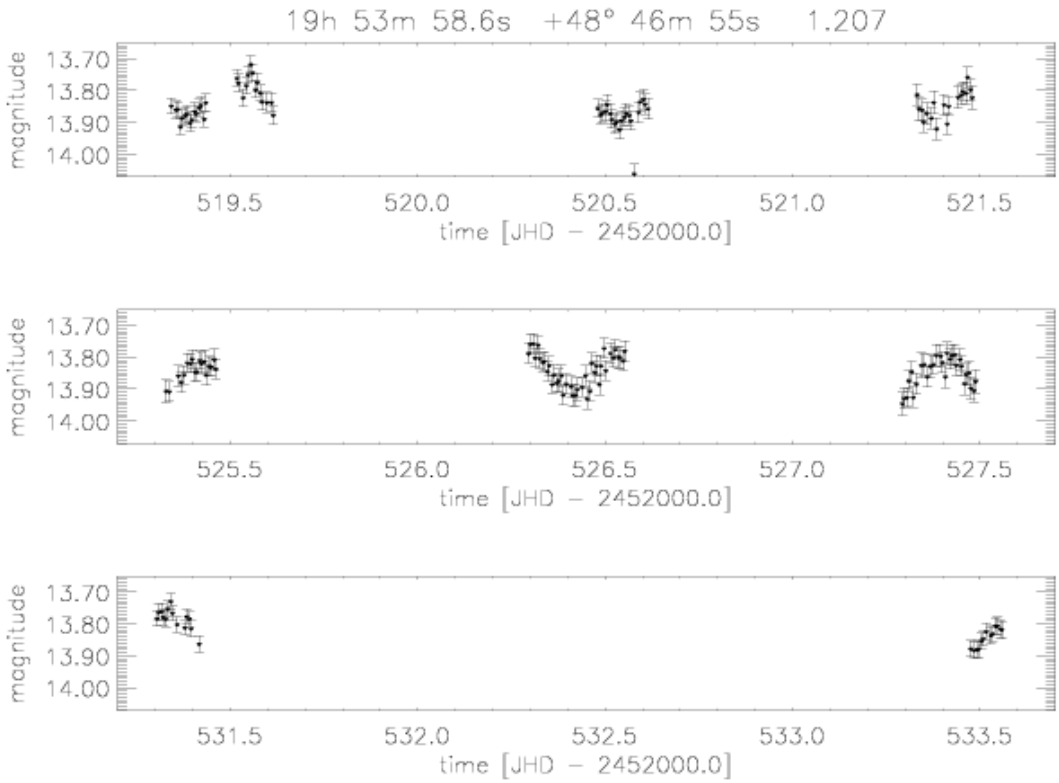

Appendix B: Light curves of variable stars detected in the TLS data set

F15 Var 58

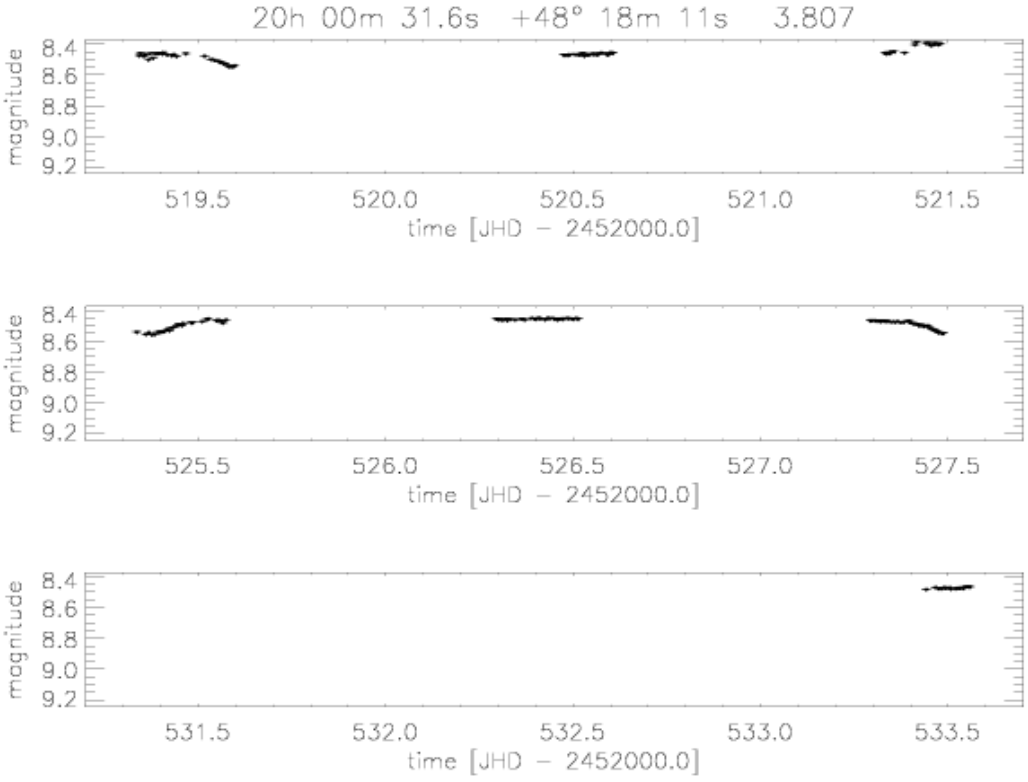

F15 Var 60

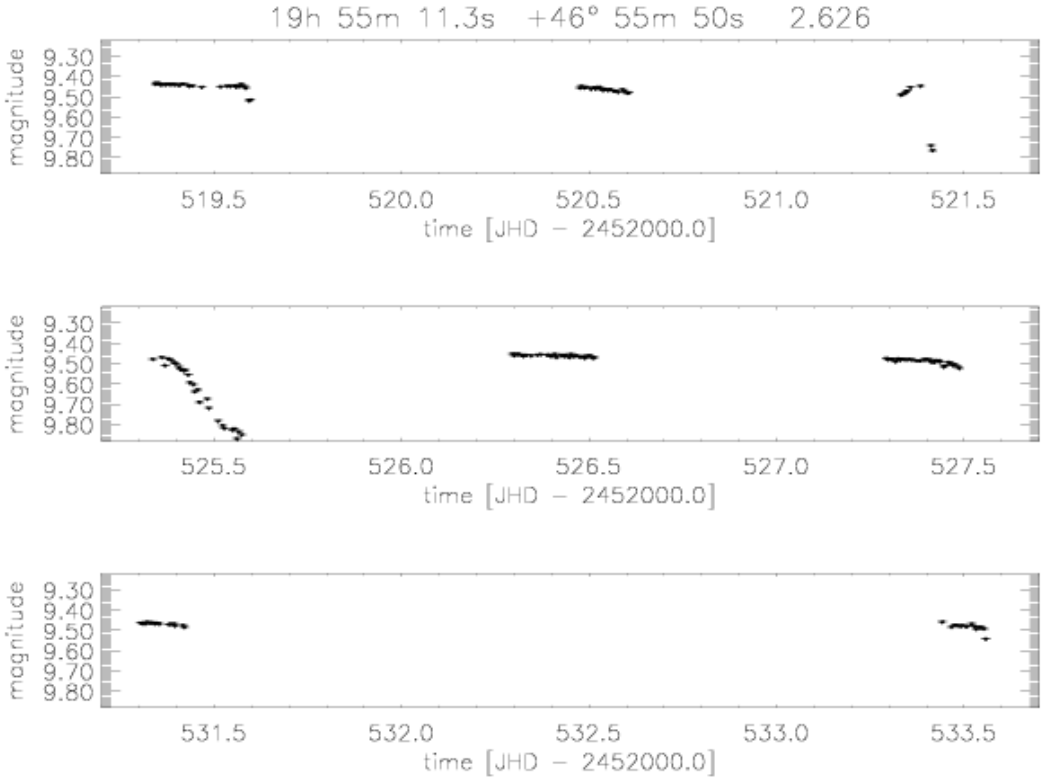

Appendix B: Light curves of variable stars detected in the TLS data set

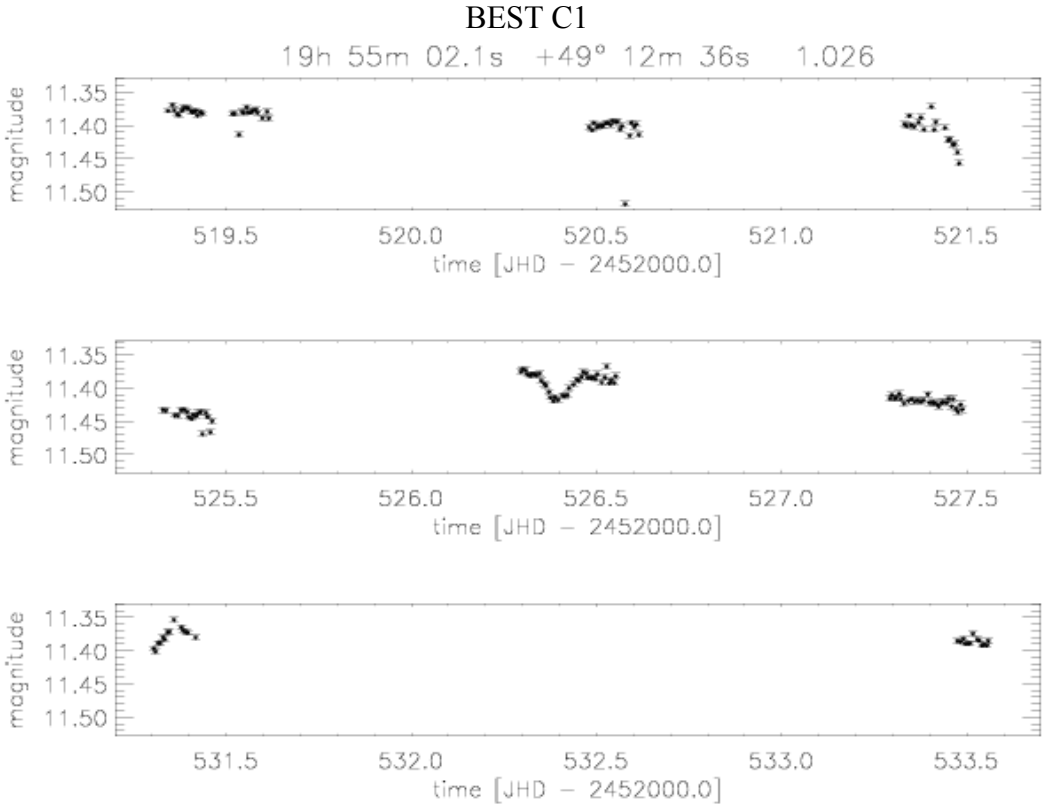

Appendix C:
Information about the BEST observations from TLS

Target field No.15

date	*UT time*	*CCD-T [°C]*	*weather*	*airmass*	*background*	*remarks*	*Number of data Cds*	*Status reduction*	*Transit search*
01/10/13	18:00-22:00	-23	Increasing mist	1.00-1.33	Medium, increasing	Bad seeing, no bias after 240er frames	2	V2	transitfilter
01/10/14	18:00-19:25	-22	Very misty	1.00-1.05	High	No bias after 240er frames	2	V2	transitfilter
01/10/18	17:50-21:00	-29	Misty	1.01-1.22	Medium, unstable	High humidity abort, residual tests	1	V2	transitfilter
01/10/20	20:10-22:20	-28	Clouds inbetween	1.13-1.49	high	Interrupted because of clouds, heavy drift not corrected	1	-	-
01/11/15	17:15-21:00	-29	Clouds	1.05-1.59	High, unstable	Interrupted (clouds)	1	V2	transitfilter
01/12/13	16:45-20:20	-48	Clear	1.16-1.94	Medium, unstable	High humidity abort later	1	V2	transitfilter
02/01/04	17:00-18:40	-40	Clear	1.41-1.89	High, increasing		2	-	-
02/06/04	21:15-00:20	-21	Misty, wind	1.47-1.06	Medium	Tracking problems (wind)	1	V2	transitfilter
02/06/14	22:00-22:20	-22.5	clouds	1.4	high	clouds	1	-	-
02/07/05	21:15-01:15	-23	Clear, hazy in the end	1.14-1.00-1.02	Medium, increasing		1	V2	transitfilter
02/07/06	22:10-23:50	-25	Cirrus at start	1.07-1.03	Medium	Clouds & high humidity abort	1	-	-
02/07/07	21:45-01:15	-24	Cirrus at start ?	1.09-1.00-1.02	Medium		1	V2	transitfilter
02/07/08	22:45-01:15	-17	cirrus	1.03-1.00-1.02	Medium	Tracking problems	1	V2	transitfilter
02/08/15	23:30-	-22	cirrus	1.02- 1.31	medium	CCD wet	1	-	-

date	*UT time*	*CCD-T [°C]*	*weather*	*airmass*	*background*	*remarks*	*Number of data Cds*	*Status reduction*	*Transit search*
	01:50					40 sec only			
02/08/16	21:25-22:15	-10	cirrus	1.01-1.00	medium	CCD wet	1	-	-
02/08/17	23:20-01:50	-10	clouds	1.05-1.31	Medium-high	CCD wet ?	2	V2	transitfilter
02/08/30	20:25-01:30	-19	Hazy	1.00-1.42	Medium-High (moon)	Tracking problems, Last 2 h 15, 40 sec only (bright moon)	2	V2	transitfilter
02/09/01	20:15-02:50	-27	clouds	1.00-1.86	Medium-high	Interrupted , clouds	1	V2	transitfilter
02/09/02	21:15-03:00	-26		1.01-1.94	Medium-high	ST-4 wet, 1.5 h not tracked	1	V2	transitfilter
02/09/03	20:00-02:10	-23	Clouds, hazy	1.03-1.39	Medium, unstable	ST-4 wet, 1.5 h not tracked, cloud abort	2	V2	transitfilter
02/09/04	19:50-01:20	-21.5	clouds	1.03-1.29	Medium-high, unstable	Cloud abort, ST-4 wet again, 2.3 h not tracked	1	V2	transitfilter
02/09/05	20:25-21:30	-23		1.01-1.0	medium	High humidity abort	1	V2	transitfilter
02/09/07	19:55-02:30	-22	Cirrus clouds	1.00-1.89	Medium-high	Cloud abort, clouds inbetween, skybeamer in the end !	2	V2	transitfilter
02/09/08	19:05-02:50	-20	Bad transparency	1.02-1.00-2.00	Medium-high	Increasing haze	2	V2	transitfilter
02/09/09	19:00-00:20	-20	Near front, Lightnings ?	1.02-1.33	Medium, unstable	High humidity abort	2	V2	transitfilter
02/09/13	19:15-22:15	-27	clouds	1.00-1.10	Medium, unstable	Clouds inbetween, cloud abort	1	V2	transitfilter
02/09/15	22:35-01:40	-29	clouds	1.19-1.79	Medium-high,	Clouds at start and inbetween, high	1	V2	transitfilter

date	*UT time*	*CCD-T [°C]*	*weather*	*airmass*	*background*	*remarks*	*Number of data Cds*	*Status reduction*	*Transit search*
					unstable	humidity abort			
02/09/30	18:55-21:50	-28		1.00-1.18	medium	Moisture on center CCD window ! High humidity abort	1	-	
02/10/01	18:05-22:10	-24	Cirrus, transparency bad	1.00-1.22	Medium, unstable	Cirrus inbetween, High humidity abort	1	V2	transitfilter
02/11/06	20:20-22:05	-35		1.15-1.47	Medium, unstable	wind	2	-	
02/12/09	17:00-20:30	-38		1.25-2.37	Medium, unstable	Moon, wind	2	V2	transitfilter
02/12/11	16:15-19:05	-44		1.18-1.85	high	moon	3	V2	-

Target field No.2

Date	*UT time*	*CCD-T [°C]*	*weather*	*airmass*	*background*	*remarks*	*Number of data CDs*	*Status reduction*	*Transit search*
01/10/12	22:15-03:45	-28	Misty	1.06-1.00-1.17	Low-medium	First useable tracking tests	2	V2	transitfilter
01/10/13	23:20-04:15	-23	Misty	1.00-1.23	Medium		2	V2	transitfilter
01/10/14	22:45-04:15	-25	Clear	1.03-1.00-1.24	Medium	Bad seeing	2	V2	transitfilter
02/01/04	19:40-00:15	-40	clear	1.01-1.47	High, increasing, moon	High humidity abort,	2	V2	transitfilter
02/01/05	17:15-01:40	-40	clear	0.97-1.00-1.89	High, increasing, moon	Disco laser beams !	3	V2	transitfilter
02/01/15	16:50-19:20	-40	clear	1.03-1.00-1.02	medium	High humidity abort	2	V2	transitfilter
02/02/02	19:55-23:20	-30	Clear (cirrus ?)	1.12-1.74	medium		2	V2	transitfilter
02/02/03	17:45-00:00	-28	Clear, wind	1.01-1.94	medium	Tracking problems (wind)	2	V2	transitfilter
02/02/04	17:30-21:00	-33	clear	1.01-1.25	Medium, unstable	Clouds abort	1	V2	transitfilter
02/02/06	21:10-22:40	-33	misty	1.31-1.62	Very high	Fog abort	2	-	
02/11/05	22:50-04:15	-35		1.12-1.00-1.75	Medium-high	Clouds inbetween High humidity abort	1	V2	transitfilter
02/11/06	22:35-02:20	-35	clouds	1.15-1.00-1.33	Medium-high	High humidity abort	2	V2	transitfilter
02/12/10	18:55-03:20	-40		1.04-1.00-1.84	Medium-high		2	V2	transitfilter

Date	*UT time*	*CCD-T [°C]*	*weather*	*airmass*	*background*	*remarks*	*Number of data CDs*	*Status reduction*	*Transit search*
02/12/11	19:16-04:20	-44		1.03-1.00-2.21	Medium-high		3	V2	transitfilter
02/12/12	18:45-04:00	-41		1.04-1.00-2.17	Medium-high	Clouds inbetween	2	V2	transitfilter

Target field No.8

Date	*UT time*	*CCD-T [°C]*	*weather*	*airmass*	*background*	*remarks*	*Number of data CDs*	*Status reduction*	*Transit search*
02/01/05	02:45-05:30	-40	Clear	1.00-1.12	High, moon		3	V2	transitfilter
02/01/15	03:45-05:30	-40	Clear	1.01-1.19	medium	High humidity abort earlier in the night	2	V2	transitfilter
02/02/02	00:20-5:00	-30	Clear, wind	1.00-1.29	High, moon		2	V2	transitfilter
02/02/03	01:15-02:40	-30	Clouds	1.00-1.05	High, changing	Clouds inbetween, Cloud abort	2	-	-
02/02/06	00:40-04:30	-33	Misty	1.00-1.27	Medium, changing	Clouds inbetween, Cloud abort	2	-	-
02/03/10	20:40-02:00	-37	Clear	1.05-1.00-1.19	Low	Cloud abort	1	V2	transitfilter
02/03/17	20:30-00:40	-28	Misty	1.03-1.00-1.10	Medium, changing	High humidity and fog abort, interupted	2	V1 (extremely poor results)	-
02/04/02	21:25-03:00	-29	Clear, wind strong	1.00-1.70	Low, but increasing (moon)	Tracking problems (wind)	2	V2	transitfilter
02/04/03	21:30-23:30	-33	Clear, wind	1.00-1.06	Low	Cloud abort	1	V2	transitfilter
02/04/04	21:20-03:20	-34	Clear	1.00-1.84	Low-medium		2	V2	transitfilter
02/04/05	20:40-03:05	-38	Clear, cirrus (?)	1.00-1.74	Low-medium	Laser beam	2	V2	transitfilter
02/04/07	21:00-	-38	Clear,	1.00-1.89	Low-		2	V2	transitfilter

Date	*UT time*	*CCD-T [°C]*	*weather*	*airmass*	*background*	*remarks*	*Number of data CDs*	*Status reduction*	*Transit search*
	03:15		cirrus (?)		medium				
02/04/08	21:00-03:00	-36	Clear	1.00-1.84	Low-medium		2	V2	transitfilter
02/04/09	20:50-03:15	-37	Misty, clouds	1.00-1.94	changing	Interrupted (clouds, fog)	1	V2	transitfilter
02/04/11	21:15-01:00	-34	Clear	1.01-1.37	low	Clouds during start, high humidity abort	2	V2	transitfilter
02/05/09	22:55-01:45	-21	Clear	1.31-1.74	Low-medium		1	V2	transitfilter
02/05/11	20:20-21:40	-22	Clear	1.05-1.17	Low	High humidity abort	1	-	-
02/05/13	20:25-23:15	-26	Clear	1.06-1.41	Medium-low	High humidity abort	1	V2	transitfilter
02/05/16	21:20-23:20	-21	Cirrus ?	1.17-1.49	Medium		1	-	-
02/05/20	22:10-00:55	-26	Clear	1.31-2.06	High (moon)	Only 40 sec frames	1	V2	transitfilter
02/12/09	03:20-04:55	-41	Clear	1.02-1.00-1.01	Medium	High humidity abort	2	V2	transitfilter
03/02/13	23:10-02:40	-36	clear	1.02-1.00-1.09	High	moon	2	V2	transitfilter
03/02/22	22:40-05:10	-43	clear	1.02-1.56	Medium	Moon second half Guiding problems	2	V2	transitfilter
03/02/23	23:00-05:20	-43	clear	1.01-1.58	Medium	Adapter problem, moon in the end	2	V2	transitfilter
03/02/24	22:40-05:00	-40	clear	1.00-1.56	Low-medium	Adapter problem	2	V2	transitfilter
03/02/25	23:00-05:05	-37	Clear, wind	1.00-1.56	Low-medium	Adapter problem	2	V2	transitfilter

Date	*UT time*	*CCD-T [°C]*	*weather*	*airmass*	*background*	*remarks*	*Number of data CDs*	*Status reduction*	*Transit search*
03/02/26	23:45-03:00	-35	Clouds sometimes	1.01-1.22	medium	Clouds in beginning, cloud abort	1	V2	transitfilter
03/03/07	02:30-04:30	-31	Thin clouds	1.24-1.62	Medium-high	clouds	1	-	-
03/03/13	21:30-04:20	-38	Clear, small cirrus?	1.01-1.00-1.70	Medium	Clouds in the end	2	V2	transitfilter
03/03/15	19:30-23:00	-36	Clear, cirrus?	1.10-1.00-1.01	High	Very bright moon, High humidity	1	V2	transitfilter
03/03/21	19:00-04:10	-37	clear	1.12-1.00-1.79	Low-medium	Moon second half	2	V2	transitfilter
03/03/22	18:40-04:10	-37	clear	1.14-1.00-1.84	Low-medium	Moon second half	2	V2	transitfilter
03/03/23	18:40-04:00	-30	clear	1.13-1.00-1.79	Medium	Moon second half	2	V2	transitfilter
03/03/24	18:50-00:50	-28	clear	1.12-1.00-1.15	Medium	Clouds in the end, Cloud abort	1	V2	transitfilter
03/03/28	19:50-22:40	-30.5	Clear, cirrus?	1.03-1.00-1.03	Medium	High humidity abort	1	V2	transitfilter
03/03/30	19:45-23:30	-29.1	misty	1.03-1.00-1.03		Cloud abort	1	V2	transitfilter
03/03/31	19:20-03:45	-32	misty	1.12-1.00-1.57	Medium	Transparency unstable, CCD damaged during rewarming	2	V2	transitfilter

Target field No.15 (untracked 15 & 40 sec only)

date	*UT time*	*CCD-T [°C]*	*weather*	*airmass*	*background*	*remarks*
01/07/23	21:00-23:15	-13 – -15	Clear	1.06-1.00	Low	Without booster
01/07/25	20:40-01:00	-14 – -16	Clear	1.08-1.00-1.06	Low	Without booster, Fall out inbetween
01/07/26	21:10-01:30	-13 – -17	Clear	1.05-1.00-1.11	Low - medium	Without booster
01/07/27	20:50-01:35	-11 – -14	Clear	1.06-1.00-1.12	Low-medium	Without booster
01/07/29	21:20-01:35	-14 – -17	Clear (clouds at start)	1.03-1.00-1.13	Medium	Without booster
01/07/30	21:20-01:55	-12 – -16	Clear, moon (clouds at start)	1.04-1.00-1.18	Medium-high	Without booster, clouds inbetween ?
01/08/01	20:20-02:00	-17 – -20	Clear, moon	1.07-1.00-1.21	High-medium	Without booster
01/08/07	20:15-00:10	-18 – -19	Cirrus sometimes	1.05-1.00-1.06	Medium-high	Without booster, cloud abort
01/08/15	20:00-00:45	-6 – -11	Clear	1.04-1.00-1.17	Low-medium	Without booster, Hot night, hot CCD
01/08/19	19:55-22:20	-13 – -14	Cirrus	1.03-1.00-1.02	Medium	Without booster, Cloud abort
01/08/22	19:55-02:50	-16	Misty	1.02-1.00-1.62	Medium-Low	Without booster
01/08/23	19:55-02:55	-13	Misty	1.02-1.00-1.70	High, changeable	Without booster, Fog interruption
01/08/24	00:10-03:00	-13 – -15	Clear, cirrus ?	1.17-1.74	Low-medium	Without booster
01/08/25	23:30-01:35	-9	Clouds ?	1.10-1.37	Medium	Without booster
01/08/26	19:30-02:55	-8 – -11	Clear, wind cirrus ?	1.03-1.00-1.74	Medium	Without booster

date	*UT time*	*CCD-T [°C]*	*weather*	*airmass*	*background*	*remarks*
01/09/17	21:40-22:55	-32	Cirrus ?	1.08-1.20	Medium	With booster
01/10/05	21:55-00:50	-30	Clear, moon	1.22-1.94	High	High humidity abort, with booster
01/10/12	17:50-21:00	-26	Clear	1.00-1.17	medium	With booster, Tracking tests (interruptions)

HD209458

date	*UT time*	*CCD-T [°C]*	*weather*	*airmass*	*background*	*remarks*
01/07/23	00:26-01:54	-15 – -17	Clear	1.20	Low-medium	Without booster
01/08/24	19:15-23:30	-9 – -10	Clear, clouds in the end	1.74-1.19	High-low	Without booster
01/09/14	20:05-23:15	-32	Cirrus	1.25-1.19-1.27	Low-medium	Pre transit only, cloud abort

Appendix D:
Radial velocity follow-up observations with the 2m TLS telescope

BEST C 1:

J.D. – 2,4000,000	*V [km/s]*
52547.304	-25.7741
52548.347	-1.9832
52549.360	24.6534
52572.289	-18.0221
52656.705	18.8509
52683.255	-3.1635

BEST C 4:

J.D. – 2,4000,000	*V [m/s]*
52683.353	56.2849
52684.294	79.7066
52684.514	49.8081
52685.385	41.1621
52685.567	76.9450
52744.458	102.5450
52744.479	104.0351
52745.388	-12.2357
52745.410	112.7521
52746.403	59.9497
52746.425	93.4574
52747.426	204.9077
52747.448	153.2972
52750.480	107.0702
52750.502	108.8155
52751.493	38.3992
52751.534	19.9092
52752.422	152.2584
52753.376	44.6133
52754.359	51.9642
52754.382	-23.5581
52755.412	18.7538

Appendix E:
Photometric follow-up observations with the Westerlund Telescope

date	*object*	*Obs. Time [UT]*	*filter*	*remarks*
04/10/11	BEST C 3	20:03 – 03:40	V,R,I	
04/10/27	BEST C 3	18:36 – 02:06	R	
04/11/16	BEST C 3	19:50 – 04:20	R	Eclipsing event detected
05/03/20	BEST C 5	19:23 – 01:35	R	
05/04/18	BEST C 5	21:31 – 02:02	R	
05/04/19	BEST C 5	20:34 – 01:58	R	
05/04/20	BEST C 5	20:50 – 01:00	R	
05/04/22	BEST C5	20:34 – 23:19	R	

Appendix F:
Spectroscopic follow-up observations with the Hobby-Eberly-Telescope

date	*object*	*remarks*
04/11/14	BEST C 4	2 high-resolution spectra

Bibliography

AIGRAIN S. & FAVATA F., 2002, Bayesian detection of planetary transits. A modified version of the Gregory-Loredo method for Bayesian periodic signal detection, *A&A*, **395**, 625.

AIGRAIN S. & IRWIN M., 2004, Practical planet prospecting, *MNRAS*, **350**, 331.

AIGRAIN S., FAVATA F. & GILMORE G., 2004, Characterizing stellar micro-variability for planetary transit searches, *A&A*, **414**, 1139.

ALARD C. & LUPTON R.H., 1998, A Method for Optimal Image Subtraction, *ApJ*, **503**, 325.

ALARD C., 2000, Image subtraction using a space-varying kernel, *A&AS*, **144**, 363.

ALONSO R., BROWN T.M., TORRES G., LATHAM D.W., SOZZETTI A., MANDUSHEV G., BELMONTE J.A., CHARBONNEAU D., DEEG H.J., DUNHAM E.W., O'DONOVAN FRANCIS T. & STEFANIK R.P., 2004, TrES-1: The Transiting Planet of a Bright K0 V Star, *ApJ*, **613**, L153.

ARRIBAS S., GILLILAND R.L., SPARKS W.B., LOPEZ-MARTIN L., MEDIAVILLA E. & GOMEZ-ALVAREZ P., 2006, Exploring the Potential of Integral Field Spectroscopy for Observing Extrasolar Planet Transits: Ground-based Observations of the Atmospheric Na in HD 209458 b, *PASP*, **118**, 21.

ARTYUKHINA N.M., DURLEVICH O.V., FROLOV M.S., GORANSKIJ V.P., GORYNYA N.A., KARITSKAY E.A., KAZAROVET E.V., KHOLOPOV P.N., KIREEV N.N., KUROCHKIN N.E., LIPUNOVA N.A., MEDVEDEVA G.I., PASTUKHOVA E.N., SAMUS N.N., TSVETKOVA T.M., 1995, General Catalogue of Variable Stars, 4th ed., vol.V. Extragalactic Variable Stars, "Kosmosinform", Moscow.

AUVERGNE M., BOISNARD L., BUEY J.-T.M., EPSTEIN G., HUSTAIX H., JOURET M., LEVACHER P. & BERRIVIN S., 2003, COROT-high-precision stellar photometry on a low Earth orbit: solutions to minimize environmental perturbations, *Proceedings of the SPIE*, **4854**, 170.

BAGLIN A., AUVERGNE M., BARGE P., BUEY J.-T., CATALA C., MICHEL E., WEISS W. & the COROT Team, 2002, COROT: Astroseismology and Planet Finding, In: *Proceedings of the First Eddington Workshop on Stellar Structure and Habitable Planet Finding*, editor: B. Battrick, Scientific editors: F. Favata, I. W. Roxburgh & D. Galadi, **ESA SP-485**, 17.

BAKOS G., NOYES R.W., KOVACS G., STANEK K.Z., SASSELOV D.D. & DOMSA I., 2004, Wide-Field Millimagnitude Photometry with the HAT: A Tool for Extrasolar Planet Detection, *PASP*, **116**, 266.

BALIBER N.R. & COCHRAN W.D., 2001, TeMPEST: the Texas, McDonald Photometric Extrasolar Search for Transits, Bulletin of the American Astronomical Society, **33**, 1112.

BARAFFE I. & CHABRIER G., 1996, Mass-Spectral Class Relationship for M Dwarfs, *ApJ*, **461**, 51.

BARAFFE I., SELSIS F., CHABRIER G., BARMAN T., ALLARD F., HAUSCHILDT P. & LAMMER H., 2004, The effect of evaporation on the evolution of close-in giant planets, *A&A.* , **419** , L13.

BENEDICT G.F., McARTHUR B.E., FORVEILLE T., DELFOSSE X., NELAN E., BUTLER R.P., SPIESMAN W., MARCY G.W., GOLDMAN B., PERRIER C., JEFFERYS W.H. & MAYOR M., 2002, A Mass for the Extrasolar Planet Gliese 876 b Determined from Hubble Space Telescope Fine Guidance Sensor 3 Astrometry and High-Precision Radial Velocities, *ApJ*, **581**, L115.

BENN C.R. & ELLISON S.L., 1998, Brightness of the night sky over La Palma, *New Astronomy Reviews*, **42**, 503.

BERTIN E. & ARNOUTS S., 1996, Sextractor: Software for source extraction, *A&A Suppl. Ser.*, **117**, 393.

BODENHEIMER P., LIN D. N.C. & MARDLING, R., 2001, On the Tidal Inflation of Short-Period Extrasolar Planets , *ApJ.*, **548**, 466.

BODENHEIMER P., LAUGHLIN G. & LIN D.N.C., 2001, On the Radii of Extrasolar Giant Planets, *ApJ.*, **592**, 555.

BONNAREL F., FERNIQUE P., BIENAYME O., EGRET D., GENOVA F., LOUYS M., OCHSENBEIN F., WENGER M. & BARTLETT J.G., 2000, The ALADIN interactive sky atlas. A reference tool for identification of astronomical Sources, *A&A Suppl. Ser.*, **143**, 33.

BORDÉ P., ROUAN D. & LÉGER A., 2003, Exoplanet detection capability of the COROT space mission, *A&A*, **405**, 1135.

BORUCKI W.J. & SUMMERS A.L., 1984, The photometric method of detecting other planetary systems, *Icarus*, **58**, 121.

BORUCKI W.J., CALDWELL D., KOCH D.G., WEBSTER L.D., JENKINS J.M., NINKOV Z. & SHOWEN R., 2001, The Vulcan Photometer: A Dedicated Photometer for Extrasolar Planet Searches, *PASP*, **113**, 439.

BORUCKI W.J., KOCH D.G., BASRI G., BROWN T.M., CALDWELL D., DEVORE E., DUNHAM E., GAUTIER T., GEARY J., GILLILAND R., GOULD A., HOWELL S. & JENKINS J., 2003 , Kepler Mission: a mission to find Earth-size planets in the habitable zone, In: *Proceedings of the Conference on Towards Other Earths: DARWIN/TPF and the Search for Extrasolar Terrestrial Planets,* Edited by M. Fridlund, T. Henning, compiled by H. Lacoste., 69

BOUCHY F., MAYOR M., PEPE F., QUELOZ D. & UDRY S., 2002, Precise radial velocities and Eddington's detected transits, In: *Proceedings of First Eddington Workshop on Stellar Structure and Habitable Planet Finding*, editor: B. Battrick, Scientific editors: F. Favata, I. W. Roxburgh & D. Galadi, **ESA SP-485**, 153.

BOUCHY F., PONT F., SANTOS N.C., MELO C., MAYOR M., QUELOZ D, & UDRY S., 2004 a, Two new very Hot Jupiters among the OGLE transiting candidates, *A&A.*, **421**, 13.

BOUCHY F., PONT F., MELO C., SANTOS N.C., MAYOR M., QUELOZ D., & UDRY S., 2004 b, Doppler follow-up of OGLE transiting companions in the Galactic bulge, *A&A.*, **431**, 1105.

BOUCHY F., UDRY S., MAYOR M., PONT F., IRIBARNE N., SA SILVA R., ILOVAISKY S., QUELOZ D., SANTOS N.C., SEGRANSAN D. & ZUCKER S., 2005, ELODIE metallicity-biased search for transiting Hot Jupiters II. A very Hot Jupiter transiting the bright K star HD 189733, *A&A*, **444**, 15.

BROWN T.M., 2003, Expected Detection and False Alarm Rates for Transiting Jovian Planets, *ApJ.*, **593**, 125.

BROWN T.M. & CHARBONNEAU D., 2000, Disks, Planetisimals and Planets, The STARE Project: A Transit Search for Hot Jupiters, *ASP Conference Series*, **219**, 584.

BROWN T., CHARBONNEAU D., GILLILAND R., NOYES R. & BURROWS A., 2001, HST Time-Series Photometry of the Transiting Planet of HD 209458, *ApJ.*, **552**, 699.

BURROWS A., HUBENY I. & SUDARSKY D., 2005, A theoretical interpretation of the measurements of the secondary eclipses of TrES-1 and HD 209458 b, *ApJ*, **625**, L135.

BUTLER R.P. & MARCY G.W., 1996, A Planet Orbiting 47 Ursae Majoris, *ApJ*, **464**, L153.

CAMPBELL B., WALKER G.A.H. & YANG S., 1988, A search for substellar companions to solar-type stars, *ApJ*, **331**, 902.

CHARBONNEAU D., BROWN T., LATHAM D., MAYOR M. & MAZEH T., 1999, Detection of Planetary Transits Across a Sun-like Star, *ApJ.*, **529**, 45.

CHARBONNEAU D., BROWN T., NOYES R.W. & GILLILAND R.L., 2002, Detection of an Extrasolar Planet Atmosphere*, ApJ*, **568**, 377.

CHARBONNEAU D., 2003, Current Challenges Facing Current Transit Surveys, in *ISSI Workshop on Planetary Systems and Planets in Systems*, eds. S. Udry, W. Benz, and R. von Steiger, *Space Sci. Rev.*, astro-ph/0302216

CHARBONNEAU D., BROWN T., DUNHAM E., LATHAM D., LOOPER D. & MANDUSHEV G., 2004, Astrophysical False Positives Encountered in Wide-Field Transit Searches, In: *AIP Conference Proceedings 'The Search for Other Worlds',* **713**, 151.

CHARBONNEAU D., ALLEN L., MEGEATH S., TORRES G., ALONSO R., BROWN T., GILLILAND R., LATHAM D., MANDUSHEV G., O'DONOVAN F. & SOZZETTI A., 2005, Detection of Thermal Emission from an Extrasolar Planet, *ApJ*, **626**, 523.

CINCOTTA P.M., MENDEZ M. & NUNEZ J.A., 1995, Astronomical Time Series Analysis. I. A Search for Periodicity Using Information Entropy, *ApJ*, **449**, 231.

CLARET A., 1998, Very low mass stars: non-linearity of the limb-darkening laws, *A&A*, **335**, 647.

CLARET A., 2000, new non-linear limb-darkening law for LTE stellar atmosphere models. Calculations for –5.0 <= log[M/H] <= +1, 2000 K <= T_{eff} <= 50000 K at several surface gravities, *A&A*, **363**, 1081.

Carlsberg Meridian Catalogs (CMC) Number 1-11, Copenhagen University Obs., Royal Greenwich Obs., and Real Instituto y Observatorio de la Armada en San Fernando, 1999.

COCHRAN W.D. & HATZES A.P., 1990, The McDonald Observatory Planetary Search, *BAAS*, **22**, 1082.

COCHRAN W.D., ENDL M., McARTHUR B., PAULSON D.B., SMITH V.V., MacQUEEN P.J., TULL R.G., GOOD J., BOOTH J., SHETRONE M., ROMAN B., ODEWAHN S., DEGLMAN F., GRAVER M., SOUKUP M. & VILLARREAL M. L. Jr., 2004, The First Hobby-Eberly Telescope Planet: A Companion To HD 37605, *ApJ*, **611**, L133

COX A.N., 2000, Allen's astrophysical quantities, 4th ed., ed. A.N. COX, Springer (New York)

CUYPERS J., 1987, New observations and frequency analysis of the Beta Cephei star Tau1 LUPI, *A&AS*, **69**, 445.

CUTRI R.M., SKRUTSKIE M.F., VAN DYK S., BEICHMAN C.A., CARPENTER J.M., CHESTER T., CAMBRESY L., EVANS T., FOWLER J., GIZIS J., HOWARD E., HUCHRA J., JARRETT T., KOPAN E.L., KIRKPATRICK J.D., LIGHT R.M, MARSH K.A., McCALLON H., SCHNEIDER S., STIENING R., SYKES M., WEINBERG M., WHEATON W.A., WHEELOCK S., ZACARIAS N., 2003, The 2MASS All-Sky Catalog of Point Sources.

SA SILVA R., UDRY S., BOUCHY F., MAYOR M., MOUTOU C., PONT F., QUELOZ D., SANTOS N.C., SEGRANSAN D. & ZUCKER S., 2006, ELODIE metallicity-biased search for transiting Hot Jupiters I. Two Hot Jupiters orbiting the slightly evolved stars HD 118203 and HD 149143, *A&A*, **446**, 717.

DEEG H.J., DOYLE L.R., KOZHEVNIKOV V.P., MARTIN E.L., OETIKER B., PAPAIOLOGOU E., SCHNEIDER J., AFONSO C., DUNHAM E.W., JENKINS J.M., NINKOV Z., STONE R.P.S. & ZAKHAROVA P.E., 1998, Near-term detectability of terrestrial extrasolar planets: TEP network observations of CM Draconis, *A&A*, **338**, 479.

DEEG H.J., DOYLE L.R., KOZHEVNIKOV V.P., BLUE J.E., MARTIN E.L. & SCHNEIDER J., 2000, A search for Jovian-mass planets around CM Draconis using eclipse minima timing, *A&A*, **358**, 5.

DEEG H. J. & HORNE K., 2002, Eddington's planet finding capabilities, In: *Proceedings of the First Eddington Workshop on Stellar Structure and Habitable Planet Finding*, editor: B. Battrick, Scientific editors: F. Favata, I. W. Roxburgh & D. Galadi, **ESA SP-485**, 123.

DEEG H.J., ALONSO R., BELMONTE J.A., ALSUBAI K., HORNE K. & DOYLE L., 2004, PASS: An All Sky Survey for the Detection of Transiting Extrasolar Planets and for Permanent Variable Star Tracking, *PASP*, **116**, 986.

DEFAŸ C., DELEUIL M. & BARGE P., 2001, A Bayesian method for the detection of planetary transits, *A&A*, **365**, 330.

DEMING D., BROWN T.M., CHARBONNEAU D., HARRINGTON J. & RICHARDSON L.J. & HARRINGTON J., 2005 a, A New Search for Carbon Monoxide Absorption in the Transmission Spectrum of the Extrasolar Planet HD 209458b, *ApJ*, **622**, 1149.

DEMING D., SEAGER S., RICHARDSON L.J. & HARRINGTON J., 2005 b, Infrared radiation from an extrasolar planet, *Nature*, **434**, 740.

DÍAZ-CORDOVÈS J., 1990, Ph.D. Thesis, Univ. Complutense, Madrid.

DOYLE L.R., DEEG H.J., KOZHEVNIKOV V.P., OETIKER B., MARTIN E.L., BLUE J.E., ROTTLER L., STONE R.P.S., NINKOV Z., JENKINS J.M., SCHNEIDER J., DUNHAM E.W., DOYLE M.F. & PAPEOLOGOU E., 2000, Observational Limits on Terrestrial-sized Inner Planets around the CM Draconis System Using the Photometric Transit Method with A Matched-Filter Algorithm, *AJ*, **535**, 338.

DRAKE A., 2003, On the selection of photometric planetary transits, *ApJ.*, **589**, 1020.

DUNHAM E.W., MANDUSHEV G.I., TAYLOR B.W. & OETIKER B., 2003, PSST: The Planet Search Survey Telescope, *PASP*, **116**, 1072.

EGRET D., DIDELON P., McLEAN B.J., RUSSELL J.L. & TURON C., 1992, Tycho Input Catalogue, Revised version, *A&A*, **258**, 217.

EYER L. & GRENON M., 1997, In: *Photometric Variability in the HR Diagram, Proceedings of the ESA Symposium 'Hipparcos-Venice '97'*, **ESA SP-403**, 467.

FISCHER D.A., LAUGHLIN G., BUTLER R.P., MARCY G.W., JOHNSON J.A., HENRY G. W., VALENTI J.A., VOGT S.S., AMMONS M., ROBINSON S., SPEAR G., STRADER J., DRISCOLL P., FULLER A., JOHNSON T., MANRAO E., McCARTHY C., MUÑOZ M., TAH K.L., WRIGHT J.T., IDA S., SATO B., TOYOTA E. & MINITTI D. 2005, The N2K Consortium. II. A Hot Saturn Planet Orbiting HD 88133, *ApJ*, **620**, 481.

GAUDI B.S., BURKE C.J., DE POY D.L., MARSHALL J.L.& POGGE R.W., 2002, Survey for Transiting Extrasolar Planets in Stellar Systems (STEPSS), *Bulletin of the American Astronomical Society*, **34**, 1264

GRAY D.F., 1992, The Observations and Analysis of Stellar Photospheres, 2nd ed., Cambridge University Press, 417

GRENON M., 1993, Low-level stellar variability, In: *Proceedings of the 137th IAU Colloquium*, 693

GUILLOT T. & SHOWMAB A.P., 2002, Evolution of "51 Pegasus b-like" planets, *A&A*, **385**, 156.

GUIS V. & BARGE P., 2005, An Image-Processing Method to Detect Planetary Transits: The 'Gauging' Filter, *PASP*, **117**, 160.

HATZES A.P., COCHRAN W.D., McARTHUR B., BALIUNAS S.L., WALKER G.A.H., CAMPBELL B. IRWIN A.W., YANG S., KÜRSTER M., ENDL M., ELS S., BUTLER R.P. & MARCY G.W., 2000, Evidence for a Long-Period Planet Orbiting ε Eridani, *ApJ*, **544**, L145.

HATZES A.P., GUENTHER E.W., ENDL M., COCHRAN W.D., DÖLLINGER M.P. & BEDALOV A., 2005, A giant planet around the massive giant star HD 13189, *A&A*, **437**, 743.

HENRY G.W., MARCY G., BUTLER R.P. & VOGT S.S., 1999, HD 209458, *IAU Circ.*, **7307**, 1**.**

HIDAS M.G., WEBB J.K., ASHLEY M.C.B. & LINEWEAVER C.H., 2003, An Automated Search for Extrasolar Planet, In: *Scientific Frontiers in Research on Extrasolar Planets, ed. D. Deming and S. Seager, ASP Conference Series***., 294**, 383**.**

HOG E., FABRICIUS C., MAKAROV V.V., URBAN S., CORBIN T., WYCOFF G., BASTIAN U., SCHWEKENDIEK P. & WICENEC A., 2000, The Tycho-2 Catalogue of the 2.5 million brightest stars, *A&A*, **355**, L37**.**

HONEYCUTT R.K., 1992, CCD ensemble photometry on an inhomogeneous set of exposures, *PASP*, **104**, 435**.**

HORNE K., 2003, Status and Prospects of Planetary Transit Searches: Hot Jupiter Galore, In: *Scientific Frontiers in Research on Extrasolar Planets, ed. D. Deming and S. Seager, ASP Conference Series***., 294**, 361**.**

HOWELL S.B., WARNOCK A. & MITCHELL K.J., 1988, Statistical error analysis in CCD time-resolved photometry with applications to variable stars and quasars, *AJ*, **95**, 247.

HOWELL S.B. & EVERETT M.E., 2001, Ultra-High Precision CCD Photometry, *Third Workshop on Photometry* , 1.

INFANTE L., 1987, A faint object processing software – Description and testing, *A&A*, **183**, 177.

JENKINS J.M., DOYLE L.R. & CULLERS D.K., 1996, A Matched Filter Method for Ground-Based Sub-Noise Detection of Terrestrial Extrasolar Planets in Eclipsing Binaries: Application to CM Draconis, *Icarus*, **119**, 244.

JENKINS J.M., CHANDRASEKARAN H., CALDWELL D.A., BATALHA N.M., SILVA N., KOCH D.G. & GAUTIER T.N., 2005, Kepler Mission Moved: Forwarding Address RA=19h 22m 40s, Dec=+44° 30' 00'', *AAS DPS meeting*, **37**, 31.08.

KANE S.R., HORNE K., STREET R.A., PALLACCO D.L., JAMES D., TSAPRAS Y. & COLLIER CAMERON A., 2003, Recent Results from the Wide Angle Search for Planets (WASP) Prototype, In: *Scientific Frontiers in Research on Extrasolar Planets, ed. D. Deming and S. Seager, ASP Conference Series***., 294**, 387**.**

KAROFF C., RAUER H., ERIKSON A. & VOSS. H., 2006, Milli-Magnitude Time-Resolved Photometry with BEST, *Astrophysics of Variable Stars*, **349**, 261.

KAZAROVETS E.V. & DURLEVICH O.V. Editor-in-Chief Samus N.N., 1998, New Catalogue of Suspected Variable Stars. Supplement, Moscow.

KHARCHENKO N.V., 2001, All-sky Compiled Catalogue of 2.5 million stars (ASCC-2.5, 2nd version), *Kinematics and Physics of Celestial Bodies*, **17**, 409.

KOCH D. & BORUCKI W., 1996, A Search For Earth-Sized Planets in Habitable Zones Using Photometry, *First International Conf on Circumstellar Habitable Zones*, Travis House Pub., 229.

KONACKI M., TORRES G., JHA S. & SASSELOV D.D., 2003, A New Transiting Extrasolar Giant Planet, *Nature*, **421**, 507.

KONACKI M., TORRES G., SASSELOV D.D & JHA S., 2003, High resolution spectroscopic follow-up of OGLE planetary transit candidates in the Galactic bulge: two possible Jupiter-mass planets and two blends, *ApJ*, **597**, 1076.

KONACKI M., TORRES G., SASSELOV D.D., PIETRZYNSKI G., UDALSKI A., JHA S., RUIZ M.T., GIEREN W. & MINNITI, D., 2004, The transiting extrasolar giant planet around the star OGLE-TR-113, *ApJ Letters*, **609**, 37.

KONACKI M., TORRES G., SASSELOV D.D & A., JHA S., 2005, A transiting extrasolar giant planet around the star OGLE-TR-10, *ApJ*, **624,** 372.

KOVÁCS G., ZUCKER S. & MAZEH T., 2002, A box-fitting algorithm in the search for periodic transits, *A&A*, **391**, 369.

KRON R.G., 1980, Photometry of a complete sample of faint galaxies, *ApJS*, **43**, 305.

KRAUTTER J., SEDLMAYR E., SCHAIFERS K. & TRAVING G., 1994, *Meyers Handbuch Weltall*, 234.

KUKARKIN B.V., KHOLOPOV P.N., ARTIUKHIN N.M., FEDOROVICH V.P., FROLOV M.S., GORANSKIJ V.P., GORYNYA N.A., KARITSKAYA E.A., KIREEVA N.N., KUKARKINA N.P., KUROCHKIN N.E., MEDVEDEVA G.I., PEROVA N.B., PONOMAREVA G.A., SAMUS N.N., SHUGAROV S.Yu., 1982, New Catalogue of Suspected Variable Stars, Nauka, Moscow

KURUCZ R.L., 1998, LTE Models, *Highlights of Astronomy*, **11A**, 646.

LANZA, A.F., RODONÒ M., PAGANO I., BARGE P. & LLEBARIA A., 2003, Modelling the rotational modulation of the Sun as a star, *A&A*, **403**, 1135.

LASKER B.M., STURCH C., LOPEZ C., MALLAMA A.D., McLAUGHLIN S.F., RUSSELL J.L., WISNIEWSKI W.Z., GILLESPIE B.A., JENKNER H., SICILIANO E.D., KENNY D., BAUMERT J.H., GOLDBERG A.M., HENRY G.W., KEMPER E. & SIEGEL M.J. , Guide Star Photometric Catalog, Updated Version 1 (Lasker+ 1988, 1996), Vizier On-line Data Catalog II/143.

LUYTEN W.J., 1979, New Luyten Catalogue of stars with proper motions larger than two tenths of an arcsecond (NLTT), Minneapolis, University of Minnesota.

MADDOX S.J., EFSTATHIOU G. & SUTHERLAND W.J., 1990, The APM Galaxy Survey – Part Two – Photometric Corrections, *MNRAS*, **246**, 433.

MANDEL K. & AGOL E., 2002, Analytic Light Curves for Planetary Transit Searches, *ApJ*, **580**, L171 .

MARCY G.W. & BENITZ K.J., 1989, A search for substellar companions to low-mass stars, *ApJ*, **344**, 441.

MARCY G.W. & BUTLER R.P., 1996, A Planetary Companion to 70 Virginis, *ApJ*, **464**, L147.

MARCY G.W., BUTLER P.R., FISCHER D. & VOGT S., 2003, Properties of Extrasolar Planets, In: *Scientific Frontiers in Research on Extrasolar Planets, ed. D. Deming and S. Seager, ASP Conference Series*, **294**, 1.

MARCY G.W., BUTLER P.R., FISCHER D., VOGT S., WRIGHT J.T., TINNEY C.G. & JONES J.R.A., 2005, Observed Properties of Exoplanets: Masses, Orbits, and Metallicities, *Progress of Theoretical Physics Supplement*, **158**, 24.

MASON B.D., WYCOFF G. L., HARTKOPF W.I., DOUGLASS G.G. & WORLEY C.E., The 2001 US Naval Observatory Double Star CD-ROM. I. The Washington Double Star Catalog, *AJ*, **122**, 3466.

MAYOR M., DUQUENNOY A., HALBWACHS J.-L. & MERMILLIOD J.-C., 1992, CORAVEL Surveys to Study Binaries of Different Masses and Ages, In: *Complementary Approaches to Double and Multiple Star Research, ASP Conference Series*, **32**, 73.

MAYOR M. & QUELOZ D., 1995, A Jupiter-Mass Companion to a Solar-Type Star, *Nature*, **378**, 355.

MAZEH T., NAEF D., TORRES G., LATHAM D.W., MAYOR M., BEUZIT J.-L., BROWN T.M., BUCHHAVE L., BURNET M., CARNEY B. W., CHARBONNEAU D., DRUKIER G.A., LAIRD J.B., PEPE F., PERRIER C., QUELOZ D., SANTOS N.C., SIVAN J.-P., UDRY S. & ZUCKER S., 2000, The Spectroscopic Orbit of Planetary Companion Transiting HD 209458, *ApJ*, **532**, L55**.**

MAZEH T., ZUCKER S. & PONT F., 2005, An intriguing correlation between the masses and periods of the transiting planets, *MNRAS*, **356**, 955.

McMILLAN R.S., SMITH P.H., FRECKER J.E., MERLINE W.J. & PERRY M.L., 1986, A Longterm Radial Velocity Program of High Accuracy with a Small Telescope, In: *Proceedings of the 118th Symposium of the International Astronomical Union*, **118**, 459.

MOCHEJSKA B.J., STANEK K.Z., SASSELOV D.D. & SZENTGYORGYI A.H., 2002, Discovery of 47 Low-amplitude Variables in the Metal-Rich Cluster NGC 6791 with Millimagnitude Image subtraction Photometry, *AJ*, **123**, 346.

MONET D., BIRD A., CANZIAN B., DAHN C., GUETTER H., HARRIS H., HENDEN A., LEVINE S., LUGINBUHL C., MONET A.K.B., RHODES A., RIEPE B., SELL S., STONE R., VRBA F., WALKER R., 1998, USNO-A V2.0, A Catalog of Astrometric Standards, U.S. Naval Observatory Flagstaff Station (USNOFS) and Universities Space Research Association (USRA) stationed at USNOFS.

MONET D.G., LEVINE S.E., CANZIAN B., ABLES H.D., BIRD A.R., DAHN C.C., GUETTER H.H., HARRIS H.C., HENDEN A.A., LEGGETT S.K., LEVISON H.F., LUGINBUHL C.B., MARTINI J., MONET A.K.B., MUNN J.A., PIER J.A., RHODES A.R., RIEPE B., SELL S., STONE R.C., VRBA F.J., WALKER R.L., WESTERHOUT G., BRUCATO R.J., REID I.N., SCHOENING W., HARTLEY M., READ M.A. & TRITTON S.B., 2003, The USNO-B Catalog, *AJ*, **125**, 984

MONTENBRUCK O. & PFLEGER T.**,** 1994, Astronomie mit dem Personal Computer, Springer-Verlag Berlin Heidelberg New York.

MONTES D., RAMSEY L.W. & WELTY A.D., 1999, Library of Medium-Resolution Fiber Optic Echelle Spectra of F, G, K, and M Field Dwarfs to Giant Stars, *ApJS*, **123**, 283.

MOUTOU C., COUSTENIS A., SCHNEIDER J., ST.GILLES R., MAYOR M., QUELOZ D. & KAUFER A., 2001, Search for spectroscopical signatures of Transiting HD 209458b's exosphere, *A&A*, **371**, 260.

MOUTOU C., PONT F., BOUCHY F. & MAYOR M., 2004, Accurate radius and mass of the transiting exoplanet OGLE-TR-132b, *A&A*, **424**, L31.

MOUTOU C., PONT F., BARGE P., AIGRAIN S., AUVERGNE M., BLOUIN D., CAUTAIN R., ERIKSON A.R., GUIS V., GUTERMAN P., IRVIN M., LANZA A.F., QUELOZ D., RAUER H., VOSS H. & ZUCKER S., 2005, Comparative blind test of five planetary transit detection algorithms on realistic synthetic light curves, *A&A*, **437**, 355.

NARITA N., SUTO Y., WINN J.N., TURNER E.L., AOKI W., LEIGH C.J., SATO B., TAMURA M. & YAMADA T., 2005, Subaru HDS Transmission Spectroscopy of the Transiting Extrasolar Planet HD 209458b, *PASJ*, **57**, 471.

NEWBERRY M.V., 1991, Signal-to-Noise Considerations for Sky-Subtracted CCD Data, *PASP*, **103**, 122

PÄTZOLD M. & RAUER H., 2002, Where are the Massive Close-In Extrasolar Planets?, *ApJ*, **568**, 117.

PEPPER J., GOULD A.& DEPOY D.L., 2003, Using All-Sky Surveys to find planetary transits, *Acta Astronomica*, **53**, 213.

PEPPER J., GOULD A.& DEPOY D.L., 2004, KELT: The Kilodegree Extremely Little Telescope, In: *AIP Conference Proceedings: The Search for OtherWorlds, eds. S. S. Holt & D. Deming*, **713**, 185.

PONT F., BOUCHY F., QUELOZ D., SANTOS N. C., MELO C. H. F., MAYOR M. & UDRY S., The "missing link": a 4-day period transiting exoplanet around OGLE-TR-111, *A&A*, **426**, L15.

PONT F., 2005, Photometric searches for transiting planets: results and challenges, astro-ph/0510846.

PONT F., MELO C. H. F., BOUCHY F., UDRY S., QUELOZ D, MAYOR M. & SANTOS N. C., 2005, A planet-sized transiting star around OGLE-TR-122. Accurate mass and radius near the hydrogen-burning limit, *A&A*, **433**, 21.

RACKHAM T.W., Astronomical photography at the telescope, 1972, London, Faber.

RAUER H. & Voß H., 2002, Die Transit-Methode zur Suche nach extrasolaren Planeten, *SuW*, **2**, 32.

RAUER H., EISLOEFFEL J., ERIKSON A., GUENTHER E., HATZES A.P., MICHAELIS H. & VOSS H., 2004 a, The Berlin Exoplanet Search Telescope System, *PASP*, **116**, 38.

RAUER H., VOSS H., ERIKSON A., HATZES A.P., EISLOEFFEL J. & GUENTHER E., 2004 b, Recent results from the Berlin Exoplanet Search Telescope, In: Second Eddington Workshop: Stellar structure and habitable planet finding, 9 - 11 April 06 2003, Palermo, Italy. Edited by F. Favata, S. Aigrain and A. Wilson., **ESA SP-538**, 201 – 203.

RAUER H., ERIKSON A., VOSS H., TITZ R., HATZES A.P., EISLOEFFEL J. & GUENTHER E., 2004 c, New results from BEST: the search for Planetary transits, *Astron. Nachr*., **325**, 574.

RIVERA E.J., LISSAUER J.J., BUTLER R.P., MARCY G.W., VOGT S.S., FISCHER D.A., BROWN T.M. & LAUGHLIN G., 2005, A ~7.5 Earth-Mass Planet Orbiting the Nearby Star GJ 876, *ApJ*, submitted.

ROBIN A.C., REYLÉ C., DERRIÉRE S. & PICAUD S., 2004, A synthetic view on the structure and evolution of the Milky Way, *A&A*, **409**, 523.

ROSENBLATT F., 1971, A Two-Color Photometric Method for Detection of Extra solar Planetary Systems, *Icarus*, **14**, 71.

SALIM S. & GOULD A., 2003, Improved astrometry and photometry for the Luyten catalog. II. Faint stars and the revised catalog, *AJ*, **582**, 1011.

SANTOS N., ISRAELIAN G., MAYOR M., REBOLO R. & UDRY S., 2003, Statistical properties of exoplanets II. Metallicity, orbital parameters, and space velocities, *A&A*, **398**, 363

SANTOS N., ISRAELIAN G. & MAYOR M. , 2004, Spectroscopic [Fe/H] for 98 extra-solar planet-host stars: Exploring the probability of planet formation, *A&A*, **415**, 1153.

SATO B., FISCHER D.A., HENRY G. W., LAUGHLIN G., BUTLER R.P., MARCY G.W., VOGT S.S., BODENHEIMER P., IDA S., TOYOTA E., WOLF A., VALENTI J.A., BOYD L.J., JOHNSON J.A., WRIGHT J.T., AMMONS M., ROBINSON S., STRADER J., McCARTHY C., TAH K.L. & MINITTI D. 2005, The N2K Consortium. II. A Transiting Hot Saturn Around HD 149026 With a Large Dense Core, *ApJ*, **633**, 465.

SIRKO, E. & PACZYNSKI B., 2003, Ellipsoidal Variability in the OGLE Planetary Transit Candidates, *AJ*, **592**, 1217.

STRUVE O., 1952, Proposal for a project of high-precision stellar radial velocity work, *The Observatory*, **72**, 199.

STREET R.A., PALLACCO D.L., FITZSIMMONS A., KEENAN F.P., HORNE K., KANE S.R., COLLIER CAMERON A, LISTER, T.A., HASWELL C.A., NORTON A.J., JONES B.W., SKILLEN I., HODGKIN P., WHEATLEY P., WEST R. & BRETT D., 2003, SuperWASP: Wide Angle Search for Planets, In: *Scientific Frontiers in Research on Extrasolar Planets, ed. D. Deming and S. Seager, ASP Conference Series*, **294**, 405.

TAMUZ O., MAZEH T. & ZUCKER S., 2005, Correcting systematic effects in a large set of photometric light curves, *MNRAS*, **356**, 1466.

THOMMES E.W. & LISSAUER J.J., 2005, Planet migration, In: Astrophysics of life. Proceedings of the Space Telescope Science Institute Symposium, edited by Mario Livio, I. Neill Reid, William B. Sparks. Vol. 16., 41.

TINGLEY B., 2003, Improvements to existing detection algorithms and their comparison, *A&A*, **408**, L5.

TOKUNAGA A.T., 2000, *Allen's Astrophysical Quantities*, 4th edition, ed. A.N. Cox, Springer-Verlag (New York), 143.

TORRES G., KONACKI M., SASSELOV D. & JHA S., 2004, New Data and Improved Parameters for the Transiting Planet OGLE-TR-56b, *ApJ.*, **609**, 1071.

TULL R.G., MacQUEEN P..J., SNEDEN C. & LAMBERT D.L., 1995, The high-resolution cross-dispersed echelle white-pupil spectrometer of the McDonald Observatory 2.7m telescope, *PASP*, **107**, 251.

TULL R.G., MacQUEEN P..J., GOOD J., EPPS H.W. & the HET HRS Team, 1998, High Resolution Spectrograph for the Hobby-Eberly Telescope, *Bulletin of the American Astronomical Society*, **30**, 1263.

UDALSKI A., PACZYNSKI B., ZEBRUN K., SZYMANSKI M., KUBIAK M., SOSZYNSKI I., SZEWCZYK O., WYRZYKOWSKI L. & PIETRZYNSKI G., 2002 a, The Optical Gravitational Lensing Experiment. Search for Planetary and Low-Luminosity Object Transits in the Galactic Disk. Results of 2001 Campaign, *Acta Astron.*, **52**, 1.

UDALSKI A., ZEBRUN K., PIETRZYNSKI G., SZYMANSKI M., KUBIAK M., SOSZYNSKI I. & WYRZYKOWSKI L., 2002 b, The Optical Gravitational Lensing Experiment. Search for Planetary and Low-Luminosity Object Transits in the Galactic Disk. Results of 2001 Campaign – Supplement, *Acta Astron.*, **52**, 115.

UDALSKI A., ZEBRUN K., SZYMANSKI M., KUBIAK M., SOSZYNSKI I., SZEWCZYK O., WYRZYKOWSKI L.& PIETRZYNSKI G., 2002 c, The Optical Gravitational Lensing Experiment. Planetary and Low-Luminosity Object Transits in the Carina Fields of the Galactic Disk, *Acta Astron.*, **52**, 317.

UDALSKI A., PIETRZYNSKI G., SZYMANSKI M., KUBIAK M., ZEBRUN K., SOSZYNSKI I., SZEWCZYK O. & WYRZYKOWSKI L., 2003, The Optical Gravitational Lensing Experiment. Additional Planetary and Low-Luminosity Object Transits from the OGLE 2001 and 2002 Observational Campaigns, *Acta Astron.*, **53**, 133.

UDALSKI A., SZYMANSKI M., KUBIAK M., PIETRZYNSKI G., SOSZYNSKI I., ZEBRUN K., SZEWCZYK O. & WYRZYKOWSKI L., 2004, The Optical Gravitational Lensing Experiment. Planetary and Low-Luminosity Object Transits in the Fields of Galactic Disk. Results of the 2003 OGLE Observing Campaigns, *Acta Astron.*, **54**, 313.

URBAN S.E., CORBIN T.E. & WYCOFF G.L., 1997, The ACT Reference Catalog, *AAS*, **191**, 5707

URBAN S.E., CORBIN T.E., WYCOFF G.L., HOEG E., FABRICIUS C. & MAKAROV V.V., 2001, AC 2000.2: The Astrographic Catalogue on the Hipparcos System, *AJ*, **115**, 1212

URBAN S.E., ZACHARIAS N. & WYCOFF G.L., 2004, The UCAC2 Bright Star Supplement, VizieR On-line Data Catalog: I/294.

VANZI L., HAINAUT O.R., 2003, Sky Background at ESO - La Silla in the Visible and Near IR, In: Light Pollution: The Global View. Edited by H.E. Schwarz, Cerro Tololo Inter-American Observatory, NOAO, La Serena, Chile. Astrophysics and Space Science Library, **284**, 181.

VIDAL-MADJAR A., LECAVELIER DES ETANGS A., DÉSERT J.-M., BALLESTER G.E., FERLET R., HÉBRARD G. & MAYOR M., 2003, An extended upper atmosphere around the extrasolar planet HD 209458b, *Nature*, **422**, 143.

VIDAL-MADJAR A., DÉSERT J.-M., LECAVELIER DES ETANGS A., HÉBRARD G., BALLESTER G.E., EHRENREICH D., FERLET R., McCONNELL J.C., MAYOR M. & PARKINSON C.D., 2004, Detection of Oxygen and Carbon in the Hydrodynamically Escaping Atmosphere of the Extrasolar Planet HD 209458b, *ApJ*, **604**, 69.

VOGES W., ASCHENBACH B., BOLLER T., BRAUNIGER H., BRIEL U., BURKERT W., DENNERL K., ENGLHAUSER J., GRUBER R., HABERL F., HARTNER G., HASINGER G., PFEFFERMANN E., PIETSCH W., PREDEHL P., SCHMITT J., TRUMPER J. & ZIMMERMANN U., 2000, ROSAT All-Sky Survey Faint Source Catalogue (RASS-FSC), *IAU Circ*., 7432.

WOLSZCZAN A. & FRAIL D.A., 2002, A planetary system around the millisecond pulsar PSR1257 +12, *Nature*, **355**, 145.

WUCHTERL G., GUILLOT T. & LISSAUER J.J, 2000, Giant Planet Formation, In: Protostars and Planets IV, eds Mannings, V., Boss, A.P., Russell, S. S., 1081.

YOUNG A.T., 1967, Photometric error analysis: VI. Confirmation of Reiger's theory of scintillation, *AJ*., **72**, 747.

YOUNG A.T., 1993, Scintillation noise in CCD photometry, *The Observatory*, **113**, 41.

ZACHARIAS N., URBAN S.E., ZACHARIAS M.I., WYCOFF G.L., HALL D.M., GERMAIN M.E., HOLDENRIED E.R. & WINTER L., The Second U.S. Naval Observatory CCD Astrograph Catalog (UCAC2), *AJ* **127**, 3043.

ZHANG X.-B., DENG L.-C., XIN Y. & ZHOU X., 2003, Searching for Variable Stars in the Field of NGC 7789, *ChJAA*, **3**, 151.

Used physical constants and identities

$G = 6.684 \cdot 10^{-11} m^3 kg^{-1} s^{-2}$

1 A.U. $= 1.49597870 \cdot 10^{11} m$

$1 M_{Jup} = 1.8988 \cdot 10^{27} kg = 9.5465 \cdot 10^{-4} M_{Sun} = 317.826 M_{Earth}$

$1 R_{Jup} = 6.98985 \cdot 10^{7} m = 1.0039 \cdot 10^{-1} R_{Sun} = 10.97134 R_{Earth}$

1 parsec $= 3.08567758130573 \cdot 10^{16} m$

Acknowledgement

It was a long way to go until this thesis was finished. Sometimes the long ways are the more interesting and important ones. Hopefully this is true for this way, too.

Many people were helping me on this way and therefore I have to be very thankful. First I want to thank Prof. Heike Rauer for giving me the chance to work in this new and challenging scientific field of research on extrasolar planets at the Institute for Planetary Research at the Deutsches Zentrum für Luft- und Raumfahrt (DLR) and attending the dissertation. As a mentor she has patiently given as much as support as possible for my thesis work.

I would like to thank Prof. Erwin Sedlmayr of the Zentrum für Astronomie und Astrophysik, TU Berlin for the second report on my thesis and his recommendation for getting a chance to work in this field. I appreciate the presidency of the promotion committee to Prof. Dr. Eichler.

The work with the Berlin Exoplanet Search Telescope (BEST) has been made possible by several people. The project was initialized by Prof. Heike Rauer and technically supported by Dr. Harald Michaelis. My thanks go to Anders Erikson for his help setting-up the BEST system and giving an introduction into photometric observations. His participation in the observations from TLS had made this work possible. Many thanks for additional BEST observations go to Michael Weiler, Joern Helbert, Christoph Goldmann, Florian Nehonsky and Andy Chwatal.

I would like to thank all the collaboration partners at the observational site Thüringer Landessternwarte (TLS) Tautenburg. I would like to express my thanks for the director of the observatory Prof. Artie Hatzes for giving me the chance to finish my thesis work at the TLS during setting-up the new transit search system TEST. I have to thank Prof. Hatzes, Jochen Eislöffel, Eike Guenther and Alexander Scholz for their collaboration and follow-up observations. Special thanks go for the technical staff for the help maintaining and improving the BEST system. Furthermore I would like to thank to night assistants of the TLS observatory for sharing many interesting night hours with me during the observations.

Additionally Michael Endl has performed spectroscopic follow-up observations with the Hobby-Eberly telescope and the Harlan-J.-Smith telescope at the McDonald Observatory. Photometric follow-up observations were performed by Ola Karlsson and Pär Nilsson with the Swedish Westerlund telescope led by Prof. Lagerkvist.

My thanks go to Anders Erikson and Ruth Titz for reading carefully the script and giving valuable comments helping to bring my chaotic thoughts into a more structured way. Special thanks go to Lee Grenfell for improving my German English to an acceptable level for a native speaker.

Ein besonderer Dank sei meinen Eltern, meiner Schwester und den anderen Verwandten für das Verständnis und Unterstützung meiner nicht zu irdischen Leidenschaften gewidmet. Ich weiß es war nicht immer einfach mit mir.

Ich danke meinen wenigen, doch dafür guten Freunden (Ihr wisst wer ihr seid), welche mich durch die verschiedensten Lebensabschnitte begleitet haben. Ihr habt mit Eurer Unterstützung in den verschiedensten Formen (von Gesprächen, Briefen, e-mails (thanks Bea) bis hin zur Musik (danke Eugen und Rotorfon)) mir viel Kraft gegeben. Ich hoffe, dass ich auch etwas zurückgeben konnte. Danke Euch allen. Mögen auch alle Eure Träume in Erfüllung gehen. Herzlichen Dank, many thanks, muchas gracias.

Zuguterletzt bedanke ich mich bei meiner Frau Tamara. Ohne ihre unglaubliche Unterstützung, ihr Verständnis und ihre Liebe hätte ich es nie bis zu diesem Punkt gebracht. Nur mit ihrer Hilfe war es möglich den langen und nicht immer einfachen Weg auf dem Gebiet der Weltraumwissenschaften zu gehen und damit meinen Träumen zu folgen.